

Advances in Science, Technology & Innovation
IEREK Interdisciplinary Series for Sustainable Development

Attila Çiner · Stefano Naitza · Ahmed E. Radwan · Zakaria Hamimi ·
Federico Lucci · Jasper Knight · Ciro Cucciniello · Santanu Banerjee ·
Hasnaa Chennaoui · Domenico M. Doronzo · Carla Candeias ·
Jesús Rodrigo-Comino · Roohollah Kalatehjari · Afroz Ahmad Shah ·
Matteo Gentilucci · Dionysia Panagoulia · Helder I. Chaminé ·
Maurizio Barbieri · Zeynal Abiddin Ergüler *Editors*

Recent Research on Sedimentology, Stratigraphy, Paleontology, Geochemistry, Volcanology, Tectonics, and Petroleum Geology

Proceedings of the 2nd MedGU, Marrakesh 2022
(Volume 2)

Advances in Science, Technology & Innovation

IEREK Interdisciplinary Series for Sustainable Development

Editorial Board

Anna Laura Pisello, Department of Engineering, University of Perugia, Italy

Dean Hawkes, University of Cambridge, Cambridge, UK

Hocine Bougdah, University for the Creative Arts, Farnham, UK

Federica Rosso, Sapienza University of Rome, Rome, Italy

Hassan Abdalla, University of East London, London, UK

Sofia-Natalia Boemi, Aristotle University of Thessaloniki, Greece

Nabil Mohareb, Faculty of Architecture—Design and Built Environment,
Beirut Arab University, Beirut, Lebanon

Saleh Mesbah Elkaffas, Arab Academy for Science, Technology and Maritime Transport,
Cairo, Egypt

Emmanuel Bozonnet, University of La Rochelle, La Rochelle, France

Gloria Pignatta, University of Perugia, Italy

Yasser Mahgoub, Qatar University, Qatar

Luciano De Bonis, University of Molise, Italy

Stella Kostopoulou, Regional and Tourism Development, University of Thessaloniki,
Thessaloniki, Greece

Biswajeet Pradhan, Faculty of Engineering and IT, University of Technology Sydney,
Sydney, Australia

Md. Abdul Mannan, Universiti Malaysia Sarawak, Malaysia

Chaham Alalouch, Sultan Qaboos University, Muscat, Oman

Iman O. Gawad, Helwan University, Helwan, Egypt

Anand Nayyar , Graduate School, Duy Tan University, Da Nang, Vietnam

Series Editor

Mourad Amer, International Experts for Research Enrichment and Knowledge Exchange
(IEREK), Cairo, Egypt

Advances in Science, Technology & Innovation (ASTI) is a series of peer-reviewed books based on important emerging research that redefines the current disciplinary boundaries in science, technology and innovation (STI) in order to develop integrated concepts for sustainable development. It not only discusses the progress made towards securing more resources, allocating smarter solutions, and rebalancing the relationship between nature and people, but also provides in-depth insights from comprehensive research that addresses the **17 sustainable development goals (SDGs)** as set out by the UN for 2030.

The series draws on the best research papers from various IEREK and other international conferences to promote the creation and development of viable solutions for a **sustainable future and a positive societal** transformation with the help of integrated and innovative science-based approaches. Including interdisciplinary contributions, it presents innovative approaches and highlights how they can best support both economic and sustainable development, through better use of data, more effective institutions, and global, local and individual action, for the welfare of all societies.

The series particularly features conceptual and empirical contributions from various interrelated fields of science, technology and innovation, with an emphasis on digital transformation, that focus on providing practical solutions to **ensure food, water and energy security to achieve the SDGs**. It also presents new case studies offering concrete examples of how to resolve sustainable urbanization and environmental issues in different regions of the world.

The series is intended for professionals in research and teaching, consultancies and industry, and government and international organizations. Published in collaboration with IEREK, the Springer ASTI series will acquaint readers with essential new studies in STI for sustainable development.

ASTI series has now been accepted for Scopus (September 2020). All content published in this series will start appearing on the Scopus site in early 2021.

Attila Çiner · Stefano Naitza ·
Ahmed E. Radwan · Zakaria Hamimi ·
Federico Lucci · Jasper Knight ·
Ciro Cucciniello · Santanu Banerjee ·
Hasnaa Chennaoui · Domenico M. Doronzo ·
Carla Candeias · Jesús Rodrigo-Comino ·
Roohollah Kalatehjari · Afroz Ahmad Shah ·
Matteo Gentilucci · Dionysia Panagoulia ·
Helder I. Chaminé · Maurizio Barbieri ·
Zeynal Abiddin Ergüler
Editors

Recent Research on Sedimentology, Stratigraphy, Paleontology, Geochemistry, Volcanology, Tectonics, and Petroleum Geology

Proceedings of the 2nd MedGU, Marrakesh
2022 (Volume 2)

Editors

Attila Çiner
Eurasia Institute of Earth Sciences
Istanbul Technical University
Istanbul, Türkiye

Ahmed E. Radwan
Faculty of Geography and Geology
Institute of Geological Sciences
Jagiellonian University
Kraków, Poland

Federico Lucci
Dipartimento di Scienze della Terra e Geoambientali
Università degli Studi di Bari "Aldo Moro"
Bari, Italy

Ciro Cucciniello
Complesso Universitario Monte Sant'Angelo
Università di Napoli Federico II
Naples, Italy

Hasnaa Chennaoui
Department of Geology
Hassan II University of Casablanca
Casablanca, Morocco

Carla Candéias
GeoBioTec, Geosciences Department
University of Aveiro
Aveiro, Portugal

Roohollah Kalatehjari
Auckland University of Technology
Auckland, New Zealand

Matteo Gentilucci
Geology Division
School of Science and Technology
University of Camerino
Camerino, Italy

Helder I. Chaminé
Polytechnic of Porto
School of Engineering (ISEP)
Porto, Portugal

Zeynal Abiddin Ergüler
Kütahya Dumlupınar University
Kütahya, Türkiye

Stefano Naitza
Università degli Studi di Cagliari
Cagliari, Italy

Zakaria Hamimi 
Geology Department
Faculty of Science
Benha University
Benha, Egypt

Jasper Knight
University of the Witwatersrand
Johannesburg, South Africa

Santanu Banerjee
Indian Institute of Technology Bombay
Mumbai, India

Domenico M. Doronzo
Istituto Nazionale di Geofisica e Vulcanologia
Naples, Italy

Jesús Rodrigo-Comino
University of Granada
Granada, Spain

Afroz Ahmad Shah
Universiti of Brunei Darussalam
Gadong, Brunei Darussalam

Dionysia Panagoulia
National Technical University of Athens
Athens, Greece

Maurizio Barbieri
University of Rome La Sapienza
Rome, Italy

ISSN 2522-8714 ISSN 2522-8722 (electronic)
Advances in Science, Technology & Innovation
IEREK Interdisciplinary Series for Sustainable Development
ISBN 978-3-031-48757-6 ISBN 978-3-031-48758-3 (eBook)
<https://doi.org/10.1007/978-3-031-48758-3>

© The Editor(s) (if applicable) and The Author(s), under exclusive license to Springer
Nature Switzerland AG 2024

This work is subject to copyright. All rights are solely and exclusively licensed by the Publisher, whether the whole or part of the material is concerned, specifically the rights of translation, reprinting, reuse of illustrations, recitation, broadcasting, reproduction on microfilms or in any other physical way, and transmission or information storage and retrieval, electronic adaptation, computer software, or by similar or dissimilar methodology now known or hereafter developed.

The use of general descriptive names, registered names, trademarks, service marks, etc. in this publication does not imply, even in the absence of a specific statement, that such names are exempt from the relevant protective laws and regulations and therefore free for general use.

The publisher, the authors, and the editors are safe to assume that the advice and information in this book are believed to be true and accurate at the date of publication. Neither the publisher nor the authors or the editors give a warranty, expressed or implied, with respect to the material contained herein or for any errors or omissions that may have been made. The publisher remains neutral with regard to jurisdictional claims in published maps and institutional affiliations.

This Springer imprint is published by the registered company Springer Nature Switzerland AG
The registered company address is: Gewerbestrasse 11, 6330 Cham, Switzerland

Paper in this product is recyclable.

About the Conference

About MedGU



Steps Toward the Creation of a Mediterranean Geosciences Union (MedGU)

Mediterranean Geosciences Union (MedGU) aims to create a unique federation that brings together and represents the Mediterranean geoscience community specializing in the areas of Earth, planetary, and space sciences.

MedGU will be structured along the lines of American Geophysical Union (AGU) and European Geosciences Union (EGU).

The plan is to establish a large organization for the Mediterranean region that is more influential than any one local geoscience society with the objective of fostering fundamental geoscience research, as well as applied research that addresses key societal and environmental challenges.

MedGU's overarching vision is to contribute to the realization of a sustainable future for humanity and for the planet.

The creation of this union will give the Earth sciences more influence in policy-making and in the implementation of solutions to preserve the natural environment and to create more sustainable societies for the people living in the Mediterranean region. It is hoped that the union will also provide opportunities to Mediterranean geoscientists to undertake interdisciplinary collaborative research. MedGU plans to recognize the work of the most active geoscientists with a number of awards and medals.

Although MedGU has not yet been officially inaugurated, its first annual meeting was organized in November 2021 in Istanbul (MedGU-21). This has provided a forum to achieve a consensus for the formation of this non-profit international union of geoscientists. Membership will be open to individuals who have a professional engagement with the Earth, planetary, and space sciences and related studies, including students and retired seniors.

Nabil Khélifi (MedGU Founder, Germany) and Attila Çiner (MedGU Interim President, Turkey) in collaboration with Abdelaziz Mridekh (MedGU-22 Local Chair, Morocco) have taken an ambitious approach to the launch of the second MedGU Annual Meeting 2022 and hope to develop it in the near future into the largest international geoscience event in the Mediterranean and the broader MENA region. Its mission is to support geoscientists based in this region by establishing a Global Geoscience Congress.

It is expected that hundreds of participants from all over the world will attend this second MedGU Annual Meeting 2022, making it one of the largest and most prominent geosciences events in the region. So far, over 1300 abstracts have been submitted from 95 countries. The meeting's sessions will cover a wide range of topics with more details available on the conference tracks.

This second 2022 Annual Meeting will have a "hybrid" format, with both in-person and virtual participation. Springer, its official partner, will publish the proceedings in a book series (indexed in Scopus) as well as a number of special issues in diverse scientific journals (for more details, see Publications). The official journal of MedGU is *Mediterranean Geoscience Reviews* (Springer).

Conference Tracks

The scientific committee of the MedGU invites research papers on all cross-cutting themes of Earth sciences, with a main focus on the following 18 conference tracks:

- Track 1. Atmospheric Sciences, Meteorology, Climatology, Oceanography
- Track 2. Biogeochemistry, Geobiology, Geoecology, Geoagronomy
- Track 3. Earthquake Seismology and Geodesy
- Track 4. Environmental Earth Sciences
- Track 5. Applied and Theoretical Geophysics
- Track 6. Geo-Informatics and Remote Sensing
- Track 7. Geochemistry, Mineralogy, Petrology, Volcanology
- Track 8. Geological Engineering, Geotechnical Engineering
- Track 9. Geomorphology, Geography, Soil Science, Glaciology, Geoarchaeology, Geoheritage
- Track 10. Hydrology, Hydrogeology, Hydrochemistry
- Track 11. Marine Geosciences, Historical Geology, Paleoceanography, Paleoclimatology
- Track 12. Numerical and Analytical Methods in Mining Sciences and Geomechanics
- Track 13. Petroleum and Energy Sciences and Engineering
- Track 14. Sedimentology, Stratigraphy, Paleontology, Geochronology
- Track 15. Structural Geology, Tectonics and Geodynamics, Petroleum Geology
- Track 16. Special Session on Astrogeology, Impact Craters and Meteorites
- Track 17. Special Session on climate and sea-level change during the Cenomanian-Turonian Anoxic Event: Synthesis of sedimentological, micropaleontological and geochemical records
- Track 18. Special Session on hydrogeological and climatic risks, their management and the effect of climate change on groundwater quality.

About the Conference Steering Committee

General Committee

Honorary Chair



A. M. Celâl Sengör

Associate Editor, *Mediterranean Geosciences Reviews* (Springer)

Eurasia Institute of Earth Sciences, Istanbul Technical University Istanbul, Turkey

Conference Supervisor



Nabil Khélifi

Senior Publishing Editor

MedGU-22 Supervisor

Program Chair



Mustapha Meghraoui

Editorial Board Member, *Mediterranean Geosciences Reviews* (Springer)

Editor of *Arabian Journal of Geosciences* (Springer)

IPG Strasbourg, France

Publications Chair



Attila Çiner

MedGU (Interim) President

Founding Editor-in-Chief, *Mediterranean Geosciences Reviews* (Springer)

Chief Editor—Tracks 11 and 14, *Arabian Journal of Geosciences* (Springer)

Eurasia Institute of Earth Sciences, Istanbul Technical University, Turkey

Conference Manager



Mohamed Sahbi Moalla

Performer—The Leading Conference Organiser, Tunisia

Journal Coordinator, *Euro-Mediterranean Journal for Environmental Integration* (Springer)

ISET, University of Sfax, Tunisia

Conference Support



Mourad Amer

Founder and CEO of IEREK

Editor of ASTI Series (Springer/IEREK)

IEREK, Alexandria, Egypt

Local Committee

Chair



Abdelaziz Mridekh

Associate Editor, *Arabian Journal of Geosciences* (Springer)
University Ibn Tofail, Kenitra, Morocco

Coordinators



El Hassane Chellai

University Cadi Ayyad, Marrakech, Morocco



Bouabid El Mansouri

University Ibn Tofail, Kenitra, Morocco



Nouredine Laftouhi
University Cadi Ayyad, Marrakech, Morocco



Azzouz Kchikach
University Cadi Ayyad, Marrakech, Morocco



Jean-Louis Bodinier
Program Lead Geology and Sustainable Mining
Mohammed VI Polytechnic University

Members

Abdallah El Hmaidi, Moulay Ismail University, Meknes, Morocco
Abdelhadi El Ouali, Moulay Ismail University, Meknes, Morocco
Aicha Benmohammadi, Ibn Tofail University, Kenitra, Morocco
Ali Essahlaoui, Moulay Ismail University, Meknes, Morocco
Annis Moumen, National Applied School, Kenitra, Morocco
Atika Fahmi, Ibn Tofail University, Kenitra, Morocco
Driss El Azzab, Sidi Mohamed Ben Abdellah University, Fes, Morocco
Hassan Echarfaoui, Ibn Tofail University, Kenitra, Morocco
Jamal Chao, Ibn Tofail University, Kenitra, Morocco
Jaouad Dabounou, Hassan 1 University, Settat, Morocco
Malika Kili, Ibn Tofail University, Kenitra, Morocco
Mohamed Bouhaddioui, National School of Mine, Rabat, Morocco
Mohamed Jaffal, Cadi Ayyad University, Marrakech, Morocco
Mohammed Ouhcine, Ibn Tofail University, Kenitra, Morocco
Moulay Hachem Awragh, Moulay Ismail University, Meknes, Morocco
Mustapha Boualoul, Moulay Ismail University, Meknes, Morocco
Mustapha Boujemaoui, Moulay Ismail University, Meknes, Morocco
Nabil El Mouçaid, Central School of Engineering, Casablanca, Morocco
Souad Haida, Ibn Tofail University, Kenitra, Morocco
Abdullah Sukkar, Department of Geomatics Engineering, Istanbul Technical University, Istanbul, Turkey
Melek Rebai, Performer—The Leading Conference Organiser, Tunisia
M. Bassem Abdelhedi, Performer—The Leading Conference Organiser, Tunisia
Oumayma Abidi, Performer—The Leading Conference Organiser, Tunisia
Toka M. Amer, IEREK—International Experts for Research Enrichment and Knowledge Exchange, Egypt

Advisory Committee



Hans Thybo

President of International Lithosphere Program (ILP)

Editor-in-Chief of *Earth and Planetary Science Letters* (EPSL)

Professor at:

- Eurasia Institute of Earth Sciences, Istanbul Technical University, Turkey
- Center for Earth Evolution and Dynamics, University of Oslo, Norway



A. M. Celâl Sengör

Associate Editor, *Mediterranean Geosciences Reviews* (Springer)

Eurasia Institute of Earth Sciences, Istanbul Technical University Istanbul, Turkey



François Roure

Chief Editor—Track 15

Arabian Journal of Geosciences (Springer)

IFP—Energies Nouvelles, France



Giovanni Bertotti

Associate Editor, *Mediterranean Geosciences Reviews* (Springer)

Geoscience and Engineering, Delft University of Technology, The Netherlands

**Abdullah Al-Amri**

Founder and Editor-in-Chief

Arabian Journal of Geosciences (Springer)

King Saud University, Saudi Arabia

**Akiça Bahri**

Director for Africa at the International Water Management Institute (IWMI), Ghana (2005–2010)

Coordinator of the African Water Facility (AWF) at the African Development Bank (2010–2015)

Director of Research at the National Research Institute for Agricultural Engineering, Water, and Forestry (INRGREF), Tunisia (since 2016)

Professor at the National Agricultural Institute of Tunisia (INAT), Tunisia (since 2017)

Awardee of the International Water Association (IWA) Women in Water Prize (2018)

Associate Editor, *Euro-Mediterranean Journal for Environmental Integration* (Springer) (since 2019)

Minister of Agriculture, Water Resources and Fisheries in Tunisia (2019–2020)

Program Committee

Chair



Mustapha Meghraoui

Editorial Board Member, *Mediterranean Geosciences Reviews* (Springer)

Editor of *Arabian Journal of Geosciences* (Springer)

IPG Strasbourg, France

Members



Attila Çiner

MedGU (Interim) President

Founding Editor-in-Chief, *Mediterranean Geosciences Reviews* (Springer)

Chief Editor—Tracks 11 and 14, *Arabian Journal of Geosciences* (Springer)

Eurasia Institute of Earth Sciences, Istanbul Technical University, Turkey



Luc Bulot

North Africa Research Group
The University of Manchester, UK



Sami Khomsi

Georesources Lab, CERTE, University of Carthage, Tunis, Tunisia



Hasnaa Chennaoui Aoudjehane

Meteoritical Society Fellow
Laureate, “Prix Paul Doistau–Émile Blutet” from the French Academy of Sciences
Editor of *Arabian Journal of Geosciences* (Springer)
Professor, Hassan II University of Casablanca, Morocco



Catherine Kuzucuoglu

Associate Editor, *Mediterranean Geosciences Reviews* (Springer)

Research Director Emeritus

CNRS, Laboratoire de Géographie Physique

UMR 8591, Meudon, France



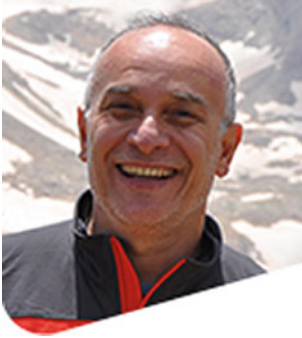
Elena Xoplaki

Chief Editor, *Euro-Mediterranean Journal for Environmental Integration* (Springer)

Justus-Liebig-University Giessen, Germany

Publications Committee

Chair



Attila Çiner

MedGU (Interim) President

Founding Editor-in-Chief, *Mediterranean Geosciences Reviews* (Springer)

Chief Editor—Tracks 11 and 14, *Arabian Journal of Geosciences* (Springer)

Eurasia Institute of Earth Sciences, Istanbul Technical University, Turkey

Members



Zeynal Abiddin Erguler

Chief Editor—Track 8

Arabian Journal of Geosciences (Springer)

Dumlupinar University, Kutahya, Turkey



Amjad Kallel

Chief Editor—Track 4

Arabian Journal of Geosciences (Springer)

Managing and Development Editor, *Euro-Mediterranean Journal for Environmental Integration* (Springer)

ENIS, University of Sfax, Tunisia



Mourad Bezzeghoud

School of Sciences and Technology (ECT)

Institut of Earth Sciences (IIFA)

University of Évora, Portugal



Hesham El-Askary

Professor of Remote Sensing and Earth Systems Science

Editor of *Arabian Journal of Geosciences* (Springer)

Director Computational and Data Sciences Graduate Programs

Center of Excellence in Earth Systems Modeling and Observations

Schmid College of Science and Technology, Chapman University, USA

**Zakaria Hamimi**

President of ArabGU

IAGETH VP for Africa and IAGETH National Chapter for Egypt

Editor of *Arabian Journal of Geosciences* (Springer)

Professor, Benha University, Benha, Egypt

**Syed E. Hasan, Ph.D.; RG; FGS**

Chair, Environmental Characterization and Remediation Technical Working Group, AEG

Department of Earth and Environmental Sciences

University of Missouri-Kansas City, USA

**François Roure**

Chief Editor—Track 15

Arabian Journal of Geosciences (Springer)

IFP—Energies Nouvelles, France



Anastasia Kiratzi

Professor of Seismology

Faculty of Sciences, Aristotle University of Thessaloniki, Greece



Broder Merkel

Chief Editor—Track 10

Arabian Journal of Geosciences (Springer)

Associate Editor of *Environmental Earth Science* (Springer)

Publisher of Freiberg Online Geoscience (FOG)

Institute of Geology, Technische Universität Bergakademie Freiberg, Germany

Preface

The proceedings of the 2nd Mediterranean Geosciences Union (MedGU-2) held in Marrakesh onsite and online in November 2022 consisted of four volumes titled:

Proceedings Volume 1: Recent Advancements from Aquifers to Skies in Hydrogeology, Geoecology, and Atmospheric Sciences

Proceedings Volume 2: Recent Research on Sedimentology, Stratigraphy, Paleontology, Geochemistry, Volcanology, Tectonics, and Petroleum Geology

Proceedings Volume 3: Recent Research on Geotechnical Engineering, Remote Sensing, Geophysics and Earthquake Seismology

Proceedings Volume 4: Recent Research on Environmental Earth Sciences, Geomorphology, Soil Science and Paleoenvironments

These volumes are based on the accepted conference papers for either oral/poster presentations or selected for online publication during the MedGU-2.

This second volume contains 76 papers related to (1) Sedimentology Stratigraphy and Paleontology, (2) Mineralogy and Petrology, (3) Geodynamics, Tectonics, Structural Geology, Petroleum Geology, (4) Geochemistry and Volcanology, and (5) Geoenergy Science and Engineering. The content of these research studies would provide new scientific knowledge to further understand recent advances in the above-mentioned fields. The proceedings of the MedGU-2 are of interest to all researchers, specialists, and students in all areas of geosciences.

Istanbul, Türkiye

Cagliari, Italy

Kraków, Poland

Benha, Egypt

Bari, Italy

Johannesburg, South Africa

Naples, Italy

Mumbai, India

Casablanca, Morocco

Naples, Italy

Aveiro, Portugal

Granada, Spain

Auckland, New Zealand

Gadong, Brunei Darussalam

Camerino, Italy

Athens, Greece

Porto, Portugal

Rome, Italy

Kütahya, Türkiye

June 2023

Attila Çiner

Stefano Naitza

Ahmed E. Radwan

Zakaria Hamimi

Federico Lucci

Jasper Knight

Ciro Cucciniello

Santanu Banerjee

Hasnaa Chennaoui

Domenico M. Doronzo

Carla Candeias

Jesús Rodrigo-Comino

Roohollah Kalatehjari

Afroz Ahmad Shah

Matteo Gentilucci

Dionysia Panagoulia

Helder I. Chaminé

Maurizio Barbieri

Zeynal Abiddin Ergüler

Contents

Sedimentology, Stratigraphy, Paleontology

- The Oldest Eocene Marine Vertebrate Fauna from the Sahara Desert in Southwestern Morocco** 3
Fadwa Aniny, Estelle Bourdon, Sylvain Adnet, Stephane Jouve, Hakima Zair, Philip D. Gingerich, Najia Elboudali, and Samir Zouhri
- Habitat Reconstruction of the Pleistocene Hippopotamidae from the Siwaliks of Pakistan Using Stable Isotopes** 7
Meera Sarwar, Muhammad Tahir Waseem, Mishal Afzal, Abdul Majid Khan, and Sania Zubaid
- Middle to Late Cambrian Marine Transgression Depositional System of the Peri-Gondwana Terranes: An Example from Al Bashair Formation of the Huqf Region, Oman** 11
Mohamed A. K. El-Ghali, Iftikhar Ahmed Abbasi, Olga Shelukhina, Mohamed S. H. Moustafa, Arshad Ali, Osman Salad Hersi, Mohamed Farfour, and Hezam Al-Awah
- Early to Middle Cambrian Fluvial-Aeolian Interplay and Marine Transgression Depositional System of the Peri-Gondwana Terranes: An Example from the Amin Formation of the Haushi-Huqf Region, Oman** 15
Mohamed A. K. El-Ghali, Iftikhar Ahmed Abbasi, Olga Shelukhina, Mohamed S. H. Moustafa, Arshad Ali, Osman Salad Hersi, Mohamed Farfour, and Hezam Al-Awah
- Lithofacies Associations and Depositional System of the Muti Formation, Oman Mountains** 19
Jenan Ahmed Attar, Iftikhar Ahmed Abbasi, Mohamed El-Ghali, Abdul Rahman Al- Harthi, and Abdulrazaq Al- Sayigh
- Middle Cambrian Marine Transgressive-Regressive Depositional System of the Peri-Gondwana Terranes: An Example from Miqrat Formation of the Haushi-Huqf Region, Oman** 23
Mohamed A. K. El-Ghali, Iftikhar Ahmed Abbasi, Olga Shelukhina, Mohamed S. H. Moustafa, Arshad Ali, Osman Salad Hersi, Mohamed Farfour, and Hezam Al-Awah
- Late Cambrian-Early Ordovician Hybrid-Energy Deltaic System of the Peri-Gondwana Terranes: An Example from the Barik Formation of the Haushi-Huqf Region, Oman** 27
Mohamed A. K. El-Ghali, Iftikhar Ahmed Abbasi, Olga Shelukhina, Mohamed S. H. Moustafa, Arshad Ali, Osman Salad Hersi, Mohamed Farfour, and Hezam Al-Awah

Genesis of Grain-Coating Clays and Their Effect on the Development of Feldspar Overgrowths: A Case Study of the Late Cambrian to Early Ordovician Barik Formation Sandstone Reservoir, Haushi-Huqf Region, Central Oman	31
Mohamed A. K. El-Ghali, Iftikhar Ahmed Abbasi, Olga Shelukhina, Mohamed S. H. Moustafa, Arshad Ali, Osman Salad Hersi, Shahad Al Mahrooqi, Khalid Al-Ramadan, Abdulwahab Muhammad Bello, Hezam Al-Awah, and Abdullah Alqubalee	
Was There a Massive Sediment Transport System from Northwestern Arabia to the Levant Basin During the Oligo-Miocene?	37
Yossi Mart	
Depositional Facies and Sea-Level Variation of the Cryogenian Glacial System: An Example from the Outcropping Fiq Formation, Abu Mahara Group, Jabal Akhdar Area, Northern Oman	43
Razan Y. Al Naabi, Mohamed A. K. El-Ghali, Mohamed S. H. Moustafa, and John Smweing	
Sedimentary and Stratigraphic Description of the Castellón B Borehole Cores (Offshore Western Mediterranean)	47
Telm Bover-Arnal, Carles Ferràndez-Cañadell, Julio Aguirre, Ulrich Heimhofer, and Mateu Esteban	
New Carbon-Isotope, Conodont, and Magnetostratigraphic Data from the Key Kulyumbe River Section (NW Siberia) and the Problem of Location of the Cambrian-Ordovician Boundary on the Siberian Platform	51
Vladimir Pavlov, Andrei Dronov, Tatiana Tolmacheva, Elizaveta Krasnova, and Alexander Larionov	
The Aptian Incised Valleys Recorded in the Maestrat Basin (E Iberia)	55
Telm Bover-Arnal, Ramon Salas, Joan Guimerà, and Josep Anton Moreno-Bedmar	
The Composition of Acervulinid – Red Algal Macrooids from the Paleogene of Croatia and Their Distribution in the Wider Mediterranean Region	59
Jasenka Sremac, Filip Huić, Marija Bošnjak, and Tihomir Marjanac	
Middle Miocene Chemosymbiotic Bivalves from the SW Margin of the Central Paratethys (Medvednica Mt., N Croatia)	63
Marija Bošnjak, Jasenka Sremac, and Elen Zukon Kolić	
Systematic and Taxonomic Investigations of Newly Discovered Mammalian Fauna from Late Pliocene of the Siwalik Sub-group of Pakistan	67
Sania Zubaid, Muhammad Tahir Waseem, Abdul Majid Khan, and Ghulam Sarwar	
The Iberian Evaporite Structure Database (IESDB): An Evaporite Radar for Energy, Carbon, and Nuclear Waste Storage Facilities	73
Eloi González-Esvertit, Juan Alcalde, and Enrique Gomez-Rivas	
Basilosauridae (Mammalia, Cetacea) from the Sahara Desert of Southwestern Morocco	77
Ayoub Amane, Hakima Zair, Fadwa Aniny, Philip Gingerich, and Samir Zouhri	
Paleoseasonality During the Early Pleistocene Revealed Through Stable Isotope Analysis of <i>Equus</i> from the Siwalik Sub-Group of Pakistan	81
Mishal Afzal, Muhammad Tahir Waseem, Abdul Majid Khan, Meera Sarwar, Ghulam Sarwar, and Rana Manzoor Ahmad	

Mineralogy and Petrology

- The Ti-Substitution in Phlogopite from the Jersey Minette (Channel Islands, UK) as Revealed by FTIR Spectroscopy** 87
Giancarlo Della Ventura, Nacir El Moutaouakkil, Boubker Boukili, Manuela Nazzari, and Federico Lucci
- Solution, Mixing and Formation Enthalpy Determination of Neodymium-Bearing Silicate–Oxyapatite** 91
Kaouther Ardhaoui
- Effect of Fly Ash (FA) Characteristic on Geopolymer Product Quality** 95
Sonia Cantika Wijayanti, Ferian Anggara, and Himawan T. B. M. Petrus
- Characteristics and Potential Concentration of Cenospheres in Fly Ash from Tanjung Jati B Combustion Power Plant, Jepara, Central Java, Indonesia** 99
Rafif Dhia Ulhaq, Ferian Anggara, and Himawan Tri Bayu Murti Petrus
- Experimental Stimulation of Sublimating Water Ice on the Earth and the Moon with Measuring D/H Ratios** 103
Vyacheslav Sevastyanov, Artem Krivenko, Sergey Voropaev, and Mikhail Marov
- An Improved Method for Carbonates Evaluating from Carbonaceous Chondrites** 107
Elena Tkachenko, Sergey Voropaev, and Veniamin Fedulov
- Efficiency of Soil Geochemistry as a Powerful Tool in Targeting of Hidden Deposits During Mineral Exploration: A Case Study of the Sediment-Hosted Kibamba Copper-Cobalt Deposit of the Lufilian Arc, Democratic Republic of Congo** 111
Katombe Kisumbule Paul, Mukendi Shambuyi Eddy, and Anani Tebagwe Jean-Michel
- Salts in SPA Therapies—Characterization and Risk Assessment** 117
Carla Candeias and Fernando Rocha
- Petrography and Mineral Chemistry of the Granitoids in the Eastern Part of Central India, Central Indian Tectonic Zone (CITZ)** 121
Indrajeet Saket, Meraj Alam, Md. Atif Raza, and Mohammad Sadiq
- Geochemical Constraints on the Petrogenesis of Tirodi Gneissic Complex (TGC) from Central India** 127
Mukesh Mishra, Meraj Alam, Tatiana Kaulina, and Talat Ahmad
- Petrogenesis and Tectonic Setting of Igneous Rocks from Kassa Area, Zing, Northeastern Nigeria: Geological and Geochemical Constraints** 131
Hafizullah Abba Ahmed, Ismaila Vela Haruna, Usman Kaigama, Maimunatu Halilu, Marcel Pius Apagu, Solomon Ahmed, Jonathan Abiukwoybe Aboh, Mohammed Babi Saleh, and Musa Bala Girei
- Miocene Magmatism in Northern Tunisia: Characterization and Geodynamic Implications** 135
Randa Ben Abdallah and Mohamed Mansour Abdelmalak
- Amphibole-Veins Formation Within a Syn-Tectonic Contact Aureole (Elba Island, Italy)** 141
Martina Zucchi, Andrea Brogi, and Domenico Liotta

Diagenesis of Diapir Flanking Successions: The Moroccan High Atlas and Other Tethyan Salt-Related Basins	145
Mar Moragas, David Cruset, Vinyet Baqués, Juan Diego Martín-Martín, Jordi Martín, Anna Travé, and Jaume Vergés	
Radiogenic Heat Production and Rare-Metal Mineralization Affinity of Anorogenic Acid Volcano-Plutonic Rocks from Neoproterozoic Tusham Ring Complex, NW Indian Shield. Constraints on Radioactive, Trace and Rare Earth Element Distributions	149
Naresh Kumar and Naveen Kumar	
Iron Ore Hypogene Mineralization in the São Francisco Craton	153
Carlos A. Rosière, Leonardo E. Lagoeiro, Flavia C. Silveira Braga, and Ricardo Pagung de Carvalho	
Indicative Role of Trace and Rare-Earth Elements of the North West Manganese Ore Deposit (South Africa) in Constraining the Genetic Model of Supergene Orebodies	157
Benedict Kinshasa Pharoe	
The Ophiolite-Hosted Cu–Fe–Zn Ores in Tuscany (Italy): VMS Deposits from a Jurassic Slow-Spreading Ridge	163
Andrea Dini, Chiara Boschi, Paolo Di Giuseppe, and Andrea Rielli	
Lithostratigraphy, Whole-Rock, and Sm–Nd Isotopic Data of the Ediacaran Magmatic Rocks from the Zgounder Ag–Hg Deposit (Siroua Massif, Central Anti-Atlas, Morocco)	167
Abdelhay Ben-Tami, Said Belkacim, Bouchra Baidada, Jamal El Kabouri, Mohamed Assalmi, Mohamed Bhilisse, and Mohammed Bouabdellah	
Characterization and Valorization of Clay Deposits from the Region of Beni Mellal-Khenifra in the Ceramic Industry (Morocco)	173
Soukaina Bedda, Toufik Remmal, Fouad Amraoui, and Assia Laroussi	
3D Modeling and Resources Estimation of Coal Old Piles in Jerada Mine, Oriental Morocco	179
Ayoub El Aallaoui, Mustapha El Ghorfi, Abdellatif Elghali, Hamza Zine, Ayoub Bayoussef, Yassine Taha, Mostafa Benzaazoua, and Rachid Hakkou	
Investigation on the Flotation Recovery of Mixed Copper Ore Through an Integrated Mineralogical Approach	185
Rachid Faouzi, Khalid Naji, Intissar Benzakour, Hakim Faqir, Hind Tahari, Hassan Oumesaoud, and Moulay Abdelazize Aboulhassan	
Sensor-Based Sorting in Mining Industry: Selection of Appropriate Sensing Technologies for a Copper Deposit	189
Samira Es-sahly, Brahim Lakssir, Khalid Naji, Hakim Faqir, Jihad Zahir, Abdelaziz El Basbas, and Slimane Dadi	
A Kinetic Test Method to Assess the Long-Term Acid Generation Behavior of Sludge/Slag and Mine Tailings of Mine a (Quebec, Canada)	193
Mohamed Jalal El Hamidi, Abdelkabar Maqsoud, and Tikou Belem	

Geodynamics, Tectonics, Structural Geology, Petroleum Geology	
The First Geological Investigation of Mekong River Rapids, Loei Province: Implications for a New Geologic Map and Tectonics in the Thai-Laos Boundary	199
Vimoltip Singtuen and Prawit Bumroongroch	
Multi-scale Analysis of the Mylonitized Giant Quartz Veins of the Cap de Creus and Canigó Massifs (Pyrenees)	203
Eloi González-Esvertit, Josep Maria Casas, Àngels Canals, Paul D. Bons, Claudia Prieto-Torrell, Gabriel Cofrade, and Enrique Gomez-Rivas	
Tracking the Southern Tethys Margin in NW Africa (Rif Belt, Morocco)	207
André Michard, Aboubaker Farah, Omar Saddiqi, Youssef Driouch, Abdeltif Lahfid, Ahmed Chalouan, Hervé Bertrand, Moulley Charaf Chabou, and Nasrrddine Youbi	
Les Avellanes Diapir, South-Central Pyrenees: Reconstructing the Kinematics of a Salt Diapir Inside a Fold-and-Thrust Belt: Preliminary Results	211
Gabriel Cofrade, Òscar Gratacós, Irene Cantarero, Oriol Ferrer, Pedro Ramirez-Perez, Eduard Roca, and Anna Travé	
Using Paleomagnetic and Field Data for the Paleogeometric Reconstruction of the Northern Border of the Central High Atlas	215
Bennacer Moussaid, Antonio Casas-Sainz, Juan José Villaláin, Hmidou El Ouardi, Belen Oliva, Sara Torres-López, Teresa Roman-Berdiel, Ruth Soto, Nawal Bouya, and Hassan El Makrini	
Evidence of Brittle Tectonic Continuity Between Precambrian Basement of Air and Its Sedimentary Cover (Northeast Niger)	219
Souley Baraou Idi, Abdoulwahid Sani, and Moussa Konaté	
Tectonics and Geodynamics of a Narrow Continental Rift: Barmer Basin, Rajasthan, India	223
Swagato Dasgupta, Soumyajit Mukherjee, and Rima Chatterjee	
Successive Fracturing and Fluid Flow Events During Thrust Sheet Emplacement: The Montsec Thrust Sheet (Southern Pyrenees)	229
Daniel Muñoz-López, Wissam Aziz, David Cruset, Irene Cantarero, Vinyet Baqués, Ardiansyah Koeshidayatullah, and Anna Travé	
CTX Gale Crater Basemap	233
FatimaEzzahra Jadid and Hasnaa Chennaoui Aoudjehane	
On the Nature of Fossil Fuel	237
Andrey Shilovskiy	
Reservoir Characteristic of Sa'adi Formation, Southern Iraq	241
Mohanad Al-Jaberi and Adyan Ali Musban	
Interpretation of Geophysical and Spectrometric Airborne Data of the Eastern Part of the Moroccan Central Massif	245
Nawal Bouya, Bennacer Moussaid, Ahmed Manar, and Hmidou El Ouardi	
Hydrocarbon Generation Centers in the Meso-Cenozoic Complex of the Black Sea-Caspian Region	249
Rustam MustaeV, Vagif Kerimov, Elena Lavrenova, and Uliana Serikova	

Modeling Hydrocarbon Migration and Accumulation Processes in the Meso-Cenozoic Complex of the Black Sea-Caspian Region	253
Vagif Kerimov, Rustam Mustaev, Elena Lavrenova, and Pavel Romanov	
The Impact of Structural-Geodynamic Systems on the Formation and Distribution of Hydrocarbon Potential in the Black Sea-Caspian Region	257
Boris Senin, Rustam Mustaev, Vagif Kerimov, and Uliana Serikova	
Generation and Emigration of Hydrocarbons in the Meso-Cenozoic Complex of the Black Sea-Caspian Region	261
Vagif Kerimov, Rustam Mustaev, Elena Lavrenova, and Uliana Serikova	
Geochemistry and Volcanology	
Model Validation of Passive Gas Dispersion: Examples from La Solfatara (Campi Flegrei, Italy) and Caldeiras Da Ribeira Grande (São Miguel Island, Azores)	267
Silvia Massaro, Manuel Stocchi, Giancarlo Tamburello, Fabio Dioguardi, Antonio Costa, Laura Sandri, Jacopo Selva, Giovanni Macedonio, Arnau Folch, Fátima Viveiros, Giovanni Chiodini, Stefano Caliro, and César Andrade	
Vertical Geochemical Trends in the Juvenile Clasts from the 79 AD Plinian Fallout Deposits	271
Giulia Chiominto, Lorenzo Fedele, Claudio Scarpati, Annamaria Perrotta, and Ileana Santangelo	
The Role of the White Pumice Clasts in the 79 AD Vesuvius Post-plinian PDC Deposits	275
Ileana Santangelo, Lorenzo Fedele, Claudio Scarpati, Annamaria Perrotta, and Giulia Chiominto	
Long-Term Probabilistic Volcanic Hazard Assessment for Tephra Fallout from Neapolitan Volcanoes on Southern Italy	279
Manuel Stocchi, Silvia Massaro, Beatriz Martínez Montesinos, Laura Sandri, Jacopo Selva, Antonio Costa, Roberto Sulpizio, Biagio Giaccio, Massimiliano Moscatelli, Edoardo Peronace, Marco Nocentini, Roberto Isaia, and Manuel Titos Luzòn	
Evidence for the Voluminous Silicic Volcanic Activity in the Permian–Triassic West Siberia	283
Anton Latyshev, Ivan Panchenko, Maria Smirnova, Petr Kulikov, Anastasia Tokmakova, and Yuliya Trushkova	
Geochemical Perspective on the Diagenesis of the Buah Carbonates from the Jabal Al Akhdar, Oman Mountains	287
Arshad Ali, Mohamed El-Ghali, Iftikhar Abbasi, Leonardo Brandão Nogueira, and Mohamed Moustafa	
Quantifying Gas Hazard with VIGIL (Automatized Probabilistic Volcanic Gas Dispersion Modelling)	293
Fabio Dioguardi, Silvia Massaro, Giovanni Chiodini, Antonio Costa, Arnau Folch, Giovanni Macedonio, Laura Sandri, Jacopo Selva, and Giancarlo Tamburello	

Geochemical Characterization of Borehole Production Water in Southern Tunisia: Relationship with the Nature of the Reservoir and Environmental Quality of the Water Discharge	297
Amel Triki, Amina Mabrouk El Asmi, and Sonia Barbouchi	
Peculiarities of the Vertical Profiles of CH₄ and CO₂ Concentrations in the Arctic Seas Sediments	303
Elena Tkachenko, Vyacheslav Sevastyanov, Veniamin Fedulov, Valery Fedulova, Olga Kuznetsova, Sergei Naimushin, Nikita Dushenko, Artem Krivenko, and Alyona Vinnikova-Malova	
Geoenery Science and Engineering	
A Novel Practical Method to Determine the Crude Oil Brine Rock System Wettability from Modified Amott Test	309
Abhijit Dandekar	
Kick Behavior Analysis and Modeling Methodologies	313
Fotios Zachopoulos and Nikolaos Kokkinos	
Insights on EU Strategy for Building Partnerships in Mediterranean Energy Policy to Meet Decarbonization Goals	317
Giacomo Di Foggia and Massimo Beccarello	
The Clustering of Source Rocks: A Spectral Approach	321
Vagia Ioanna Makri and Dimosthenis Pasadakis	
CNN-Transfer Learning-Based Prediction for Porosity and Absolute Permeability from Carbonate Rock Images	327
Ramanzani Kalule, Hamid Ait Abderrahmane, Waleed Alameri, and Mohamed Sassi	
Petrophysical Properties of the Late Carboniferous and Early Permian Glaciogenic Reservoirs: An Example from Al Khlata Formation, Block 56, Eastern Flank of South Oman Salt Basin	331
Elham K. S. Al-Nadabi, Mohamed A. K. El-Ghali, and Alex Ilic	
Microfacies and Depositional Analysis of Mauddud Formation in Selected Wells at Three Oilfields—Southern Iraq	335
Zainab Abdul-Wahhab and Mohanad Al-Jaberi	
Setting Up an Infinite Slope Stability Analysis on a High-Resolution DEM (0.21 × 0.21 m²) of a Mechanically Terraced Slope in Cyprus	339
Corrado Camera, Mattia Gentile, Hakan Djuma, Christos Zoumides, Christos Keleshis, Andreani Papageorgiou, Christos Constantinides, Andreas Leonidou, Marina Faka, and Adriana Bruggeman	

About the Editors



Attila Çiner Istanbul Technical University, Turkey

Attila Çiner is Sedimentology and Quaternary Geology Professor at the Eurasia Institute of Earth Sciences at Istanbul Technical University, Turkey. After graduating from the Middle East Technical University in Ankara (1985), he obtained his M.Sc. degree at the University of Toledo, USA (1988) and his Ph.D. at the University of Strasbourg, France (1992). He works on the tectono-sedimentary evolution of basins and Quaternary depositional systems such as moraines, fluvial terraces, alluvial fans, and deltas. He uses cosmogenic nuclides to date these deposits. He primarily focuses on the glacial deposits and landscapes and tries to understand paleoclimatic and paleoenvironmental changes since the Last Glacial Maximum. Lastly, he was part of the Turkish Antarctic Expedition. He spent two months working on the site recognition and decision of the future Turkish scientific research station to be implemented on the continent. He is Founding Editor-in-Chief of *Mediterranean Geoscience Reviews* and Chief Editor of *Arabian Journal of Geosciences*, both published by Springer. He received the Humboldt Foundation Georg Forster lifetime achievement award in 2022. He has published more than 100 peer-reviewed articles and book chapters.



Stefano Naitza Università degli Studi di Cagliari, Italy

Dr. Stefano Naitza was born on 29/05/1965 in Cagliari and graduated in Geological Sciences at the University of Cagliari. In 1992–93, he attended the Degree Course in Prospecting and Evaluation of Minerals at the Institute of Mineral Deposits at the University of Cagliari. In 1993–96, Ph.D. in Mineral Prospecting (IX Cycle) was completed at the University of Cagliari—Department of Geoengineering and Environmental Technologies. In 1998–2000, he was a research contractor at the University of Sassari—Institute of Geological-Mineralogical Sciences. In 2000–2002, he is the winner of a research grant at the Department of Geoengineering and Environmental Technologies at the University of Cagliari. In 2002, he was the winner of the public competition University Researcher—disciplinary sector D03D—GEOLOGY OF MINERAL DEPOSITS at the University of Cagliari. He has served as Researcher at the Department of Civil Engineering, Environmental, and Architecture (DICAAR), Faculty of Engineering, University of Cagliari from 2002 to February 2017 and currently belongs to the Department of Chemical and

Geological Sciences, where he is currently in charge of the ECONOMIC GEOLOGY Course for the Master Degree Course in Geological Sciences and Technologies. In the period 2012–2017, he was appointed to the Lithology and Geology Module in Applied Geology and Geology—Degree Course in Environmental Engineering. For the same degree course, he was in the past years in charge of the Rock and Industrial Minerals Course, the Solids Characterization Course, and the Ore Mineralogy Laboratory (2005–2010). His current research guidelines include: Studies on geology and metallogenesis of mineral deposits in the Variscan basement of Sardinia; studies on petrology and metallogenesis of Sardinian late-Variscan granitoids; studies on mineralization of precious (Au) and strategic (REE, Co, W, etc.) metals in the Sardinian basement and in the Arabian-Nubian Shield (Saudi Arabia) environmental characterization and assessment of pollution in past mining sites; research and geo-archeological study of historical mining sites.



Ahmed E. Radwan Institute of Geological Sciences, Jagiellonian University, Krakow, Poland

Dr. Ahmed E. Radwan is Adjunct Professor at the Institute of Geological Sciences of the Jagiellonian University (Poland). Dr. Radwan has academic and industrial experience, since he obtained his Ph.D. in geophysics at Sohag University, Egypt, besides his proficient work in the oil and gas industry as Section Head at the exploration department of the Gulf of Suez petroleum company (Gupco), Egypt. As Post-doctoral Research Scientist, he attended Innsbruck University in Austria in 2019. In 2020, he joined the Jagiellonian University in Poland. Despite his youth, he has received numerous awards from international organizations such as the International Union of Geological Sciences (IUGS), the Geochemical Society (GS), the Clay Minerals Society (CMS), the Austrian Forschungsgemeinschaft (FG), the Narodowa Agencja Wymiany Akademickiej (NAWA), the Austrian Federal Ministry of Education, Science, and Research (BMBWF), and petroleum companies. Dr. Radwan has authored more than 100 papers in highly indexed international peer-reviewed journals, published four book chapters, and presented at numerous international conferences. Dr. Radwan is Associate Editor in *Asian Earth Sciences*, *Marine and Petroleum Geology*, *Geoenergy Sciences and Engineering*, *Petroleum Exploration and Production Technology*, *The Geological Journal*, *Energy Geosciences*, and *Petroleum Research*, in addition to being Editorial Board Member of *Unconventional Resources*. Dr. Radwan is Book Reviewer and Research Article Reviewer for several publishers and journals, and he organizes many special issues in different journals with the leading publishers. His research interests focused on multidisciplinary research integrating geosciences (geophysics, geochemistry, and geology), petroleum engineering, and reservoir engineering, as follows: (1) geology areas include: petroleum geology, reservoir characterization, sedimentology, facies analysis, depositional environment, diagenesis, paleoenvironment

interpretations, subsurface analysis, basin analysis, reservoir quality, fluid flow, fractures, formation evaluation, and unconventional and conventional resources; (2) petroleum engineering (petroleum geomechanics, drilling, fluids, and casing design); (3) reservoir engineering (reservoir geology and geophysics, reservoir damage, production optimization, water flooding, stimulations, fluid flow, and enhanced recovery); (4) the geophysics fields of study (ex. formation evaluation, petrophysics, borehole geophysics, and rock typing); (5) geochemistry fields of study include geochemical characterization, basin modeling, petroleum systems, and isotope analysis; (6) petroleum geomechanics (pore pressure, wellbore stability, in-situ stress orientation, and magnitudes); (7) machine learning applications in the energy industry; and (8) energy storage.



Zakaria Hamimi Benha University, Benha, Egypt

Zakaria Hamimi is a structural geologist who spent the majority of his academic career at Benha University (Egypt) along with some years at Sana'a University (Yemen) and King Abdulaziz University (Saudi Arabia). He graduated (1984) from Assiut University (distinction with honor degree) and holds the M.Sc. (1988) from Zagazig University (Egypt) and the Ph.D. in Structural Geology and Tectonics (1992) from Cairo University. His research interests focus on structural geology, microstructures, and tectonics. He has worked in many field-related sub-disciplines of Earth Sciences including geologic mapping, microstructural analysis, strain analysis, paleostress reconstruction, active tectonics, tectonic geomorphology, crustal deformation, and image processing. He used all these fields to study key areas in the Arabian-Nubian Shield and to decipher their deformation history. He is the president, and one of the founding team, of the Arabian Geosciences Union since 2012. He received the medal of the Egyptian Geological Society of Egypt in 2015 and also the medal of the Arab Mining and Petroleum Association in 2016. He has co-published 50 research articles in national and international indexed and refereed journals and authored several books. In 2016, he (1) joined the AJGS as Associate Editor responsible for evaluating submissions in the fields of structural geology, microstructures and tectonics, (2) selected as a Member of the Egyptian Universities Promotion Committee, the Supreme Council for Universities (SCU, Egypt), (3) nominated as a Secretary of the National Committee for Geological Sciences, Academy of Scientific Research and Technology, and (4) designated as the IUGS-Representative for Egypt. In November 2017, he attended the Gondwana 16 International Conference held at Bangkok, Thailand, as the Representative of the National Committee for Geological Sciences, Academy of Scientific Research and Technology, Egypt. September 15, 2020, he was nominated as the President of the Egyptian National Committee for Geological Sciences, Academy of Scientific Research and Technology. In January 2022, he joined the *Journal of African Earth Sciences* as an Associate Editor.



Federico Lucci Dipartimento di Scienze della Terra e Geoambientali, Università degli Studi di Bari “Aldo Moro”, Bari, Italy

Federico Lucci holds a B.Sc. in Earth Sciences (2004), a M.Sc. in Earth Sciences (2006), and a Ph.D. degree in Earth Sciences (2010) from Università degli Studi Roma Tre (Italy). Theses and specialties related to the degrees are petrography, multivariate statistics in Earth Sciences and igneous petrology-structural geology, respectively. He holds Associate Professor Qualification 04/A1 (2022)—ASN-MIUR in Petrology, Mineralogy, Geochemistry, and Volcanology. His main research is focused on modeling and timing of magmatic complexes as key-constraint for understanding regional tectonics and geodynamic scenarios, through a multidisciplinary approach that integrates field survey, rock fabric characterization, mineral chemistry (SEM-EDS-BSE, SEM-CL, EMPA, in situ LA-ICP-MS), geochemistry, geochronology, inverse and forward thermobarometry and FC-AFC-mixing modeling. He has done extensive fieldwork in Alpine and Hercynian orogens (Rif Chain, Corsica, Sardinia, Pyrenees, Central Iran), Gondwanan orogens (Central Iran), Pacific-Cocos convergence zone (Trans-Mexican Volcanic Belt), intraplate volcanic chains (Cameroon Line). His investigations are related to the definition of the magmatic heat source in areas of geothermal interests (Eastern Trans-Mexican Volcanic Belt), understanding the granulite-granite connection (Rif Chain and Pyrenees), unraveling the Mesozoic geodynamic scenario of the Neo-Tethys realm of Iran through its magmatic record and its Cadomian basement, understanding the processes of crust-forming and growth through anatexis processes (Rif Chain in Morocco; Sanandaj-Sirjan Zone of Iran), and understanding the existing relationships between ore deposits, magmatism, and crust structure (Iran). In 2012, together with Prof. John C. White (Eastern Kentucky University), he created the informal group of Theoretical Petrology with the aim to develop and discuss numerical models applied to natural case studies for a better understanding of the genesis and evolution of the Earth crust. Results obtained are published in many international peer-reviewed papers. Recently, he also focused on the characterization of naturally occurring asbestos (NOA) and anthropic pollutants (e.g., particulate matter, black carbons, and micro-fibers) through spectroscopic techniques, with the aim to develop new low-cost devices dedicated to real-time monitoring of airborne pollutants. Since February 2022, he is Researcher in Petrography and Petrology at the University of Bari, where is dealing with the teaching course petrography of metamorphic rocks (semester). He organized in 2022 the short course for Ph.D. candidates dealing with the scientific language required for publishing papers in international journals. He was co-tutor of numerous bachelor, master, and Ph.D. theses, the bulk of them dealing with the evolution of crystalline basements petrographic fieldwork and laboratory activity were always part of the work in each thesis.



Jasper Knight University of the Witwatersrand, South Africa

I am Geoscientist with research interests in the spatial and temporal variability in morphosedimentary system responses to rapid hemispheric-scale climatic and environmental changes during the late Pleistocene and Holocene. I focus thematically on glaciers, rivers, coasts, and mountains. I focus geographically on Africa, Ireland, northwest USA, Australia, the European Alps, and various places in Asia and South America.



Ciro Cucciniello Università degli Studi di Napoli Federico II, Naples, Italy

Academic Position • Researcher in Petrology and Petrography (GEO/07) from 30/12/2013 to 26/12/2020 • Associate Professor in Petrology and Petrography (GEO/07) from 27/12/2020 to present
Main Scientific Interests • Petrological and geochemical study of large igneous provinces (e.g., Madagascar, Deccan, Karoo) • Petrological and geochemical study of intrusive complexes from ultramafic to felsic (e.g., India) • Petrological and geochemical study of alkaline, strongly alkaline, and peralkaline rocks (e.g., Madagascar, Libya) • Analytical chemistry of magmatic rocks and minerals using X-ray fluorescence spectrometry (XRF), scanning electron microscopy (SEM), and energy dispersive X-ray spectroscopy (EDS) • Isotopic analysis ($^{87}\text{Sr}/^{86}\text{Sr}$, $^{143}\text{Nd}/^{144}\text{Nd}$, $^{206}\text{Pb}/^{204}\text{Pb}$, $^{207}\text{Pb}/^{204}\text{Pb}$, $^{208}\text{Pb}/^{204}\text{Pb}$) of magmatic rocks by thermal ionization mass spectrometry (TIMS)
Research Funding Principal Investigator • Research Project Ateneo 2016 Università di Napoli, Federico II “Geochemistry, petrogenesis and mineralogy of alkaline and peralkaline rocks in northern and central Madagascar, rare metal (REE and HFSE) mineralization and their potential exploitation”
Participant • PRIN 2017 (P.I. Coltorti Massimo), ID Number: 20178LPCPW_004 “Micro to Macro—How to unravel the nature of the Large Magmatic Events” • PRIN 2015 (P.I. Conticelli Sandro), ID Number: 20158A9CBM_004 “Geochemical and isotopic budget of highly metasomatized subcontinental mantle in the Africa and Europe geodynamic systems: modern and fossil analogues” • PRIN 2010-2011 (P.I. Conticelli Sandro), ID Number: 2010 TT22SC_006 “Genesi e differenziazione dei magmi in relazione all’ambiente geodinamico ed alle caratteristiche petrologiche e geochimiche delle loro sorgenti: implicazioni per l’evoluzione del sistema convergente Africa-Europa” • PRIN 2008 (P.I. Coltorti Massimo), ID Number: 2008HMHYFP_003 “Il magmatismo cenozoico orogenico in Sardegna: sorgenti di mantello, evoluzione magmatica ed implicazioni geodinamiche” • PRIN 2008 (P.I. Marzoli Andrea), ID Number: 2008CR4455_002 “Petrogenesi, paleogeografia ed implicazioni paleoambientali del vulcanismo Cretacico in Madagascar ed India meridionale”.



Santanu Banerjee Indian Institute of Technology Bombay, India

Santanu Banerjee currently works as a Professor at the Department of Earth Sciences, Indian Institute of Technology Bombay. He does research in sedimentology and petroleum geology. His research areas include authigenic iron silicates, microbially induced sedimentary structures, basin analysis, provenance interpretations, and alternate potash fertilizer. He is on the editorial board of *Journal of Palaeogeography*, *Minerals*, *Arabian Journal of Geosciences* and *Journal of Earth Systems Science*. He teaches sedimentology, sedimentary basins, and petroleum exploration in his institute. He has published close to 130 papers in SCI-indexed journals, which received more than 5000 citations.



Hasnaa Chennaoui Hassan II University of Casablanca, Morocco

Education and Research: Hasnaa Chennaoui is a Moroccan scientist in the field of Meteoritics and Planetary Sciences and Geochemistry. She is a Professor in the Department of Geology at the Hassan II University of Casablanca, former Director of the GAIA Laboratory, and Coordinator of the Centre of Research on Georesources and the Environment. She became the first woman to graduate with a degree in meteoritics in Morocco and the Arabic countries. She obtained her first Ph.D. in noble gas geochemistry from the Université Pierre et Marie Curie Paris 6, France in 1992. She defended a “Thèse d’état” at the Hassan II University of Casablanca, Morocco in meteoritics in 2007. She has studied and classified many meteorites from Morocco including the latest 14 falls. One of her most influential projects characterized “Tissint”, the fifth eyewitnessed Martian meteorite, which proved the origin of all Martian meteorites and demonstrated the presence of fluids on Mars in these Martian rocks. *Honors and Awards:* She has received several honors and awards for her research, including the Paul Doistau-Émile Blutet Prize from the French Academy of Sciences in 2009 and the Moroccan National TV SNRT Trophy for “Distinguished Women in Morocco” in 2016. She was selected in 2013 for the US Department of State’s International Visitors Leadership Program (IVLP) for the Women Innovations in Science and Engineering (WISE) focus and was awarded the Women in Science Hall of Fame Award in 2014 by the US Department of State. In recognition for her outreach in geology and meteoritics, she was selected as an Africa Science Leadership Program Fellow (Pretoria, SA) in 2016 and as a Guest Lecturer for the Outreach Program of the European Association of Geochemistry in 2019. In recognition of her significant work on meteoritics, planetary science, and contributions toward impact events, she was elected Fellow of the Meteoritical Society in 2018. She received on 2021 the Hypatia International Award for research impacting society. Her name “Chennaoui” was given to asteroid in recognition to

her efforts on developing and promoting planetary sciences in Morocco and MENA region. Service to the Meteoritical Society. She has been a member of the Meteoritical Society for two decades and has served the Society in several capacities. She served on the Nomenclature Committee of the Meteoritical Society from 2005 to 2010 and joined again in 2015 and is currently a member. She was elected to the Council of the Meteoritical Society from 2011 to 2015 and served before that on the Membership Committee and the Ethical Committee. Since 2020, she is member of the membership committee. She organized the 77th Meteoritical Society Meeting in September 2014 in Casablanca, Morocco, which was the first meeting in an Arabic and Muslim country. She has also convened sessions dedicated to meteorites and impact studies at other conferences and participated on the scientific organizing committee for several workshops and conferences including multiple annual Arab Impact Cratering and Astrogeology Conference (AICAC) meetings. *Teaching and Outreach:* She has been introducing students to meteoritics and impact cratering in Morocco and the Arabic countries through coursework and research in these areas, and she developed a curriculum for the study of cosmochemistry and meteoritics in Moroccan universities for geology bachelor students. She has supervised many Ph.D. theses in Morocco, including three directed toward identifying and characterizing impact craters. In April 2019, she created the International ATTARIK Foundation for Meteoritics and Planetary Science, an NGO dedicated to the promotion of planetary sciences. ATTARIK supports education through public and private institutions, and cooperation among teachers, students, citizens, and civic leaders beginning with Morocco, but extending throughout the Arab World and African countries in an effort to develop an understanding of meteorites, astronomy, and planetary science, promote sustainable development, and preserve the heritage of this underserved region. In only a few years, ATTARIK Foundation succeeds in organizing many events for the general public and children in cities and villages. Since June 2021, this NGO launched an exhibit museum “Meteorites: messengers of the sky” that was very successful, so far it welcomed more than 8000 visitors. It presents for the first time in Morocco a collection of Moroccan meteorite falls, impactites, as well as a sketch of the solar system, an impact crater (the Meteor Crater), Apollo 11 rocket, discovery space shuttle, and dinosaurs footprints. She wrote a storybook about “Tamdakht” an important meteorite that fell in the south of Morocco in December 2008.



Domenico M. Doronzo Istituto Nazionale di Geofisica e Vulcanologia, Italy

Dr. Domenico M. Doronzo holds a B.Sc., a M.Sc., and a Ph.D. degree in Earth Sciences from Università degli Studi di Bari Aldo Moro, Italy. Investigation specialties related to those degrees are physical volcanology, experimental, and computational fluid dynamics, petrology, and natural hazards. Then, he has worked in volcanology and sedimentology, fluid dynamics and combustion, environmental sciences, and rock physics in the USA, Mexico, Spain, and Italy. Currently, he is a contract Researcher at Istituto Nazionale di Geofisica e Vulcanologia, Osservatorio Vesuviano, Italy. Particularly, he has received the Rittmann Medal from Associazione Italiana di Vulcanologia and Istituto Nazionale di Geofisica e Vulcanologia, which is assigned to the best young Italian volcanologist. His research interests focus on integrating theory, field measurements, numerical modeling, laboratory and outdoor experiments to study geological processes and products in volcanic areas (Vesuvio, Campi Flegrei, Etna, Vulcano, Colli Albani, Tenerife, Altiplano Puna, Colima) from fluid dynamic and natural hazard perspectives. He studies specifically pyroclastic energy currents, pre-eruption conditions, ground deformations, eruption forecasting, lahars and debris flows, flow-building interactions, sand and dust storms, turbidity currents, man-made environmental phenomena, and georesources. Recently, he has published the first comprehensive review on the famous 79 CE “Pompeii” Plinian eruption of Vesuvius by means of a multidisciplinary approach in volcanology, including magma chamber growth and pre-eruption ground deformation. He is a Chief Editor of the *Arabian Journal of Geosciences* responsible for evaluating submissions in the fields of geochemistry, mineralogy, petrology, and volcanology.



Carla Candeias GeoBioTec, Geosciences Department, University of Aveiro, Portugal

Carla Candeias is Researcher at GeoBioTec Research Centre, Geosciences Department, University of Aveiro, 3810-193 Aveiro, Portugal; candeias@ua.pt, Researcher ID: A-2521-2014/Scopus: 37062910200/Ciencia ID: D912-6FC4-79CC/ORCID: 0000-0001-6664-8545 Keywords: Medical geology, water and sediment quality, soil quality, air quality, indoor and outdoor dust, pelotherapy, environmental geochemistry, human health risk assessment, epidemiology, geophagy students’ supervisor. Carla Candeias is Member of international and national projects, including as PI. She is Member of scientific and organizing committees of international conferences. Knowledge dissemination in the scientific and social communities. She is Editor of books and special issues. She published papers indexed on Science Citation Index, e.g.: (1) Carla Candeias, Paula Ávila, Cristina Sequeira, Albuquerque Manuel, Fernando Rocha (2022). Potentially toxic elements dynamics in the soil rhizospheric-plant system in

the active volcano of Fogo (Cape Verde) and interactions with human health. *Catena* 209(1), 105843, <https://doi.org/10.1016/j.catena.2021.105843>. (2) Lara Almeida, Fernando Rocha, Carla Candeias (2022). Geochemical and mineralogical characterization of Ria de Aveiro (Portugal) saltpan sediments for pelotherapy application. *Environmental Geochemistry and Health*, <https://doi.org/10.1007/s10653-022-01407-5>. (3) Archi Mishra, Shamsh Pervez, Madhuri Verma, Carla Candeias, et al. (2023). Chemical fractionation of particulate-bound metal(loid)s to evaluate its bioavailable fractions, sources and assessment of associated cancer risk. *Science of the Total Environment*, <https://doi.org/10.1016/j.scitotenv.2022.159516>. (4) Retshepile Evelyn Malepe, Carla Candeias, Hassina Mouri (2023). Geophagy and its potential human health implications—A review of South African cases. *Journal of African Earth Sciences*, <https://doi.org/10.1016/j.jafrearsci.2023.104848>. (5) Bernardino Bernardo, Carla Candeias, Fernando Rocha (2022). Soil properties and environmental risk assessment of soils in the surrounding area of Hulene-B waste dump, Maputo (Mozambique). *Journal of Environmental Earth Sciences* 81:542, <https://doi.org/10.1007/s12665-022-10672-7>. Projects, e.g., (1) European Commission/Directorate-General for Research and Innovation Grant Agreement with European Plate Observing System—European Research Infrastructure Consortium (EPOS ERIC) and other beneficiaries (number 871121—EPOS SP—H2020-INFRADEV-2018-2020/H2020-INFRADEV-2019-2). Key Researcher, responsible for the Environmental Geology and Medical Geology studies. (2) FIRE—Fogo Island volcano: multidisciplinary Research on 2014 Eruption. FCT (PTDC/GEO-GEO/1123/2014). Task 9 Coordinator. (3) COST Action IS1408, Industrially Contaminated Sites and Health Network (ICSHNet). Project Member. (4) Scientific Cooperation Agreement Portugal and Poland, Waters Geochemical evolution in abandoned mining areas in Portugal and Poland. Funding FCT 31027/2014. Project Member. (5) Wireless sensors network as a base solution for environmental water quality assessment and monitoring. Funding OHM/CNRS (France), competitive call. Project Coordinator.



Jesús Rodrigo-Comino University of Granada, Spain

Ph.D. D.Eng. Jesús Rodrigo-Comino is Member of the Department of Regional and Physical Geography at the University of Granada (Spain). He completed his first Ph.D. in Geography at the University of Málaga (Spain) and Trier (Germany) in 2018 and the second one in the engineering of Geomatics and Topography at the Polytechnic University of Valencia (2023). His current research interests include soil geography, regional geography, and land degradation. He coordinates the Terra Lab 2 EGEMAP (Environmental Geography and Mapping) www.egemap.eu.



Roohollah Kalatehjari Auckland University of Technology, New Zealand

Dr. Roohollah (Roo) Kalatehjari is Highly Accomplished Academic and Researcher with over 15 years of experience in geotechnical engineering. He is Senior Lecturer in Geotechnical Engineering, Associate Head of School—Learning and Teaching at the School of Future Environments (SoFE) at Auckland University of Technology (AUT), Director of the Advanced Construction Research cluster, and Founder and Director of the Geotechnical Engineering Laboratory. His research focuses on preserving the environment and finding sustainable and environmentally friendly solutions for soil stabilization and slope stability. Roo is also Active Member of several professional engineering and education organizations, including Engineering New Zealand, the New Zealand Geotechnical Society, and the International Society for Soil Mechanics and Geotechnical Engineering. He is Fellow of HEA, UK, and Member of Life Cycle Assessment New Zealand.



Afroz Ahmad Shah Universiti of Brunei Darussalam, Brunei

Afroz Ahmad Shah is Senior Assistant Professor of Structural Geology at the Department of Geosciences, Universiti of Brunei Darussalam (UBD). He graduated from IIT Kanpur India in 2006 and then completed Ph.D. at James Cook University, Australia, in 2010, a post-doctorate at Earth Observatory of Singapore in 2013, and joined his first academic job as Senior Lecturer of Structural Geology at Curtin Sarawak, Miri, Malaysia, before joining UBD. His research mainly involves the brittle deformation of lithospheric plates, focusing on earthquake-causing faults in South and Southeast Asia. It also includes floods, landslides, and land subsidence hazards. Shah works on earthquake science education and outreach and frequently writes in newspapers, magazines, and blogs. He is National Geographic Explorer, and his work on earthquake hazards in Kashmir has been featured in the National Geographic Magazine. He loves writing and has been involved in writing about geological and climatic hazards.



Matteo Gentilucci University of Camerino, School of Science and Technology, Geology division, Camerino, Italy

Matteo Gentilucci had his B.Sc. degree in “Geological Sciences” from University of Camerino, Italy, in 2009 and then earned M.Sc. degree in 2012 from University of Camerino, Italy, in “Geoenvironmental Resources and Risks”. He earned a first-level master’s degree in GIS for the governance of the territory in 2012 and a Ph.D. in “Sciences and technology: Earth Science” from the University of Camerino in 2017. From February 2017 to October 2018, he is Researcher at the Experimental Geophysical Observatory of Macerata, and in 2018, he became Honorary Fellow in Advanced GIS. In 2018 and 2019, he is Contract Professor of the University of Camerino. Since 2022, he has been Researcher at the

University of Camerino and holds courses in meteorology, climatology, and GIS. He is Editorial Board Member of the *Journal of Experimental Sciences*, of the *Journal Sustainability*, of the *Arabian Journal of Geosciences*, and of the International Research Conference Committee. He is Author of numerous articles in international journals. Dr. Matteo Gentilucci is involved in numerous research projects related to climate. The main topics of interest and expertise are: geographic information systems applied to the environment, relationship between climate and phenology, climate change, global warming, and extreme events. <https://www.scopus.com/authid/detail.uri?authorId=57201441740>



Dionysia Panagoulia National Technical University of Athens, Greece

Dr. Dionysia Panagoulia is Associate Professor at the National Technical University of Athens, Greece, with expertise in hydrology, hydroclimatology, and water systems. She is Author of more than 145 published research works, including being Co-editor of the book *River Basin Management—Under a Changing Climate* and lately has extended her research work to water economics theory and complex time/dark matter approaches. She has over 30 years of research experience in floods and their risk and hazard, extreme events, precipitation, global climate contribution to local climate, climate change, low flows, droughts, maximum/minimum temperatures, sediment transport, groundwater/streamflow interaction, ANN, WEF Nexus, and water economics and management. She has cooperated in joint research with the University of Stuttgart, Germany; CNRS Laboratory of Oceanology and Geosciences Wimereux, France; Wageningen University, Netherlands; and McGill University, Canada. She was/is Member of twelve scientific societies, Reviewer and Guest Editor for thirty-two international journals, and Recipient of the 2018 Outstanding Reviewer Award from Water MDPI.



Helder I. Chaminé School of Engineering of Porto (ISEP), Portugal

Helder I. Chaminé is Skilled Geologist (B.Sc., Ph.D., D.Sc.) and Professor of engineering geosciences at the School of Engineering (ISEP) of the Polytechnic of Porto, Portugal, with over 33 years of experience in multidisciplinary geosciences research and practice. Before joining the academy in 2001, he worked for over 13 years on international and national projects for mining hydrogeomechanics and geology, structural geology mapping, applied mineralogy, rock engineering, exploration geology, and groundwater. His major research interests are GIS mapping techniques for applied geology, geotechnics and natural hazards, engineering geosciences and hydrogeomechanics, hard-rock hydrogeology, urban groundwater, water resources, and thermal waters management. He has interests in geomining heritage, geothics, history of cartography, military geosciences, higher education dissemination, and geoprofessional

core values. Presently, he is Head of the Laboratory of Cartography and Applied Geology (LABCARGA|ISEP), Senior Researcher at Centre GeoBioTec|U. Aveiro and Centre IDL|U. Lisbon, as well as belongs to the executive board of the M.Sc. Geotechnical and Geoenvironmental Engineering program (OE+EUR-ACE Label) and the Department of Geotechnical Engineering (ISEP). Furthermore, he was Consultant and responsible for over 70 projects of applied geology, hydrogeomechanics, slope geotechnics, mining geology, exploration hydrogeology, hard-rock hydrogeology, water resources, urban groundwater, and applied mapping (Mozambique, Portugal, and Spain). He has co-authored over 220 publications in indexed journals, conference proceedings/full papers, book chapters, and technical and professional papers. He co-edited over 16 special volumes (journals and Springer Series Books) and is presently editing topical collections for several international journals. He serves as Associate Editor (*SN Applied Sciences*, *Discover Water*, *Arabian Journal of Geosciences*, *Euro-Mediterranean Journal for Environmental Integration*) and on the editorial or advisory boards (*Mediterranean Geoscience Reviews*, *Geotechnical Research ICE*, *Journal of Geoethics and Social Geosciences*, *Cadernos do Laboratório Xeolóxico de Laxe*, *Revista Geotecnia SPG*, *Geología Aplicada a la Ingeniería y al Ambiente ASAGAI*). He also served as Associate Editor in the *Hydrogeology Journal*. In addition, he has a broad activity as Reviewer for several international journals. In 2021, the journal *SN Applied Sciences* awarded him an outstanding Guest Editor and Editorial Board Member. In addition, he integrates as Moderator or Session Chair in several conferences, workshops, and meetings. He is Vice-President of the Portuguese Chapter of the International Association of Hydrogeologists (IAH) and Deputy Secretary of the Technical Commission of Environmental Geotechnics from the Portuguese Geotechnical Society (SPG). Furthermore, he served as Invited Expert Evaluator of the Bologna Geoscience program for DGES (Portugal) and Scientific Projects Evaluation for NCST, 2017–2019 (Kazakhstan), and NRF|RISA, 2019 (South Africa), as well as Coordinator of “Geology on Summer/Ciência Viva” program at ISEP (2005–2019) for geoscience dissemination. He has also been active in teaching and supervising many Ph.D., M.Sc., and undergraduate students.



Maurizio Barbieri University of Rome La Sapienza, Italy

Maurizio Barbieri is a skilled geologist (B.Sc., Ph.D.) with over 27 years of experience and a full professor of Geochemistry at the Department of Chemical, Materials, and Environmental Engineering (DICMA) of the Sapienza University of Rome, Italy. Presently, he is Fellow of the Association of Applied Geochemists and European Chair (Italy) of the Society for Environmental Geochemistry and Health (<https://segh.net/about-us>). He has been on the editorial board of the *Arabian Journal of Geosciences*, *Chemie der Erde*, *Environmental Geochemistry and Health*, *Euro-Mediterranean Journal for Environmental Integration*, *Water*, *Geofluids*, and *Discover Water*. In addition, he is an editor-in-chief (hydrogeology section) for *Geosciences MDPI*. The main R&D fields are: environmental geochemistry; environmental hydrogeology; hydrogeochemistry; water-rock interaction; water resources management; and geoenvironment and geohazards.



Zeynal Abiddin Ergüler Kutahya Dumlupinar University, Geological Engineering Department, Kutahya, Turkey

Prof. Dr. Zeynal Abiddin Ergüler is Full Professor in the geological engineering department at Kutahya Dumlupinar University (Turkey). Dr. Ergüler holds a B.Sc. (1998), an M.Sc. (2001), and a Ph.D. degree (2007) in Geological Engineering from Hacettepe University (Turkey). His research interests mainly focus on rock mechanics, engineering geology, environmental geology, and soil mechanics. His current investigation is to understand and model the thermo-hydro-mechanical behavior of shale rocks in the area of shale gas production. In addition to performing many types of research and industry-funded projects, he has also taught and supervised undergraduate and graduate students. In 2017, Dr. Ergüler joined the *Arabian Journal of Geosciences* (AJGS) as Editor responsible for evaluating submissions in the fields of rock mechanics, engineering geology, environmental geology, and soil mechanics.

Sedimentology, Stratigraphy, Paleontology



The Oldest Eocene Marine Vertebrate Fauna from the Sahara Desert in Southwestern Morocco

Fadwa Aniny, Estelle Bourdon, Sylvain Adnet, Stephane Jouve, Hakima Zair, Philip D. Gingerich, Najia Elboudali, and Samir Zouhri

Abstract

The Sabkha of El Breij has yielded the oldest marine Eocene vertebrate fauna from the Sahara Desert in southwestern Morocco. Fossils come from three distinct layers in the Samlat Formation sequence. Selachian teeth are abundant at all levels. The selachian assemblage in the lower level indicates a Lutetian-early Bartonian age. The selachian taxa of the two upper levels indicates an upper Bartonian age. The lower horizon yields abundant fossil remains of two protocetids, the very large *Papocetus lugardi* and a smaller medium-sized protocetid. Protocetids are associated with rare remains of bony fishes, turtles, crocodyliforms, and a paleohipiid snake (cf. *Palaeophis moghrebianus*). The two upper fossiliferous levels (Bartonian) are about 20 m above the

lower level. They yielded remains of three genera of Basilosauridae: *Chrysocetus*, *Platyosphys*, and *Eocetus*, associated with abundant chondrichthyans, and remains of bony fish, turtles, crocodyliforms, and seabirds. Turtles are represented by a pleurodire species of the subtribe Stereogenyina, probably *Cordichelys antiqua*, and another pleurodire form remains to be determined. The crocodile vertebrae show that it is a Eusuchian, and the shape of the quadrate suggests a gavialoid. The two specimens of pseudotoothed birds (Odontopterygiformes, Pelagornithidae) are tentatively assigned to the genus *Pelagornis*, which together with *Pelagornis* from the Bartonian of Gueran constitutes one of the earliest records of this genus.

Keywords

Sahara Desert • Morocco • Vertebrates • Middle Eocene • Palaeontology

F. Aniny (✉) · H. Zair · S. Zouhri
Laboratory of Health and Environment, Faculty of Sciences Ain Chock, Hassan II University of Casablanca, Casablanca, Morocco
e-mail: fadwa.aniny-etu@etu.univh2c.ma

E. Bourdon
National Museum of Natural History, CNRS, EPHE, Sorbonne University, 57 rue Cuvier, 75231 Paris Cedex 05, France

S. Adnet
UMR 5554, Montpellier Institute of Evolutionary Sciences, University of Montpellier, Place E. Bataillon, 34095 Montpellier Cedex 5, France

S. Jouve
Palaeontology Research Center, National Museum of Natural History MNHN, CNRS, Sorbonne University, 4 Place Jussieu, 75252 Paris Cedex 05, France

P. D. Gingerich
Museum of Paleontology, Research Museum Center, University of Michigan, 3600 Varsity Drive, Ann Arbor, MI 48108-2228, USA

N. Elboudali
Geosciences Applied to Development Engineering Laboratory, Faculty of Sciences Ain Chock, Hassan II University of Casablanca, Casablanca, Morocco

1 Introduction

The Sahara Desert in southwestern Morocco is rapidly developing into an important region for documentation of archaeocete whale evolution, complementing the Indo-Pakistan sub-continent and the Fayum Depression of Egypt. We first described a Priabonian marine fauna from coastal sites in the Samlat Formation near Ad-Dakhla (Adnet et al., 2010; Zouhri et al., 2014, 2018b). Later, we described a marine fauna from the Aridal Formation of the Sabkha of Gueran (Gingerich & Zouhri, 2015; Jouve et al., 2019; Zouhri et al., 2018a, 2021). Here, we report the discovery of new middle Eocene localities in the Aridal Formation of the Sabkha of El Breij. At El Breij, the vertebrate remains come from three distinct levels. The interest of this new locality lies in the fact that the lower level that yielded remains of Protocetidae would be of the Lutetian age according to the

Elasmobranchs assemblage. This makes it one of the oldest stratigraphic levels yielding marine vertebrates from the Eocene of the Sahara Desert. The upper two fossiliferous levels at El Breij yielded remains of Basilosauridae associated with other marine vertebrates. The upper levels, yielding a fauna like that of Gueran, are Bartonian in age according to the selachians.

2 Geological Setting

Vertebrate fauna reported here comes from the Aridal Formation in the El Breij depression in the Sahara Desert of southwestern Morocco. Geologically, this formation belongs to the Atlantic basin of Tarfaya-Laayoun-Ad-Dakhla. This basin is the onshore proximal part of the Atlantic passive margin. Gingerich and Zouhri (2015) summarized the geological context of the study area. In the Depression of El Breij, the stratigraphic sequence comprises three lithostratigraphic units. The three fossiliferous beds are located in the lower lithostratigraphic unit. The lower unit outcrops over a thickness of seven to eight meters. It consists of alternating whitish marls indurated and cut into plates, sandy marls, and three levels of coarse-grained marly sands rich in vertebrates, separated from each other by a very persistent yellowish sandstone. The two upper lithostratigraphic units did not yield marine Eocene vertebrates.

3 Materials and Methods

Fossils described in this work were collected at Sabkha of El Breij during a field trip carried out in 2019 and 2022. They come from three fossiliferous layers visible along several kilometers in the lower lithostratigraphic unit. This material is housed in the Paleontological Collections of the Department of Geology of the Faculty of Sciences Ain Chock, Hassan II University of Casablanca. The fossils are catalogued: FSAC–Breij n°.

4 Systematic Palaeontology

Chondrichthyes: The Elasmobranch assemblage from the lower fossiliferous level in the lower unit suggests an early Lutetian-Bartonian age. This assemblage is very similar to that of the Lutetian phosphate deposits in Morocco and Senegal. Selachian assemblages from the other two fossiliferous levels in the lower unit indicate a late Bartonian age based on the presence of large *Carcharhinus* generally encountered in the Priabonian.

Actinopterygii: The actinopterygian fauna of El Breij is represented by fragmentary material composed of remains of perciforms, siluriforms, and *Cylindracanthus*.

Chelonii: Turtles are represented by a pleurodire species of the subtribe Stereogenyina, probably *Cordichelys antiqua*, and another pleurodire that probably represents a variant of the first form, another species, or even another family (Bothremydidae?).

Crocodylia: Interesting material belonging to a single individual represents a crocodyliform. The vertebrae show that it is an eusuchian, and the shape of the quadrate suggests a gavialoid.

Serpentes: An isolated snake vertebra was found in the lower level (Ypresian-lower Bartonian). It has large dimensions: the length of the centrum on the ventral side is 33.5 mm; the width and the height of the cotyle are 23.6 and 21.8 mm, respectively. This vertebra shows practically no lateral compression. According to its dimensions and its “primitive” grade morphology, the vertebra is attributed to *Palaeophis moghrebianus* known from the Ypresian deposits in the phosphates of Morocco (Houssaye et al., 2013).

Aves: The distal end of a right humerus and the distal end of a right tibiotarsus from one of the upper layers (Bartonian) have been assigned to the Pelagornithidae or Odontopterygi pseudotoothed birds based on anatomical features of the group listed by Bourdon et al. (2010). The first specimen represents a humerus that was at least 400 mm in total length and belonged to a large pelagornithid. This size is smaller than that of many species of *Pelagornis* (Ksepka, 2014; Mayr & Rubilar-Rogers, 2010) and smaller than the beak fragment from the Bartonian of Gueran (Zouhri et al., 2018a). The tibiotarsus belonged to a gigantic pelagornithid. Its size approximates that of the largest species of *Pelagornis* (Ksepka, 2014; Mayr & Rubilar-Rogers, 2010). The size range of the tibiotarsus from El Breij is similar to that of the beak fragment from the Bartonian of Gueran (Zouhri et al., 2018a).

Cetacea: The early Lutetian-early Bartonian horizon yields abundant fossil remains of two protocetids, the very large *Pappocetus lugardi* and a smaller medium-sized protocetid. *P. lugardi* is now known from a rostrum, and for the first time from vertebrae and associated limb bones, confirming that the genus was a semi-aquatic georgiacetine. The second protocetid is about 20% smaller than *Pappocetus*. The two upper fossiliferous levels at El Breij (Bartonian) have yielded remains of three Basilosauridae: *Chrysocetus* sp., *Pachycetus* sp., and *Eocetus schweinfurthi* similar to those of Gueran.

5 Conclusion

The sabkha of El Breij is the third locality in the Moroccan Sahara to have yielded remains of an Eocene marine fauna. The lower fossiliferous level is Lutetian-early Bartonian in age; hence, it is the oldest marine fauna from the Moroccan Eocene. The two upper fossiliferous levels yielded a Bartonian fauna similar to Gueran. The Lutetian-early Bartonian fauna with *Pappocetus* supports a close bio-geographical connection with the faunas of the Atlantic coast of West Africa, while that of the Bartonian supports faunal exchanges between the southeastern and southwestern coasts of the Mediterranean Sea.

References

- Adnet, S., Cappetta, H., & Tabuce R. (2010). A middle-late Eocene vertebrate fauna (marine fish and mammals) from southwestern Morocco preliminary report: age and palaeobiogeographical implications. *Geological Magazine* 147, 860–870.
- Bourdon, E., Amaghaz, M., & Bouya, B. (2010). Pseudo-toothed birds (Aves, Odontopterygiformes) from the Early Tertiary of Morocco. *American Museum Novitates*, 3704, 1–71.
- Gingerich, P. D., & Zouhri, S. (2015). New fauna of archaeocete whales (Mammalia, Cetacea) from the Bartonian middle Eocene of southern Morocco. *Journal of African Earth Sciences*, 111, 273–286.
- Houssaye, A., Rage, J.-C., Bardet, N., Vincent, P., Amaghaz, M., & Meslouh, S. (2013). New highlights about the enigmatic marine snake *Palaeophis maghrebianus* (Palaeophiidae; Palaeophiinae) from the Ypresian (Lower Eocene) phosphates of Morocco. *Palaeontology*, 56, 647–661.
- Jouve, S., Khalloufi, B., & Zouhri, S. (2019). New Longirostrine crocodyliforms from the Bartonian of Morocco and Paleogene climatic and sea-level oscillations in peri-Tethys area. *Journal of Vertebrate Paleontology*, 39(3), e1617723.
- Ksepka, D. T. (2014). Flight performance of the largest volant bird. *Proceedings of the National Academy of Sciences*, 111(29), 10624–10629.
- Mayr, G., & Rubilar-Rogers, D. (2010). Osteology of a new giant bony-toothed bird from the Miocene of Chile, with a revision of the taxonomy of Neogene Pelagornithidae. *Journal of Vertebrate Paleontology*, 30(5), 1313–1330.
- Zouhri, S., Gingerich, P. D., Adnet, S., Bourdon, B., Jouve, S., Khalloufi, B., Amane, A., Elboudali, N. S., Rage, J.-C., de Lapparent de Broin, F., Kaoukaya, A., & Sebti, S. (2018a). Middle Eocene vertebrates from the sabkha of Gueran, Atlantic coastal basin, Saharan Morocco, and their peri-African correlations. *Comptes Rendus Geosciences*, 350, 310–318.
- Zouhri, S., Gingerich, P. D., Elboudali, N., Sebti, S., Noubhani, A., Rahali, M., & Meslouh, S. (2014). New marine mammal faunas (Cetacea and Sirenia) and sea level change in the Samlat Formation, Upper Eocene, near Ad-Dakhla in southwestern Morocco. *Comptes Rendus Palevol*, 13, 599–610.
- Zouhri, S., Gingerich, P. D., Khalloufi, B., Bourdon, E., Adnet, S., Jouve, S., Elboudali, N., Amane, A., Rage, J.-C., Tabuce, R., & de Lapparent de Broin, F. (2021). Middle Eocene vertebrate fauna from the Aridal Formation, Sabkha of Gueran, southwestern Morocco. In J.-S. Steyer, M. L. Augé, & G. Métais (Eds.), *Memorial Jean-Claude Rage: A life of paleo-herpetologist. Geodiversitas*, 43(5), 121–150.
- Zouhri, S., Khalloufi, B., Bourdon, E., de Lapparent de Broin, F., Rage, J.-C., M'Haidrat, L., Gingerich, P. D., & Elboudali, N. (2018b). Marine vertebrate fauna from the late Eocene Samlat Formation of Ad-Dakhla, southwestern Morocco. *Geological Magazine*, 1–25.



Habitat Reconstruction of the Pleistocene Hippopotamidae from the Siwaliks of Pakistan Using Stable Isotopes

Meera Sarwar, Muhammad Tahir Waseem, Mishal Afzal, Abdul Majid Khan, and Sania Zubaid

Abstract

Stable isotopes of carbon and oxygen ($\delta^{13}\text{C}$ and $\delta^{18}\text{O}$) archived in fossil tooth enamel are essential tools to reconstruct the palaeoecology and palaeohabitat of mega-herbivores. Among the mega-herbivores, hippopotamus (Hippos) are the third-largest existing artiodactyls. The family Hippopotamidae consists of semi-aquatic, mostly herbivorous non-ruminant animals. Hippos first appeared in the late Miocene (~ 6 Ma) which was the time of substantial faunal turnover and expansion of C_4 vegetation in low latitude regions globally, due mainly to lowered atmospheric CO_2 as well as other environmental factors. However, studies regarding the habitat of mega-herbivores are inadequate. In this paper, we reconstruct the habitat of *Hexaprotodon sivalensis* recovered from the early Pleistocene (ca. 2.5–2.2 Ma), Pabbi Hills locality of the Siwalik sub-Group of Pakistan. We used bulk stable isotope analyses of oxygen and carbon which provide temporal and environmental information on the animal's ecology and diet. The average $\delta^{13}\text{C}_{\text{enamel}}$ and $\delta^{18}\text{O}_{\text{enamel}}$ are $-0.6 \pm 1.4\text{‰}$ and $-2.1 \pm 2.1\text{‰}$, respectively, which indicate that during the early Pleistocene, the diet of *H. sivalensis* was dominantly composed of C_4 vegetation which was present mainly in the form of open grasslands. The high $\delta^{18}\text{O}_{\text{enamel}}$ values indicate that *H. sivalensis* inhabited freshwater ponds under drier climatic conditions where they fed upon the C_4 vegetation exclusively. However, enamel thickening/complexity and high crowns also

provide direct evidence for pure C_4 grass-dominated vegetation along with higher $\delta^{13}\text{C}_{\text{enamel}}$ in the Siwaliks, like modern hippos from Africa.

Keywords

Hexaprotodon • Pinjor formation • Palaeoclimate • Palaeodiet • Climate change

1 Introduction

The family Hippopotamidae (Hippos) consists of large, semi-aquatic artiodactyls, mostly herbivores and non-ruminant animals. Most recent studies demonstrate that hippos and Cetaceans have common ancestors. They live in semi-aquatic habitats, submerged in water during the daytime and come out at night, moving < 3 km away from water to feed. There are only two species of Hippopotamidae that exist today, which are the common hippopotamus (*Hippopotamus amphibius*) and pygmy hippopotamus (*Hexaprotodon sivalensis*) (Lihoreau & Brunet, 2005). Overall hippos are considered herbivores, whereas some cases of carnivores are reported in common hippos. Generally, paleoecological data provide evidence that hippopotamus fed on herbaceous strata which mainly incorporate C_3 and C_4 grasses in eastern, central, and southern Africa and in Asia (Boisserie et al., 2005).

Hippopotamus diversified during the late Miocene in the eastern and central region of the Arabo-African continent. During the late Miocene, expansion of C_4 vegetation indicates reorganization of open grassland landscapes. *H. amphibius* crops heavily and systematically on fresh grasses, and recent stable isotope analysis of *H. amphibius* shows opportunistic diets along with regular and significant intake of C_3 vegetation, while other extant *Choeropsis liberiensis* is more versatile in its diet. The diet of extant hippos is dominated by herbaceous plants. Various common hippopotamus

M. Sarwar · M. Afzal · A. M. Khan · S. Zubaid
Ecology and Evolutionary Biology Laboratory, Institute of
Zoology, University of the Punjab, Lahore, 54590, Pakistan

M. T. Waseem (✉)
Zoological Science Division, Pakistan Museum of Natural
History, Shakarparian, Islamabad, 44000, Pakistan
e-mail: tahirmuhammad1213@gmail.com

have a rostral morphology which prevents fine food selection, which means that C₃ plants can be ingested alongside C₄ plants in lawns with diverse vegetation. It is worth noting that early hippos lived in more open habitats compared to extant *C. liberiensis* (Vignaud et al., 2002). During the early Pliocene, hippos mostly lived in intermediate habitats and fed exclusively on C₄ grasses. At the end of the Pliocene due to Himalayan uplift (~ 3 Ma), hippo habitats became drier and open grassland expanded, where C₄ vegetation become widespread and C₃ plants were constrained to fewer places. During the Pleistocene, tectonic uplift led to the evolution of lowland sedimentary basins which become suitable habitats for most hippos (Barry & Flynn, 1989). However, studies regarding the habitat of *H. sivalensis* are inadequate. In this paper, we reconstruct the habitat of *H. sivalensis* from the middle Pleistocene (ca. 1.8–1.6 Ma) locality of the Siwalik sub-Group of Pakistan by using stable isotope analysis of carbon and oxygen. This analysis is an essential tool to reconstruct the paleoecology and paleohabitat of mega-herbivores (Quade et al., 1997). The specimens for this study were collected from Pinjor district Pabbi Hills, north Punjab, of Pakistan. The stable isotope analysis of $\delta^{13}\text{C}$ and $\delta^{18}\text{O}$ allows us to explore the paleohabitat of *H. sivalensis* from the upper Siwaliks of Pakistan. The Hippos habitat is still a mystery in the Siwaliks of the Pakistan. Thus, this study is an attempt to address this issue by using sophisticated and new approach of stable isotope analysis.

2 Materials and Methods

For stable isotope analysis, we select 30 samples of *H. sivalensis* from the middle Pleistocene (ca. 1.8–1.6 Ma) locality of the Siwalik sub-Group of Pakistan. We examine enamel because it is least susceptible to diagenetic alteration and its large size crystals make it useful tissue for stable isotope analysis. We use bulk sampling which is taken perpendicular to the crystal growth axis. For the extraction of enamel, a foredom dental drill was used which extracted 10–15 mg of enamel from all teeth (include the premolar and molar). Samples were stored in plastic vials. The fine powder tooth enamel was pre-treated for 1 h by 10 ml of 2% NaOCl and the solution was rinsed and decanted by distilled water three times. The sample was further treated for 1 h with 10 ml 0.1% acetic acid after which the sample was dried in an oven. Isotope ratio mass spectrometry was undertaken at Islamabad PINSTECH. All samples were loaded in a continuous flow elemental mass spectrometer for analysis of carbon and oxygen stable isotopes, following the manufacturer's standard procedures. Oxygen and carbon values are report to isotope standards such as:

$$\delta^{13}\text{C} \text{ or } \delta^{18}\text{O} = (R_{\text{sample}}/R_{\text{standard}} - 1)/1000$$

where R_{sample} and R_{standard} refer to the $^{18}\text{O}/^{16}\text{O}$ and $^{13}\text{C}/^{12}\text{C}$ ratios for sample and the standard of $\delta^{13}\text{C}$ or $\delta^{18}\text{O}$. The standard isotope reference is V-PDB for isotopes of oxygen and carbon. We applied a student *t*-test by using SPSS for statistical analysis to estimate the major difference in isotopic ratios of carbon and oxygen. Before every statistical analysis, we evaluate all data for normality by using the Shapiro–Wilk test.

3 Results

3.1 Carbon Isotope Values

Carbon isotope values range between – 3.8 and 0.9‰ which were calculated from all fifteen samples of *H. sivalensis*. This finding is consistent with the previously established hypothesis of grasslands dominance on the Siwalik floodplain during the Pleistocene (reference needed). The mean for all samples is – 0.6‰ and the standard deviation is $-0.6 \pm 1.4\%$. The *t*-test revealed significant differences ($p < 0.05$; $p = 0.02$) among the Pleistocene samples (average $\delta^{13}\text{C}_{\text{enamel}} = -0.6\%$) (Fig. 1a).

3.2 Oxygen Isotope Values

Oxygen isotope values range from – 4.65 to 4.70‰; the average value is $-2.1 \pm 2.1\%$. A *t*-test reveals a significant difference ($p = 0.00$) among Pleistocene samples (Fig. 1b, c). The highly depleted oxygen isotope values are in agreement with those of African Hippos which directly reflects their semi-aquatic lifestyle (Cerling et al., 2008).

4 Discussion

Stable isotopes of carbon and oxygen archived in fossil tooth enamel are essential tools to reconstruct the palaeoecology and paleohabitat of extinct fauna. *H. sivalensis* is a unique hippopotamid lineage in Asia and it has been found in all main stratigraphic units of the Pinjor and Tatrot formations of Pakistan, while it occupies less frequently as compared to other related groups (Boisserie & White, 2004). Stable isotope analysis of dental enamel provides evidence that earlier hippos live in closed canopy forests with some open habitats, and their carbon isotope values indicate that their diet contains a significant portion of C₃ plants along with C₄

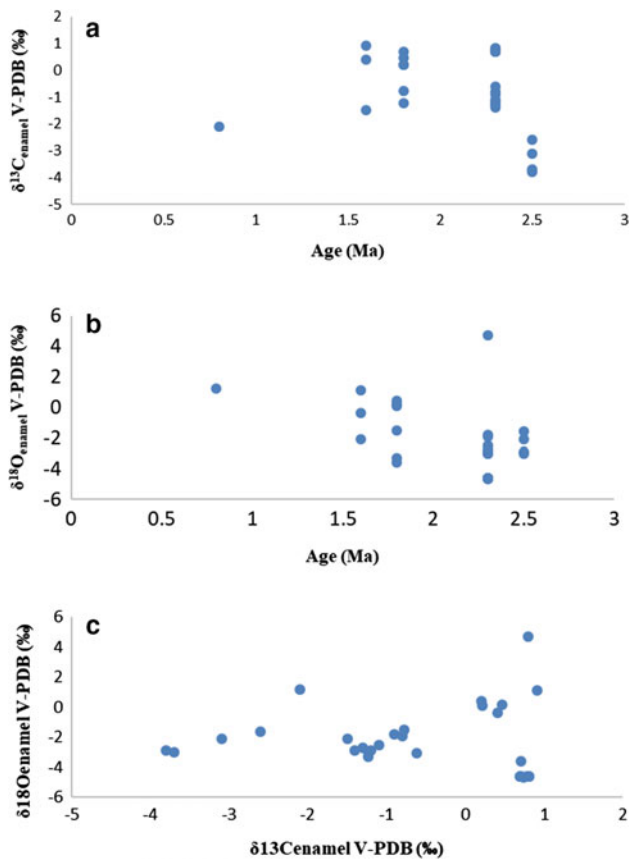


Fig. 1 **a** Time series of $\delta^{13}\text{C}$ ratios of *Hexaprotodon sivalensis* tooth enamel from the Pleistocene Siwaliks of Pakistan. **b** Time series of $\delta^{18}\text{O}$ ratios of *Hexaprotodon sivalensis* tooth enamel from upper Siwaliks of Pakistan. **c** Comparison of $\delta^{13}\text{C}_{\text{enamel}}$ and $\delta^{18}\text{O}_{\text{enamel}}$ values across the Pleistocene *Hexaprotodon sivalensis* samples from the upper Siwaliks of Pakistan

plants. In the Siwaliks during the middle Miocene, isotopic composition of hippopotamus indicates that they are browsers (C_3) and live in relatively closed forest as well as drink water from ^{18}O -depleted sources like ponds and streams. During the late Miocene, hippo habitats shifted and the forested landscape changed to grassland which was initially linked with decreased atmospheric CO_2 as well as Himalayan uplift that led to drier habitats. Extant *H. amphibius* diet was mainly C_4 plants (Cerling et al., 2008). During the early Pliocene, the landscape was not dominated by extensive open grasslands and was instead a mosaic with only a few grasses (Ungar et al., 2007). The difference between the extant *H. amphibius* and early hippo's diet is chiefly linked with the lack of C_4 and abundance of C_3 vegetation. It suggests that C_4 expansion in the late Miocene provided new feeding niches, although hippopotamus species play important roles in the expansion of herbaceous communities (i.e., C_4 plants) in wet habitats by intensive grazing. Therefore, this study suggests a direct correlation between C_4 plant

expansion and increased grassland habitats, implying rapid expansion of these open, grassy biomes (Beerling & Osborne, 2006). The $\delta^{13}\text{C}_{\text{enamel}}$ isotope contents within samples of *H. sivalensis* from the middle Pleistocene Siwaliks of Pakistan show that *H. sivalensis* relied upon mixed to exclusive C_4 vegetation which was present preferably in the form of open grasslands. Enamel thickening and higher hypsodont indices indicate that the diet is dominantly composed of rougher and tougher vegetation (grasses). The $\delta^{18}\text{O}_{\text{enamel}}$ isotope contents indicate that hippos were relying on open water bodies like ponds for their water intake. High oxygen values show that hippos are mostly present in that environment which is evaporation insensitive and serves as a valuable resource for mammals that are more sensitive to aridity.

5 Conclusions

Our findings indicate that in the Pleistocene, the diet of *H. sivalensis* shifted from a mixed C_3/C_4 to exclusive C_4 vegetation which was present preferably in open grasslands. High $\delta^{18}\text{O}_{\text{enamel}}$ values indicate that *H. sivalensis* inhabited freshwater ponds under drier climatic conditions where they fed upon C_4 vegetation exclusively. This finding is consistent with the previously established hypothesis of grasslands dominance on the Siwalik floodplain during the Pleistocene (ref needed).

References

- Barry, J. C., & Flynn, L. J. (1989). Key biostratigraphic events in the Siwalik sequence. In *European Neogene mammal chronology* (Vol. 180, pp. 557–571).
- Beerling, D. J., & Osborne, C. P. (2006). The origin of the savanna biome. *Global Change Biology*, 12, 2023–2031.
- Boisserie, J. R., & White, T. D. (2004). A new species of Pliocene Hippopotamidae from the Middle Awash, Ethiopia. *Journal of Vertebrate Paleontology*, 24, 464–473.
- Boisserie, J. R., Zazzo, A., Merceron, G., Blondel, U., Vignaud, P., & Likies, A. (2005). Diets of modern and late Miocene hippopotamids: Evidence from carbon isotope composition and micro-wear of tooth enamel. *Palaeogeography, Palaeoclimatology, Palaeoecology*, 221, 153–174.
- Cerling, T. E., Harris, J. M., Hart, J. A., Kaleme, P., Klingel, H., Leakey, M. G., Levin, N. E., Lewison, R. L., & Passey, B. H. (2008). Stable isotope ecology of the common hippopotamus. *Journal of Zoology*, 276, 204–212.
- Lihoreau, F., & Brunet, M. (2005). The position of Hippopotamidae within Cetartiodactyla. *Proceedings of the National Academy of Sciences*, 102, 1537–1541.
- Quade, J., McIntosh, W. C., & Latorre, C. (1997). The expansion of C_4 grasses and global change in the late Miocene: Stable isotope evidence from the Americas. *Earth and Planetary Science Letters*, 146, 83–96.

- Ungar, P. S., Merceron, G., & Scott, R. S. (2007). Dental microwear texture analysis of Varswater bovids and early Pliocene paleoenvironments of Langebaanweg, Western Cape Province, South Africa. *Journal of Mammalian Evolution*, 4, 163–181.
- Vignaud, P., Douring, P., Mackaye, H. T., Likius, A., Blondel, C., Boisserie, J. R., & Brunet, M. (2002). Geology and palaeontology of the Upper Miocene Toros-Menalla hominid locality, Chad. *Nature*, 418, 152–155.



Middle to Late Cambrian Marine Transgression Depositional System of the Peri-Gondwana Terranes: An Example from Al Bashair Formation of the Huqf Region, Oman

Mohamed A. K. El-Ghali, Iftikhar Ahmed Abbasi, Olga Shelukhina, Mohamed S. H. Moustafa, Arshad Ali, Osman Salad Hersi, Mohamed Farfour, and Hezam Al-Awah

Abstract

The Al Bashair Formation corresponds to the lowermost part of the Andam Group (Haima Supergroup) that crops out in the Huqf region of central Oman. Al Bashair Formation is an important deep hydrocarbon-producing subsurface reservoir in the interior Oman Salt Basin. The current outcrop-based stratigraphic and facies analysis of the Al Bashair Formation in the Huqf region has shed new insights to better understand the spatial and temporal distribution of the depositional facies and construct a reliable depositional model. The results have shown that the Al Bashair Formation can be divided into two informal members. The lower informal member contains ca. 120 m thick interval of thinly interbedded (ca. 5–25 cm) sandstone, siltstone, and red mudstone packages with (ca. 1 m) carbonate layers. The mudstones sometimes exhibit the presence of desiccation mud cracks. The sandstones show different body fossils, such as trilobites, brachiopods, and echinoderms, trace fossils

and halite molds. The carbonate layers include stromatolites and oolitic grainstones. The oolitic grainstones show the presence of herringbone cross beddings. The upper member of the Al Bashair Formation contains about 160 m thick interval of coarsening upward cycles of red mudstones, siltstones, and sandstones. The sandstones lack body fossils and show less frequent trace fossils including Cruziana and U-shape (*Arenicolites*) borrows. The sandstones show the presence of hummocky and swaley cross-stratifications. The described rock intervals of Al Bashair Formation support deposition in tide- and frequently storm-dominated shallow marine ranging from supratidal to subtidal settings.

Keywords

Late Cambrian • Marine transgression • Peri-Gondwana • Al Bashair Formation • Huqf region • Oman

M. A. K. El-Ghali (✉) · I. A. Abbasi · M. S. H. Moustafa · M. Farfour
Earth Sciences Research Center, Sultan Qaboos University,
Muscat, Oman
e-mail: melghali@squ.edu.om

M. A. K. El-Ghali · A. Ali
Department of Earth Sciences, College of Science,
Sultan Qaboos University, Muscat, Oman

O. Shelukhina
Research and Education Center, Novosibirsk State University,
Novosibirsk, Russia

O. S. Hersi
Department of Geology, University of Regina,
Saskatchewan, Canada

H. Al-Awah
Department of Chemistry and Earth Sciences,
Qatar University, Doha, Qatar

1 Introduction

The Late Cambrian Al Bashair Formation is exclusively exposed in the Huqf-Haushi region in Central Oman and is a tight hydrocarbon-producing subsurface reservoir in the interior Oman Salt Basin (Fig. 1a–c) (Droste, 1997; Forbes et al., 2010). Stratigraphically, the Al Bashair Formation represents the lowermost part of the Andam Group (Haima Supergroup) and is overlying the Miqrat Formation and underlying the Barik Formation (Fig. 1c) (Droste, 1997; Forbes et al., 2010). Previous researchers suggested that the Al Bashair Formation was deposited in a marginal marine to shallow marine systems (Droste, 1997; Forbes et al., 2010). This study aims to utilize the collected outcrop data of the logged Al Bashair Formation from the open sections in the Haushi-Huqf region and present an appropriate depositional environment interpretation.

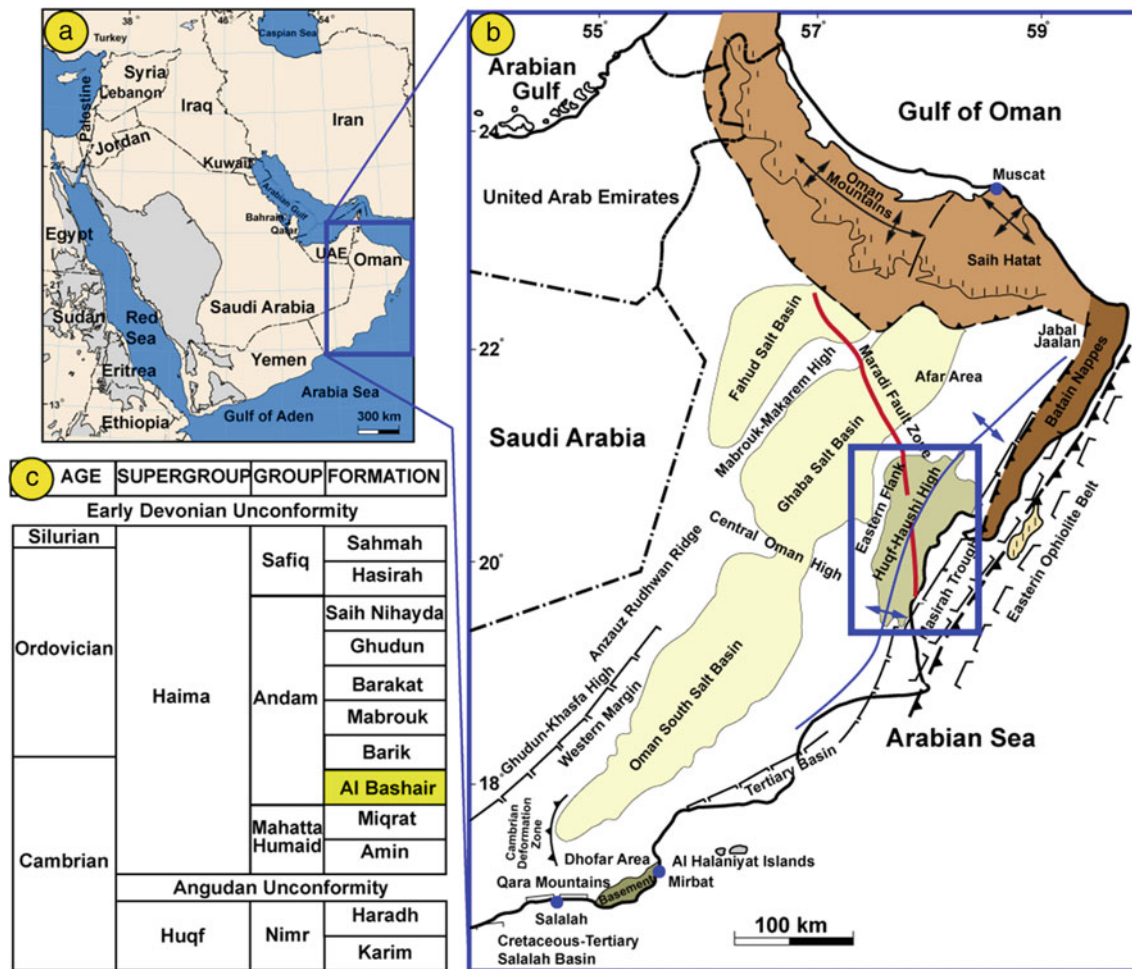


Fig. 1 Maps showing **a** the position of the Sultanate of Oman on the southeastern corner of the Arabian Peninsula and **b** the location of the studied area, namely Huqf-Haushi region in Central Oman (modified

after Droste, 1997). **c** Stratigraphic nomenclature of the Haima Supergroup showing the studied Al Bashair Formation (modified after Forbes et al., 2010)

2 Materials and Methods

To achieve the aim of this study, detailed sedimentological investigations were carried out on numerous exposed sections of the Al Bashair Formation. The investigations include lithology, grain size, bed thickness, bed contact nature, sedimentary structures, and trace fossils. These investigations were used to identify numerous lithofacies to understand the dominant depositional processes. The identified lithofacies were grouped into facies associations representing the basis for depositional environment interpretation. Moreover, the regionally correlated lithological attributes of the identified facies associations bounding surfaces enabled the subdivision of Al Bashair Formation into the two dominant lithostratigraphic informal members.

3 Results

The Al Bashair Formation, based on this study, can be subdivided into two informal members: (i) lower member, dominated by red-green mudstones, sandstones, and carbonates and (ii) upper member, dominated by red-green mudstones and sandstones (Fig. 2a).

The lower informal member of the Al Bashair Formation comprises ca. 120 m thick interval of coarsening upwards sequences of mudstones, siltstones, sandstones, and limestones (Fig. 2b). The mudstones are dominantly red and less commonly green in color. The mudstones display desiccation mud cracks. The sandstones are dominantly sheet-like bodies displaying trough cross-bedding, low angle planar cross-bedding, and seldom hummocky cross-stratification.

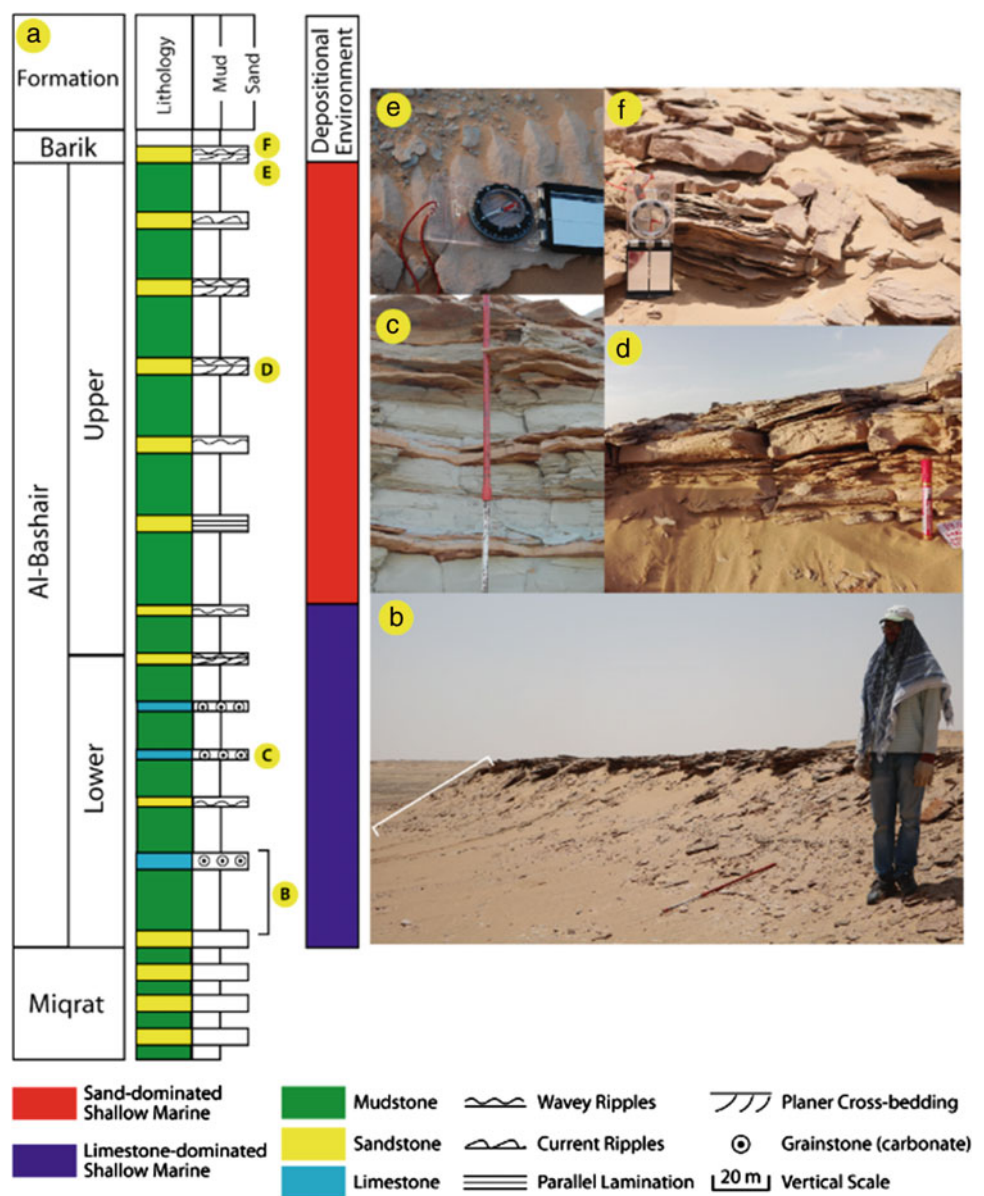
The sandstones show current and wave ripples. The sandstones contain diverse types of body fossils, such as trilobites, brachiopods, and echinoderms, trace fossils and halite molds. The limestone is dominantly composed of stromatolites and oolitic grainstones (Fig. 2c). The algal stromatolites are usually composed of irregularly laminae of micritic carbonates with some scattered quartz grains between the laminations. The oolitic grainstones display herringbone cross beddings. The upper member of the Al Bashir Formation contains about 160 m thick intervals of coarsening upward sequences of mudstones, siltstones, and sandstones. The mudstones are red in color and display desiccation mud cracks. The sandstones show low angle planar cross-bedding (Fig. 2d), and hummocky and swaley cross-stratifications and current to wave

ripples (Figs 2e–f). The sandstones lack body fossils and show less frequent trace fossils including the *Cruziana* and U-shape (*Arenicolites*) burrows.

4 Discussion

The occurrence of hummocky cross-stratification, wave ripples, fossil bodies, and trace fossils is indicative of deposition in a marine setting ranging from marginal to the storm-wave base. However, the lower informal member characterized by the presence of oolitic grainstone indicates the deposition under a high energy shallow marine conditions (Wright, 1990). Stromatolites suggest the deposition in

Fig. 2 a Composite sedimentological logs of the studied Al Bashair Formation in the Huqf-Haushi area displaying the identified lithofacies associations and depositional environmental system, and field photos showing **b** a coarsening upward cycle, **c** parallel bedding oolitic grainstone carbonate, **d** low angle planar cross-bedding sandstones, **e** plane view of the wave rippled sandstones, and **f** side view of the wave rippled sandstones



intertidal to subtidal settings. The upper informal member, which lacks the oolitic grainstones and stromatolites, was probably deposited in a relatively deeper shallow marine settings compared with the lower informal member.

5 Conclusions

This study aimed to shed new insights into the stratigraphy and depositional environment model of the Al Bashair Formation. This study revealed that:

1. The Al Bashair Formation can be subdivided into the two informal members, namely the lower and upper informal member.
2. The lower informal member is characterized by coarsening upward cycles of red-to-green mudstones and sandstones and limestones, deposited in a tidally- to storm-dominated shallow marine environment.
3. The upper informal member is characterized by coarsening upward cycles of red-to-green mudstones and

sandstones from tidally- to storm-dominated shallow marine environment.

The proposed stratigraphic and depositional environmental scheme can be used as an analogue for similar surface and subsurface rocks.

Acknowledgements This work is supported by His Majesty Strategic Grant [SR/SCI/ETHS/15/01] for Sultan Qaboos University. Thanks go to the editor's time and the reviewers' for their provided constructive comments on the final version of the manuscript.

References

- Droste, H. J. (1997). Stratigraphy of the lower Palaeozoic Supergroup of Oman. *GeoArabia*, 2, 419–471.
- Forbes, G. A., Jansen, H. S. M., & Schreurs, J. (2010). Lexicon of Oman, subsurface stratigraphy. *GeoArabia Special Publication*, 5.
- Wright, V. P. (1990). Carbonate sediments and limestones: Constituents. In M. E. Tucker & V. P. Wright (Eds.), *Carbonate sedimentology* (pp. 1–27). Blackwell Scientific.



Early to Middle Cambrian Fluvial-Aeolian Interplay and Marine Transgression Depositional System of the Peri-Gondwana Terranes: An Example from the Amin Formation of the Haushi-Huqf Region, Oman

Mohamed A. K. El-Ghali, Iftikhar Ahmed Abbasi, Olga Shelukhina, Mohamed S. H. Moustafa, Arshad Ali, Osman Salad Hersi, Mohamed Farfour, and Hezam Al-Awah

Abstract

The Amin Formation, the lowermost part of the Mahatta Humaid Group (Haima Supergroup), is a tight oil-producing reservoir in the interior Oman Salt Basin. It is exposed in the Huqf region of central Oman and was previously interpreted as braided fluvial, aeolian, and dry sabkha deposits. This study is an outcrop-based stratigraphic and facies analysis to furnish new insights into the Amin Formation in the Huqf region to understand the spatial and temporal distribution of the depositional facies and interpret the depositional environment. The results have shown that the formation can be stratigraphically divided into three informal members. The lowermost member is poorly exposed and comprises intervals of red to reddish-green claystones and siltstones enclosing greenish-gray, very fine-grained sandstone lenses. This member grades upward into brown, fine- to medium-grained, trough cross-bedded sandstone. The member fills relatively low topographic depression on the underlying Huqf Supergroup surface and lacks marine signatures reflecting deposition in an isolated inland freshwater lake. The middle member comprises intervals of cobble conglomerates grading upward into pebbly to granule

sandstones, coarse-grained sandstones, and rarely, siltstones and claystones. The conglomerates are clast- to matrix-supported of large-scale, trough- to tabular cross-bedded, exhibiting a low relief erosional base. The interbedded pebbly to granule sandstones contain cosets of high- to low-angle trough and tabular cross-bedding with pebble lags at the bottom. The claystone, occasionally intervening in the sandstone, is yellow and parallel-laminated, enclosing lenticular-shaped bodies of siltstones. The erosional scours with lag deposits, fining upward trends, and lack of marine features indicate deposition in braided channels where the mudrocks represent overbank, floodplain, and crevasse splay. The uppermost member is fine- to very fine-grained sandstone interval with trough and tabular cross-bedding, ladder to wave ripples, and horizontal (*Cruziana*-like) to inclined (*Psilonichnus*-like) trace fossils reflecting deposition in shallow marine conditions. There are also localized transverse dunes of very fine- to fine-grained sandstones comprising cosets of medium to high-angle planar cross-bedding with current ripples reflecting their deposition as aeolian dunes. The Amin Formation can be envisaged as a complex system that is graded from an inland freshwater lake to fluvial (lower two members) and shoreface environments with subordinate coastal aeolian dunes in its upper member.

M. A. K. El-Ghali (✉) · A. Ali
Earth Sciences Research Center, Sultan Qaboos University,
Muscat, Oman
e-mail: melghali@squ.edu.om

M. A. K. El-Ghali · I. A. Abbasi · M. S. H. Moustafa · M. Farfour
Department of Earth Sciences, College of Sciences,
Sultan Qaboos University, Muscat, Oman

O. Shelukhina
Research and Education Center, Novosibirsk State University,
Novosibirsk, Russia

O. S. Hersi
Department of Geology, University of Regina,
Saskatchewan, Canada

H. Al-Awah
Department of Chemistry and Earth Sciences,
Qatar University, Doha, Qatar

Keywords

Early to Middle Cambrian · Fluvial · Aeolian · Marine transgression · Peri-Gondwana · Amin Formation · Huqf region · Oman

1 Introduction

The Early-Middle Cambrian Amin Formation is well exposed in the Huqf-Haushi region in Central Oman. It is a tight oil-producing subsurface reservoir in the interior Oman

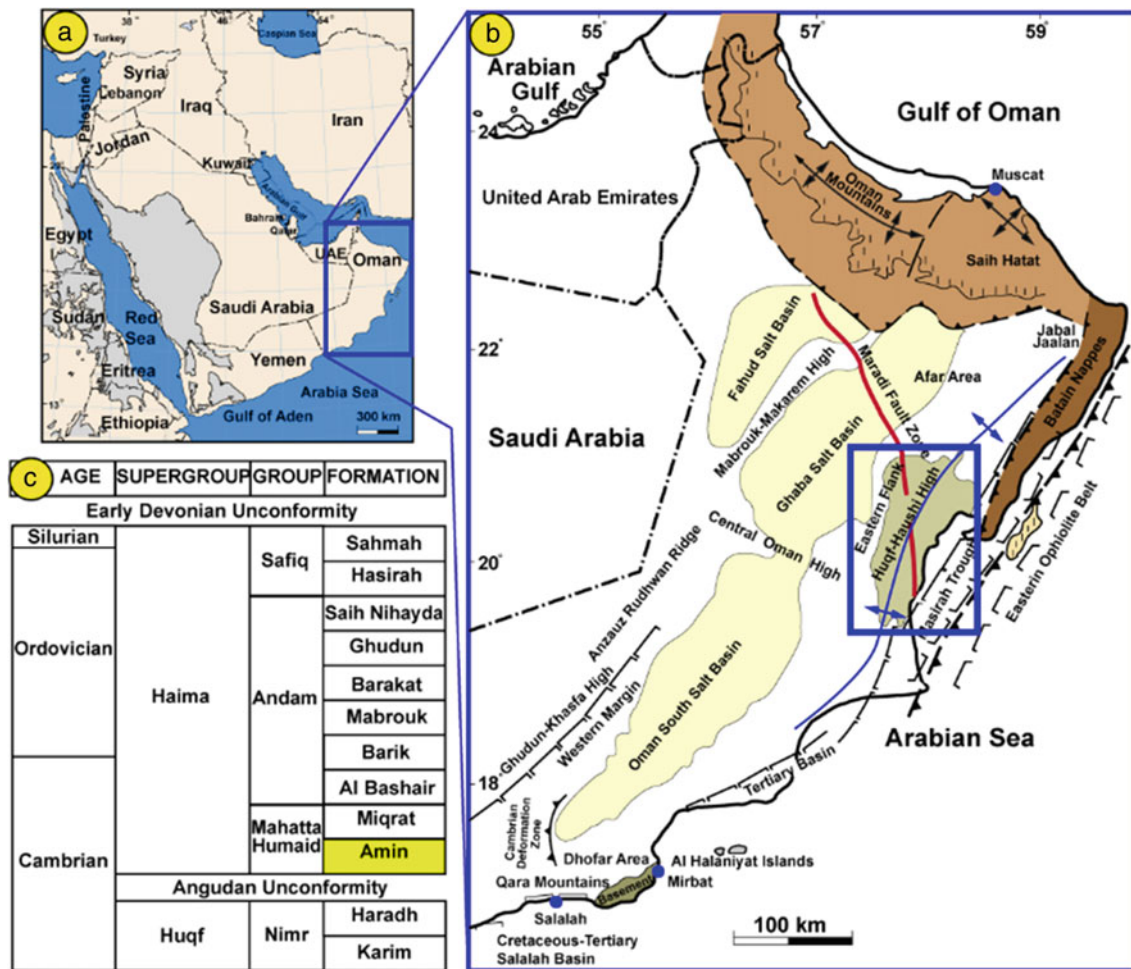


Fig. 1 Maps showing **a** the position of the Sultanate of Oman on the southeastern corner of the Arabian Peninsula and **b** the location of the studied area, namely Huqf-Haushi region in Central Oman (modified

after Droste, 1997). **c** Stratigraphic nomenclature of the Haima Supergroup showing the studied Amin Formation (after Forbes et al., 2010)

Salt Basin (Figs. 1a–c) (Droste, 1997; Forbes et al., 2010). Stratigraphically, the Amin Formation represents the lowermost part of the Mahatta Humaid Group (Haima Supergroup). It unconformably overlies the Huqf Supergroup and conformably underlies the Miqrat Formation (Fig. 1c) (Droste, 1997; Forbes et al., 2010). The Amin Formation was deposited in braided fluvial, aeolian, and dry sabkha systems (Droste, 1997; Forbes et al., 2010). This study aims to utilize the newly collected outcrop data of the logged Amin Formation outcropped sections in the Haushi-Huqf region and propose a suitable depositional environment interpretation.

2 Materials and Methods

Detailed sedimentological investigations were carried out on numerous well-exposed sections of the Amin Formation. The investigations include lithology, grain size, bed

thickness, bed contact nature, sedimentary structure, and trace fossils. These investigations were used to identify numerous lithofacies to understand the dominant depositional processes. The identified lithofacies were grouped into facies associations representing the basis for depositional environment interpretation. Moreover, the regionally correlated lithological attributes of the identified facies associations helped the subdivision of the Amin Formation into three dominant lithostratigraphic informal members.

3 Results

This study subdivided the Amin Formation in the studied outcrops into three informal members (Fig. 2a), namely (i) lower-dominated red-green mudstones member, (ii) middle-dominated conglomerate-conglomeratic sandstones member, and (iii) upper-dominated sandstone member. The lower informal member appears to fill relatively low

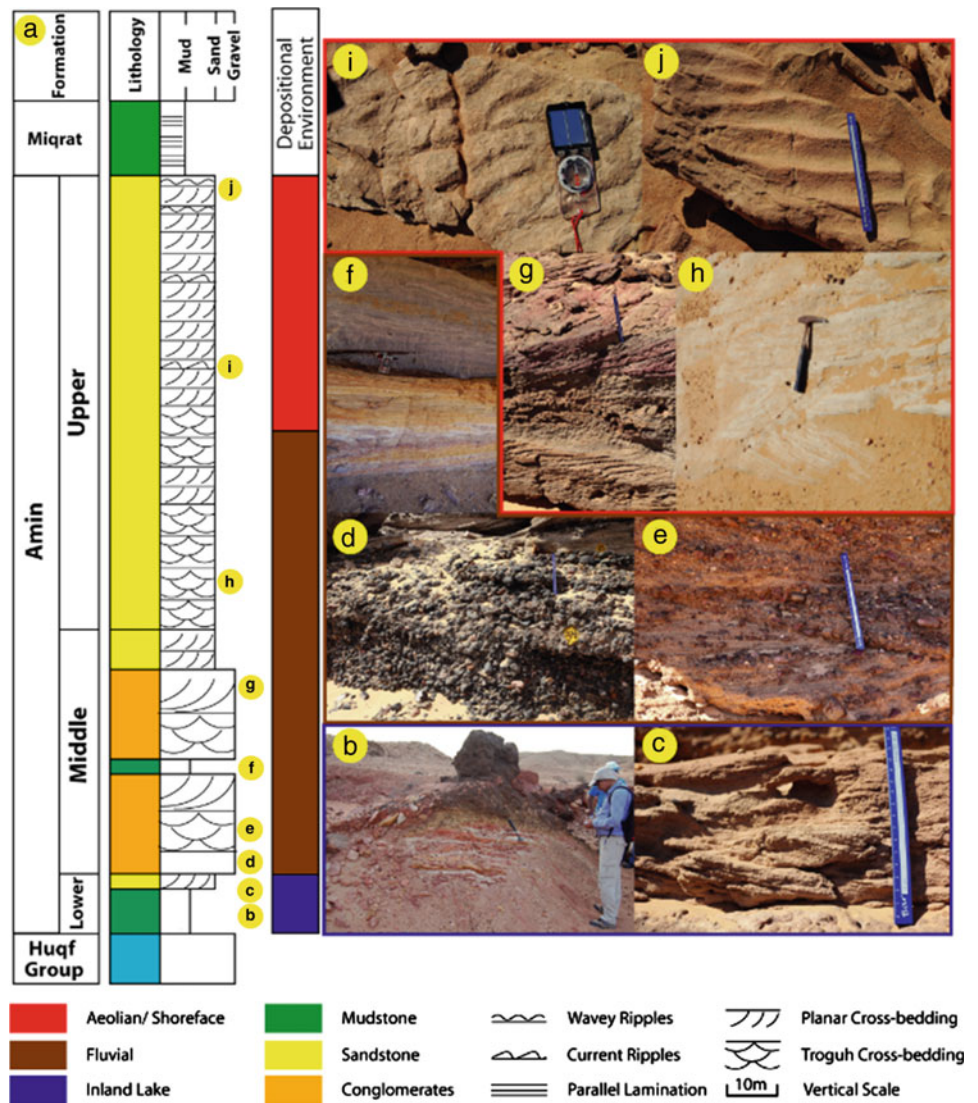
topographic relief on the Angudan Unconformity. This member is dominantly red and green claystones and siltstones, passing upward into trough cross-bedded sandstones (Figs. 2b, c). The informal middle member is composed of a meter-scale thickness of clast- and sandy matrix-supported conglomerates that interbed with very coarse to pebbly sandstones and barely end with claystones. The conglomerates are made of large-scale troughs and tabular cross-beddings with erosive bases scouring down into the underlying sandstones and conglomerates (Figs. 2d, e). The sandstones are made of lateral sheets to lenticular bodies of troughs and planar cross-beddings with erosive bases. The claystones are rare, white-yellow, reddish, and very poorly preserved (Fig. 2f). The informal upper member comprises amalgamated sets of planar and small- and large-scale trough cross-bedding sandstone—both planar and trough cross-beddings show high- and low-angle

bedforms (Figs. 2g, h). Occasionally, the planar cross-bedding sandstones are interbedded with the trough cross-bedding. The trough cross-bedding sandstones usually show scouring surfaces with lag deposits at the base. The trough and planar cross-bedding sandstones grade, in most cases, upwards into current ripples and, in rare cases, wave ripples in the uppermost part (Figs. 2i, j). Moreover, ladderback ripples and trace fossils are observed.

4 Discussion

The occurrences of the lower informal member deposits within the depression vicinity and lacking marine signatures suggest deposition in shallow-depth inland freshwater lakes. The claystone and siltstone facies represent the settlement of the suspension load within the lake depocenter.

Fig. 2 a Composite sedimentological logs of the studied Amin Formation in the Huqf-Haushi region displaying the identified lithofacies associations and depositional environmental system, b poorly exposed mudstone, c planar cross-bedding sandstones, d clast- to mud-supported clast conglomerate, e planar cross-bedding conglomeratic sandstones, f mudstone, g planar cross-bedding sandstone, h trough cross-bedding sandstones, i current ripples sandstones, and j wave ripples sandstones



The relatively shallow depth nature of the lake could facilitate the presence of sporadic exposures and thus partiality resulted in oxidizing the claystone facies with red color. The trough cross-bedded sandstones may record deposition along the lake margins. The fining-upward cycles with erosive bases of the informal middle member, conglomerate-sandstone-claystone nature is supportive of deposition in a braided fluvial system (cf. Bhattacharyya et al., 2015). The conglomerates, pebbly sandstones, and sandstone facies represent channel bars, whereas the claystones facies represent floodplains (Bhattacharyya et al., 2015). The scarcity of claystones facies could be attributed to the non-deposition or erosion due to high energy in the braided fluvial system; the later process may result in partial or entire erosion of pre-deposited floodplain facies. The fining-upward nature with scouring and presence of lag deposits at bases followed by the trough and planar cross-bedding and current ripples at the top of the informal upper member represent deposition in channel bars. The preservation of wave ripples within the uppermost part of the informal upper member and ladder-back ripples and trace fossils indicates marine invasion and thus may represent beach facies (cf. Rossi et al., 2017). The meter-scale and high-angle planar cross-bedding intercalated with the beach facies suggests the deposition of aeolian sand dunes near the shoreline (cf. Schwan, 1988).

5 Conclusions

This study aimed to shed new insights into the stratigraphy and depositional environment model of the Amin Formation. This study revealed that:

1. The lower informal member is red-to-green mudstones and sandstones of shallow-depth inland freshwater lakes system,
2. The informal middle member is dominantly conglomerate to conglomeritic sandstones of braided fluvial system, and
3. The informal upper member is predominantly sandstones of fluvial, aeolian, and beach systems. The proposed stratigraphic and depositional environmental scheme can be used as an analogue for similar subsurface equivalents.

Acknowledgements This work is supported by His Majesty Strategic Grant [SR/SCI/ETHS/15/01] for Sultan Qaboos University. The editors and the reviewers are thanked for their provided constructive comments.

References

- Bhattacharyya, P., Bhattacharya, J. P., & Khan, S. D. (2015). Paleo-channel reconstruction and grain size variability in fluvial deposits, Ferron Sandstone, Notom Delta, Hanksville, Utah. *Sedimentary Geology*, 325, 17–25.
- Droste, H. J. (1997). Stratigraphy of the lower Palaeozoic Supergroup of Oman. *GeoArabia*, 2, 419–471.
- Forbes, G. A., Jansen, H. S. M., & Schreurs, J. (2010). Lexicon of Oman, subsurface stratigraphy. *GeoArabia Special Publication*, 5.
- Rossi, V. M., Perillo, M. M., Steel, R. J., & Olariu, C. (2017). Quantifying mixed-process variability in shallow-marine depositional systems: What are sedimentary structures really telling us? *Journal of Sedimentary Research*, 87, 1–15.
- Schwan, J. (1988). The structure and genesis of Weichselian to early Holocene aeolian sand sheets in western Europe. *Sedimentary Geology*, 55, 197–232.



Lithofacies Associations and Depositional System of the Muti Formation, Oman Mountains

Jenan Ahmed Attar, Iftikhar Ahmed Abbasi, Mohamed El-Ghali, Abdul Rahman Al- Harthi, and Abdulrazaq Al- Sayigh

Abstract

The Upper Cretaceous Muti Formation of the Aruma Group was the first unit deposited in the Oman foreland basin in the Oman Mountains. The Oman foreland basin is a major hydrocarbon-producing basin with great future exploration potential. A few studies were published in the early 1990; however, no detailed work on the sediments of the Muti Formation has been done since then. The closure and compression of the southeast margin of the Tethys Ocean during the Upper Cretaceous resulted in thrusting and obduction events and erosion of the Arabian platform, known as the Wasia-Aruma break. The Semail Ophiolite and Hawasina Complex were obducted over the eastern margin in northeast Oman, and the platform drowned, flexed, and faulted, resulting in the foreland basin development. The Muti Formation is well exposed around the Jabal Akhdar Dome, and a total of 14 outcrop sections are measured and described to identify the lithofacies associations and depositional setting of the formation. These lithofacies are correlated across various sections to help understand their distribution and depositional environments. The Muti Formation thickness ranges from 13.4 to 179 m and comprises nine lithofacies. These lithofacies are grouped into four lithofacies associations, namely wackestone to mudstone,

monomictic conglomerate, laminated claystone, and ferruginous clays. Based on these results, the formation is lithologically subdivided into a lower and upper parts. A diverse fossil assemblage was observed within the wackestone to mudstone lithofacies, including ammonites, bryozoans, bivalves, brachiopods, and gastropods. The Muti Formation records the transition from a passive margin to a foreland basin deposited in a shallow marine environment. The lower part is dominated by wackestone to mudstone lithofacies association rich in fossils accumulated in the middle carbonate shelf. The upper part of the formation is composed of siliciclastic lithofacies deposited on the outer shelf under low energy conditions. The findings of this study shed light on the lithofacies distribution and depositional system of the Muti Formation across the foreland basin.

Keywords

Aruma Group • Oman Foreland Basin • Muti Formation • Jabal Akhdar Dome • Oman Mountains

1 Introduction

The Muti Formation belongs to the Aruma Group, deposited in the Oman foreland basin (Fig. 1) during the Late Cretaceous (Ali et al., 2013; Boote et al., 1990; Glennie et al., 1974). The Oman Foreland Basin is a significant hydrocarbon-producing basin with substantial future exploration potential. The basin developed because of the Semail Ophiolite and Hawasina Nappe emplacement over the northeast part of the Arabian platform (Glennie et al., 1974; Warburton et al., 1990). Based on seismic data, the basin is asymmetric in shape and deepest along the northern east margin of Oman Mountains and thinning to the west with thicknesses up to 4.3 km (Ali et al., 2013; Cooper et al., 2014). The earliest sediments deposited in the foreland basin

J. A. Attar (✉) · I. A. Abbasi · M. El-Ghali · A. Al- Sayigh
Department of Earth Sciences, Sultan Qaboos University,
Muscat, Oman
e-mail: jenanattar@hotmail.com

M. El-Ghali
Earth Science Research Center, Sultan Qaboos University,
Muscat, Oman

A. R. Al- Harthi
Petroleum Development of Oman, Muscat, Oman

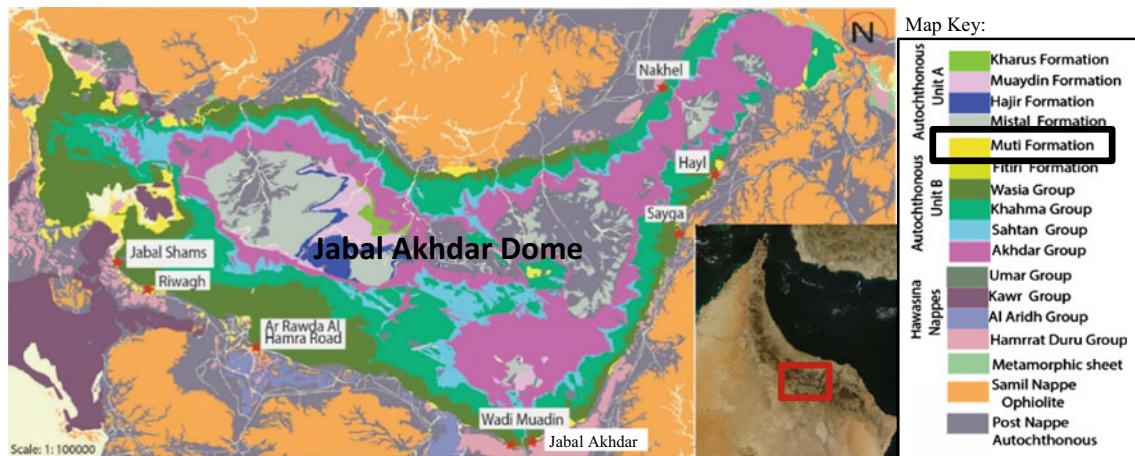


Fig. 1 Location and geological map of the study area showing Jabal Akhdar Dome in northern Oman (red square) and the locations of studied outcrops in the eight different regions; (Rustaq map, Nakhal

map and Birkat Al Mawz map). Modified after Beurrier (1986), Rabu (1986) and Hutin (1986)

belong to the Muti Formation, subdivided into Sayga and Riyamah members in the Oman Mountains. The Sayga Member is well exposed around Jabal Akhdar Dome (Fig. 1), Saih Hatat, and Jebel Salakh (Cooper, 1990; Glennie et al., 1974; Robertson, 1987) and is described in detail in this study. The outcrops of the Muti Formation correlate to the Shargi Member of the Fiqa Formation in the subsurface (Forbes et al., 2010). The Muti Formation (Sayga Member) lies unconformably over the Natih Formation or Mahil Formation and underlies either the Hawasina Nappe or Samail Ophiolite Nappe (Beurrier, 1986; Rabu, 1986; Robertson, 1987). This research aims to study the stratigraphy and lithology of the Muti Formation (Sayga member) around Jabal Akhdar Dome.

2 Materials

To achieve the aim of this research, fieldwork was carried out in eight different locations around Jabal Akhdar Dome; Nakhal, Hayl, Sayga, Wadi Muadin, Jabal Akhdar, Riwaq, Ar Rawda Al Hamra road, and Jabel Shams areas (Fig. 1). A total of 14 surface sections cropped out at the Muti Formation have been examined; 10 of them have been logged and discussed in detail, while samples from the other four sections have been collected. In the latter sections, it was difficult to identify their upper and lower contact, because of their monotonous shaley lithofacies. The first ten sections were studied to identify the lithofacies and lithofacies associations based on their lithology and texture. These lithofacies were correlated across the area to understand the distribution and depositional environment of the Muti Formation. Genetically related lithofacies are grouped into four different lithofacies associations.

3 Results

The base of the Muti Formation in the studied areas is marked by a hardground surface (Fig. 2a). The thickness of examined sections ranges from 13.4 to 179 m. The Muti Formation is divided into a lower and upper parts, based on various lithofacies. These lithofacies are classified into: wackestone to mudstone, monomictic conglomerate, laminated claystone, and ferruginous clays (Table 1). The wackestone to mudstone and facies association are well developed in the lower part of the Muti Formation and contain a diverse fossil assemblage, such as ammonites, bryozoans, bivalves, brachiopods, and gastropods (Fig. 2b, c). It consists of bedded limestone, micrite, and nodular limestone. The monomictic conglomerate facies association constitutes a small portion of the Muti Formation. It is subdivided into two lithofacies: based on their texture and dominant clast type (chert and carbonate). These lithofacies are oligomictic breccia and paraconglomerate. The laminated claystone lithofacies association is mainly deposited in the upper part of the Muti Formation. This facies association is composed of shale, which splits into mm-thick flakes, and claystone, compacted and well bedded. The last facies association contains iron-rich sediments and Ferruginous clays. The latter constitutes a minor proportion of the Muti Formation and is divided into iron bed and red clay.

4 Discussion

The lithofacies of the Muti Formation indicates its deposition in a shallow marine environment. The wackestone to mudstone lithofacies associated with well-preserved fossils

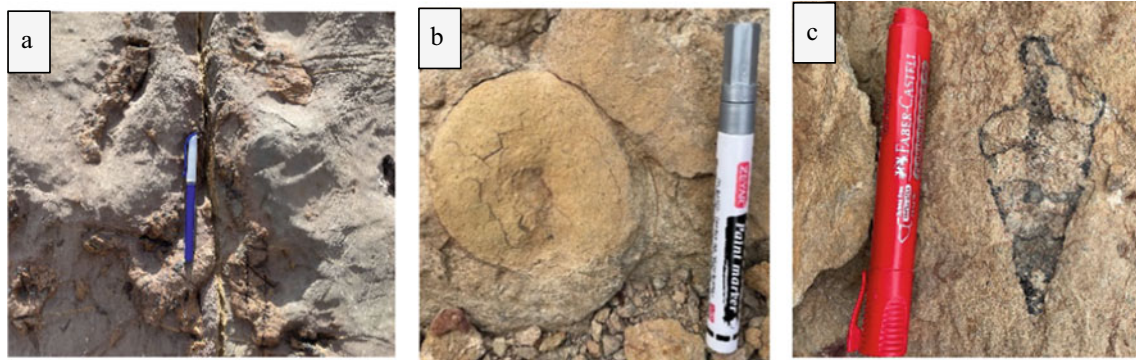


Fig. 2 Field photographs showing **a** hardground surface, **b** ammonite and **c** gastropod

Table 1 A summary table showing the facies association, lithofacies, distribution, and properties

Facies association	Facies code	Lithofacies	Distribution/properties
FA1 wackestone to mudstone	<ul style="list-style-type: none"> • BL • MI • NL 	<ul style="list-style-type: none"> • Bedded limestone • Micrite • Nodular limestone 	Found in the lower part of Fm. and contains diverse fossil assemblage (ammonites, bryozoans, bivalves, brachiopods and gastropods) (Fig. 2), iron concretion, clasts (chert and carbonate), and veins filled by calcite. NL, the nodules are gray varying from 5 to 20 cm in diameter, embedded in a calcareous matrix
FA2 monomictic conglomerate	<ul style="list-style-type: none"> • OB • PC 	<ul style="list-style-type: none"> • Oligomictic breccia • Paraconglomerate 	Constitutes a small portion of the Muti Fm. in the N and NE portion and dominant in the S. Two groups of clast types are recognized: (1) angular black color chert and (Sg and Hy sections), (2) rounded gray color carbonate (Ma, RHR, Ha, and S sections)
FA3 laminated claystone	<ul style="list-style-type: none"> • SH • CL 	<ul style="list-style-type: none"> • Shale • Claystone 	Discovered in the upper part of the Muti Fm. SH, it is soft and splits easily into mm-thick flakes, CL compacted
FA4 ferruginous clays	<ul style="list-style-type: none"> • IB • RC 	<ul style="list-style-type: none"> • Iron bed • Red clay 	Constitutes a minor proportion of the Muti Fm. IB very hard bed contains black color chert clasts at the surface. RC found in different forms such as soft, massive, and strips

in the lower part of the Muti Formation indicate that deposition took place under calm to moderate energy condition including warm water settings characterized by normal marine salinity (Boggs, 2001; James & Walker, 1992; Scholle et al., 1983). On the other hand, the siliciclastic lithofacies in the upper part of the Muti Formation were deposited on the outer shelf. When there is a sediment influx, the Muti Formation contains claystone and shale lithofacies. The source of the influx could be from the moving allochthonous sheet. The laminations in claystone indicate fluctuations in depositional conditions due to changes in clay contents and mineral composition. The claystone was deposited under low energy conditions below the wave/storm currents (Boggs, 2001; Flugel, 2010). The monomictic conglomerate developed downslope is due to significant thrusts and gravity sliding (Boggs, 2001). The well-rounded carbonate clasts from the Arabian platform (Wasia Group) were transported long distances and deposited within channels in the South and Southeast portions of Jabal Akhdar Dome. The angular black color chert clasts

found in the north and northeast sections of Jabal Akhdar Dome. The source of cherts was derived mainly from the Hawasina allochthonous units (Robertson, 1987). The ferruginous clays were deposited in the deeper part of the basin when the sedimentation rates were low and clay was exposed to oxidizing water for a long time (Boggs, 2001).

5 Conclusions

This research was conducted on the surface section of the Upper Cretaceous Muti Formation, located in the Oman foreland basin, to identify its lithofacies and depositional environment around Jabal Akhdar Dome. This study revealed the following:

- (1) The total thickness of the Muti Formation ranges from 13.4 to 179 m.
- (2) The Muti Formation is lithologically subdivided into an upper clastic rocks and lower calcareous rocks.

- (3) The Muti Formation was deposited in a shallow marine environment in the middle and outer part of the carbonate shelf.

References

- Ali, M. Y., Watts, A. B., & Searle, M. P. (2013). Seismic stratigraphy and subsidence history of the United Arab Emirates (UAE) rifted margin and overlying foreland basins. *Frontiers in Earth Sciences*, 5, 127–143.
- Beurrier, M. (1986). *Geological map, Oman 1:100,000. Sheet NF 40-3D*. Ministry of Petroleum and Minerals.
- Boggs, S. (2001). *Principles of stratigraphy and sedimentology* (3rd ed.). Prentice Hall, America.
- Boote, D. R. D., Mou, D., & Waite, R. I. (1990). Structural evolution of the Suneinah Foreland, Central Oman Mountains. *Geological Society Special Publication*, 49, 397–418.
- Cooper, D. J. W. (1990). Sedimentary evolution and palaeogeographical reconstruction of the Mesozoic continental rise in Oman: Evidence from the Hamrat Duru Group. *Geological Society Special Publication*, 49, 161–187.
- Cooper, D. J. W., Ali, M. Y., & Searle, M. P. (2014). Structure of the northern Oman Mountains from the Semail Ophiolite to the foreland basin. *Geological Society, London, Special Publications*, 392(1), 129–153.
- Flügel, E. (2010). *Microfacies of carbonate rocks* (2nd ed.). Springer-Verlag Berlin Heidelberg.
- Forbes, G. A., Janseni, H. S. M., & Schreurs, J. (2010). Lexicon of Oman subsurface stratigraphy. *GeoArabia*.
- Glennie, K. W., Boeuf, M. G. A., Hughes Clarke, M. W., Moody-Stuart, M., Pilaar, W. F. H., & Reinhardt, B. M. (1974). *Geology of the Oman Mountains (parts 1, 2 and 3)*, *Verhandelingen Koninklijk Nederlands geologisch mijnbouwkundig Genootschap*.
- Hutin, G. (1986). *Geological map, Oman 1:100,000. Sheet NF 40-7B*. Ministry of Petroleum and Minerals.
- James, N. P., & Walker, R. G. (1992). *Facies models: Response to sea level changes* (2nd ed.). Geological Association of Canada.
- Rabu, D. (1986). *Geological map, Oman 1:100,000. Sheet NF 40-3E, Nakhl*. Ministry of Petroleum and Minerals.
- Robertson, A. H. F. (1987). Upper Cretaceous Muti Formation: Transition of a Mesozoic carbonate platform to a foreland basin in the Oman Mountains. *The Journal of the International Association of Sedimentology*, 34(6), 1123–1142.
- Scholle, P. A., Bebout, D. G., & Moore, C. H. (1983). Carbonate depositional environments. In *American Association of Petroleum Geologists*.
- Warburton, J., Burnhill, T. J., Graham, R. H., & Isaac, K. P. (1990). The evolution of the Oman Mountains Foreland Basin. *Geological Society Special Publication*, 49, 419–427.



Middle Cambrian Marine Transgressive-Regressive Depositional System of the Peri-Gondwana Terranes: An Example from Miqrat Formation of the Haushi-Huqf Region, Oman

Mohamed A. K. El-Ghali, Iftikhar Ahmed Abbasi, Olga Shelukhina, Mohamed S. H. Moustafa, Arshad Ali, Osman Salad Hersi, Mohamed Farfour, and Hezam Al-Awah

Abstract

The Miqrat Formation is the uppermost lithostratigraphic unit of the Mahatta Humaid Group (Haima Supergroup) that crops out in the Huqf region of central Oman. The formation is among the complex, deep tight gas reservoirs in the interior Oman Salt Basin. The formation has been previously interpreted as deposits of interconnected ephemeral playa lakes, aeolian dunes, and wet and dry sabkha environments. Lithologic reevaluation of the rocks in the Huqf region unveils new geologic information that allows reassessment of the spatial and temporal distribution of the depositional facies and the construction of the updated and improved depositional model. The Miqrat Formation can be stratigraphically divided into three informal members. The lowermost member is about 80-m-thick section characterized by coarsening-upward cycles of dark brown to reddish-brown mudstones to sandy siltstones that grade to fine-grained sandstones. The sandstones show parallel to low-angle cross lamination and wave ripples, whereas the mudstone and siltstone interbeds display large-scale desiccation cracks. The middle member contains about 40-m-thick light-brown

to buff, fine- to coarse-grained sandstone containing low- to high-angle tabular to trough cross-bedding and wave ripples. Near the uppermost part of this unit, the sandstone contains *Thalassinoides* trace fossils, which are reported here for the first time, indicating the deposition in the marine system—subtidal environments. The uppermost member of the formation is poorly exposed interval and lithologically appears to be similar to that of the lower member. The sedimentary properties and trace fossils suggest that the formation accumulated in a marginal marine setting characterized by tidally-influenced supratidal to intertidal environments (lower and upper members) and subtidal (middle member) depositional setting. This interpretation may further indicate a possibly 3rd-order sea level change represented by initial low sea level (lower member) through relatively higher sea level (middle member) and lastly back to lower sea level (upper member).

Keywords

Late Cambrian • Transgression-regression • Peri-Gondwana • Miqrat Formation • Huqf region • Oman

M. A. K. El-Ghali (✉) · A. Ali
Earth Sciences Research Center, Sultan Qaboos University,
Muscat, Oman
e-mail: melghali@squ.edu.om

M. A. K. El-Ghali · I. A. Abbasi · M. S. H. Moustafa · M. Farfour
Department of Earth Sciences, College of Science,
Sultan Qaboos University, Muscat, Oman

O. Shelukhina
Research and Education Center, Novosibirsk State University,
Novosibirsk, Russia

O. S. Hersi
Department of Geology, University of Regina, Saskatchewan,
Canada

H. Al-Awah
Department of Chemistry and Earth Sciences, Qatar University,
Doha, Qatar

1 Introduction

The Middle Cambrian Miqrat Formation is exceptionally exposed in the Huqf-Haushi region in Central Oman and represents a complex, deep tight gas-producing subsurface reservoir in the interior Oman Salt Basin (Figs. 1a–c) (Droste, 1997; Forbes et al., 2010). Stratigraphically, the Miqrat Formation represents the uppermost part of the Mahatta Humaid Group (Haima Supergroup) and is overlying the Amin Formation and underlying Al-Bashair Formation (Fig. 1c) (Droste, 1997; Forbes et al., 2010). It is

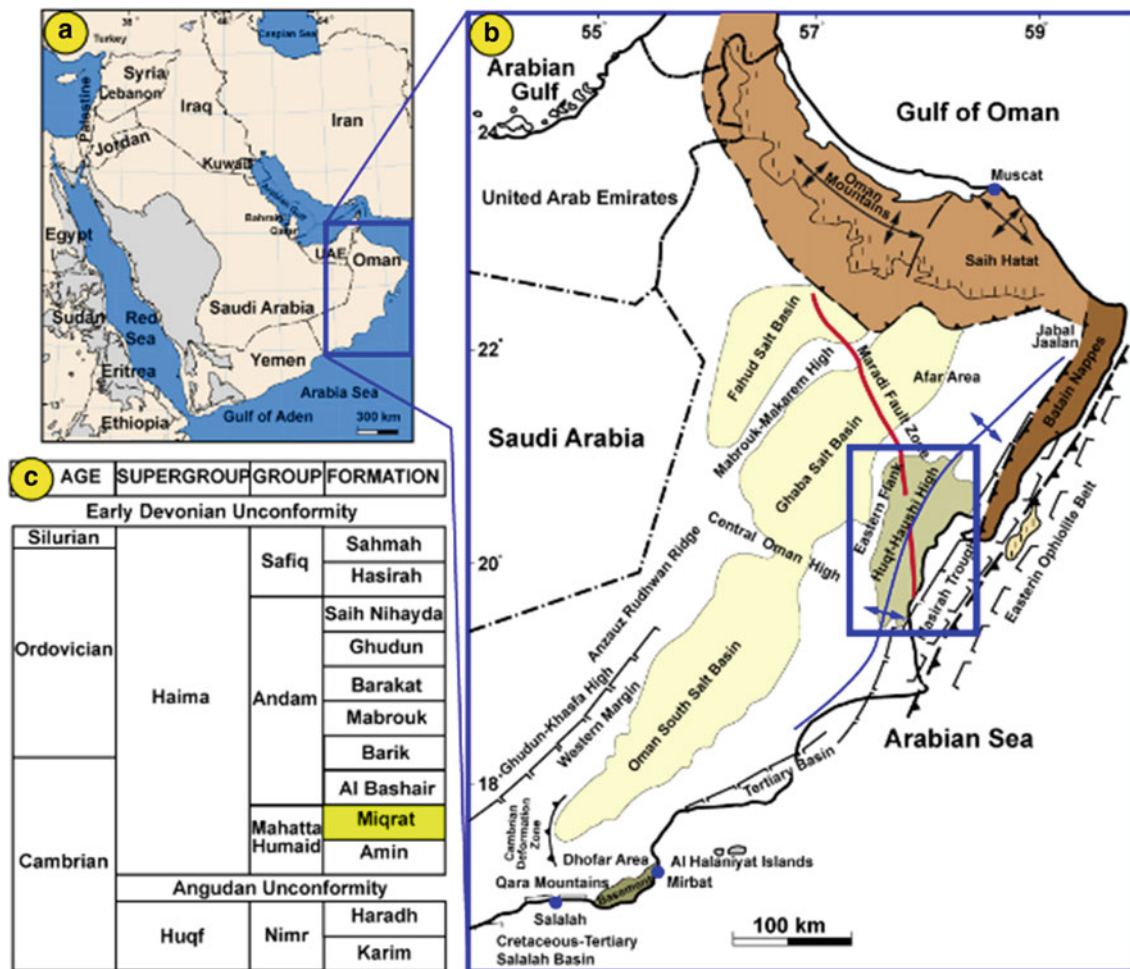


Fig. 1 Maps showing **a** the position of the Sultanate of Oman on the southeastern corner of the Arabian Peninsula and **b** the location of the studied area, namely Huqf-Haushi region in Central Oman (modified

after Droste, 1997). **c** Stratigraphic nomenclature of Haima Supergroup showing the studied Miqrat Formation (after Forbes et al., 2010)

known in the literature that Miqrat Formation was deposited in interconnected ephemeral playa lakes, aeolian dunes, and wet and dry sabkha systems (Droste, 1997; Forbes et al., 2010). This study aims to use the newly gathered outcrop data of the logged Miqrat Formation outcropped sections in the Haushi-Huqf region and provides a proper depositional model.

2 Materials and Methods

A detailed sedimentological study was performed on several exceptionally exposed sections of Miqrat Formation. The study focused on investigating lithology, grain size, bed thickness, bed contact nature, sedimentary structure, and trace fossils. These investigations were taken as a basis for the recognition of numerous lithofacies to understand the governing depositional processes. The recognized lithofacies were grouped into facies associations forming the basis for

depositional environment interpretation. Moreover, the regionally correlated lithological attributes of the identified facies associations enabled the subdivision of Miqrat Formation into three lithostratigraphic informal members.

3 Results

According to this study, the Miqrat Formation can be subdivided into three informal members (Figs. 2a): (i) lower-dominated red-green mudstones, (ii) middle-dominated sandstones, and (iii) upper-dominated red-green mudstones. However, the lower and upper informal members are similar although the upper informal member is poorly exposed. The lower and upper informal member is dominantly composed of mottled red siltstones and very fine-grained sandstones; it forms fairly coarsening-upward cycles in which the sandstones beds thicken upward (Figs. 2b–e). The sandstones display a very weakly developed trough

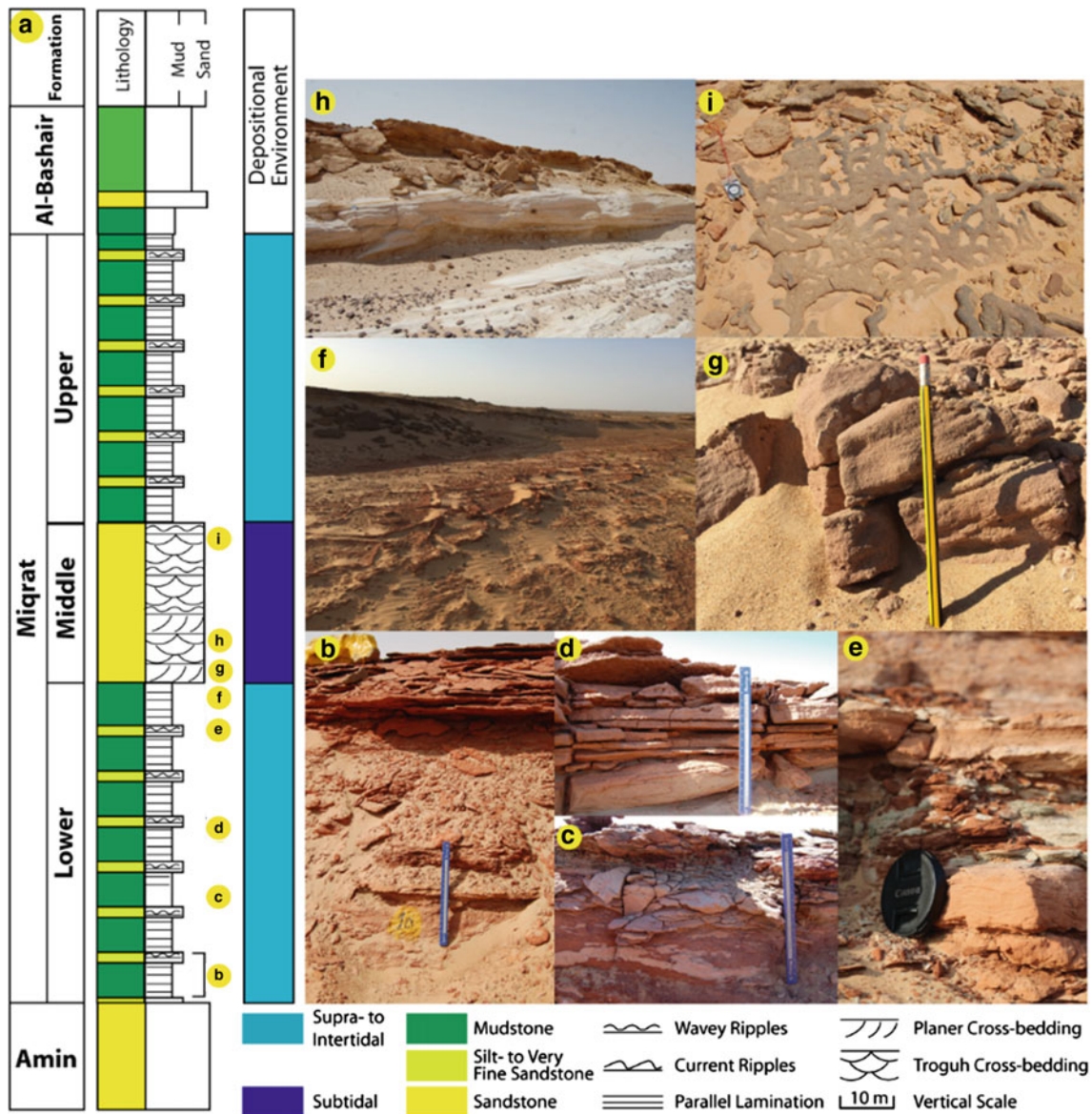


Fig. 2 a Composite sedimentological logs of the studied Miqrat Formation in Huqf-Haushi area displaying the identified lithofacies associations and depositional environmental system, b coarsening-upward cycle, c mottled mudstones, d parallel lamination

sandstones, e wave rippled sandstones, f desiccation cracks, g planar cross-bedding sandstones, h trough cross-bedding sandstones, i *Thalassinoides* like trace fossils

cross-bedding and sometimes low-angle planar cross-bedding and starved ripples. The sandstone and siltstones are laterally traceable for km's scale. The upper contact of lower informal member is marked by a meter scale of desiccation cracks on tops (Fig. 2f). The middle informal member is dominantly composed of very fine- to coarse-grained sandstones that interbed with siltstones (Figs. 2g-h). The sandstones appear to be quartz to feldspathic arenites in composition. The sandstones are made of amalgamated sets of large-scale, low-angle planar, and trough cross-bedding, mostly with current and wave ripples at tops (Fig. 2h). The sandstones of the uppermost part of this informal member

were bioturbated; at least 5 horizons of trace fossils (*Thalassinoides* like trace fossils) were recognized (Fig. 2i). The sandstones are laterally traceable for km's scale. The siltstones are parallel laminated and sometimes display ripples (Fig. 2).

4 Discussion

The interpretation of the depositional environment of lower and upper informal members can be arguable; it has been interpreted by Buckley (1997) as aeolian, sabkha, and playa

lake environment. However, the presence of marine signatures immediately underneath the lower informal member (i.e., uppermost upper Amin Member) and the presence of sandstones with parallel to low-angle cross lamination and wave ripples and large-scale desiccation cracks may suggest deposition in a marginal marine environment—supratidal to intertidal. The middle informal member also was interpreted by Buckley (1997) and other researchers as an aeolian in origin. The presence of low- to high-angle tabular to trough cross-bedding, wave ripples, and *Thalassinoides* like trace fossils at the uppermost part points to the deposition in the marine system as subtidal environments.

5 Conclusions

This study aimed to shed new insights into the stratigraphy and depositional environment model of Miqrat Formation. This study revealed that:

1. Miqrat Formation can be subdivided into three informal members, namely lower, middle, and upper informal members.
2. The lower and upper informal members are characterized by coarsening-upward cycles of red-to-green mudstones
3. The middle informal member is dominantly composed of sandstones with *Thalassinoides* like trace fossils suggesting deposition in a subtidal environment.

The proposed stratigraphic and the depositional environmental scheme can be used as an analogue for similar surface and subsurface rocks.

Acknowledgements This work is supported by His Majesty Strategic Grant [SR/SCI/ETHS/15/01] for Sultan Qaboos University. Thanks to the editors and the reviewers for the provided constructive comments.

References

- Buckley, R. C. (1997). *The sedimentary evolution of the Cambrian of east-central Oman: An outcrop study of the Haima Supergroup* [unpublished Ph.D. thesis] (331 pp.).
- Droste, H. J. (1997). Stratigraphy of the lower Palaeozoic Supergroup of Oman. *GeoArabia*, 2, 419–471.
- Forbes, G. A., Jansen, H. S. M., & Schreurs, J. (2010). Lexicon of Oman, subsurface stratigraphy. *GeoArabia Special Publication*, 5.



Late Cambrian-Early Ordovician Hybrid-Energy Deltaic System of the Peri-Gondwana Terranes: An Example from the Barik Formation of the Haushi-Huqf Region, Oman

Mohamed A. K. El-Ghali, Iftikhar Ahmed Abbasi, Olga Shelukhina, Mohamed S. H. Moustafa, Arshad Ali, Osman Salad Hersi, Mohamed Farfour, and Hezam Al-Awah

Abstract

The Barik Formation corresponds to the uppermost part of the Andam Group (Haima Supergroup) and is well exposed in the Huqf region of central Oman. It is a complex, deep, tight gas reservoir in Oman's interior Salt Basin and has been previously interpreted as braid delta deposits. This study illustrates a detailed outcrop-based stratigraphic and facies analysis of the Barik formation in the Huqf region. It offers new insights into the spatial and temporal distribution of the depositional facies and provides more information to enhance the depositional environment interpretation of the Barik Formation in the outcrop. The results revealed a complex depositional system indicated by various lithofacies, which have been grouped to represent four facies associations, including (i) mouth bar/shoreface, (ii) tidal flat, (iii) tidal channel, and (vi) delta distributary channels. The mud drapes, large-scale reactivation surfaces, sigmoidal cross-bedding, climbing ripples, and flaser bedding indicate tidal flats and delta distributary channels of the lower delta plains. Wave and storm facies, including wave ripples and small-scale hummocky cross-stratification, represent a mouth bar/shoreface of the delta front depositional setting. The

presence of basal scouring surfaces with lag deposits at channel bases and desiccation cracks of red mudstones indicated fluvial and subaerial facies. This study serves as an analogue for the ancient hybrid energy prograding delta over a broad and low relief shelf in a vegetation-free system, where the deposition is controlled by an interplay of multi-related tidal, wave/storm, and fluvial processes.

Keywords

Late Cambrian • Hybrid energy delta • Peri-Gondwana • Barik Formation • Huqf region • Oman

1 Introduction

The Late Cambrian-Early Ordovician Barik Formation is a hydrocarbon-producing subsurface reservoir in Oman's interior Salt Basin (Figs. 1a–c) (Droste, 1997; Forbes et al., 2010). It is exclusively exposed in the Huqf-Haushi region in Central Oman and stratigraphically represents a portion of the lowermost part of the Andam Group (Haima Supergroup). The Barik was interpreted as a braid delta system (Droste, 1997; Forbes et al., 2010) and conformably overlies the Al-Bashair Formation, and sand dunes cover its upper contact in the study area. However, in the subsurface, it is overlain by the Mabrouk Formation (Fig. 1c) (Droste, 1997; Forbes et al., 2010). This study aims to utilize outcrops observations of the Barik Formation in the Mahatta Humaid of the Haushi-Huqf region to have an appropriate depositional environment interpretation.

2 Materials and Methods

We carried out comprehensive sedimentological studies on several well-exposed sections of the Barik Formation in the Haushi-Huqf region. Lithology, grain size, bed thickness,

M. A. K. El-Ghali (✉) · M. S. H. Moustafa · A. Ali
Earth Sciences Research Center, Sultan Qaboos University,
Muscat, Oman
e-mail: melghali@squ.edu.om

M. A. K. El-Ghali · I. A. Abbasi · M. Farfour
Department of Earth Sciences, College of Science,
Sultan Qaboos University, Muscat, Oman

O. Shelukhina
Research and Education Center, Novosibirsk State University,
Novosibirsk, Russia

O. S. Hersi
Department of Geology, University of Regina,
Saskatchewan, Canada

H. Al-Awah
Department of Chemistry and Earth Sciences,
University of Qatar, Doha, Qatar

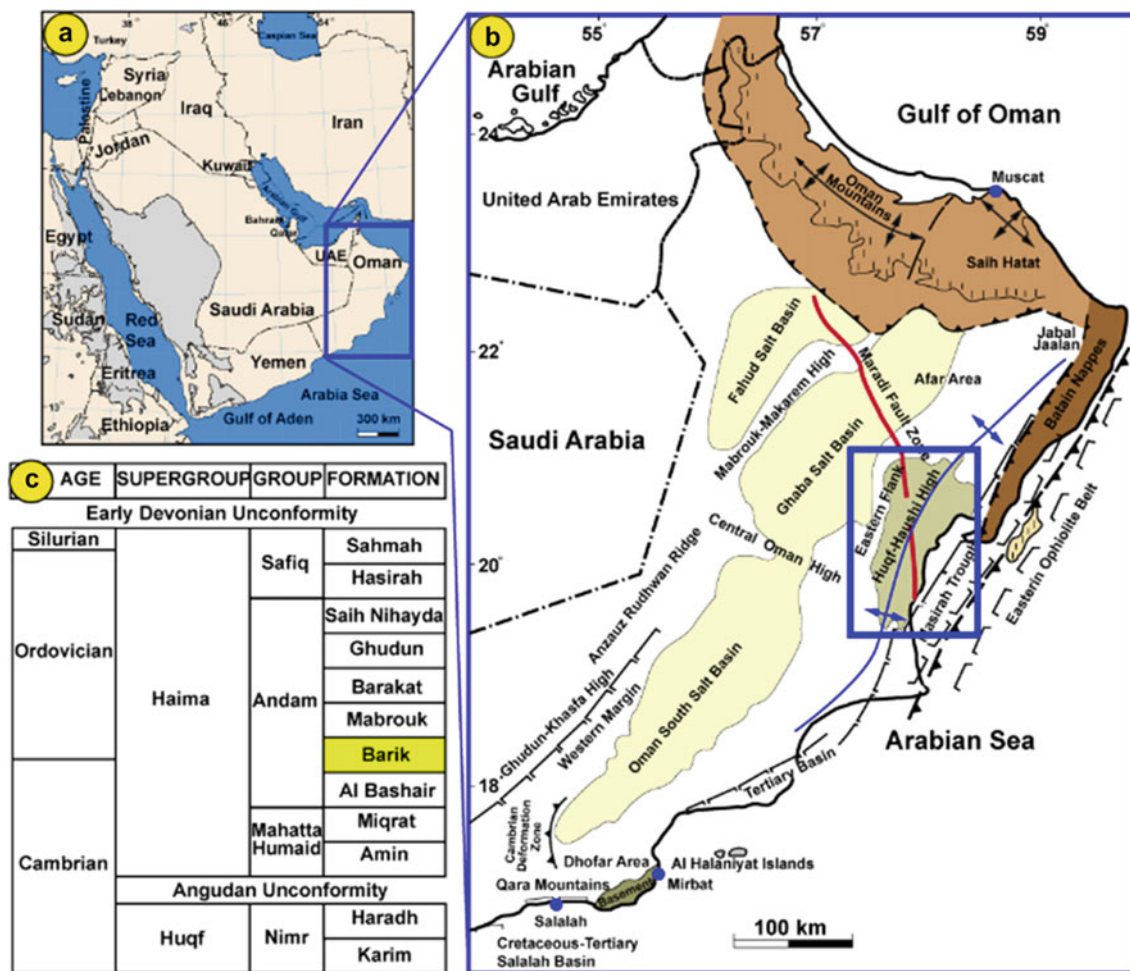


Fig. 1 Maps showing **a** the position of the Sultanate of Oman on the southeastern corner of the Arabian Peninsula and **b** the location of the studied area, namely Huqf-Haushi region in Central Oman (modified

after Droste, 1997). **c** Stratigraphic nomenclature of Haima Supergroup showing the studied Barik Formation (modified after Forbes et al., 2010)

bed contact nature, sedimentary structure, and trace fossils in the formation were investigated. Such investigations help to recognize several lithofacies and understand their dominant depositional processes. The recognized lithofacies were grouped into facies associations, demonstrating the basis for depositional environment interpretation.

3 Results

Four facies associations (FA1–FA4) were interpreted from the Barik Formation in the studied outcrops (Figs. 2a–g). FA1 (Fig. 2b) comprises brown to reddish-brown sandstones exhibiting sheet-like and locally lenticular bodies. The sheet-like sandstone bodies show small-scale hummocky cross-stratification. The sandstones display ripples at the upper interval, mostly asymmetrical and infrequently symmetrical—the asymmetrical rippled sandstones demonstrating north-northeast and northwest paleoflow directions. They

exhibit flakes and clasts of mudstones and are frequently intercalated with mudstones with desiccation cracks. FA2 is composed of mostly red to greenish mudstones that are interbedded with thin beds of sandstones. The mudstones are massive and display parallel lamination (Fig. 2c), while the sandstones display asymmetrical and symmetrical ripples (Fig. 2d) and contain trace fossils assemblage, mostly *Skolithos*. FA3 comprises sheet-like bodies of white sandstones interbedded with a thin mudstone. The sandstones show parallel lamination, low-angle planar cross-bedding, and tangential planar cross-bedding that grades upwards into intercalations of climbing asymmetrical and symmetrical ripples and flaser beds (Fig. 2e). The trace fossils assemblage in FA3 comprises *Skolithos*, *Planolites*, and *Thalassinoides*. FA4 includes amalgamated channelized sandstone bodies exhibiting tangential and sigmoidal planar and trough cross-bedding that grades upwards to parallel laminated and low-angle planar cross-bedding sandstone (Figs. 2f–g). They are intercalated with red to green, thinly laminated mudstones.

4 Discussion

The occurrences of small-scale hummocky cross-stratification and wave-rippled sandstones in FA1 suggest deposition in shallow marine (Basilici et al., 2012; Shelukhina et al., 2021). The desiccation mud cracks represent frequent subaerial exposures subsequent waning periods and red mudstone settlement. FA1 indicates deposition in shoreface and mouth bar settings. FA2 with interlaminated mudstones and sandstones displaying asymmetrical and symmetrical ripples and *Skolithos* trace fossils implies deposition in a tidal flat setting (Plint, 2013). FA3 of sandstones with parallel lamination, low-angle planar cross-bedding, and tangential planar cross-bedding that are intercalated into climbing asymmetrical and symmetrical ripples, flaser beds, and mudstone with *Skolithos*, *Planolites*, and *Thalassinoides* is indicative of deposition in tidal channels (Rossi et al., 2017). FA4 with amalgamated channelized sandstone bodies displaying tangential and sigmoidal planar and trough that grades upward to low-angle planar cross-bedding sandstone supports deposition in delta distributary channels (Aschoff et al., 2018; Shelukhina et al., 2021).

5 Conclusions

This study aimed to shed new insights into the stratigraphy and depositional environment model of the Barik Formation. It revealed the following points:

1. The Barik Formation in the outcrop of the Huqf-Haushi region comprises four facies associations, namely shoreface and mouth bar (FA1), tidal flats (FA2), tidal channels (FA3), and delta distributary channels (FA4).
2. The Barik Formation in the outcrop is represented by a shallowing upward interval starting by FA1 of the deeper and distal setting of mouth bar and shoreface deposits

and ending by FA4 of the shallower and proximal setting of delta distributary channel, through FA2 of tidal flat setting and FA3 of tidal channels.

The proposed stratigraphic and depositional environmental scheme can be used as an analogue for surface and subsurface equivalents.

Acknowledgements This work is supported by His Majesty Strategic Grant [SR/SCI/ETHS/15/01] for Sultan Qaboos University. We appreciate the editor's time and the reviewers' constructive comments, which assisted us to improve the manuscript.

References

- Aschoff, J. L., Olariu, C., & Steel, R. J. (2018). Recognition and significance of bayhead delta deposits in the rock record: A comparison of modern and ancient systems. *Sedimentology*, 65, 62–95.
- Basilici, G., De Luca, P. H., & Poiré, D. G. (2012). Hummocky cross-stratification-like structures and combined-flow ripples in the Punta Negra Formation (Lower-Middle Devonian, Argentine Precordillera): A turbiditic deep-water or storm-dominated prodelta inner-shelf system. *Sedimentary Geology*, 267–268, 73–92.
- Droste, H. J. (1997). Stratigraphy of the lower Palaeozoic Supergroup of Oman. *GeoArabia*, 2, 419–471.
- Forbes, G. A., Jansen, H. S. M., & Schreurs, J. (2010). Lexicon of Oman, subsurface stratigraphy. *GeoArabia Special Publication*, 5.
- Plint, G. (2013). Mud dispersal across a Cretaceous prodelta: Storm-generated, wave-enhanced sediment gravity flows inferred from mudstone microtexture and microfacies. *Sedimentology*, 61(3), 609–647.
- Rossi, V. M., Perillo, M. M., Steel, R. J., & Olariu, C. (2017). Quantifying mixed-process variability in shallow-marine depositional systems: What are sedimentary structures really telling us? *Journal of Sedimentary Research*, 87, 1–15.
- Shelukhina, O., El-Ghali, M. A. K., Abbasi, I. A., Khan, J. A., Khalifa, M. K., Rajendran, S., & AlSayigh, A. (2021). Facies architecture and depositional model for a fine-grained hybrid-energy delta: An example from the Upper Cambrian to Lower Ordovician Barik Formation, Central Oman. *Geological Journal*, 56, 4254–42791.



Genesis of Grain-Coating Clays and Their Effect on the Development of Feldspar Overgrowths: A Case Study of the Late Cambrian to Early Ordovician Barik Formation Sandstone Reservoir, Haushi-Huqf Region, Central Oman

Mohamed A. K. El-Ghali, Iftikhar Ahmed Abbasi, Olga Shelukhina, Mohamed S. H. Moustafa, Arshad Ali, Osman Salad Hersi, Shahad Al Mahrooqi, Khalid Al-Ramadan, Abdulwahab Muhammad Bello, Hezam Al-Awah, and Abdullah Alqubalee

Abstract

The Barik Formation sandstones accumulated under a deltaic system and constituted important deep and tight gas reservoirs in the Interior Oman Salt Basin. This study aims to understand the genesis of grain-coating clays and their role in controlling the development of feldspar overgrowths. The study is based on integrated different analytical techniques, including thin-section petrography, scanning electron microscopes coupled with dispersed energy spectrometers, and X-ray diffraction analyses. These are achieved to determine the mineralogical and chemical composition, texture and mode of occurrence of the grain-coating clays. These analyses revealed that the

grain-coating clays are typically illite and, to a smaller extent, chlorite. The observed illite forms $\sim 5 \mu\text{m}$ thick envelop rimming partially to entirely the detrital grain surfaces and also along grain-to-grain contacts. The illite shows honeycomb-like texture and cornflake textures with filamentous terminations. The chlorite forms $\sim 3 \mu\text{m}$ thick envelop rimming, seemingly the entire detrital grains and at grain-to-grain contacts. The chlorite also shows a honeycomb-like texture and curved platelet morphologies. The described illite and chlorite textural morphologies and mode of occurrence strongly support their growth through a transformation process from smectite precursors. The transformation of smectite to illite and chlorite were taken place during the mesodiagenesis. The smectite clay precursors are naturally near-surface clay fractions that are ultimately introduced mechanically into sandstones by hydrodynamic pumps during high tides. The larger extent of illite compared to chlorite can be related to the enrichment of the system by potassium ions, which are sourced internally via the widespread dissolution of detrital potassium feldspar grains. It is noticed that when the illite and chlorite, partially to entirely, envelop the detrital feldspar grains, they effectively hinder and inhibit the precipitation of authigenic feldspar overgrowth by limiting the nucleation sites on the detrital grains. This study may be regarded as an analogue for similar sandstone reservoirs to understand better the genesis and role of grain-coating clays on reservoir quality.

M. A. K. El-Ghali (✉) · I. A. Abbasi · A. Ali
Earth Sciences Research Center, Sultan Qaboos University,
Muscat, Oman
e-mail: melghali@squ.edu.om

M. A. K. El-Ghali · M. S. H. Moustafa · S. Al Mahrooqi
Department of Earth Sciences, College of Science, Sultan Qaboos
University, Muscat, Oman

O. Shelukhina
4Research and Education Center, Novosibirsk State University,
Novosibirsk, Russia

O. S. Hersi
Saskatchewan, University of Regina, Saskatchewan, Canada

K. Al-Ramadan
Department of Geosciences, King Fahd University of Petroleum
and Minerals, Dhahran, Saudi Arabia

A. M. Bello · A. Alqubalee
Center for Integrative Petroleum Research, College of Petroleum
Engineering and Geosciences, King Fahd University of Petroleum
and Minerals, Dhahran, Saudi Arabia

H. Al-Awah
Department of Chemistry and Earth Sciences, Qatar University,
Doha, Qatar

Keywords

Late Cambrian · Early Ordovician · Grain-coating
clays · Illite · Chlorite · Feldspar overgrowths ·
Barik Formation · Oman

1 Introduction

Grain-coating clays in sandstones occur as allogenic and/or authigenic constituent that form in a wide-ranging depositional settings, climatic conditions, and diagenetic realms (El-Ghali et al., 2006a, 2006b, 2009, 2019; El-Khatiri et al., 2015; Moraes & De Ros, 1990; Usman et al., 2020; Worden & Morad, 2003). Identifying grain-coating clays type, texture, the timing of formation, and spatial and temporal distribution is essential for predicting their control on a reservoir property (Al-Ramadan et al., 2013; Moraes & De Ros, 1990; Worden et al., 2020). However, grain-coating clays are strongly governing reservoir properties by preventing the formation of quartz and feldspar overgrowths in deeply-buried reservoirs (Bjørlykke & Aagaard, 1992; Worden & Morad, 2003). Authigenic illite and chlorite are common grain-coating clays and typically form during the mesodiagenetic regime in sandstone reservoirs (Ehrenberg, 1993; El-Ghali et al., 2006a, 2006b; Millson et al., 2008; Morad et al., 2010; Usman et al., 2020).

This study targets to examine and document the grain-coating clays genesis and governor on the formation of feldspar overgrowths in the outcropped fine-grained hybrid-energy delta sandstones of the lower Paleozoic (i.e., Upper Cambrian-Lower Ordovician) Barik Formation in Huqf-Haushi region (Figs. 1a–c). Barik Formation is a major tight gas-producing reservoir in the subsurface of Oman Interior Basin (Droste, 1997) and understanding the effect of grain-coating clays on feldspar overgrowths formation utilizing the available outcropped Barik Formation sections will significantly help to better plan for hydrocarbon exploration, production, and enhanced oil recovery, and energy storage in the basin.

2 Materials and Methods

To achieve the main aims of this study, about 30 sandstone samples were collected throughout Barik Formation sections in the Huqf-Haushi region of Central Oman (Fig. 1b). The 30 collected sandstone samples were thin-sectioned subsequent to impregnation with blue-epoxy resin to easiness porosity recognition. The thin sections were first described under the optical microscope highlighting the type, texture, and distribution of grain-coating clays. Six fresh sandstone samples with relatively widespread grain-coating clays were carefully examined using the JEOL-scanning electron microscope equipped with a dispersed energy spectrometer (EDS) at the Central Analytical and Applied Research Unit (CAARU) of Sultan Qaboos University in Oman, highlighting the textural habits and paragenetic relationships among grain-coating clays and other diagenetic minerals. The samples were coated with gold and examined using

SEM under a 20 kV, and 4.5×10^{-11} A current beam of wavelength and the EDS interpretation was performed using AZtech 2.0 Software. The same 6 samples were further examined using X-Rays Diffraction (XRD) for structural determination of the contained minerals at CAARU of Sultan Qaboos University in Oman. The pattern was analyzed and indexed using HighScore Plus Software. The XRD patterns were recorded on PANalytical X Pert PRO diffractometer using graphite filtered $\text{CuK}\alpha$ radiation ($\lambda = 1.5405 \text{ \AA}$) at 45 kV and 40 mA within a scanning rate of 0.2307/s from 0° (start angel) to 70° (end angel).

3 Results

Illitic Clays

The grain-coating illite clays in the studied samples exhibit (i) a yellow interference appearance rimming detrital grains under cross-polarized light (XPL) microscope (Fig. 2a), (ii) a honeycomb and cornflakes textural habits under SEM, (iii) a presence of peaks of oxygen (60.4 wt%), silica (15.9 wt%), aluminum (9.1 wt%), potassium (1.6 wt%), magnesium (2.1 wt%), and small amounts of calcium (0.5 wt%) under EDS examinations, and (iv) XRD peaks confirming the occurrence of illitic-type clays. The illitic clays occur commonly as continuous and infrequently discontinuous rims that are tangentially projected around detrital grains and along grain-to-grain contact (i.e., feldspar grains) with variable thicknesses not exceeding $5 \mu\text{m}$ (Figs. 2a–c). Detrital feldspar grains rimmed by thick and continuous illitic clays lack the development of feldspar overgrowths (Fig. 2c), whereas feldspar grains with discontinuous illitic rims are cemented by feldspar overgrowths (Fig. 2d–g).

Chloritic Clays

The grain-coating chloritic clays in the studied samples exhibit (i) a grayish-interference appearance rimming detrital grains under cross-polarized light (XPL) microscope, (ii) a honeycomb and platelet-like textural habits under SEM, (iii) a presence of peaks of oxygen (59.6 wt%), silica (22.1 wt%), aluminum (10.9 wt%), iron (1.5 wt%), magnesium (2.1 wt%), and variable amounts of potassium (3.0 wt%) and calcium (0.7 wt%) under EDS examinations, and (iv) XRD peaks confirming the occurrence of chloritic-type clays. The chloritic clays occur commonly as continuous and infrequently discontinuous rims that are perpendicularly projected around detrital grains and along grain-to-grain contact (i.e., feldspar grains) with variable thicknesses not exceeding $3 \mu\text{m}$ (Figs. 2h–i). Detrital feldspar grains rimmed by thick and continuous illitic clays lack the

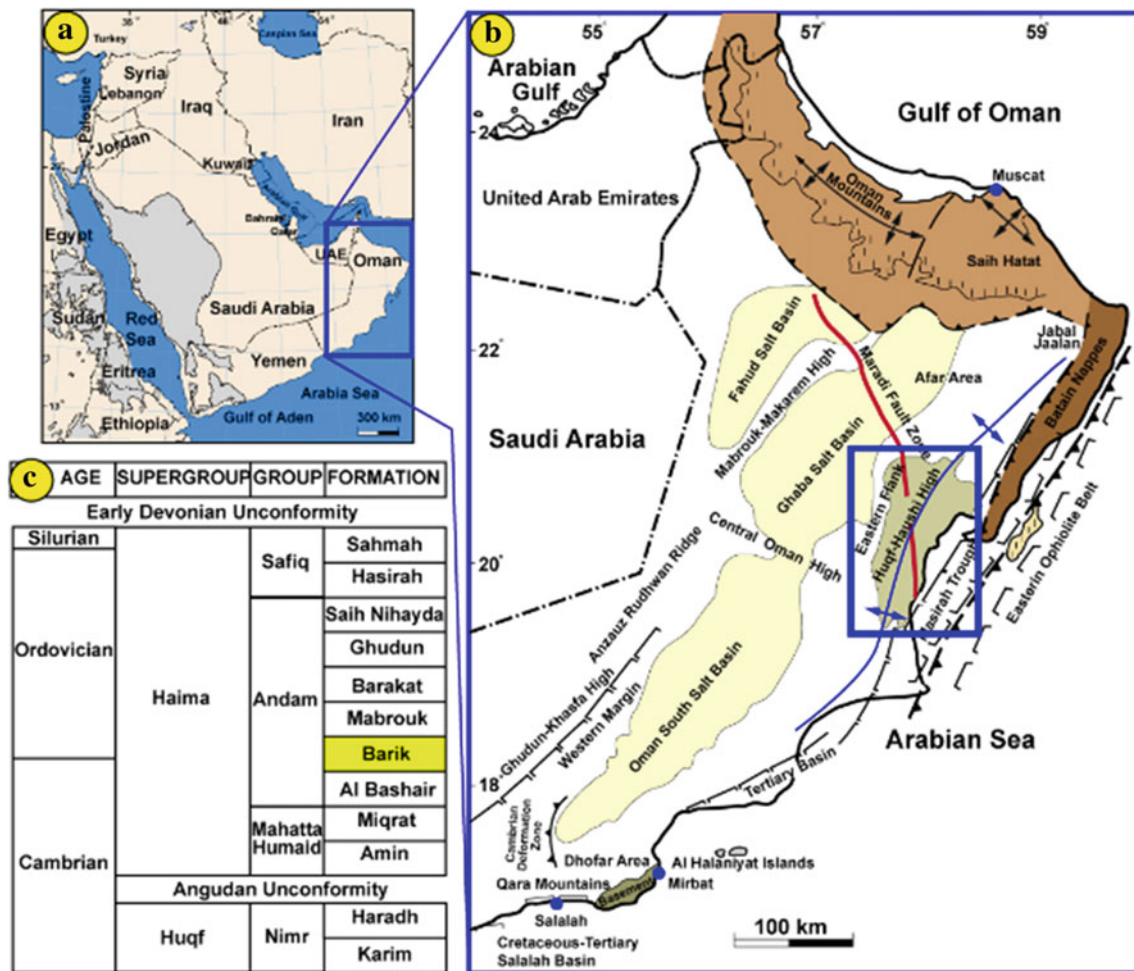


Fig. 1 Maps showing **a** the location of the Sultanate of Oman on the southeastern portion of the Arabian Peninsula and **b** the location of the studied area, namely Huqf-Haushi region in Central Oman (modified

after Forbes et al., 2010). **c** Haima Supergroup stratigraphic nomenclature comprising the studied Barik Formation (based on McBride, 1963)

development of feldspar overgrowths, whereas feldspar grains with discontinuous illitic rims are cemented by feldspar overgrowths (Fig. 2i).

4 Discussion

Grain-Coating Clays Genesis

The yellow- and grayish-interference appearance of grain-coating illitic and chloritic clays confirmed by SEM, EDS, and XRD investigations and displaying continuous tangential- and perpendicular-projected rims around and along grain-to-grain detrital feldspar surfaces prove to form by mechanical infiltration at near-surface diagenesis (cf. Moraes & De Ros, 1990; El-Ghali et al., 2006a, 2006b, 2009; Worden & Morad, 2003). The nature of grain-coating illitic and chloritic clays textural habits of honeycombs and cornflakes texture indicates smectitic clay precursors

(El-Ghali et al., 2023; Worden & Morad, 2003) that are introduced into the hybrid-energy delta sandstones of Barik Formation by the tidal pumps process hydrodynamically. The tidal pumps assist the muddy enriched waters to penetrate through the sandstones and eventually form clay rims around detrital grains. The recognized spiny terminations of the honeycombs and cornflakes and the platelet-like texture prove the conversion of the smectitic clay precursors into illite and chlorite with the availability of potassium and iron ions in the pore-water, respectively, during progressive burial, i.e., mesodiagenesis (cf. El-Ghali et al., 2006a, 2006b, 2009).

Grain-Coating Clays Control the Development of Feldspar Overgrowths

It is noted that the absence of feldspar overgrowths in the studied sandstone samples of the Barik Formation is closely related to the occurrence of the grain-coating

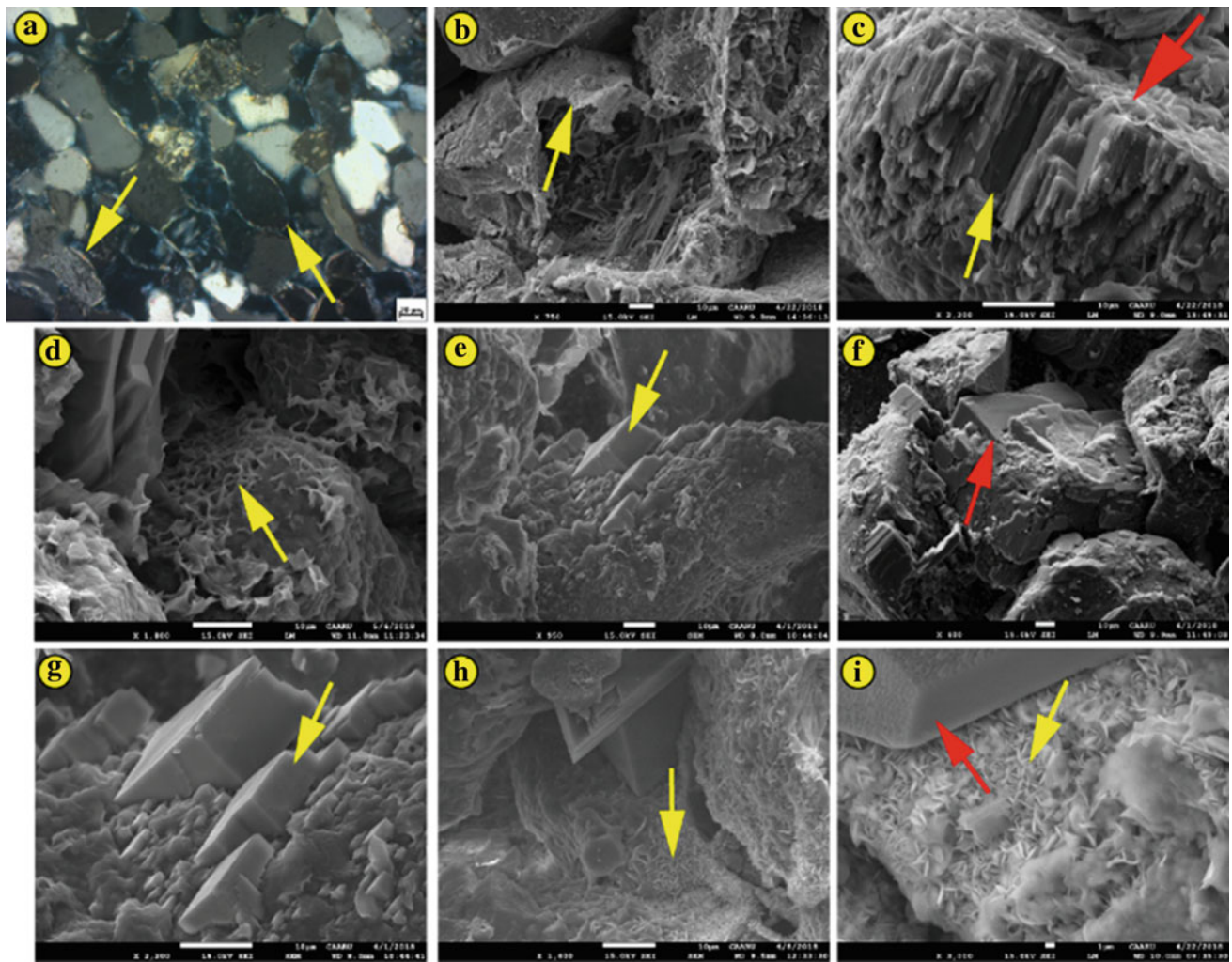


Fig. 2 a Microphotograph showing grain-coating clays around feldspar and quartz detrital grains (yellow arrows), SEM images showing b illitic grain-coating clays coating dissolved feldspar grains, c thin illitic grain-coating clays (red arrow) around partially dissolved feldspar grain (yellow arrow), d honeycomb texture of illitic clays

(yellow arrow), e, f, g feldspar overgrowths postdating illitic grain-coating clays, h chloritic grain-coating clay (yellow arrow), and i feldspar overgrowth (red arrow) postdating chloritic grain-coating clays (yellow arrow)

clays. The continuous illitic and chloritic rims around detrital feldspar grains acted as barriers reducing the nucleation sites for the development of feldspar overgrowths. The barriers will eventually hinder the saturated formation waters with ions required to form feldspar overgrowths from accessing the detrital feldspar grain surfaces and thus inhibit the growth of feldspars (Al-Ramadan et al., 2013; El-Ghali et al., 2023; Shelukhina et al., 2021). On the other hand, the detrital feldspar grains with discontinuous illitic and chloritic clay rims reveal the presence of well-developed feldspar overgrowths. This reflects the availability of substantial clay-free detrital feldspar grains surface, allowing the saturated formation waters with ions required to form feldspar overgrowths to access the feldspar grains surface and develop the feldspar overgrowths.

5 Conclusions

The petrographic and geochemical techniques shed light on the genesis and controls of grain-coating clays on feldspar overgrowths in the hybrid-energy delta sandstones of the Barik Formation. This study revealed that:

1. Grain-coating clays are illitic and chloritic-type clays with honeycombs and cornflakes and honeycombs and platelet textural habits, respectively demonstrating the conversion from smectitic clays precursors during mesodiagenesis.
2. Grain-coating clays are introduced into the sandstones by tidal pump processes hydrodynamically via the percolation of the muddy waters.

3. Grain-coating clays inhabited the development of feldspar overgrowths on detrital feldspar grains entirely rimmed by continuous clays.
4. Grain-coating clays with discontinuous rims around detrital feldspar grains show the development of feldspar overgrowths; the discontinuous rims provide the occurrence of nucleation sites on detrital feldspar grains for cementation by feldspar overgrowths.

This study can act as an analog to decipher the grain-coating clays genesis and control on cementation by feldspar overgrowths in deeply-buried sandstones.

Acknowledgements This study is supported by the Ministry of Higher Education, Research, and Innovation Grant Fund # **RC/RG-DVC/ESRC/21/01**. We greatly appreciate the editor's time and the reviewers' constructive feedback, which helped us to improve the manuscript.

References

- Al-Ramadan, K., Morad, S., Norton, A. K., & Hulver, M. (2013). Linking diagenesis and porosity preservation versus destruction to sequence stratigraphy of gas condensate reservoir sandstones; the Jauf Formation (Lower to Middle Devonian), Eastern Saudi Arabia. In *Linking diagenesis to sequence stratigraphy* (pp. 297–336).
- Bjørlykke, K., & Aagaard, P. (1992). Clay minerals in the North Sea. In D. W. Houseknecht & E. D. Pittman (Eds.), *Origin, diagenesis, and petrophysics of clay minerals in sandstones. Society of Economic Paleontologists and Mineralogists Special Publication* (Vol. 47, pp. 65–80), Tulsa, OK.
- Droste, H. J. (1997). Stratigraphy of the lower Palaeozoic Supergroup of Oman. *GeoArabia*, 2, 419–471.
- Ehrenberg, S. N. (1993). Preservation of anomalously high-porosity in deeply buried sandstones by grain coating chlorite—Examples from the Norwegian continental shelf. *American Association of Petroleum Geologists Bulletin*, 77(7), 1260–1286.
- El-Ghali, M. A. K., Al-Hinai, N., Mandhari, K., & Khan, J. (2019). Diagenesis and reservoir quality of glacio-lacustrine sandstones: An example from the Upper Carboniferous-Lower Permian Al Khlata Formation in Wadi Daiqa, Northern Oman. In M. Boughdiri, B. Bádenas, P. Selden, E. Jaillard, P. Bengtson, & B. Granier (Eds.), *Paleobiodiversity and tectono-sedimentary records in the Mediterranean Tethys and related eastern areas. CAJG 2018. Advances in Science, Technology & Innovation (IEREK Interdisciplinary Series for Sustainable Development)* (pp. 151–153). Springer.
- El-Ghali, M. A. K., Mansurbeg, H., Morad, S., Al-Aasm, I., & Ajdanlisky, G. (2006a). Distribution of diagenetic alterations in fluvial and paralic deposits within sequence stratigraphic framework: Evidence from the Petrohan Terrigenous Group and the Svidol Formation, Lower Triassic, NW Bulgaria. *Sedimentary Geology*, 190, 299–321.
- El-Ghali, M. A. K., Morad, S., Al-Aasm, I., Ramseyer, K., & Mansurbeg, H. (2006b). Distribution of diagenetic alterations in glaciogenic sandstones within a depositional facies and sequence stratigraphic framework: Evidence from the Upper Ordovician of the Murzuq Basin, SW Libya. *Sedimentary Geology*, 190, 299–327.
- El-Ghali, M. A. K., Morad, S., Mansurbeg, H., Caja, M. A., Ajdanlisky, G., Ogle, N., Al-Aasm, I., & Sirat, M. (2009). Distribution of diagenetic alterations within depositional facies and sequence stratigraphic framework of fluvial sandstones: Evidence from the Petrohan Terrigenous Group, Lower Triassic, NW Bulgaria. *Marine and Petroleum Geology*, 26, 1212–1227.
- El-Khatri, F., El-Ghali, M. A. K., Mansurbeg, H., Morad, S., Neil, O., & Robert, K. (2015). Diagenetic alterations and reservoir quality evolution of lower cretaceous fluvial sandstones: Nubian formation, Sirt Basin, north-central Libya. *Journal of Petroleum Geology*, 38, 217–239.
- El-Ghali, M. A. K., Shelukhina, O., Abbasi, I. A., Moustafa, M. S. H., Hersi, O. S., Siddiqui, N. A., Al-Ramadan, K., Alqubalee, A., Bello, A. M., & Amao, A. O. (2023). Depositional and sequence stratigraphic controls on diagenesis in the upper cambrian-lower ordovician Barik Formation, central Oman: Implications on prediction of reservoir porosity in a hybrid energy delta system. *Marine and Petroleum Geology*, 106611. <https://doi.org/10.1016/j.marpetgeo.2023.106611>
- Forbes, G. A., Jansen, H. S. M., & Schreurs, J. (2010). Lexicon of Oman, subsurface stratigraphy. *GeoArabia Special Publication*, 5.
- McBride, E. (1963). A classification of common sandstones. *Journal of Sedimentary Petrology*, 33, 664–669.
- Millson, J. A., Quin, J. G., Idiz, E., Turner, P., & Al-Harthy, A. (2008). The Khazzan gas accumulation, a giant combination trap in the Cambrian Barik Sandstone Member, Sultanate of Oman: Implications for Cambrian petroleum systems and reservoirs. *AAPG Bulletin*, 97(7), 885–917.
- Morad, S., Al-Ramadan, K., Ketzer, J. M., & De Ros, L. F. (2010). The impact of diagenesis on the heterogeneity of sandstone reservoirs: A review of the role of depositional facies and sequence stratigraphy. *American Association of Petroleum Geologists Bulletin*, 94(8), 1267–1309.
- Moraes, M. A. S., & De Ros, L. F. (1990). Infiltrated clays in fluvial Jurassic sandstones of origin, diagenesis, and petrophysics of clay minerals in sandstones (Vol. 47, pp. 241–255).
- Shelukhina, O. I., El-Ghali, M. A. K., Abbasi, I. A., Hersi, O. S., Farfour, M., Ali, A., Al-Awah, H., & Siddiqui, N. A. (2021). Origin and control of grain-coating clays on the development of quartz overgrowths: Example from the lower Paleozoic Barik Formation sandstones, Huqf Region, Oman. *Arabian Journal of Geosciences*, 14, 1–20.
- Usman, M., Siddiqui, N. A., Mathew, M., Zhang, S., El-Ghali, M. A., Ramkumar, M., Jameel, M., & Zhang, Y. (2020). Linking the influence of diagenetic properties and clay texture on reservoir quality in sandstones from NW Borneo. *Marine and Petroleum Geology*, 104509.
- Worden, R. H., Griffiths, J., Wooldridge, L. J., Utley, J. E. P., Lawan, A. Y., Muhammed, D. D., Simon, N., & Armitage, P. J. (2020). Chlorite in sandstones. *Earth-Science Reviews*, 204, 103105.
- Worden, R. H., & Morad, S. (2003). Clay minerals in sandstones: Controls on formation, distribution, and evolution. In R. H. Worden & S. Morad (Eds.), *Clay mineral cements in sandstones* (Vol. 34, pp. 3–41). Special Publication of the International Association of Sedimentologists.



Was There a Massive Sediment Transport System from Northwestern Arabia to the Levant Basin During the Oligo-Miocene?

Yossi Mart

Abstract

Seismic reflection profiles that were shot along the Levant Basin and its eastern margin show considerable thickening of the Oligo-Miocene sequence shelf-to-basin transition compared with overlying and underlying stratigraphic units. Numerous erosional channels were depicted in that sequence, suggesting a massive flow system of sedimentary supply from the source in the east to the sink in the west. The dimensions of these channels vary, but together they form a dense submarine system of sediment transport. Reconstruction of the Oligo-Miocene land-to-sea drainage system, from northwestern Arabia to the Mediterranean Sea, was active before the tectonic evolution of the Levant Rift and its uplifted flanks. Consequently, analog experiments showed that the tectonic evolution of the rift under the tectonic regime of oblique extension would generate a simultaneous break-up of detached series of discrete structural basins, which would interconnect gradually. That gradual connection enabled the westwards sediment supply concurrently with the structural evolution of the Levant Rift, but during the late Miocene and the early Pliocene, the growth of the rift and its elevated flanks gradually truncated the westwards fluvial flow. Since the middle Pliocene, only small rivers were left behind to supply Levantine sediments to the Mediterranean, and at present, the Levant Basin derives most of its sediments from the Nile River.

Keywords

Levant Basin • Oligo-Miocene • Submerged sedimentary channels • Land-to-sea sedimentary supply

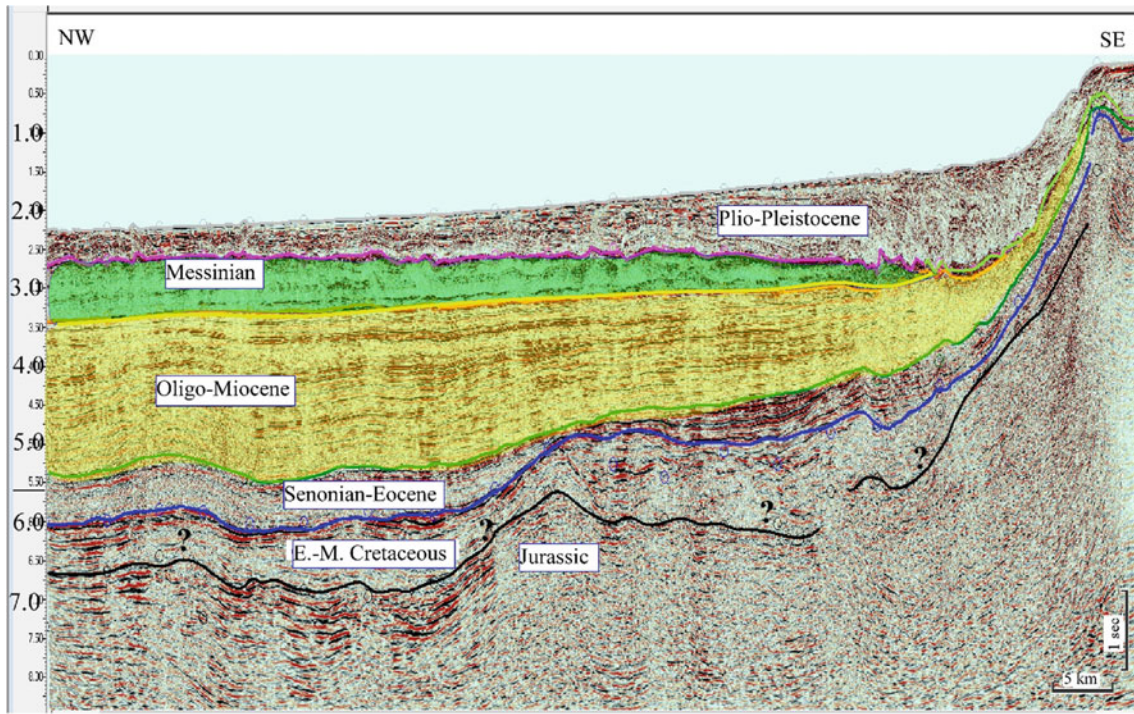
1 Introduction

Extensive petroleum exploration in the Levant Basin uncovered a thick sequence of mostly clastic sediments (Fig. 1a) that were geophysically charted, drilled, and dated to the Oligo-Miocene Epoch (ca. 34–5 Ma). While the distribution of Oligocene strata on land is variable and unabundant, and the Miocene deposits are mostly fluvial or shallow marine, the exceptional thickness of the marine Oligo-Miocene sequence, as well as the rock samples of the exploration boreholes, indicates an extensive sedimentary supply seawards (e.g., Bar et al., 2013). The source of the Oligo-Miocene sediments in the Levant Basin could have been either from NE Africa—a Nilotic source—or from the Levant—an Arabian source, or both. Observing the present geomorphology of both terrains, it seems obvious that had the present landscape of NE Africa been similar to that of some 20 Ma, the Nile was a ready source for the sediments of the Levant Basin. It is also very plausible to presume that if the Levant Rift and its raised flanks existed during the middle Miocene, there would have been no Arabian sediments in that basin (Fig. 2).

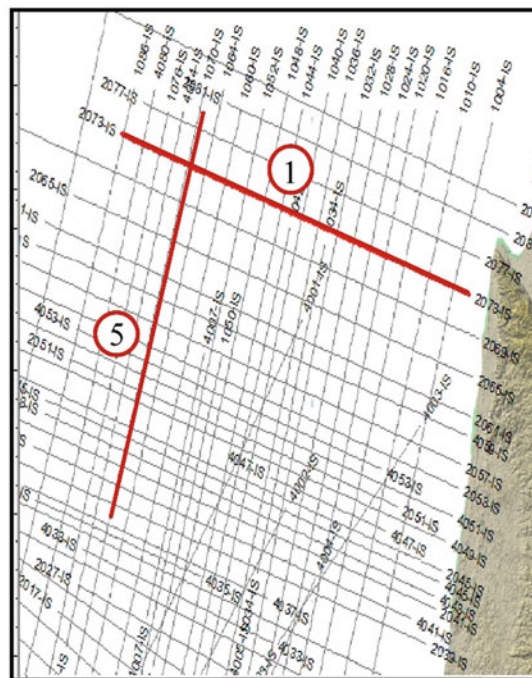
The present investigation encountered abundant sedimentological evidence that there was sediment supply from the Arabian source to the Levant Basin sink, suggesting that the Levant regional rift and its raised flanks have not yet existed during most of the Oligo-Miocene epoch. The evidence shows further that the dwindling of the Arabian sedimentary supply started in the late Miocene and terminated in the early-middle Pliocene, when the developing Levant Rift system truncated that source from its Mediterranean Basin.

Y. Mart (✉)

Recanati Institute of Maritime Studies, University of Haifa,
3498838 Haifa, Israel
e-mail: y.mart@research.haifa.ac.il



(a)



(b)

Fig. 1 a Regional seismic profile NW off Haifa, emphasizing the stratigraphic setting of the Messinian evaporites (green) and the rest of the Oligo-Miocene sequence (yellow). Pre-Oligocene seism stratigraphy is speculative. Faults were not depicted. Note scale at the lower

right. Left panel shows location. Vertical scale is reflection time in seconds. See b for location and location chart, numbers indicate figure numbers

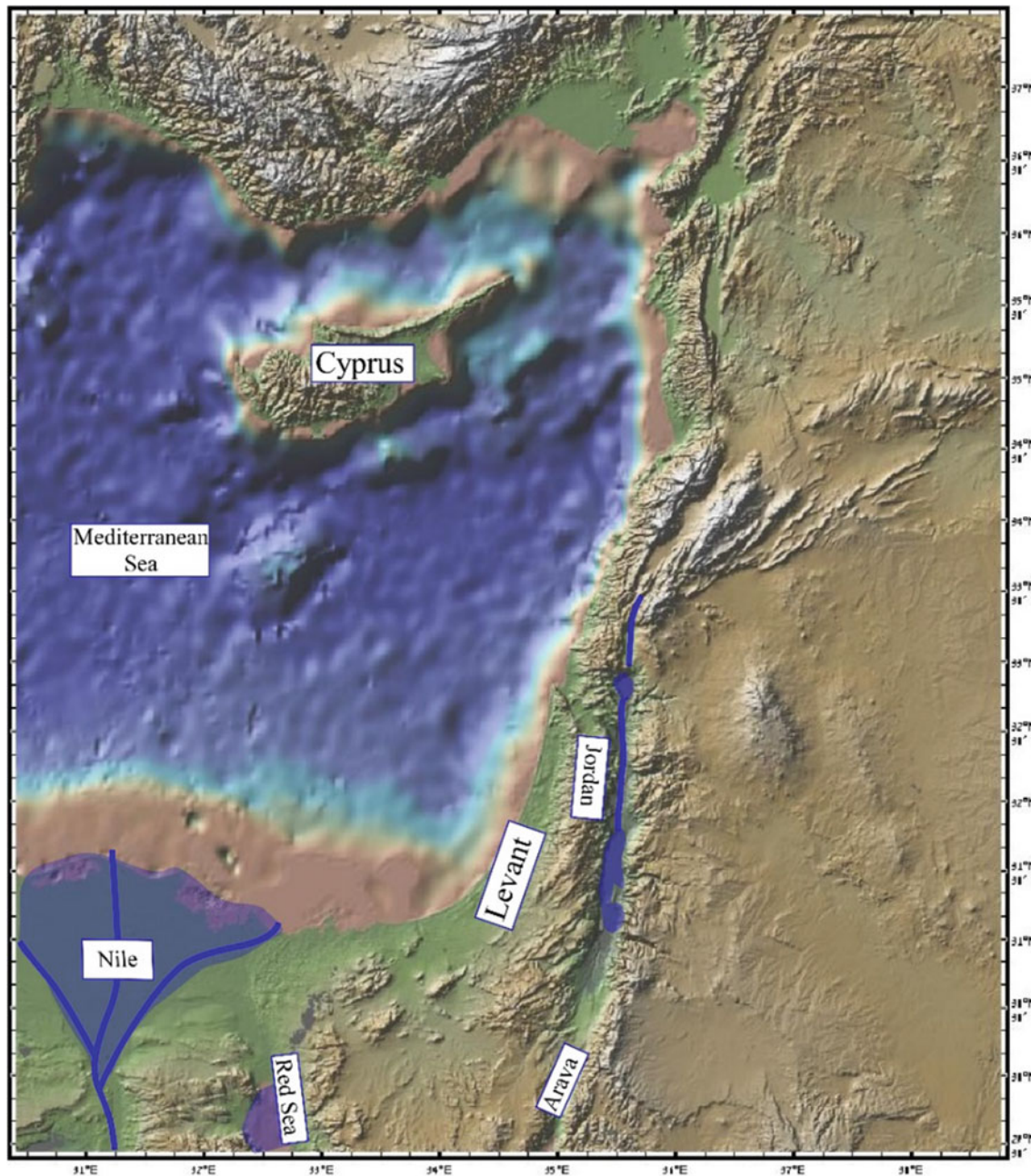


Fig. 2 Geographic setting of the Levant Basin and the domains of the Levant and the Nile. The Jordan River flows in a segment of the Levant Rift, which is bound on both flanks by mountainous chains. Topography and bathymetry courtesy www.geomapapp.org

2 Geological Setting

The paleogeographic location of the Levant during the early Oligocene was probably at the latitudinal range of 10–15° N, where the initiation of the East African mantle plume uplifted the Arabo-Nubian Massif and generated the co-occurrence of the subsidence of several surrounding basins, one of which is the Levant Basin (Moucha & Forte, 2011). The co-occurrence of the uplifted terrain above the

mantle plume and the subsidence of the Levant Basin could have generated the source area for the extensive sedimentary accretion in that marine basin, as the African tectonic plate continued its northeastwards migration, to gradually close the NeoTethys seaway.

Extensive outcrops of Miocene lithologies in central Israel show sediments of fluvial and shallow marine provenance (Fig. 3). It seems obvious that the present system of the Levant Rivers, which is small, short, and carry mostly mud and sand, could not have supplied the sediments that



Fig. 3 Mid-Miocene fluvial conglomerate in central Israel is evidence for sediment-rich flow in the large rivers that crossed the Levant from NW Arabia to the Mediterranean Sea. After Mart and Vachtman (2015)

filled the Levant Basin during the Oligo-Miocene, which carried boulders on land and generated turbidites in the basin (Figs. 3 and 4). Therefore reconstructions of the fluvial system of the Levant during the Miocene (Calvo & Bartov, 2001; Horowitz, 1979; Zak & Freund, 1981) that suggested that the rivers had fast-flowing floods that carried large boulders during the Miocene and into the early Pliocene seem valid (Fig. 3). Extensive terrains of boulders in several locations west of the Levant Rift suggest wide floodplains of fast-flowing large rivers that crossed the Levant from northern Arabia to the Mediterranean during the Oligo-Miocene and formed these boulder terrains.

The thick marine sequence of Oligo-Miocene sediments in the Levant Basin could consequently be divided into three time units. The Oligocene/early Miocene unit was deposited over probably Eocene strata, where turbidites channels abound. The unit above is probably Tortonian, where the fewer turbidites channels suggest early truncation of the fluvial system on land due to early development of the Levant Rift system. The upper unit dates to the Messinian where the sediments are evaporitic, indicating the desiccation of the Mediterranean Sea (Fig. 4).

The faulting pattern along the Levant Rift is normal, and first-motion solutions of active earthquakes suggest transtensional displacement, and indeed, satellites measured left-lateral offset along the rift of ca. 5.0 mm/yr. The accumulation of such displacements since the end of the Miocene indicates lateral offset of some 25 km, if indeed the offset

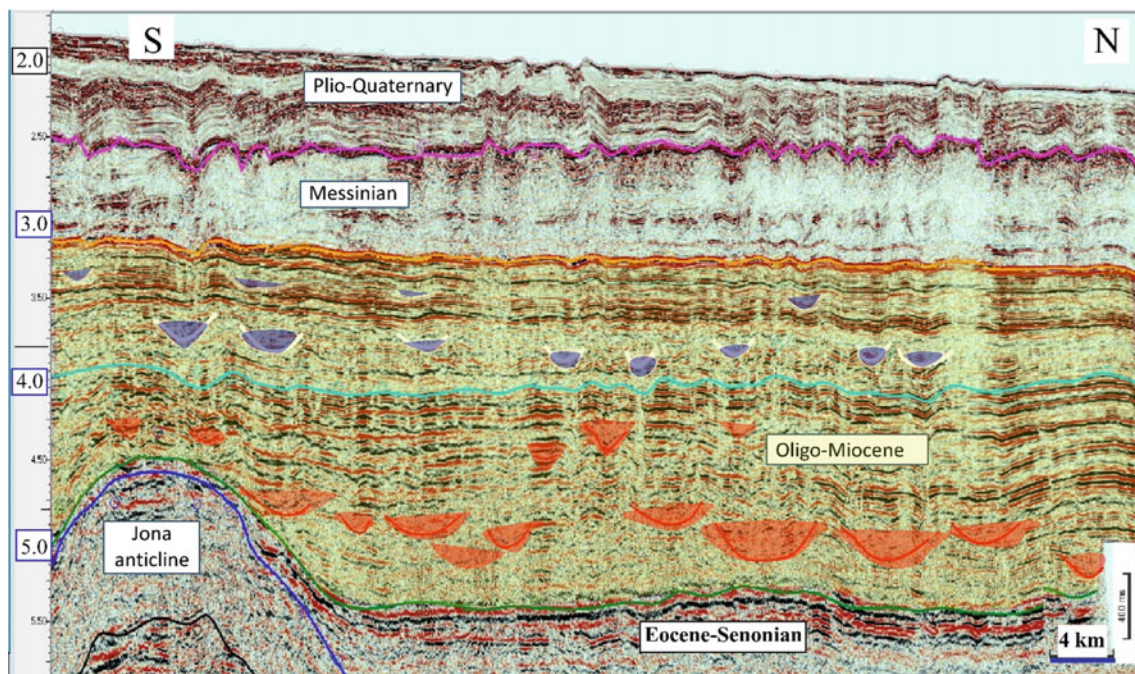


Fig. 4 Detailed north to south trending seismic reflection profile showing wealth of turbidites-entrained channels in the late Miocene (blue) and the Oligocene/early Miocene (red) strata. Vertical scale in

reflection time and left panel is a location chart (heavy red line). Note the horizontal scale on the lower right corner of the profile. See Fig. 1b for location

was conducted at a steady rate (e.g., Mart & Vachtman, 2015; Oren et al., 2020).

Structural evidence suggested that the tectonic regime along the Levant Rift is that of oblique extension (e.g., Mart & Horowitz, 1981), and the presumed 107 km left-lateral offset along the rift (e.g., Freund et al., 1970) is accompanied by large extensional normal faulting. The structural depressions in the domains of the Dead Sea and the Sea of Galilee, where thick sequences of salt were deposited in the early Pliocene, suggest that the composite displacement of the Levant Rift started probably in the early Messinian (Mart & Ryan, 2008). Furthermore, observations in the northern Red Sea showed that the early stages of the continental break-up and rifting there comprise the ascent of a linear series of magmatic diapirs that interconnect gradually to form the continuous rift (Bonatti, 1985). Analog experiments have indicated that oblique extension generates such linear series of small rifts that gradually interconnect (Mart & Dauteuil, 2000), like the structures of the northern Red Sea (Fig. 5).

3 Conclusions

The reconstruction of Oligo-Miocene large rivers of land and mass-transport sediment system at sea indicates that fluvial flow of sediments to the Levant Basin differed drastically from the present depositional system, which derives most of its sediments from the north-flowing Nile River. The sedimentological feed of the Levant Basin in the Oligo-Miocene derived probably from the contemporaneous rivers that flowed westwards from northwestern Arabia to the Mediterranean Sea. The seismic data show that the Oligo-Miocene marine turbidites channels were disrupted by the tectonic evolution of the Levant Rift and its elevated flanks, but a few large rivers still flowed during the Messinian desiccation of the Mediterranean Sea (Mart & Ryan, 2008). The Plio-Quaternary tectonic evolution of the Levant Rift system truncated the Oligo-Miocene fluvial system and left the Nile as the principal sedimentary source of the Levant Basin since the Pliocene.

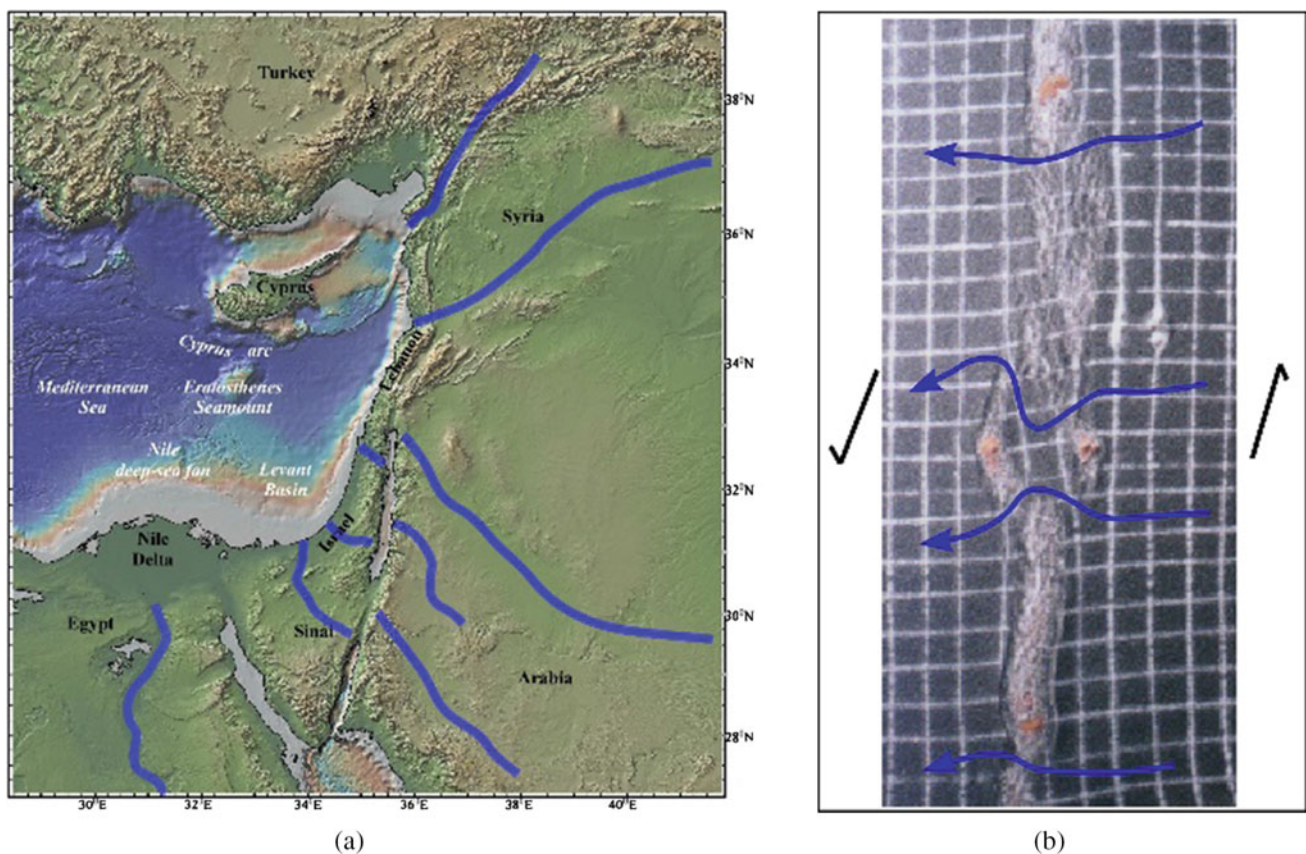


Fig. 5 **a** Reconstructed fluvial system of the Levant during the early Pliocene, partly after Zak and Freund (1981), and Mart and Vachtman (2015). These rivers were offset sinistrally by the oblique displacement along the Levant Rift. **b** Sand-box experiment of oblique extension,

where a series of basins develop simultaneously as small basins, which gradually extend mostly along their long axis, and rivers could still flow between the basins. See Mart and Dauteuil (2000) for details

References

- Bar, O., Gvirtzman, Z., Feinstein, S., & Zilberman, E. (2013). Accelerated subsidence and sedimentation in the Levant Basin during the Late Tertiary and concurrent uplift of the Arabian platform: Tectonic versus counteracting sedimentary loading effects. *Tectonics*, *32*, 334–350.
- Bonatti, E. (1985). Punctiform initiation of seafloor spreading in the Red Sea during transition from a continental to an oceanic rift. *Nature*, *316*, 33–37.
- Calvo, R., & Bartov, Y. (2001). Hazeva Group, southern Israel: New observations, and their implications for its stratigraphy, paleogeography, and tectono-sedimentary regime. *Israel Journal of Earth Sciences*, *50*, 71–100.
- Freund, R., Garfunkel, Z., Zak, I., Goldberg, M., Weissbrod, T., & Derin, B. (1970). The shear along the Dead Sea rift. *Transactions of the Royal Society, London, Series A*, *267*, 107–130.
- Horowitz, A. (1979). *The quaternary of Israel*. Academic Press.
- Mart, Y., & Dauteuil, O. (2000). Analogue experiments of propagation of oblique rifts. *Tectonophysics*, *316*, 121–132.
- Mart, Y., & Horowitz, A. (1981). The tectonics of the Timna region in southern Israel and the evolution of the Dead Sea rift. *Tectonophysics*, *79*, 165–199.
- Mart, Y., & Ryan, W. (2008). The Levant slumps and the Phoenician structures: Collapse features along the continental margin of the southeastern Mediterranean Sea. *Marine Geophysical Researches*, *28*, 297–307.
- Mart, Y., & Vachtman, D. (2015). The internal grabens of the Levant Rifts and their geodynamic significance. *Comptes Rendus Geoscience*, *347*, 191–200.
- Moucha, R., & Forte, A. M. (2011). Changes in African topography driven by mantle convection. *Nature Geoscience*, *4*, 707–712.
- Oren, O., Nuriel, P., Kylander-Clark, A. R. C., & Haviv, I. (2020). Evolution and propagation of an active plate boundary: U-Pb ages of fault-related calcite from the Dead Sea transform. *Tectonics*, *39*, e2019TC005888.
- Zak, I., & Freund, R. (1981). Asymmetry and basin migration in the Dead Sea rift. *Tectonophysics*, *80*, 27–38.



Depositional Facies and Sea-Level Variation of the Cryogenian Glacial System: An Example from the Outcropping Fiq Formation, Abu Mahara Group, Jabal Akhdar Area, Northern Oman

Razan Y. Al Naabi, Mohamed A. K. El-Ghali, Mohamed S. H. Moustafa, and John Smweing

Abstract

The Cryogenian Snowball Earth episode is represented in Oman by the Fiq Formation of the Abu Mahara Group. Although the Fiq Formation is an important hydrocarbon target in Oman, its spatial and temporal depositional facies distribution is still poorly understood. This study aims to build on previous outcrop studies and develop a depositional model based on detailed sedimentological logging of the well-exposed Fiq Formation in the Jabal Akhdar area of northern Oman. This study has revealed that the Fiq Formation is of glaciomarine (i.e., proximal and distal) and proglacial facies. Proximal glaciomarine facies consist of discontinuous, thin, clast-rich diamictite intervals. The clast-rich nature suggests rainout diamictites formed by the continuous source of debris below an ice sheet, extending some distance from the grounded ice margin. Distal glaciomarine facies make up most of the logged section and consist of thick massive mud-prone, clast-poor dilute diamictite intervals. They are of rainout ice-rafted based diamictites, sourced by iceberg-based debris flows, and deposited towards the distal area of the basin, distant from an active ice margin. Local glacier features (i.e., ice-rafted granitic dropstones) display clear evidence of active glaciation during the deposition of the Fiq Formation. The proglacial, gravity flow elements comprise gravity flow facies consisting of massive, locally graded sandstones with rippled tops, displaying pulse-like features, representing bottom-current-based turbidites, sourced from meltwater

bottom-currents from sub-glacial tunnel-mouth outlets, and deposited on unstable slope setting. Proglacial, gravity flow facies are also represented by parallel and thinly laminated siltstones and deformed mudstones, massive pebbly sandstones and clast-supported conglomerates with moderate to well-sorted texture, and rippled fine-grained sandstones and siltstones. Altogether this suggests suspension fallout from turbid plumes, intensively reworked debris and dilute current-based ripples formed in a deep water setting. Thick intervals of structureless sandstone represent lithofacies deposited in a braided fluvial environment. The Fiq Formation represents cycles of sea-level rise and fall events formed during local and multiple glaciation and deglaciation events. The outcome of this study may serve as a reference to test Fiq's potential development as a play and to define its regional variation in further studies.

Keywords

Neoproterozoic • Cryogenian • Snowball Earth • Diamictite • Glaciomarine • Fiq Formation • Abu Mahara Group • Huqf Supergroup • Wadi Hajir • Jabal Akhdar area • Oman

1 Introduction

In Oman, the Cryogenian Fiq Formation (600–500 Ma) of the Abu Mahara Group of the Huqf Supergroup preserves a Neoproterozoic stratigraphic record of the Marinoan glaciation (Allen et al., 2011a, 2011b; Leather, 2001). It overlies the Sturtian Ghubrah Formation (Allen et al., 2011a, 2011b; Fig. 1a; 760–700 Ma). The Neoproterozoic glaciomarine facies of the Fiq are well exposed, in the Jabal Akhdar area, Mirbat area, and Saih Hatat window (Fig. 1b; Allen 2011a). The Fiq Formation is of syn-rift sedimentation, deposited on an extensional fault-bounded rift basin,

R. Y. Al Naabi (✉) · M. A. K. El-Ghali · M. S. H. Moustafa
Department of Earth Sciences, College of Science,
Sultan Qaboos University, Muscat, Oman
e-mail: razan.y.alnaabi@gmail.com

M. A. K. El-Ghali
Earth Sciences Research Center, Sultan Qaboos University,
Muscat, Oman

J. Smweing
Earth Resources Ltd., Hendy, Swansea, UK

and formed when Oman was separated into a series of horsts and grabens (Fig. 1c; Cozzi et al., 2012; Le Guerroué et al., 2005; Romine & Stuart-Smith, 2003). This study aims to understand the temporal and lateral distribution of the outcropping Fiq Formation and to build an illustrative depositional model on previous studies.

2 Materials and Methods

The main objective of the study is to adopt sedimentological and stratigraphic approaches to identify lithological units, sedimentary structures and features, along with facies analysis of a well-exposed outcrop section of the Fiq Formation, located in Wadi Hajir, Sahtan Bowl, northern Jabal Akhdar area, Oman. Sequences stratigraphic concepts, and relationship with glacial advance and retreat cycles and associated sea-level rise and drop were applied to the identified facies associations to come up with a simplified explanation of the sequence stratigraphic evolution of the Fiq Formation.

3 Results

The logged section of the Fiq Formation comprises four facies associations (Fig. 2). The first facies association consists of discontinuous thin intervals of clast-supported diamictites interbedded with massive coarse-grained sandstones (Fig. 2a). The second facies association consists predominantly of thick units of matrix-supported diamictites which make most of the studied section (Fig. 2b). Dilute

matrix-supported, clast-poor diamictites consist of local isolated cobble-sized, elongated, rounded to subrounded extraformational granitic clasts displaying clear bending below the clasts within the fine-grained matrix (Fig. 2c). The third facies association consists of sheet-like, sharp-based massive to graded, coarse to very coarse-grained sandstones, locally with rippled tops, displaying pulse-like features (Fig. 2d). This facies association consists also of a well-sorted pebbly sandstones and clast-supported conglomerates (Fig. 2d). The sharp-based graded, pulse-like sandstones are interbedded with laminated and planar laminated, and convoluted/deformed very fine-grained sandstones, siltstones, and mudstones (Fig. 2d, g, h). It also consists of rippled very fine-grained rippled sandstones, siltstones, and mudstones (Fig. 2e). This facies association displays local soft-sediment deformation structures (e.g., slumps, slumped folds, load casts, and flame structures; Fig. 2f). These graded sandstone beds are millimeter to decimeter thick. The fourth facies association consists of thick units (> 10 m) of massive structureless units, showing fining upward sequences (Fig. 2i).

4 Discussion

The discontinuous clast-rich diamictites, interbedded with massive sandstone beds are suggestive of rainout diamictites formed by a continuous source of debris below an ice sheet, close to the grounded ice margin of the basin, in ice-proximal glaciomarine setting (Allen et al., 2011a; Eyles & Januszczak, 2004; Miller, 1996). The matrix-supported,

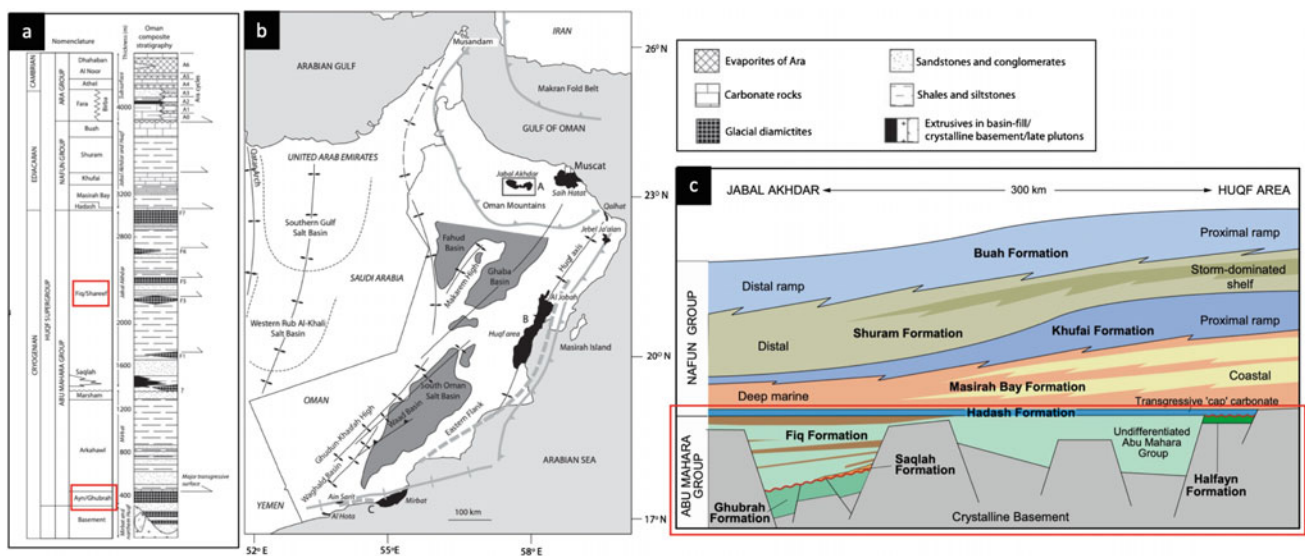
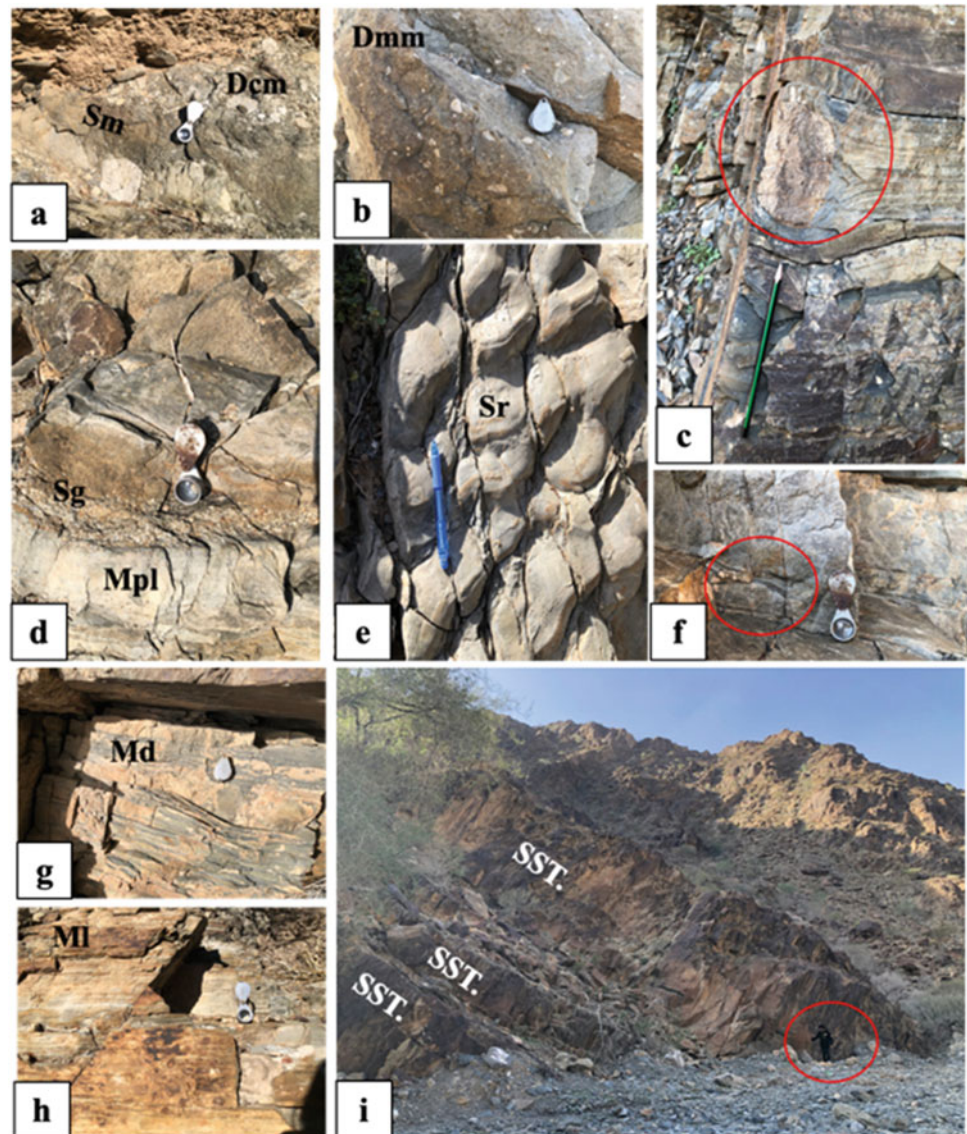


Fig. 1 **a** Composite lithostratigraphic column of the Neoproterozoic Huqf Supergroup deposits in Oman. Note the labeled Ghubrah and Fiq formations. **b** Location map of the Neoproterozoic outcrops of the Huqf Supergroup in the Jabal Akhdar area, Huqf area, Mirbat area.

c Tectonostratigraphic model of the Abu Mahara Basin showing the created horsts and graben structures (modified after Allen et al., 2011a; Cozzi et al., 2012; Le Guerroué et al., 2005)

Fig. 2 Field photographs showing outcrop lithofacies of the Cryogenian Fiq Formation in Wadi Hajir, Sahtan Bowl, Jabal Akhdar area of northern Oman. **a** Massive, clast-supported diamictite (Dcm) interbedded with massive sandstone (Sm). **b** Massive, matrix-supported diamictite (Dmm). **c** Granitic elongated ice-rafted dropstone. **d** Interbedded unit of planar laminated siltstone and sharp-based graded sandstone (Sg). **e** Rippled siltstone (Sr). **f** Soft sediment deformation (slumped fold). **g** Deformed siltstone (Md). **h** Laminated siltstone (Ml). **i** Massive thick units of structureless sandstones. Note the scale (red circle; SST.: sandstone)



clast-poor diamictites sourced by iceberg-based debris and deposited as rainout diamictites, towards the distal area of the basin, representing ice-distal glaciomarine diamictites, with evidenced glacial ice-rafted dropstones (Gilbert, 1990). The massive sheet-like sandstones, locally graded with rippled tops, suggest sand-rich turbiditic, gravity flow-induced facies, deposited in an unstable slope setting (Allen et al., 2011a; Eyles & Januszczak, 2004; Leather, 2001). This is supported by soft sediment deformations indicative of an unstable slope (Novak & Egenhoff, 2019). The planar laminated and convoluted siltstones and mudstones are suggestive of suspended deposits formed by the gradual settlement of dilute turbid plumes (Allen et al., 2011a; Leather, 2001; Stow et al., 1996). The rippled tops

fine-grained sandstones, siltstones, and mudstones are current-based ripples formed by dilute mass flow turbidity current in deep water setting (Allen et al., 2011a). The presence of thick units of dilute matrix-supported diamictites in the logged section in Wadi Hajir implies that most of the Fiq Formation strata were deposited during glacial retreat (i.e., sea-level rise; Hu et al., 2011; Miall, 1985). Massive thick units of sandstones imply deposition in a braided fluvial environment during the local glacial advance. Sequential deposition of glaciomarine and proglacial facies indicates that the Fiq Formation represents cycles of sea-level rise and fall events formed during local and multiple glaciation and deglaciation events (Hu et al., 2011; Miall, 1985).

5 Conclusions

The study aimed to build on previous outcrop studies, a detailed illustrative depositional model of the Cryogenian Fiq Formation. The study revealed that Fiq Formation is of glacial origin, evidenced by the proximal to distal glaciomarine diamictites and the granitic dropstones. The Fiq Formation consists also proglacial facies associations, including massive and locally graded sandstones with rippled tops, pebbly sandstones and conglomeratic beds, laminated and deformed siltstones. The Marinoan glaciation dynamic preserved in the Fiq Formation displays cyclic deposition of glacial advance and glacial retreat cycles during the Cryogenian, formed during local cyclic sea-level fall and rise.

Acknowledgements This study is funded by Tethys Oil Ltd, done in partial fulfillment of the requirements for the degree of Master of Science in Petroleum Geology in the Sultan Qaboos University (SQU), Oman. The authors are grateful to the anonymous reviewers for critically reading the manuscript and improving the text.

References

- Allen, P. A., Leather, J., Brasier, M. D., Rieu, R., McCarron, M., Guerroué, E. L., Etienne, J. L., & Cozzi, A. (2011a). The Abu Mahara Group (Ghubrah and Fiq formations), Jabal Akhdar, Oman. *Geological Society Memoir*, 36(1).
- Allen, P. A., Rieu, R., Etienne, J. L., Matter, A., & Cozzi, A. (2011b). The Ayn Formation of the Mirbat Group, Dhofar, Oman. In E. Arnaud, G. P. Halverson, & G. Shields-Zhou (Eds.), *The geological record of Neoproterozoic glaciations*. Geological Society, London, *Memoirs*, 36, 239–249.
- Cozzi, A., Rea, G., & Craig, J. (2012). From global geology to hydrocarbon exploration: Ediacaran-early Cambrian petroleum plays of India, Pakistan and Oman. *Geological Society Special Publication*, 366(1).
- Eyles, N., & Januszczak, N. (2004). “Zipper-rift”: A tectonic model for Neoproterozoic glaciations during the breakup of Rodinia after 750 Ma. *Earth-Science Reviews*, 65(1–2).
- Gilbert, R. (1990). Rafting in glaciomarine environments. In J. A. Dowdeswell & J. D. Scourse (Eds.), *Glaciomarine environments: Processes and sediments*. Geological Society Special Publication, 53, 105–120.
- Hu, J., Wang, J., Chen, H., Wang, Z., Xie, L., & Lin, Q. (2011). Multiple cycles of glacier advance and retreat during the Nantuo (Marinoan) glacial termination in the Three Gorges area. *Frontiers of Earth Science*, 6.
- Le Guerroué, E., Allen, P. A., & Cozzi, A. (2005). Two distinct glacial successions in the Neoproterozoic of Oman. *GeoArabia*, 10, 17–34.
- Leather, J. (2001). *Sedimentology, chemostratigraphy and geochronology of the lower Huqf Supergroup, Oman* [Ph.D. thesis]. Trinity College Dublin, Ireland. Unpublished.
- Miall, A. D. (1985). Sedimentation on an early Proterozoic continental margin under glacial influence: The Gowganda Formation (Huronian), Elliot Lake area, Ontario, Canada. *Sedimentology*, 32(6), 763–788.
- Miller, J. M. G. (1996). Glacial sediments. In H. G. Reading (Ed.), *Sedimentary environments: Processes, facies and stratigraphy* (pp. 454–484). Blackwell Science Ltd.
- Novak, A., & Egenhoff, S. (2019). Soft-sediment deformation structures as a tool to recognize synsedimentary tectonic activity in the middle member of the Bakken Formation, Williston Basin, North Dakota. *Marine and Petroleum Geology*, 105, 124–140.
- Romine, K., & Stuart-Smith, P. (2003). *Regional seismic interpretation: Western deformation front, South Oman Salt Basin*. SRK confidential report to PDO (65 pp.).
- Stow, D. A. V., Reading, H. G., & Collinson, J. D. (1996). Deep seas. In H. G. Reading (Ed.), *Sedimentary environments: Processes, facies and stratigraphy* (pp. 395–453). Blackwell Science.



Sedimentary and Stratigraphic Description of the Castellón B Borehole Cores (Offshore Western Mediterranean)

Telm Bover-Arnal, Carles Ferràndez-Cañadell, Julio Aguirre, Ulrich Heimhofer, and Mateu Esteban

Abstract

The Castellón B-1, 2, 3, 4, 11, and 12 cores were studied to establish the precise age and the stratigraphic framework of the Cenozoic offshore sedimentary succession from eastern Iberia. Six stratigraphic units were recognized: (i) a Black Sandstone Unit, (ii) a Red Beds Unit, (iii) the Alcanar Conglomerates, (iv) the Tarraco “Shale,” (v) the Amposta Limestone, also known as “Amposta Chalk,” and (vi) the San Carlos Group. The Black Sandstone Unit corresponds to non-fossiliferous slightly foliated fault breccias that resemble the Carboniferous Scala Dei Formation cropping out in the Priorat area (onshore Catalonia, NE Spain). The Red Beds Unit consists of fine-grained sandstones and red clays containing *Classopollis* sp. pollen grains, which range from the Late Triassic to the Paleocene. According to the known stratigraphy of onshore deposits from eastern Iberia, they are comparable with the red beds of the uppermost Cretaceous-Paleocene Mediona Formation. The Alcanar Conglomerates are mainly made up of Paleozoic clasts indicating the existence of nearby subaerially exposed Paleozoic rocks. The Tarraco “Shale” is made up of siliciclastic-influenced wackestone-packstone textures with planktonic foraminifera. Above, the Amposta Limestone comprises platform carbonates rich in coralline red algae, as well as larger benthic foraminifera including *Borelis* sp., *Heterostegina* sp., *Amphistegina mammilla*,

and *Amphistegina bohdanowiczi*. The foraminiferal association suggests an early-mid Langhian age. The drowning of the Amposta Limestone is marked by the deposition of the planktonic foraminifera-rich deposits of the lower part of the San Carlos Group.

Keywords

Miocene • Iberian Plate • Western Mediterranean • Carbonate Platform • Amposta Limestone

1 Introduction

The Castellón B borehole cores were drilled by Shell España between 1968 and 1986 on the Castellón High (offshore Eastern Mediterranean; Fig. 1). The offshore succession drilled yielded non-economic hydrocarbon reservoirs, and thus, these wells were soon abandoned. Much information on the geology of these borehole materials is not yet public and has only been described in internal reports of oil companies. The study of these rocks is thus an opportunity to gain geological knowledge and better characterize the stratigraphy and age of the succession from the offshore western Mediterranean. An improved chronostratigraphic framework for this succession will allow better correlations to be drawn between offshore and onshore successions.

2 Materials and Methods

The Castellón B-1, 2, 3, 4, 11, and 12 cores studied (Fig. 1b) are stored at the core facilities of the Spanish Geological Survey (IGME) in Peñarroya-Pueblonuevo (Province of Córdoba, S Spain). The six borehole cores were logged and sampled. A total of 127 samples were collected to produce thin sections to characterize the microfacies and search for age-diagnostic fossil remains.

T. Bover-Arnal (✉) · C. Ferràndez-Cañadell
Universitat de Barcelona, Martí i Franquès s/n,
08028 Barcelona, Spain
e-mail: telm.boverarnal@ub.edu

J. Aguirre
Universidad de Granada, Fuentenueva s/n, 18002 Granada, Spain

U. Heimhofer
Leibniz University Hannover, Callinstraße 30,
30167 Hannover, Germany

M. Esteban
07314 Caimari, Mallorca, Spain

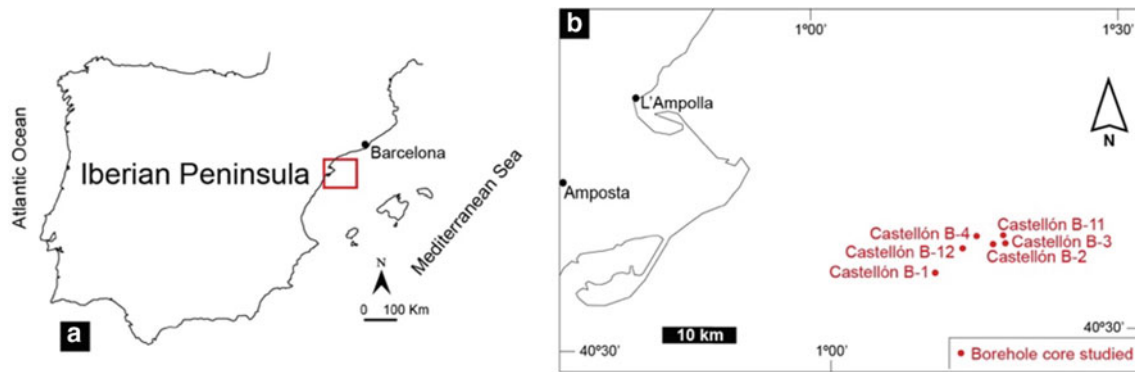


Fig. 1 Geographical setting in the offshore eastern Iberia (a) of the borehole cores studied (b)

3 Results

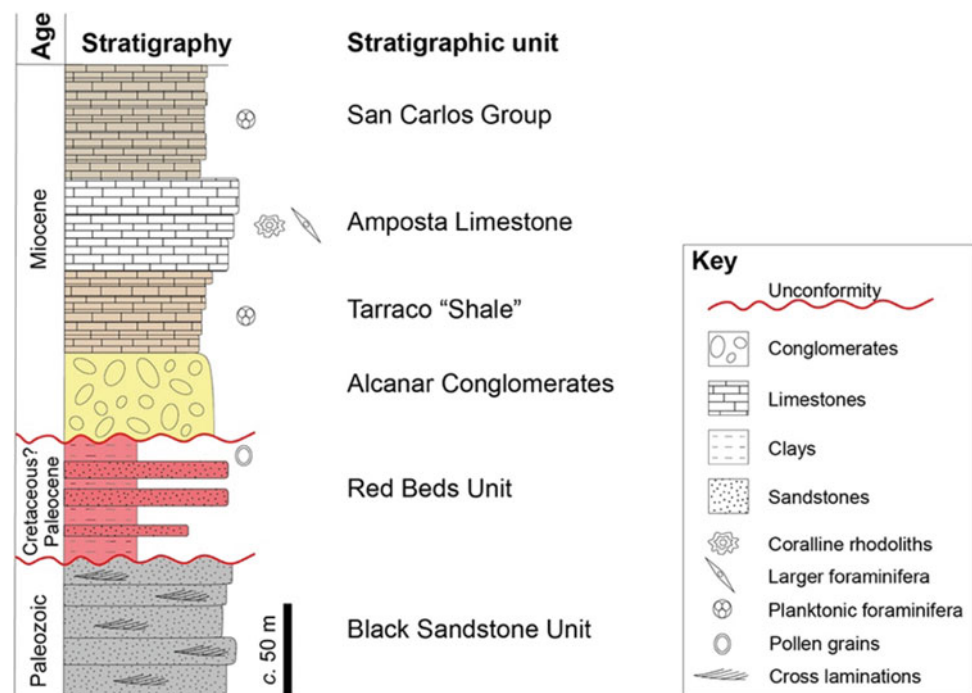
3.1 Description of the Sedimentary Succession and Fossil Content

The Paleozoic and Cenozoic sedimentary succession studied in the cores (Fig. 1b) can be subdivided into six stratigraphic units (Fig. 2). From older to younger, these are (i) a Black Sandstone Unit (> 50 m thick), (ii) a Red Beds Unit (> 50 m thick), (iii) the Alcanar Conglomerates (between 40 and 75 m thick), (iv) the Tarraco “Shale” (between 10 and 90 m thick), (v) the Amposta Limestone, also known as “Amposta Chalk” (between 40 and 60 m thick), and (vi) the San Carlos Group (> 60 m thick).

The Black Sandstone Unit consists of brecciated and slightly foliated meta-sandstones, which exhibit laminations and quartz-filled fractures (Fig. 3a). This unit is barren of fossil remains. The Red Beds Unit is formed by red clays and red and gray sandstones (Fig. 3b). The clay of the Red Beds Unit yielded pollen grains belonging to the genera *Classopollis* and *Cycadopites*.

The Alcanar Conglomerates unit is constituted by dolomitized sandstones and conglomerates, including Paleozoic metamorphic and Mesozoic carbonate clasts. This unit contains very scarce marine fossils such as unidentified bivalves remains and foraminifera. The Tarraco “Shale” is mainly made up of fine-grained wackestone to packstone textures with planktonic foraminifera (Fig. 3c), siliciclastic grains, and radioactive detrital dolomite.

Fig. 2 Chronostratigraphy of the sedimentary succession recovered from the Castellón B boreholes. See also (Seemann et al., 1990) for a generalized stratigraphic column of the offshore western Mediterranean area



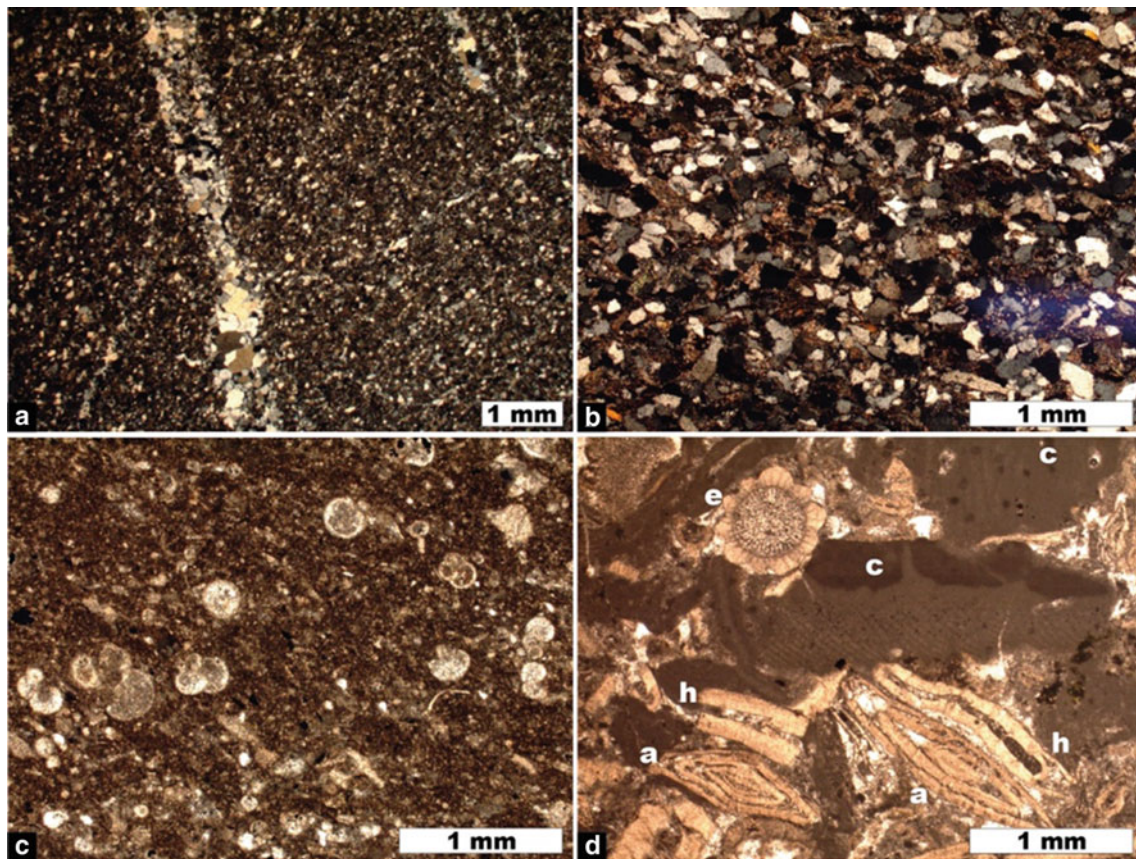


Fig. 3 **a** Paleozoic Black Sandstone Unit exhibiting fractures filled with quartz. **b** Sandstone of the Red Beds Unit. **c** Hemipelagic planktic foraminifera-rich facies of the Tarraco “Shale.” **d** Grain-supported

texture of the Amposta Limestone, including *Amphistegina mammilla* (a), *Heterostegina* sp. (h), coralline algae (c), and echinoid fragments (e)

The Amposta Limestone consists of grain-supported carbonate textures, mainly rudstones, containing coralline algae (mainly forming rhodoliths together with gypsinids), larger foraminifera, bryozoans, and echinoid fragments (Fig. 3d). The coralline algae identified includes *Lithothamnion* spp., *Mesophyllum* spp., *Sporolithon* sp., *Spongites* sp., and *Lithoporella* sp., whereas the larger foraminifera recognized are *Borelis*, *Heterostegina*, *A. mammilla* (Fig. 3d), and *A. bohdanowiczi*. The Amposta Limestone is pervasively micritized due to strong diagenetic overprinting: it exhibits a friable condition and a “chalky” appearance. The San Carlos Group is made up of hemipelagic fine-grained packstones with planktonic foraminifera and scarce fragments of skeletal components derived from more proximal settings such as *Amphistegina* or bryozoan colonies.

4 Concluding Remarks

The non-fossiliferous slightly foliated fault breccias named herein as Black Sandstone Unit resemble the Carboniferous Scala Dei Formation cropping out in the Priorat area

(onshore Catalonia, NE Spain). The Red Beds Unit consisting of fine-grained sandstones and red clays contains *Classopollis* sp. pollen grains, a long-ranging genus extending from the Late Triassic to the Paleocene. According to the known stratigraphy of onshore deposits from eastern Iberia, they are only comparable with the red beds of the uppermost Cretaceous-Paleocene Mediona Formation.

The Alcanar Conglomerates are made up of Paleozoic and Mesozoic clasts indicating the existence of nearby subaerially exposed Paleozoic and Mesozoic rocks. The Tarraco “Shale” is made up of siliciclastic-influenced wackestone-packstone textures with planktonic foraminifera and indicates a transgressive interval.

The Amposta Limestone comprises platform carbonates rich in coralline algae, as well as larger foraminifera including *Borelis*, *Heterostegina*, and *Amphistegina*. This foraminiferal association suggests an early-middle Langhian age. Platform carbonates of Langhian age with larger foraminifera, oysters, coralline algae, and corals, which locally formed small reefs, are found in the Penedès Basin (onshore Catalonia, NE

Spain) and thus would be correlatable with the Amposta Limestone. The drowning of the Amposta Limestone is marked by the deposition of the planktonic foraminifera-rich deposits of the lower part of the San Carlos Group, which is interpreted as a hemipelagic transgressive unit.

Reference

- Seemann, U., Pümpin, V.F., & Casson, N. (1990). Amposta oil field. In *American association of petroleum geologists treatise of petroleum geology* (pp. 1–20). Atlas of Oil and Gas Fields. American Association of Petroleum Geologists, Tulsa



New Carbon-Isotope, Conodont, and Magnetostratigraphic Data from the Key Kulyumbe River Section (NW Siberia) and the Problem of Location of the Cambrian-Ordovician Boundary on the Siberian Platform

Vladimir Pavlov, Andrei Dronov, Tatiana Tolmacheva, Elizaveta Krasnova, and Alexander Larionov

Abstract

The Kulyumbe River section (NW of the Siberian Platform) is one of the most complete, best exposed, well-studied, and relatively easily accessible Cambrian-Ordovician (Cm-O) successions on the entire Siberian Platform. It is a key section for regional correlation of the Furongian-lower Ordovician interval in Siberia. However, the exact position of the Cm-O boundary as well as the boundaries of the global Ordovician stages in the section is still a matter of debate. We present new magneto-, chemo-, and biostratigraphic data, which allow us to discuss the position of the Cm-O and Tremadocian-Floian boundaries in the Kulyumbe River section. These data determine a new confident levels for correlation of transitional Siberian Cm-O layers with the International Stratigraphic Scale.

Keywords

Cambrian-Ordovician boundary • Tremadocian-Floian boundary • Siberian platform • Carbon isotope data • Conodonts • Magnetostratigraphy

1 Introduction

The Kulyumbe River section is a key section for regional correlation of the Furongian-lower Ordovician interval in Siberia. The exact position of the Cm-O boundary in the section has long been hotly debated, mainly due to the endemism of the Siberian fauna and the absence of a global stratotype of this boundary. Shortly after the base of the Ordovician system has been officially defined at the level of the first appearance of *Iapetognathus fluctivagus*, detailed study of conodonts from the Cm-O transition in the Kulyumbe River section was carried out (Tolmacheva & Abaimova, 2009). This study showed that the Cm-O boundary in the section should be placed in the middle part of the Nyaian Regional stage. Results of our investigations support this conclusion. The next important issue is tracing the boundaries of the global Ordovician stages in the Kulyumbe section, in particular, determining the position of the Tremadoc-Floian boundary. Below, we present our preliminary results that constrain the location of this boundary. Magneto- and chemostratigraphic characteristics of stratigraphic units and their boundaries are of great importance for their regional and global correlation. In the course of our study, we have obtained detailed records of changes in magnetic polarity and $\delta^{13}\text{C}$ in the reference Kulyumbe section. Here, we demonstrate these records and discuss their important features that can be used for correlation of Ordovician sections.

2 Short Geological Description of the Section

The transitional Cm-O layers crop out along the Kulyumbe River (68.0°N, 88.8°E; NW of the Siberian platform) over a distance of about 1 km and represent the most complete and

V. Pavlov (✉)

Institute of Physics of the Earth, Russian Academy of Sciences,
128242 Moscow, Russia
e-mail: pavlov.ifz@gmail.com

A. Dronov

Geological Institute, Russian Academy of Sciences,
119017 Moscow, Russia

T. Tolmacheva · A. Larionov

Russian Geological Research Institute,
199106 St. Petersburg, Russia

E. Krasnova

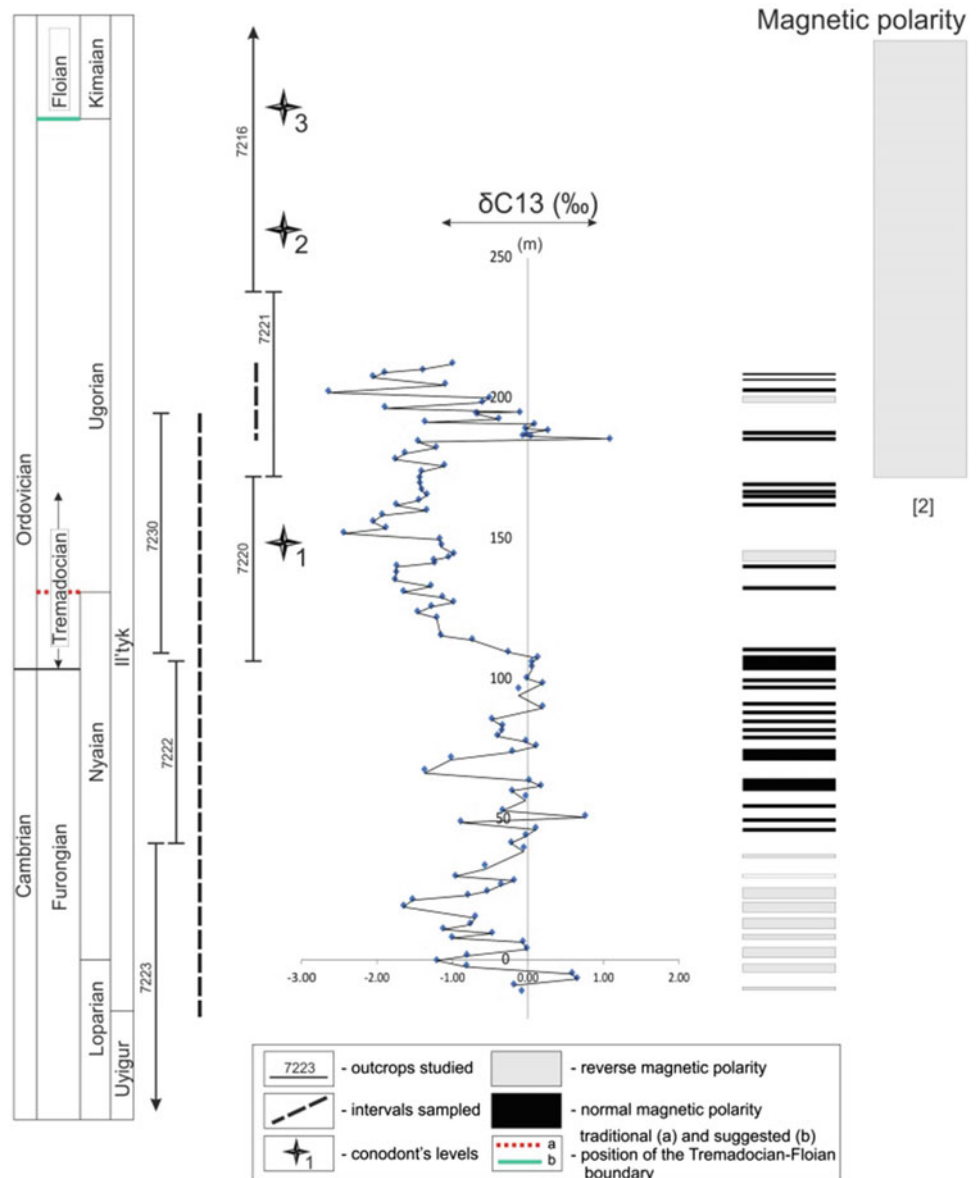
Lomonosov Moscow State University, 119991 Moscow, Russia

longest Siberian section across the Cm-O boundary. The succession is remarkably uniform in lithology; it lacks visible unconformities and sharp lithological changes. The lower half of the section is represented by gray and yellowish dolomites and limestones referred to the Uyghur Formation. The upper half of the section, assigned to the Il'tyk Formation, consists of gray limestones and variegated dolomites and siltstones. The succession embraces the Loparian, Nyaian, and Ugorian biostratigraphic regional stages, which are distinguished by the distribution of endemic benthic faunas and are easily recognizable over the whole territory of Siberia. The Kulyumbe section is traditionally regarded as the reference section for these three regional stages.

3 Results

Conodont studies. During the field works 2021, the transitional Cm-O interval of the Kulyumbe section has been sampled. From samples located stratigraphically slightly above the level proposed by Tolmacheva and Abaimova (Tolmacheva & Abaimova, 2009) for the Cm-O boundary (Fig. 1, level 1), we have recovered conodonts *Semiacontiodus* sp., *Monocostodus severiensis* (Miller), *Semiacontiodus* cf. *S. iowensis* (Furnish), and *Teridontus* sp. These conodonts are characteristic for the lower Tremadocian; therefore, their finding supports the conclusion of Tolmacheva and Abaimova. Until recently, the boundary of the Tremadocian and Floian stages in the Siberian sections was

Fig. 1 Magneto- and chemostratigraphic data from Cm-O transition in the Kulyumbe section



drawn along the boundary of the Nyaian and Ugorian regiestages of the Siberian regional stratigraphic scale.

However, our study has shown that the conodonts *Glyptoconus quadruplicatus* and *Histiodelpha angulata*, typical for the upper Tremadoc, occur significantly above this boundary in the upper part of the Ugorian (Fig. 1, level 2). On the other hand, the first elements of *Prioniodus*, which can formally mark the lower boundary of the Floian stage for the Kulumbe section, first appear only at the lowest levels of the Kimaian Regiostage (Fig. 1, level 3). These results clearly indicate that the Tremadocian-Floian boundary in the Kulumbe section, as well as on the Siberian platform as a whole, should be placed close to the base of the Kimaian Regiostage that is much higher than previously thought.

Magnetostratigraphy. The establishment of new position of the Cm-O boundary prompted us to conduct detailed study of the magnetic polarity record and $\delta^{13}\text{C}$ changes in the Cm-O transitional layers, namely in layers corresponding to upper Loparian, Nyaian, and lower Ugorian regiestages. The detail of our research is several times higher than that in previous works. The rocks composing the studied interval of the section are severely remagnetised by neighboring trap intrusions. Nevertheless, thermal demagnetization reveals in a part of the samples clear circles of remagnetization, which make it possible to identify zones of magnetic polarity. Upper Loparian and lower Nyaian layers have been formed when geomagnetic field had a reverse polarity. The rest of the Nyaian Regiostage corresponds to thick normal polarity zone. The lower part of the Ugorian Regiostage is characterized by alternating reverse and normal polarity with predominance of the latter. And finally, as it was shown in Rodionov and Gurevich (2010), the rocks of the rest of the Ugorian Regiostage and the entire overlying Kimaian Regional stage have been formed during an epoch of reverse polarity (Fig. 1).

Chemostratigraphy. Obtained chemostratigraphic record is rather noisy and does not reveal any high-amplitude anomalies. Nevertheless, the tendencies of $\delta^{13}\text{C}$ changes are quite obvious and can be described as follows. The Cambrian part of the record shows moderate values of $\delta^{13}\text{C}$ with one or two relatively small negative anomalies, the amplitudes of which are about -1.5% . At the Cm-O boundary, the value of $\delta^{13}\text{C}$ oscillates about 0% and then rapidly decreases to -2.5 to -3.5% . Upper Nyaian and lower Ugorian rocks record a fairly wide (but moderate in amplitude) negative anomaly, interrupted for a short time by an increase in $\delta^{13}\text{C}$ to a value of $\sim 0\%$ and even more.

4 Discussion

Our data allow to present new characteristics that can probably be used to trace the Cm-O boundary and for regional and worldwide correlation of sections of this age. In particular, our

results show that the Cm-O transition occurred when the geomagnetic field had normal polarity, and at least, the early Tremadocian was also characterized by the predominance of normal polarity. On the other hand, taking into account the magnetostratigraphic data from Rodionov and Gurevich (2010), we can assume that the onset of the Ordovician superchron of reverse polarity did not occur at the very beginning of Arenig (Floian), as previously thought, but probably several million years earlier. Chemostratigraphic data from the transition interval of the Kulyumbe River section are generally consistent with chemostratigraphic data found in other section around the world. The rapid decrease in the values of $\delta^{13}\text{C}$ immediately after the Cm-O boundary can be an important marker of this boundary, unless it is due to some incomformity in this part of the section, as suggested in Tolmacheva and Abaimova (2009). Other important feature of the obtained record is short-term increase of the $\delta^{13}\text{C}$ values in the middle part of the Ugorian Regional stage. It may tentatively be correlated with the well-known TSICE anomaly.

5 Conclusions

(1) New data obtained from conodonts of the Kulyumbe section support the location of the Cm-O boundary proposed in Tolmacheva and Abaimova (2009). The Tremadocian-Floian boundary does not correspond to the boundary of the Nyaian and Ugorian regiestages (as it was previously accepted) and located much higher, probably, close to the base of the Kimaian Regiostage; (2) the Cm-O transition occurred when the geomagnetic field had normal polarity. The Ordovician superchron of reverse polarity probably extends several million years further into the past than previously thought; (3) the chemostratigraphic record obtained from the transitional Cm-O layers of the Kulyumbe section has significant potential for regional and global correlations. The work is supported by RSF Grant #20-17-00198.

References

- Rodionov, V. P., & Gurevich, E. L. (2010). Key magnetostratigraphic sequence of the Lower Ordovician deposits, northwestern Siberian platform. *Neftegazovâ Geologîâ Teoriâ i Praktika*, 5, 3.
- Tolmacheva, T., & Abaimova, G. (2009). Late Cambrian and early Ordovician conodonts from the Kulumbe River section, northwest Siberian platform. *Memoirs of the Association of Australasian Palaeontologists*, 37, 427–451.



The Aptian Incised Valleys Recorded in the Maestrat Basin (E Iberia)

Telm Bover-Arnal, Ramon Salas, Joan Guimerà, and Josep Anton Moreno-Bedmar

Abstract

Carbonate platforms flourished in the Maestrat Basin (E Iberian Plate) during the Aptian recorded two episodes of major sea-level fall. The sedimentary results of lowering sea level during the Aptian were studied in two sub-basins of the Maestrat Basin, namely, Galve (in the western margin) and Morella (in the northern margin). The oldest episode occurred within the *Dufrenoyia furcata* ammonite zone, during the late early Aptian, whereas the youngest event had an early late Aptian age and occurred around the boundary between the *Epicheloniceras martini* and *Parahoplites melchioris* ammonite zones. The sedimentary evidence of such drops in sea level includes erosional, locally incised, subaerial unconformities with paleokarst developed at the platform tops. The amplitudes of sea-level fall are estimated to be in the order of 50 to > 100 m and were measured from the depths of the incised valleys recorded. There are no angular stratal relationships between the truncated sedimentary successions and the incised valley fills. Therefore, these drops in relative sea level are interpreted to be mainly of eustatic origin. The late early and early late Aptian sea-level drops occurred respectively in < 0.9 and < 3 Myr according to the current version of the Geological Time Scale. Such amplitudes (> 10 m) and durations (< 0.9 Myr) of relative sea-level fall and subsequent rise are considered rapid in geological terms, and thus could be the result of glacial eustasy. Nevertheless, clear sedimentological, paleontological, and/or isotopic evidence of significant portions of Earth's surface covered by extensive ice sheets during the Aptian has not been reported so far.

Keywords

Aptian • Maestrat Basin • Carbonate platform • Sea-level changes • Sequence stratigraphy

1 Introduction

Carbonate platforms developed in low-latitude settings during the Phanerozoic were sensitive recorders of past relative sea-level changes. During the Aptian, the margins of the Tethys Ocean witnessed the development of extensive carbonate platforms characterized by the presence of rudist bivalves and corals. In the Maestrat Basin (Fig. 1a), which formed owing to two rifting episodes that affected the eastern part of the Iberian Plate during the Late Jurassic-Early Cretaceous, the Aptian platform carbonates recorded two episodes of major loss of accommodation that led to the development of deeply incised subaerial unconformities.

The incised subaerial unconformities were studied in the Morella and Galve sub-basins (Fig. 1b). These episodes of major relative sea-level drops are recorded at the upper part of the lower Aptian Villarroya de los Pinares Formation and the top of the platform carbonates of the lower part of the upper Aptian Benassal Formation (Fig. 1c). The finding of Aptian incised subaerial unconformities is of significance, in that it permits to measure reliable amplitudes of relative sea-level drop during this stage and thus, it provides valuable data to calibrate global eustatic charts.

2 Materials and Methods

The deeply incised subaerial unconformities, other key sequence-stratigraphic surfaces, stratigraphic geometries, and the facies architectures were mapped on panoramic photographs of the outcrops (Figs. 2 and 3). Depths of

T. Bover-Arnal (✉) · R. Salas · J. Guimerà
Universitat de Barcelona, Martí i Franquès s/n,
08028 Barcelona, Spain
e-mail: telm.boverarnal@ub.edu

J. A. Moreno-Bedmar
Universidad Nacional Autónoma de México,
04510 Coyoacán, Ciudad de México, Mexico

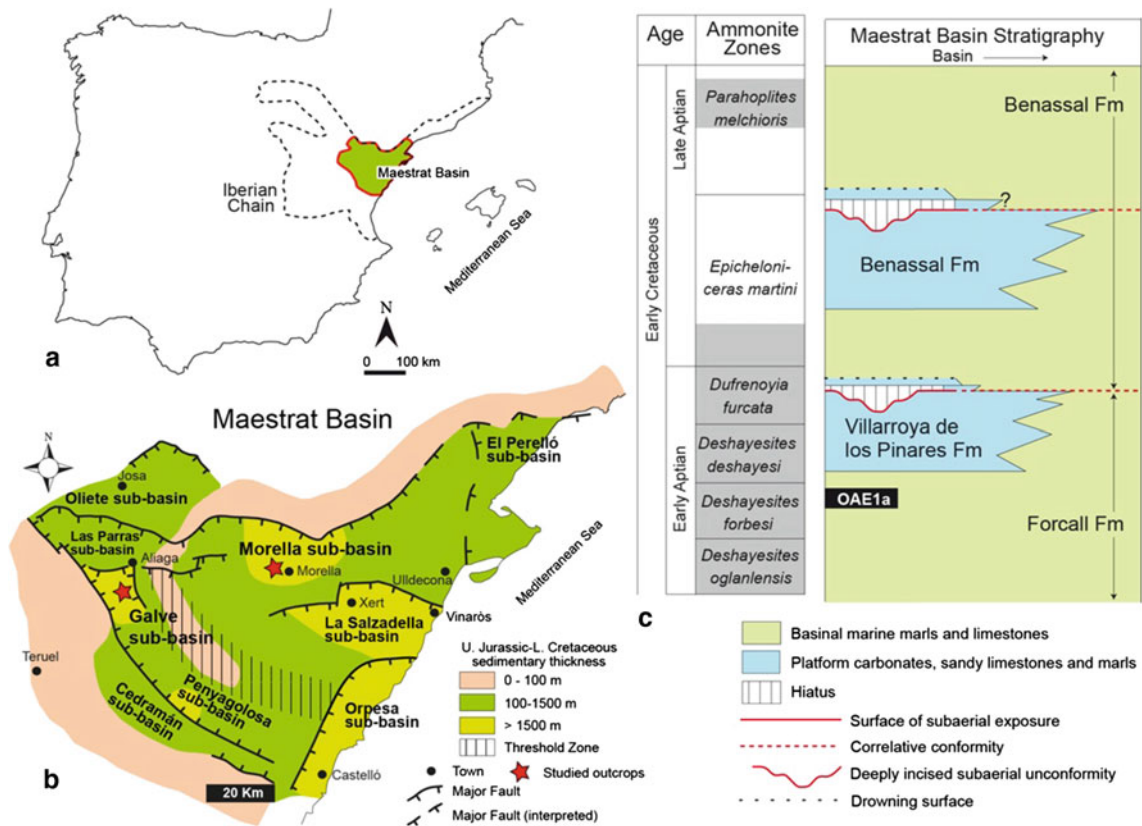


Fig. 1 **a** Geographical location of the Maestrat Basin in the eastern part of the Iberian Chain in eastern Iberia. **b** Paleogeographic map of the Maestrat Basin displaying the Upper Jurassic-Lower Cretaceous sedimentary thickness and its interpreted subdivision into nine sub-basins. **c** Stratigraphic framework and age of the Aptian

sedimentary succession of the Maestrat Basin. The Aptian deeply incised subaerial unconformities studied are indicated. The ammonoid zones identified in the Morella and Galve sub-basins are highlighted in gray. Modified after (Bover-Arnal et al., 2022)

incised valleys were measured on LiDAR- and drone-based models. The ages of the rocks analyzed were taken from Bover-Arnal et al. (2022).

3 Results

3.1 The Upper Lower Aptian Deeply Incised Subaerial Unconformity

In the Galve sub-basin (Fig. 1b), an upper lower Aptian (intra *Dufrenoyia furcata* zone; Fig. 1c) incised valley is well exposed. This incised valley is carved into aggrading highstand platform carbonates with rudists and corals of the Villarroya de los Pinares Formation (Fig. 2). The depth of the incision is around 50 m. Accordingly, the amplitude of the relative sea-level fall associated would have had a similar magnitude. The incised platform carbonates exhibit similar dips and dip directions to those of the transgressive valley fill, which onlaps the incised subaerial unconformity (Fig. 2). The truncation surface

exhibits paleokarst features. In the current version of the Geological Time Scale 2020, the *D. furcata* zone spanned 0.9 Myr.

3.2 The Lower Upper Aptian Deeply Incised Subaerial Unconformity

An example of an incised subaerial unconformity with the development of paleokarst of early late Aptian age is found in La Mola d'en Camaràs in the Morella sub-basin (Fig. 1b). The depth of the incised valley indicates that the amplitude of the relative sea-level drop and subsequent base-level rise was at least 115 m. The stratal relationship between the incised highstand succession of the Benassal Formation and the overlying transgressive valley fill is non-angular (Fig. 3). The subaerial exposure surface is dated around the boundary between the *Epicheloniceras martini* and the *Parahoplites melchioris* ammonite zones (Fig. 1c). According to the Geological Time Scale 2020, the duration of this fluctuation of relative sea level would have been < 3 Myr.

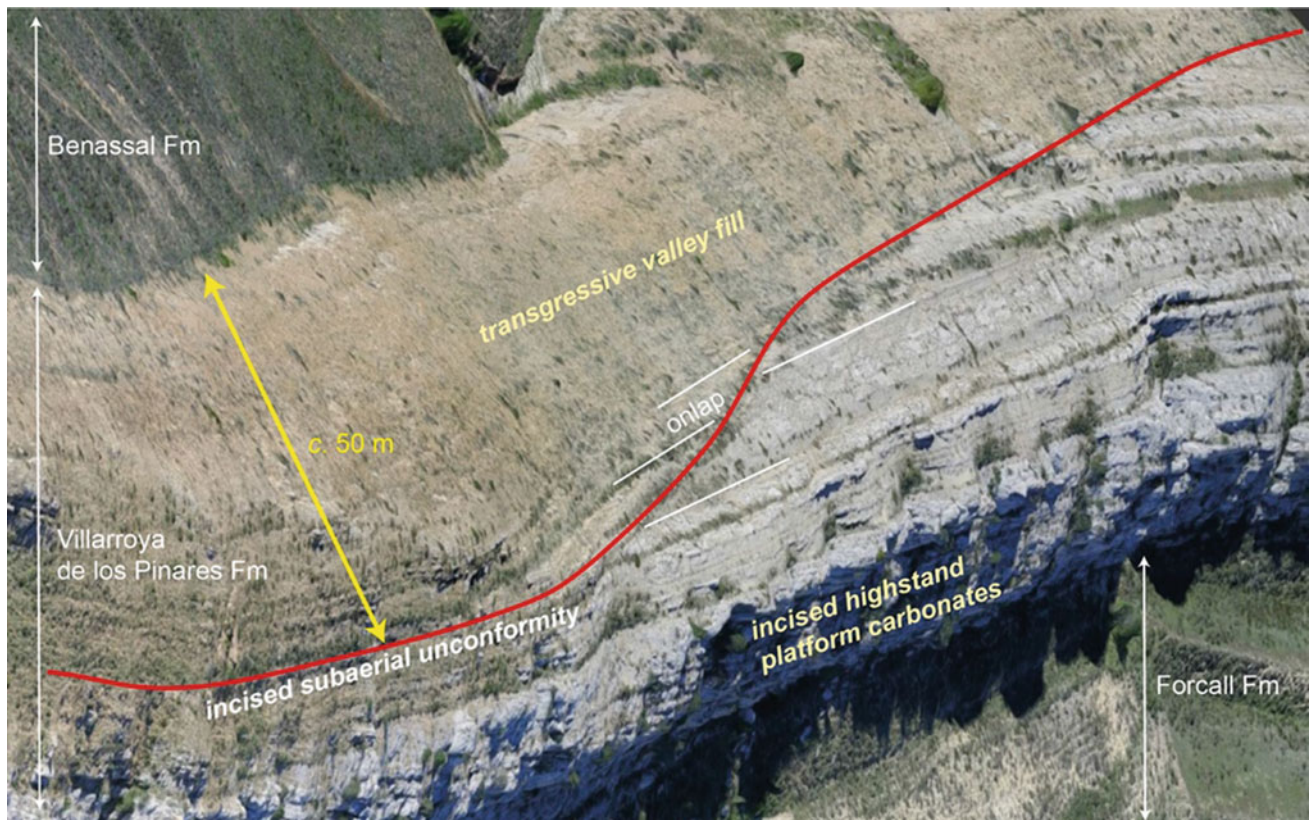


Fig. 2 Aerial image captured by a drone of the upper lower Aptian deeply incised subaerial unconformity outcropping in the Galve sub-basin (Fig. 1b). The photogrammetric model is courtesy of

Riccardo Rocca and available at http://riccardorocca.github.io/home/Camarillas_Platform.html, accessed 15 August 2022. See (Bover-Arnal et al., 2022) for the precise location of the section



Fig. 3 Panoramic view of La Mola d'en Camaràs in the Morella sub-basin (Fig. 1b) displaying the upper lower Aptian deeply incised subaerial unconformity. See (Bover-Arnal et al., 2022) for the precise location of the section

4 Discussion

The bedding of both the incised strata and the deposits filling in the incisions studied is nearly horizontal. Accordingly, the surfaces separating the truncated sedimentary successions below from the overlying valley fills above correspond to disconformities. The absence of angular unconformities suggests that eustasy played a key role in controlling the major fluctuations of the relative sea level analyzed.

In a rift basin, syn-rift subsidence must have played a part in controlling accommodation. However, tectonic tilting or folding is unlikely to be the main trigger of these major relative sea-level drops. To generate such disconformities mainly through tectonics, it would imply a > 50 m uplift, subaerial exposure, and incision of the sedimentary successions studied, and then a subsidence of > 50 m without any stratal deformation while marine sedimentation resumes, and everything occurring in < 0.9 Myr.

5 Conclusions

The Aptian Stage was punctuated by two episodes of major eustatic fluctuations of late early and early late Aptian age. The eustatic mechanism or mechanisms that controlled such changes in accommodation are unknown. The magnitude of these major sea-level variations (amplitudes of tens of meters and durations of < 1 Myr) would fall within the domain of glacial eustasy. Nevertheless, clear geological evidence of significant portions of Earth's surface covered

by extensive ice sheets during the Aptian has not been documented so far.

Reference

- Bover-Arnal, T., Salas, R., Guimerà, J., Moreno-Bedmar, J.A.: Eustasy in the Aptian world: A vision from the eastern margin of the Iberian Plate. *Glob. Planet. Change* 214, 103849. <https://doi.org/10.1016/j.gloplacha.2022.103849> (2022)



The Composition of Acervulinid – Red Algal Macroids from the Paleogene of Croatia and Their Distribution in the Wider Mediterranean Region

Jasenka Sremac, Filip Huić, Marija Bošnjak, and Tihomir Marjanac

Abstract

This research is a continuation of the previous biometrical study of the Eocene macroids in Dalmatia (southern Croatia), with the aim to determine the principal bioconstructors and reveal the composition and distribution patterns of macroids during the Paleogene Period. We randomly collected 322 samples of extracted macroids and 12 samples of host rocks, from the beaches between Omiš and Mimice in Dalmatia. Thin sections were prepared at the University of Zagreb/Faculty of Science, studied and photographed using a light microscope with camera. Macroids occur within the Eocene “Nummulitic” packstones, floatstones to rudstones, dominated by the large benthic foraminifera, a common facies of ramp crests, deposited along the coasts of the Tethys Ocean. Algal-dominant genera are *Sporolithon* and *Lithoporella*. Among the encrusting foraminifera, *Acervulina* and *Solenomeris* prevail. Serpulids, corals, bryozoans, echinoids, crinoids, and other biota also occur as bioclasts, but they are less abundant. Regularly shaped macroids can be classified as rhodoliths, as they are dominated by the genus *Sporolithon*. Irregularly shaped macroids were formed by the intercalation of red algal and encrusting foraminiferal layers, pointing to the slightly deeper depositional environment. The subsequent demise of green and then red algae, and their replacement with encrusting foraminifera during the Paleogene can be correlated with the basin subsidence and/or increased turbidity, a scenario related to the Alpine tectonics in this area.

Keywords

Acervulinidae • Florideophyceae • Macroids • Paleogene • Croatia

1 Introduction

During the Eocene Epoch, the Mediterranean region was in the midst of the Alpine tectonic episode. Due to the collision of the African and the European Plate, new continental masses were uplifted from the Neotethys Ocean, and vast shelf areas were formed, suitable for colonization of the benthic biota (Fig. 1a, blue areas). Foraminifera and red algae were the most common bioconstructors, particularly on wave ramps, where “Nummulitic limestones” (foraminiferal packstones/floatstones/rudstones) were deposited (e.g., Martín-Martín et al., 2021; Payros et al., 2010, and references therein).

The position of today’s Croatia was at the center of these events (see Fig. 1b) (e.g., Babić & Zupanić, 2007; Čosović et al., 2008, 2018; Marjanac & Čosović, 2000, and references therein). Due to the Eocene synsedimentary tectonics, platform margins partly collapsed, producing a regionally recognizable megabed in the Mediterranean region, with blocks composed of foraminiferal bioclastic limestones (e.g., Marjanac, 1991; Marjanac & Čosović, 2000; Petrinjak et al., 2021, and references therein). These olistoliths are today scattered along the Dalmatian beaches, where the wave erosion extracts from them bioclasts and macroids, which are the main topic of our research.

2 Materials and Methods

During the initial research, performed during 2019–2020, 322 macroid samples, washed out from the Eocene olistoliths, were randomly collected at the beaches between Omiš

J. Sremac (✉) · F. Huić
University of Zagreb, 10000 Zagreb, Croatia
e-mail: jsremac@geol.pmf.hr

M. Bošnjak
Croatian Natural History Museum, 10000 Zagreb, Croatia

T. Marjanac
ProGEO-Croatia, 10000 Zagreb, Croatia

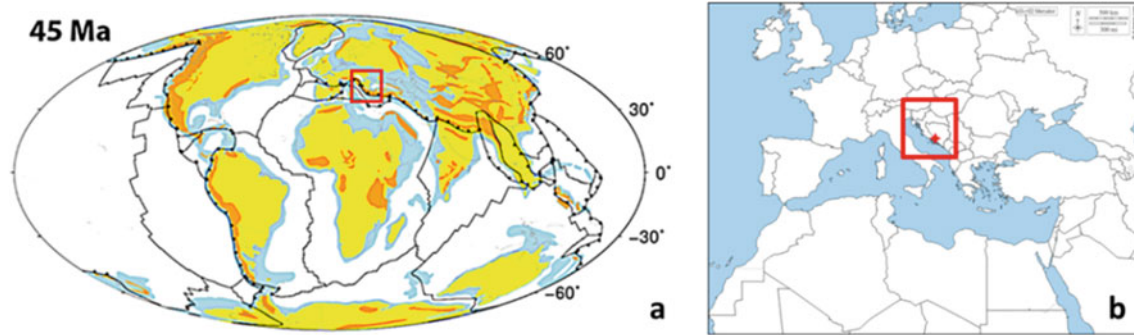


Fig. 1 **a** Global paleogeography during the Middle Eocene (Lutetian), ca. 45 Ma BP, with the approximate position of Croatia. Reconstruction is from Cao et al. (2017), with the plate motion model after (Matthews et al., 2016). Yellow = landmasses, orange = mountains;

blue = marine shallows; white = deep ocean; **b** Modern map of the Mediterranean region (white = land; blue = sea) (D-maps, 2022). The position of the study area is marked by the red asterisk in the red square

and Mimice, together with some fossil clasts and 12 samples of their host rocks. The main research locality was Stanići Beach. The initial analysis of the extracted macroids revealed variations in size and shape and their complex composition (Sremac et al., 2020). Thin sections were prepared at the University of Zagreb/Faculty of Science, studied and photographed with an Olympus SZX10 microscope equipped with a Canon EOS 1100D Camera. This research includes a detailed determination of the main bioconstructors and associated biota and their paleobiogeographic distribution.

3 Results

Large benthic foraminifera, dominantly of the genus *Nummulites*, were the most important carbonate producers during the middle-late Eocene in the study area, as well as in the whole Mediterranean region. Sometimes they occur together with rhodoliths and other macroids (e.g., Španiček et al., 2017).

The main bioconstructors of macroids in the Omiš area are rhodophytes and encrusting foraminifera (Fig. 2).

Among the red algae, Corallinophycidae prevails, with the most common genera being: *Sporolithon* (Order Sporolithales) (Fig. 2a) and *Lithoporella* (Order Corallinales) (Fig. 2b). *Sporolithon*-dominated rhodoliths are subspherical in form (Fig. 2a), while the complex macroids vary in shape, size, and composition (Fig. 2b). Red algae dominate among the macroid constructors: *Sporolithon lugeonii* (Pfender) Ghosh and Maithy, 1996, *Sporolithon* sp., *Lithoporella melobesioides* (Foslie) Foslie, 1909, *L. minus* Johnson, 1964, *Mesophyllum mengaudii* (Lemoine, 1934), *Polystrata alba* (Pfender) Denizot, 1968. Foraminifera *Acervulina linearis* Hanzawa, 1947 and *Solenomeris ogormani* Douvillé, 1924 are also quite common, while some other bioconstructors occur sporadically, e.g., red algae *Lithothamnion*, *Neogoniolithon* and *Hydrolithon*, textularian foraminifera *Placopsilina*, and miliolid foraminifera *Nubecularia*. Serpulid *Rotularia spirulea* (Lamarck, 1818) is also common, while *Rotularia* (*Praerotularia*) *marcinowskii* Radwanska, 1996 occurs sporadically. Rotaliid foraminifera can be found incorporated within macroid layers (Fig. 2b), or represent bioclasts in the matrix.

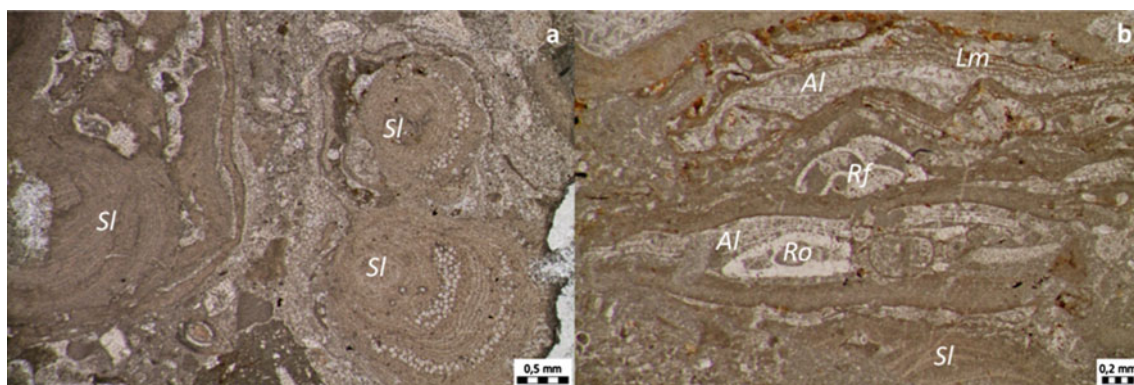


Fig. 2 The main bioconstructors of Eocene macroids from Dalmatia: *Sl* = *Sporolithon* sp.; *Al* = *Acervulina linearis* Hanzawa, 1947; *Lm* = *Lithoporella melobesioides* (Foslie) Foslie, 1909, *Ro* = *Rotorbinella* Bandy, 1944, *Rf* = sessile rotaliid foraminifera (*Haddonina*? sp.)

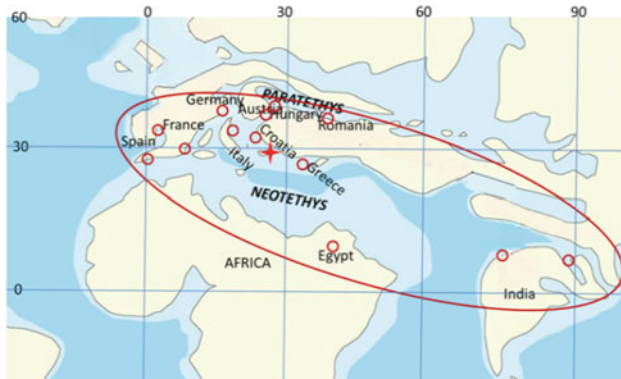


Fig. 3 The positions of the recorded Eocene macroid findings in the wider Mediterranean region, according to the available published data, are marked by red circles within a red ellipse. Yellow = land, light blue = marine shallows, blue = deep sea. The study area is marked by the red asterisk. Paleogeography inspired by Scotese (2022)

Solitary and colonial corals, gastropods, bivalves, bryozoans, echinoids, and crinoids (*Isselicrinites* sp.) can be recognized on weathering surfaces or are sometimes washed out from the host rock.

4 Discussion

The sites with Eocene macroids are the most abundant around the 30°N latitude, along the indented coasts of the NW Neotethys (Fig. 3).

By analogy with modern biota, *Sporolithon*-dominated, subspherical rhodoliths were deposited in the shallower, sunlit part of the middle ramp, compared to the complex *Acervulina*-rhodalgal, variably shaped macroids, which today occur in lower parts of the fore-reef zone (e.g., Bassi et al., 2011, and references therein). Sessile foraminifera *Acervulina linearis* was a cosmopolite bioencruster in Eocene seas, occurring together with the coralline alga *Lithoporella melobesioides*, and, during the middle-late Eocene, red alga *Sporolithon lugeonii*, which prefers less complex buildups.

Paleogene marine communities with large benthic foraminifera, similar to other Mediterranean (Neotethys) sites, comprise first green and then red algae, which are subsequently replaced with encrusting foraminifera and, finally, large orthofragmines (e.g., Čosović et al., 2018; Özcan et al., 2022, and references therein) and planktonic foraminifera. Changes in marine communities and depositional processes (from carbonate to clastic-carbonate deposition) are a consequence of basin subsidence and increased turbidity related to the synsedimentary tectonics in this area.

5 Conclusions

Eocene macroids from the Omiš area (S Croatia) occur within widespread Nummulitic bioclastic carbonate rocks. Two main types can be distinguished: *Sporolithon*-dominated rhodoliths (deposited on a shallow middle ramp) and complex acervulinid-rhodalgic macroids (deposited in slightly deeper ramp parts). Basin subsidence and increased turbidity caused a faunal turnover and prevalence of syn-orogenic, flysch-type deposition.

References

- Babić, Lj., & Zupanić, J. (2007). Major events and stages in the sedimentary evolution of the Paleogene Promina basin (Dinarides, Croatia). *Natura Croatica*, 16(4), 215–232.
- Bassi, D., Humblet, M., & Iryu, Y. (2011). Recent ichnocoenosis in deep water macroids, Ryukyu Islands, Japan. *Palaios*, 26(4), 232–238.
- Cao, W., Zahirovic, S., Flament, N., Williams, S., Golonka, J., & Müller, R. D. (2017). Improving global paleogeography since the late Paleozoic using paleobiology. *Biogeosciences*, 14, 5425–5439.
- Čosović, V., Marjanac, T., Drobne, K., & Moro, A. (2008). Outer Dinarides: Eastern Adriatic coast. Paleogene and Neogene. In: T. McCann (Ed.), *The geology of Central Europe, Volume 2: Mesozoic and Cenozoic* (pp. 1031–1139). The Geological Society London, London.
- Čosović, V., Mrinjek, E., Nemeč, W., Španiček, J., & Terzić, K. (2018). Development of transient carbonate ramps in an evolving foreland basin. *Basin Research*, 544(30/4), 746–765.
- D-maps. (2022). https://d-maps.com/carte.php?num_car=3138&lang=en. Accessed 19 Aug 2022.
- Marjanac, T. (1991). Importance of megabeds for reconstruction of Paleogene Flysch basin in Split hinterland (Middle Dalmatia). *Geološki vjesnik*, 44, 201–213.
- Marjanac, T., & Čosović, V. (2000). Tertiary depositional history of Eastern Adriatic realm. *Vijesti Hrvatskoga geološkog društva*, 37(2), 93–103.
- Martin-Martín, M., Guerrero, F., Tosquella, J., & Tramontana, M. (2021). Middle Eocene carbonate platforms of the westernmost Tethys. *Sedimentary Geology*, 415, 105861.
- Matthews, K. J., Maloney, K. T., Zahirovic, S., Williams, S. E., Seton, M., & Müller, R. D. (2016). Global plate boundary evolution and kinematics since the late Paleozoic. *Global and Planetary Change*, 146, 226–250.
- Özcan, E., Yücel, A. O., Erkızan, L. S., et al. (2022). Atlas of the Tethyan orthofragmines. *Mediterranean Geoscience Reviews*, 4, 3–213.
- Payros, A., Pujalte, V., Tosquella, J., & Orue-Etxebarria, X. (2010). The Eocene storm-dominated foralgal ramp of the western Pyrenees (Urbasa–Andia Formation): An analogue of future shallow-marine carbonate systems? *Sedimentary Geology*, 228(3–4), 184–204.
- Petrinjak, K., Budić, M., Bergant, S., & Korbar, T. (2021). Megabeds in Istrian Flysch as markers of synsedimentary tectonics within the Dinaric foredeep (Croatia). *Geologia Croatica*, 74(2), 99–120.

- Scotese, C. R. (2022). Plate tectonic maps and Continental drift animations. PALEOMAP Project. www.scotese.com. Accessed 19 Aug 2022.
- Španiček, J., Čosović, V., Mrinjek, E., & Vlahović, I. (2017). Early Eocene evolution of carbonate depositional environments recorded in the Čikola Canyon (North Dalmatian Foreland Basin, Croatia). *Geologia Croatica*, 70(1), 11–25.
- Sremac, J., Huić, F., Bošnjak, M., & Drempetić, R. (2020). Morphometric characteristics and origin of Paleogene macroids from beach gravels in Stanići (vicinity of Omiš, Southern Croatia). In: T. Malvić, U. Barudžija, M. Bošnjak, J. Sremac, & J. Velić (Eds.), *Mathematical methods and terminology in geology 2020*, Proceedings of reviewed papers, 49–61. University of Zagreb, Faculty of Mining, Geology and Petroleum Engineering, Zagreb.



Middle Miocene Chemosymbiotic Bivalves from the SW Margin of the Central Paratethys (Medvednica Mt., N Croatia)

Marija Bošnjak, Jasenka Sremac, and Elen Zukon Kolić

Abstract

Chemosymbiotic bivalves are rare and specialized biota, able to survive in hostile environments. We recorded their presence in the Middle Miocene (Badenian—Langhian/Serravallian) deposits of Northern Croatia. Bivalve specimens, representatives of the families Solemyidae (11 specimens) and Lucinidae (998 specimens), are in most cases preserved as casts and molds. Newly collected specimens (10 lucinids and 2 solemyids) were cleaned up, determined, and housed at the Croatian Natural History Museum and the University of Zagreb, Faculty of Science. Lucinid bivalves are widely dispersed and comprise several taxa, including the most numerous *Lucinoma borealis* (Linnaeus, 1767), particularly common *Lucina (Eomiltha) polymorpha* Kochansky, 1944 and *Megaxinus ellipticus* (Borson, 1825). They were found in deposits of different lithologies, varying from argillaceous marls to limestones. Lucinids are generally considered the most diverse among the chemosymbiotic bivalves, and are widely distributed in various habitats. Some of the collected lucinids lived in the shallower marine, oxygen-depleted environments. We also recorded solemyids and lucinids together with planktic molluscs (pteropods) pointing to the deeper marine environments. The age of the deposits comprising these findings coincides with the Langhian opening of the marine corridors between the Paratethys and the Mediterranean during the highstands, a major faunal turnover event in the Central Paratethys and Miocene Climatic Optimum. Records of chemosymbiotic bivalves and accompanied fauna in the investigated area could point to the further

diversification of the Badenian marine environments in this part of the Central Paratethys and their correlation with similar contemporaneous environments and fauna in the Mediterranean.

Keywords

Chemosymbiotic bivalves • Middle Miocene • Central Paratethys • Croatia

1 Introduction

During the Miocene, the Paratethys Sea covered vast marine areas, including today's Northern Croatia (e.g., Pavelić & Kovačić, 2018; Piller et al., 2007; Rögl, 1998). One of the well described Middle Miocene (Badenian—Langhian/Serravallian) marine successions in Northern Croatia is located at the Medvednica Mt. (e.g., Bošnjak et al., 2017a; Kochansky, 1944; Kochansky-Devidé, 1957; Vrsaljko et al., 2006), paleogeographically situated at the southwestern margin of the Central Paratethys (Fig. 1) (e.g., Piller et al., 2007; Rögl, 1998). The presence of chemosymbiotic bivalves was recorded in the Badenian deposits of the Medvednica Mt. (Bošnjak et al., 2017b) (Fig. 1). The aim of this study is to distinguish and describe their biotopes, from oxygen-depleted shallows, to deep basins.

2 Materials and Methods

Recorded chemosymbiotic bivalves are represented by the taxa belonging to the families of Lucinidae (998 specimens) and Solemyidae (11 specimens), and representatives of the family Thyasiridae are also present. These bivalves are, in most cases, preserved as casts and molds. Newly collected specimens (10 lucinids and 2 solemyids) were cleaned up with a soft brush, determined according to the relevant

M. Bošnjak (✉)
Croatian Natural History Museum, 10000 Zagreb, Croatia
e-mail: marija.bosnjak@hpm.hr

J. Sremac
University of Zagreb, 10000 Zagreb, Croatia

E. Zukon Kolić
University of Trieste, 34127 Trieste, Italy

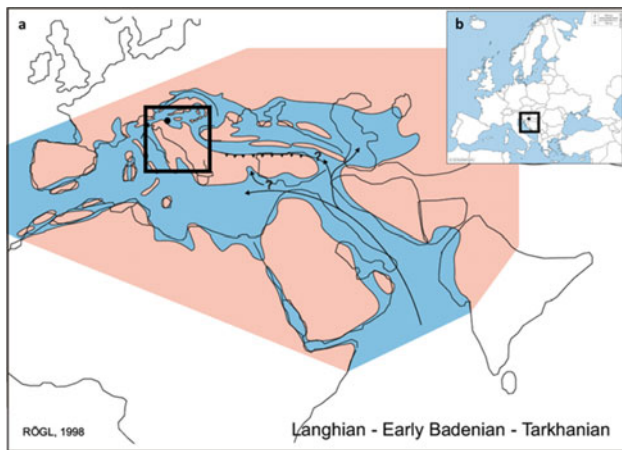


Fig. 1 a Paleogeographic position of today's area of Northern Croatia during the Middle Miocene (Badenian-Langhian) modified after (Rögl, 1998), marked within the black square by a black circle; b Geographic position of the investigated area in Northern Croatia marked by a black circle within the black square, modified after (D-maps.com., 2022). Legend: blue = marine environments; brown (Fig. 1a) and white (Fig. 1b) = land; arrows = marine connections

literature and housed together with the already inventoried collections of the Croatian Natural History Museum and the University of Zagreb, Faculty of Science.

3 Results

Among the inventoried chemosymbiotic bivalves, lucinids are widely dispersed and comprise several taxa. The most numerous taxa are *Lucinoma borealis* (Linnaeus, 1767) (291 specimens), particularly common *Lucina (Eomiltha) polymorpha* Kochansky, 1944 (236 specimens) and *Megaxinus ellipticus* (Borson, 1825) (206 specimens). Species *Myrtea spinifera* (Montagu, 1803) is also recorded (more than 30 specimens). The presence of rare solemyid chemosymbiotic bivalves *Solemya* (= *Acharax*) *doderleini* (Mayer, 1861) is recorded with 11 specimens. Representatives of the family Thyasiridae are recorded as well.

The Badenian bivalves were found in deposits of different lithologies, varying from argillaceous marls to limestones in different areas (Kochansky, 1944; Kochansky-Devidé, 1957) of Medvednica Mt. in Northern Croatia (Fig. 1). The most numerous and diversified chemosymbiotic fossil fauna is found in the central area of the Medvednica Mt., where also the deepest marine deposits were recorded (e.g., Bošnjak et al., 2017a and references therein). A single species from the family Solemyidae, *Solemya* (= *Acharax*) *doderleini* (Mayer, 1861), was found in platy limestones only in the central part of the Medvednica Mt.

4 Discussion

Chemosymbiotic bivalves are identified in all representatives of the families Lucinidae and Solemyidae, and in some members of the family Thyasiridae (e.g., Taylor & Glover, 2010). Lucinids are considered the most diverse family among the chemosymbiotic bivalves, and are widely distributed in various marine habitats from intertidal to over 2000 m depth (e.g., Taylor et al., 2011). Solemyids also have a wide range of marine habitats and depths (e.g., Taylor & Glover, 2010 and references therein).

Some of the collected Badenian lucinids from Northern Croatia (Fig. 1) lived in the shallower marine, oxygen-depleted environments, with associated fauna of corbulids and tellinids (Kochansky, 1944; Kochansky-Devidé, 1957). In the central part of the Medvednica Mt., we recorded solemyids and lucinids together with planktic molluscs (pteropods) pointing to the deeper marine environments (e.g., Bošnjak et al., 2017a; Kochansky, 1944; Kochansky-Devidé, 1957). Solemyids are rather scarce in the Miocene deposits. They are also recorded in the Middle Miocene deposits of the neighboring area close to the "Trans-Tethyan corridor" in Slovenia (Mikuž & Gašparič, 2014), as well as in the Miocene deposits of the Mediterranean Basin, where they also live today (Taviani et al., 2011 and references therein).

The age of the deposits comprising the chemosymbiotic bivalves with accompanying deeper water fauna of the Medvednica Mt. corresponds to the Langhian opening of the marine corridors between the Paratethys and the Mediterranean (Fig. 1) during the highstands (e.g., Pavelić & Kovačić, 2018; Piller et al., 2007; Rögl, 1998 and references therein). The opening of the marine corridors enabled a major faunal turnover event in the Central Paratethys coinciding with the Miocene Climatic Optimum (e.g., Harzhauser et al., 2003; Zachos et al., 2001, and references therein).

5 Conclusions

Records of chemosymbiotic bivalves and accompanying fauna in the investigated area point to the diversification of the Badenian shallow and deep marine environments, including those with unfavorable oxygen-reduced conditions, in this part of the Central Paratethys. Correlation with similar contemporaneous environments and fauna in neighboring areas of the Central Paratethys and in the Mediterranean, as well as the correlation with current knowledge on the present specialized biota could give more insight into the paleoecological conditions in the southwestern margin of the Central Paratethys during the Middle Miocene (Badenian-Langhian/Serravallian).

References

- Bošnjak, M., Sremac, J., Vrsaljko, D., Aščić, Š., & Bosak, L. (2017a). Miocene “Pteropod event” in the SW part of the Central Paratethys (Medvednica Mt, northern Croatia). *Geologica Carpathica*, 68, 329–349.
- Bošnjak, M., Sremac, J., & Vrsaljko, D. (2017b) Deep-marine mollusk assemblages in Middle Miocene (Badenian) deposits of the Medvednica Mt., Northern Croatia-today’s point of view. In: M. Horvat, & L. Wacha (Eds.), *Proceedings of the 7th international workshop on the Neogene of the Central and South-Eastern Europe Abstracts book* (pp. 13–15). Croatian Geological Society.
- D-maps.com. (2022). https://d-maps.com/carte.php?num_car=2232&lang=en. Accessed 16 Aug 2022
- Harzhauser, M., Mandic, O., & Zuschin, M. (2003). Changes in Paratethyan marine molluscs at the Early/Middle Miocene transition: Diversity, palaeogeography and palaeoclimate. *Acta Geologica Polonica*, 53(4), 323–339.
- Kochansky, V. (1944). Fauna marinskog miocena južnog pobočja Medvednice (Zagrebačke gore) (Miocene marine fauna of the southern slope of the Medvednica Mt. (Zagrebačka gora Mt.)) [Miozäne marine Fauna des südlichen Abhanges der Medvednica (Zagreber Gebirge)]. *Vjestnik Hrv. drž. geol. zavoda i Hrv drž. geol. muzeja*, 2(3), 171–280.
- Kochansky-Devidé, V. (1957). O fauni marinskog miocena i o tortonskom “šliru” Medvednice (Zagrebačke gore) (About Miocene marine fauna and Tortonian “schlier” of the Medvednica Mt. (Zagrebačka gora Mt.)) [Ueber die Fauna des marinen Miozäns und über den Tortonischen “schlier” von Medvednica (Zagreber Gebirge)]. *Geološki vjesnik*, 10, 39–50.
- Mikuž, V., & Gašparič, R. (2014). Some rare fossils from Slovenske gorice. *Slovenia. Geologija*, 57(2), 155–166.
- Pavelić, D., & Kovačić, M. (2018). Sedimentology and stratigraphy of the Neogene rift-type North Croatian Basin (Pannonian Basin System, Croatia): A review. *Marine and Petroleum Geology*, 91, 455–469.
- Piller, W. E., Harzhauser, M., & Mandic, O. (2007). Miocene Central Paratethys stratigraphy: Current status and future directions. *Stratigraphy*, 4, 151–168.
- Rögl, F. (1998). Palaeogeographic considerations for Mediterranean and Paratethys Seaways (Oligocene to Miocene). *Annalen des Naturhistorischen Museums in Wien*, 99A, 279–310.
- Taviani, M., Angeletti, L., & Ceregato, A. (2011). Chemosynthetic bivalves of the family Solemyidae (Bivalvia, Protobranchia) in the Neogene of the Mediterranean Basin. *Journal of Paleontology*, 85(6), 1067–1076.
- Taylor, J.D., & Glover, E.A. (2010) Chemosymbiotic bivalves. In: S. Kiel (Ed.), *The vent and seep biota, topics in geobiology* (Vol. 33, pp. 107–135). Springer
- Taylor, J. D., Glover, E. A., Smith, L., Dyal, P., & Williams, S. T. (2011). Molecular phylogeny and classification of the chemosymbiotic bivalve family Lucinidae (Mollusca: Bivalvia). *The Linnean Society of London, Zoological Journal of the Linnean Society*, 163, 15–49.
- Vrsaljko, D., Pavelić, D., Miknić, M., Brkić, M., Kovačić, M., Hećimović, I., Hajek-Tadesse, V., Avanić, R., & Kurtanek, N. (2006). Middle Miocene (Upper Badenian/Sarmatian) palaeoecology and evolution of the environments in the area of Medvednica Mt. (North Croatia). *Geologia Croatica*, 59(1), 51–63.
- Zachos, J., Pagani, M., Sloan, L., Thomas, E., & Billups, K. (2001). Trends, rhythms, and aberrations in global climate 65 Ma to present. *Science*, 292, 686–693.



Systematic and Taxonomic Investigations of Newly Discovered Mammalian Fauna from Late Pliocene of the Siwalik Sub-group of Pakistan

Sania Zubaid, Muhammad Tahir Waseem, Abdul Majid Khan, and Ghulam Sarwar

Abstract

Some new mammalian remains have been discovered in the new localities (Kangar, Dhillomora, Rasool pur, Nikki Rawal Wali) of the late Pliocene (3.5–2.58 Ma) of the Siwalik sub-group, Pakistan. This work describes the comprehensive systematic and taxonomic investigations of new fossils comprising molars and nasal horns belonging to three families including Bovidae (*Kobus porrecticornis*), Anthracotheriidae (*Merycopotamus dissimilis*), Rhinocerotidae (*Rhinoceros sondaicus*). The present study adds to the scanty data of Pliocene mammals of the Siwalik sub-group of Pakistan. Taxonomic and morphological studies of these new fossils give a novel insight to the dietary habitats of the late Pliocene fauna as higher hypsodonty indices and complex dental patterns indicate a coarser and tougher diet available to these mammals which coincide with the hypothesis of grasslands expansion after the famous late Miocene climatic and vegetational change in low-latitude regions, worldwide.

Keywords

Tatrot • Upper Siwaliks • Mammals • Diet

1 Introduction

The Siwalik Formation of Pakistan exhibits an excellent fossil record from the middle Miocene to the late Pleistocene (Dennell et al., 2006). Siwalik fauna are taxonomically diverse and in close resemblance to the mammalian fauna of Africa because of their shared continental drift and rejoining of the Eurasian and African landmasses (Patnaik, 2015). Although the Siwalik sub-group of Pakistan has been documented in fossil collections for its well-preserved fossil record, the fauna of the Upper Siwaliks are not comprehensively reported. This current study has been designed to detail the comparative dental morphology and taxonomical analysis of less studied taxa of the Upper Siwaliks with a special focus on the Tatrot Formation which is late Pliocene in age (Dennell et al., 2006).

The studied samples belong to three families and four species. These are the family Bovidae (*Kobus porrecticornis*, *Antelope subtrota*), Rhinocerotidae (*Rhinoceros sondaicus*), Anthracotheriidae (*Merycopotamus dissimilis*). Comparative dental taxonomy has helped establish a biogeographic perspective of species dispersal among different regions of Upper Siwaliks and give an insight to their dietary patterns.

1.1 Geologic Settings

Lithologically, the Upper Siwaliks comprises of orange and pale pinkish clays with interbedded brown siltstones and conglomerates (Maung-Thein et al., 2010; Sen, 2013). The studied localities are located within Tatrot Formation of the Siwalik sub-group and within the late Pliocene (Fig. 1b). The Tatrot Formation is mainly comprised of sandstone, mudstone, and claystone in alternating fashion which are not much thick. The samples were yielded from the main locality and nearby localities including Dhillomora (32.86° Latitude; 73.33° Longitude), Rasool Pur (32.97° Latitude; 73.39° Longitude), Nikki Rawal Wali (32.85° Latitude;

S. Zubaid · A. M. Khan · G. Sarwar
Ecology and Evolutionary Biology Lab, Institute of Zoology,
University of the Punjab, Lahore, India

M. T. Waseem (✉)
Zoological Science Division, Pakistan Museum of Natural
History, Shakarparian, Islamabad, India
e-mail: tahirmuhammad1213@gmail.com

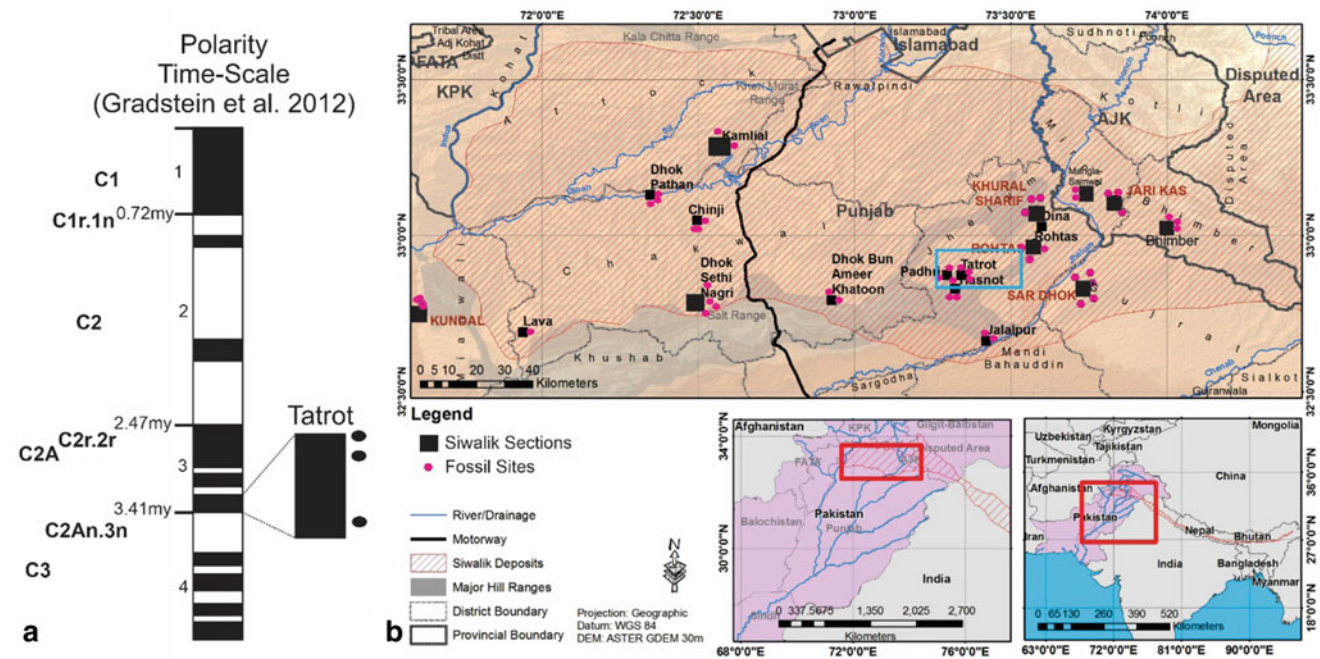


Fig. 1 A generalized map of the Siwalik sub-group of Pakistan indicating different sites along with the studied localities (a) and geomagnetic polarity timescale and its correlation with the studied localities (b) (Gradstein et al., 2012)

73.34°Longitude), and Kangar (32.78°Latitude; 73.30°Longitude). The Tatrot type locality is normally magnetized and lies below the Gauss/Matuyama boundary (~ 2.47 Ma). The upper limit of the section lies around the Chron C2r.2r and lower limit lies around C2An.2n giving an age from ~ 2.5 to ~ 3.5 Ma (late Pliocene). Opdyke et al. (1979) reports that the sediments of Tatrot type locality and related localities are normally magnetized which can be correlated with the section given in Fig. 1b.

2 Materials and Methods

All the material for the current study was collected during a field trip (2019). The studied material consists of 7 samples collected from new localities of Tatrot outcrops. The collected samples were cleaned with water and detergent to remove dust whereas, adhesive dust was removed with the help of micro-rotary drills. Samples were catalogued with the serial number (e.g., EB1/19), where EB represented the Environmental Biology lab followed by serial number and collection year. The collected samples were identified on the basis of their morphometric characteristics and measurements. Gentry et al. (1997) was used as reference for terminology of dentition (Upper Molar, M^u and Lower Molar, M^l) and teeth were compared to previously reported data for detailed dental and morphological studies.

A one-way analysis of variance (ANOVA) was performed with Post hoc Tukey HSD test for multiple

comparisons of mean values between different species in IBM SPSS Statistics 26 to determine the significant differences between the measurements of studied specimen and different reported species. Origin 2021b was used for graphical representation of the studied sample data of different reported species.

Systematic Paleontology

Kingdom	Animalia
Phylum	Chordata
Sub Phylum	Vertebrata
Class	Mammalia Linnaeus 1758
Order	Artiodactyla Owen, 1848
Family	Bovidae Gray, 1821
Subfamily	Antilopinae Gray, 1821
Tribe	Reduncini Blaine, 1914, Simpson, 1945
Genus	<i>Kobus</i> A. Smith, 1840

K. porrecticornis

New Material: EB1/19 (rM²), EB2/19 (lM²), and EB3/19 (P⁴).

Description: The studied samples, EB1/19, EB2/19, EB3/19, EB18/21, and EB19/21 (Fig. 2(1a–4c)), consist of premolar and molars of the maxilla. These are medium-sized, well-preserved hypsodont upper molars with

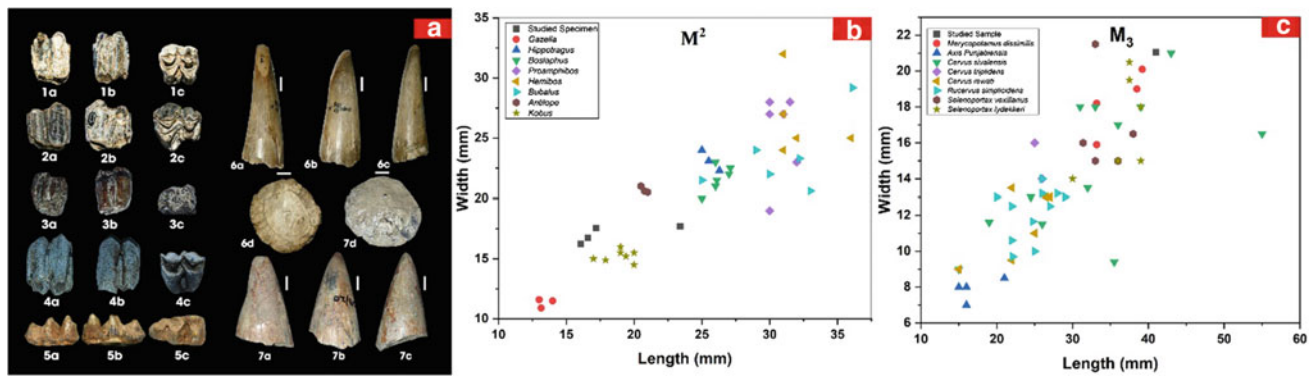


Fig. 2 a The newly discovered dental remains of *K. porrecticornis* and *M. dissimilis*. a (Labial view), b (Lingual view), c (Occlusal view). 1 (EB1/19), 2 (EB2/19), 3 (EB18/21), 4 (EB19/21), 5 (EB8/19), and

Nasal horn of *R. sondaicus*. a (Latero-lingual view), b (Labial view), c (Latero-labial view), d (Cross section), 6 (PUPC 67/145F), 7 (EB13/20). **b** (M^2 of *K. Porrecticornis*), **c** (M_3 of *M. dissimilis*)

less rugose enamel. Specimens are in early stage of wear and contain comparatively thick layer of cementum. A clear transverse flange with a strong goat fold and median basal pillar is present lingually in the upper molars. On the basis of protocones shape, EB1/19 is identified as rM^2 and EB2/19 is assigned as IM^2 . Morphometrically, the samples under study exhibit the characteristics of *K. porrecticornis* documented by Iqbal et al. (2015) and Gentry (1997) in having a clear goat fold with complex rounded cusps and strong basal pillar (Table 1; Fig. 2a(1a–4c), b). They have clear transverse flange according to the *Kobus* dental morphology reported by Iqbal et al. (2015). Strong basal pillar is characteristic feature of *K. porrecticornis* as reported by Gentry (1997).

Family Anthracotheriidae Leidy, 1869
 Subfamily Bothriodontinae Scott, 1940
 Genus *Merycopotamus* Falconer and Cautley, 1847

M. dissimilis

New Material: EB8/19 (rM_3).

Description: The studied specimen (Fig. 2(16a–c)) is rM_3 of *M. dissimilis*. Sample is pentacuspoid teeth with selenodont appearance. It has well-preserved conids with triangular labial conids and convoluted metaconid and entoconid.

Table 1 Comparative measurements of the dental remains of *K. porrecticornis*, *Antelope subtorta*, *M. dissimilis*

Taxa	Number	Position	Length (mm)	Width (mm)	Height (mm)	W/L	H/W
<i>K. porrecticornis</i>	EB1/19	rM^2	16.05	16.25	26.6	1.01	1.63
	EB2/19	rM^2	17.2	17.55	21.3	1.02	1.21
	EB18/21	IM^2	23.4	17.7	24.8	0.75	1.40
	EB19/21	rM^2	16.6	16.75	24.1	1.00	1.44
<i>K. porrecticornis</i>	PUPC 13/335	IM^2	20.0	15.5	–	0.77	–
	PUPC 13/345a	IM^2	19.0	16.0	–	0.84	–
	PUPC13/347	M^2	19.0	19.0	–	0.81	–
	PUPC 14/190	IM^2	20.0	14.5	–	0.725	–
<i>K. porrecticornis</i> (Siddiq et al., 2014)	PUPC 66/149	rM^2	19.4	15.2	–	0.78	–
<i>K. porrecticornis</i>	PUPC 82/13	IM^2	17.0	15.0	–	0.88	–
<i>K. aff. Porrecticornis</i> (Gentry, 1997)	WM 969/92	rM^2	17.9	14.9	–	0.83	–
<i>M. dissimilis</i> (Studied specimens)	EB8/19	rm^3	41.01	21.05	19.06	0.51	0.90
<i>M. dissimilis</i>	PUPC 14/152	rm^3	38.5	19.0	–	0.49	–
<i>M. medioximus</i> (Lihoreau et al., 2007)	N ° Injana	m^3	33.2	18.2	–	0.54	–
<i>M. dissimilis</i> (Lihoreau et al., 2007)	M18442	m^3	39.2	20.1	–	0.51	–

Traces of cementum are visible on highly rugose enamel. Mesolingual central fossettes are deeper between the anterior conids than the posterior ones. Posthypocristid joins with hypoconulid posteriorly and posthypocristulid are partially damaged. On the basis of hypsodonty and previously reported data, the studied specimen is assigned to *M. dissimilis* (Table 1; Fig. 2a(5a–5c), c).

Family	Rhinocerotidae Gray, 1821
Subfamily	Rhinocerotini Gray, 1821
Genus	<i>Rhinoceros</i> Linnaeus, 1758

R. sondaicus Desmarest, 1822

New Material: EB 13/20 and PUPC 67/145F.

Description: The studied samples (Fig. 2a(6a–7d)) are nasal horn of *R. sondaicus*. The samples are striated with clearly visible crimson-red keratin fibers. Average diameter of keratin fibers is 0.5 mm. The preserved length of EB 13/20 is 135.3 mm with slightly damaged anterior margin whereas, diameter of posterior end is 79 mm. The sample is smooth, broader, and less curved. PUPC 67/145 is less long, flat, and less curved at lateral side. The horn is dusky gray striated with visible keratin fibers on the surface. Keratin fibers are ~ 0.5 mm. There are no cut marks or stiff bristles. Although the nasal horn is slightly broken at the posterior side, the preserved length is about 168 mm. These nasal horns are less curved and have shorter length and are different from nasal horn of *Coelodonta antiquitatis* (UHMP 43) documented by Fortelius (1983).

3 Comparison and Discussion

The Upper Siwalik mammals exhibited several characteristic features, i.e., higher hypsodonty indices, complex dental patterns, increased dental size, and molarization. These features suggest a move from less fibrous and less grittier diet (which was present in the form of tress or plants), and closed habitats to more fibrous and more grittier diet (grasses), and open habitats after the appearance of *Hipparion* (during the late Miocene) (Bibi, 2007; Waseem et al., 2021), as well as, they enabled the surviving and migrating mammals to cope with new climatic regime (Behrensmeyer & Barry, 2005). The ancestral characteristics of Family Bovidae evinced them as forest-dwelling browsers (Bibi, 2007) with little enamel complications, and sharp-wearing cusps but bovids of the Upper Siwaliks exhibit teeth characterized with complex enamel folds, strong basal pillars, and round-wearing cusps and higher hypsodonty indices, mesowear and occlusal complexity, indicating that bovids

feed on tougher diets and endured the drier and more open environments as C_4 grasses are posited to be more abrasive to teeth than C_3 grasses (Waseem et al., 2016). Family Anthracotheriidae has low crowned and selenodont dentition (Lihoreau et al., 2007). After the Pliocene, they became extinct because their dental characteristics were not enough for them to cope with more arid abrasive grasslands (Barry et al., 2002). *M. dissimilis* was water-dependent and preferred closed habitats than the open grasslands. Vegetational changes and competitive pressure led the extinction of this family from the Siwalik sub-group (Croitor, 2017). Family Rhinocerotidae was the most stable family among all the mammalian families in this study (Khan et al., 2021). Their living relatives are still present in sub-tropical settings of Myanmar and Java (Maung-Thein et al., 2010). Members of this family exhibited sub-hypsodont dentition with moderate complexity and moderate rugosity indicated them as mixed feeders on both plants and grasses (Siddiq et al., 2014). This species inhabited near shade and water and thus indicated their competitive success during the Pliocene (Waseem et al., 2020). Many researchers have studied the taxonomy and paleoclimate of faunal items from the middle and late Miocene but the Upper Siwaliks mammals (Plio-Pleistocene) have received less attention (Iqbal et al., 2015). The evolution of Himalayan tectonics, the origins of the monsoon system, major shifts in animal diversity, and vegetational changes are all interlinked (Patnaik, 2015), but the major driving forces behind these changes are still debatable.

References

- Barry, J. C., Morgan, M. E., Flynn, L. J., Pilbeam, D., Behrensmeyer, A. K., Raza, S. M., Khan, I. A., Badgley, C., Hicks, J., & Kelley, J. (2002). Faunal and environmental change in the late Miocene Siwaliks of northern Pakistan. *Paleobiology*, 28(S2), 1–71.
- Behrensmeyer, A. K., & Barry, J. (2005). Biostratigraphic surveys in the Siwaliks of Pakistan: A method for standardized surface sampling of the vertebrate fossil record. *Palaeontologia Electronica*, 8(1), 1–24.
- Bibi, F. (2007). Origin, paleoecology, and paleobiogeography of early Bovini. *Palaeogeography, Palaeoclimatology, Palaeoecology*, 248 (1–2), 60–72.
- Croitor, R. (2017). Description of a new deer species (Cervidae, Mammalia) from the early Pliocene of Eastern Europe, with a review of early dispersals and palaeobiogeography of the subfamily Cervinae. *Neues Jahrbuch Für Geologie Und Paläontologie-Abhandlungen.*, 283(1), 85–108.
- Dennell, R., Coard, R., & Turner, A. (2006). The biostratigraphy and magnetic polarity zonation of the Pabbi Hills, northern Pakistan: An upper Siwalik (Pinjor stage) upper Pliocene-Lower Pleistocene fluvial sequence. *Palaeogeography, Palaeoclimatology, Palaeoecology*, 234(2–4), 168–185.
- Fortelius, M. (1983). The morphology and paleobiological significance of Horns of *Coelodonta antiquitatis* (Mammalia, Rhinocerotidae). *Journal of Vertebrate Paleontology*, 3(2), 125–135.

- Gentry, A. W. (1997). Fossil ruminants (mammalia) from the Manonga valley, Tanzania. In: *Neogene paleontology of the Manonga Valley, Tanzania* (pp. 107–135). Springer
- Gradstein, F. M., Ogg, J. G., Schmitz, M. B., & Ogg, G. M. (Eds.). (2012). *The geologic time scale*. Elsevier
- Iqbal, A., Khan, A. M., & Akhtar, M. (2015). *K. porrecticornis* (Reduncini) from the Upper Siwaliks of Tatrot, Pakistan. *Journal of Animal and Plant Sciences*, 25(3), 466–471.
- Khan, A. M., Waseem, M. T., Ahmad, R. M., Iqbal, A., Naz, H. I., Rafah, A., & Ameen, M. (2021). First record of *Eotragus noyei* from the Late Miocene Siwaliks of Pakistan. *Pakistan Journal of Zoology*, 53(2), 423.
- Lihoreau, F., Barry, J., Blondel, C., Chaimanee, Y., Jaeger, J. J., & Brunet, M. (2007). Anatomical revision of the genus *Merycopotamus* (Artiodactyla; Anthracotheriidae): Its significance for Late Miocene mammal dispersal in Asia. *Palaeontology*, 50(2), 503–524.
- Maung-Thein, Z. M. M., Takai, M., Tsubamoto, T., Egi, N., Htike, T., Nishimura, T., Maung, M., & Win, Z. (2010). A review of fossil rhinoceroses from the Neogene of Myanmar with description of new specimens from the Irrawaddy Sediments. *Journal of Asian Earth Sciences*, 37, 154–165.
- Opdyke, N. D., Johnson, G. D., Johnson, N. M., Tahirkheli, R. A. K., & Mirza, M. A. (1979). Magnetic polarity stratigraphy and vertebrate palaeontology of the Upper Siwaliks subgroup of Northern Pakistan. *Palaeogeography, Palaeoclimatology, Palaeoecology*, 27, 1–34.
- Patnaik, R. (2015). Diet and habitat changes among Siwalik herbivorous mammals in response to Neogene and Quaternary climate changes: An appraisal in the light of new data. *Quaternary International*, 371, 232–243.
- Sen, S. (2013). Dispersal of African mammals in Eurasia during the Cenozoic: Ways and whys. *Geobios*, 46(1–2), 159–172.
- Siddiq, M. K., Akhtar, M., Khan, M. A., Ghaffar, A., Sarwar, K., & Khan, A. M. (2014). New fossils of Rhinoceros (Rhinocerotidae) from the Soan Formation (Plio-Pleistocene) of Northern Pakistan. *Pakistan Journal of Zoology*, 48, 3.
- Waseem, M. T., Khan, A. M., Ghaffar, A., Iqbal, A., & Ahmad, R. M. (2021). Palaeodietary and palaeoclimatic reconstruction for late Miocene hipparionines from the Siwaliks of Pakistan. *Pakistan Journal of Zoology*, 35(1), 69–76.
- Waseem, M. T., Khan, A. M., Khalid, S., Ahmad, R. M., Iqbal, A., & Ameen, M. (2020). Systematic Study of Boselaphine Remains from the Late Miocene of Hasnot. *Pakistan Punjab University Journal of Zoology*, 35(1), 69–76.
- Waseem, M. T., Sarwar, M. A., Ahmad, R. M., & Khan, A. M. (2016). Newly discovered fossil remains of *Selenoportax vexillarius* from Hasnot, locality of Siwaliks of Pakistan. *Punjab University Journal of Zoology*, 31(1), 053–058.



The Iberian Evaporite Structure Database (IESDB): An Evaporite Radar for Energy, Carbon, and Nuclear Waste Storage Facilities

Eloi González-Esvertit, Juan Alcalde, and Enrique Gomez-Rivas

Abstract

Evaporite formations may represent suitable subsurface storage sites for carbon, nuclear waste, and Geo-energy applications, which are key for the Energy Transition. Consequently, the systematic indexation of the knowledge on evaporite structures is key for developing geoscience-based technologies to address the pressing societal challenges. However, vast amounts of subsurface and surface data about the stratigraphy, structure, petrophysics, and geochemistry of evaporite structures are often segregated, not systematically organized, and, sometimes, inaccessible. The Iberian Evaporite Structure DataBase (IESDB; <https://iesdb.eu>) is a collection of 150 inventoried evaporite structures in Spain and Portugal, constituting the first comprehensive assessment from any region of the world that is focused on these type of structures. The IESDB is sourced from more than 1500 published and unpublished references and databases and includes varied information and figures of undeformed evaporite successions, outcropping and buried diapirs, evaporite-cored anticlines, evaporite-detached thrusts, and allochthonous bodies. Compiled data include key bibliographic references and a complete summary of the structure, stratigraphy, chronology, subsurface data, and mining activity. The IESDB meets the FAIR principles of data management and is presented as an open-access webpage where indexed structures can be selected by a multi-criteria search engine or visualized in an interactive map. The information compiled in the IESDB represents an opportunity to boost the scientific research

on Iberian evaporites to tackle important societal challenges, and it can also foster similar initiatives in other regions.

Keywords

Evaporite • Database • Geo-resources • Geo-energy • Iberia

1 Introduction

Evaporite structures flow in a viscous manner under relatively low stresses. This results in the formation of diapiric provinces and large-scale detachment levels that control the evolution of many sedimentary basins and orogens worldwide (Fig. 1a). Due to the viscous behavior of evaporites, their encasing rocks are often folded and faulted creating traps for underground fluids like hydrocarbons. Moreover, subsurface evaporite structures are preferentially targeted as repositories for storing oil, natural gas, or renewable energy vectors such as hydrogen, and have also been proposed as suitable hosts for nuclear waste storage (von Berlepsch & Haverkamp, 2016; Ozarslan, 2012). In addition, some evaporite minerals contain critical elements such as lithium, a key element in the electrification of the economy, and are key resources for production of raw materials like gypsum and potash (Fig. 1a).

The indexation, classification, and characterization of evaporite rocks are thus essential for the implementation of new geoscience-based technologies, especially aiming at climate change mitigation. Due to their strategic relevance, vast amounts of surface and subsurface data about their stratigraphy, structure, geochemistry, or petrophysical properties have been generated by geoscientists from (among others) national geological surveys, research institutions, and mining companies. In most cases, however, these data are widely disseminated and not well organized.

E. González-Esvertit (✉) · E. Gomez-Rivas
Departament de Mineralogia, Petrologia i Geologia Aplicada,
Facultat de Ciències de La Terra, Universitat de Barcelona,
08028 Barcelona, Spain
e-mail: e.gonzalez-esvertit@ub.edu

J. Alcalde
Geosciences Barcelona (GEO3BCN), CSIC,
08028 Barcelona, Spain

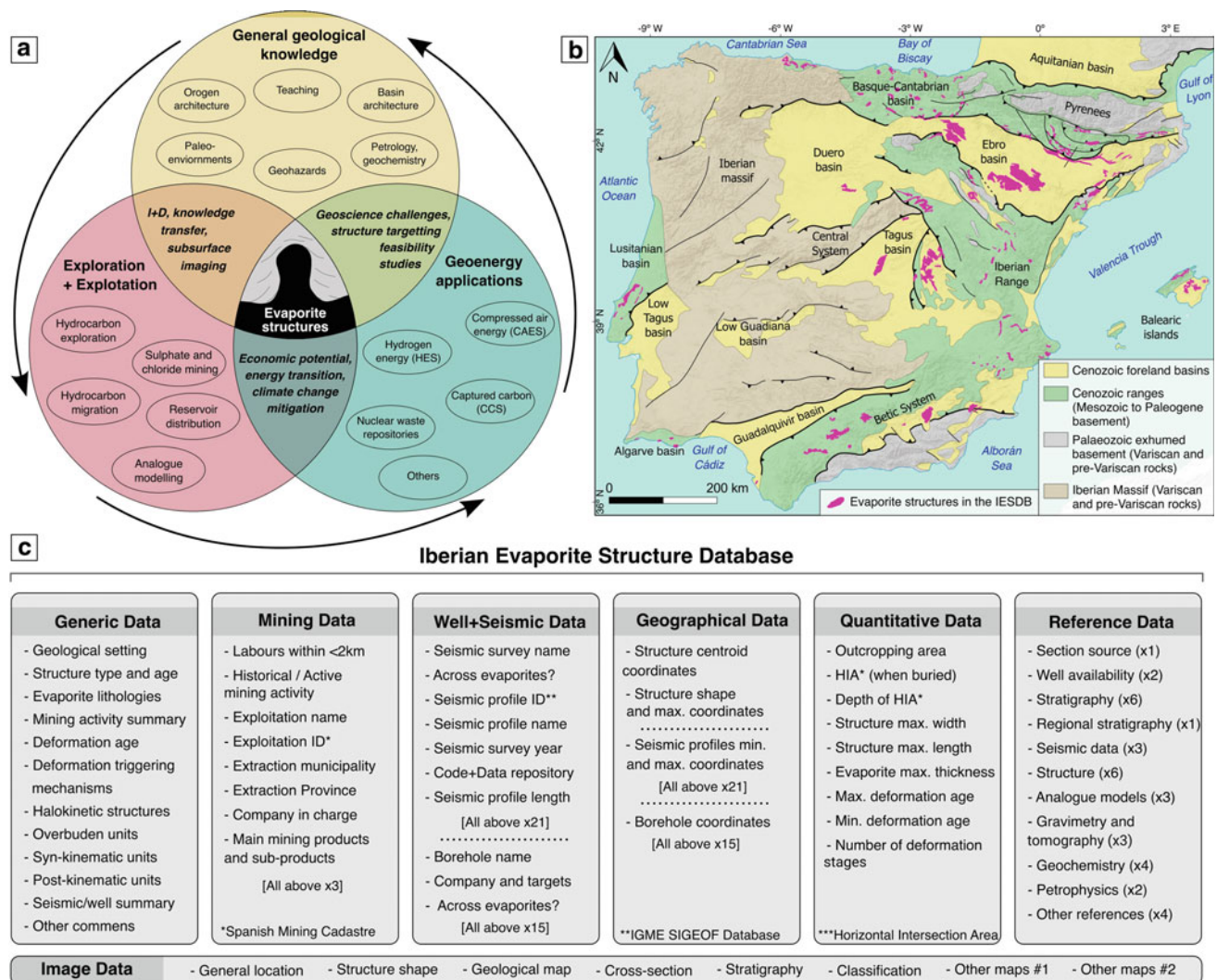


Fig. 1 a Role of evaporite structures from the point of view of general geologic knowledge, resource exploration and exploitation, and subsurface storage. b Geological sketch map of Iberia and the evaporite

structures included in the Iberian Evaporite Structure DataBase (IESDB). c Structure, datasets, and potential data entries of the IESDB

To address the systematic study of evaporite structures, it is necessary to collect and curate these massive datasets in order to make them accessible to potential end users.

Here we present the Iberian Evaporite Structure DataBase (IESDB) (González-Esvertit et al., 2023), which contains all the relevant information about 150 Spanish and Portuguese evaporite structures and represents a pioneering database for their geological knowledge and Geo-energy applications (Fig. 1a).

2 Iberian Evaporites and the IESDB

Evaporite structures are present in all post-Paleozoic tectonic regions in the Iberian Peninsula (Fig. 1b). Mesozoic evaporites of Iberia strongly influenced the Mesozoic extension

period and the Alpine mountain range development during the Cenozoic (Fig. 1b). Triassic evaporites correspond to the epicontinental Buntsandstein, Muschelkalk, and Keuper facies. Buntsandstein “Röt” and Muschelkalk “M2” evaporites crop out scarcely along NW Iberia, while the Keuper facies can be found in all the Mesozoic basins (Ortí et al., 2017). Jurassic evaporites include the Anhydrite Member along northern and eastern Iberia, the Hettangian Evaporites in the Algarve basin, and the Dagorda Formation in the Lusitanian basin, while the scarce Cretaceous evaporite outcrops are geographically restricted. Deformation of Mesozoic evaporites (Early Jurassic-Late Cretaceous) mainly consisted of the mobilization and diapirism of the Upper Triassic-Lower Jurassic salt in all the Iberian Mesozoic basins (Fig. 1b). During the Cenozoic, geodynamics in Iberia were governed by contractional tectonics that

produced asynchronous deformation along the plate margins and within intraplate domains. Deformation was highly controlled by the distribution of Mesozoic-Paleogene evaporites, caused the inversion of Mesozoic rift basins, and gave rise to the Cenozoic ranges and foreland basins (Quesada and Oliveira, 2019) and the references thereof). The Duero, Ebro, and Tagus Cenozoic basins evolved from exorheic to endorheic settings during the Paleogene and Neogene producing more evaporite deposition (Fig. 1b). In the Betic System, several Neogene to Quaternary basins were also isolated since the late Miocene, giving rise to a diachronic evaporite precipitation followed by the basins continentalization (Galindo-Zaldívar et al., 2019).

The IESDB (González-Esvertit et al., 2023) stores systematically organized information about the stratigraphy, structure, event chronology, seismic and well data availability, and mining activity of 150 evaporite structures (salt diapirs, undeformed successions, evaporite-cored anticlines, evaporite-detached thrusts, and allochthonous bodies) (Fig. 1c). The database is built with information compiled from data repositories and from more than 1500 relevant documents, such as published and unpublished research articles, books and book chapters, industry reports, and conference abstracts (Fig. 1c). The IESDB aims to serve as a basis and starting point for further studies of the inventoried structures. The IESDB is also conceived to act as an “evaporite radar” for the targeting of suitable sites for energy, carbon, or nuclear waste storage. The IESDB is freely available at <https://iesdb.eu> (CC BY 4.0 License).

3 Potential Use of the IESDB in Geo-energy Applications

The evaporite structures indexed in IESDB are located in both Spanish and Portuguese territories. Spain is one of the main evaporite producers worldwide, and their calculated reserves are large and accessible (e.g., Escavy et al., 2012). In the IESDB, a large number of evaporite structures that are currently being exploited or have an economic potential are indexed, so the database can be useful for mining companies and governmental organizations looking for geological information of these evaporite resources. Furthermore, evaporite structures have important applications in Geo-energy. Salt caverns developed in subsurface evaporite structures are one of the most suitable geological options for underground energy storage of hydrogen and compressed air (e.g., von Berlepsch & Haverkamp, 2016), due to their technological maturity, production flexibility, and large storage capacity. Specifically in Iberia, onshore buried evaporite structures from the Basque-Cantabrian basin, Southern Pyrenees, Lusitanian basin, and Pre-Betic cordillera (most of them indexed in IESDB) have been proposed

as “eligible” for the underground storage of hydrogen or compressed air (Caglayan et al., 2020; Carneiro et al., 2019), and Spain ranks third (after Germany and Poland) in the European national storage potential classification (Caglayan et al., 2020).

Evaporites may also serve as sealing structures for subsurface storage of CO₂ (Espinoza & Santamarina, 2017), a secure option for climate change mitigation that is already being implemented in worldwide depleted oil and gas fields. Examples of active CO₂ subsurface storage sites with evaporitic caprocks are facilities from the ROAD project offshore Netherlands (Arts et al., 2012), or the Weyburn field in Canada (Li et al., 2005). In Iberia, prospective studies proposed some evaporite structures indexed in IESDB as a suitable seals for CO₂ geological storage facilities, in the Lusitanian basin, the Basque-Cantabrian basin, and Betic System (Llamas et al., 2017; Pereira et al., 2021; Sun et al., 2021; Urquiza, 2012). Evaporite structures have also been postulated as suitable hosts for nuclear waste repositories by both the US Committee of Waste Disposal and, more recently, the International Atomic Energy Agency. Nowadays, only two active storage sites constructed within salt structures host nuclear wastes in New Mexico, USA (Waste Isolation Pilot Plant, WIPP) and Morsleben, Germany (Endlager für radioaktive Abfälle Morsleben, ERAM) (von Berlepsch & Haverkamp, 2016). Further suitable deep nuclear waste repositories, some with evaporitic rocks as host rocks, have been investigated in the last decades by different countries (Metlay, 2016). However, the safety and durability of these sites must be ensured prior to the development of these nuclear waste repositories (Warren, 2017).

In summary, the geological knowledge on evaporite structures, such as that provided by the IESDB (González-Esvertit et al., 2023) (Fig. 1c), will be crucial for the energy transition.

References

- Arts, R. J., Vandeweyer, V. P., Hofstee, C., Pluymaekers, M. P. D., Loeve, D., Kopp, A., & Plug, W. J. (2012). The feasibility of CO₂ storage in the depleted P18–4 gas field offshore the Netherlands (the ROAD project). *International Journal of Greenhouse Gas Control*, 11, S10–S20. <https://doi.org/10.1016/j.ijggc.2012.09.010>
- Caglayan, D. G., Weber, N., Heinrichs, H. U., Linßen, J., Robinius, M., Kukla, P. A., & Stolten, D. (2020). Technical potential of salt caverns for hydrogen storage in Europe. *International Journal of Hydrogen Energy*, 45, 6793–6805. <https://doi.org/10.1016/j.ijhydene.2019.12.161>
- Carneiro, J. F., Matos, C. R., & van Gessel, S. (2019). Opportunities for large-scale energy storage in geological formations in mainland Portugal. *Renewable and Sustainable Energy Reviews*, 99, 201–211. <https://doi.org/10.1016/j.rser.2018.09.036>
- Escavy, J. I., Herrero, M. J., & Arribas, M. E. (2012). Gypsum resources of Spain: Temporal and spatial distribution. *Ore Geology Reviews*, 13, 38.

- Espinoza, D. N., & Santamarina, J. C. (2017). CO₂ breakthrough—caprock sealing efficiency and integrity for carbon geological storage. *International Journal of Greenhouse Gas Control*, *66*, 218–229. <https://doi.org/10.1016/j.ijggc.2017.09.019>
- Galindo-Zaldívar, J., Braga, J. C., Marín-Lechado, C., Ercilla, G., Martín, J. M., Pedrera, A., Casas, D., Aguirre, J., Ruiz-Constán, A., Estrada, F., et al. (2019). Extension in the Western Mediterranean. In C. Quesada & J. T. Oliveira (Eds.), *The geology of Iberia: A geodynamic approach* (pp. 61–103). Regional Geology Reviews; Springer International Publishing.
- González-Esvertit, E., Alcalde, J., & Gomez-Rivas, E. (2023). IESDB – the Iberian Evaporite Structure Database. *Earth System Science Data*, *15*, 3131–3145. <https://doi.org/10.5194/essd-15-3131-2023>
- Li, S., Dong, M., Li, Z., Huang, S., Qing, H., & Nickel, E. (2005). Gas breakthrough pressure for hydrocarbon reservoir seal rocks: Implications for the security of long-term CO₂ storage in the Weyburn field—gas breakthrough pressure for different gas/liquid systems. *Geofluids*, *5*, 326–334. <https://doi.org/10.1111/j.1468-8123.2005.00125.x>
- Llamas, B., Cruz Castañeda, M., Laín, C., & Pous, J. (2017). Study of the Basque-Cantabrian basin as a suitable region for the implementation of an energy storage system based on compressed air energy storage (CAES). *Environmental Earth Science*, *76*, 204. <https://doi.org/10.1007/s12665-017-6515-y>
- Metlay, D. S. (2016). Selecting a site for a radioactive waste repository: A historical analysis. *Elements*, *12*, 269–274. <https://doi.org/10.2113/gselements.12.4.269>
- Ortí, F., Pérez-López, A., & Salvany, J. M. (2017). Triassic evaporites of Iberia: Sedimentological and palaeogeographical implications for the Western Neotethys evolution during the middle Triassic-earliest Jurassic. *Palaeogeography, Palaeoclimatology, Palaeoecology*, *471*, 157–180. <https://doi.org/10.1016/j.palaeo.2017.01.025>
- Ozarslan, A. (2012). Large-scale hydrogen energy storage in salt caverns. *International Journal of Hydrogen Energy*, *37*, 14265–14277. <https://doi.org/10.1016/j.ijhydene.2012.07.111>
- Pereira, P., Ribeiro, C., & Carneiro, J. (2021). Identification and characterisation of geological formations with CO₂ storage potential in Portugal. *Petroleum Geoscience*, *13*, petgeo2020-123. <https://doi.org/10.1144/petgeo2020-123>
- Quesada, C., Oliveira, J.T. (Eds.). (2019). Regional geology reviews. In: *The Geology of Iberia: A geodynamic approach: Volume 3: The alpine cycle*. Springer International Publishing
- Sun, X., Alcalde, J., Bakhtbidar, M., Elío, J., Vilarrasa, V., Canal, J., Ballesteros, J., Heinemann, N., Haszeldine, S., Cavanagh, A., et al. (2021). Hubs and clusters approach to unlock the development of carbon capture and storage: Case study in Spain. *Applied Energy*, *300*, 117418. <https://doi.org/10.1016/j.apenergy.2021.117418>
- Urquiza, M. R. (2012). Estudio de Las Formaciones Favorables Para Almacenamiento de CO₂ En Un Sector Del Borde Meridional de Las Béticas Orientales. PhD thesis, Universidad de Oviedo
- von Berlepsch, T., & Haverkamp, B. (2016). Salt as a Host Rock for the Geological Repository for Nuclear Waste. *Elements*, *12*, 257–262. <https://doi.org/10.2113/gselements.12.4.257>
- Warren, J. K. (2017). Salt usually seals, but sometimes leaks: Implications for mine and cavern stabilities in the short and long term. *Earth-Science Reviews*, *165*, 302–341. <https://doi.org/10.1016/j.earscirev.2016.11.008>



Basilosauridae (Mammalia, Cetacea) from the Sahara Desert of Southwestern Morocco

Ayoub Amane, Hakima Zair, Fadwa Aniny, Philip Gingerich,
and Samir Zouhri

Abstract

The Sahara Desert in southwestern Morocco is today an important paleontological region for its richness of archaeocete whale remains from the middle and late Eocene. Remains of Basilosauridae have been reported from Gueran and El Breij of the Bartonian age and Ad-Dakhla of the Priabonian age. There are no complete skeletons, meaning it is rarely possible to associate the skull and the post-cranial bones directly. However, analysis of the size and shape of the recovered sequential vertebrae enables distinction and comparison of the species of basilosaurids. Lumbar vertebrae best distinguish the different species of Basilosauridae, and eight different species are present in the three localities combined. Reexamination of the characteristics of the vertebrae of the different species of basilosaurids allows a better expansion of knowledge concerning their taxonomy, stratigraphic distribution, and paleogeography.

Keywords

Cetacea • Archaeoceti • Basilosauridae • Vertebral morphology • Eocene • Morocco

1 Introduction

Over several field missions in the Sahara Desert in southwestern Morocco, we collected a rich material of archaeocete cetaceans, Protocetidae and Basilosauridae, from the

A. Amane (✉) · H. Zair · F. Aniny · S. Zouhri
Laboratory of Health and Environment, Aïn Chock Faculty of Sciences, Hassan II University of Casablanca, Casablanca, Morocco
e-mail: ayoub.amane-etu@unih2c.ma

P. Gingerich
Museum of Paleontology, Research Museum Center, University of Michigan, 3600 Varsity Drive, Ann Arbor, MI 48108-2228, USA

middle and upper Eocene (Gingerich & Zouhri, 2015; Zouhri et al., 2014). Basilosaurid remains come from three different localities in the Sahara Desert in southwestern Morocco: Gueran and El Breij, both of Bartonian age and Ad-Dakhla, of Priabonian age.

Fifteen genera and twenty-three species of Basilosauridae from all over the world appear valid and distributed among three subfamilies (Gingerich et al., 2022). However, skulls and associated skeletons have been described for only four genera and species. Associated skulls and skeletons are rare in the Moroccan Sahara, and analysis of the size and shape of the vertebrae in each locality is necessary to distinguish and characterize the species present in each locality.

2 Materials and Methods

The material studied here comes from three sites in the Sahara Desert in southwestern Morocco. Specimens are housed in the paleontological collections of the Faculty of Sciences Aïn Chock, University Hassan II, Casablanca [FSAC]. Ad-Dakhla specimens are cataloged as FSAC-Dak-n°; Gueran specimens as FSAC-Bouj-n°; and El Breij specimens as FSAC-Breij-n°.

3 Systematic Paleontology

Basilosauridae Cope, 1868

Basilosaurinae Cope, 1868

Basilosaurus isis Beadnell in Andrews, 1904

Referred material: *B. isis* is known only from Ad-Dakhla. FSAC-DAK-43, eight posterior lumbar or anterior caudal centra; FSAC-DAK-44, two posterior lumbar or anterior caudal centra.

Stratigraphic provenance: All specimens come from the Priabonian level in the Aridal Formation south of Ad-Dakhla.

Description: The posterior lumbar vertebrae and the anterior caudal vertebrae of *B. isis* from Ad-Dakhla have elongated centra (Fig. 1). They are characterized by short transverse processes, an anteroposteriorly short neural spine, and short prezygapophyses. *B. isis* differs from *Eocetus schweinfurthi* in having an anteroposteriorly shorter neural arch and neural spine, and prezygapophyses that stop well before the anterior border of the centrum.

Eocetus schweinfurthi Fraas, 1904

Referred material: *E. schweinfurthi* has been recovered from Gueran and, more recently, El Breij.

The material from Gueran consists of two thoracic vertebrae (FSAC-Bouj-617, 19), three lumbar vertebrae (FSAC-Bouj-20, 8, 164), and five caudal vertebrae (FSAC-Bouj-748, 747, 749, 746, 30). The material from El Breij consists of a partial post-cranial skeleton including six cervicals, seven thoracics, and four lumbar (FSAC-Breij-1).

Stratigraphic provenance: In Gueran, the material comes from the single Bartonian fossil level (Aridal Formation). In El Breij, the fossils of *E. schweinfurthi* come from the Bartonian upper fossiliferous level (Aridal Formation).

Description: *E. schweinfurthi* has lumbar vertebrae as elongated as those of *B. isis*, but its caudals appear to be a

little shorter. The transverse processes in thoracic and lumbar vertebrae of *E. schweinfurthi* are shorter than those of *B. isis*. *E. schweinfurthi* is clearly distinguished from all other species of Basilosauridae at Gueran and El Breij by the large dimensions of its vertebrae (Fig. 2).

Pachycetinae Gingerich, Amane and Zouhri, 2022

Antaectus aithai Gingerich, Amane and Zouhri, 2022

Referred material: The material from Gueran is listed in Gingerich and Zouhri (Gingerich & Zouhri, 2015). The material from El Breij includes two cervical vertebrae (FSAC Breij-307, 290), four thoracic vertebrae (FSAC Breij-304, 306, 288, 305), and five lumbar vertebrae (FSAC-Breij-316, 317, 330, 314, 315).

Stratigraphic provenance. Specimens from Gueran come from the single Bartonian sandstone fossiliferous layer (Aridal Formation) and specimens from El Breij from the Priabonian two upper levels.

Description: Vertebrae of *A. aithai* have centra that are clearly shorter than those of the Basilosaurinae, particularly the thoracic and caudal centra. Posterior thoracic and lumbar vertebrae are relatively longer than in all Dorudontinae (Fig. 1).

Dorudontinae Müller, 1923

Masracetus markgrafi Gingerich, 2007

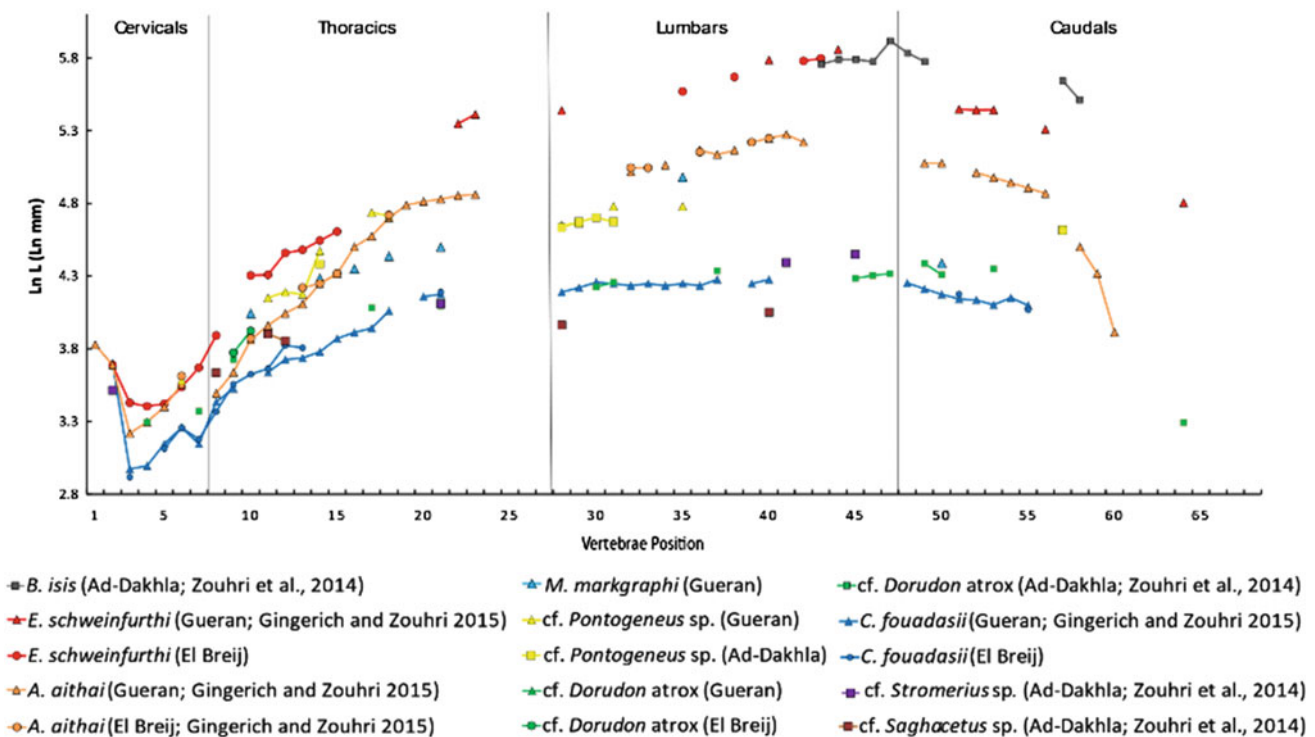


Fig. 1 Comparison of profiles of vertebral centrum length of different Basilosauridae species from the Sahara Desert in southwestern Morocco. Each series of dots corresponds to a given taxon and can

represent a series of vertebrae from the same individual or composite specimens. Key: A, Antaectus; B, Basilosaurus; C, Chrysocetus; E, Eocetus; L, Length; M, Masracetus

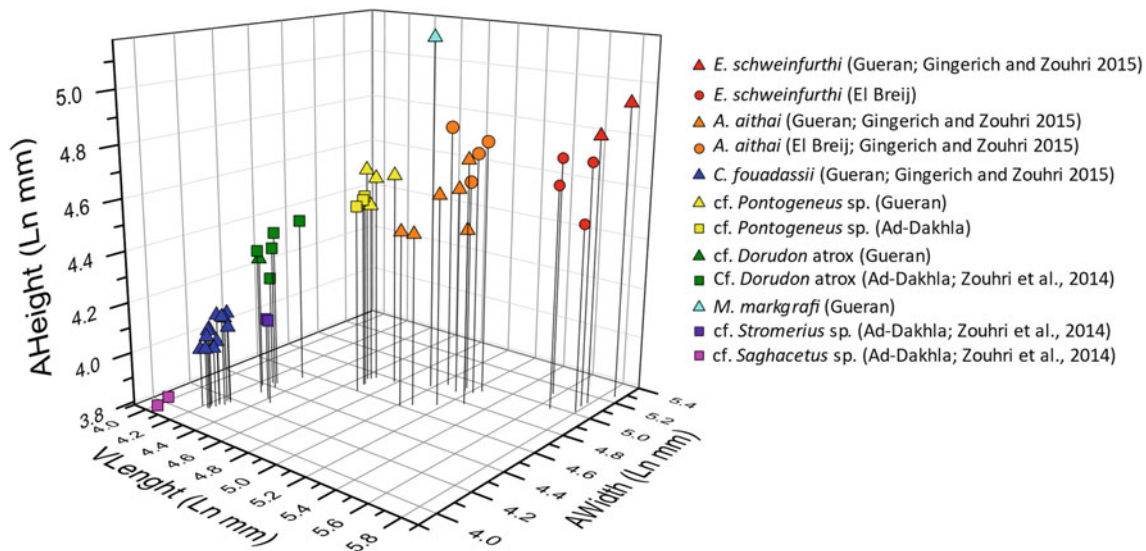


Fig. 2 Comparison of profiles of lumbar vertebral centrum ventral length, anterior height, and anterior width of different Basilosauridae species from the Sahara Desert in southwestern Morocco. Key: circles, El Breij; triangles, Gueran; squares, Ad-Dakhla

Referred material: *M. markgrafi* is known in Gueran and Ad-Dakhla. The material from Gueran consists of five thoracic vertebrae (FSAC-Bouj-20, 183, 29, 184, 163), a lumbar vertebra (FSAC-Bouj-197), and a caudal vertebra (FSAC-Bouj-37). The material from Ad-Dakhla consists of a single lumbar vertebra (FSAC-Dak-404).

Stratigraphic provenance: Specimens from Gueran come from the single Bartonian sandstone fossiliferous layer and the single specimen from Ad-Dakhla comes from the Priabonian bonebed B1.

Description: *M. markgrafi* is distinguished from other dorudontines by its noticeably very short vertebrae in relation to their width and height. The average width-to-length ratio, in this case, is about 1.6. In contrast, although relatively short, the lumbar vertebrae are relatively wider and higher than those of the same vertebrae of *B. isis* and *E. schweinfurthi* (Fig. 2). They are much larger than those of the other dorudontines, all dimensions combined.

cf. *Pontogeneus* Leidy 1852

Referred material: The material from Gueran consists of one cervical vertebra (FSAC-Bouj-285), six thoracic vertebrae (FSAC-Bouj-281, 273, 275, 269, 274, 270), and a series of four lumbar vertebrae (FSAC-Bouj-197). The material from Ad-Dakhla consists of a thoracic vertebra (FSAC-Dak-389), four lumbar vertebrae (FSAC-Dak-388, 385, 386, 383), and a caudal vertebra (FSAC-Dak-384).

Stratigraphic provenance: Specimens from Gueran come from the single Bartonian sandstone fossiliferous layer and specimens from Ad-Dakhla come from the Priabonian bonebed B1.

Description: *Pontogeneus* sp. has much shorter lumbar vertebrae than those of *B. isis* and those of *E. schweinfurthi* (Fig. 1). They are also slightly shorter than those of *M. markgrafi* (Fig. 1). Its lumbar vertebrae are relatively smaller than those of *B. isis*, *E. schweinfurthi*, and *M. markgrafi* given the fact that they are also relatively much narrower and lower (Fig. 2). The lumbar vertebrae of *Pontogeneus* sp. are significantly larger than those of other smaller dorudontine species.

cf. *Dorudon atrox* (Andrews, 1906)

Referred material: The material of cf. *D. atrox* comes from Gueran (Gingerich and Zouhri, 2015) and Ad-Dakhla (Zouhri et al., 2014).

Stratigraphic provenance: Specimens from Gueran come from the single Bartonian sandstone fossiliferous layer. At Ad-Dakhla, specimens come from the Priabonian bonebed B1 (Samlat Formation).

Description: In general, the vertebrae of *D. atrox* fall in terms of length of the centrum among those of the small species of Basilosauridae (Fig. 1). Nevertheless, the thoracics of *D. atrox* have centra slightly wider and higher than those of *Chrysocetus fouadassii*, *Stromerius* sp., and *Saghacetus* sp. (Fig. 2).

***Chrysocetus fouadassii* Gingerich and Zouhri, 2015**

Referred material: *C. fouadassii* is known from the type locality of Gueran (Gingerich and Zouhri, 2015) and from El Breij. The material from El Breij consists of three cervical vertebrae (FSAC-Breij-55, 56, 39), six thoracic vertebrae (FSAC-Breij-58, 48, 63, 61, 38), a lumbar vertebra

(FSAC-Breij-52), and two caudal vertebrae (FSAC-Breij-51 and 46).

Stratigraphic provenance: Specimens of *C. fouadassii* come from the single Bartonian sandstone fossiliferous layer, and specimens from El Breij come from the two Bartonian upper fossiliferous levels (Aridal Formation).

Description: *C. fouadassii* is one of the smallest basilosaurids, distinguished from Cf. *Stromerius* by its slightly shorter and narrower lumbar vertebrae and is distinguished from Cf. *Saghacetus* in having relatively shorter thoracic vertebrae (Fig. 2).

Cf. *Stromerius* Gingerich, 2007

Referred material: Lumbar vertebrae FSAC-Dak-10, 21, 35 from Ad-Dakhla.

Stratigraphic provenance. All specimens come from the Priabonian bonebed B1.

Description: The vertebrae of *Stromerius* sp. are smaller than those of *D. atrox*, and are distinguished from those of *C. fouadassii* by their larger size (Fig. 2).

Cf. *Saghacetus* Gingerich, 1992

Referred material: Thoracic vertebrae (FSAC-Dak-13, 15, 20, 24), lumbar vertebrae (FSAC-Dak-7, 12), and caudal vertebra (FSAC-Dak-25).

Stratigraphic provenance: All specimens come from the Priabonian bonebed B1 from Samlat Formation, southwestern Ad-Dakhla.

Description: cf. *Saghacetus* sp. has relatively longer thoracic vertebrae centra than those of *C. fouadassii* and cf. *Stromerius*. On the other hand, cf. *Saghacetus* has the shortest basilosaurid vertebrae (Figs. 1 and 2).

4 Discussion and Conclusion

Abundant fossil remains of Basilosauridae come from three localities in the Sahara Desert of southwestern Morocco. Several species of Basilosauridae are present in each of these localities. The species are represented predominantly by isolated vertebrae. Analysis of the dimensions and proportions of the vertebrae makes it possible to distinguish and characterize the different species present. The lumbar vertebrae are more informative than the others, although it is difficult to distinguish the posterior lumbar from the anterior caudals. Eight different species have been distinguished in the Moroccan Sahara Desert, which makes it one of the richest and most diversified regions for Eocene archaeocete cetaceans.

References

- Gingerich, P. D., & Zouhri, S. (2015). New fauna of archaeocete whales (Mammalia, Cetacea) from the Bartonian middle Eocene of southern Morocco. *Journal of African Earth Sciences*, *111*, 273–286. <https://doi.org/10.1016/j.jafrearsci.2015.08.006>
- Gingerich, P. D., Amane, A., & Zouhri, S. (2022). Skull and partial skeleton of a new pachycetina genus (Cetacea, Archaeoceti, Basilosauridae) from the Aridal Formation, Bartonian middle Eocene, of southwestern Morocco. *PLoS ONE*, *17*(10), e0276110. <https://doi.org/10.1371/journal.pone.0276110>
- Zouhri, S., Gingerich, P. D., Elboudali, N., Sebti, S., Noubhani, A., Rahali, M., & Meslouh, S. (2014). New marine mammal faunas (Cetacea and Sirenia) and sea level change in the Samlat Formation, Upper Eocene, near Ad-Dakhla in southwestern Morocco. *Comptes Rendus Palevol*, *13*, 599–610. <https://doi.org/10.1016/j.crpv.2014.04.002>



Paleoseasonality During the Early Pleistocene Revealed Through Stable Isotope Analysis of *Equus* from the Siwalik Sub-Group of Pakistan

Mishal Afzal, Muhammad Tahir Waseem, Abdul Majid Khan, Meera Sarwar, Ghulam Sarwar, and Rana Manzoor Ahmad

Abstract

Fossil tooth enamel archives the isotopic variability during its formation, an essential tool to reconstruct the paleo-seasonal changes during an animal's life. Stable isotopes of carbon and oxygen from enamel ($\delta^{13}\text{C}_{\text{enamel}}$ and $\delta^{18}\text{O}_{\text{enamel}}$) reveal an animal's dietary and drinking preferences and are helpful in the reconstruction of paleoclimate and seasonality. The current study attempts to probe these paleoclimatic and seasonal changes during the Early Middle Pleistocene (2.5–1.6 Ma) and their impact on mammals of the Siwalik sub-Group of Pakistan using the intra-tooth analysis of Family Equidae for $\delta^{13}\text{C}_{\text{enamel}}$ and $\delta^{18}\text{O}_{\text{enamel}}$ ($n = 87$). The $\delta^{13}\text{C}_{\text{enamel}}$ values of the Family Equidae ($-3.1 \pm 1.3\text{‰}$) indicate that the Pleistocene mammals consumed C_4 diet (grasses) dominantly. Whereas, $\delta^{18}\text{O}_{\text{enamel}}$ values of Equidae ($0.2 \pm 1.5\text{‰}$) provide evidence for a dry and open habitat where animals were drinking from open evaporating water sources, most preferentially, ponds or streams. A positive correlation between intra-tooth $\delta^{13}\text{C}_{\text{enamel}}$ and $\delta^{18}\text{O}_{\text{enamel}}$ indicates that C_4 grasses spread more under dry conditions. The higher variations in intra-tooth $\delta^{18}\text{O}_{\text{enamel}}$ values (4–5‰) indicate an intense seasonal influence on the Siwalik floodplain. Our results conclude that the Early Middle Pleistocene time span (~ 2.5 –1.6 Ma) in the Siwaliks was dominated by C_4 grasses favored under the dry and highly seasonal climate, as revealed through the intra-tooth isotopic signals.

Keywords

Pliocene • Pleistocene • Aridity • Monsoon • Climate

1 Introduction

Paleoenvironmental and paleoclimatic changes have triggered several floral and faunal variations worldwide over the past 20 million years, modeling current climatic and ecologic regimes. Several factors have contributed to these ecologic changes, which include grassland fires, lowering of partial pressure of carbon dioxide ($p\text{CO}_2$), increased seasonality, and strengthening of monsoon (Karp et al., 2018). Conditions during the Pleistocene were dynamic and went through dramatic change because of patterns of climatic change and the development of ice sheets in the northern part of the hemisphere. These changes impacted all areas of the Earth; however, these ecological changes fluctuated from one spot to another. The isotopic study of oxygen and carbon of vertebrate teeth, enamel, or bone can be used in reconstructing climatic conditions during bioapatite formation.

Carbon isotopes present in bioapatite could be utilized in remodeling animals' climate and dietary behavior (Waseem et al., 2021). Carbon isotopes in an animal's tissues are associated with food intake that can be C_3 , C_4 , or CAM. Seasonal changes in rainfall and temperature or the reconstruction of aridity and humidity cycles are primarily centered on oxygen isotopes (Blumenthal et al., 2017). The evaporation-insensitive (EI) taxa are preferred for reconstructing seasonality because they are better recorders of seasonal variation. $\delta^{18}\text{O}_{\text{enamel}}$ values tend to be more negative under more humid conditions in contrast with $\delta^{18}\text{O}_{\text{enamel}}$ of drier season, where heavy isotopes are in high concentration because of evaporation, giving a positive value (Hempson et al., 2015). Here, we analyzed the enamel of the Equid molars based on its large crystal size, smaller pores,

M. Afzal · A. M. Khan · M. Sarwar · G. Sarwar
Institute of Zoology, University of the Punjab,
Lahore, 54590, Pakistan

M. T. Waseem (✉)
Zoological Science Division, Pakistan Museum of Natural
History, Shakarparian, Islamabad 44000, India
e-mail: tahirmuhammad1213@gmail.com

R. M. Ahmad
Department of Zoology, Government College University, Lahore,
Punjab, Pakistan

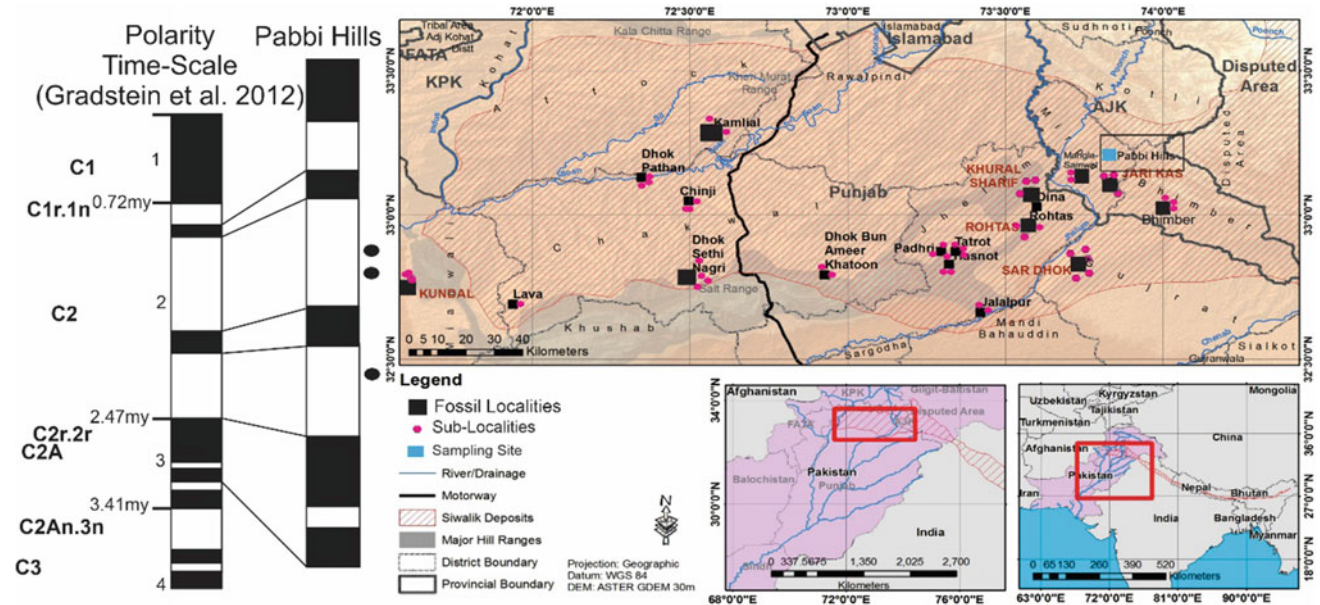


Fig. 1 Map of the Siwaliks along with the sampling localities and paleomagnetic polarity timescale

and resistance against the diagenesis process (Waseem et al., 2021). The study aims to probe the seasonality during the early to middle Pleistocene time span (2.5–1.6 Ma) in the Siwalik sub-group of Pakistan (Fig. 1).

2 Materials and Methods

Six Molars of *Equus sivalensis* were examined for analysis of isotopic ratios of oxygen and carbon present in tooth enamel. A sum of 87 samples were made from the six molars. These samples were collected from the different localities of Pabbi Hills (Pleistocene), Pakistan. A rotary dental drill was used to extract the enamel in powdered form. Serial samples were made horizontally from the lingual side of the tooth and placed in 5 ml vials (Eppendorf). The powdered enamel samples were treated with hydrogen peroxide (H_2O_2) and acetic acid (CH_3COOH) to neutralize the effects of organic and inorganic impurities, as given by Koch et al. (1997). For drying out the samples, ethanol was added and left for 24 h. CO_2 production takes place by dissolving the enamel samples in 95% H_3PO_4 . The CO_2 was examined with the help of Isotope Ratio Mass Spectrometry (IRMS) at PINSTECH, Islamabad. The samples containing extract of enamel were analyzed at the Isotope Ratio Mass Spectrometer in PINSTECH (Pakistan Institute of Nuclear Science and Technology) Islamabad. Statistical analysis used Statistical Package for the Social Sciences (SPSS) 21.0 version. The normality of the data is checked by using the normality test, and after that one-way ANOVA (Analysis of Variance) test was used with Duncan's to analyze the results.

3 Results

3.1 Isotopic Ratios of Carbon and Oxygen

One-way ANOVA and Duncan's post hoc test were performed to compare the means of six samples. According to the Duncan test, significant differences exist among the samples collected from the localities with an age of 2.5, 2.3, and 1.6 Ma. Variations among *Equus* samples range from -5.7 to -0.7% . The average $\delta^{13}C_{enamel}$ value of tooth enamel is $-3.2 \pm 1.3\%$.

Variations among oxygen values range from -3.1 to 2.8% . The average $\delta^{18}O_{enamel}$ value of tooth enamel is $0.17 \pm 1.54\%$. One-way ANOVA was carried out to compare the means of six groups. Duncan's test reveals that samples with an age of 2.5 Ma are non-significantly different from each other but significantly different from the samples collected from 2.3 to 1.6 Ma. All the samples show a positive correlation between carbon and oxygen values.

4 Discussion

Intra-tooth differences of carbon and oxygen isotopes archived in the bioapatite reveal the seasonal climatic changes, changes in vegetation, humidity/aridity cycles, and rainfall throughout the year that help in paleoseasonality reconstruction (Balasse et al., 2012). According to our results, the $\delta^{13}C_{enamel}$ values of *Equus* samples (PUPC 352, 351) from 2.5 Ma range from -5.7 to -3.3% which show that they were mixed feeders and consumed about 43–50%

grass in their diet whereas $\delta^{18}\text{O}_{\text{enamel}}$ (-3.10 to 2.2%) demonstrated seasonal changes in aridity which are shown by a variation in the values of oxygen (Fig. 2). The $\delta^{13}\text{C}_{\text{enamel}}$ (-3.8 to -2.4%) and $\delta^{18}\text{O}_{\text{enamel}}$ (-0.9 to -2.8%) of samples (PUPC 313, 317) from 2.3 Ma proposed (Fig. 2) mixed to dominantly C_4 feeding with 50–70% grass in their diet, i.e., more monocot and fewer dicot plants in open habitat and their water intake is from evaporating ponds or streams under drier conditions. The $\delta^{13}\text{C}_{\text{enamel}}$ (-2.6 to -0.7%) and $\delta^{18}\text{O}_{\text{enamel}}$ (-2.4 to 2.4%) from 1.6 Ma samples (PUPC 312, 314) indicated an exclusively C_4 diet and exhibited pure grazing and drier seasonal conditions (Fig. 2). Earlier in the Pleistocene, *Equus* from the Pinjor Formation has been considered as a C_4 grazer with over 90% grass consumption in its diet but probably acquired its food and water from moderate to drier regions. The *Equus* species around that time were obligate drinkers and pure grazers. A dramatic rise in C_4 plants during a C_3 -dominated environment throughout the Late Miocene was reported from the Himalayan Foreland Basin (HFB) of the Siwaliks. A few hypotheses, like higher seasonal precipitation, particularly in summer, low atmospheric $p\text{CO}_2$, and low latitude aridity, along with temperature variations, recurrent wildfires, and substrate nature, have been suggested to describe the above-mentioned environmental change (Sanyal et al., 2010). A warm seasonal rainfall describes the monsoon system of India and is frequently related to lightning, a driving force to instigate forest fires. It was quite possible that initiating a strong monsoon could make a genuine disturbance in the landscape ecology and lead to C_4 expansion. The collision of the Indian Plate with the Eurasian Plate brought about the development of the Himalayan-Tibet Plateau in the Neogene period, swaying Asia's regional environment and influencing the overall climate (Wang et al., 2014). Investigations concerning climatic changes in the Siwaliks are rare. Besides, they don't hold comprehensive records for the last 15 Ma. Hardly any work presents the sequences in the seasonality of Siwaliks during the Pleistocene, though others present the evolution of the Asiatic Monsoon (Nelson, 2005; Patnaik et al., 2019).

5 Conclusion

We present the climatic and vegetational changes from Pakistan's Siwalik sub-group (Pinjor formation) using serial stable isotope analysis of *Equus* molars. We utilized this proxy to estimate the seasonality, dietary preferences, and monsoonal intensification from the early to the middle Pleistocene period (~ 2.5 – 1.6 Ma). We propose a significantly higher seasonality during the early middle Pleistocene time. The $\delta^{13}\text{C}_{\text{enamel}}$ values suggested that C_4 grasses were widespread in open habitats. Oxygen isotopic analyses

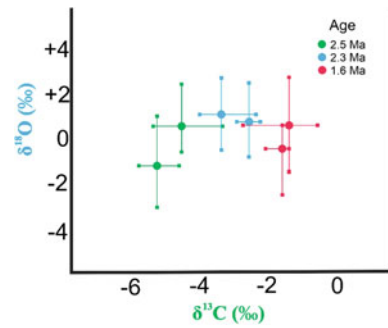


Fig. 2 $\delta^{13}\text{C}_{\text{enamel}}$ and $\delta^{18}\text{O}_{\text{enamel}}$ values and intra-tooth sampling ranges of the samples along with their ages

provide evidence of climatic change, with a trend showing higher $\delta^{18}\text{O}_{\text{enamel}}$ values over time with water intake from open evaporating ponds or streams. Paleovegetational reconstruction gives proof of the extension of C_4 grasslands, while the $\delta^{18}\text{O}_{\text{enamel}}$ values of the teeth profiles demonstrate an open habitat along with the reduction in precipitation over time. Thus, the isotopic examination of equid teeth from the Siwalik sub-group, proposes that the Pleistocene was dominated by a seasonal and monsoonal rainfall system, with a diminution in rainfall over time due to which C_4 grasslands expanded.

References

- Balasse, M., Obein, G., Ughetto-Monfrin, J., & Mainland, I. (2012). Investigating seasonality and season of birth in past herds: a reference set of sheep enamel stable oxygen isotope ratios. *Archaeometry*, *54*(2), 349–368.
- Blumenthal, S. A., Levin, N. E., Brown, F. H., Brugal, J.-P., Chritz, K. L., Harris, J. M., Jehle, G. E., & Cerling, T. E. (2017). Aridity and hominin environments. *Proceedings of the National Academy Sciences*, *114*, 7331–7336.
- Hempson, G. P., Archibald, S., & Bond, W. J. (2015). A continent-wide assessment of the form and intensity of large mammal herbivory in Africa. *Science*, *350*(6264), 1056–1061.
- Karp, A. T., Behrensmeier, A. K., & Freeman, K. H. (2018). Grassland fire ecology has roots in the late Miocene. *Proceedings of the National Academy of Sciences of the United States of America*, *115* (48), 12130–12135.
- Koch, P. L., Tuross, N., & Fogel, M. L. (1997). The effects of sample treatment and diagenesis on the isotopic integrity of carbonate in biogenic hydroxylapatite. *Journal of Archaeological Science*, *24*, 417–429.
- Nelson, S. V. (2005). Paleoseasonality inferred from equid teeth and intra-tooth isotopic variability. *Palaeogeography, Palaeoclimatology, Palaeoecology*, *222*(1–2), 122–144.
- Patnaik, R., Singh, N. P., Paul, D., & Sukumar, R. (2019). Dietary and habitat shifts in relation to climate of Neogene-Quaternary and associated mammals of Indian subcontinent. *Quaternary Science Reviews*, *224*, 105968.
- Sanyal, P., Sarkar, A., Bhattacharya, S. K., Kumar, R., Ghosh, S. K., & Agrawal, S. (2010). Intensification of monsoon, microclimate and asynchronous C_4 appearance: Isotopic evidence from the Indian

- Siwalik sediments. *Palaeogeography, Palaeoclimatology, Palaeoecology*, 296(1–2), 165–173.
- Wang, P. X., Wang, B., Cheng, H., Fasullo, J., Guo, Z. T., Kiefer, T., & Liu, Z. Y. (2014). The global monsoon across timescales: Coherent variability of regional monsoons. *Climatic past*, 10, 2007–2052.
- Waseem, M. T., Khan, A. M., Quade, J., Krupa, A., Dettman, D. L., Rafeh, A., & Ahmad, R. M. (2021). Stable isotope analysis of middle Miocene mammals from the Siwalik sub-group of Pakistan. *Acta Palaeontologica Polonica*, 66, s123–s132.

Mineralogy and Petrology



The Ti-Substitution in Phlogopite from the Jersey Minette (Channel Islands, UK) as Revealed by FTIR Spectroscopy

Giancarlo Della Ventura, Nacir El Moutaouakkil, Boubker Boukili, Manuela Nazzari, and Federico Lucci

Abstract

Phlogopite solid-solutions have a wide physico-chemical stability field; they are thus ubiquitous in a wide variety of geological environments. Phlogopite may provide important insight into the physico-chemical parameters of its crystallization conditions thus representing a tool for understanding magma storage conditions and petrogenesis. This paper focuses on the study of some intriguing single-crystals occurring within a lamprophyre minette from Fort Regent, St. Helier (Jersey Island, UK). The primary assemblage is represented by phlogopite + clinopyroxene + alkali-feldspar + apatite. Phlogopite occurs as both euhedral to subhedral phenocrysts and as euhedral microcrystals. Phlogopite phenocrystals associated with mica-lamprophyres generally present normal and continuous compositional zonings, however, the crystals from the studied minette are characterized by dark chestnut patchy cores enveloped by euhedral oscillatory rims. Preliminary results indicate (i) cores with a $Mg\# = Mg/(Mg + Fe_{tot})$ of ≈ 0.73 and high TiO_2 contents of $\approx 10\%$; (ii) inner rims having $Mg\# \approx 0.90$ with TiO_2 not exceeding 2% ; and (iii) external rims with $Mg\# \approx 0.67$ and TiO_2 contents up to 5.5% . Combination of EMP and single-crystal FTIR results in the OH-stretching region shows that, differently to what observed in other occurrences, the substitution mechanism responsible for the exceptional Ti zoning during the biotite crystallization is the Ti-vacancy mechanism that is known to be typical of HP/HT crystallization environments.

G. Della Ventura (✉)
Università Roma Tre, Roma, Italy
e-mail: giancarlo.dellaventura@uniroma3.it

N. El Moutaouakkil · B. Boukili
University Mohammed V, Rabat, Morocco

M. Nazzari · F. Lucci
Institute of Volcanology and Geophysics (INGV), Rome, Italy

F. Lucci
University of Bari, Bari, Italy

Keywords

Biotite · Titanium · Jersey Island (UK) · EMPA · FTIR imaging

1 Introduction

Phlogopite/biotite shows a wide physico-chemical stability field and its composition covers a wide range of solid-solutions (Guidotti, 1984); phlogopite phenocrysts associated with mica-lamprophyres generally present normal and continuous compositional zoning, however the Jersey minette contains relative large phenocrystals (up to 1–2 mm) with a systematic discontinuous inverse zonation (Velde, 1969), particularly evident for the Ti content.

We present here preliminary microchemical and FTIR results in the OH-stretching region with the aim of characterizing the substitutional mechanism responsible for the entry of usual amount of Ti in the mica structure.

2 Materials and Methods

The phlogopite samples studied here were manually extracted from a lamprophyric dyke outcropping at Fort Regent, St. Helier (Jersey Island, UK).

Electron Microprobe (EMP) and scanning electron microscopy (SEM) data were acquired at Istituto Nazionale di Geofisica e Vulcanologia (INGV), Rome by using a Jeol Superprobe. Used standards were all natural minerals. Single-crystal FTIR spectra in the OH-stretching medium-infrared (MIR) region were collected with unpolarized light using a Bruker Hyperion 3000 microscope equipped with an MCT (Mercury Cadmium Telluride) detector and a KBr beam splitter at Istituto Nazionale di Fisica Nucleare (INFN, Frascati, Rome).

3 Results

3.1 Results: Petrography and Mineral Chemistry

The studied minette shows a holocrystalline porphyritic texture as indicated by the presence of biotite and clinopyroxene phenocrysts. The main primary phases are phlogopite, clinopyroxene, and alkali-feldspar with apatite as dominant accessory mineral. The mica phenocrysts have euhedral to subhedral habit and invariably show dark chestnut patchy cores enveloped by alternate euhedral light- and dark-brown rims. Preliminary SEM-BSE imaging and EMP chemical investigations confirm the oscillatory texture consisting of: (i) cores with a $Mg\# = Mg/(Mg + Fe_{tot})$ of ≈ 0.73 and high TiO_2 contents up to 9–10%; (ii) inner rims having higher $Mg\# \approx 0.90$ but lower TiO_2 (< 2%); and (iii) external rims with lower $Mg\# \approx 0.67$ but increasing TiO_2 contents (up to 5.5%).

3.2 Results: FTIR Spectroscopy

The OH-stretching bands in micas may be classified (Robert & Kodama, 1988) into three types: N-bands (“normal”) when the hydroxyl oxygen is shared by three divalent metals, I-bands (“impurity”) when a trivalent cation (Al, Fe^{3+}) is present at one octahedral site, and V-bands (“vacancy”) when one octahedron is locally empty; this type occurs in dioctahedral micas. The local arrangements affect the charge balance on the hydroxyl oxygen, thus the vibrational frequency of the OH bond provides a very efficient tool to understand the relation between structure and local chemistry of mica (Boukili et al., 2003; Redhammer et al., 2000).

In end-member phlogopite, the OH vibrational frequency is 3724 cm^{-1} . For compositions along the phlogopite-annite join this band shifts to lower frequencies and broadens due to the presence of Fe^{3+} (and/or Al) at the octahedral sites. In dioctahedral mica, one over three OH-bonded octahedra is vacant, and the OH-stretching frequency shifts to wavenumber values $< 3600\text{ cm}^{-1}$ (Boukili et al., 2003; Redhammer et al., 2000; Robert & Kodama, 1988). Figure 1 compares the spectra collected at the crystal core and at the rim of the studied biotite. The former shows two very broad absorptions at 3700 and 3550 cm^{-1} , respectively, while the latter shows a most intense peak at 3700 cm^{-1} and a minor absorption at 3550 cm^{-1} . The higher frequency absorption at 3700 cm^{-1} is assigned to trioctahedral configurations; a tentative deconvolution (Fig. 1, right) indicates that this broad peak is due to several overlapping components due to the distribution of Mg and Fe^{2+} at the octahedral sites. The lower frequency (3550 cm^{-1}) absorption is related to the local dioctahedral configurations; considering that this V-band type is related to the crystal core, and based on the crystal-chemical compositional variations across the sample, it is assigned to local (Mg, Fe^{2+})Ti-OH clusters.

4 Discussion

There are essentially three mechanisms whereby Ti^{4+} can enter the phlogopite structure (Sassi et al., 2008): (1) The *Ti-Tschermak*, where the entry of Ti^{4+} in the structure is balanced by a simultaneous substitution of Al for Si at the tetrahedral sites; (2) the *oxy substitution*, whereby the Ti^{4+} entry is balanced by a local deprotonation; and (3) the *Ti-vacancy*, whereby the Ti^{4+} entry is balanced by the

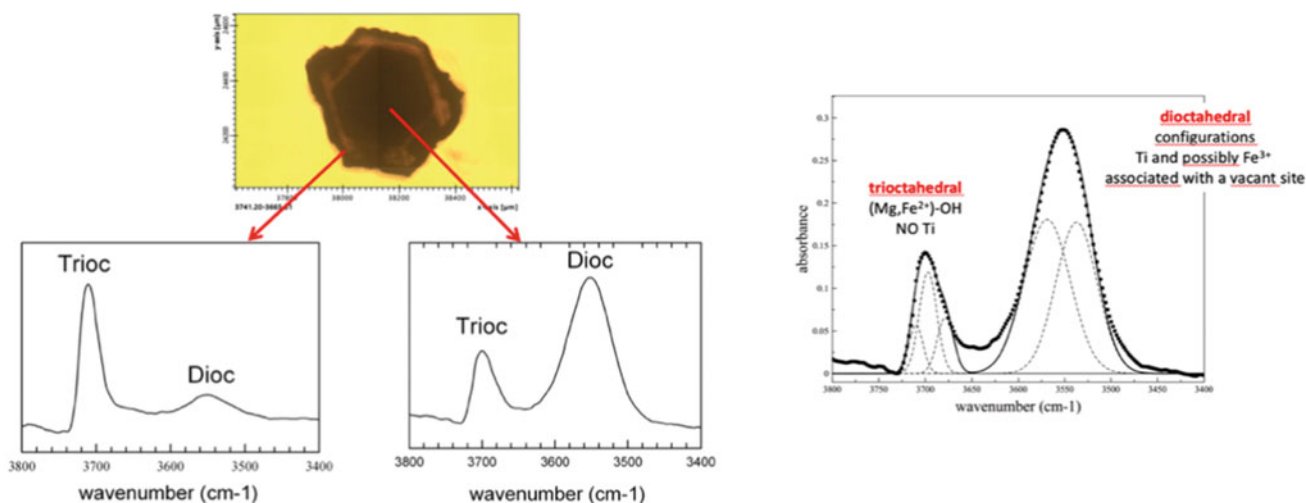


Fig. 1 Left: the single-crystal FTIR spectra collected in the OH-stretching region at the core and rim of the studied zoned biotite (also shown in the figure). Right: example of the spectral decomposition into single Gaussian components

formation of local dioctahedral configurations (i.e., those configurations involving a vacant octahedral site). The spectra of Fig. 1 show unambiguously that in the studied sample, the Ti enters the structure via mechanism (3).

Revision of data from petrologically well-constrained occurrences seems to indicate that the Ti-oxy substitution predominates in H₂O poor environments while Ti-vacancy predominates in H₂O-rich conditions (Cesare et al., 2003; Sassi et al., 2008). Experimental work on the Ti-Tschermak substitution (Robert, 1976) shows a significant increase of Ti for increasing temperature, and a decrease of Ti with pressure. On the other hand, the Ti-vacancy substitution was shown to increase for both increasing T and P (Forbes & Flower, 1974).

5 Conclusions

Combination of petrographic observations, EMP analyses, and FTIR single-crystal spectroscopy shows that the studied rock is a fragment of a volcanic dyke that, based on the chemical and mineralogical composition can be classified as a minette. The biotite has a Ti-rich core and shows extreme compositional zoning, which is the result of variation of the crystallizing system rather than to evolving P–T conditions. FTIR spectroscopy shows that the entry of Ti in the structure is mainly related to a Ti-vacancy mechanism in H₂O-rich conditions. Such a conclusion is in agreement with previous literature showing (Forbes & Flower, 1974) that the Ti-vacancy mechanism is typically related to HP/HT crystallization environments.

References

- Boukili, B., Holtz, F., Robert, J.-L., Joriou, M., Bény, J.-M., & Naji, M. (2003). Infrared spectra of annite in the O-H stretching vibrational range. *Swiss Bulletin of Mineralogy and Petrology*, 83, 331–340.
- Cesare, B., Cruciani, G., & Russo, U. (2003). Hydrogen deficiency in Ti-rich biotite from anatectic metalelites (El Joyazo, SE Spain): Crystal-chemical aspects and implications for high-temperature petrogenesis. *American Mineralogist*, 88, 583–595.
- Forbes, W. C., & Flower, M. F. J. (1974). Phase relations of titan-phlogopite, $K_2(Mg_4Ti)(Si_6Al_2)O_{20}(OH)_2$: A refractory phase in the upper mantle? *Earth and Planetary Science Letters*, 22, 60–66.
- Guidotti, C.V. (1984) Micas in metamorphic rocks. In: S. W. Bailey (Ed.), *Micas Review in Mineralogist* (Vol. 13, pp. 357–467). Mineralogical Society of America
- Redhammer, G. J., Beran, A., Schneider, J., Amthauer, G., & Lottermoser, W. (2000). Spectroscopic and structural properties of synthetic micas on the annite-siderophyllite binary: Synthesis, crystal structure refinement, Mossbauer, and infrared spectroscopy. *American Mineralogist*, 85, 449–465.
- Robert, J.-L. (1976). Titanium solubility in synthetic phlogopite solid solutions. *Chemical Geology*, 17, 213–227.
- Robert, J.-L., & Kodama, H. (1988). Generalization of the correlation between hydroxyl-stretching wavenumbers and composition of micas in the system $K_2O-MgO-Al_2O_3-SiO_2-H_2O$: A single model for dioctahedral and trioctahedral micas. *American Journal of Science*, 288A, 196–212.
- Sassi, R., Cruciani, G., Mazzoli, C., Nodati, L., & Craven, J. (2008). Multiple titanium substitutions in biotite from high-grade metapelitic xenoliths (Euganean Hill, Italy): Complete crystal-chemistry and appraisal of petrologic control. *American Mineralogist*, 93, 339–350.
- Velde, D. (1969). Les micas des lamprophyres: Kersantites, minettes et lamproïtes. *Bulletin De Minéralogie*, 92, 203–223.



Solution, Mixing and Formation Enthalpy Determination of Neodymium-Bearing Silicate–Oxyapatite

Kaouther Ardhaoui

Abstract

Apatite is a common phosphate mineral in crustal rocks, recognized as being the main feedstock for fertilizer industry, but also due to its rich composition, which makes this mineral a source for rare earth elements. Moreover, apatite has a structure stability and durability under radiation conditions in geological situation and in synthetic products. Thus, britholite, which is a phospho-silicate-apatite-containing rare earth elements, is considered as one of the possible candidates for actinides and fission products immobilization. Hence, the management of apatite, in this environment protection view, suggests the knowledge of their stability, thermodynamic properties, dissolution, and potential reactions. The calorimetry of dissolution is a powerful technique to study the stability of materials in various solvents, like water and acid solutions, which leads to the determination of numerous thermodynamic values. In this work, the thermochemical stability of an apatite solid solution was studied, named Neodymium-bearing silicate-oxyapatite or britholite $\text{Ca}_{10-x}\text{Nd}_x(\text{PO}_4)_{6-x}(\text{SiO}_4)_x\text{O}$ having different substitution rate x , with $1 < x < 6$. The calorimetric study consisted of measuring the enthalpies of a solution in nitric acidic aqueous solution (46% w) at 298.15 K using a swinging differential Tian-Calvet calorimeter. The formation enthalpies from the elements were reached by a thermochemical cycle and complementary experiments. Moreover, the mixing enthalpies in the studied solid solution were also deduced. The results revealed that the solution reactions are exothermic and display a notable increase of the absolute values of energies with the rate of

substitution. Furthermore, the mixing enthalpies are positive and the formation enthalpies are decreasing with the amount of substitution x . Such experimental results are readily usable thermodynamic data for geochemical studies on the stability of apatite.

Keywords

Apatite • Britholite • Heat of solution • Mixing enthalpy • Heat of formation

1 Introduction

Apatites are phosphate materials allowing a large array of substitution. The composition of apatite compounds is expressed as $\text{Me}_{10}(\text{PO}_4)_Z\text{O}$; with Me = alkaline earth ion or vacancy; and $Z = \text{F}^-$, OH^- , O^{2-} or vacancy (Elliott, 1994). The majority of apatite crystallize in the hexagonal system (spatial symmetry group $\text{P6}_3/\text{m}$).

This research on the thermodynamic stability of the chosen solid solution $\text{Ca}_{10-x}\text{Nd}_x(\text{PO}_4)_{6-x}(\text{SiO}_4)_x\text{O}$ with $1 < x < 6$, has the aim of corroborating the efforts of several studies to valorize apatite as material for the immobilization of trivalent actinides in geological disposals (Strzelecki et al., 2022; Zhou et al., 2023). This paper presents the results of synthesis and the characterization of neodymium-bearing silicate-oxyapatite. Then in the second part, the results of the solution calorimetry of the britholites are displayed. The enthalpies of solution in the nitric acid allowed the deduction of the formation and the mixing enthalpies.

2 Methodology

Britholites were prepared by solid state reaction through cold pressing and sintering (Orlova & Ojovan Aug., 2019). A stoichiometric mixture of $\text{Nd}_2\text{O}_3/\text{CaCO}_3/\text{Ca}_2\text{P}_2\text{O}_7/\text{SiO}_2$

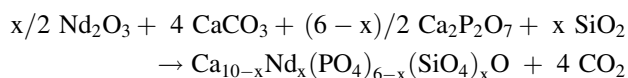
K. Ardhaoui (✉)
Higher Institute of Applied Biology of Medenine,
Gabes University, Gabes, Tunisia
e-mail: ardhaouikaouther@gmail.com

K. Ardhaoui
Laboratory of Eremology and Combating Desertification,
IRA Medenine, Medenine, Tunisia

Table 1 Solution enthalpies, mixing enthalpies, and formation enthalpies of the neodymium-bearing silicate-oxyapatite studied

X	Neodymium Oxybritholite	$\Delta_{\text{sol inf dil}}H^\circ(\text{kJmol}^{-1})$	$\Delta_{\text{mix}}H^\circ/\text{kJ mol}^{-1}$	$\Delta_fH^\circ/\text{kJ mol}^{-1}$
0	$\text{Ca}_{10}(\text{PO}_4)_6\text{O}$	–	0	– 12,917 (Ardhaoui, 2006)
1	$\text{Ca}_9\text{Nd}(\text{PO}_4)_5(\text{SiO}_4)\text{O}$	– 605.5	126.1	– 13,258
2	$\text{Ca}_8\text{Nd}_2(\text{PO}_4)_4(\text{SiO}_4)_2\text{O}$	– 712.7	132.6	– 13,718
3	$\text{Ca}_7\text{Nd}_3(\text{PO}_4)_3(\text{SiO}_4)_3\text{O}$	– 816.01	142.9	– 14,175
4	$\text{Ca}_6\text{Nd}_4(\text{PO}_4)_2(\text{SiO}_4)_4\text{O}$	– 843.2	229.4	– 14,555
5	$\text{Ca}_5\text{Nd}_5(\text{PO}_4)_1(\text{SiO}_4)_5\text{O}$	– 1110.2	75.9	– 15,176
6	$\text{Ca}_4\text{Nd}_6(\text{SiO}_4)_6\text{O}$	– 1299.8	0	– 15,718

was calcined at 1400 °C in order to attain the britholites, giving to the following equation:



where $0 < x < 6$.

Solution calorimetry in nitric acid solutions (46% w) was realized at room temperature using a differential calorimeter named Calsol (Ganteaume et al., 1991). This apparatus allows studding either quick kinetic or slow kinetic phenomena. Due to its 100 cm³-Kel-F[®]-cell, Calsol provides wide spectra of experiments. The solution enthalpies of the studied neodymium oxybritholite were measured in an acidic aqueous solvent which is a mixture of nitric acid 46 weight % containing hydrofluorhydric acid HF to facilitate the dissolution of silicates. Powdered britholites quantities did not exceed 12 mg. As dissolving higher quantities may lead to the precipitation of calcium and neodymium fluorides, as it was described in a previous work (Ganteaume et al., 1991). The mixing enthalpies were then deduced. By means of the dissolution mechanism of the britholites, the formation enthalpies were also determined.

3 Results

3.1 Characterization

The powders obtained are pure and well crystallized and the infrared spectra present only characteristic bands transmittance of phosphate and silicate groups as described previously (Ardhaoui et al., 2018).

3.2 Determination of the Thermodynamic Properties of Neodymium Oxybritholite: Solution Enthalpies, Mixing and Formation Enthalpies

See Table 1.

Discussion

The formation enthalpy of britholites $\text{Ca}_{10-x}\text{Nd}_x(\text{PO}_4)_{6-x}(\text{SiO}_4)_x\text{O}$ decrease versus the rate x, indicating an increase in stability of oxybritholite, as the double substitution (Ca^{2+} ; PO_4^{3-}) \leftrightarrow (Ln^{3+} ; SiO_4^{4-}) rises. This evolution can be explained by the fact that Si–O ($D^\circ 298 = 799.6 \text{ kJ mol}^{-1}$) and Nd–O ($D^\circ 298 = 703 \text{ kJ mol}^{-1}$) bonds are harder to break than P–O ($D^\circ 298 = 599.1 \text{ kJ mol}^{-1}$) and Ca–O ($D^\circ 298 = 402.1 \text{ kJ mol}^{-1}$) bonds respectively (Wagman, 1982).

Thermodynamical data on britholite and similar materials are needed to understand the nucleation and growth kinetics of various RE-phases and their crystallization in RE-bearing slag (Lan et al., 2021), and to complement information on the physico-chemical properties and application of apatite in the field of photocatalysis (Kumar et al., 2021), biomaterials (Owens et al., 2019) and industry (Singh, 2021). For this reason, handling these materials implies the knowledge of their stability and other dissolution and thermodynamic properties.

4 Conclusions

This research was dedicated to study the stability of a solid solution of neodymium-bearing silicate-oxyapatite $\text{Ca}_{10-x}\text{Nd}_x(\text{PO}_4)_{6-x}(\text{SiO}_4)_x\text{O}$ with $1 < x < 6$, which was prepared by solid state solution. The solution calorimetric study headed to the solution, mixing, and formation enthalpies of the studied britholites. These results are useful to comprehend the relative stability of the solid solutions of neodymium-bearing silicate-oxyapatite and lanthanum-bearing silicate-oxyapatite.

References

- Elliott, J. C. (1994). *Structure and Chemistry of the Apatites and Other Calcium Orthophosphates*. Elsevier Science.
- Strzelecki, A. C., et al. (2022). Structure and thermodynamics of calcium rare earth silicate oxyapatites, $\text{Ca}_2\text{RE}_8(\text{SiO}_4)_6\text{O}_2$ (RE = Pr, Tb, Ho, Tm). *Physics and Chemistry of Minerals*, 49(5), 13. <https://doi.org/10.1007/s00269-022-01187-5>

- Zhou, Y., Tang, Y., Liao, C., Su, M., & Shih, K. (2023). Recent advances toward structural incorporation for stabilizing heavy metal contaminants: a critical review. *Journal of Hazardous Materials*, *448*, 130977. <https://doi.org/10.1016/j.jhazmat.2023.130977>
- Orlova, A. I., & Ojovan, M. I. (2019). Ceramic mineral waste-forms for nuclear waste immobilization. *Materials*, *12*(16), 2638. <https://doi.org/10.3390/ma12162638>
- Ganteaume, M., Coten, M., Decressac, M. (1991). Un nouveau calorimetre de solution: Le calsol. *Thermochim Acta*, *178*. doi: [https://doi.org/10.1016/0040-6031\(91\)80300-8](https://doi.org/10.1016/0040-6031(91)80300-8)
- Ardhaoui, K., ben Chérifa, A., Rogez, J. (2018). Standard enthalpy of formation of Neodymium oxybritholites. In *7th international chemistry conference (ICC 2018)*. King Saud University.
- Ardhaoui, K., Rogez, J., ben Chérifa, A., Jemal, M., & Satre, P. (2006). Standard enthalpy of formation of lanthanum oxybritholites. *Journal of Thermal Analysis and Calorimetry*, *86*(2). doi: <https://doi.org/10.1007/s10973-005-7369-1>
- Wagman, D. D. (1982). The NBS tables of chemical thermodynamic properties. Selected values for inorganic and C1 and C2 organic substances in SI Units. 8725 John J. Kingman Road, Fort Belvoir, VA 22060-6218: DEFENSE TECHNICAL INFORMATION CENTER.
- Lan, X., Gao, J., Li, Y., & Guo, Z. (2021). Phase equilibria of CaO–SiO₂–CaF₂–P₂O₅–Ce₂O₃ system and formation mechanism of britholite. *Ceramics International*, *47*(9), 11966–11972. <https://doi.org/10.1016/j.ceramint.2021.01.038>
- Kumar, A. N., et al. (2021). La₁₀Si₆O₂₇: Tb³⁺ nanomaterial; its photocatalytic and electrochemical sensor activities on Disperse Orange and Fast Blue dyes. *Sensors International*, *2*, 100076. <https://doi.org/10.1016/j.sintl.2020.100076>
- Owens, C. L., Nash, G. R., Hadler, K., Fitzpatrick, R. S., Anderson, C. G., & Wall, F. (2019). Apatite enrichment by rare earth elements: A review of the effects of surface properties. *Advances in Colloid and Interface Science*, *265*, 14–28. <https://doi.org/10.1016/j.cis.2019.01.004>
- Singh, Y. (2021). Indian rare-earth deposits: related industry, balance problem and Atmnirbhar Bharat. 91–117. doi: https://doi.org/10.1007/978-981-16-4122-0_7



Effect of Fly Ash (FA) Characteristic on Geopolymer Product Quality

Sonia Cantika Wijayanti, Ferian Anggara, and Himawan T. B. M. Petrus

Abstract

Fly Ash and Bottom Ash (FABA), a waste product in the form of ash from the burning coal at coal-fired power plants, is considered to have many advantages as the raw material for construction. One of the construction product examples is a geopolymer. This research aimed to determine the effect of the FABA characteristic on the compressive strength of geopolymer products. The source of fly ash (FA) used in this study is FA from Tanjung Jati B combustion power plant, Java, Indonesia which was characterized using petrographic analysis, XRD analysis, XRF analysis. Geopolymer was made with wet mixing methods and characterized using compressive strength tests and FTIR analysis. This study characterized the fly ash as having the dominant major oxides being Al_2O_3 , SiO_2 , and Fe_2O_3 . The inorganic components consist of glass, quartz, mullite, *k*-feldspar, fe-spinel, mg-spinel, hematite, magnetite, calcite, and kaolinite, while the inorganic components are dominated by glass materials, and the organic component consists of unburned coal (UC). Geopolymer, which is made, has a

compressive strength average of 33 Mpa. A high value of $\text{SiO}_2/\text{Al}_2\text{O}_3$, a high value of reactive SiO_2 , a low value of unburned carbon, and a low value of Fe_2O_3 affect the bond structure formed in the geopolymer and have a direct effect on increasing compressive strength. The results of this study could be used as a guide for determining the initial characteristics of FA in the manufacture of geopolymers with maximum quality.

Keywords

Geopolymer • Fly ash • Wet mixing method

1 Introduction

Coal combustion waste, FABA, in Indonesia is predicted to increase along with the increasing demand for electrical energy that is used (Anggara et al., 2021). The accumulation of FABA has an impact on the environment, such as polluting air, soil, or water (Damayanti, 2018). Therefore, it is necessary to increase the use of FABA, that is, as a geopolymer.

FA is used as a pozzolanic material to replace Ordinary Portland Cement (OPC) in the production of geopolymer concrete as an alternative of conventional concrete. The use of geopolymer concrete has the advantages of relatively low cost, good mechanical and physical properties, low energy consumption, and can reduce greenhouse emissions (Živica et al., 2015). The type and feature of the raw materials used in the production of geopolymers will directly affect the physical and chemical properties of the resulting geopolymer (Živica et al., 2015). Therefore, further research on the effect of FA characteristics as a raw material for the production of geopolymers on the quality of geopolymer products is important, so that the appropriate characteristics of FA can be determined in increasing the use value of the waste products of coal combustion.

S. C. Wijayanti · F. Anggara (✉)
Departement of Geological Engineering, Faculty of Engineering,
Universitas Gadjah Mada, Jalan Grafika No.2 Kampus UGM
Bulaksumur, D.I. Yogyakarta, 55281, Indonesia
e-mail: ferian@ugm.ac.id

F. Anggara · H. T. B. M. Petrus
Unconventional Geo-Resources Research Group, Faculty of
Engineering, Universitas Gadjah Mada, Jalan Grafika No.2
Kampus UGM Bulaksumur, D.I. Yogyakarta, 55281, Indonesia

H. T. B. M. Petrus
Departement of Chemical Engineering, Faculty of Engineering,
Universitas Gadjah Mada, Jalan Grafika No.2 Kampus UGM
Bulaksumur, D.I. Yogyakarta, 55281, Indonesia

2 Materials and Methods

FA samples in this study were collected from PLTU Tanjung Jati B unit 4 with feed coal from PT. Berau and PT. Indominco with a ratio of 50:50%. The feed coal is taken from Berau Basin and Kutai Basin with rank sub-bituminous to high-volatile bituminous which is burned using a pulverized coal combustion system and ESP ash catcher. FA characteristics were analyzed using XRF analysis to determine major oxide, XRD to determine mineralogy on details, and petrography to determine its organic and inorganic components.

Geopolymer concrete was produced using the wet mixing method referred to by (Bayuaji et al., 2017; Petrus et al., 2019) with the concentration of NaOH used being 12 M according to the optimum conditions based on research from (Herwani et al., 2018). An alkaline activator is produced by mixing NaOH with sodium silicate (Na_2SiO_3) with a 1:1 ratio. FA is mixed with an alkaline activator using the wet mixing method to produce geopolymer paste that is homogeneous. The geopolymer paste was then printed on a $5 \times 5 \times 5 \text{ cm}^3$ mold and dried at room temperature (30°C) for 28 days. Samples of dried geopolymer paste were taken for a compressive strength test to determine the resulting compressive strength and an FTIR analysis to determine the geopolymerization bond formed.

3 Results

3.1 Chemical Composition

Chemical composition of FA (Table 1) shows that the dominant major oxide is Al_2O_3 , SiO_2 , and Fe_2O_3 with the $\text{SiO}_2/\text{Al}_2\text{O}_3$ is 2.65.

3.2 Organic and Inorganic Composition

Petrography analysis indicated that FA samples consist of organic and inorganic components which can be seen in the optical appearance of each component in Fig. 1. With percentage of organic and inorganic components on FA shown in Table 2. The dominant organic component is unburned coal while the dominant inorganic component is glass (cenosphere and pleiosphere).

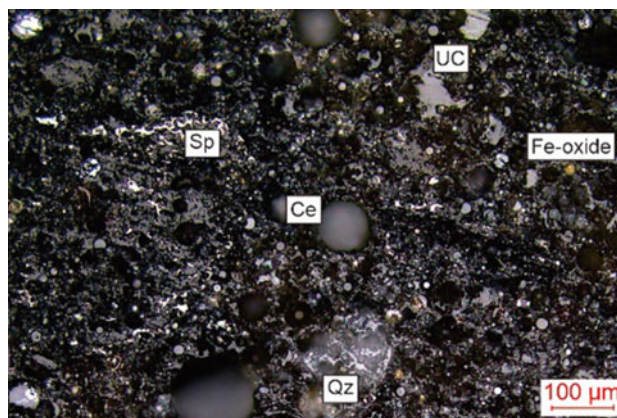


Fig. 1 Fly ash component: cenosphere (Ce), quartz (Qz), spinel (Sp), oxide minerals (Fe-oxide), and unburned carbon (UC)

3.3 Mineralogy Composition

Mineralogy variations based on XRD analysis were identified as quartz, mullite, calcite, spinel which are detailed into fe-spinel and mg-spinel, and the last oxide minerals which are detailed into hematite and magnetite. Dominant mineral based on XRD analysis is quartz (Fig. 2 and Table 3).

3.4 Compressive Strength

One FA sample produces 3 geopolymers with each compressive strength as 20.04, 36.08 and 42.55 Mpa to determine the average compressive strength produced. The average compressive strength is 32.89 Mpa, and based on SNI 03-0691-1996, it belongs to category B-grade concrete, which can conclude that the geopolymer can be used for parking equipment.

3.5 FTIR

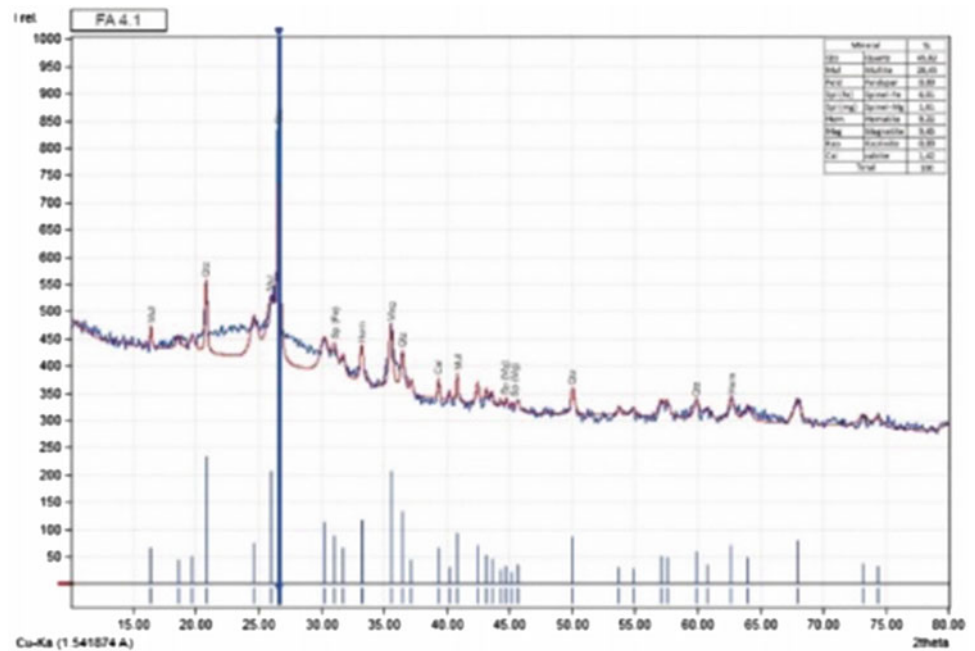
FTIR analysis shows that the existence of Si-O-Al in the sample is relatively low in comparison to the standard zeolite used in this experiment. Other bonds formed are O-H and H-O-H which are present in sufficient quantities to help hydrate the alumina-silica and will produce a homogeneous mixture (Fig. 3).

Table 1 Chemical composition of FA Tanjung Jati B unit 4

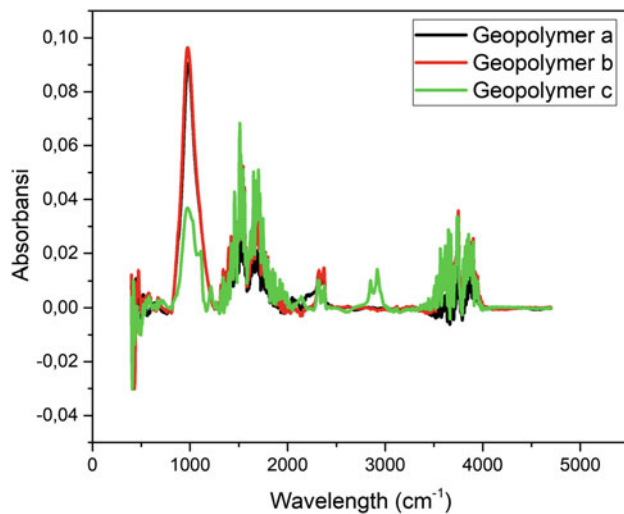
Sample	wt%						
	Al_2O_3	SiO_2	SO_3	K_2O	CaO	TiO_2	Fe_2O_3
FA	17.74	47.08	0.39	3.00	7.20	1.49	21.43

Table 2 Organic and inorganic composition of FA Tanjung Jati B unit 4

Sample	Unburned carbon (%)	Glass (%)	Quartz (%)	Spinel (%)	Oxides minerals (%)
FA	20.96	39.43	2.83	9.87	26.91

Fig. 2 XRD pattern shows the type of minerals from FA Tanjung Jati B unit 4**Table 3** Mineralogy composition of FA Tanjung Jati B unit 4

Sample	Quartz (%)	Mullite (%)	Fe-spinel (%)	Mg-spinel (%)	Hematite (%)	Magnetite (%)	Calcite (%)
FA	45.82	26.45	6.01	1.61	9.22	9.45	1.42

**Fig. 3** FTIR pattern from FA Tanjung Jati B unit 4

4 Discussion

The FA sample has a high $\text{SiO}_2/\text{Al}_2\text{O}_3$ value with a high composition of quartz (SiO_2) based on XRD analysis followed by high composition of glass (reactive SiO_2) values. FA sample also has low unburned carbon (UC) values and low Fe_2O_3 values. A high value of $\text{SiO}_2/\text{Al}_2\text{O}_3$ will produce more Si-O-Si bonds formed than Si-O-Al (Faradilla et al., 2020). This Si-O-Si bond has a stronger bond than the Si-O-Al bond, so concrete with high compressive strength will be formed (Faradilla et al., 2020). The high composition of quartz (SiO_2) based on XRD analysis, followed by a high composition of glass (reactive SiO_2) value, indicates that more and more SiO_2 reacts and forms bonds so that it will accelerate the geopolymerization reaction and produce concrete with high compressive strength (Kucharczyk et al.,

2019). The low UC content in FA samples based on Fernandez-Jimenez (Fernández-Jiméne & Palomo, 2003) and Diaz (Diaz & Barrios, 2010) will cause more surface to react and less activator solution required to activate the active material, resulting in high compressive strength and saving raw materials. Based on Choi (Choi & Lee, 2012) Low Fe₂O₃ content in the sample will accelerate the formation of CSH bonds so that the resulting compressive strength value will be higher. The FA characteristics are compared with the compressive strength and the formed geopolymerization bond, which shows a compressive strength value of 32.89 with category B grade, which can be used as parking equipment (Badan Standarisasi Nasional, 1996) and produces a low Si-O-Al geopolymerization.

5 Conclusions

The FA were class F with SiO₂/Al₂O₃ ratio is 2.65. The inorganic components of FA based on petrography analysis were dominated by glass (cenosphere and pleiosphere) with a percentage of 39.43%. Other inorganic components are quartz, spinel, and oxide minerals. The inorganic components of FA based on XRD analysis are dominated by quartz with a percentage of 45.82%. Other inorganic components are mullite, Fe-spinel, Mg-spinel, hematite, magnetite, and calcite. The organic component contained in FA is UC with a percentage of 20.96%. The high percentage of UC composition will increase the porosity of the FA so that more activator solution is needed to fill the pores and activate the main reaction material. UC can reduce the surface that reacts with the activator solution so that the presence of UC will inhibit the production of geopolymer bonds in the reaction and decrease the compressive strength. The compressive strength produced by the FA sample has an average of 32.89 MPa with the category B-grade concrete, according to SNI 03-0691-1996, which can be used as parking equipment.

Acknowledgements The authors would like to thank you Research Directorate Gadjah Mada University (Program Rekognisi Tugas Akhir Batch I Tahun Anggaran 2022) for its funding to publish this research.

References

- Anggara, F., Petrus, H. T. B. M., Anisa, D., Besari, A., Manurung, H., Yulindra, F., & Saputra, A. (2021). Tinjauan Pustaka Karakterisasi dan potensi Pemanfaatan fly ash dan bottom ash. *Buletin Sumber Daya Geologi*, 16, 53–70.
- Bayuaji, R., Yasin, A. K., Susanto, T. E., & Darmawan, M. S. (2017). A review in geopolymer binder with dry mixing method (geopolymer cement). *American Institute of Physics Inc, AIP Conference Proceedings*, 1887, 1–6.
- Badan Standarisasi Nasional. (1996).: Bata Beton (Paving Block): SNI 03-0691-1997.
- Choi, S. C., & Lee, W. K. (2012). Effect of Fe₂O₃ on the physical property of geopolymer paste. *Advanced Materials Research*, 586, 126–129.
- Damayanti, R. (2018). Abu batubara dan pemanfaatannya: Tinjauan teknis karakteristik secara kimia dan toksikologinya. *Jurnal Teknologi Mineral Dan Batubara*, 14, 213–231.
- Diaz, E. E. S., & Barrios, V. A. E. (2010). Development and use of geopolymers for energy conversion: An overview. *Construction and Building Material*, 315, 1–14.
- Faradilla, F. S., Nugroho, D. T., Hidayati, R. E., Nurlina, Bayuaji, R., Hartanto, D., & Fansuri, H. (2020). Optimization of SiO₂/Al₂O₃ ratio in the preparation of geopolymer from high calcium fly ash. In *IOP conference series: earth and environmental science* (Vol. 616, pp. 1–7).
- Fernández-Jiméne, A., & Palomo, A. (2003). Characterisation of fly ashes. *Potential Reactivity as Alkaline Cements, Fuel*, 82, 65.
- Herwani, P. I., Imran, I., Budiono, B. (2018). Compressive strength of fly ash-based geopolymer concrete with a variable of sodium hydroxide (NaOH) solution molarity. In *EDP sciences, MATEC web of conferences* (Vol. 147, pp. 1–5)
- Kucharczyk, S., Zajac, M., Stabler, C., Thomsen, R. M., Ben Haha, M., Skibsted, J., & Deja, J. (2019). Structure and reactivity of synthetic CaO-Al₂O₃-SiO₂ glasses. *Cement and Concrete Research*, 120, 77–91.
- Petrus, H. T. B. M., Adelizar, A. S., Widiyatmoko, A., Olvianas, M., Suprpta, W., Perdana, I., Prasetya, A., and Astuti, W. (2019). Kinetics of fly ash geopolymerization using semi quantitative fourier-transform infrared spectroscopy (FTIR); corr data. In *IOP conference series: materials science and engineering, institute of physics publishing* (Vol. 532, 1–9)
- Živica, V., Palou, M. T., & Krížma, M. (2015). Geopolymer cements and their properties: A review. *Building Research Journal*, 61, 85–100.



Characteristics and Potential Concentration of Cenospheres in Fly Ash from Tanjung Jati B Combustion Power Plant, Jepara, Central Java, Indonesia

Rafif Dhia Ulhaq, Ferian Anggara, and Himawan Tri Bayu Murti Petrus

Abstract

Fly ash and bottom ash (FABA) are residual products from a power plant coal combustion that can be processed into products with economic value. One component of FA that has the potential to proceed is the cenospheres. However, the concentration of cenospheres in FA is limited so further analysis is needed to maximize this potential. The study was conducted using FA samples at Tanjung Jati B combustion power plant covering units 1 and 2, unit 3, and unit 4 located in Jepara, Central Java, Indonesia. Samples were analyzed to determine the composition of FA and the concentration of cenospheres within. The main oxide compounds in FA were determined by XRF analysis. The organic and inorganic components of FA were identified through petrographic observations. The mineralogical composition of FA was generated by XRD analysis. The cenospheres retrieval test used the sink-float method with three trials on each sample and the presence of the cenospheres was confirmed through SEM analysis. The results showed that the inorganic components of FA consist of glass, quartz, Fe-spinel, Mg-spinel, hematite, magnetite, mullite, kaolinite, smectite, K-feldspar, and calcite, while the organic component found in FA is Unburned Carbon (UC). The cenospheres concentration values obtained were in the global range of cenospheres concentrations. The relationship between the constituent components of FA and the concentration of the cenosphere indicates that the presence of quartz in the FA sample positively

correlated with the amount of cenospheres that can be observed through petrographic analysis.

Keywords

Cenospheres • Fly ash • Sink-float method

1 Introduction

The more a country's economy grows, the more energy is required to run their activity, including coal. Coal production in Indonesia is expected to continuously increase, especially to meet domestic needs until 2027 with a total of 162 Mt. The coal combustion will produce Fly Ash and Bottom Ash (FABA) reaching 16.2 Mt assuming 10% of coal consumption (Hower, 2012). If FABA in large volumes is not managed properly, it will cause serious environmental and economic problems. Some components in FABA can be used as products with an economic value, while especially FA can be used for cenosphere recovery.

Cenospheres are amorphous silica (glass) composed predominantly by aluminosilicate compounds obtained from FA in coal combustion at boilers of a power plant. Compared to other particles, cenospheres have superior properties, such as light density, high compressive strength, low conductivity, and effective insulation (Fomenko et al., 2013). These superior properties provide opportunities for the use of cenosphere in various industries like paints, coatings, construction, petroleum, and pharmaceuticals (Danish & Mosaberpanah, 2020). Thus, cenospheres have the potential to be the most economical component to be processed from FA. However, study on cenospheres in Indonesia were limited and the concentration of cenospheres in FA were quite small. Therefore, a research about the potential of FA as a source of cenospheres needs to be conducted. Furthermore, the correlation between the constituent components of

R. D. Ulhaq · F. Anggara (✉)
Department of Geological Engineering, Faculty of Engineering,
Universitas Gadjah Mada, Jalan Grafika No.2 Kampus UGM
Bulaksumur, D.I. Yogyakarta, 55281, Indonesia
e-mail: ferian@ugm.ac.id

H. T. B. M. Petrus
Department of Chemical Engineering, Faculty of Engineering,
Universitas Gadjah Mada, Jalan Grafika No.2 Kampus UGM
Bulaksumur, D.I. Yogyakarta, 55281, Indonesia

FA with the concentration of cenospheres contained will be examined in this study.

2 Materials and Methods

The samples of FA used in this research came from PLTU Tanjung Jati B, Jepara, Central Java, Indonesia consisting of units 1 and 2 (FA 1), 3 (FA 3), and 4 (FA 4). Comparison of coal composition from PT. Berau and PT. Indomico were 50:50%. This sub-bituminous-rank coal is mined from the Kutai Basin and Berau Basin in East Kalimantan. The combustion system used was pulverized coal combustion with an ESP ash collection system. The constituent components of FA were determined from petrographic observations of polished block. In order to detail the mineralogy of FA, an XRD analysis was performed using the bulk method. Then the main oxide compound was determined through the results of XRF analysis.

The cenosphere samples were taken from fly ash by the quantitative method using the sink-float method according to (Petrus et al., 2020). The ratio of distilled water to FA were 1:10. Distilled water was first added to beaker with a volume of 500 mL, then put 50 g of FA. After that, the beaker was put into the ultrasonicator for 15 min to ensure the stability of the individual particles and allowed to stand for 4–5 h. Then the floating material was filtered using filter paper and dried for 1 day. The filtered material consists of cenospheres and some impurities such as Unburned Carbon (UC). To remove the carried UC material, calcination was carried out in the furnace at 800 °C for 90 min. Therefore, the cenospheres that obtained has lower density than distilled water, which is $< 1 \text{ gr/cm}^3$. Furthermore, to ensure the presence of cenospheres in the floating material, each sample was analyzed by SEM.

3 Results

3.1 Chemical Composition

The major oxide compounds in FA samples analyzed using XRF included SiO_2 , Al_2O_3 , Fe_2O_3 , CaO , MgO , SO_3 , K_2O , TiO_2 , SrO , and BaO (see Table 1).

3.2 Components of FA

The constituent components of FA can be grouped into two broad categories: inorganic and organic (Hower, 2012). Inorganic components consist of glass, iron oxide minerals, spinel, quartz, and metal, while the organic component consists of unburned carbon as shown in Fig. 1. Furthermore, the percentage of the presence of each constituent component through petrographic analysis can be seen in Table 2.

3.3 Mineralogy Data of FA

The results of XRD analysis on three samples of FA showed that the type of mineral that appeared with the highest intensity in all samples was quartz. The mineral variations found in all FA samples tend to be similar, consisting of quartz, mullite, K-feldspar, Mg-spinel, Fe-spinel, hematite, magnetite, maghemite, smectite, kaolinite, and calcite.

3.4 Concentration of Cenospheres

The concentration of cenospheres is calculated in units of weight percent (wt%) resulting from the weight of the float material after being calcined, divided by 50 g of FA, and multiplied by 100%. The experiment was conducted three times on each sample and the cenosphere concentration was calculated from the average value. As seen in Table 3, the sample of FA 1 has the highest concentration of cenospheres, compared to FA 4 and FA 3.

4 Discussion

The concentration of cenospheres obtained from the FA samples of PLTU Tanjung Jati B is in the global concentration range of 0.01–4.80 wt% (Petrus et al., 2020). The concentrations of cenospheres from the uptake test and petrographic analysis showed different results. The uptake test showed FA 1 has the highest concentration of cenospheres, while the petrographic analysis presents FA 4 as the highest one. It can be interpreted that FA 4 contains more

Table 1 Chemical composition of FA from Tanjung Jati B combustion power plant

No	Samples code	Major oxide compound (wt%)										Total (wt%)
		SiO_2	Al_2O_3	Fe_2O_3	CaO	MgO	SO_3	K_2O	TiO_2	SrO	BaO	
1	FA 1	47.09	18.54	21.33	6.55	0	1.10	2.96	1.53	0.26	0.14	99.50
2	FA 2	46.03	17.17	22.09	8.11	0.85	0.55	2.70	1.44	0.30	< 0.01	99.24
3	FA 3	47.08	17.75	21.43	7.20	0.85	0.39	3.00	1.49	0.18	0.14	99.49

Fig. 1 Fly ash components: cenospheres (Ce), pleiospheres (Ple), quartz (Qz), spinel (Spl), and unburned carbon (UC)

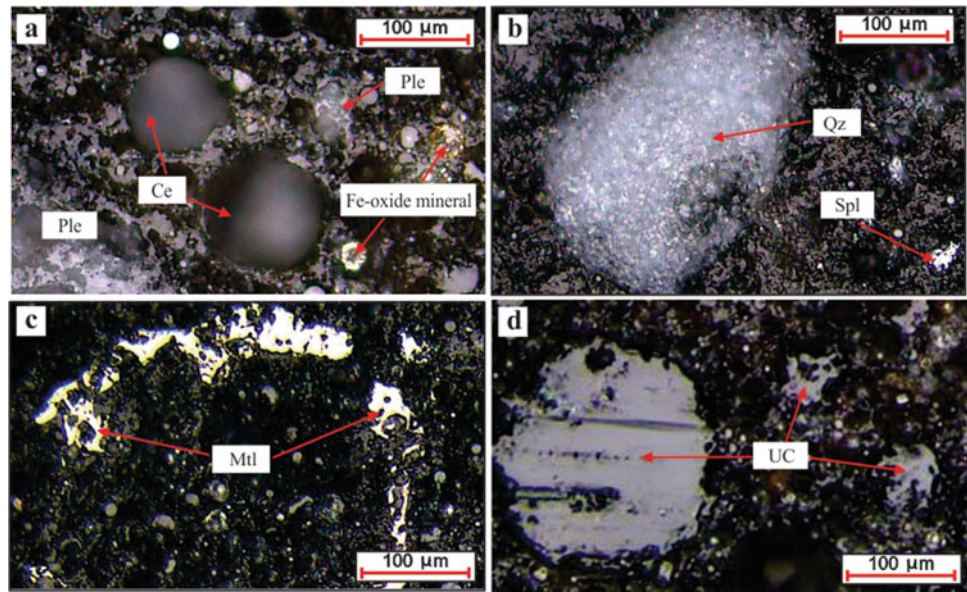


Table 2 Percentage of components FA based on petrographic analysis

Samples code	Glass (%)		Minerals (%)			Unburned Carbon (%)	Metal (%)
	Cenosphere	Pleiosphere	Quartz	Spinel	Oxide minerals		
FA 1	6.94	32.56	1.18	9.65	30.61	18.52	0.55
FA 2	2.84	24.78	0.87	17.18	22.7	30.23	1.41
FA 3	11.55	25.07	1.79	11.69	26.6	22.17	1.14
Average	7.11	27.47	1.28	13	26.64	23.64	1.03

Table 3 Cenospheres concentration data in FA

Samples code	Experiment (wt%)			Average (wt%)
	1	2	3	
FA 1	0.59	0.89	0.91	0.80
FA 3	0.04	0.08	0.07	0.06
FA 4	0.09	0.10	0.26	0.15

cenosphere with greater density than water. Therefore, when the sampling test was conducted, FA 1 could have a higher cenosphere concentration than FA 4.

Cenospheres which have bigger density than water can be caused by two factors, by the content of iron oxide as well as the influence of both shell along with the number and the size of gas inclusions (Acar & Atalay, 2016). The effect of iron oxide content in this study cannot be explained, since each FA sample has a high percentage (22.7–30.61%). The number and the size of gas inclusions estimated to influence the density of cenospheres in this study, where it could have a varying shell size with different numbers and sizes of gas inclusions.

Furthermore, the effect of the FA’s constituent components on the amount of cenospheres was observed. It was

found that quartz was positively correlated with the observed cenospheres through petrographic analysis. It is known that silica in quartz changes the viscosity so that it has an impact on increasing the diameter and shell of cenospheres (Fomenko et al., 2013).

5 Conclusions

Based on these analysis, the constituent components of each FA are dominated by inorganic components in the form of glass and oxidized minerals and organic components, namely UC. The chemical components are dominated by SiO₂, Al₂O₃, and Fe₂O₃ compounds which are known to be important components in the formation of the cenosphere.

The concentration of cenospheres in FA has average value for FA 1 of 0.80 wt%, FA 3 of 0.06 wt%, FA 4 of 0.15 wt%. FA 1 has the highest concentration of cenospheres compared to FA 4 and FA 3. Contrary to the results of petrographic analysis, it is observed that the highest percentage of cenospheres is in FA 4. This can be interpreted as FA 4 has a cenosphere with greater density than water as described in the publication recently that the cenosphere can have a greater density than water.

For the utilization of cenospheres on FA 1 and FA 3, they can be applied as a light filler in polymers, ceramics, and cement. Whereas FA 4 is dominated by cenospheres with a density greater than water, it has a high value application in the construction industry as a filler and reinforcement because of its greater wall thickness, which can contribute to the strength of the final product. However, it is necessary to characterize the physical and chemical properties of the cenospheres so that the use of the cenospheres is on target. Furthermore, it is known that the abundance of quartz in FA is positively correlated with the number of cenospheres observed through petrographic analysis, meaning that the higher the quartz content, the more cenospheres that can be observed will also increase.

Acknowledgements The authors would like to thank you Research Directorate Gadjah Mada University (Program Rekognisi Tugas Akhir Batch I Tahun Anggaran 2022) for its funding to publish this research.

References

- Acar, I., & Atalay, M. U. (2016). Recovery potentials of cenospheres from bituminous coal fly ashes. *Fuel*, 180, 97–105. doi: <https://doi.org/10.1016/j.fuel.2016.04.013>
- Danish, A., & Mosaberpanah, M. A. (2020). Formation mechanism and applications of cenospheres: a review. *Journal of Materials Science*, 55, 4539–4557. doi: <https://doi.org/10.1007/s10853-019-04341-7>
- Fomenko, E. V., Anshits, N. N., Solovyov, L. A., Mikhaylova, O. A., & Anshits, A. G. (2013). Composition and morphology of fly ash cenospheres produced from the combustion of Kuznetsk coal. *Energy and Fuels*, 27, 5440–5448. doi: <https://doi.org/10.1021/ef400754c>
- Hower, J. C. (2012). Petrographic examination of coal-combustion fly ash. *International Journal of Coal Geology*, 92, 90–97. doi: <https://doi.org/10.1016/j.coal.2011.12.012>
- Petrus, H. T. B. M., Olvianas, M., Suprpta, W., Setiawan, F. A., Prasetya, A., Sutijan, & Anggara, F. (2020). Cenospheres characterization from Indonesian coal-fired power plant fly ash and their potential utilization. *Journal of Environmental Chemical Engineering*, 8, 104116. doi: <https://doi.org/10.1016/j.jece.2020.104116>



Experimental Stimulation of Sublimating Water Ice on the Earth and the Moon with Measuring D/H Ratios

Vyacheslav Sevastyanov, Artem Krivenko, Sergey Voropaev, and Mikhail Marov

Abstract

In this paper, we present a draft new experimental setup for studying the sublimation of water ice at low temperatures under different conditions. The sublimation temperature could be varied from -196 to 0 °C. Also, the unit is connected to an Isotope Ratio Mass spectrometer (IRMS). An isotopic mass spectrometer allows measuring the isotopic composition of vapors of an evaporating substance and the rate of sublimation under specified physic-chemical conditions. The gas input into the mass spectrometer on-line mode distinguishes the developed setup from the existing analogues. The developed setup is equipped with a transparent quartz window through which the surface of the test substance can be heated using a halogen lamp. The setup can also be used to study the sublimation of gas hydrates and CO_2 , to study the sorption of gases on the surface of various samples.

Keywords

Ice • Sublimation • Isotope • Gas hydrates • Kinetic effects

1 Introduction

The key to a sustainable future in space is developing and utilizing space resource. Recent experiments have shown that the sublimation of water ice is not a simple and steady process (Brown et al., 2012). After the discovery of water on the Moon, interest in lunar resources increased significantly (Berezhnoy et al., 2012). Currently, methods are being developed to extract water from the shadowed regions of the

moon (Mortimer et al., 2018; Sower & Dreyer., 2019). It is known that isotopically heavy water leads to a violation of human metabolism and can affect the operation of rocket engines (Rouillard, 2010). The aim of this work is to create a setup and develop a method for studying the process of sublimation of ice or hoarfrost on Earth and under lunar conditions.

2 Settings of Experimental Setup

The experimental setup is currently at the testing stage (see Fig. 1). The setup includes a chamber with a sample located on a cooled support, a cooled trap for water vapor condensation and providing the possibility of sampling without depressurization of the entire system for isotope analysis, as well as a system for pumping the setup to the required vacuum. The first series of experiments includes the deposition of water on the surface of a basalt in vacuum ($\sim 10^{-3}$ mbar) and at temperatures from -150 to -20 °C. The surface temperature of samples will be changed by means of a heater or by the radiation of a halogen lamp. In this case, water vapor will move into the shadowed areas.

Setup is made of stainless steel and shown schematically in Fig. 2. 1 ml sample of initial water of known D/H ratio is placed in trap 1 and quantitatively transferred to the reactor; trap 2 is used for periodic extraction of water vapor; and trap 3 is used to collect water from the reactor remaining after sublimation. The entire installation is heated with a heating tape to a temperature of ~ 150 °C to prevent the sorption of water vapor on the metal surfaces of connecting tubes and valves. The reactor is pumped out by the Value VRD 6 vacuum pump (China) to a pressure of 10^{-4} mbar. The pressure is measured using ERSTEVAC MTP4D (Germany) pressure gauges near the vacuum pump and reactor.

The ice contained in the traps is thawed with a heat gun and when the valves locking the trap are opened, by turning the 6-way multi-position valve (position 2), the helium flow

V. Sevastyanov (✉) · A. Krivenko · S. Voropaev · M. Marov
Vernadsky Institute of Geochemistry and Analytical Chemistry,
119991 Moscow, Russia
e-mail: vsev@geokhi.ru

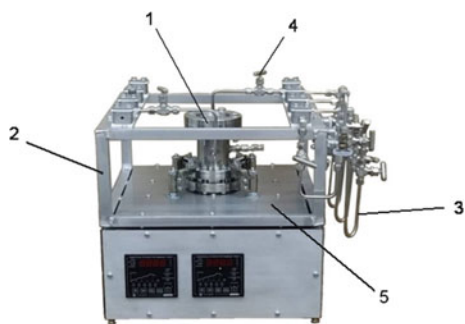


Fig. 1 Overall view of the experimental installation: 1—reactor, 2—the frame of the installation, 3—water traps, 4—valves, 5—protective heat shields of heaters

is directed into the trap with a sample, and then into the TC/EA pyrolyzer connected to the Delta Plus XP isotope ratio mass spectrometer (Thermo Fisher Scientific, Bremen, Germany). An isotopic mass spectrometer allows measuring the isotopic composition of vapor of an evaporating substance and the rate of sublimation under specified physico-chemical conditions. The presence of gas input into the mass spectrometer on-line distinguishes the developed installation from foreign analogues.

In position 1 of the 6-way valve, the helium flow enters directly into the pyrolyzer and mass spectrometer, bypassing the trap system. Into the TC/EA pyrolyzer at a temperature of 1450 °C, water molecules on the surface of the glassy carbon granulate decompose into hydrogen and CO. Next,

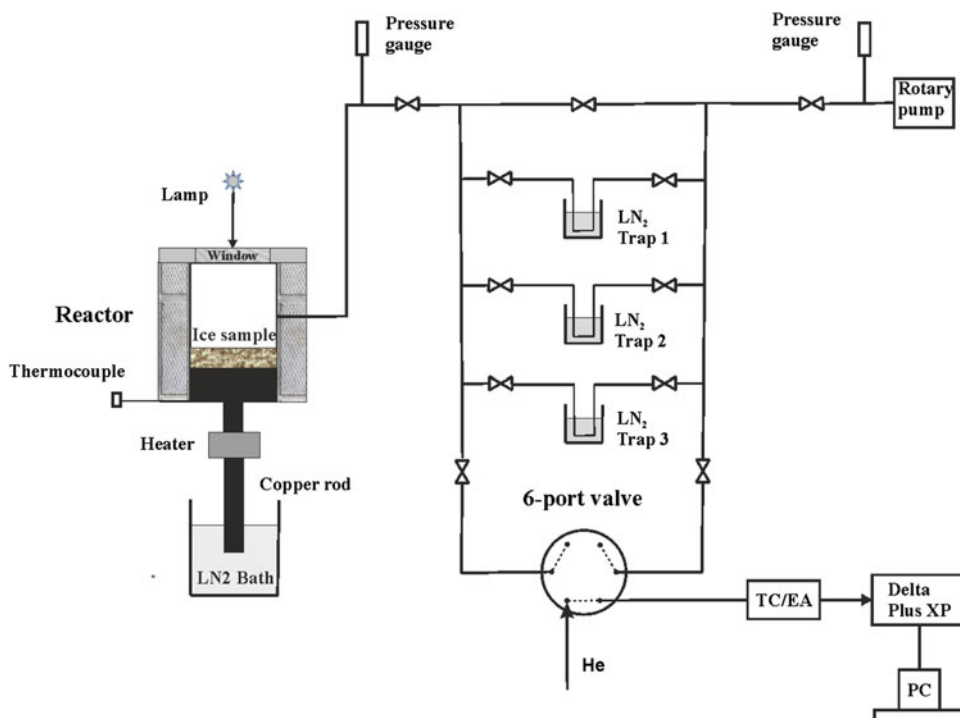
gas molecules are ionized in the ion source of the mass spectrometer and ion currents are measured. Using the ratios $2\text{H}^+/1\text{H}^+$ and $\text{C}^{18}\text{O}^+/\text{C}^{16}\text{O}^+$, the isotopic composition of hydrogen $\delta^2\text{H}_{\text{VSMOV}}$ and oxygen $\delta^{18}\text{O}_{\text{VSMOV}}$ are calculated relative to the international water standard VSMOV.

The reactor (see Fig. 1), in which ice sublimation occurs, consists of a cooled copper rod and a heater that allows changing the temperature of the sample from -196 to 0 °C. At the top of the reactor, there is a flange with a transparent quartz window through which the surface of the test substance can be heated using a halogen lamp.

3 Discussion

The design of the developed setup will allow reproducing the processes of sublimation of ice (snow) and condensation of water vapor under conditions simulating conditions near the lunar surface (Sower & Dreyer., 2019). A series of test measurements of isotopic fractionation of hydrogen and oxygen of water vapor during sublimation of ice with a known isotopic composition at temperatures -20 and -70 °C will be carried out and compared with existing literature data. The process of sublimation of ice in the form of frost on mineral grains of basalt, modeling the composition of lunar marine basalt, and the fractionation of hydrogen and oxygen isotopes accompanying this process when heating the surface with a light source will be studied in detail.

Fig. 2 Schematic of experimental setup for water ice sublimation



Based on the results of the research, estimates of the isotopic kinetic effect will be made during the movement of water vapor through cracks and pores of fragmented lunar marine basalts, as well as during degassing into vacuum. Numerical calculations will be carried out on the rate of retention and accumulation of water ice on the surface of the particles of lunar marine basalt in the processes of sublimation and resorption, shock processes, and subsequent burial in the regolith thickness.

4 Conclusions

A draft of an experimental setup has been developed to study the sublimation of ice at low temperatures and pressures simulating lunar conditions. The installation allows on-line measurement of the sublimation rate of water ice and the change in the isotopic composition of steam. The presence of a transparent window makes it possible to simulate the heating of the lunar surface by sunlight and to study the condensation of water molecules on shadowed surfaces. The created installation is multifunctional and allows obtaining

unique data on the sublimation of ice, gas hydrates, and CO₂, on the sorption and desorption of gases at various temperatures and pressures.

Acknowledgements This work was supported by Russian Science Foundation, project 21-17-00120.

References

- Brown, R. H., Lauretta, D. S., Schmidt, B., & Moores, J. (2012). Experimental and theoretical simulations of ice sublimation with implications for the chemical, isotopic, and physical evolution of icy objects. *Planetary and Space Science*, 60(1), 166–180.
- Berezhnoy, A. A., Kozlova, E. A., Sinitsyn, M. P., Shangaraev, A. A., & Shevchenko, V. V. (2012). Origin and stability of lunar polar volatiles. *Advances in Space Research*, 50(12), 1638–1646.
- Mortimer, J., Lecuyer, C., Fourel, F., Carpenter, J. (2018). D/H fractionation during sublimation of water ice at low temperatures into a vacuum. *Planetary and Space*, 158, 25–33.
- Sower, G. F., Dreyer, C. (2019). Ice mining in lunar permanently shadowed regions. *New Space*, 7(4), 235–244.
- Rouillard, M. K. (2010). Isotopes and life: Considerations for space colonization. *EIR Science*, 37(25), 36–47.



An Improved Method for Carbonates Evaluating from Carbonaceous Chondrites

Elena Tkachenko, Sergey Voropaev, and Veniamin Fedulov

Abstract

We have updated the standard method for estimating the amount of carbonates in carbonaceous chondrites on the example of the Murchison meteorite (CM2). In contrast to the existing technique (passing carbon dioxide released from carbonates through brine and weighing the remainder of the substance, when a small volume of gas may be too small for analysis using a mass spectrometer, our method is more reliable because all carbonates are collected in the form of a precipitate and then decompose at once at high temperature to carbon dioxide CO_2 and divalent metal oxides. This required the creation of a laboratory setup and development of the technique to calibrate mixtures of (Volcano Tolbachik, Kamchatka, Russia) with pure calcium carbonate CaCO_3 for analysis (from 0.1 to 1.0 wt.% with an interval of 0.1). The error estimation method was made on the basis of physico-chemical calculations of the content of carbon dioxide gas in the installation air. Results are tested and confirmed using gas chromatograph.

Keywords

Meteorite powders • Carbonaceous chondrites • Isotopy • Murchison meteorite • Allende meteorite • Volcanic ash • Carbon dioxide • Precipitation • Thermal decomposition • Degassing • Hydrochloric acid • Calcium carbonate

1 Introduction

The isotopic composition of carbon in meteorites was studied by several ways: direct decomposition of a ground sample before and after degassing at various temperatures; gas samples during meteorite degassing at various temperatures; removal of carbonates from meteorite powders before and after degassing at different temperatures to selectively determine the isotopic composition of carbon in carbonates. (CV3) and Murchison (CM2) carbonaceous chondrites have been studied.

2 Settings, Methods, and Materials

The carbonate decomposition method using hydrochloric acid and the subsequent carbon isotopic composition of the released CO_2 measurement have been proposed to determine the carbon isotopic composition of meteorite carbonates. Several model mixtures of pure CaCO_3 and volcanic ash were made to test this method. The CaCO_3 contents were 0.5, 1.0, and 1.5 wt. %. The calcium carbonate and ash mixture were ground in the ball mill until homogeneity was achieved. The model mixture (0.5–1.0 g) is poured into a test tube furnished with a vacuum cap. The test tube with the model mixture is purged then with helium to remove air. The control was carried out using Gas Chromatographer. Purging from the air continued for 15–20 min. Vacuum was created in an airless test tube using a water jet pump. This is necessary to escape a problem with the vacuum stopper when CO_2 is released after hydrochloric acid. Then 3 ml of 10% hydrochloric acid solution was added to the tube to decompose CaCO_3 and release CO_2 . At the end of the reaction 0.1 N KOH solution was added also to the test tube—no hydrochloric acid vapors in the gaseous medium remained and there was no destruction of the device.

E. Tkachenko · S. Voropaev (✉) · V. Fedulov
Vernadskii Institute of Geochemistry and Analytical Chemistry
of Russian Academy of Sciences (GEOHKI RAS),
Ulitsa Kosygina 19, Moscow, Russia
e-mail: voropaev@geokhi.ru

Technique for Isotope Measurements of Gases

The carbon isotope of the gas composition was determined using DELTA Plus mass spectrometer in combination with a GC Combustion III combustion interface and an Agilent 6890 Gas Chromatograph equipped with an HP-Plot (30, 0.32 mm) quartz capillary column (Agilent Technologies). The temperature of the oxidizing reactor at the combustion interface was 950 °C. The IAEA NGS3 standard methane sample ($\delta^{13}C_{VPDB} = -73.29\%$) was used as a standard sample. The isotopic composition was calculated using the formula:

$$\delta^{13}C = [(R_{s\text{amp.}}/R_{s\text{tand.}}) - 1]1000\%_{\text{oo}} \quad (1)$$

where $R_{s\text{amp.}}$ and $R_{s\text{tand.}}$ are the abundance ratios of $^{13}C/^{12}C$ isotopes in the analyzed sample and standard, respectively.

Procedure for Isotopic Measurements of Solid Samples

Samples weighing 0.1 mg were placed in tin capsules to determine the carbon isotopic composition and then analyzed using a Delta Plus isotope mass spectrometer connected to a Flash 1112 elemental analyzer via a ConFlo 3 interface unit (Thermo Scientific, Germany). Oxidation reactor temperature is 1020 °C, reagents: chromium oxide (+3), silver-plated cobalt oxides (+ 2/+ 3) granules. The temperature of the reduction reactor is 650 °C, reagents: copper. The correctness of measurements was checked according to the international oil standard NBS 22 ($\delta^{13}C_{VPDB} = -29.7\%$). The isotopic composition was calculated using the formula:

$$\delta^{13}C_{VPDB} = [(R_{s\text{amp.}}/R_{s\text{tand.}}) - 1]1000\%_{\text{oo}},$$

where $R_{s\text{amp.}}$ and $R_{s\text{tand.}}$ are the abundance ratios of $^{13}C/^{12}C$ isotopes in the analyzed sample and standard, respectively.

3 Results

Three series of experiments with 0.5, 1.0, and 1.5% wt. of $CaCO_3$ in volcanic ash were carried out. Table 1 shows the carbon dioxide isotopic results for calcium carbonate.

The isotopic composition of carbon was measured for 3 samples of CO_2 gas releasing. Table 2 indicates the $\delta^{13}C$ (CO_2), ‰ in $CaCO_3$ model mixture with ash with and without He gas, respectively.

4 Discussion

Earlier studies of the mineral composition of carbonaceous chondrites (Hartmann, 1972) showed the presence of a significant amount of isotope-heavy carbonates: from 0.1 to 1.1 wt %, $\delta^{13}C > +10$. Similar deposits of carbonates were found in ordinary chondrites (Monica et al., 1988; Voropaev et al., 2021). In this work, we were interested in determining the total carbon CO_2 isotopic composition. We have updated the standard method for amount of carbonates in carbonaceous chondrites estimation in Murchison meteorite (CM2): all carbonates were collected in the form of a precipitate and then decomposed at once at high temperature to carbon dioxide CO_2 and divalent metal oxides. We have created a laboratory setup for the method.

Table 1 Carbon isotopic composition of the initial $CaCO_3$ used in the model mixture $CaCO_3$ (pure) initial powder

$CaCO_3$ (pure)	Initial powder	Method ^a	
		With He gas	Without He gas ^b
$\delta^{13}C$ (CO_2), ‰	- 31.59	- 31.45	- 31.43

^a Decomposed according to the method mentioned above

^b Without helium: In the process of work according to the proposed method, the helium purge stage was omitted, the test tube with the model mixture was immediately sent to the water jet pump for dilution

Table 2 Isotopic composition of $CaCO_3$ carbon in a certain composition

0.5% wt.	Mix. 1	Mix. 2	Mix.3	Mix.4
$\delta^{13}C(CO_2)$, ‰	- 29.01	- 27.79	- 27.88	- 28.83
1.0% wt.	Mix.1	Mix.2 (without He)	Mix.3	Mix.4 (without He)
$\delta^{13}C(CO_2)$, ‰	- 30.91	- 30.56	- 30.46	- 30.61
1.5% wt.	Mix.1	Mix.2	Mix.3	Mix.4
$\delta^{13}C(CO_2)$, ‰	- 30.17	- 31.06	- 30.84	- 30.61

5 Conclusions

The carbon isotopic composition in meteorites was studied in several ways: direct ground sample decomposition before and after degassing at various temperatures with gas samples during meteorite degassing at various temperatures. The determination error (isotope composition of carbonates) is large enough in comparison with our method of acidic removal of carbonates from meteorite powders. The error of determination ($\delta^{13}\text{C}$) is almost absent here, which is why we can recommend this method for the study of samples of small quantities, such as a meteorite. Table 2 shows the results of our measurements: determination error for each sample is minimal.

At this stage, the Allende (CV3) and Murchison (CM2) carbonaceous chondrites have been studied. Murchison carbonates (CM2) isotopic composition turned out to be very

heavy— $\delta^{13}\text{C}(\text{CO}_2)$, ‰ = + 36.31. Allende carbonates (CV3) isotopic composition turned out to be much lighter— $\delta^{13}\text{C}(\text{CO}_2)$, ‰ = - 7.97.

Acknowledgements This work was supported by the grant Russian Science Foundation # 21-17-00120.

References

- Hartmann, W. K. (1972). Paleocratering of the moon: review of the post-Apollo data. *Astrophysics and Space Science*, 17, 48–64.
- Voropaev, S., Boettger, U., Pavlov, S., Hanke, F., Petukhov, D. (2021). Raman spectra of the Markovka chondrite (H4). *Journal of Raman spectroscopy*, 1–9.
- Monica, M., Grady, I. P., Wright, P. K., & Swart, C. T. (1988). Pillinger. *The Carbon and Oxygen Isotopic Composition of Meteoritic Carbonates Geochimica Et Cosmochimica Acta*, 52(12), 2855–2866.



Efficiency of Soil Geochemistry as a Powerful Tool in Targeting of Hidden Deposits During Mineral Exploration: A Case Study of the Sediment-Hosted Kibamba Copper-Cobalt Deposit of the Lufilian Arc, Democratic Republic of Congo

Katombe Kisumbule Paul, Mukendi Shambuyi Eddy,
and Anani Tebagwe Jean-Michel

Abstract

The Lufilian Arc of Neoproterozoic formed during the Pan-African orogeny in the Democratic Republic of Congo and to its south-east in the Republic of Zambia, and the Westward extension of similar rock sequences into southern Africa. Due to the global demand for metal ores such as copper, cobalt, nickel, lithium, etc. which continues to increase for the foreseeable future, the needs of new technology (e.g., batteries for electronic devices and electric vehicles, etc.) and the desire and efforts to improve living standards worldwide are some of the key drivers which dictate the aggressive ongoing exploration and mining activities in the Democratic Republic of Congo. The Lufilian Arc is a zone known to hosting world-class high-grade Cu-Co-U and Pb-Zn mineralization. The use of soil geochemistry as one of the targeting tools in mineral exploration, especially in the search of copper/cobalt shallow and blind sub-outcropping deposits, has proven to be very successful and efficient at early stage of exploration. The purpose of this study aims at reviewing and demonstrating the effectiveness of soil geochemical exploration technique in the discoveries of different Cu-Co deposits, like Kibamba Cu-Co deposit of the Congolese Copperbelt. It has been observed that shallow-seated orebodies express anomalies in soils through dispersion processes over time. Mapping of

chemical element signatures, identification of pathfinders, scavengers within *in-situ* soil covers, interpretation of regoliths (allochthonous vs. autochthonous), etc. in targeting of metal anomalies in soils and prioritization can help remarkably in revealing a presence of mineral bodies under cover. To reach our goals, a data summary of soil geochemistry at selected exploration areas within the Copperbelt where soil surveys were conducted at early phases of exploration, particularly at Kibamba area has been processed using MapInfo software combined to Discover for basic statistics and interpretation for a definition of orders of anomalism for priorities. Then, a follow-up by other exploration techniques such as geophysical surveys, structural and lithological mapping then drilling (reverse circulation and coring) to test and confirm anomalies have been complimentary for resources definition and estimates.

Keywords

Lufilian arc • Soil geochemistry • Targeting tool • Anomaly definition • Cu-Co deposits

K. K. Paul (✉) · A. T. Jean-Michel
Département de Géologie, Université de Lubumbashi,
B.P.1825, Lubumbashi, Democratic Republic of the Congo
e-mail: paul.katombe@gmail.com

K. K. Paul
Department of Geology, Kore Potash Ltd. (www.korepotash.com),
B.P.: 662, Pointe Noire, Democratic Republic of the Congo

M. S. Eddy · A. T. Jean-Michel
Exploration Geology Department, Samta Natural Resources
D.R. of Congo, Lubumbashi, Haut-Katanga,
Democratic Republic of the Congo

1 Introduction

The Lufilian Arc belongs to the system of orogenic belts extended across eastern Angola, the Katanga province in the south-east of the Democratic Republic of Congo and the north-western region of the Republic of Zambia (Hitzman et al., 2012) in Southern Africa. The Democratic Republic of Congo is known to be one of the destinations in Africa for base metals such as copper, cobalt, zinc, lead, uranium, just to name a few, which are hosted in the Neoproterozoic Katangan Belt also known as the Central African Copperbelt or the Lufilian Arc. Rocks in the Neoproterozoic Katanga Belt (D.R. of Congo) are classified into three groups of the

Katangan Supergroup, namely (from bottom to top): Roan Group, Nguba Group, and Kundelungu Group.

In comparison to the Nguba and Kundelungu Groups, the Roan Group has been deeply investigated for decades, explored, and detailed-studied in terms of lithostratigraphy, metallogeny, mineralogy, petrography, and more due to its economic facts by hosting world-class stratiform and stratabound mineral deposits whereas previously the Nguba and Kundelungu Groups were believed to be of less economic interests. However, some exploration works were conducted in places of Zn-Pb occurrences such as at Kipushi, Kengere, and for construction materials (limes and cements). But recently, exploration activities have been increasingly growing with the discovery of the giant world-class Kamoa, Kakula copper deposits, and the presence of some economic deposits like Dikulushi and Lufukwe hosted in the Nguba and Kundelungu Groups.

Soil geochemical exploration technique has been effectively applied in the search of copper and cobalt in numerous areas on the Congolese and Zambian sides of the Copperbelt with reference to copper deposits detected through soil anomalies. For instance, Lonshi, Frontier, Kibamba, Kamoa copper deposits and Sentinel deposit in the Northwestern province in Zambia.

The main aim of this paper is to demonstrate the efficiency of geochemical exploration technique conducted in Kibamba area (PR851, *as per the DRC Carte de la Retombe Miniere Cadastre Minier—2005*) as a showcase located in the Central Copperbelt (within the Lufilian Arc) in the D.R. of Congo with an emphasis on the use of soil sampling survey although complimented by the application of other exploration techniques.

2 Methodology

To achieve the purposes of the current work, a review of historical data coupled with real soil assay results from the field work undertaken under the banner of the Compagnie Minière de Sakania sarl was done.

Thereafter, a target generation and ranking of target priorities for a follow-up with reverse circulation drilling then coring were executed. Subsequently logging of rock chips, drill cores, and core assaying were done for drill section interpretation and resource estimates. Simultaneously, input from the author's proven experience in mineral exploration was considered after nearly two decades of work to date in sediment-hosted copper mineralization of the Central African Copperbelt in the Democratic Republic of Congo and Zambia including five consecutive dedicated years of work from 2003 to 2008 for Cu-Co exploration within the Kibamba area from Greenfield exploration to the discovery of copper-cobalt deposits at RSF and Subo sites.

Hitzman et al. (2012), Fleischer (1984), and Broughton and Rodgers (2010) argued that the use of soil surveys as an exploration tool in the search of copper and cobalt deposits has been a successful prospection technique in the discovery of low- to high-grade deposits in the Central African Copperbelt and elsewhere in some regions of the world. From desk review, soil sampling procedure in the Kibamba area was established through a grid design. At a regional first phase of reconnaissance soil survey, 7000 samples spaced at 100 m intervals on an 800 m spaced east–west and north–south oriented lines were planned to cover and screen the entire prospect area. Then followed by a later detailed and localized soil sampling on 400 × 100 m and after 200 × 100 m grids spacing on the second and third phases. Sampling lines were planned perpendicularly to the strike of the mineralization host rock units with at least two traverse lines and two to three soil samples being collected over the anticipated potential Cu-Co target. In D.R. of Congo, most of the stratiform and stratabound economic Cu and/or Cu-Co ore deposits contained in the Central African Copperbelt extend along strike than they do on width. Soil sampling convention was conducted in an old-school 'square grid' and/or 'rectangular grid' method as opposed to a new-school 'off-set grid' which is believed to increase the sample search space and reduce the level of uncertainty.

Equipment during the soil survey included a list of the following, but not limited to, a geological map, a topographic map, a basic map of the sampling plan in the area, handheld GPS, magnetic compasses, a laptop to load and download GPS coordinates, sampling ticket books, sampling sheets, picks, shovels, sieves (180 µm size), plastic zip lock bags, permanent markers, pens and pencils, camping gears, and appropriate well-equipped all-terrain vehicles.

During sampling, small pits were dug into the top of the B horizon between 25 and 30 cm below ground surface or shallower in rocky areas away from organic rich, dark-colored horizon. Once the sample was collected, the exact depth was recorded on the sampling sheet. Soil sampling was compliant with standards operating procedures already put in place. Samples collected from the field went through a preparation process to ensure they comply with laboratory specifications and requirements.

Soil samples collected were initially submitted for copper and cobalt analyses only using the C/AAS analytical method (two acid digestion-high temperature perchloric acid oxidative attacks with a hydrochloric acid final leach) for first pass analysis at the accredited Genalysis Laboratory Services Pty Ltd in Perth Western Australia.

Thereafter, a follow-up soil sample analysis of all significant copper as well as cobalt anomaly results were re-assayed by using the AX/AAS analytical method (Four acid digestion- Multi-acid attack including hydrofluoric, nitric, perchloric, and hydrochloric acids in Teflon beakers).

Suitable for dissolving silica-based samples requiring low levels of detection. These digest approach total dissolution for most minerals and are recommended for high precision ore-body evaluation.

QAQC samples consisted of blanks, field duplicates, and certified reference materials and were systematically inserted into a batch of samples sequence prior to dispatch to the laboratory for analyses.

For the sake of ranking priorities for follow-up, it was necessary to define different 'orders' of anomalism (1st order, 2nd order, and 3rd order). And so, anomaly threshold definition was based on different principles such as literature comparison, statistical methods, spatial analysis, and domainning.

All soil samples data with corresponding laboratory assay results attached next to their relevant soil sample ID's before being loaded and stored onto a database.

3 Soil Samples Data Processing

3.1 Anomaly Threshold and Interpretation

Soil sampling data were processed using MapInfo combined to Discover and ioGAS softwares for statistical applications, map geo-referencing, data plotting, data interpolation (gridding and contouring), point classification for target generation, prioritization, and interpretation.

Basic statistics for copper and cobalt were concerned initially with measures of central tendency (mean, median, and mode) and dispersions (range, variance, standard deviation, percentiles, and coefficient of variation) of unbiased samples, as parameters that were useful and important in describing attributes of the probability density function of soil sampling data set from PR851 prospect area. Two data sets were taken into consideration. At first, a data set of 3536 soil samples from 800×100 m to 200×100 m grids implemented over localized fragments of Roan Group lithology sequence. And secondly, a data population of the first 3536 samples combined with an addition of 1493 soil samples collected from 400×400 m grid conducted to cover the rest of PR851 concession area.

Statistical analysis helped to understand and visualize the nature of data distribution from diagrams and also to determine the anomaly thresholds. A measure of similarity between paired Cu-Co assays data have been estimated by mean of a correlation. So the *R*-mode statistical treatment dealing with correlation between pairs of variables (Cu and Co in our case), has been used. Therefore, with considerations to soil samples with Cu and Co lab results only, the correlation coefficient (*R*) has been calculated to 0.6549. This shows that the two paired Cu-Co data are increasing sympathetically illustrating a strong positive correlation and

can be interpreted that both copper and cobalt are originally from the same mineral source and probably from the same mineral assemblage or paragenesis.

Rumsey, 2011 demonstrated that in statistics, the correlation coefficient (*R*) is always between + 1 and - 1 and a value closest to + 0.70 illustrates a strong positive linear relationship. The simple Cu-Co linear correlation in the Kibamba area remains consistent with numerous cupro-cobaltiferous deposits examined in the surrounding areas within the Lufilian Arc such as Menda, Kambove, Kamoya, and Tenke Fungurume deposits. In these different Cu-Co deposits, sulfide and oxide ores are characterized by chalcopyrite, bornite, heterogenite, malachite, carrollite, chrysocolla, vaesite, nickeliferous pyrite, and siegenite, which are in form of disseminations, vug fillings, veins, bedding controlled, massive, and blebby which some of them were found and intersected in places of old artisanal diggings and drill holes in Kibamba area.

However, when defining anomaly threshold by literature comparison for the Kibamba area, we took into account our geological knowledge of the area as well as our personal experience as exploration geologist. Considering that the regional background value of Cu in the Copperbelt is relatively very high, we used a cutoff of 100 ppm as a subjective threshold to implement initial test drilling although it remains uncertain and not precise to set up in mind the definition of anomalies based on literature comparison only.

Calculated standard deviations for Cu was 162.62 and 9.69 for Co. From the recorded laboratory analytical results, standard deviations showed large values which were not necessarily a bad thing and have just reflected a large amount of variation in the data set which has been studied. Second- and third-order standard deviations were calculated to estimate the 1st and 2nd anomaly thresholds.

And so, any values above 325.24 and 19.38 for Cu then Co respectively are interpreted to be the 2nd anomaly threshold and values above 487.86 for Cu and 29.07 for Co will then be 1st anomaly threshold.

Anomaly thresholds defined by literature comparison and standard deviation were supported by points classification; graduated symbols and colors, spatial analysis, gridding and contouring maps (Fig. 1).

3.2 Targeting Criteria and Results of Reconnaissance Drilling of Targets

Soil geochemistry data set was considered to be the first criteria for target generation. However, it has been complemented by real and factual data sets from other exploration methods deployed in the area for targeting and prioritization. Drilling for reconnaissance targeted high-grade copper and cobalt anomalies in soils.

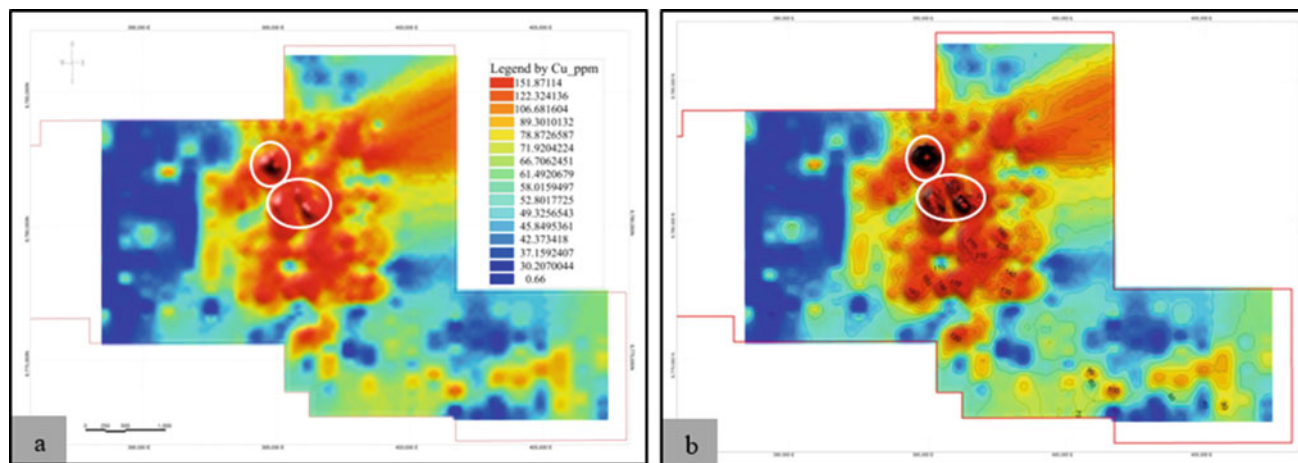


Fig. 1 a and b Illustrations of a gridded map a and a contours map b of Cu_ppm assays from central part of PR851 area showing zones of high anomalies. Peaks in Cu_ppm anomalies circled in white

Taylor et al. (2010) stated that the formation of Cu-Co and stratabound types of deposits stands on a number of conditions like: the metal source rocks, the brines, the fluid flow and pathways, the organic matters, and the confining beds and containment structures. Syn-sedimentary and post-depositional complex fault structures in the area of interest could have been probably critical in providing focused fluid flow or served as fluid pathways. Carbonaceous shale of the Mwashya Subgroup at PR851 prospect area was considered to have acted as a possible reductant rock unit in place of organic matters needed as a reductant agent at the site of any copper mineral deposition in the stratiform-stratabound copper type of the Central African Copperbelt. The Kibamba anticline with confining beds in PR851 area, like one of the containment structures among others like stratigraphic pinch outs, is indicated to focus fluid flow of the copper-bearing brines to rock units containing organic material that could have caused sulfide precipitation. Therefore, after understanding copper/cobalt deposition environment in the Katangan basin and the targeting criteria, numerous targets were selected in the prospect area and few of them have been following up with drilling (reverse circulation and diamond drilling). Likely one of those targets revealed an economic Cu-Co deposit which was investigated and studied up to the reserve estimation.

4 Discussions

The Central African Copperbelt in the Democratic Republic of Congo is known to host about 60% of global cobalt reserves and accounted for 7.2% of the estimated global mine production of stratiform-stratabound copper in 2011 Taylor et al. (2010) after copper derived from porphyries.

In terms of tectonics vs. Cu-Co mineralization, it has been understood that deformation events that occurred in the Katangan basin in general resulted in a complex structural architecture of the region (folding, faulting, and brecciation). At PR851 prospect area, the Kibamba anticline as a structural trap and the transfer fault toward the north of the prospect resulting from tectonics that could have enabled fluid flow and accumulation of hydrocarbons in the basin might have localized copper as well as cobalt mineralization.

In terms of Cu-Co anomalies in soils vs. landform, precautions were taken when interpreting Cu/Co anomalies in soils with regard to the landform. Integration of different geological data sets of the Kibamba area was compulsory in the interpretation of transported versus *in-situ* anomalies.

Weathering process at Kibamba prospect area has been of very significant importance. The high grades are results of supergene enrichment in a very deep weathering profile. Primary copper sulfide minerals are changed to sulfates, oxides, carbonates, and/or silicates during weathering process. At Kibamba area, copper released by weathering reactions precipitated as sulfide minerals in the form of chalcopyrite and chalcocite, then oxidized copper and iron minerals include but not limited to malachite, chrysocolla, azurite and hematite.

5 Conclusions

For many years, exploration for base metals has been increasingly conducted in the Lufilian Arc due to the global demand and everlasting needs of the growing population for living standards, electrical construction demands for modern cities around the world and specially copper as well as cobalt for electrical vehicles and batteries in support of clean

energy initiatives. Both Cu/Co high tonnage low grade and/or low tonnage high grade deposits can be found in the Central African Copperbelt which remains a great opportunity up until now.

Soil geochemistry as an exploration tool has proven to be very effective in detecting shallow Cu/Co anomalies in sediments of the Lufilian Arc and particularly in Kibamba area covered by PR851. Nevertheless, a combination of soil geochemical survey with other exploration techniques like stream sediment survey, water sampling, remote sensing, geophysics methods (induced polarization, electromagnetics), outcrops, and regolith mapping and targeting has always been beneficial in targets definition for a follow-up with drilling and later resource estimate.

At Kibamba area, environmental, social, and community concerns were at the center of exploration activities. Prior to exercising the right to Cu/Co exploration in the area, commitments to complying with environmental, social, and community obligations as stated in the country mining code and regulations and besides requirements of international financial institutions that subscribe to the Equator Principles were carefully honored. As an example, environmental and social studies were conducted, management plans written to guide in the assessment, preventing and mitigating of impacts. Soil sampling at PR851 area was environmental friendly as no big trees were cut off; deforestation was

avoided to the possible maximum and during the survey, all sampling pits dug were filled out, packed down, and rehabilitated as close to its original condition as possible.

References

- Broughton, D., Rogers, T. (2010). Discovery of the Kamoia copper deposit, Central Africa Copperbelt, D.R. of Congo. *Society of Economic Geologists, Special Publication*, 15(1), 287–298.
- Fleischer, V. (1984). Discovery, geology and genesis of copper-cobalt mineralization at Chambishi South-East prospect. *Zambia. Precambrian Research*, 25(1), 119–133.
- Hitzman, M. W., Broughton, D., Selley, D., Woodhead, J., Wood, D., & Bull, S. (2012b). The Central African Copperbelt: Diverse stratigraphic, structural, and temporal settings in the world's largest sedimentary Copper District. Society of economic geologists, Inc. *Special Publication*, 16, 487–514.
- Rumsey, D. J. (2011). *Statistics for Dummies*, 2nd Edn., p 384. ISBN: 978-0-470-91108-2.
- Taylor, C. D., Douglas Causey, F. D., Denning, P., Hammarstrom, J. M., Hayes, T. S., Horton, J. D., Kirschbaum, M. J., Parks, H. L., Wilson, A. B., Wintzer, N. E., Zientek, M. L. (2010). Descriptive models, grade-tonnage relations, and databases for the assessment of sediment-hosted copper deposits-with emphasis on deposits in the central African Copperbelt, Democratic Republic of the Congo and Zambia. *Scientific Investigations Report 2010–5090-J*. U.S. Department of the Interior, U.S. Geological Survey.



Salts in SPA Therapies—Characterization and Risk Assessment

Carla Candeias and Fernando Rocha

Abstract

Salt water and dissolved salts themselves have been used in dermal therapies since ancient times. Dead Sea salts are the most known ones used for dermal curative and cosmetic purposes. Studies recognized their dermal application benefits in conditions such as psoriasis and eczemas. Elements (e.g., Na, Mg, K, Ca) present in salts can be absorbed by the skin, and aid in processes such as cellular respiration, or act as anti-inflammatory agents, among others. Therapeutical results could be enhanced with the presence of certain minerals. The present study aims to characterize the mineralogical and chemical composition of salts produced in Portugal salt pans of two different areas, Ria de Aveiro and Ria Formosa and a commercial coarse salt subjected to purification. Potential positive and negative outcomes by dermal applications are assessed in this study. Samples show chemical and mineralogical composition variation. Further laboratorial analysis and results interpretation are being conducted.

Keywords

Salt • SPA therapies • Geochemistry • Mineralogy

1 Introduction

Salted water and the dissolved salts have been used since ancient times by different civilizations, e.g., Greeks, Romans, for therapeutical applications. Previous studies demonstrated the scientific validity of these practices. Dead Sea salts studies, confirmed beneficial effects when used for dermatological and rheumatological diseases, such as an

effective treatment in osteoarthritis, anti-aging, and psoriasis cases, this last one with the contribution of Mg content in salts (Katz et al., 2012; Sornnen & Nicrotha, 2021). In these types of diseases, Mg and S content play an important role when applied on the skin. Mg-rich salt solutions improve the skin barrier functions, enhancing skin hydration, and reducing inflammation in atopic dry skin (Harari, 2012). The Na, Cl, and K present in salts, help to maintain the adequate equilibrium of intra-cellular and extra-cellular electrolytes in the human body (Almeida et al., 2022; Bergamaschi et al., 2020; Crisan-Dabija et al., 2021). Studies in patients treated with Dead Sea salts and artificial UVB (ultraviolet B) showed a reduction in the number of Langerhans' cells in the epidermis (Gruner et al., 1990). Nevertheless, the human stratum corneum (HSC) is a barrier against most substances, especially solutes such as water and salts, which can be reduced with temperature and hydrostatic pressure in therapeutical applications (Carbajo & Maraver, 2018). Additionally, the study of salts used in respiratory diseases (halotherapy) showed their usefulness in treating patients with chronic obstructive pulmonary disease (COPD) within a chamber that mimics a salt cave environment (Crisan-Dabija et al., 2021). There are few studies on salts used directly in the skin or applied in cosmetics preparations, but there is evidence that encourages research and development of products using these materials. This study aims the characterization of salts from two different regions in Portugal as a starting point for further investigation on their use for medical purposes.

2 Materials and Methods

2.1 Salt Samples

Two representative salt samples were collected directly in artificial salt pans, one in Ria de Aveiro (#1) and one in Ria Formosa (#2) regions (Portugal), without any purification

C. Candeias (✉) · F. Rocha
GeoBioTec Research Center, Department of Geosciences,
University of Aveiro, Campus de Santiago,
3810-193 Aveiro, Portugal
e-mail: candeias@ua.pt

treatment, and accessible to be used by users. A third sample was considered, for comparison, a commercial coarse sea salt (#3) subjected to purification before being available for consumers.

Ria de Aveiro (NW Portugal; 40° 38' N, 8° 45' W) is a shallow 45 × 10 km coastal lagoon, that receives Atlantic Ocean, and Vouga and Antuã rivers waters. The lagoon is separated from the Ocean by a sand bar, except on an artificial channel (Mil-Homens et al., 2014). Is characterized by narrow channels and large areas of mud flats, with a large area occupied by artificial saltpans (> 270), mostly currently abandoned (Teixeira & Zbyszewski, 1976). Ria Formosa is a barrier lagoon, with 55 × 6 km, on the Algarve coast (S Portugal; 36° 59' N, 7° 55' W), receiving Atlantic Ocean and Gilão river waters. This area includes ~ 4000 ha of salt extraction ponds (Bebianno, 1995). Both mesotidal lagoons experienced water quality degradation over the years, reflecting the economic development by anthropogenic activities, including chemical, fishing, and mariculture industries, with tidal transport of potentially toxic elements (PTEs) (Gadelha et al., 2019). The lack of control over human activities can be reflected in the lagoons' salted waters quality, being enriched in PTEs, e.g., Cr, Cu, Pb, that can be found also in distant areas from the source, being saltpans and resulting salts affected by these waters quality.

2.2 Samples Analysis

Quantitative chemical analysis of major elements and potentially toxic elements (PTEs) was conducted by XRF (Panalytical Axios spectrometer PW4400/40 X-ray) operating on a Rh tube under argon/methane. Mineral phases were determined on samples, after being for 24 h on an exicator at 30 °C (oven), using a Phillips/Panalytical power diffractometer, model X'Pert-Pro MPD, carrying an automatic slit, with Cu-X-ray tube operated at 50 kV and 30 mA, which allowed data to be collected from 2 to 70° 2θ with a step size of 1° and a counting interval of 0.02 s. Individual particles' morphology and size determination were performed with a Tescan scanning electron microscope (SEM), model VEGA LMU, operating in a high and low vacuum and capable of image acquisition through secondary and back-diffused electron detectors. Particles' semi-quantitative chemical characterization was determined by elemental chemical analysis using an Energy Dispersive Spectrometer (EDS). The pH was measured using a calibrated Hanna HI98494 model, with a 1:5 ratio of sample: and deionized water (ISO 10390:1994). Internal standards, certified reference material, and quality control blanks were used for monitoring the precision and accuracy of the analyses. Results were within the 95% confidence limits.

3 Results and Discussion

Samples pH was, #1 7.51, #2 7.03, and #3 7.83, that are typical values for salted materials. These salts were produced in alkaline conditions, as seawater pH was ~ 8.3, slightly varying with composition (Bebianno, 1995). During salt production, pH decreases mainly due to CaCO₃ precipitation and organic matter decomposition. Summer temperatures (in July up to 40 °C in locations of samples #1 and #2) and seawater pH lead to NaCl crystallization.

Identified mineral phase in all samples was halite [NaCl], with trace amounts of gypsum [CaSO₄·2H₂O] in sample #2 (Fig. 1). These results were expected taking into consideration the chemical concentration and origin of the analyzed salt samples (Fig. 2), with Cl⁻ and Na₂O being the main constituents in all samples, ranging 48.877–52.437%, and 39.748–46.578%, respectively in samples #1 and #2. Sample #2 MgO content, represented 5.547%, and SO₃ 4.040%, possible related to the presence of epsomite [MgSO₄·7H₂O], kieserite [MgSO₄·H₂O], or its efflorescence sanderite [MgSO₄·2H₂O], not identified by XRD. The higher content of MgO and SO₃ in sample #2, was confirmed by SEM–EDS analysis (Fig. 3b), i.e., with 13.1% MgO, and 6.4% SO₃. Additionally, sample #2 salt particles, when compared, presented more distinctive cubic shapes, with the purification that sample #3 was subjected being quite noticeable, with rounded edges and smaller particles (Fig. 3c, d). This sample presented slightly higher Pb, and Mn content, possibly due to the purification technique (equipment?). The comparison of Cr and Pb content with other studies (Gad et al., 2020; Mostafaii et al., 2020), revealed higher values, nevertheless, despite these PTEs are classified as carcinogenic, risk of these samples was considered acceptable.

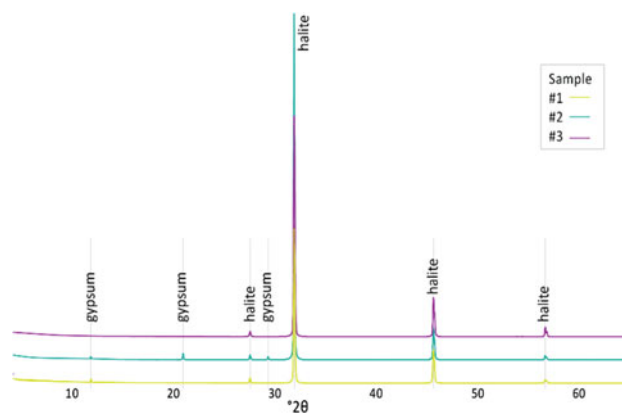


Fig. 1 XRD patterns of the collected samples #1, #2, and #3

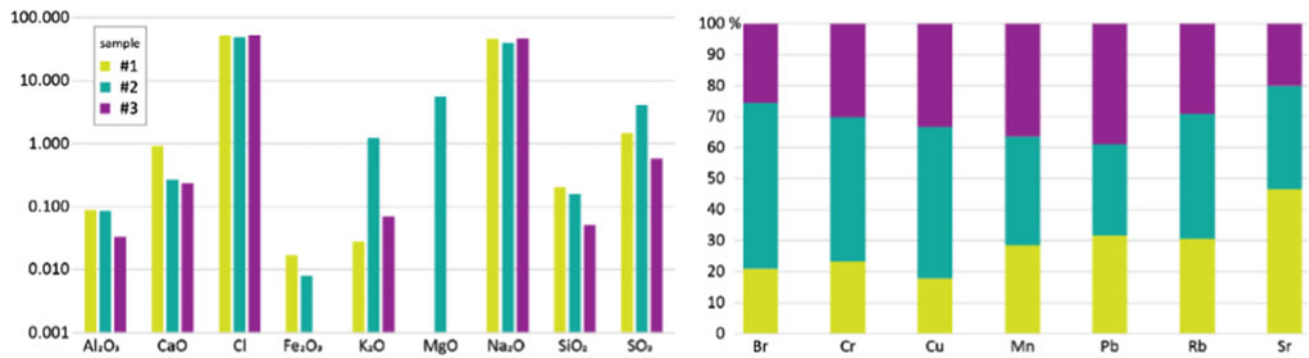
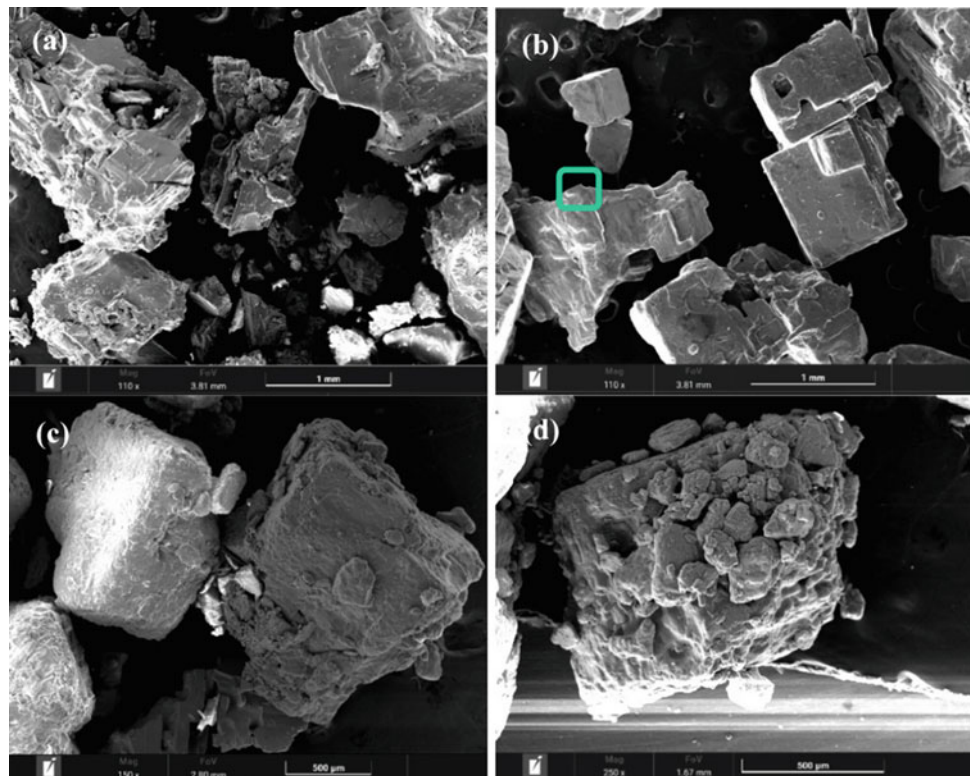


Fig. 2 Major (left; logarithmic scale based on elemental %) and minor (right; samples relative %) elements chemical concentration

Fig. 3 SEM images of samples #1 (a); #2 (b); and #3 (c and d)



4 Conclusions

Salt samples #1 and #2 revealed a potential to be applied in skin and respiratory treatments, especially sample #2, due to the MgO content. Nevertheless, this sample Br content, if ingested/inhaled, can lead to adverse health outcomes, such as mental impairment. Further tests, including in vitro bioaccessibility, are needed for further interpretation.

Acknowledgements This work was supported by GeoBioTec Research Centre (UIDB/04035/2020). The authors are thankful to Dr. Luis Rodrigues for the Ria Formosa sample.

References

- Almeida, L., Rocha, F., & Candeias, C. (2022). Geochemical and mineralogical characterization of Ria de Aveiro (Portugal) saltpan sediments for pelotherapy application. *Environmental Geochemistry and Health*.
- Bebianno, M. J. (1995). Effects of pollutants in the Ria Formosa Lagoon, Portugal. *Science of the Total Environment*, 171, 107–115.
- Bergamaschi, B., Marzola, L., Radice, M., Manfredini, S., Baldini, E., Vicentini, C. B., Marrocchino, E., Molesini, S., Ziosi, P., Vaccaro, C., & Vertuani, S. (2020). Comparative study of SPA Mud from “Bacino Idrominerario Omogeneo dei Colli Euganei (B.I.O.C.E.)—Italy” and industrially optimized Mud for skin applications. *Life*, 10, 78.

- Carbajo, J., & Maraver, M. (2018). Salt water and skin interactions: New lines of evidence. *International Journal of Biometeorology*, 62, 1345–1360.
- Crisan-Dabija, R., Sandu, I., Popa, I., Scripcariu, D., Covic, A., & Burlacu, A. (2021). Halotherapy—An ancient natural ally in the management of Asthma: A comprehensive review. *Healthcare*, 9, 1604.
- Gad, A., Bakey, S., & Sakr, S. (2020). Concentrations of heavy metals and associated human health risk in unrefined salts of inland hypersaline lakes, Egypt. *International Journal of Environmental Analytical Chemistry*, 102(6), 1278–1291.
- Gadelha, J. R., Rocha, C., Camacho, C., Eljarrat, E., Peris, A., Aminot, Y., Readman, J., Boti, V., Nannou, C., Kapsi, M., Albanis, T., Rocha, F., Machado, A., Bordalo, A., Valente, L., Nunes, M., Marques, A., & Almeida, C. (2019). Persistent and emerging pollutants assessment on aquaculture oysters (*Crassostrea gigas*) from NW Portuguese coast (Ria de Aveiro). *Science of the Total Environment*, 666, 731–742.
- Gruner, S., Zwirner, A., Boonen, H., & Sönnichsen, N. (1990). Effect of treatment with salt from the Dead Sea (*Tomesa therapy*) on epidermal Langerhans cells—a clinical study. *Zeitschrift für Hautkrankheiten*, 65(12), 1146–1151.
- Harari, M. (2012). Beauty is not only Skin Deep: The Dead Sea features and Cosmetics. *Anales Hidrología Médica*, 5(1), 75–88.
- Katz, U., Shoenfeld, Y., Zakin, V., Sherer, Y., & Sukenik, S. (2012). Scientific evidence of the therapeutic effects of dead sea treatments: A systematic review. *Seminars in Arthritis and Rheumatism*, 42(2), 186–200.
- Mil-Homens, M., Vale, C., Raimundo, J., Pereira, P., Brito, P., & Caetano, M. (2014). Major factors influencing the elemental composition of surface estuarine sediments: The case of 15 estuaries in Portugal. *Marine Pollution B*, 84(1–2), 135–146.
- Mostafaii, G., Moravveji, A., Hajirostamloo, B., Arani, M., Dehghani, M., Heidarnejad, Z., Fakhri, Y., & Khaneghah, A. (2020). The concentration and risk assessment of potentially toxic elements (PTEs) in unrefined salt: A case study of Aran and Bidgol Lake, Iran. *International Journal of Environmental Analytical Chemistry*, 102(5), 1192–1204.
- Sornnen, T., & Nicrotha, S. (2021). Salt mist generation control unit (SMGCU) for SPA business. *International Journal of Research Publications*, 86(1), 99–109.
- Teixeira, C., & Zbyszewski, G. (1976). *Geological map of Portugal at scale 1:50000. Sheet 18–C—Aveiro*. Portugal Geological Survey, Lisbon.



Petrography and Mineral Chemistry of the Granitoids in the Eastern Part of Central India, Central Indian Tectonic Zone (CITZ)

Indrajeet Saket, Meraj Alam, Md. Atif Raza, and Mohammad Sadiq

Abstract

The NE-SW trending Central Indian Tectonic Zone (CITZ) is a prominent suture zone that was brought out by the amalgamation of the Northern Indian Block (NIB), constituted by the Aravalli-Bundelkhand craton in the north and Southern Indian Block (SIB), constituted by the Bastar-Singhbhum and Dharwar cratons to the south. The CITZ is traversed by major tectonic lineaments parallel to its length: the Son-Narmada North Fault (SNNF), the Son-Narmada South Fault (SNSF), the Gavilgarh-Tan Shear Zone (GTSZ), and the Central Indian Suture/Shear (CIS) from north to south. The study area located in the eastern part of Central India, near the GTSZ records different phases of granite intrusions. They are comprised mainly of two types of granite facies: coarse to medium-grained pink granite and medium to fine-grained gray granite. Pink granite are composed by K-feldspar, plagioclase, biotite with accessory hornblende, apatite, zircon, titanium-magnetite and garnet with rare muscovite, chlorite; whereas the gray granite is more enriched in ferromagnesian phases. Mineral chemistry data sets are used to constrain the physicochemical, pressure-temperature condition of magmatic origin and depth of emplacement of studied granite. Previous results from the study area were not subjected to the genesis and tectonic setting of these granites. Biotite composition with low MgO content (5.05–5.59) and high FeO (23.66–24.60) suggests iron enrichment, and the narrow range of the $\text{Fe}^{2+}/\text{Fe}^{2+} + \text{Mg}$ suggests their magmatic nature. The $10^* \text{TiO}_2 - (\text{FeO}^f + \text{MgO}) - \text{MgO}$ ternary diagram is used to determine the nature of biotite, where primary biotite is most likely affected by post-magmatic fluids. In the

ternary diagram of $\text{FeO}^f - \text{MgO} - \text{Al}_2\text{O}_3$, biotite compositions suggested that these granitic rocks are S-type with peraluminous characteristics and originated by syn-collisional tectonic setting. The ferromagnesian minerals of biotites composition fall in the Fe-rich siderophyllite field in the ternary plot $(\text{Al}^{\text{VI}} + \text{Fe}^{3+} + \text{Ti}) - \text{Mg} - (\text{Fe}^{2+} + \text{Mn})$ and the $\text{FeO}^f/(\text{FeO}^f + \text{MgO})$ versus MgO (wt.%) correlation plot indicates a crustal source. The Ti content in biotite thermometry suggests crystallization at 716–730 °C at 4.24 to 5.57 kbar pressure. The biotites characteristics suggest the magma that initially derived from metasomatized crust through melting in plate interiors.

Keywords

Granitoids • Petrogenesis • Biotite chemistry • S-type granite • CITZ

1 Introduction

The continental crust preserved old and significant rock records and that evolved in space and geologic time through magmatic emplacement under different tectonic settings. The continental crustal growth is believed to occur mainly by subduction-related magmatism, at the convergent plate margins, and by within-plate magmatism initiated by rising mantle plumes (Rudnick & Fountain, 1995). The granitic rocks are an important component to understand the crustal evolution in a geologic province; during the evolution of the continental crust, partial melting in the lower to middle crust and transfer of melt to the upper crust is believed to have caused the chemical differentiation of the continental crust. The Precambrian Indian shield presents a diverse rock assemblage from early Archaean to late Proterozoic age exposed in different tectonic settings. The eastern part of Central India has less information on petrogenetic and

I. Saket · M. Alam (✉)

Department of Geology, Indira Gandhi National Tribal University,
Amarkantak, 484887, India
e-mail: merajdu@gmail.com

Md.A. Raza · M. Sadiq

Geological Survey of India, Faridabad, 212001, India

© The Author(s), under exclusive license to Springer Nature Switzerland AG 2024

A. Çiner et al. (eds.), *Recent Research on Sedimentology, Stratigraphy, Paleontology, Geochemistry, Volcanology, Tectonics, and Petroleum Geology*, Advances in Science, Technology & Innovation, https://doi.org/10.1007/978-3-031-48758-3_28

tectonic relationships hitherto. The present study aims to establish a petrogenetic and tectonic relationship of studied granitoids, and discuss their crystallization history.

2 Geological Setting

The NE-SW trending Central Indian Tectonic Zone (CITZ) has been brought out by the collision of two cratonic blocks, namely Northern Indian Block (comprising Aravalli and Bundelkhand cratons) and Southern Indian Block (comprising Bastar, Singhbhum and Dharwar Cratons) (Fig. 1a). The Precambrian Indian shield has experienced multiple events of crustal collision and accretion (Chattopadhyay et al., 2017; Radhakrishna & Naqvi, 1986; Roy & Prasad, 2003). The CITZ is traversed by major tectonic lineaments parallel to its length, i.e., Son-Narmada North Fault (SNNF), Son-Narmada South Fault (SNSF), Gavilgarh-Tan Shear Zone (GTSZ), and Central Indian Suture/Shear (CIS) from north to south (Fig. 1b). The CITZ comprises three major supracrustal belts, including the Mahakoshal, Betul, and Sausar belts from north to south that are made of different lithological units of mafic to acidic compositions. Three granulite belts, namely Makrohar granulite (MKG), Ramakona-Katangi granulite (RKG), and Bhandara-Balaghat granulite (BBG) belts exposed along the Central

Indian Shear (Fig. 1b) also demarcate the CITZ. The study area is located in the eastern part of Central India near the GTSZ and is characterized by different phases of granites (Fig. 1c).

3 Texture and Petrography

The study area is located in the Anuppur district, Madhya Pradesh in the eastern part of Central India between the latitude $22^{\circ} 54' 01''$ N– $23^{\circ} 05' 22''$ N and longitude $81^{\circ} 36' 24''$ E– $81^{\circ} 55' 56''$ E. The studied rocks comprise mainly two types of granite facies; coarse- to medium-grained pink granite and a medium to fine-grained grey granite. Pink granite is coarse to medium-grained with large megacrysts of K-feldspar and shows porphyritic texture (Fig. 2a). Gray granite is medium to fine-grained and shows equigranular texture (Fig. 2b). Pink granites comprise quartz, K-feldspar, plagioclase, biotite, and hornblende with accessory phases of apatite, chlorite, muscovite, titanium-magnetite, zircon, and garnet. Gray granite shows a hypidiomorphic texture, essentially composed of quartz, plagioclase, K-feldspar, and biotite with the accessory phases of apatite, titanium-magnetite, epidote, chlorite, muscovite, hornblende, and zircon. Anhedral to subhedral quartz, sericitization of plagioclase feldspar with albite twinning, and

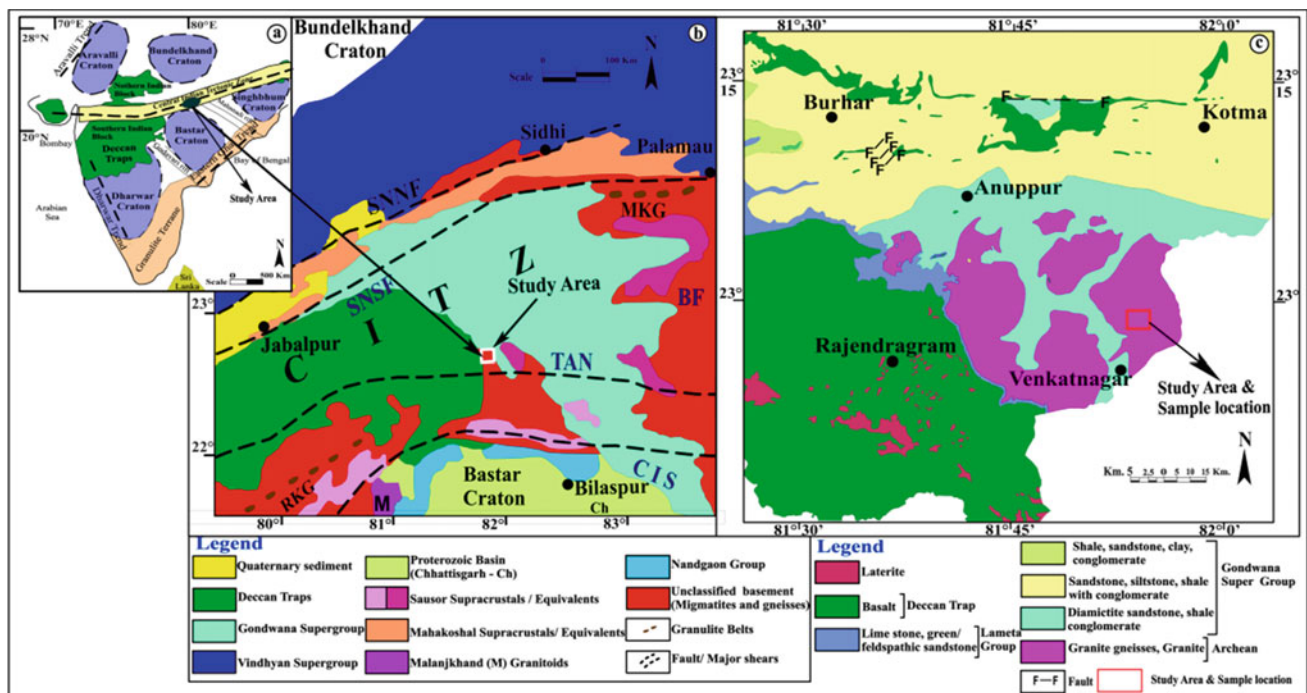


Fig. 1 a Major tectonic divisions of the Indian sub-continent. b Geological map of the Central Indian Tectonic Zone (CITZ) and different geological units with respect to the study area (Ramachandra & Roy, 2001; Roy et al., 2002). Abbreviations: BF–Balram Fault, Ch–

Chhattisgarh Basin, M–Malanjhand Granitoids. c Shahdol DRM modified map showing the study area (Geological District Resource Map of Shahdol, 2002)

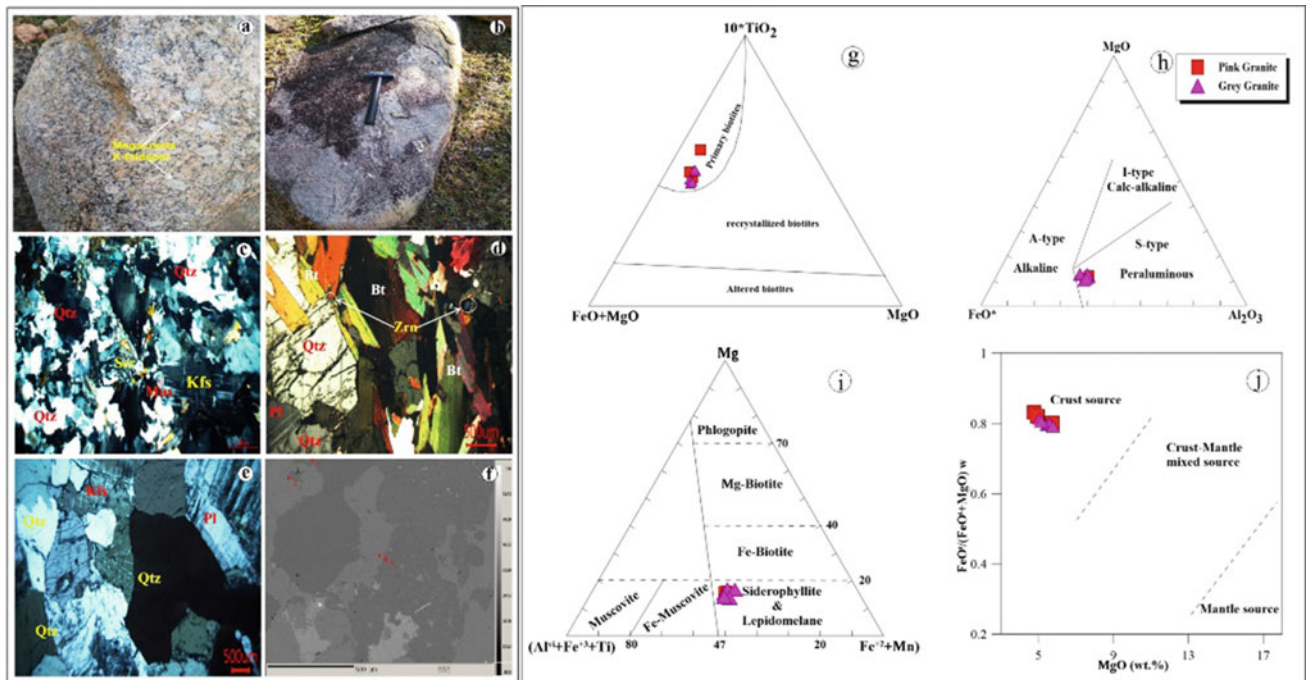


Fig. 2 a Porphyritic pink granite with tabular to rounded megacrysts of K-feldspar from the location of Jaithari. b Medium to fine-grained gray granite from Venkatnagar area. c Grain to grain relationship showing Qtz and K-feldspar with interlocking texture, plagioclase occurs as anhedral to subhedral and shows sericitization due to the presence of hydrothermal alteration. d Biotite showing flaky laths with pleochoric haloes, zircon also occurs as inclusions within biotite. e Coarse-grained quartz with myrmekitic texture. f EPMA (BSE) image

points-1, 4: Plagioclase rim, 2, 3: Alkali-feldspar rim. g 10^*TiO_2 - FeO - MgO ternary diagram type and source of biotite plots using EPMA data (Foster, 1960; Nachit et al., 2005). h FeO - MgO - Al_2O_3 biotite discriminate ternary diagram (Abdel-Rahman, 1994). i Chemical composition of biotites on the $(Al^{VI} + Fe^{3+} + Ti)$ - Mg - $(Fe^{2+} + Mn)$ ternary diagram of Foster (1960). j $(\Sigma FeO)/(\Sigma FeO + MgO)$ w ratio versus MgO (wt.%) using biotite compositions for the studied granitoids (Zhou, 1986)

Table 1 Ti in Biotite Thermobarometry

Sample	Minerals (temperature)	Minerals (pressure)	T (°C)	P (kbar)	Reference for PT
VPGG49	Bt	Hbl (BtPlQtz)	730.212	5.571	Wu and Chen, 2015; Schmidt, 1992
VPGG49	Bt	Hbl (BtPlQtz)	722.806	4.891	Wu and Chen, 2015; Anderson and Smith, 1995
VPGG49	Bt	Hbl (BtPlQtz)	715.756	4.238	Wu and Chen, 2015; Mutch et al., 2016

microcline are also observed (Fig. 2c). Biotite grains occur as subhedral to euhedral shape and zircons, present as inclusions in the biotite, shows pleochoric haloes (Fig. 2d). Intergrowth textures of myrmekite due to late magmatic or post-consolidation reaction indicate that these granites were affected by low temperature alteration (Fig. 2e). The relationships of plagioclase and alkali-feldspar are observed in Back Scattered Electron (BSE) image (Fig. 2f).

4 Methodology

Representative polished and carbon-coated thin sections were chosen for Electron Probe Micro Analyzer (EPMA) study of silicate mineral chemistry aimed to geothermobarometric

determination. These thin sections were analyzed by CAMECA SX-100 electron microprobe installed at EPMA Laboratory, Geological Survey of India, Faridabad with the method of Sadiq et al., (2017), and the data is illustrated in Table 1.

5 Results and Discussion

The EPMA data were evaluated using an Excel Spreadsheet version from a biotite-calculated structural formula based on 11 oxygen. The biotites in granitoid show variation in SiO_2 content from 34.76 to 36.48 wt.%, have high Al_2O_3 (15.45–15.92 wt.%) and low TiO_2 (2.52–3 wt.%) contents reflecting the characteristic of Ilmenite series. The low Ti content in

biotite correlates to the low temperature of crystallization (Henry et al., 2005). According to Ishihara (1977) Ilmenite series, granitoids were crystallized under oxygen-reducing conditions in contrast to those belonging to the magnetite series. The high FeO (23.66–24.60 wt.%) and low MgO (5.05–5.59 wt.%) contents suggest iron enrichment. The Mg/(Fe²⁺ + Mg) ratios range from 0.27 to 0.30, showing Mg poor nature, whereas (Fe/(Fe + Mg)) values range from 0.70 to 0.73 wt.%, suggesting iron enrichment. These pieces of evidence and the narrow range of Fe²⁺/Fe²⁺ + Mg indicate the magmatic nature of biotites characterizing the studied granites. Moreover, using the 10*TiO₂–FeO^l–MgO ternary discrimination diagram (Nachit et al., 2005), the biotite compositions plot within the primary magmatic biotite field (Fig. 2g), indicating a direct crystallization from magma (Stone, 2000). The FeO*MgO–Al₂O₃ (Abdel-Rahman, 1994) biotite discriminate diagram indicates the biotite in paraluminous rocks, including collision and S-type granite and have aluminum-rich siderophyllitic composition and are generally associated with muscovite, garnet, and andalusite minerals. These signatures also indicate that the studied granitoids are evolved by the subduction-related syn-collisional tectonic activity (Fig. 2h). Ternary biotite classification diagram (Al^{VI} + Fe³⁺ + Ti)–Mg–(Fe²⁺ + Mn), commonly used for the Fe-rich biotite granites classification, they belong to the siderophyllite suite (Fig. 2i) (Foster, 1960). Moreover, FeO^l/(FeO^l + MgO)–MgO wt.% binary plot (Fig. 2j) indicative of the magma source, which was the crustal-derived source for these biotite granites (Zhou, 1986). Finally, the Ti content used in the biotite geothermometer (Henry et al., 2005) and the Al^T content in the hornblende geobarometer for studied granitoids with a common mineral assemblage are crystallization temperatures ranging from 716 to 730 °C and pressure ranges from 4.24 to 5.57 kbar.

6 Conclusions

Petrographically, the two types of granites have been identified, viz., coarse- to medium-grained pink granite (K-feldspar enriched) and medium to fine-grained gray granite (mafic minerals and Na-rich feldspar). Geochemical characteristics for biotite granites suggest peraluminous, including S-type granitic nature, and they were evolved by the subduction-related syn-collisional tectonic setting. The (Al^{VI} + Fe³⁺ + Ti)–Mg–(Fe²⁺ + Mn) ternary diagram indicates a Fe-rich biotite with siderophyllitic affinity for the host granite. The Ti content in the biotite geothermometer and Al^T contents in the hornblende geobarometer suggests crystallization temperatures ranging from 716 to 730 °C and pressure ranges from 4.24 to 5.57 kbar for biotite granite. This study sheds light on the physicochemical condition of the

magmatic source (crustal-derived), pressure and temperature of the derivation of studied granites. Geochemical data of biotite granites suggests the initial derivation of crustal-derived magma from metasomatized crust through melting in plate interiors.

References

- Abdel-Rahman, A. M. (1994). Nature of biotites from alkaline, calc-alkaline, and peraluminous magmas. *Journal of Petrology*, 35, 525–541.
- Anderson, J. L., & Smith, D. R. (1995). The effects of temperature and *f*O₂ on the Al-in-hornblende barometer. *American Mineralogist*, 80, 549–559.
- Chattopadhyay, A., Chatterjee, A., Das, K., & Sarkar, A. (2017). Neoproterozoic transpression and granite magmatism in the Gavilgarh-Tan Shear Zone, central India: Tectonic significance of U–Pb zircon and U–Th-total Pb monazite ages. *Journal of Asian Earth Sciences*, 147, 485–501.
- Foster, M. D. (1960). Interpretation of the composition of trioctahedral micas. *U.S. Geological Survey Professional Paper*, 354-B, 11–49.
- Geological District Resource Map of Shahdol. (2002). *The Published map by Geological Survey of India*.
- Henry, D. J., Guidotti, C. V., & Thomson, J. A. (2005). The Ti-saturation surface for low- to medium pressure metapelitic biotites: Implications for geothermometry and Ti-substitution mechanisms. *American Mineralogist*, 90(2–3), 316–328.
- Ishihara, S. (1977). The magnetite-series and ilmenite-series granitic rocks. *Mining Geology (Tokyo)*, 27, 293–305.
- Mutch, E. J. F., Blundy, J. D., Tattitch, B. C., Cooper, F. J., & Brooker, R. A. (2016). An experimental study of amphibole stability in low-pressure granitic magmas and a revised Al-in-hornblende geobarometer. *Contributions to Mineralogy and Petrology*, 171(85), 1–27. <https://doi.org/10.1007/s00410-016-1298-9>
- Nachit, H., Ibhi, A., Abia, E. H., & Ohoud, M. B. (2005). Discrimination between primary magmatic biotites, re-equilibrated biotites and neofomed biotites. *Comptes Rendus Geoscience*, 337, 1415–1420.
- Radhakrishna, B. P., & Naqvi, S. M. (1986). Precambrian continental crust of India and its evolution. *The Journal of Geology*, 94, 145–166.
- Ramachandra, H. M., & Roy, A. (2001). Evolution of the Bhandara-Balaghat granulite belt along the southern margin of the Sausar Mobile Belt of Central India. *Proceedings of the Indian Academy of Sciences (earth Planetary Science)*, 110(4), 351–368. <https://doi.org/10.1007/BF02702900>
- Roy, A., Devarajan, M. K., & Hanuma Prasad, M. (2002). Ductile shearing and syntectonic granite emplacement along the southern margin of the Palaeoproterozoic Mahakoshal supracrustal belt: Evidence from Singrauli Area, Madhya Pradesh. *Journal of Geological Society of India*, 59, 9–21.
- Roy, A., & Prasad, H. (2003). Tectonothermal events in Central Indian Tectonic Zone (CITZ) and its implications in Rodinian crustal assembly. *Journal of Asian Earth Sciences*, 22, 115–129.
- Rudnick, R. L., & Fountain, D. M. (1995). Nature and composition of the continental crust: A lower crustal perspective. *Reviews of Geophysics*, 33, 267–309.
- Sadiq, M., Umrao, R. K., Sharma, B. B., Chakraborti, S., Bhattacharyya, S., & Kundu, A. (2017). Mineralogy, geochemistry and geochronology of mafic magmatic enclaves and their significance in evolution of Nongpoh granitoids, Meghalaya, NE India. In S. Sensarma & B. C. Storey (Eds.), *Large igneous provinces from*

- Gondwana and Adjacent Regions. Geological Society, London, Special Publications* (Vol. 463, pp. 171–198). <https://doi.org/10.1144/SP463.2>
- Schmidt, M. W. (1992). Amphibole composition in tonalite as a function of pressure: An experimental calibration of the Al-in-hornblende barometer. *Contributions to Mineralogy and Petrology*, 110(2–3), 304–310.
- Stone, D. (2000). Temperature and pressure variations in suites of Archean felsic plutonic rocks, Berens River area, northwest Superior Province, Ontario, Canada. *The Canadian Mineralogist*, 38, 455–470.
- Wu, C.-M., & Chen, H.-X. (2015). Revised Ti-in-biotite geothermometer for ilmenite-or rutile bearing crustal metapelites. *Science Bulletin*, 60(1), 116–121. <https://doi.org/10.1007/s11434014-0674-y>
- Zhou, Z. X. (1986). The origin of intrusive mass in Fengshandong, Hubei Province. *Acta Petrologica Sinica*, 2, 59–70.



Geochemical Constraints on the Petrogenesis of Tirodi Gneissic Complex (TGC) from Central India

Mukesh Mishra, Meraj Alam, Tatiana Kaulina, and Talat Ahmad

Abstract

The Tirodi Gneissic Complex (TGC) from central India represents part of the basement gneisses. The TGC comprises a combination of pink and grey granitic gneiss assemblages, and it is petrographically characterized by biotite-rich granite gneisses. The geochemistry and isotope (Rb–Sr) data set is used to constrain the petrogenesis of TGC granitoids and Precambrian crustal evolution. Previous geochemical results from the study area were not focused on the genesis and crustal evolution of these granitoids. The present contribution addresses these issues by using new geochemical and isotopic data sets. The studied samples were analyzed by WD-XRF (Siemens SRS 3000) and ICP-MS (Perkin Elmer, Elan DRC-e) facility at Wadia Institute of Himalayan Geology Dehradun. These granitoids classified as calc-alkaline granite-trondhjemite with metaluminous to peraluminous composition. The negative correlation of ferromagnesian oxide with silica suggests primary magmatic igneous parental melt. Multi-element patterns for the TGC granitoids are characterized by large ion lithophile elements (LILE) enrichment, depletion in high field strength elements (HFSE: Nb, P and Ti) and positive Pb and Zr anomalies. Negative anomalies in HFSE correspond to crustal/lithospheric sources with some influence of K-feldspar, plagioclase and Ti-oxide fractionation.

M. Mishra
Geological Survey of India, Jhalana Doongri,
Jaipur, 302004, India

M. Alam (✉)
Department of Geology, Indira Gandhi National Tribal University,
Amarkantak, 484887, India
e-mail: merajdu@gmail.com

T. Kaulina
Geological Institute of the Kola Science Centre, RAS,
Apatity, 184209, Russia

T. Ahmad
Department of Geology, University of Delhi,
New Delhi, 110007, India

Isotopic data presents the Initial $^{87}\text{Sr}/^{86}\text{Sr}_{(t=1.6 \text{ Ga})}$ ratio that varies from 0.70595 to 0.73191 for TGC granitoid. Such a range of initial $^{87}\text{Sr}/^{86}\text{Sr}$ ratios (> 0.706), corresponding to the TGC granitoid, indicate they are generated within the crust. The elevated value of the initial $^{87}\text{Sr}/^{86}\text{Sr}$ ratio may also correspond to the alteration. The geochemical results on the TGC granitoids indicate transitional tectonic settings from “within plate granite” to “volcanic arc syn-collisional granite”.

Keywords

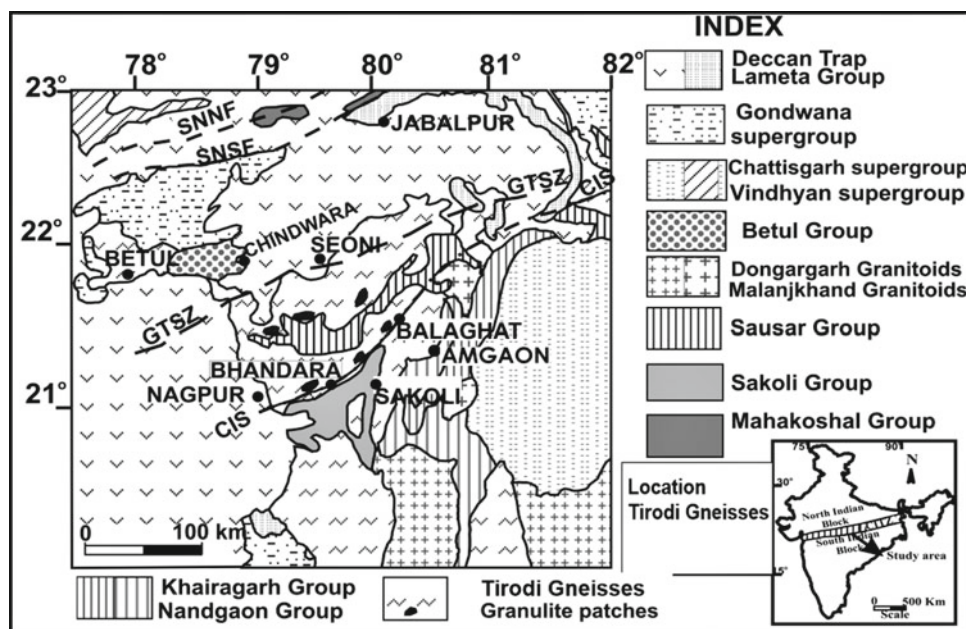
Geochemistry • Sr isotopes • Petrogenesis • Tirodi gneissic complex • Central India

1 Introduction

The Tirodi Gneissic Complex (TGC) from Central Indian Tectonic Zone (CITZ), central India, represents portions of the basement gneisses. The CITZ is an important suture zone, which has been developed by the collision of two Indian blocks (North Indian Block and South Indian Block) (Fig. 1). The various litho-units depicted within the CITZ include the Ramakona-Katangi granulite belt in the north, Sausar Mobile Belt (SMB) in the center and Bhandara-Balaghat granulite belt in the southern margin of CITZ (Fig. 1). The SMB comprises two major litho-tectonic units, viz., TGC, which is also known as Tirodi biotite gneiss and migmatite (Phadke, 1990; Sarangi & Mohanty, 1998) and metasedimentary unit (Chattopadhyay et al., 2020) (Fig. 1a). The metasediments are primarily sandy, shaly and calcareous sediments with the absence of volcanic suites, which are deposited in the basin margin (Mohanty, 2003; Roy, 1981).

Although a significant amount of data has been generated on granitoids from CITZ in the last few decades, it still needs to be clarified to establish any petrogenetic and tectonic relationship between these studied gneisses. We aim to

Fig. 1 Geological map shows the study area and major lineaments and super-groups within the CITZ, central India. CIS: Central India shear; GTSZ: Gavilgarh-Tan shear zone; SNSF: Son-Narmada South Fault; SNNF: Son-Narmada North Fault



address these issues using new elemental and isotopic (Rb–Sr) data on these TGC rocks from central India.

2 Analytical Methods

The studied samples were analyzed by WD-XRF (Siemens SRS 3000) and ICP-MS (Perkin Elmer, Elan DRC-e) facility at Wadia Institute of Himalayan Geology, Dehradun. We followed Saini et al. (Saini et al., 1998) and Bhattacharya et al. (Bhattacharya et al., 2012) for precision and accuracy. The Rb–Sr isotopic analyses were carried out at the Geological Institute of the Kola Science Centre, RAS, Apatity, and the method was followed by Kunakkuzin et al. (2020).

3 Results

3.1 Whole-Rock Geochemistry

TGC has high SiO_2 content (65–75 wt.%), low TiO_2 content (< 1 wt.%), Al_2O_3 content (13–16 wt.%), low $\text{Fe}_2\text{O}_3^{\text{T}}$ content (2–5 wt.%), very low MgO content (< 1–1 wt.%), CaO content (< 1–4 wt.%), Na_2O content (1–5 wt.%), K_2O content (1–4 wt.%) and low P_2O_5 content (<1 wt.%). Harker variation diagrams negatively correlate with SiO_2 , indicating primary magmatic characteristics. However, K_2O shows a scattered relationship against SiO_2 , probably suggesting the mobile nature of potash. In the normative An–Ab–Or (Barker & Barker, 1979; O'Connor & J, 1965) diagram, rock

samples plot in granite to trondjemite fields (Fig. 2a). Other geochemical discriminant diagrams suggest a calc-alkaline affinity with peraluminous to metaluminous composition (Fig. 1b).

Trace elements show Rb content (94–266 ppm), high Ba content (254–1085), U content (2–15 ppm), Nb content (11–48 ppm), Sr content (25–300 ppm), Zr content (126–879 ppm) Y content (8–70 ppm), V content (9–37 ppm) and Ni content (9–30 ppm). Primitive mantle (PM) normalized multi-element patterns show enrichment of LILE and other incompatible trace elements with prominent positive Th, U, Zr and Pb anomalies and negative anomalies for HFSE–Nb, P, Ti and Sr (Fig. 1c). Tectonic discrimination plots based on trace element compositions and variation plot of Rb versus $\text{Nb} + \text{Y}$ (ppm) are shown in Fig. 1d. In the tectonic diagrams, TGC granitoids sample plots within the volcanic arc granite (VAG) field to within the plate granite (WPG) field.

4 Isotope Geochemistry

The value of initial $^{87}\text{Sr}/^{86}\text{Sr}$ ratios, and the concentrations of Rb and Sr (in ppm) for the selected four samples are illustrated in Table 1. Rb–Sr data of studied rock presents the ranges of initial $^{87}\text{Sr}/^{86}\text{Sr}_{(t=1.6 \text{ Ga})}$ ratios from 0.70595 to 0.73191. These isotopic ratios of Rb–Sr can suggest the nature of the melts' sources and constrain the crustal evolution processes. Sr isotopes have not been of much use owing to their mobile nature and appear to have been disturbed by post-crystallization processes.

Fig. 2 Discriminant diagrams for TGC rocks from CITZ. **a** An–Ab–Or normative classification (Barker & Barker, 1979; O'Connor, 1965). **b** Aluminum saturation index (ASI) or A/CNK plot (Maniar & Piccoli, 1989). **c** Rock/primitive mantle normalized multi-element patterns, normalization values of primitive mantle use after Sun and McDonough (1989). **d** Nb + Y versus Rb (ppm) plots (Pearce et al., 1984)

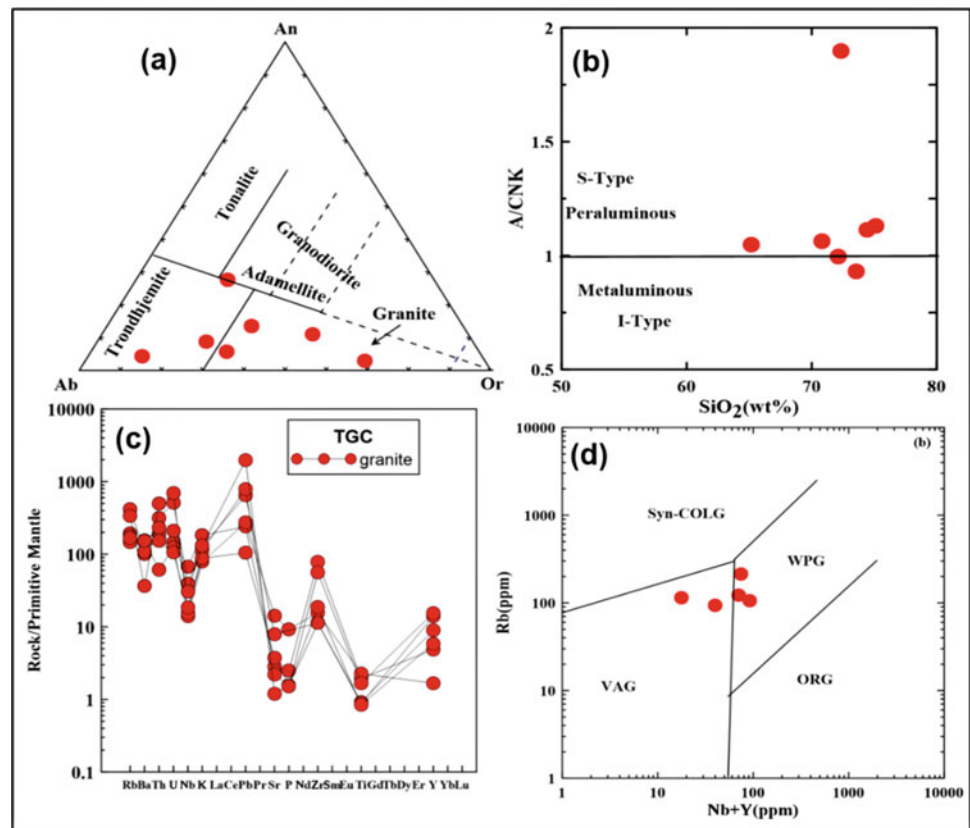


Table 1 Isotopic (Rb–Sr) data of representative samples of TGC granitoids from central India

Sample	Rb (ppm)	Sr (ppm)	$^{87}\text{Rb}/^{86}\text{Sr}$	$^{87}\text{Sr}/^{86}\text{Sr}$	$(^{87}\text{Sr}/^{86}\text{Sr})_{i(1.6)}$
MU-2	141.13	177.3	2.31936	0.76722	0.71392
MU-3	7.63	407.58	0.05443	0.73316	0.73191
MU-5	90.86	236.13	1.11824	0.73464	0.70894
TG-01	45.14	86.2	1.52254	0.74094	0.70595

5 Discussion

The studied rocks are classified as granites to trondhjemites. Other geochemical signatures indicate a calc-alkaline affinity with peraluminous to metaluminous composition. The negative correlation between ferromagnesian major elements and silica indicates the conservation of primary magmatic characteristics of the studied granitoids. However, major oxides like K_2O and P_2O_5 show scattered relationships against silica, probably due to the mobile nature of potash. Multi-element patterns show enrichment of LILE with prominent positive Th, U, Zr and Pb anomalies and negative anomalies for HFSE–Nb, P, Ti and Sr. These observed anomalies are probably related to crustal/lithospheric sources with some influence of fractionations of K-feldspar, plagioclase and Ti-oxides. Rb–Sr data for TGC granitoid presents initial $^{87}\text{Sr}/^{86}\text{Sr}_{(t=1.6 \text{ Ga})}$ ratios from 0.70595 to 0.73191,

considering the 1.6 Ga crystallization age used after (Ahmad et al., 2009; Alam et al., 2022) for the calculation of the initial ratios. Higher initial $^{87}\text{Sr}/^{86}\text{Sr}$ (> 0.706) ratios correspond to crustal-derived magma generated by partial melting within the crust. The elevated value of the initial $^{87}\text{Sr}/^{86}\text{Sr}$ ratio may correspond to a metasedimentary source. The tectonic discrimination plot of Rb versus Nb + Y (ppm) suggests probably a post-collision tectonic setting.

6 Conclusions

The TGC granitoids from the CITZ are classified as granite-trondhjemite and have calc-alkaline lineage with metaluminous to peraluminous characteristics. The geochemical signatures suggest the primary magmatic characteristics. Negative anomalies in trace element patterns correspond to crustal/lithospheric sources with some extent

to K-feldspar, plagioclase and Ti-oxide fractionation. Moreover, Sr isotopic results correspond to a crustal/lithospheric sources for the TGC granitoids. Other geochemical characteristics support volcanic arc granite (VAG) to within plate granite (WPG) tectonic environment for the TGC granitoids.

References

- Ahmad, T., Kaulina, T. V., Wanjari, N., Mishra, M. K., & Nitkina, E. A. (2009). U–Pb zircon chronology and Sm–Nd isotopic characteristics of the Amgaon and Tirodi Gneissic Complex, Central Indian Shield: Constraints on Precambrian crustal evolution. In *Precambrian Continental Growth and Tectonism* (pp. 137–138). Excel India Publishers.
- Alam, M., Mishra, M. K., Kaulina, T. V., Ahmad, T., & Choudhary, A. K. (2022). Geochemistry and petrogenesis of proterozoic granitoids from central Indian Tectonic Zone (CITZ): Elemental and isotopic constraints. *Geochemical Journal*, 56(5), 160–176.
- Barker, F. (1979). Trondhjemites: definition, environment and hypotheses of origin. In F. Barker (Ed.), *Trondhjemites, dacites and related rocks* (pp. 1–12). Elsevier.
- Bhattacharya, S., Chaudhary, A. K., & Basai, M. (2012). Original nature and source of khondalites in the Eastern Ghats province, India. In R. Mazumdar & D. Saha (Eds.), *Paleoproterozoic of India: Geological Society, London, Special Publications* (Vol. 365, pp. 147–159).
- Chattopadhyay, A., Bhowmik, S. K., & Roy, A. (2020). Tectonothermal evolution of the Central Indian Tectonic Zone and its implications for Proterozoic supercontinent assembly: The current status. *Episodes*, 43(1), 132–144.
- Kunakkuzin, E., Borisenko, E., Nerovich, L., Serov, P., Bayanova, T., & Elizarov, D. (2020). The origin and evolution of ore-bearing rocks in the Loypishnun deposit (Monchetundra Massif, NE Fennoscandian Shield): Isotope Nd–Sr and REE geochemical data. *Minerals*, 10, 286.
- Maniar, P. D., & Piccoli, P. M. (1989). Tectonic discrimination of granitoids. *Geological Society of America Bulletin*, 101, 635–643.
- Mohanty, S. (2003). Structural stratigraphic relations in Precambrian rocks of Sausar belt, central India. *Gondwana Geological Magazine*, 7, 109–117.
- O'Connor, J. T. (1965). A classification for quartz-rich igneous rocks based on feldspar ratios. *U.S. Geological Survey Professional Paper*, 525(B), 79–84.
- Pearce, J. A., Harris, N. B. W., & Tindle, A. G. (1984). Trace element discrimination diagrams for the tectonic interpretation of granitic rocks. *Journal of Petrology*, 25, 956–983.
- Phadke, A. V. (1990). Genesis of the granitic rocks and the status of the “Tirodi Biotite Gneiss” in relation to the metamorphites of the Sausar group and the regional tectonic setting. *Geological Society of India Special Publications*, 28, 287–302.
- Roy, S. (1981). *Manganese deposits* (p. 458). Academic Press.
- Saini, N. K., Mukherjee, P. K., Rathi, M. S., Khanna, P. P., & Purohit, K. K. (1998). A new geochemical reference sample of Granite (DG-H) from Dalhouse, Himachal Himalaya. *Journal of the Geological Society of India*, 52, 603–606.
- Sarangi, S., & Mohanty, S. (1998). Structural studies in the Chhotanagpur Gneissic complex near Gomoh, Dhanbad district, Bihar. *Indian Journal of Geology*, 70, 73–80.
- Sun, S. S., McDonough, W. F. (1989). Chemical and isotopic systematics of oceanic basalts: Implications for mantle composition and processes magmatism in ocean basins. In A. D. Saunders & M. J. Norry (Eds.), *Geological society special publication* (Vol. 42, pp. 313–345).



Petrogenesis and Tectonic Setting of Igneous Rocks from Kassa Area, Zing, Northeastern Nigeria: Geological and Geochemical Constraints

Hafizullah Abba Ahmed, Ismaila Vela Haruna, Usman Kaigama, Maimunatu Halilu, Marcel Pius Apagu, Solomon Ahmed, Jonathan Abiukwobye Aboh, Mohammed Babi Saleh, and Musa Bala Girei

Abstract

Pan-African granitoids of variable mineralogical compositions are emplaced in Kassa, Zing area, which form part of the Adamawa Massif of Northeastern Nigeria Basement complex. In this study, 16 samples obtained during fieldwork were subjected to geochemical analysis using XRF techniques in order to shed more light on the origin and tectonic setting of the rocks. Studied rock suites include ijolite, syenite, quartz syenite, quartz monzonite, biotite granite and granodiorite. The silica contents of the rocks range from 47.10 wt.% to 71.00 wt.%, exhibiting alkalic, calc-alkalic and calcic affinities. All the studied granitoids plot within the peralkaline and metaluminous fields on the A/NK versus A/CNK diagram. The decrease in Fe_2O_3T , MgO, CaO and TiO_2 with increasing SiO_2 and increase in Ba and Sr with increasing SiO_2 is an indication of formation through fractional crystallization. Based on the field, petrographic and geochemical data, it can be inferred that the ijolite, syenite, quartz syenite, quartz monzonite and biotite granite are formed by the fractional crystallization of basic melts. On the other hand, plots of normative albite anorthite-orthoclase and Mg# versus SiO_2 indicate that the granodiorite was emplaced via partial melting of tonalitic rocks from the deeper crust. In conclusion, the crystalline basement of Kassa area represents two different settings: Syn-collision and late orogenic stage. The oldest pluton, granodiorite, intruded during collision by partial melting of crustal rocks of tonalitic composition at temperatures between 850 and 950 °C. The emplacement of the ijolite, syenite,

quartz syenite, quartz monzonite and biotite granite occurred during late orogenic times, via fractional crystallization of mantle-derived mafic melts.

Keywords

Ijolite • Adamawa Massif • Quartz monzonite • Petrogenesis • Tonalitic rocks

1 Introduction

Imprints of the Neoproterozoic Pan-African orogeny are well represented by large granitic batholiths that extend from Adamawa Massif in northeastern Nigeria to the Bamenda Massif in Cameroun. This region forms parts of the network of orogenic belts that extend from NW Africa southward into the Borborema province of Brazil. These orogenic belts consist largely of Pan-African (600 ± 150 Ma) granites that intruded into migmatites and gneisses of Eburnean (Paleoproterozoic) age (Dada, 1998). Despite their significance in reconstructing the tectonic evolution of western Gondwana, the granitic rocks of the Adamawa Massif have not been studied in detail before.

Accordingly, this contribution presents an integrated petrographic and geochemical data of co-existing calc-alkaline and alkaline rocks from Kassa area, Adamawa Massif, northeastern Nigeria. Our aim is to determine the petrogenesis and tectonic implications of the rocks.

2 Geological Background, Sampling and Analysis

Adamawa Massif occupies a large region between the Benue Trough to the west and the Cameroon volcanic line to the east. The Adamawa Massif, together with the Hawal Massif and Oban Massif, constitute the Eastern Nigeria Terrain

H. A. Ahmed (✉) · I. V. Haruna · U. Kaigama · M. Halilu · M. P. Apagu · S. Ahmed · J. A. Aboh · M. B. Saleh
Department of Geology, Modibbo Adama University,
P.M.B. 2076 Yola, Nigeria
e-mail: ahmedha@mau.edu.ng

M. B. Girei
Department of Geology, Bayero University, Kano,
P.M.B. 3011 Kano, Nigeria

(ENT) that extends into the neighboring Cameroon Republic. They are crosscut by Neoproterozoic (ca. 580–640 Ma; (Tubosun, 1983)) granites consisting of hornblende granites, biotite granite and undifferentiated granites. Some of these undifferentiated granites may include the alkaline rocks covered in this study.

Whole rock major element compositions of sixteen samples from Kassa area (Fig. 1), were measured using X-Ray Fluorescence Spectrometry (XRF) (Rigaku NEX DE 1233) at the Geology Department Laboratory of Gombe State University, Nigeria.

The rocks range from fine to coarse-grained and porphyritic in texture and commonly composed of biotite,

K-feldspars, plagioclase, quartz, hornblende, garnet, nepheline and pyroxene as the major minerals and magnetite, apatite, muscovite and zircon as accessory minerals. They were geochemically classified (Roche et al., 1980) as ijolite, syenite, quartz syenite, quartz monzonite, granite and granodiorite (Fig. 2a). The major elements compositions in Kassa area are highly variable with SiO₂ ranging from 47.815 wt.% for the ijolite, 64.13–70.53 wt.% syenite, 63.22–71.34 wt.% quartz syenite, 65.87–68.72 wt.% quartz monzonite, 65.93–69.98 wt.% biotite granite and 67.43–73.91 wt.% granodiorite, Na₂O contents of 6.97 wt.% ijolite, 6.39–7.72 wt.% syenite, 4.63–6.57 wt.% quartz syenite, 3.83–4.39 wt.% quartz monzonite, 2.65–2.84 wt.% biotite

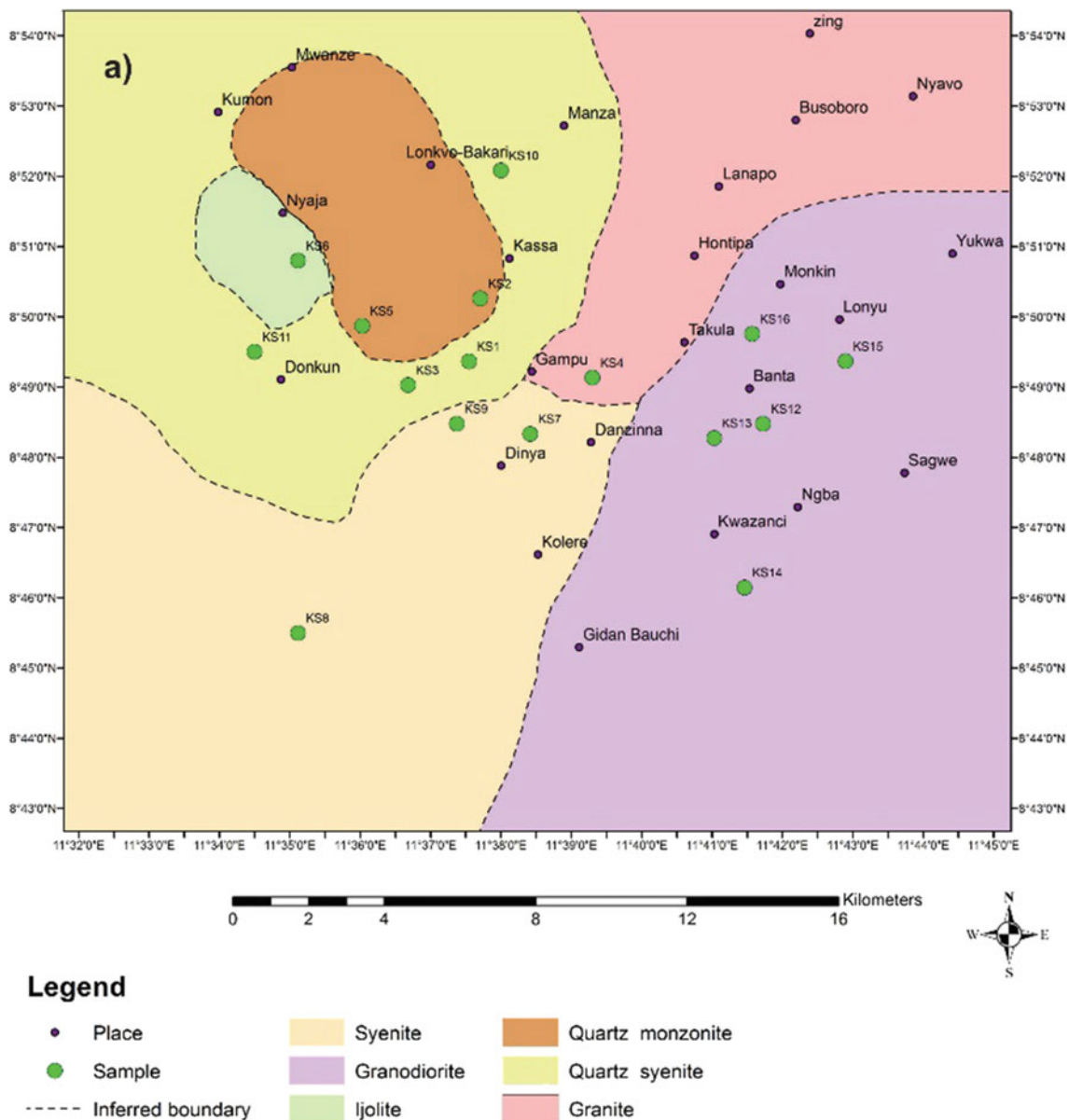


Fig. 1 Showing the geologic map of the study area

granite and 0.83–2.34 wt.% granodiorite. The K₂O contents range from 1.68 wt.% (ijolite), 5.22–5.97 wt.% (syenite), 4.76–5.54 wt.% (quartz syenite), 4.24–5.49 wt.% (quartz monzonite), 4.23–6.37 wt.% (biotite granite) and 3.45 wt.%–5.79 wt.% (granodiorite). Other contents also vary: MgO 6.2 wt.% (ijolite), 0.38–1.60 wt.% (syenite), 0.28–1.34 wt.% (quartz syenite), 0.5–1.40 wt.% (quartz monzonite), 0.29–1.15 wt.% (biotite granite), 0.33–0.79 wt.% (granodiorite). CaO is up to 10.5 wt.% (ijolite), 1.03–3.27 wt.% (syenite), 1.66–2.33 wt.% (quartz syenite), 1.58–2.48 wt.% (quartz monzonite), 1.58–3.66 wt.% (biotite granite) and 2.97–5.79 wt.% (granodiorite). Fe₂O₃T content of the samples includes 10.6 wt.% (ijolite), 1.1–4.11 wt.% (syenite), 1.56–3.46 wt.% (quartz syenite), 2.86–4.00 wt.% (quartz monzonite), 3.18–8.2 wt.% (biotite granite) and 2.24–6.58 wt.% (granodiorite). TiO₂ composition is 1.35 wt.% (ijolite), 0.08–0.79 wt.% (syenite), 0.19–0.38 wt.% (quartz syenite), 0.38–0.78 wt.% (quartz monzonite), 0.46–1.44 wt.% (biotite granite) and 0.21–2.59 wt.% (granodiorite). P₂O₅ 0.49 wt.% (ijolite), 0.10–0.34 wt.% (syenite), 0.14–0.28 wt.% (quartz syenite), 0.11–0.20 wt.% (quartz monzonite), 0.11–0.48 wt.% (biotite granite) and 0.01–3.98 wt.% (granodiorite). In general, the ijolite sample has the highest content of MgO and CaO of 6.832 wt.% and 10.659 wt.%, respectively, more than the rest of the samples.

SiO₂ shows negative, almost linear, correlation with MgO and CaO and weaker correlation with Fe₂O₃^T, Na₂O, K₂O, MnO₂ and TiO₂. The rocks in the study area range from peralkaline to metaluminous (A/CNK = 0.45–1.01). The A/CNK versus SiO₂ plot indicates that the rocks under study are I-type granitoids.

3 Discussion

The rocks of the area belong to a Syn-collisional to late orogenic calc-alkaline and alkaline suites that represent an intrusive phase of Late Precambrian to Early Paleozoic Pan-African Orogeny in Nigeria. They exhibit geochemical features ranging from shoshonite to high-K-calc-alkaline.

The geochemical features of the studied granodiorites suggest that their parental magma was largely derived through partial melting of crustal sources. According to Chappell and White (1984), the high-K-calc-alkaline are mostly granodiorite and tonalite. Typically, magma generated from melting of some greywackes is depleted in Al₂O₃, K₂O, Ba and Rb. Thus, the enrichment of these major elements in the investigated granitoids suggests that greywackes (pelites) do not constitute a major component of their parental magma. Instead, this geochemical feature is more consistent with their formation through partial melting of tonalitic rocks at 7 kbar around 850–950 °C (Liu et al., 2014). Using silica (SiO₂) as an index of differentiation, most of the major oxides show decreasing trend with increasing SiO₂, which is consistent with magma evolution involving fractionation of feldspars, ferromagnesian minerals and apatite.

On the other hand, the Si undersaturated (alkaline) rocks represented by the syenites, quartz monzonite and biotite granite are peralkaline to slightly metaluminous in composition. Based on Frost et al. (2001), the geochemical affinity of Kassa rocks shows that they are majorly ferroan and range from calcic-calc-alkalic to alkalic, indicating their high level of evolution. The linear geochemical variations shown by

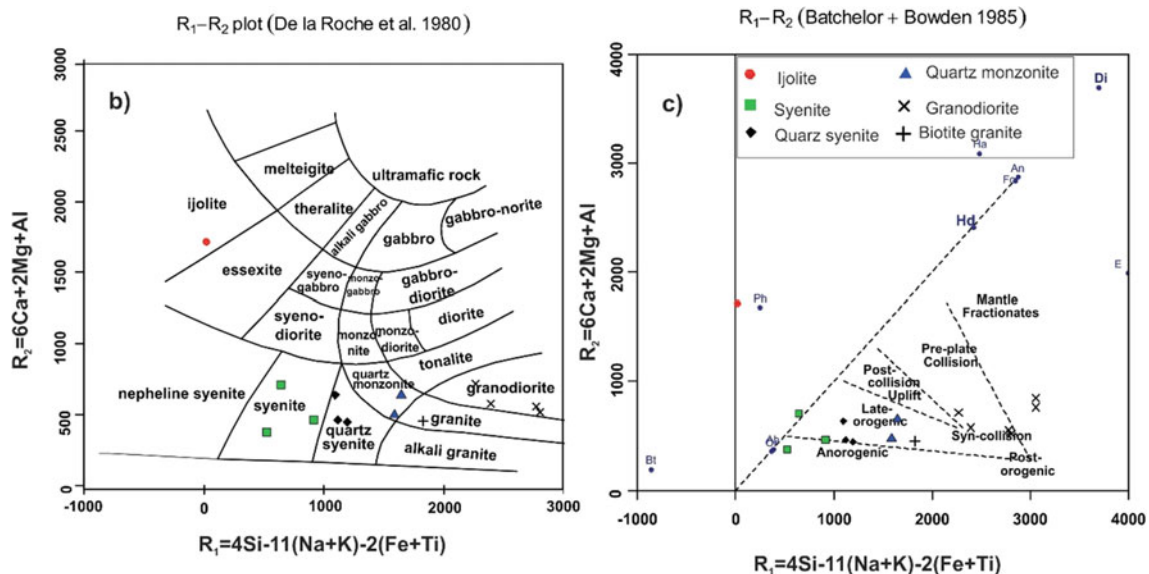


Fig. 2 a Rock classification after (Roche et al., 1980), b Tectonic discrimination plot after (Batchelor & Bowden, 1985)

Harker plots are indicative of the genetic relationships between the rocks which is an indication of possible fractional crystallization during formation from a common source. Most of the rocks correlate with SiO_2 . However, Fe_2O_3 , Na_2O , MnO_2 and TiO_2 have weak correlations as they show scatter plots.

The ijolite together with the other alkaline rocks most probably originate from the mantle rather than the crust due to their low Silica (SiO_2) through the process of fractional crystallization of early formed minerals which tend to separate from the silicate melt and settle at the bottom by gravity settling. The variation of SiO_2 from 47.01 to 71 wt. % is a clear indication of formation of Kassa alkaline rocks through fractional crystallization, with ijolites being the first to crystallize followed by syenites, quartz syenite, quartz monzonite and biotite granite based on their SiO_2 gradation. The quartz monzonite, quartz syenite and syenite form outside the region of pure crustal melt at 7 kbar at 1000–1050 °C. This high temperature is consistent with rocks formed from fractional crystallization of mantle sources (Liu et al., 2014).

Geotectonic classification (Batchelor & Bowden, 1985) from the study area shows that Kassa granodiorites are syn-collisional (Fig. 2b). This is similar to the granites from southernmost Nigeria (Obiora, 2008), Cameroon (Djouka-Fonkwe et al., 2008) and granitoids from northern Adamawa Massif (Haruna, 2014). However, similar plot defines the tectonic setting of the alkaline rocks as late orogenic (Fig. 2b). In general, the orientations of the geologic structures in the study area are mainly NE–SW, and NW–SE in consonance with the Pan-African orogeny (Rahaman, 2003).

4 Conclusions

In conclusion, the Kassa area experienced at least two tectonic regimes, which defined the outcrops in the study area. The syn-collisional tectonics aided the formation of the granodiorite in the area, which is supposedly the oldest. This rock was probably formed by partial melting of crustal rocks at temperatures between 850 and 950 °C. We propose that the granodiorite formed from partial melting of tonalitic rocks. On the other hand, the second regime marked the emplacement of ijolite, syenite, quartz syenite, quartz

monzonite and biotite granite during the late orogenic stage. This event aided their emplacement via fractional crystallization of mafic magmas from the mantle. This study reports for the first time the presence of ijolite and syenitic rocks in this region of northeastern Nigeria basement terrain.

Acknowledgements We acknowledge the TETFund for the IBR 7th batch 2021 grant awarded for this study. The support of the management of Center for Research and Development, Modibbo Adama University Yola, is also highly acknowledged.

References

- Batchelor, R. A., & Bowden, P. (1985). Petrogenetic interpretation of granitoid rock series using multicationic parameters. *Chemical Geology*, 48(1–4), 43–55.
- Chappell, B. W., & White, A. J. R. (1984). I- and S-type granites in the Lachlan Fold Belt, Southeastern Australia. In K. Xu & G. Tu (Eds.), *Geology of granites and their metallogenic relations* (pp. 87–101). Science Press.
- Dada, S. S. (1998). Crust-forming ages and Proterozoic crustal evolution in Nigeria: A reappraisal of current interpretations. *Precambrian Research*, 87(1–2), 65–74.
- De La Roche, H., Leterrier, J., Grandclaude, P., & Marchal, M. (1980). A classification of volcanic and plutonic rocks using R1–R2 diagram and major element analyses—its relationships with current nomenclature. *Chemical Geology*, 29(1–4), 183–210.
- Djouka-Fonkwe, M. L., Schulz, B., Schussler, U., Tchouankoue, J. P., & Nzolang, C. (2008). Geochemistry of the Bafoussam Pan-African I- and S-type granitoids in Western Cameroon. *Journal of African Earth Sciences*, 50(50), 148–167.
- Frost, B. R., Barnes, C. G., Collins, W. J., Arculus, R. J., Ellis, D. J., & Frost, C. D. (2001). A geochemical classification for granitic rocks. *Journal of Petrology*, 42, 2033–2048.
- Haruna, I. V. (2014). Petrology and geochemistry of granitoids of the Northern Part of Adamawa Massif, N. E. Nigeria. *Journal of Geology and Geosciences*, 3(6), 100–0177. <https://doi.org/10.4172/2329-6755.1000177>
- Liu, L., Qiu, J. S., Zhao, J. L., & Yang, Z. L. (2014). Geochronological, geochemical, and Sr–Nd–Hf isotopic characteristics of Cretaceous monzonitic plutons in western Zhejiang Province, Southeast China: New insights into the petrogenesis of intermediate rocks. *Lithos*, 196, 242–260.
- Obiora, S. C. (2008). Geology and mineral resources of the Precambrian basement complex of Nigeria. In *A Talk Presented at the National Geophysical Research Institute Hyderabad, India on 25th November as a CSIR-TWAS Post-Doctoral Fellow*.
- Rahaman, M. A. (2003). An address delivered by president, NMGS at the Annual International Conference, Itakpe. *The Crust*, 26(2).
- Tubosun, I. A. (1983). *Geochronologie U/Pb du socle précambrien du Sud Ouest Nigéria* [Thesis Doct 3ème cycle]. Université des Sciences et Techniques du Languedoc, Montpellier, France.



Miocene Magmatism in Northern Tunisia: Characterization and Geodynamic Implications

Randa Ben Abdallah and Mohamed Mansour Abdelmalak

Abstract

The Nefza mining district in northern Tunisia comprises a wide variety of magmatic rocks related to the Cenozoic Mediterranean geodynamic history. Magmatic rocks consist mainly of granodiorite and rhyodacite emplaced during the Serravallian–Tortonian (14–8 Ma) and basalts emplaced during the Messinian (8–6 Ma). This magmatism belongs to the magmatic belt that extends along the Mediterranean coast of the Maghreb from eastern Tunisia to northern Morocco. The differences in geochemical composition were attributed to changes in mantle dynamics but the implications are still unclear in northern Tunisia due to the paucity of data. In this contribution, we present new bulk-rock geochemical data of the granodiorite and rhyodacite of Nefza recovered from OB45 drill core. Samples from the OB45 drill core give a unique opportunity to follow the geochemical evolution of the magmatic rocks with depth. Geochemical (major and trace elements) compositions of OB45 drill core rocks indicate a peraluminous and potassic nature. In the total alkali versus silica (TAS) classification diagram, samples plot in the rhyolite, dacite and trachydacite fields. Trace element compositions of Nefza magmatic rocks show typical subduction-related signatures, with relative depletion of high field strength elements (HFSE: Nb, Zr, Ta, Hf), large ion lithophile elements (LILE: Rb, Ba, Pb) and light rare earth elements (LREE: La, Ce, Nd, Gd, Sm), compared to the Continental Arc Andesite (CAA) geochemical composition. However, most of the OB45 drill core rocks show negative Eu anomalies. The wide

geochemical composition of the igneous rocks emplaced during this tectonic evolution confirms a strong heterogeneity of the Mediterranean upper mantle composition. The comparison of the major and trace element as well as isotope characteristics of the magmatism in the Nefza and nearby regions (such as Kabylies and Sardinia) provides insights into the petrogenesis of the magmas and the nature of the main mantle source and its geodynamics.

Keywords

Northern Tunisia • Cenozoic magmatism • Geochemical composition • Geodynamic evolution

1 Introduction

The western Mediterranean area displays a complex tectonic evolution attributed to the interplay between different geodynamic processes including collision of continents, subduction of oceanic plates, slab rollback, slab detachment and associated back-arc basin spreading, crustal thinning, and possible upwelling of mantle plume. Consequently, a wide variety of igneous rocks of Cenozoic and Quaternary age characterize the area (Fig. 1a). A 1200 km-long linear magmatic belt extends from eastern Tunisia to Morocco (Maury et al., 2000) and resulted from the collision between the African and Eurasian plates. These magmatic rocks are mostly composed of Miocene (14–8 Ma), K-rich or medium-K calc-alkaline granites, granodiorites, andesites and rhyolites and younger (8–6 Ma) sodic alkali basalts and basanites (Carminati et al., 1998; Coulon et al., 2002; Decrée et al., 2014; Lustrino & Wilson, 2007; Maury et al., 2000). In northern Tunisia, calc-alkaline volcanic activity started during the Serravallian (12 Ma) and was followed by the emplacement of alkali basalts and basanites since the Tortonian to the Pliocene (8–5 Ma). However, the significant variations in geochemical composition between the different

R. Ben Abdallah (✉)
University of Carthage, 7021 Bizerte, Jarzouna, Tunisia
e-mail: randa.benabdallah@gmail.com

M. M. Abdelmalak
University of Oslo, Blindern, P.O. Box 1028 0316 Oslo, Norway
e-mail: m.m.abdelmalak@geo.uio.no

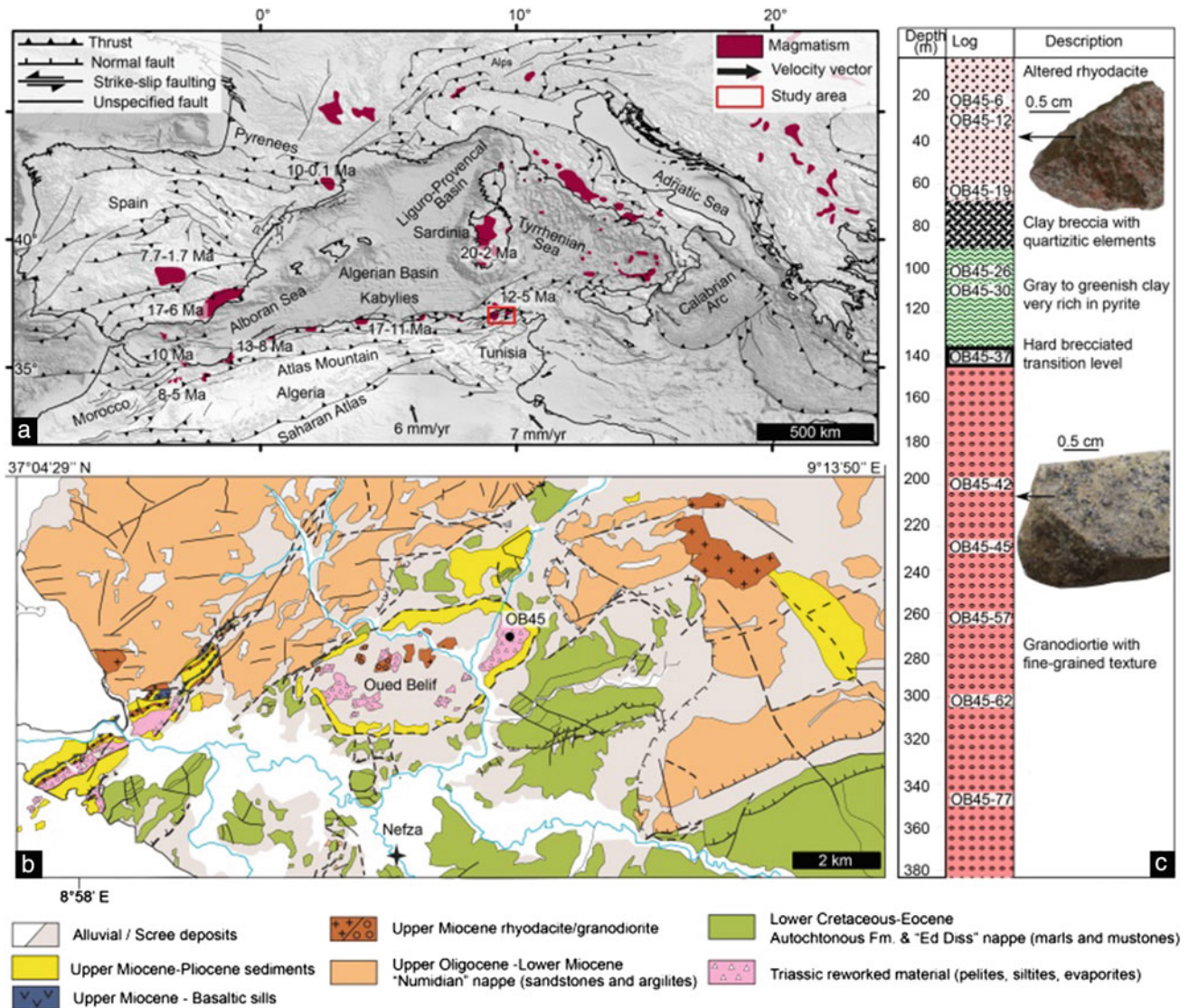


Fig. 1 **a** Tectono-magmatic map of the western Mediterranean area. **b** Geological map of the Nefza mining district with location of OB45 drill core. **c** Lithology of the OB45 drill core

volcanic units and the implication of the mantle dynamics in the area are still unclear, notably in northern Tunisia due to the paucity of data.

The aim of this study is to characterize the Miocene magmatism in the Nefza mining district using field and OB45 drill core samples, thus giving a unique opportunity to follow the geochemical evolution of magmatic rocks with depth.

2 Geological Settings

The northern Tunisia displays a wide variety of magmatic rocks related to the Mediterranean geodynamic history that occurred during the convergence of the African and Eurasian

plates in the Cenozoic (Fig. 1a). The Nefza mining district, studied here, is well-known for iron deposits that were first mined at the end of the nineteenth century. In this area, magmatic rocks (granodiorite and rhyodacite) were emplaced during the Serravallian to Tortonian period (14–8 Ma) and the basalts during the Messinian (8–6 Ma) (Decrée et al., 2014; Faccenna et al., 2005; Lustrino & Wilson, 2007; Le Maitre et al., 2002; Maury et al., 2000). These magmatic rocks enhanced fluid circulation, leading to mineralization and ore deposits.

Eighteen magmatic rocks were sampled from the Nefza mining district and from the OB45 drill core (total depth of 356m) located in the Oued Béliif area (Fig. 1b). From top to bottom of the OB45 drill core, the following units were encountered: (1) Rhyodacite (from 0 to 65 m); (2) a

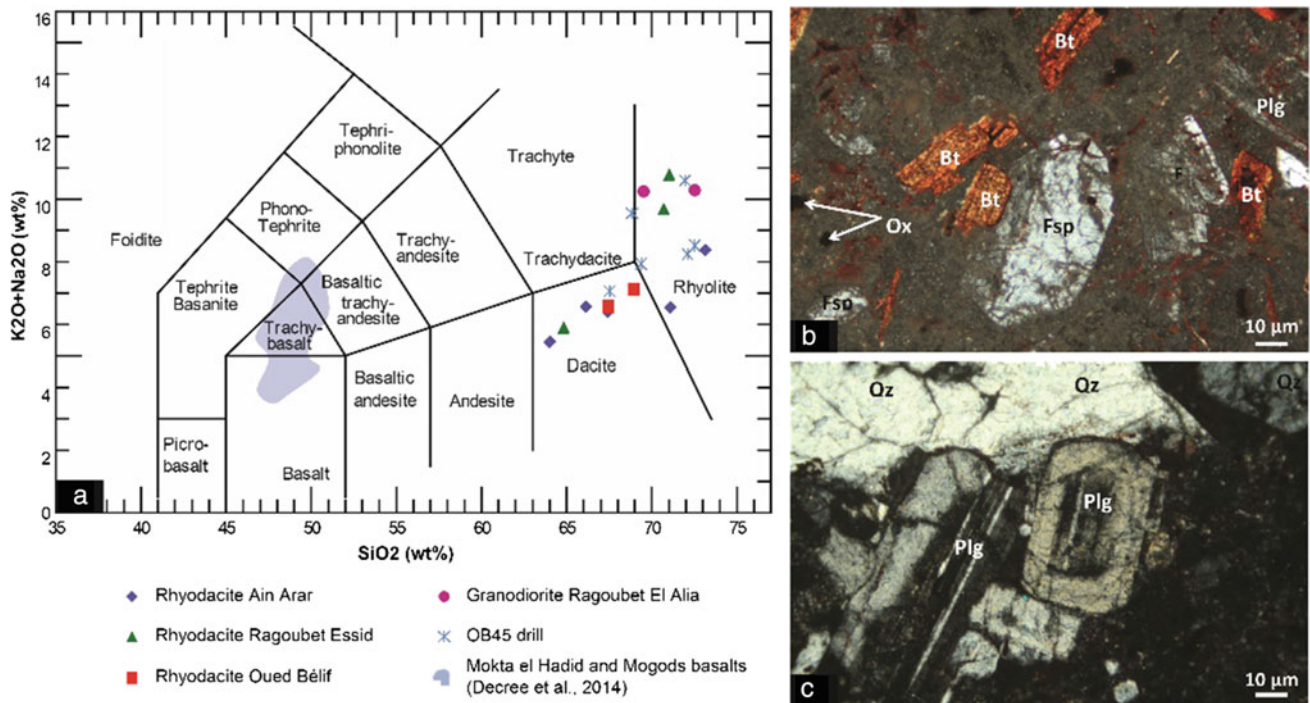


Fig. 2 a Total alkalis–silica (TAS) diagram (Le Maitre et al., 2002) showing the classification of the Miocene magmatic rocks in the Nefza area. b Photomicrograph of rhyodacite (OB45-12). c Photomicrographs

of granodiorite (OB45-77). Bt: biotite, Fsp: feldspar, Ox: oxide, Qz: quartz, Pl: plagioclase

polygenic breccia (65 to 90 m depths), sometimes greenish and rich in pyrite; (3) granodiorite (depth range from 90 to 380 m) (Fig. 1c).

3 Materials

The mineralogy and texture of the rocks were determined by standard petrography using transmitted and polarized light microscopy. Geochemical analyses (major and trace elements) were performed at the Geology Department of the Royal Museum for Central Africa, Belgium. All major element analysis were recalculated to 100% on anhydrous basis, following the recommendation of the International Community (Le Maitre et al., 2002).

4 Results

4.1 Major Elements and Petrography

The total alkali versus silica (TAS) classification diagram indicates an alkaline composition for the Nefza mining district and OB45 samples. Samples plot in the rhyolite, dacite and trachydacite fields (Fig. 2a) and consist mainly of granodiorite and rhyodacite. The rhyodacite is white-green

to light gray with a microlitic texture. It contains quartz, plagioclase (often zoned) with Carlsbad twinning sanidine, biotite and mesostasis glass (Fig. 2b). The granodiorite is made up of quartz (~ 20%), albite (\pm 30%) and orthoclase (35–40%). It has a fine-grained texture with crystal size of 2–3 mm (Fig. 2c).

4.2 Traces Elements Geochemistry

The chondrites normalized REE patterns (Fig. 3a) show that the rhyodacite and the granodiorite in OB45 have Σ REE 86–596 ppm and 147–366 ppm, respectively. Most rocks from the OB45 drill core show negative Eu anomalies ($0.51 < \text{Eu}/\text{Eu}^* < 0.68$ for rhyodacite and $0.40 < \text{Eu}/\text{Eu}^* < 0.61$ for granodiorite) indicating plagioclase fractionation. The La_N/Yb_N elemental abundance ratio is ranging from 28.4 to 80.6 and from 10.7 to 27.7 for the rhyodacite and granodiorite samples, respectively. The most altered samples from the OB45 drill core (OB45-26) have higher Σ REE (596 ppm) and higher La_N/Yb_N (80.6) suggesting LREE mobility during alteration.

The Nefza magmatic rocks exhibit primitive mantle-normalized spider diagrams (Fig. 3b) characterized by negative anomalies in Sr, Ba, Nb and positive anomalies in Rb, Pb and W. The Nefza granodiorite and rhyodacite rocks are

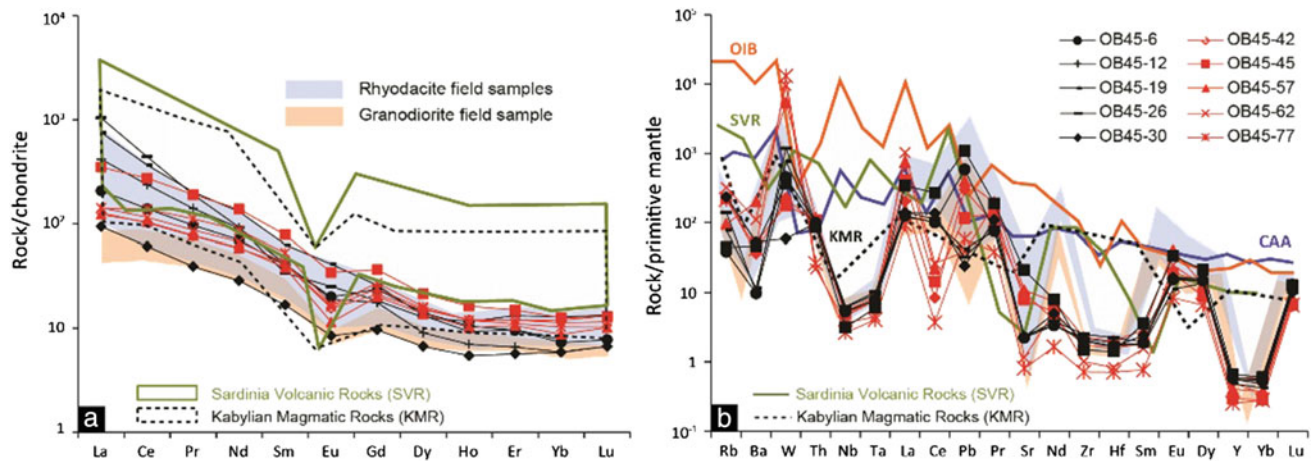


Fig. 3 REE patterns (a) and spider diagrams (b) of the Nefza magmatic rocks. Normalization values to the chondrites from Sun and McDonough (1989). Normalization values to the primitive mantle from Sun and McDonough (1989). Granodiorite are plotted in black and

rhyodacite in red. The OB45 sample locations are indicated in Fig. 1c. CAA: continental arc basalt; KMR: Kabylian Magmatic Rocks; OIB: Oceanic Island Basalt; SVR: Sardinia Volcanic Rocks

enriched in LILE (Rb, Ba, Pb) relative to HFSE (Nb, Ta, Hf, Zr). The granodiorite samples from the OB45 drill core are less enriched in LILE and more enriched in Zr, Hf and Y than the rhyodacite samples. For all samples, our results show enrichment in La, Pb, W and U. The surface samples of Nefza magmatic rocks have the same tendency as the OB45 drill samples.

5 Discussion and Conclusion

The Nefza magmatic rocks are depleted in HFSE (Hf, Zr, Nb and Ta) compared to the Continental Arc Andesite (CAA) and Oceanic Island Basalt (OIB) geochemical composition (Fig. 3b), which is characteristic of convergent plate boundaries (Zheng, 2019). The negative Nb–Ta anomaly measured in our samples is characteristic of calc-alkaline lavas which is also detected in the nearby Kabylian and Sardinia magmatic rocks (Fig. 1a). The Nefza calc-alkaline rocks (granodiorite and rhyodacite) are interpreted to be the result of partial melting of the lithospheric mantle. In this scenario, the lithosphere was metasomatized due to the uprise of the asthenosphere, in turn controlled by the oceanic subduction in the Eocene (Maury et al., 2000). However, the origin of the alkali basalts and basanites is most likely the result of mixing with deeper materials from an enriched asthenospheric mantle (Maury et al., 2000).

Regarding the geodynamic evolution, the magmatism associated with the slab breakoff started in Central Eastern Algeria at 16 Ma and then propagated eastwards and westwards (Carminati et al., 1998). We propose that the Algerian slab breakoff was responsible for the calc-alkaline volcanic activity in our studied area during the Serravallian (12 Ma).

Later, the rupture or the tearing of Calabrian slab, that occurred along the northern margin of Tunisia, produced Late Miocene volcanism (~ 8 Ma) (Faccenna et al., 2005). This slab breakoff or slab tearing can trigger upwelling and mixing of the mantle material and thus can explain the variations in geochemical composition of the magmatic rocks in the Nefza mining district.

Finally, we suggest that the geology of northern Tunisia may need to be revised to link the geodynamic evolution with deeper mantle processes. Additional samples and geochemical analyses are needed in combination with precise radiometric ages to date the timing of the different magmatic rocks in the area and reveal the mantle dynamic and the tectono-magmatic evolution of the western Mediterranean area.

References

- Carminati, E., Wortel, M. J. R., Spakman, W., & Sabadini, R. (1998). The role of slab detachment processes in the opening of the western-central Mediterranean basins: Some geological and geophysical evidence. *Earth and Planetary Science Letters*, 160(3–4), 651–665.
- Coulon, C., Megartsi, M., Fourcade, S., Maury, R. C., Bellon, H., Louni-Hacini, A., Cotten, J., Coutelle, A., & Hermitte, D. (2002). Post-collisional transition from calc-alkaline to alkaline volcanism during the Neogene in Oranie (Algeria): Magmatic expression of a slab breakoff. *Lithos*, 62(3–4), 87–110.
- Decrée, S., Marniac, C., Liégeois, J.P., Yans, J., Ben Abdallah, R., & Demaiffe, D. (2014). Miocene magmatic evolution in the Nefza district (Northern Tunisia) and its relationship with the genesis of polymetallic mineralizations. *Lithos*, 192–195, 240–258 (2014).
- Faccenna, C., Civetta, L., D’Antonio, M., Funicello, F., Margheriti, L., & Piromallo, C. (2005). Constraints on mantle circulation around the deforming Calabrian slab. *Geophysical Research Letters*, 32, L06311. <https://doi.org/10.1029/2004GL021874>

- Le Maitre, R. W., Streckeisen, A., Zanettin, B., Le Bas, M. J., Bonin, B., Bateman, P., Bellieni, G., Dudek, A., Efremova, S., Keller, J., Lameyre, J., Sabine, P. A., Schmid, R., Sorensen, H., & Woolley, A. R. (2002). *Igneous rocks: A classification and glossary of terms: Recommendations of the International Union of Geological Sciences, Subcommittee on the Systematics of Igneous Rocks* (236pp). Cambridge University Press (2002).
- Lustrino, M., & Wilson, M. (2007). The circum-Mediterranean anorogenic Cenozoic igneous province. *Earth-Science Reviews*, *81*, 1–65.
- Maury, R. C., Fourcade, S., Coulon, C., El Azzouzi, M., Bellon, H., Coutelle, A., Ouabadi, A., Semroud, B., Megartsi, M., Cotten, J., Belanteur, O., Louni-Hacini, A., Piqué, A., Capdevila, R., Hernandez, J., & Réhault, J.-P. (2000). Post-collisional Neogene magmatism of the Mediterranean Maghreb margin: A consequence of slab breakoff. *Comptes Rendus De L'academie Des Sciences. Serie III, Sciences De La Vie*, *331*, 159–173.
- Sun, S. S., & McDonough, W. F. (1989). Chemical and isotopic systematics of oceanic basalts: Implication for Mantle composition and processes. *Geological Society of London Special Publication*, *42* (1989).
- Zheng, Y.-F. (2019). Subduction zone geochemistry. *Geoscience Frontiers*, *10*, 1223–1254.



Amphibole-Veins Formation Within a Syn-Tectonic Contact Aureole (Elba Island, Italy)

Martina Zucchi, Andrea Brogi, and Domenico Liotta

Abstract

The eastern part of Elba Island (northern Tyrrhenian Sea, Italy) is an exhumed sector of thinned continental crust, intruded by a monzogranitic pluton during the Messinian. Pluton emplacement occurred at a depth of c. 6 km as a consequence of permeability enhancement in the upper crust due to extensional tectonics. The contact aureole records coeval intense circulation of geothermal fluids and deformation. Here, we describe syn-tectonic amphibole + quartz veins that cross the contact aureole and are associated with extensional structures that formed during contact metamorphism. These veins (shear and extensional veins) are perpendicular or sub-parallel to the main foliation of the host rock and are either arranged in en-echelon arrays or developed in extensional jogs. Calcite, chlorite and titanite occur as accessory minerals in the veins. The interaction between hot fluids and host rocks produced localized metasomatism indicated by white haloes symmetrically developed adjacent to the veins. Fluid inclusions in quartz from amphibole + quartz veins are of two types: (i) two-phase liquid-rich and (ii) two-phase vapor-rich, in which the vapor phase includes mostly CO₂ with minor amounts of CH₄ and N₂, the latter detected by Raman spectroscopy. Microthermometry indicates maximum temperatures of ~ 500 °C, assuming a maximum P of about 0.8 kbar and salinity up to 6.4 wt% NaCl equivalent, suggesting a metamorphic origin.

Keywords

Contact aureole • Extensional tectonics • Fluid-rock interaction • Fluid inclusions • Elba Island

1 Introduction

When magma cooling is coeval with crustal extension, the development of its contact aureole is mostly controlled by the fault activity responsible for granite unroofing and exhumation (e.g., Bouillin et al., 1993; Dilek et al., 2009; Peccerillo, 2003). Thus, the heat released by the magmatic intrusion produces thermal perturbations impelling metamorphic processes in the host rocks and geothermal fluid circulation within the contact aureole. Commonly, fluids flow is focused either along fault zones, especially if rocks are characterized by very low primary permeability or within permeable levels hydraulically connected to the main fault zone. Here, we study a paleo-geothermal system recorded at the eastern sector of Elba Island (Tuscan Archipelago, Italy; Fig. 1) which is considered to be the fossil exhumed analogue of the Larderello active geothermal field (Tuscany, Italy). In the study area, the local fault system controlled the hydrothermal fluid circulation driven by the cooling of the magmatic pluton, named Porto Azzurro (6.53–6.4 Ma; Gagnevin et al., 2011; Spiess et al., 2021), and emplaced at 6–7 km depth in a regional transfer zone (Dini et al., 2008; Liotta et al., 2015; Fig. 1). The results highlight (i) how brittle deformation induces fluid flow in rocks of very low permeability triggering fluid-rock interaction processes and (ii) the chemical–physical features of the paleo-geothermal fluid (Zucchi, 2020).

2 Methods

Fieldwork included field mapping at 1:10,000 scale and structural and kinematic data collection in 13 stations. Samples of host rocks, mineralization on the fault slip

M. Zucchi (✉) · A. Brogi · D. Liotta
Department of Earth and Geoenvironmental Sciences, University of Bari, Bari, Italy
e-mail: martina.zucchi@uniba.it

A. Brogi · D. Liotta
National Research Council - Institute of Geosciences and Earth Resources, (IGG-CNR), Pisa, Italy

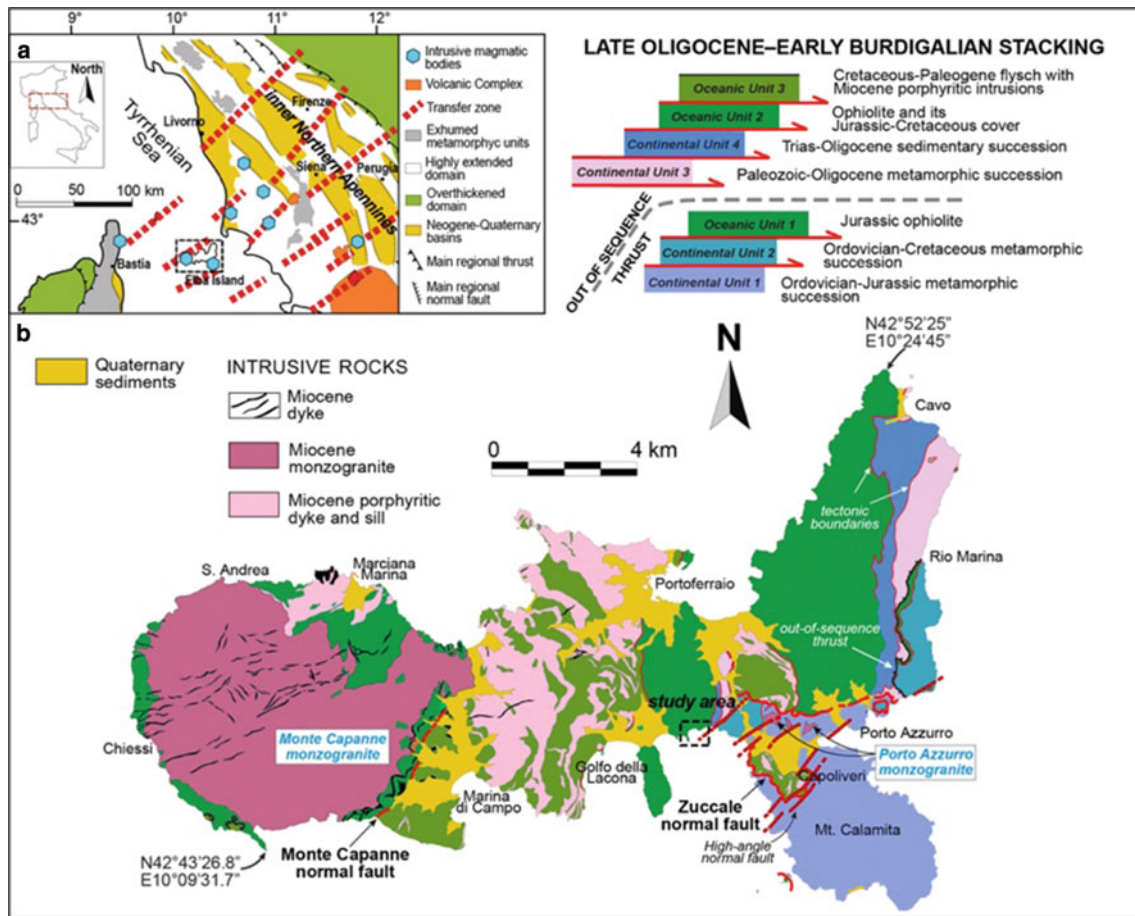


Fig. 1 a Structural sketch map of the Northern Apennines and Northern Tyrrhenian Sea; b structural sketch map of Elba Island and location of the study area (in the black dotted square)

surface and veins were collected for petrographic and fluid inclusion analyses (both performed at the University of Bari) to reconstruct the mineral paragenesis and the chemical–physical features of the paleo-fluid, respectively.

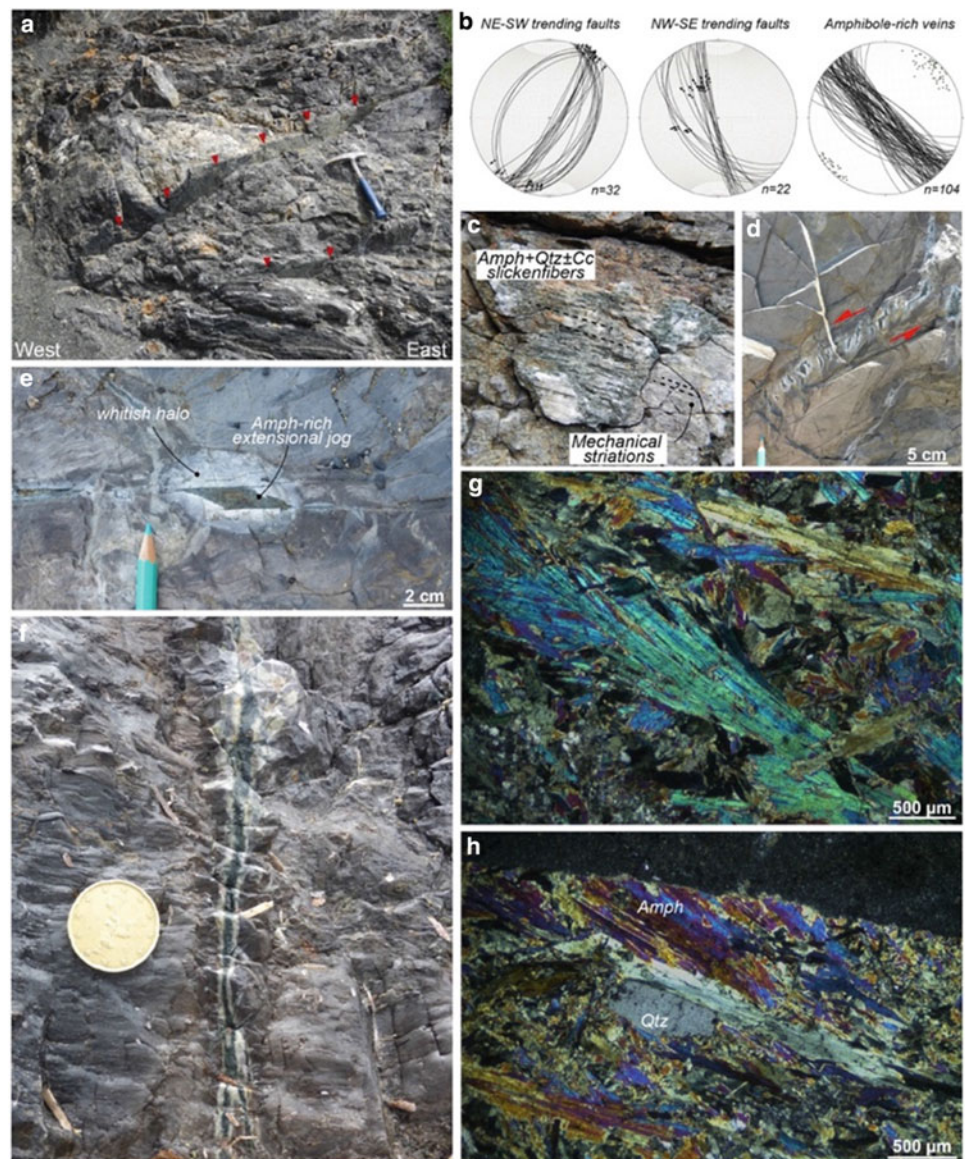
3 Results

3.1 Geological and Structural Setting

The study area includes Norsi and Acquarilli beaches and is located in the south-eastern part of Elba Island, within the Porto Azzurro contact aureole. The exposed metamorphic rocks are derived from a sedimentary succession belonging to the uppermost Ligurian Units cropping out at Elba Island. The succession consists of decimeter- to meter-thick pelites with interlayered siliceous limestone and marly levels (Argille a Palombini Fm; lower Cretaceous) tectonically interposed with the Jurassic oceanic basement (mainly serpentinitized lherzolite and harzburgite). Structural and

kinematic data indicate that different generations of faults have affected these rocks: (i) low-angle normal faults that thinned the tectonic pile at the end of the collisional processes of the Northern Apennines (Cretaceous–early Miocene), which are systematically cross-cut by (ii) high-angle normal to oblique-slip faults. The latter show two different trends: NE–SW and NW–SE, both characterized by offsets ranging from some decimeters to meters (Fig. 2). Kinematic indicators on the slip surfaces of these faults are amphibole + quartz ± calcite slickenfibers, highlighting different movements for the two faults systems and mechanical striations (Fig. 2b, c). The NE-trending faults show strike- to oblique-slip kinematics, whereas the NW-trending faults are characterized by right-lateral oblique slip movements (Fig. 2b). In both fault systems, the fault damage zone is characterized by minor structures (i.e., extensional jogs and en-echelon veins; Fig. 2d, e) with kinematics compatible with the movements observed on the fault slip surface. These structures are mineralized with the same mineral paragenesis as the slickenfibers on the fault planes.

Fig. 2 **a** Example of high-angle NW-trending normal faults; **b** stereographic diagrams (equal-area projection, lower hemisphere) of faults and striae and amphibole-rich veins; **c** kinematic indicators consisting of slickenfibers and mechanical striations; **d, e** minor structures associated with the high-angle normal faults mineralized mainly by amphibole + quartz and characterized by whitish halo; **f** sub-vertical amphibole-rich vein with millimeter thick whitish halo; **g** cross polarised light (CP) micrograph showing fibrous amphibole crystals; **h** CP micrograph of preferentially oriented amphibole crystals, indicating that minerals growth was contemporaneous with fault activity. Mineral abbreviation: Amph = amphibole; Qtz = quartz; Cc = calcite



3.2 Fluid-Rock Interaction

The emplacement and gradual heat loss of the Porto Azzurro pluton produced a thermal aureole that hosted an intense geothermal fluid circulation. In the metapelites, this fluid circulation enhanced metasomatic processes forming amphibole + quartz \pm chlorite \pm calcite \pm titanite veins that are parallel or orthogonal to the main foliation. These veins, up to 3 cm thick and 30 cm long (Fig. 2f), are characterized by a symmetrical whitish halo mainly made up of plagioclase + quartz + biotite + muscovite + ilmenite at the contact with metapelites, recording fluid-host rock interaction. The same mineral assemblage occurs on the slip surface of the high-angle normal faults and associated minor structures. This suggests syn-kinematic growth, particularly of amphibole, which usually occurs as elongated fibers oriented

parallel to the fault's kinematics (Fig. 2g, h). SEM-EDS analyses indicate that amphibole has a composition spanning from ferro-actinolite to actinolite, whereas plagioclase varies from labradorite to anorthite in composition moving from the vein to the host metapelite.

3.3 Fluid Inclusion Analyses

Fluid inclusions were studied in hydrothermal quartz and calcite developed on the fault slip surface (Zucchi, 2020). Based on optical observations at room temperature, fluid inclusions hosted in quartz vary from a few to 30 μm in size and consist of two types: (i) two-phase vapor-rich (VL) and (ii) two-phase liquid-rich (LV). The first type frequently shows elongated or rounded shapes and is arranged along

trails geometrically perpendicular to the amphibole + quartz \pm calcite slickenfibers. LV inclusions also occur along trails and usually show elongated or irregular shapes. The textural relationships between these two inclusion types indicate that LV inclusions cross-cut the VL-type suggesting that their trapping occurred subsequently. In calcite, only LV-type was recognized, usually arranged along twinning planes. Microthermometric analyses of selected FIAs (fluid inclusion assemblages) indicate the presence of CO₂, mostly in VL-type with T_{mCO2} (melting temperature of CO₂) values between -56.6 and -57.5 °C and minor amount of CH₄ and N₂. Homogenization temperatures (T_h) of VL inclusions occurred to the vapor phase, with values between 296 and 349 °C. LV inclusions in quartz show T_h (to the liquid phase) from 261 to 359.8 °C, whereas inclusions hosted in calcite show T_h from 252.6 to 351.3 °C. Salinity calculated for VL and LV inclusion types ranges between 4.2–5.0 and 1.0–6.4 wt% NaCl eq., respectively.

4 Discussion

Structural data collected in the study area revealed the occurrence of high-angle normal faults characterized by two trends. These faults, which show right-lateral oblique slip to normal movements, are characterized by amphibole + quartz \pm calcite slickenfibers on their slip surfaces. This suggests a syn-tectonic geothermal fluid flow and the simultaneous activity of both fault systems, within the same, common, stress field. This indicates that the fluid flow was strictly controlled by the geometry of the fault zones, channeling fluids from deep to shallow levels. Mechanical striations on fault slip surfaces indicates that the tectonic activity continued after mineralization. P–T trapping conditions of the geothermal fluids were estimated based on fluid inclusion microthermometry and textural relationships between VL- and LV-types. Isochores for VL inclusions were computed by ISOC software (Bakker, 2003), showing trapping temperatures (T_t) between 495 and 475 °C at a maximum P of about 0.8 kbar, whereas isochores for LV inclusions were computed by HokieFlincs Microsoft spreadsheet (Steele-MacInnis et al., 2012), indicating T_t from 430 to 330 °C and 430 to 315 °C in quartz and calcite, respectively. VL inclusions are mainly arranged along trails reflecting a cyclic cracking and sealing process in the already-formed quartz crystals (Montomoli et al., 2001). The presence of CO₂ suggests that it was derived by partial decarbonation of siliceous limestone horizons within the Argille a Palombini Fm.

5 Conclusions

Structural and kinematic data collected in the study area demonstrate how geothermal fluid circulation within a contact aureole is mostly controlled by brittle structures. Understanding fluid paths is a fundamental information, especially when dealing with low permeable rocks, which are usually assumed to be the caprocks of any geothermal system.

References

- Bakker, R.J. (2003). Package FLUIDS 1. Computer programs for analysis of fluid inclusion data and for modelling bulk fluid properties. *Chemical Geology*, 194, 3–23 (2003)
- Bouillin, J. P., Bouchez, J. L., Lespinasse, P., & Pecher, A. (1993). Granite emplacement in an extensional setting; an AMS study of the magmatic structures of Monte Capanne (Elba, Italy). *Earth Planetary Science Letters*, 118, 263–279.
- Dilek, Y., Altunkaynak, S., & Öner, Z. (2009). Syn-extensional granitoids in the Menderes core complex and the Late Cenozoic extensional tectonics of the Aegean province. *Geological Society of London Special Publications*, 321, 197–223.
- Dini, A., Westerman, D. S., Innocenti, F., & Rocchi, S. (2008). Magma emplacement in a transfer zone: The Miocene mafic Orano dyke swarm of Elba Island, Tuscany, Italy. *Geological Society of London Special Publication*, 302, 131–148.
- Gagnevin, D., Daly, J. S., Horstwood, M. S. A., & Whitehouse, M. J. (2011). In-situ zircon U-Pb, oxygen and hafnium isotopic evidence for magma mixing and mantle metasomatism in the Tuscan Magmatic province, Italy. *Earth and Planetary Science Letters*, 305(1–2), 45–56.
- Liotta, D., Brogi, A., Meccheri, M., Dini, A., Bianco, C., & Ruggieri, G. (2015). Coexistence of low-angle normal and high-angle strike-to oblique-slip faults during Late Miocene mineralization in eastern Elba Island (Italy). *Tectonophysics*, 660, 17–34.
- Montomoli, C., Ruggieri, G., Boiron, M. C., & Chatelineau, M. (2001). Pressure fluctuation during uplift of the Northern Apennines (Italy): A fluid inclusions study. *Tectonophysics*, 341, 121–139.
- Peccerillo, A. (2003). Plio-quaternary magmatism in Italy. *Episodes*, 26, 222–226.
- Spiess, R., Langone, A., Caggianelli, A., Stuart, F. M., Zucchi, M., Bianco, C., Brogi, A., & Liotta, D. (2021). Unveiling ductile deformation during fast exhumation of a granitic pluton in a transfer zone. *Journal of Structural Geology*, 147, 104326.
- Steele-MacInnis, M., Lecunberri-Sanchez, P., & Bodnar, R. J. (2012). HOKIEFLINCS_H₂O–NaCl: A microsoft excel spreadsheet for interpreting microthermometric data from fluid inclusions based on the PVTX properties of H₂O–NaCl. *Computers & Geosciences*, 49, 334–337.
- Zucchi, M. (2020). Faults controlling geothermal fluid flow in low permeability rock volumes: An example from the exhumed geothermal system of eastern Elba Island (northern Tyrrhenian Sea, Italy). *Geothermics*, 85, 101765.



Diagenesis of Diapir Flanking Successions: The Moroccan High Atlas and Other Tethyan Salt-Related Basins

Mar Moragas, David Cruset, Vinyet Baqués, Juan Diego Martín-Martín, Jordi Martín, Anna Travé, and Jaume Vergés

Abstract

During the last decade, several studies have investigated the impact of diapirism in the diagenesis of the flanking sediments, as they are potential targets for the exploration of mining and energetic resources. These diagenetic processes are closely related to the tectonic evolution of the salt structures. The Tazoult and the Toumliline diapirs case studies display excellent exposures in the Central High Atlas (Morocco). Petrographic observations and geochemical analyses of Jurassic carbonate halokinetic sequences bounding both salt diapirs reveal similar diagenetic phases, which are: (1) saddle dolomites replacing both carbonate host-rock and fracture filling cements and (2) calcite cements and calcitized dolomite linked to meteoric water percolation. Coarse crystalline saddle dolomite ($\delta^{13}\text{C}$ ranging from -3.56 to -1.79% VPDB, and $\delta^{18}\text{O}$ ranging from -7.45 to -5.19% VPDB) are attributed to the circulation of hot Mg-rich brines in the vicinity of diapir structures during their passive growth. In contrast, meteoric percolation and the associated calcite cements, characterized by Mn content above 2000 ppm, and calcitized dolomite are attributed to later stages in the evolution of diapiric structures, most likely during their Alpine compressional deformation and inversion. Results indicate similar diagenetic evolution and geodynamic context to those described in other salt-related basins in

the Tethyan domain such as in the Pyrenean Trough, Betic Margin, Cantabrian Basin, Iberian Basin, Causses Basin, and Tunisian Atlas Margin.

Keywords

Diapir • Fluid flow • Diagenesis • Tethyan basins

1 Introduction

The diagenetic history of carbonates flanking salt diapirs can be complex as fluid flow pathways and chemistry can differ substantially through space and time due to evolution of diapirs (Fischer et al., 2013; Reuning et al., 2009). The understanding of the processes that controls the diagenetic overprinting of the carbonate host rocks in diapiric settings is essential in the analysis of reservoir quality, distribution of ore deposits and other natural resources. Most of these studies, however, are handicapped by the lack of continuous outcrops or well data availability. In this regard, the well-exposed lower Jurassic carbonates flanking the Tazoult and the Toumliline diapirs (Central High Atlas of Morocco) represent an excellent opportunity to compare the diagenetic evolution in two different structures, looking for similarities and patterns that can be equivalent to those observed in others salt-related basins of the Tethyan domain.

2 Geological Setting

Field and petrographic observations, and geochemical analysis, were carried out in two diapiric structures from the Central High Atlas (Fig. 1a), which has been reported as a world-class example of a diapiric basin where salt-related structures were active during, at least, Early and Middle Jurassic times, and reactivated during the Alpine compression (Saura et al., 2014).

M. Moragas (✉) · D. Cruset · J. Vergés
Group of Dynamics of the Lithosphere (GDL), Geosciences
Barcelona (Geo3BCN-CSIC), 08028 Barcelona, Spain
e-mail: mar.moragas@uib.no

M. Moragas
Department of Earth Science, University of Bergen (UiB),
5020 Bergen, Norway

V. Baqués · J. D. Martín-Martín · A. Travé
Departament de Mineralogia, Petrologia i Geologia Aplicada,
Universitat de Barcelona (UB), 08028 Barcelona, Spain

J. Martín
Departament de Geologia, Universitat Autònoma de Barcelona,
08193 Cerdanyola del Vallès, Spain

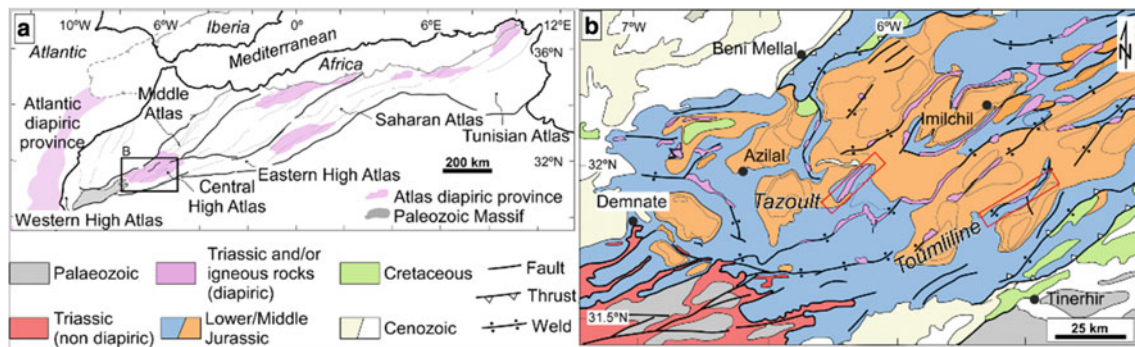


Fig. 1 **a** Synthetic map of NW Africa showing the location of the most important diapiric areas in the Atlas system (pink). **b** Geological map of the Central High Atlas showing the location of the Tazoult and the Toumliline diapirs (red square). Modified from Martín-Martín et al. (2017)

The Tazoult diapir is a NE-SW-trending elongated salt wall 20 km long and 0.6–3 km wide (Fig. 1b), characterized by a core made of Late Triassic claystones that includes blocks (slivers) of Hettangian-Lower Sinemurian carbonates and Middle Jurassic gabbro intrusions. Both flanks of the structure include sub-vertical Pliensbachian platform carbonates and late Pliensbachian-Aalenian mixed siliciclastic-carbonate successions (Martín-Martín et al., 2017).

The Toumliline is an ENE-WSW-trending elongated salt wall 8 km long and 0.5–2.5 km wide (Fig. 1b), with welded terminations and a core made of Late Triassic claystones and evaporites with Bathonian gabbro intrusions (Middle Jurassic). The eastern weld has a south flank made of Sinemurian (Early Jurassic) carbonates and a northern flank made of Aalenian-Bajocian (Middle Jurassic) carbonates (Saura et al., 2014).

3 Results

3.1 Tazoult Diapir

According to crosscut relationships, petrography and geochemistry used to build the paragenesis and link it with Tazoult diapir growth phases, the diagenetic story of the Tazoult diapir is characterized by three main stages:

Pliensbachian stage (i) is characterized by early diagenetic alterations including replacive dolomite, karstic breccias (linked to the exposure of the platform carbonates) and calcite cements (Moragas et al., 2020). Post-Pliensbachian stage (ii) is characterized by burial diagenesis, with calcite cements and saddle dolomites in fractures ($\delta^{13}\text{C}$ between -4.3 and $+2.7\text{‰}_{\text{VPDB}}$, and $\delta^{18}\text{O}$ between -16.8 and $-1.76\text{‰}_{\text{VPDB}}$ (Fig. 2). The youngest stage (iii) expands

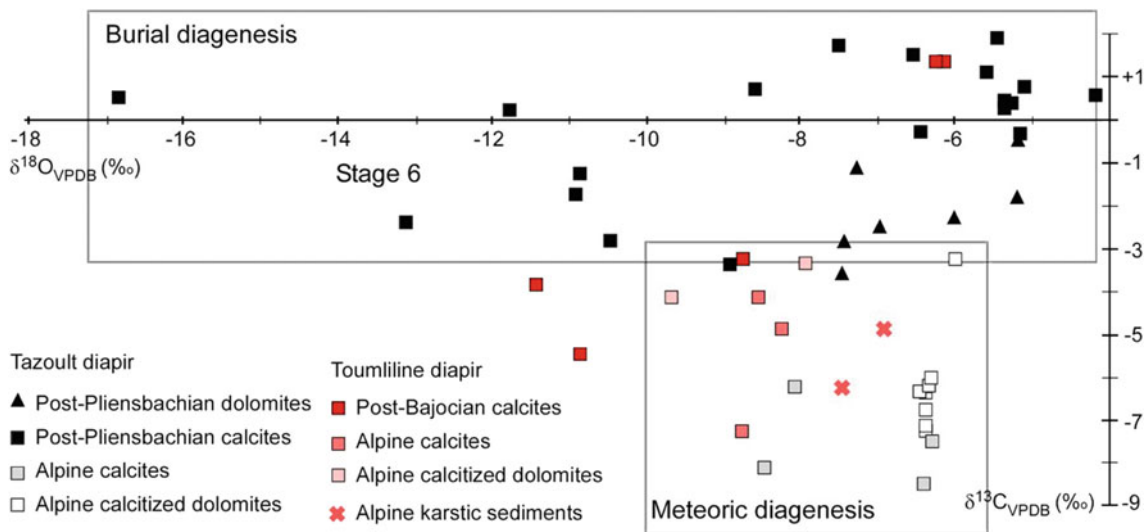


Fig. 2 $\delta^{18}\text{O}$ - $\delta^{13}\text{C}$ plot of diagenetic phases encountered in the Tazoult and the Toumliline diapirs arranged according to the defined diagenetic stages (black polygons)

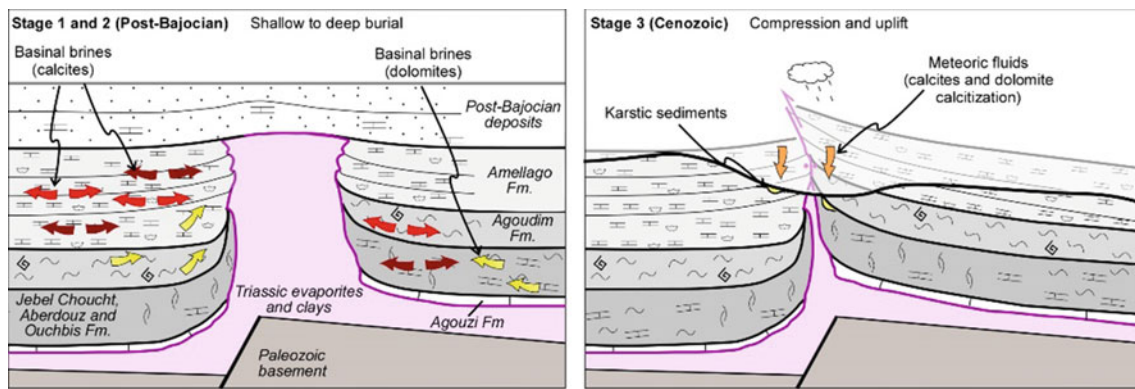


Fig. 3 Diagenetic model for the Toumliline diapir including Post-Bajocian and Cenozoic stages

from Late Cretaceous to recent times episode (Alpine Orogeny) with calcitized dolomite and calcite cements ($\delta^{13}\text{C}$ between -8.46 and $-3.25\text{‰}_{\text{VPDB}}$, and $\delta^{18}\text{O}$ between -8.41 to -6‰_{VPDB}).

3.2 Toumliline Diapir

Three main stages can be differentiated in the diagenetic story of the flanking carbonates of the Toumliline diapir. The earliest diagenetic stage, (i) pre-Bajocian in age, includes replacive dolomite. Post-Bajocian stage (ii) is characterized by several phases that record the transition from shallow to deep burial diagenesis (Fig. 2), with calcite cements and saddle dolomites in fractures ($\delta^{13}\text{C}$ from -5.56 to $+1.37\text{‰}_{\text{VPDB}}$, and $\delta^{18}\text{O}$ from -11.3 to $-6.05\text{‰}_{\text{VPDB}}$). The youngest stage (iii) is the Late Cretaceous to recent Alpine Orogeny (Fig. 2) characterized by calcitized dolomite, calcite cements and karstic sediments ($\delta^{13}\text{C}$ from -7.79 to $-3.58\text{‰}_{\text{VPDB}}$, and $\delta^{18}\text{O}$ from -9.92 to $-6.93\text{‰}_{\text{VPDB}}$).

4 Discussion

The diagenetic evolution of both structures has relevant similarities: during the passive growth of diapirs, diagenesis transitioned from shallow to deep burial realms, characterized by the precipitation of oxygen-depleted calcite cements and saddle dolomite precipitated from warmed basinal brines (Fig. 3). Contrarily, compression and inversion of diapiric basins reactivated salt tectonics resulting in salt (thrust) welds and exposure of flanking sediments. Late Cretaceous to recent (Alpine Orogeny) allowed percolation of meteoric fluids causing calcitization of dolomite, precipitation of calcite cements and karstification (Fig. 3). Observed diagenetic patterns in the Central High Atlas case study have been also reported in other diapiric structures from the Tethyan domain.

In the Cantabrian and Pyrenean Basins (Motte et al., 2021; Perona et al., 2018), saddle dolomite precipitation occurred during passive diapir growth due to circulation of basinal hydrothermal fluids. Meteoric fluid circulation during diapir inversion is reported in the Pyrenees (Cruset et al., 2021) and the Tunisian Atlas (Bejaoui et al., 2013) fold belts.

5 Conclusions

Central High Atlas examples show comparable patterns in terms of diagenetic evolution. These are characterized by periods of diapir growth and fossilization/burial dominated by the circulation of warm basinal fluids and periods of diapiric basin inversion characterized by meteoric percolation. Several diapiric basins from the Tethyan domain show similar patterns. The obtained results show that diapirs play a major role on the diagenetic evolution of minibasins and highlight that further work needs to be done to improve diapir-related diagenesis models for later apply them as subsurface analogues.

Acknowledgements This work is funded by the ALORBE project (PIE-CSIC-202030E310), the research groups “Grup de Modelització Geodinàmica de la Litosfera” (2017-SGR-847) and “Geologia Sedimentària” (2021 SGR-Cat 00349) funded by the Generalitat de Catalunya, and the DGICYT Spanish project PID2021-122467NB-C22 and PGC2018-093903-B-C22 (MICIU/AEI/10.13039/501100011033/FEDER, UE). David Cruset acknowledges the Spanish MICIU for the “Juan de la Cierva Formación” fellowship FJC2020-043488-I AEI/10.13039/501100011033.

References

- Bejaoui, J., Bouhlel, S., Cardellach, E., Canals, À., Perona, J., & Piqué, À. (2013). Mineralization and fluid inclusion studies of the Aptian carbonate-hosted PbZnBa ore deposits at Jebel Hamra, Central Tunisia. *Journal of Geochemical Exploration*, 128, 136–146.

- Cruset, D., Vergés, J., Benedicto, A., Gomez-Rivas, E., Cantarero, I., John, C. M., & Travé, A. (2021). Multiple fluid flow events from salt-related rifting to basin inversion (Upper Pedraforca thrust sheet, SE Pyrenees). *Basin Research*, 33(6), 3102–3136.
- Fischer, M. P., Kenroy, P. R., & Smith, A. P. (2013). Fluid systems around salt diapirs. *AAPG Search and Discovery*, #50902, 1–29.
- Martín-Martín, J. D., Vergés, J., Saura, E., Moragas, M., Messenger, G., Baqués, V., Razin, P., Grélaud, C., Malaval, M., Jousiaume, R., Casciello, E., Cruz-Orosa, I., & Hunt, D. W. (2017). Diapiric growth within an Early Jurassic rift basin: The Tazoult salt wall (central High Atlas, Morocco) [Article]. *Tectonics*, 36(1), 2–32.
- Moragas, M., Baqués, V., Travé, A., Martín-Martín, J. D., Saura, E., Messenger, G., Hunt, D., & Vergés, J. (2020). Diagenetic evolution of lower Jurassic platform carbonates flanking the Tazoult salt wall (Central High Atlas, Morocco). *Basin Research*, 32(3), 546–566.
- Motte, G., Hoareau, G., Callot, J.-P., Révillon, S., Piccoli, F., Calassou, S., & Gaucher, E. C. (2021). Rift and salt-related multi-phase dolomitization: Example from the northwestern Pyrenees. *Marine and Petroleum Geology*, 126, 104932.
- Perona, J., Canals, À., & Cardellach, E. (2018). Zn-Pb Mineralization Associated with Salt Diapirs in the Basque-Cantabrian Basin, Northern Spain: Geology, Geochemistry, and Genetic Model. *Economic Geology*, 113(5), 1133–1159.
- Reuning, L., Schoenherr, J., Heimann, A., Urai, J. L., Littke, R., Kukla, P. A., & Rawahi, Z. (2009). Constraints on the diagenesis, stratigraphy and internal dynamics of the surface-piercing salt domes in the Ghaba Salt Basin (Oman): A comparison to the Ara Group in the South Oman Salt Basin. *GeoArabia*, 14(3), 83–120.
- Saura, E., Vergés, J., Martín-Martín, J. D., Messenger, G., Moragas, M., Razin, P., Grélaud, C., Jousiaume, R., Malaval, M., & Homke, S. (2014). Syn-to post-rift diapirism and minibasins of the Central High Atlas (Morocco): The changing face of a mountain belt. *Journal of the Geological Society*, 171(1), 97–105.



Radiogenic Heat Production and Rare-Metal Mineralization Affinity of Anorogenic Acid Volcano-Plutonic Rocks from Neoproterozoic Tusham Ring Complex, NW Indian Shield. Constraints on Radioactive, Trace and Rare Earth Element Distributions

Naresh Kumar and Naveen Kumar

Abstract

Data on radio-elemental abundances, radiogenic heat production and rare-metal affinity of acid volcano-plutonic rocks of Riwasa, Nigana, Dulheri, Dharan, Khanak, Dadam, Devsar and Tusham areas of Neoproterozoic Tusham Ring Complex (TRC) in the NW Indian Shield, are presented in this paper. Geochemically, the investigated rock types consist of hypersolvus to subsolvus, peraluminous and high-K calc-alkaline to shoshonitic A-type granitoids that are characterized by high SiO₂ (59.56–75.73), K₂O + Na₂O (4.28–9.37), K/Na, Fe/Mg, Ga/Al, Rb/Sr, Th/U, Rb, Zr, Nb, Y, Th, U, REE (except, Eu), halogens (F & Cl) and low CaO (0.03–2.56), MgO (0.07–0.99), Sr, Cr, Ni, P and Eu in abundances. The enrichment of LILE (K, Rb, Ba) and HFSE (Zr, Nb, REE, Th, U), collectively, is attributed to high heat-producing (HHP) and rare-metal bearing granitoids. The acid volcanics of Riwasa and Tusham show wide variations of U (4.70–26.10 ppm), Th (19–145 ppm), Th/U (3.56–15.91), heat production (HP: 3.04–15.30 uWm⁻³), heat generation unit (HGU: 7.24–36.3 uWm⁻²) whereas the granitic massifs of Nigana, Dulheri, Dharan, Khanak, Devsar and Dadam show range of U (2.50–35.60 ppm), Th (17–124 ppm), Th/U (3.93–20 ppm), HP (3.03–16.63 uWm⁻³) and HGU (7.22–39.37 uWm⁻²), respectively. Moreover, the studied granitoids have much higher values of HP and HGU than the average values of continental crust (3.8 HGU), which indicate a ‘hot crust’ category and a possible linear relationship among the radioactive heat production, surface heat flow and crustal heat generation in the acid volcano-plutonic rocks of TRC. The elemental geochemistry and mineral chemistry in conjunction with

radioactive element distribution (U, Th, K) suggest the possibility of important rare metals and rare earth metals (RMREM) mineralization, i.e., Sn–W, Nb–Sn, Sn–W–Be, porphyry Cu, U–Th and Rb–Ba, respectively, in the study areas.

Keywords

A-type • Radiogenic heat production • Rare-metal granitoids • Mineralization • Tusham Ring Complex • Malani Igneous Suite

1 Introduction

Radiogenic heat production (RHP) is genetically related to the heat produced by the decay of radioactive elements, i.e., U, Th and K (Gard et al., 2019). Therefore, the granitoids which have general crustal abundances 3–4 ppm of U; 10–15 ppm of Th and Th/U ratio of 3.7 are identified as HHP granitoids (Clark et al., 1990). Such granitoids play an important role to sustain ‘heat engine’ in continental crust and enhanced the probability of circulation of ore-bearing hydrothermal fluids. The high heat-producing (HHP) granitoids in India were reported from Bundelkhand craton, Dharwar craton, Rajasthan and eastern Singhbhum and have geological ages ranging from Archaean to Neoproterozoic with heat production up to 13 μWm⁻³ (Artemieva et al., 2017). Worldwide, HHP granitoids were also found in Asia, Africa, North America, South America, Europe, Antarctica and Australia. Nevertheless, the distribution of heat-producing elements (HPEs) that heat the lithosphere internally is poorly constrained in the context of NW Indian shield.

HHP granitoids are economically important because of their association with some ore deposits and their potential for geothermal energy. To understand the heat production and related mineralization, this paper also systematizes and

N. Kumar (✉) · N. Kumar
Kurukshetra, India
e-mail: sagwal_naresh@kuk.ac.in

N. Kumar
Department of Geology, Kurukshetra University, Kurukshetra,
Kurukshetra, India

integrates the geological, geochemical and the tectono-magmatic evolutionary processes. The rocks of MIS exposed in Siwana Ring Complex, Nakora Ring Complex, Jalor Ring Complex and Jhunjhunu Ring Complex were studied very well, and we have extensive knowledge about their age, composition and origin. Unfortunately, there is lack of information about the radio-elemental distribution and related rare metals and rare earth metals (RMREM) mineralization in Tusham Ring Complex (TRC).

2 Geological Framework

The anorogenic and felsic magmatism of MIS was supposed to be operated by hotspot/mantle plume tectonics during the Neoproterozoic time (Kumar et al., 2020). The MIS (bimodal, anorogenic, plume-related, area: 55,000 km², thickness: 3–7 km, age: ~ 780–750 Ma) manifested in NW India is a Precambrian silicic large igneous province and represented later by Pan-African thermo-tectonic event (Kumar et al., 2020). The representatives of such felsic magmatism are well exposed and reported from Tusham (SW Haryana), Siwana, Nakora, Jhunjhunu, Jalor, Jodhpur, Mokalsar, Mt. Abu, Sirohi (W Rajasthan) and Kirana, Nagarparkar (SE Pakistan) areas (Kumar et al., 2020). Tusham Ring Complex (TRC) was considered as an extension of MIS (Kumar et al., 2020). The important exposures of MIS are sketched in geological map (Fig. 1a), and the

geology of the studied region is plotted in the simplified geological map of TRC (Fig. 1b).

3 Distribution of Radioactive Elements and Geochemical Controlling Factors

Granitoids, which are rich in radioactive heat-producing elements like uranium, thorium and potassium, are the most common sources of radioactive heat production. The distribution of radioactive elements is genetically linked with the lithology and formation environment. A genetic relationship was also suggested between acid magmatism and the formation of radioactive elements (Simpson and Plant, 1984). The high degree of fractionation of magma in Malani Igneous Suite was considered as an important geochemical factor in the extreme enrichment of U and Th. The geochemical variations in terms of major oxides are major controlling factors in the distribution and migration of radioactive, trace and rare earth elements in the primary magma. The present obtained values ($Th_{mean} 119.5 \pm 25.5$, $U_{mean} 12.9 \pm 6.3$ in ppm for TRC rhyolites, $Th_{mean} 69.0 \pm 52.0$, $U_{mean} 19.05 \pm 16.55$ in ppm for TRC granites and $Th_{mean} 56.0 \pm 37.0$, $U_{mean} 15.4 \pm 10.7$ in TRC felsites) are considerable above the well-established database on worldwide granites (GRANITE2017, Artemieva et al., 2017) that reported 14.8 ± 13.2 ppm as the mean Th content and 3.93 ± 3.27 ppm as the mean U content in granites.

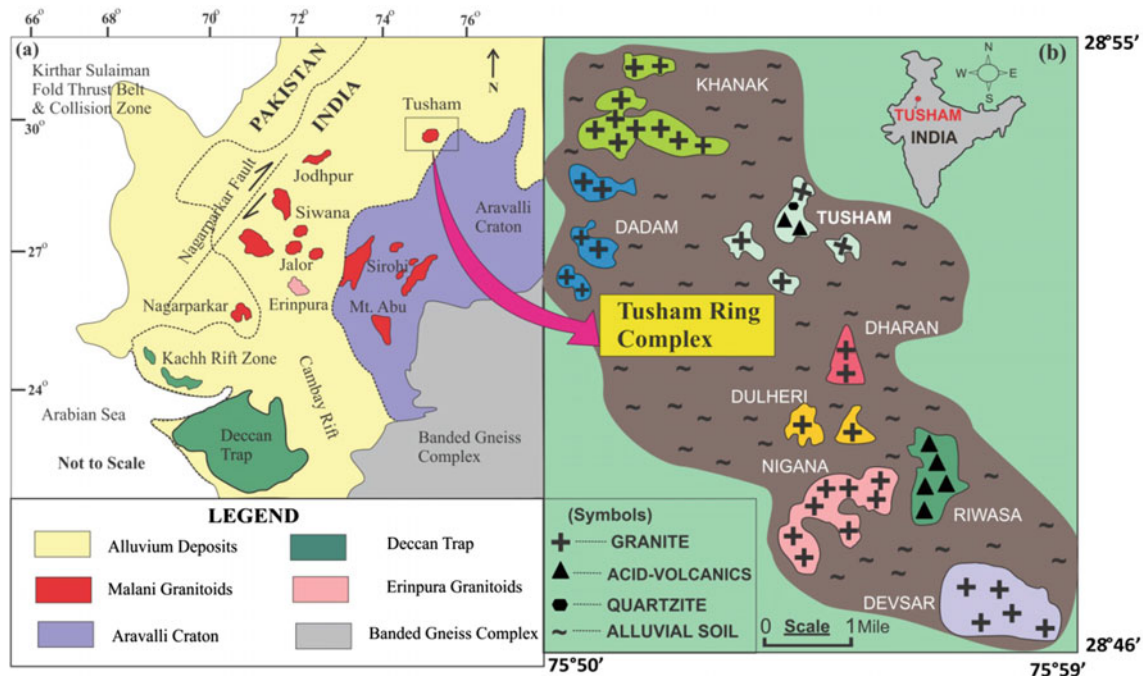


Fig. 1 a Regional geological map of Malani Igneous Suite exposed in NW Indian shield and SE Pakistan (modified after, Shakoor et al., 2019). b Simplified geological map of Tusham Ring Complex (modified after, Kumar et al., 2020)

References

- Artemieva, I. M., Thybo, H., Jakobsen, K., Sørensen, N. K., & Nielsen, L. S. K. (2017). Heat production in granitic rocks: Global analysis based on a new data compilation GRANITE2017. *Earth-Science Reviews*, *172*, 1–26.
- Clark, A. H., et al. (1990). Geological and geochronological constructions on the metallogenic evolution of the Andes of Southeastern Peru. *Economic Geology*, *85*, 1520–1583.
- Gard, M., Hasterok, D., Hand, M., & Cox, G. (2019). Variations in continental heat production from 4 Ga to the present: Evidence from geochemical data. *Lithos*, *342–343*, 391–406.
- Kumar, N., Kumar, N., Sharma, R., et al. (2020). Petrogenesis and tectonic significance of the neoproterozoic magmatism of the Tusham Ring Complex (NW Indian Shield): Insight into tectonic evolution of the Malani Igneous Suite and Rodinia Supercontinent. *Geotectonics*, *54*(3), 428–453.
- Shakoor, M. A., et al. (2019). Early Neoproterozoic evolution of Southeast Pakistan: Evidence from geochemistry, geochronology, and isotopic composition of the Nagarparkar Igneous Complex. *International Geology Review*. <https://doi.org/10.1080/00206814.2018.1512905>
- Simpson, P. R., & Plant, J. A. (1984). Role of high heat production granites in uranium province Formation. In B. De Vivo, et al. (Eds.), *Uranium geochemistry, mineralogy, geology, exploration and resources* (pp. 167–178).



Iron Ore Hypogene Mineralization in the São Francisco Craton

Carlos A. Rosière, Leonardo E. Lagoeiro, Flavia C. Silveira Braga, and Ricardo Pagung de Carvalho

Abstract

Two large-scale mineralization events associated with two orogenies generated economically important iron formation-hosted hypogene high-grade iron orebodies in the Brazilian São Francisco craton each with distinctive fabric and chemical characteristics as genetic diagnostic features. During the 2.1–2.0 Ga Trans-Amazonian orogeny, magnetite–martite–hematite massive to banded orebodies from the Quadrilátero Ferrífero District in Minas Gerais were controlled by thin-skinned tectonic structures. Metamorphic fluids promoted leaching of gangue minerals and substitution of carbonates in the Paleoproterozoic Cauê Iron Formation of the Minas Supergroup to form the orebodies. The age of the Cauê IF is bracketed by the U–Pb SHRIMP date of 2580 ± 7 Ma for the youngest detrital zircons from the underlying quartzites and the Pb–Pb isochron date of 2420 ± 19 Ma for the overlying dolostones. During the Ediacaran to Cambrian Brasiliano orogeny, modified hydrothermal fluids of magmatic and metamorphic origin recurrently mineralized the Cauê IF and the younger, carbonate-free IFs of the Serra da Serpentina Group (1990 ± 16 Ma—MDA, U–Pb SHRIMP data), lower Espinhaço Supergroup along five events with ages of 497, 508, 518, 526, and 536 Ma related to granitic intrusions. Massive Ti- and Mn-rich magnetite orebodies from the Guanhões Tectonic Block formed at the contact zone of anatectic

pegmatite intrusions in deep to intermediate crustal level. Schistose platy to granular hematite orebodies crystallized in thrust fault-related shear zones at the eastern border of the Espinhaço Fold and Thrust Belt by structurally controlled hydrothermal fluid flow. Mineralogical, chemical, and textural transformations of the Cauê Iron Formation during the first regional event were partially overprinted or obliterated by the far-reaching effects of the Brasiliano orogeny. The complex multistage evolution of schistose ore crystallized in shear zones has been tracked by micro-chemical, geochronological and EBSD petrofabric studies in the terrains eastern of the Espinhaço Range indicating a syn-deformational origin with the development of a crystallographic preferred orientation by crystal-plastic processes and hydrothermal fluid-assisted grain growth along thrust planes.

Keywords

Iron formations • Hypogene iron mineralization • Sao Francisco craton

1 Introduction

The upgrade of iron formations (IF) to hypogene high-grade iron ore (> 65 wt.% Fe) depends on circulation of large volumes of hot reactive fluids. Multiple deformational events create favorable conditions for recurrent mineralization and the formation of large deposits, with the opening of fluid pathways, enhancing quartz solubility by pressure solution and the development of a tectonic fabric (Rosière et al., 2008). The combination of geochronology, geochemical/isotopic and petro-tectonic studies applied to selected hypogene shear zone-hosted deposits aims to trace the history and help understanding the micro-scale processes involved in iron mineralization, particularly in the origin of syn-deformational high-grade orebodies.

C. A. Rosière (✉) · F. C. S. Braga
CPMTC/Department of Geology, Universidade Federal de Minas Gerais, Belo Horizonte, Minas Gerais, 31270-901, Brazil
e-mail: crosiere@gmail.com

L. E. Lagoeiro
CME/Geology Department, Universidade Federal do Paraná, Curitiba, Paraná, Brazil

R. P. de Carvalho
Graduate School, IGC, Universidade Federal de Minas Gerais, Belo Horizonte, Minas Gerais, 31270-901, Brazil

2 Geological Setting

The Neoproterozoic to early Paleoproterozoic Cauê Iron Formation of the Minas Supergroup (MSG) hosts the world-class iron deposits of the Quadrilátero Ferrífero Mining District (QFD) (Fig. 1). This unit was deposited in a Siderian passive margin associated with psamopelitic and carbonate units and the age is bracketed by the age of 2580 ± 7 Ma (Hartmann et al., 2006) for the youngest detrital zircons from the underlying Moeda Formation and the Pb–Pb isochron date of 2420 ± 19 Ma for the overlying Gandarela dolostones (Babinski et al., 1995). The main stage of mineralization developed under greenschist metamorphic conditions and is dated by the age obtained from monazite grains that yielded a $^{232}\text{Th}/^{208}\text{Pb}$ date of 2038.2 ± 6.6 Ma, in the final stages of the Transamazonian orogeny (2.1–2.0 Ga) during the Rhyacian–Orosirian transition (Rosière et al., 2021).

Northeast of the QFD along the eastern margin of the protocraton ca. 2.0–1.7 Ga psammopelitic units with IF comprises the Serra da Serpentina Group (SSG). They occur as west-verging tectonic slivers in the eastern Espinhaço Fold and Thrust Belt (EFTB) juxtaposed with the Statherian metasediments of the Espinhaço Supergroup and Transamazonian gneisses of the Guanhanês Complex (Fig. 1). The maximum depositional age (MDA) of the SSG is constrained by the U–Pb SHRIMP date of 1990 ± 16 Ma of the youngest single detrital zircon from interlayered sandstones. The sequence has undergone upper greenschist to amphibolite facies metamorphism during the evolution of the Araçuaí–West Congo orogen (Ediacaran–Cambrian Brasiliano orogeny) that lasted from 630 to 530 Ma (Alkmim et al., 2017). Syn- to post-tectonic hydrothermal events caused the iron mineralization of the SSG and overprinted the Cauê IF of the Minas Supergroup in the QFD (Rosière et al., 2021).

3 Methodology

Electron Backscatter Diffraction (EBSD)-based petrofabric studies were accomplished at the CME/UFPR (Centro de Microscopia Electronica/Universidade Federal do Paraná in

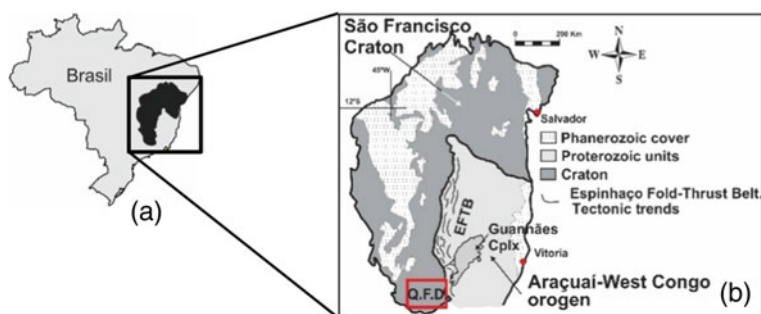
representative samples from syntectonic orebodies enclosed in the Guanhanês Complex complementary to earlier studies from deposits of the QFD (Rosière & Rios, 2004). Mineral identification X-Ray Diffraction (DRX) analyses on concentrates were conducted at the CPMTC/UFMG (Centro de Pesquisa Professor Manoel Teixeira da Costa/Universidade Federal de Minas Gerais). The ages were constrained by Sensitive High-Resolution Ion Microprobe (SHRIMP) analyses conducted in the laboratory of John de Laeter Centre for Isotope Research at the Curtin University. Chemical analyses were performed at the ALS Laboratory, Peru, using the Inductively Coupled Plasma Atomic Emission Spectrometry and Mass Spectroscopy (ICP-AES and ICP-MS) methods.

4 Mineralization Events and Genetic Ore Types

The polyphase history of the high-grade iron orebodies in the Cauê Iron Formation is not fully constrained due to limited geochronological data, but petrotectonic studies associated with trace elements and isotope geochemistry, mineral chemistry and fluid inclusions studies demonstrates two mineralization stages associated with distinct tectonic events. In the first stage, during the Transamazonian orogeny, enrichment was caused by large volumes of low-temperature and low-to-moderate salinity metamorphic fluids (Rosière & Rios, 2004). These circulated along major faults, leading to carbonatization, and leaching of gangue minerals with the crystallization of porous to massive hematite–magnetite/martite ore displaying a xeno- to hypidioblastic fabric (Rosière et al., 2013; Rosière et al., 2008).

A manifold mineralization scenario is envisioned during the Brasiliano collisional orogeny with the development of far-field hydrothermal alteration that affected Meso- to Neoproterozoic sequences as well as Archean to Paleoproterozoic terranes of the cratonic core. Episodic circulation of these fluids is likely to have been driven by seismic pumping from the Araçuaí–West Congo orogen (AWC) associated with the long-living emplacement of granite and pegmatite bodies.

Fig. 1 a Location map of the São Francisco craton. b Simplified regional map of the São Francisco craton and surrounding terranes with location of the tectonic units (see text)



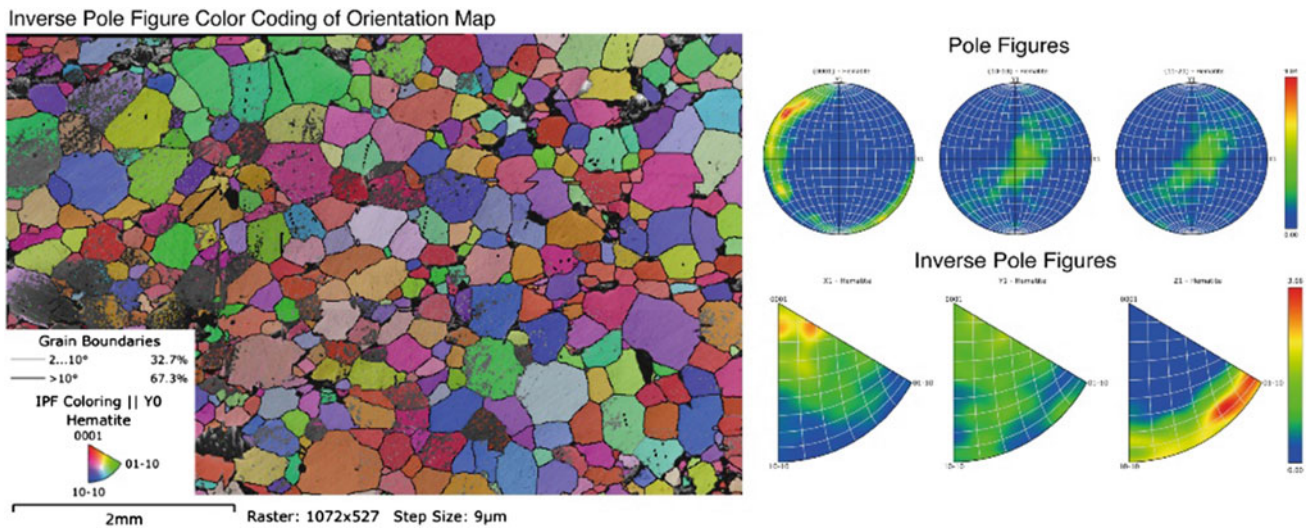


Fig. 2 EBSD orientation map of syntectonic iron ore hosted by the S. serpentina Group

The earliest mineralization phase during the Brasiliano orogeny affected iron formations of the Minas Supergroup and of the Serra da Serpentina Group. It is characterized by deformation and syntectonic crystallization of hematite with the development of a crystallographic preferred orientation (CPO) in shear zones. During this phase, desilicification occurred mainly by pressure solution.

In the late to post-tectonic stages of mineralization, massive high-grade magnetite orebodies crystallized in the IF slivers associated with granite-pegmatite bodies. Hydrothermal activity associated with the emplacement of the late to post-orogenic granitic rocks from the AWC and partial remelting of the ca. 1.74 Ga Borrachudos Felsic Suite, generated quartz and pegmatite veins. The percolating heated fluids caused quartz dissolution and recrystallization of hematite to magnetite with the formation of massive high-grade ore bodies at the contact zones of the igneous bodies.

5 Deformation, Petrofabrics and Mineralization

The specularitic orebodies of the Cauê IF in the QFD display a grain shape and crystallographic preferred orientation, where the hematite basal plane defines a continuous to anastomosed schistosity enveloping lens-shaped relics of hematite–martite aggregates (Rosiere et al., 2013). The pole figures of the (00.1) plane usually depict a single maximum or an elongated girdle perpendicular to the stretching lineation.

Petrotectonic/EBSD studies from a syn-deformational orebody hosted in a sheared iron formation from the Serra da Serpentina Group in the Guanhões Complex revealed, however, a wide variety of fabric (Fig. 2). A complex deformational history involved crystal-plastic behavior of hematite with the formation of sub-grains, oriented grain growth by fluid-assisted solution-precipitation. Late grain growth and twinning were a result of accommodation to minimize the strain energy resulting from plastic deformation. This deformational history reveals a progressive upthrusting of tectonic blocks as an efficient driving mechanism for the far-reaching hydrothermal fluids.

6 Conclusions

The petrofabric of shear zone-hosted schistose hematite ore is a key feature in establishing a diagnostic of the syntectonic mineralization phase during the Brasiliano orogeny. Petrotectonic studies in high-grade ore deposits, supported by EBSD analyses, geochemistry and geochronology indicate that compressive thrust tectonic plays a critical role as a ground preparation and driving mechanism for hydrothermal fluids to the development of a far-field regional alteration and mineralization that may affect already consolidated terranes over lengthy periods of geologic history.

Acknowledgements The authors acknowledge funding from the CNPq (Pr. Nr. 472602/2009-8) and FAPEMIG (Pr. Nr. APQ-01178-15). Fieldwork was supported by Anglo American BR, and BEMISA. Participation in the Congress is sponsored by the UFMG.

References

- Alkmim, F. F., Kuchenbecker, M., Reis, H. L. S., & Pedrosa-Soares, A. C., et al. (2017). The Araçuaí belt. In M. Heilbron (Ed.), *The São Francisco craton, eastern Brazil (Regional Geology Reviews)* (pp. 255–276). Springer.
- Babinski, M., Chemale, F., & Van Schmus, W. R. (1995). The Pb/Pb age of the Minas Supergroup carbonate rocks, Quadrilátero Ferrífero, Brazil. *Precambrian Research*, 72, 235–245.
- Hartmann, L. A., Endo, I., Suita, M. T. F., Santos, J. O. S., Frantz, J. C., Carneiro, M. A., McNaughton, N. J., & Barley, M. E. (2006). Provenance, and age delimitation of Quadrilátero Ferrífero sandstones based on zircon U-Pb isotopes. *Journal of South American Earth Sciences*, 20, 273–285.
- Rosière, C. A., Garcia, O. L., Siemes, H., & Schaeben, H. (2013). Domanial fabrics of hematite in schistose shear zone-hosted high-grade Fe ores: The product of the interplay between deformation and mineralization. *Journal of Structural Geology*, 55, 150–166.
- Rosière, C. A., & Rios, F. J. (2004). The origin of hematite in high-grade iron ores based in infrared microscopy and fluid inclusion studies: The example of the Conceição Deposit, Quadrilátero Ferrífero, Brazil. *Economic Geology*, 99(3), 611–624.
- Rosière, C. A., Santos, J. O. S., Silveira-Braga, F., Hensler, A., Rolim, V. K., & Bekker, A. (2021). Multiple hydrothermal events upgraded iron-formations in southeastern São Francisco craton, South America. *The Journal of Geology*, 129(3), 283–296.
- Rosière, C. A., Spier, C. A., Rios, F. J., & Suckau, V. E. (2008). The itabirite from the Quadrilátero Ferrífero and related high-grade ores: An overview. *Reviews in Economic Geology*, 15, 223–254.



Indicative Role of Trace and Rare-Earth Elements of the North West Manganese Ore Deposit (South Africa) in Constraining the Genetic Model of Supergene Orebodies

Benedict Kinshasa Pharoe

Abstract

The North West Province of the Republic of South Africa is famously known for its mineral wealth in chrome and platinum group metals associated with the Bushveld Igneous Complex. In addition to this, small-scale supergene manganese deposits are found to occur on the weathered upper crust of the Neoproterozoic Malmani dolostones in the Transvaal Supergroup. These deposits occur as manganese nodules, wad and crusts confined to karstic depressions, which resulted from surficial weathering and dissolution of the underlying manganiferous dolostones. This study presents the geochemistry (X-ray fluorescence and inductively coupled plasma mass spectrometry analyzed sample data) of rare-earth (REE) and trace (TE) elements and its indicative role in constraining the genesis of the North West Deposit. The ore mineralogy consists predominantly of high valence state (Mn^{4+}) Mn oxide minerals. These minerals are known to be scavengers of relatively high concentrations of trace (TE) and rare-earth elements (REE) into their tunnel crystal structures during mineral precipitation. The stability and coherent nature of these elements in natural environments have shown in their robustness when it comes to discriminating various sources of manganese ore substances. The Post-Archean Australian Shale (PAAS) normalized REE patterns of the ore samples indicated enrichment in Ba, Y, Cu, Sc, Ni, Co and other TE such as Ce, La and Zr and depletion of Zn, Nb and U. The REE + Y anomalies from the analyzed ore samples further indicated ore-enrichment in light rare-earth elements and notably

pronounced positive Ce and negative Y anomalies indicative of hydrogenetic precipitation as a governing mechanism for the formation of manganese nodules. This was supported by the observation on the high field strength (HFS) element discriminating plots; Ce anomalies and Y_{SN}/Ho_{SN} , Ce anomalies and Nd concentrations and the $Fe + Mn + (Co + Ni + Cu)*10$, which effectively discriminate between hydrogenetic, hydrothermal, diagenetic and mixed source ore precipitates. An overlap in the normalized REE-Y patterns for Mn nodules and Malmani dolostones is suggestive of a close genetic relation.

Keywords

Genesis • Supergene Mn deposits • Weathering crust • South Africa

1 Introduction

Studies on the geochemistry, mineralogy, spatial distribution, metallogenic provinces and epochs for the evolution of manganese deposits have been well captured in the literature (Hein and Bolton, 1992; Kuleshov, 2013; Roy, 1997). With regard to the genetic types of manganese deposits, Roy (1997) distinguished three classes: hydrothermal, sedimentary and supergene. Even though the processes that give rise to these classes may be interrelated, each involves distinct mechanisms (Roy, 1997). In addition, more of ore genetic-related studies were carried out with the aim of improving the approach in which various types of manganese deposits are classified (Bau et al., 2014; Heshmatbehzadi & Shahabpour, 2010; Nath et al., 1997; Roy, 1997; Toth, 1980). Polymetallic nodules from ocean floors have also sparked an interest due to their potential sources of Ni, Cu, Co, V and a number of rare-earth elements. Their genetic classifications involve the use of trace- and rare-earth element geochemistry to discriminate a variety of oceanic

B. K. Pharoe (✉)
Department of Geology, University of Fort Hare, Alice,
5700, South Africa
e-mail: BPharoe@ufh.ac.za

B. K. Pharoe
Liphakoeng Mining LTD, Germiston 1401, Johannesburg,
South Africa

settings (Bau et al., 1996, 2014; Bonatti et al., 1972; Hein et al., 2015; Josso et al., 2017).

The elevated concentrations of rare and trace elements analyzed from the North West Manganese ore samples allowed us to follow suit in applying the TE and REE geochemistry to genetically classify the ore deposit based on the source of the ore components and formation mechanism. The North West Manganese Deposit represents a near-surface accumulation of manganese wad and nodules in a supergene zone underlain by the manganiferous dolomites of the Malmani Subgroup (Fig. 1). Common manganese minerals found in these ore deposits are mainly composed of romanechite, cryptomelane, lithiophorite, pyrolusite and vernadite (Pharoe et al., 2020). These oxides are characterized by open tunnels in their octahedral crystallographic structures, which tend to scavenge high concentrations of rare and trace elements in their internal structures during precipitation from basinal waters. This study is, therefore, aimed at identifying classification fields of supergene manganese oxide deposits from the existing schemes.

2 Methodology

2.1 Sampling

Sampling was carried out along the outcrop areas of manganese mineralization in different regions underlain by manganiferous dolostones in the North West Province.

These outcrop areas were identified on the 1:250,000 geological map of the West Rand (2626 Wes-Rand). The sampled areas include: Ventersdorp, Lichtenburg and Ottoshoop. Open pits in areas of active mining were the main targets for sample collection as they provided fresh rock samples. The samples consisted mainly of manganiferous dolomites, manganese nodules and wad; where: BH1–BH14 are manganese nodules, BH15 and BH16 are manganese wad and DOL1 and DOL2 are manganiferous dolomites.

2.2 Laboratory Analyses

Twenty-two (22) samples were analyzed for twenty-one (21) rare-earth and trace elements with the use of PerkinElmer NexiON 300X Inductively Coupled Plasma Quadrupole Mass Spectrometer housed at the Geology Department, University of Johannesburg. In addition, major and trace element analyses were undertaken on MagiX Fast, X-ray fluorescence (XRF) spectrometer at the Council for Geoscience in Pretoria, South Africa. The anomalous concentrations of rare-earth elements were normalized to compositions of the Post-Archean Australian shale (Taylor & McLennan, 1985). The Ce (Ce_{SN}/Ce^*_{SN}) and Eu (Eu_{SN}/Eu^*_{SN}) are calculated as the ratio of the normalized values (subscript n, from the Post-Archean Australian Shale, Taylor and McLennan, 1985) of an element by the interpolation of the adjacent elements (superscript *) such that:

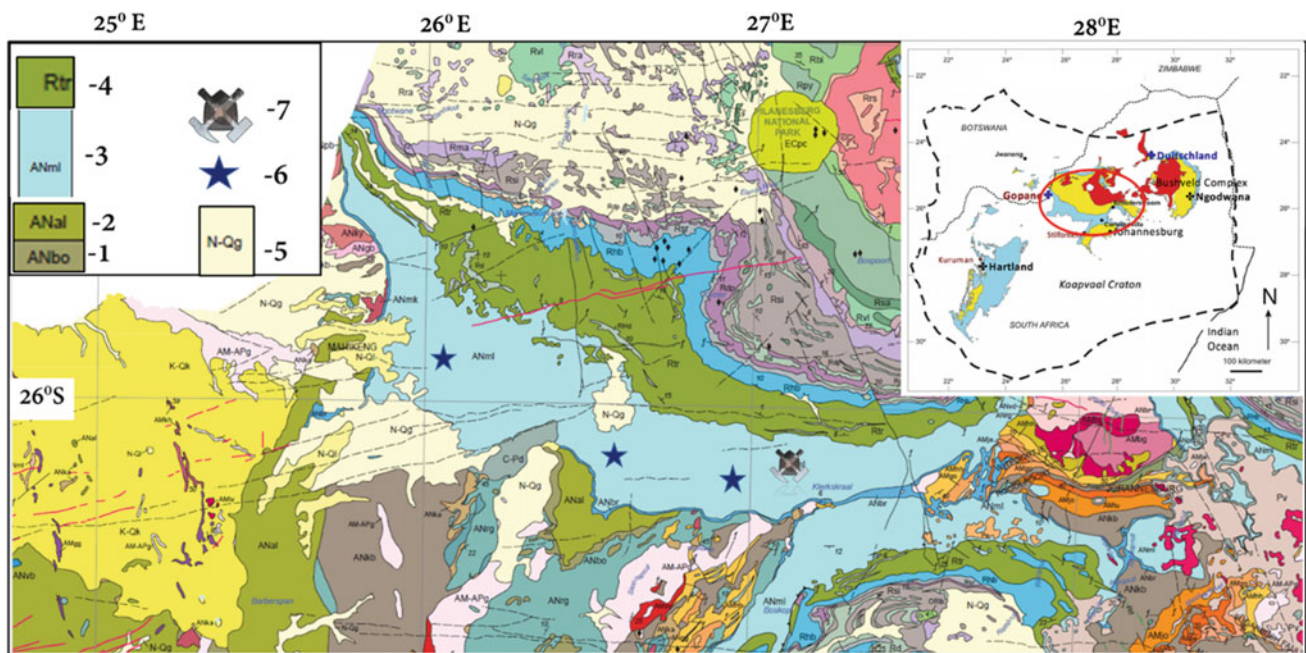


Fig. 1 Geological map of the northern flank of the Kaapvaal Craton in South Africa (CGS, 2019). 1—Siliciclastic and pyroclastic rocks of the Bothaville Formation, Ventersdorp Supergroup; 2—Diamictites and

sandstones of the Allanridge Formation, Ventersdorp Supergroup; 3—Malmani Dolomites, Transvaal Supergroup; 4—Quaternary sediments; 6—Other sampled locations; 7—General Nice Mine

$$\frac{Ce_{SN}}{Ce_{SN}^*} = \frac{2[Ce]_{SN}}{[Sm]_{SN} + [Pr]_{SN}} \quad (1)$$

$$\frac{Eu_{SN}}{Ce_{SN}^*} = \frac{2[Eu]_{SN}}{[Sm]_{SN} + [Gd]_{SN}} \quad (2)$$

3 Results

3.1 Geochemistry

The rare and trace element geochemistry from the manganese ore samples was used to deduce the probable source of ore substances and the processes that governed the formation of supergene manganese deposits in the North West Province of South Africa. The ore samples are

Fig. 2 Spider plots of the major element compositions of the North West Manganese Deposit. The values were normalized using average composition of the Oaktree Dolomites (treated as source rock) (Eroglu et al., 2015)

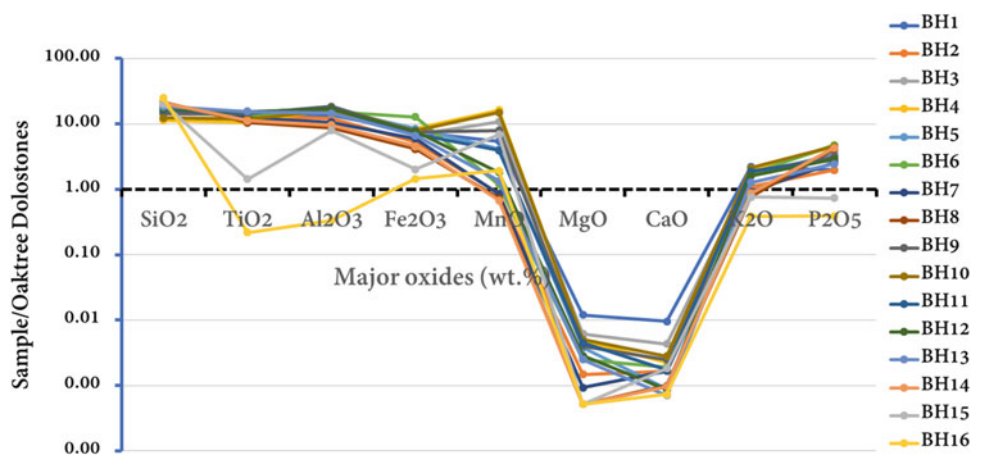
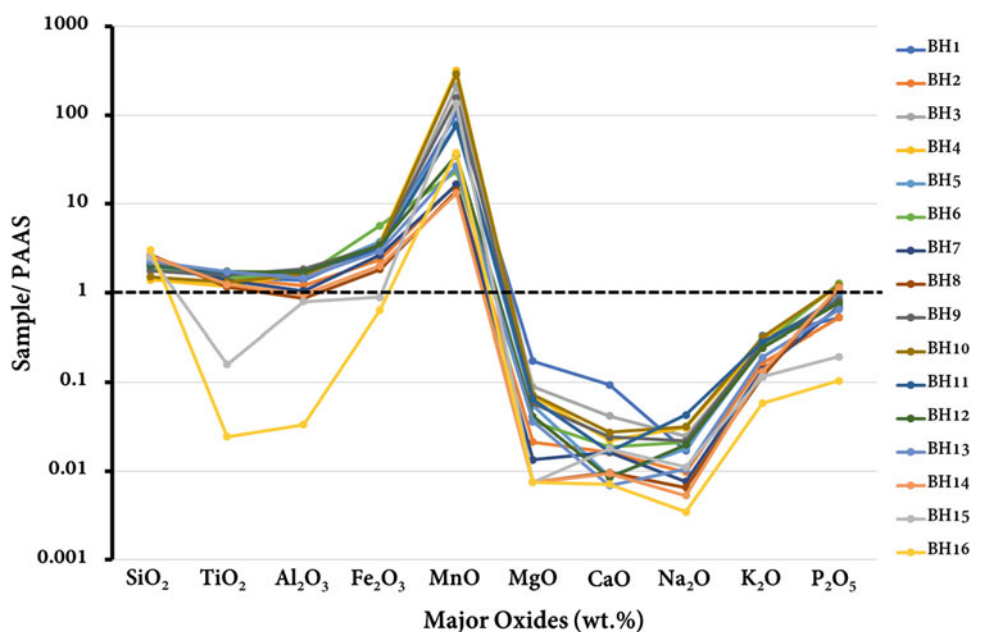


Fig. 3 Spider plots of the major element compositions of the North West Manganese Deposit. The values were normalized using average composition of the Post-Archean Australian Shale (Taylor & McLennan, 1985)



relatively enriched in major oxides (SiO_2 , Al_2O_3 , TiO_2 , Fe_2O_3 , MnO , K_2O and P_2O_5) in relation to the oxides' average values of the Oaktree protolith except for the two manganese wad samples (*BH15* and *BH16*). On the contrary, MgO and CaO concentrations are more depleted as indicated in Fig. 2. The depletion in MgO and CaO concentrations may be ascribed to dissolution and leaching processes in supergene environment. In relation to the PAAS normalization, the studied ore samples have higher contents of MnO (Fig. 3).

3.2 Ore Genetic Classification

The genetic classification of the North West Manganese Deposit was based on the geochemistry of trace and rare-earth elements. The rare-earth element contents in

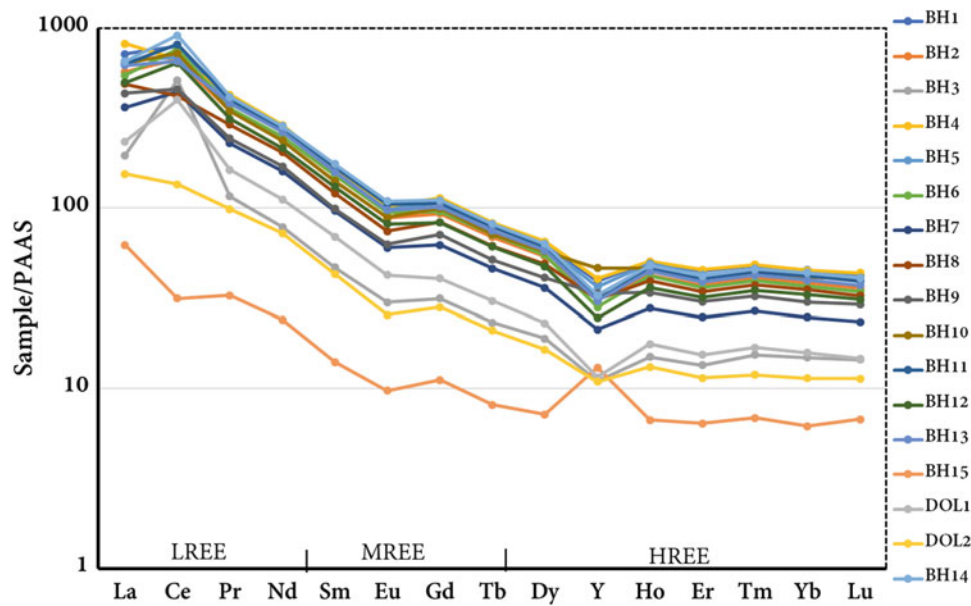


Fig. 4 PAAS shale-normalized REE distribution spectra of the North West Mn Ore Deposit (Taylor & McLennan, 1985)

manganese ores, normalized through the PAAS values are shown in Fig. 4. The ore samples are characteristically enriched in light rare-earth elements (LREEs) a characteristic of near-surface deposits. The contents of medium rare-earth elements (MREEs) are also relatively elevated compared to heavy rare-earth elements (HREEs) contents.

3.3 Ore Classification

The classification of the North West Ore Deposits on bivariate discrimination plots proposed by Bonatti et al. (1972), Hein et al. (2015), Josso et al. (2017), Bau et al. (1996, 2014) indicates that the ores were formed through

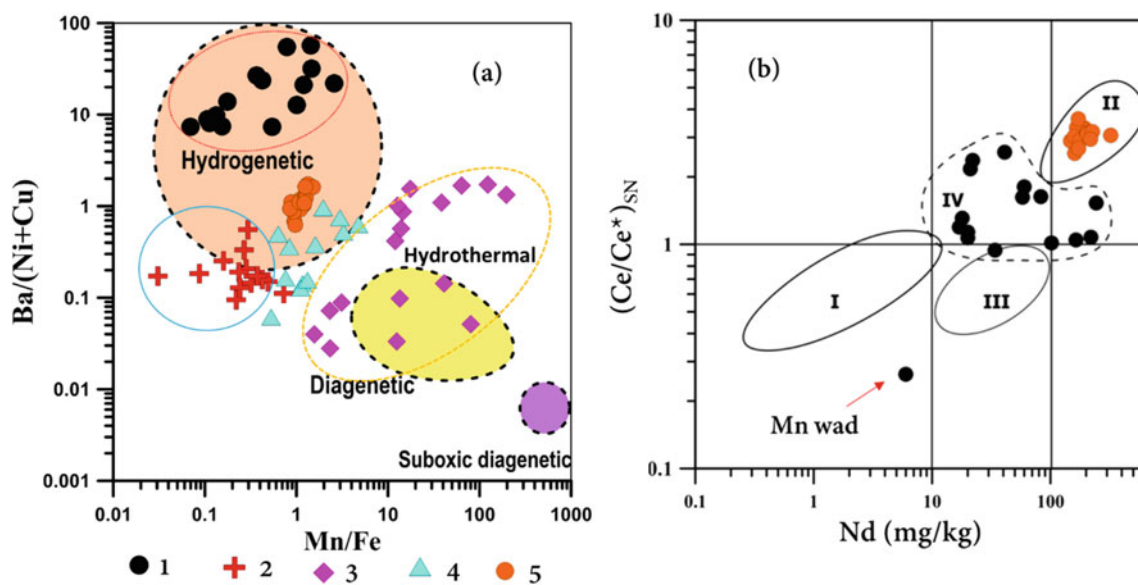


Fig. 5 Bivariate discrimination plots used to genetically classify the source of ore substances for manganese deposits based on the ore geochemistry (Bau et al., 2014; Hein et al., 2015; Josso et al., 2017). The sample points are given as follows: 1—North West Manganese Deposits; 2—Manganese wad samples from the Waterval Saprolite in West-Wits Mine (Niekerk et al., 1999); 3—Hydrothermal ferromanganese deposits South West Pacific Ocean—Wallis and Futuna deposits

(Josso et al., 2017); 4—The Karoo Supergroup hosted manganese wad deposit—Ryedale deposit (Pack et al., 2000); 5—Oceanic ferromanganese nodules from the Cook Island (Hein et al., 2015). I—Hydrothermal field; II—Hydrogenetic field; III—Diagenetic field; IV—New field suggesting hydrogenetic precipitation of Mn deposits in surface waters associated with supergene environment

hydrogenetic processes (Fig. 5). This suggests that nodular and concretionary ores were formed from precipitation of colloidal particulates carried in suspension in basin's water column. The source of the ore particulates must have been released during surficial weathering, leaching and dissolution of the underlying manganiferous dolostones of the Malmani Subgroup. The genetic relation between the ores and Malmani dolostones (samples: DOL1 and DOL2) is evident from the correlation of REE patterns in Fig. 4.

4 Discussion

The Mn ore-bearing section in the North West Manganese Province constitutes two tiers; the lower Mn wad-bearing Waterval Saprolite and the upper Mn nodule-bearing alluvial succession known as the West-Wits Alluvium. The two tiers are separated by a sharp erosional surface locally referred to as the Post African I surface of uplift and erosion. Mn wad deposits in the province are genetically linked to either: (1) supergene alteration of Malmani dolostones or (2) Permian *Ecce strata* of the Karoo Supergroup (Niekerk et al., 1999; Pack et al., 2000). The first type is associated with most deposits identified in the North West Province such as the Klipkuil, General Nice, Klipgat, West-Wits near Krugersdorp and the deposits considered in this study. On the contrary, the latter type is mostly associated with the deposits in Ryedale, Houtkoppies and Roodepan farms.

This study therefore attempts to genetically classify North West Manganese Deposit based on the trace and rare-earth element geochemistry. The trace and rare-earth elements are inherently favored in reconstruction of genesis and paleoenvironmental conditions for a number of deposits mostly due to their constrained mobility in soils. PAAS normalized rare-earth patterns of the ore deposit indicate positive correlation with that of the underlying dolostones of the Malmani Subgroup (Fig. 4). This is suggestive of genetic link between the studied ores (Mn wad and Nodules) and Malmani dolostones.

Furthermore, the positive Ce_{SN} and negative Y_{SN} anomalies are indications of hydrogenetic ore precipitation (settling out of ore colloidal sols carried in suspension in water column) (Fig. 4). This is supported in Fig. 5a where the samples from the North West Mn Deposit occupy the hydrogenetic field. It is important to note that Co ($Co/(Ni + Cu)$) from the original discrimination plot given in Josso et al. (Josso et al., 2017) was replaced by Ba ($Ba/(Ni + Cu)$) in this study. This was carried out to compensate for the lower concentrations of Co. A new hydrogenetic field representing Mn deposits in the weathering

crust was delineated in Fig. 5b. The field lies in between the existing hydrogenetic, hydrothermal and diagenetic fields as defined in Hein et al. (2015). It incorporates part of what is termed mixed field in Hein et al. (2015).

5 Conclusions

Indicative role of trace and rare-earth elements allowed us to restore the source of ore substance and the process that governed the formation of North West Manganese Deposits (Mn nodules and Wad) in the Ventersdorp area. The properties of indicative elements such as Ni, Cu, Ba, Ce, La, Y as used in this study may provide a reliable basis in determining ore sources in other analogous deposits. On the basis of this study, the following can be deduced:

1. The manganese ores in the areas under study were formed through surficial weathering, dissolution and leaching of the underlying manganiferous dolostones of the Malmani Subgroup in a typical lacustrine environment.
2. The early stage gave rise to the formation of Waterval Saprolite and subsequently Mn wad along the African surface in the late Cretaceous post-Gondwanaland.
3. The negative Ce_{SN} anomaly across Mn wad sample may suggest that Mn wad contributed to the ore supply during the formation of Mn nodules.
4. Manganese nodules and concretion's formation is associated with Post-African I surface of uplift and erosion.

References

- Bau, M., Koschinsky, A., Dulski, P., & Hein, J. R. (1996). Comparison of the partitioning behaviors of yttrium, rare-earth elements, and titanium between hydrogenetic marine ferromanganese crust and seawater. *Geochemica Et Cosmochimica Acta*, 60(10), 1709–1725.
- Bau, M., Schmidt, K., Koschinsky, A., Hein, J., Kuhn, T., & Usui, A. (2014). Discriminating between different genetic types of marine ferromanganese crusts and nodules based on rare-earth elements and yttrium. *Chemical Geology*, 318, 1–9.
- Bonatti, E., Kraemer, T., & Rydell, H. (1972). Classification and genesis of submarine iron manganese deposits. *Ferromanganese Deposits on the Ocean Floor*, 31, 149–166.
- Eroglu, S., Schoenberg, R., Wille, M., & Beukes, N. (2015). Geochemical stratigraphy, sedimentology, and Mo isotope systematics of the ca. 2.58–2.50 Ga-old Transvaal Supergroup carbonate platform. *South Africa. Precambrian Research*, 266, 27–46.
- Hein, J. R., & Bolton, B. (1992). Stable isotope composition of Nikopol and Chiatara manganese ores, USSR: Implications for genesis of large sedimentary manganese deposits. *International Geological Congress*, 1, 209.

- Hein, J. R., Spinardi, F., Okamoto, M., Mizell, K., Thorburn, D., & Tawake, A. (2015). Critical metals in manganese nodules from the Cook Islands EEZ, abundances and distribution. *Ore Geology Reviews*, *68*, 97–116.
- Heshmatbehzadi, K., & Shahabpour, J. (2010). Metallogeny of manganese and ferromanganese ores in Baft Ophiolitic Mélange, Kerman, Iran. *Australian Journal of Basic and Applied Sciences*, *4* (2), 302–313.
- Josso, P., Pelleter, E., Pourret, O., Fouquet, Y., Etoubleau, J., Cheron, S., & Bollinger, C. (2017). A new Discrimination scheme for oceanic ferromanganese deposits using high field strength and rare earth elements. *Ore Geology Reviews*, *87*, 3–15.
- Kuleshov, N. V. (2013). Manganese rocks and ores: Isotope geochemistry, genesis, evolution of ore formation. *Monograph Moscow: Nauchnyi Mir*, *14*, 508.
- Nath, B. B., Pluger, W. L., & Roelandts, I. (1997). Geochemical constraints on the hydrothermal origin of ferromanganese incrustations from the Rodriguez triple junction, Indian Ocean. *Geological Society of London, Special Publication*, *119*, 199–211.
- Pack, A., Gutzmer, J., Beukes, N., & van Niekerk, H. (2000). Supergene ferromanganese wad deposits derived from Permian Karoo Strata along the late Cretaceous-mid-Tertiary African land surface, Ryedale, South Africa. *Economic Geology*, *95*, 203–220.
- Pharoe, B. K., Evdokimov, A. N., Gembitskaya, I. M., & Bushuev, Y. Y. (2020). Mineralogy, geochemistry and genesis of the post-Gondwana supergene manganese deposit of the Caletonville-Ventersdorp area, North West Province, South Africa. *Ore Geology Reviews*, *120*, 103372.
- Roy, S. (1997). Genetic diversity of manganese deposition in the terrestrial geological record. *Geological Society*, *119*, 5–27.
- Taylor, S. R., & McLennan, S. M. (1985). *The continental crust: Its composition and evolution* (p. 312). Blackwell Scientific
- Toth, J. (1980). Deposition of submarine crusts rich in manganese and iron. *Geological Society of America Bulletin*, *91*(1), 44–54.
- van Niekerk, H. S., Beukes, N. J., & Gutzmer, J. (1999). Post-Gondwana pedogenic ferromanganese deposits, ancient soil profiles, African land surfaces and palaeoclimate change on the Highveld of South Africa. *Journal of African Earth Sciences*, *29*, 761–781.



The Ophiolite-Hosted Cu–Fe–Zn Ores in Tuscany (Italy): VMS Deposits from a Jurassic Slow-Spreading Ridge

Andrea Dini, Chiara Boschi, Paolo Di Giuseppe, and Andrea Rielli

Abstract

Small Cu–Fe–Zn VMS deposits are widespread in Tuscan ophiolites (Ligurian Units). Industrial production was small and definitively ceased from the 1960s. Locally, massive ore (chalcopyrite-bornite-chalcocite) having exceptionally high grade was found. The Montecatini Val di Cecina mine exploited the largest “bonanza” and, for few decades in nineteenth century, became one of the richest and most profitable copper mines in Europe. This study (PRIN-MUR-2017AK8C32 project) was performed in order to define the structural setting, the potential for precious-critical metals and the redox reactions involving sulfides and gangue silicates. Ophiolite-hosted Cu–Fe–Zn ores in Tuscany mostly occur in serpentinite crosscut by dykes-laccoliths of gabbro and dyke-swarms of basalt. Chalcopyrite stockworks are common but the largest deposits are hosted by cataclastic shear-zones in serpentinite-gabbro basement and at the contact with the overlying basalt. The early chalcopyrite stockworks were strongly mechanically chemically reworked with formation of chalcopyrite-bornite-chalcocite nodules embedded in a chlorite, Ca-rich amphibole, Fe-rich serpentine, quartz, andradite and xonotlite assemblage. The ores contain substantial amount of sphalerite and pyrite and ubiquitous grains of clausthalite, native tellurium and gold, in accordance with the significant Te–Se–Au content of these deposits. The overall characters of the Cu–Fe–Zn ores and host rocks suggest a formation in an active oceanic core complex along the Jurassic slow-spreading ridge of the Piedmont–Ligurian Ocean.

Keywords

VMS deposit • Ophiolites • Slow-spreading ridge • Critical metals • Northern Apennine

1 Introduction

The Northern Apennine fold and thrust belt (Italy) includes tectonic units derived from the Piedmont–Ligurian ocean basin (Ligurian domain), which separated, during Jurassic–Cretaceous times, the European and Adriatic plates (Piccardo et al., 2004). These tectonic units are characterized by the widespread occurrence of ophiolites—serpentinized peridotites, gabbros and basalt—that locally host small Cu–Fe–Zn VMS deposits (Fig. 1) (Klemm & Wagner, 1982; Zaccarini & Garuti, 2008). The geochemical characteristics of ophiolites throughout the Northern Apennine belt are relatively homogeneous, but the associated Cu–Fe–Zn ores can be divided into two distinct types on the base of structural, textural and mineralogical features: conventional pyrite-chalcopyrite massive-vein ore in Liguria and unconventional chalcopyrite-bornite-chalcocite nodular ore in Tuscany.

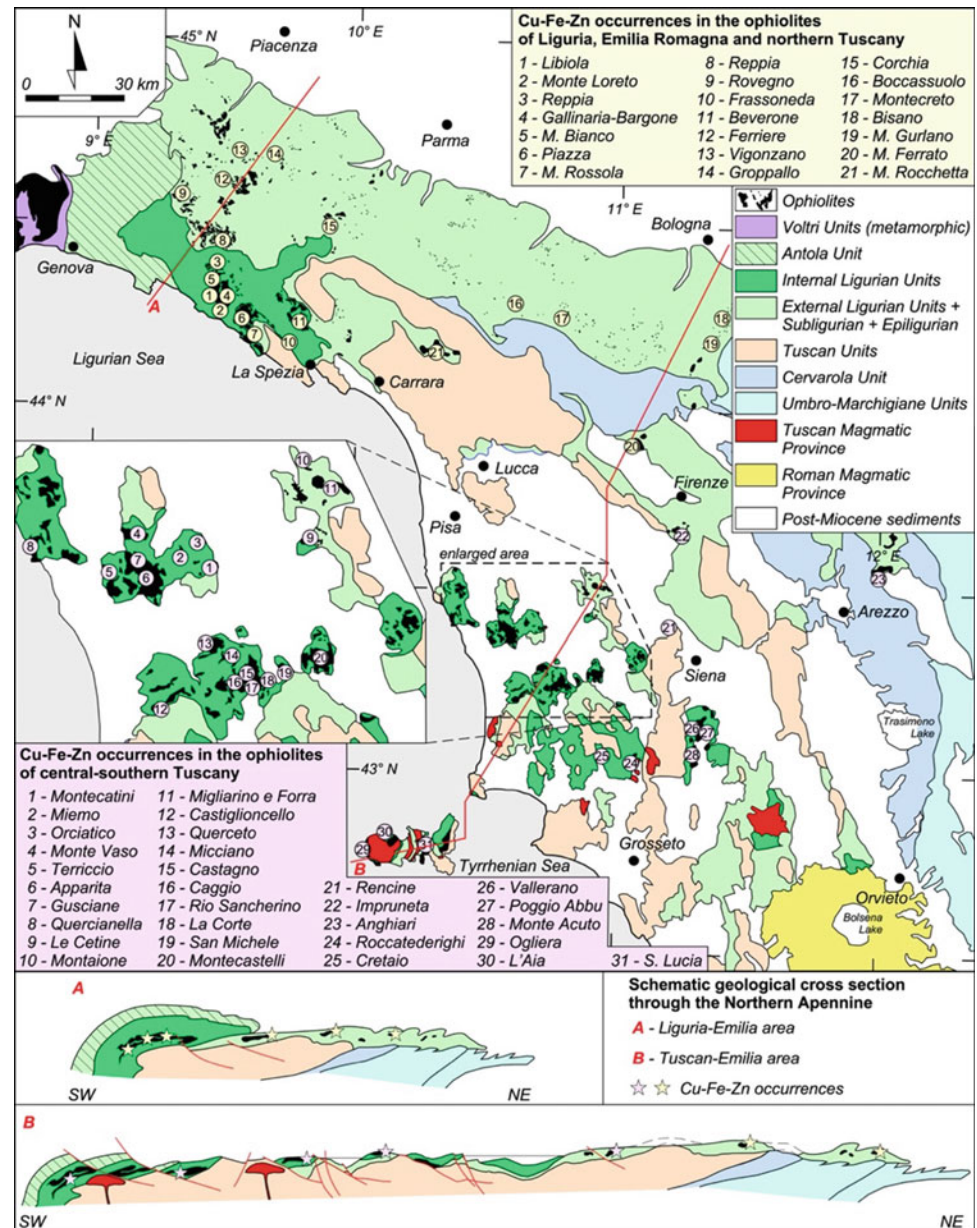
This contribution is part of an Italian scientific project (PRIN-MUR-2017AK8C32 project) aimed to compare the Ligurian and Tuscan ores, defining the structural setting, the precious-critical metal content and the chemical–physical processes responsible for the peculiar characters of the ophiolite-hosted Cu–Fe–Zn VMS deposits of Tuscany.

2 Settings

Thrusting of the Ligurian Domain units on top of the Tuscan Domain units (Fig. 1) resulted from a Late Cretaceous–middle Eocene “Alpine” stage, controlled by the east-dipping subduction of the Ligurian ocean, followed by a late Eocene–Quaternary “Appenninic” stage, related to the

A. Dini (✉) · C. Boschi · P. Di Giuseppe · A. Rielli
Istituto di Geoscienze e Georisorse—CNR, 56124 Pisa, Italy
e-mail: a.dini@igg.cnr.it

Fig. 1 Simplified tectonic map of the Northern Apennine indicating the distribution of ophiolitic rocks and VMS deposits in the Internal and External Ligurian Units. The two schematic geological sections highlight the distinct tectono-sedimentary “dispersion” experienced by the ophiolite-hosted VMS deposits in the northern area (Liguria transect) with respect to the intensely extended terrain in the south (Tuscan transect). Modified after Dini and Boschi (2017)



west-dipping subduction of the Adria plate (Conti et al., 2020). The Ligurian Domain can be divided to the Internal Ligurian Units and the External Ligurian Units (Elter, 1975). The Internal Units comprise Jurassic-early Paleogene sedimentary successions deposited on the Jurassic oceanic crust. They are characterized by large outcrops of ophiolites (Piccardo et al., 2004). The External Units lack the pre-Cretaceous succession and are distinguished by the occurrence of basal sedimentary mélanges (Upper Cretaceous) containing metric-kilometric blocks of ophiolites (Fig. 1). The Jurassic ophiolites involved in the early accretionary wedge of the “Alpine” stage (Internal Units), provided the ophiolitic debris to the Late Cretaceous, basal sedimentary mélanges of the Ligurian External Units

(Marroni et al., 2010). Thus, rocks and ores from the Jurassic slow-spreading ridge were firstly dispersed by the combined tectono-sedimentary effect of the “Alpine” deformation stage. Later, during the “Appenninic” stage, the Ligurian domain was emplaced onto the Tuscan Domain with a top-NE tectonic transport direction and then affected, since the early-middle Miocene, by extension. Tuscany and Northern Tyrrhenian basin experienced rates of extension much higher than Liguria, leading to an extreme tectonic dispersion of the ophiolitic units and ores (Fig. 1) (Dini & Boschi, 2017). The Tuscan Cu-Fe-Zn VMS deposits are mostly hosted in the Internal Ligurian Unit. The sedimentary covers of this ophiolite unit have been deposited on a very heterogeneous seafloor, characterized by strong lateral

variations. They may lay on pillow-lava basalts, on serpentinized peridotites crosscut by dykes/laccoliths of gabbro, themselves cut by dolerite dykes, as well as, directly on gabbro bodies crosscut by dolerite dykes. This evidence, coupled with the pervasive serpentinization of the peridotites (Boschi et al., 2017) and the lower hydration experienced by gabbro and dolerite bodies intruded in serpentinized peridotites, suggests a complex tectono-magmatic-hydrothermal evolution for the oceanic crust. The exhumation and hydration of mantle peridotites at the oceanic spreading ridge seem to have occurred progressively, allowing the sequential intrusion of gabbro bodies, when the serpentinized peridotite was already partially exhumed at plutonic depth, and dolerite dykes, when the system had reached a much shallower subvolcanic level.

3 Results

Old mining documentation was thoroughly studied and integrated with new surface and underground mapping. Ore samples, gangue minerals and host rocks were collected and petrographically and geochemically characterized.

In Liguria, Cu was mainly produced from typical Cu–Fe–Zn VMS deposits, including pyrite-chalcopyrite stockworks, breccias and seafloor-stratiform bodies formed throughout the entire ophiolitic sequence, up to the contact with the sedimentary cover (Zaccarini & Garuti, 2008).

However, only few typical, pillow-lava basalt-hosted, Cu–Fe–Zn VMS deposits occur in Tuscany. Most of the ores are hosted in the serpentinite-gabbro basement and at the contact with the overlying pillow-lava basalt. Chalcopyrite stockworks (Fig. 2A) are present in serpentinites and gabbro, but the largest deposits are hosted by cataclastic shear-zones developed at the contact between pillow-lava basalt and the underlying serpentinite-gabbro basement, as well as into the serpentinite-gabbro basement (Fig. 2B). Here, early chalcopyrite stockworks have been strongly mechanically and chemically reworked to form chalcopyrite-bornite-chalcocite nodules embedded in a chlorite, Ca-rich amphibole, Fe-rich serpentine, quartz, andradite and xonotlite assemblage (Fig. 2b, d).

The ores contain substantial amount of sphalerite and pyrite and ubiquitous grains of clausthalite, native tellurium and gold (Fig. 2c,d), in accordance with the significant Te–Se–Au content of these deposits.

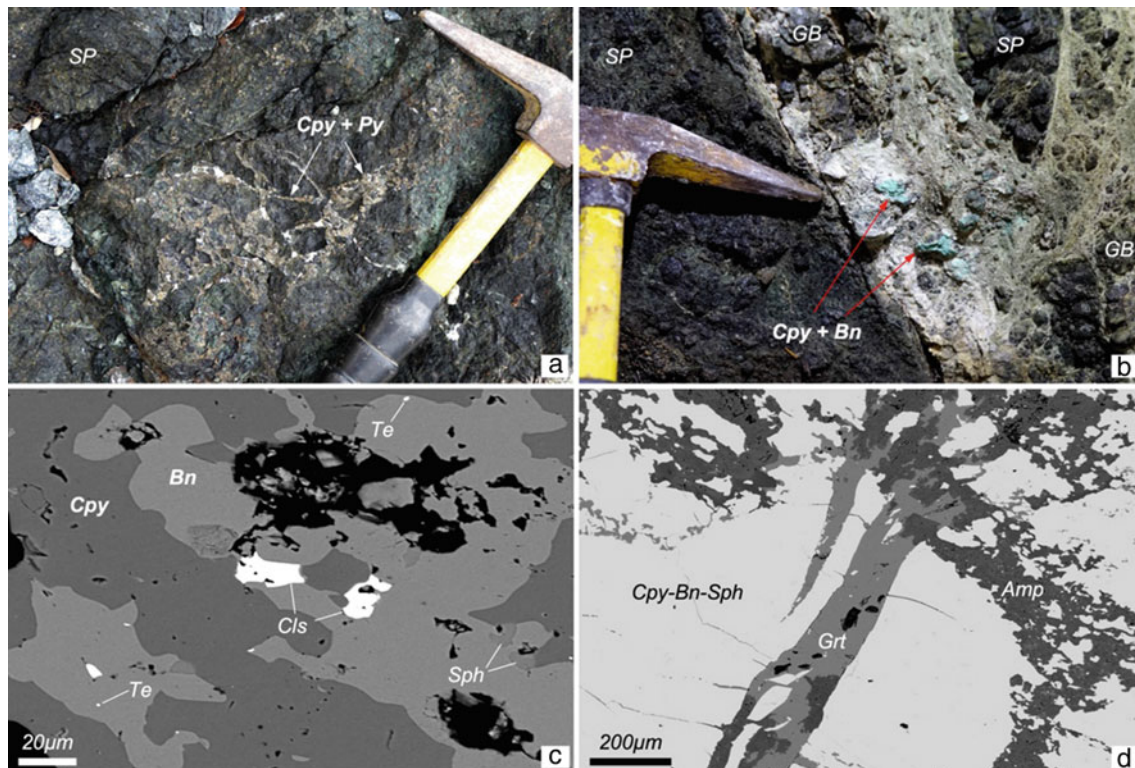


Fig. 2 **a** Chalcopyrite-pyrite stockwork (Cpy + Py) in serpentinite (SP) at Libbiano; **b** clasts of chalcopyrite-bornite (Cpy-Bn), serpentinite (SP) and gabbro (GB) in the reworked ore at Querceto; **c** clausthalite

(Cls) and native tellurium (Te) grains in a bornite (Bn)-chalcopyrite (Cpy) nodule; **d** garnet (Grt) and Ca-amphibole (Amp) hosting the Cu–Fe–Zn sulfide assemblage

4 Discussion

The overall characters of the Cu–Fe–Zn ores and host rocks suggest a formation in an active oceanic core complex along the Jurassic slow-spreading ridge of the Ligurian–Piedmont Ocean. Both the early stockwork ore and the late reworked nodular ore clearly post-date the serpentinization of ultramafic rocks and the emplacement of the plutonic bodies of gabbro and the subvolcanic bodies of dolerite. The strong mechanical and chemical reworking of the Tuscan orebodies suggests a prolonged process developed throughout the transition from the early stages of low-angle detachment to the late collapse stage (Patten et al., 2022). Transient magmatism coupled with the focalization of hydrothermal fluids along shear-zones could have occurred during the final exhumation of the oceanic core complex. The occurrence of a peculiar gangue mineral association (garnet, Ca-amphibole, xonotlite) and the specific metal enrichment (Se, Te, Au) of the reworked ore suggest a proximal position to the causative magmatic intrusion and the possible involvement of magmatic fluids.

References

- Boschi, C., Dini, A., Baneschi, I., Bedini, F., Perchiazzi, N., & Cavallo, A. (2017). Brucite-driven CO₂ uptake in serpentinized dunites (Ligurian Ophiolites, Montecastelli, Tuscany). *Lithos*, 288–289, 264–281.
- Conti, P., Cornamusini, G., & Carmignani, L. (2020). An outline of the geology of the Northern Apennines (Italy), with geological map at 1:250,000 scale. *Italian Journal of Geosciences*, 139, 149–194.
- Dini, A., & Boschi, C. (2017). I giacimenti cupriferi delle ofioliti toscane. *Rivista Mineralogica Italiana*, 42, 84–101.
- Elter, P. (1975). L'ensemble ligure. *Bulletin De La Société Géologique De France*, 17, 984–997.
- Klemm, D., & Wagner, J. (1982). Copper deposits in ophiolites of southern Tuscany. *Ofioliti*, 7, 331–336.
- Marroni, M., Meneghini, F., & Pandolfi, L. (2010). Anatomy of the Ligure-Piemontese subduction system: Evidence from Late Cretaceous–middle Eocene convergent margin deposits in the Northern Apennines, Italy. *International Geology Review*, 52, 1160–1192.
- Patten, C. G. C., Coltat, R., Junge, M., Peillod, A., Ulrich, M., Manatschal, G., & Kolb, J. (2022). Ultramafic-hosted volcanogenic massive sulfide deposits: An overlooked sub-class of VMS deposit forming in complex tectonic environments. *Earth-Science Reviews*, 224, 103891.
- Piccardo, G. B., Müntener, O., Zanetti, A., & Pettke, T. (2004). Ophiolitic peridotites of the Alpine-Appennine system: Mantle processes and geodynamic relevance. *International Geology Review*, 46, 1119–1159.
- Zaccarini, F., & Garuti, G. (2008). Mineralogy and chemical composition of VMS deposits of northern Apennine ophiolites, Italy: Evidence for the influence of country rock type on ore composition. *Mineralogy and Petrology*, 94, 61–83.



Lithostratigraphy, Whole-Rock, and Sm–Nd Isotopic Data of the Ediacaran Magmatic Rocks from the Zgounder Ag–Hg Deposit (Siroua Massif, Central Anti-Atlas, Morocco)

Abdelhay Ben-Tami, Said Belkacim, Bouchra Baidada, Jamal El Kabouri, Mohamed Assalmi, Mohamed Bhilisse, and Mohammed Bouabdellah

Abstract

In the Zgounder Ag–Hg high-grade deposit, Ediacaran magmatic rocks of different types and compositions have been intruded by several dolerite and rhyolite dike swarms. This contribution focuses on the 610–541 Ma period of the Zgounder mine region, starting with the volcano-sedimentary successions of the Bou-Salda Group (610–580 Ma), represented in the studied area by the Tadmant rhyolite. The overlaying Ouarzazate Group (580–541 Ma) consists predominantly of volcano-sedimentary series intruded by contemporaneous multipulses of felsic plutons. Geochemically, two magmatic associations are distinguished: (i) mafic metaluminous rocks of within plate and calc-alkaline to transitional affinity; and (ii) felsic-intermediate rocks of peraluminous and high-K calc-alkaline signature. For all of the samples, the hybrid isotopic signature ($\epsilon\text{Nd}_{(570)} = -0.9$ to $+4.3$) and the calculated T_{DM} model ages from 1197 to 1526 Ma indicate mixing between a depleted mantle source with an enriched source (probably a Paleoproterozoic crust).

These findings suggest that the Ediacaran magmatism of Zgounder deposit was emplaced in a long-lived syn-to-post-collisional environment during the metacratonic evolution of the northern edge of the West African Craton (WAC). During this period, huge volumes of mostly felsic magmas, typical of a Silicic Large Igneous Province (SLIP), were emplaced during multiple pulses. The last two pulses, at the final stage of the Pan-African orogeny (560–550 Ma), seem to be responsible for a pervasive hydrothermal activity recorded over the whole Anti-Atlas. Consequently, this hydrothermal activity led to the formation of numerous world-class precious and base metal porphyry-epithermal deposits, including the investigated Ag–Hg Zgounder deposit.

Keywords

Ouarzazate Supergroup • Silicic Large Igneous Provinces (SLIPs) • Ag–Hg Zgounder deposit • Siroua Massif • Sm–Nd isotopes

A. Ben-Tami (✉) · S. Belkacim
Laboratoire de Géologie Appliquée et Géo-Environnement,
Faculté des Sciences, Université Ibn Zohr, B.P.8106, Agadir,
Maroc
e-mail: abdelhaybentami@gmail.com

B. Baidada
École Supérieure de Technologie, Fkih Ben Salah, Beni Mellal,
Morocco

J. El Kabouri
Équipe de Géodynamique, Géo-Éducation, et Patrimoine
Géologique, Faculté des Sciences, Chouaib Doukkali University,
B.P. 20, 24000 El Jadida, Maroc

M. Assalmi · M. Bhilisse
Aya Gold and Silver Group, Zgounder Millennium Silver Mining
(ZMSM), Rue De L'épargne, Quartier Racine, Casablanca, Maroc

M. Bouabdellah
Laboratoire des Gîtes Minéraux, Hydrogéologie et
Environnement, Faculté des Sciences, Université Mohammed
Premier, 60000 Oujda, Maroc

1 Introduction

The studied Zgounder Ag–Hg epithermal deposit is located on the northwest flank of Siroua within the Ouzellagh-Siroua Salient (OSS), in the central Anti-Atlas Mountains, approximately 260 km east of Agadir city (Fig. 1a). The wide range of outcropping rock types and compositions attest to a complex geological history. Pan-African island arc, ophiolite and thick Ediacaran sedimentary and volcano-sedimentary units were deposited during the multiple events that mark the evolution of the Anti-Atlas segment of Morocco. Yet, the evolution of the latter is still debated and not fully understood, especially for the last two events in which the tectonic processes have changed from a complete transpressive regime around 615–580 Ma (Gasquet et al., 2008; Thomas et al., 2002) to a transtensive one

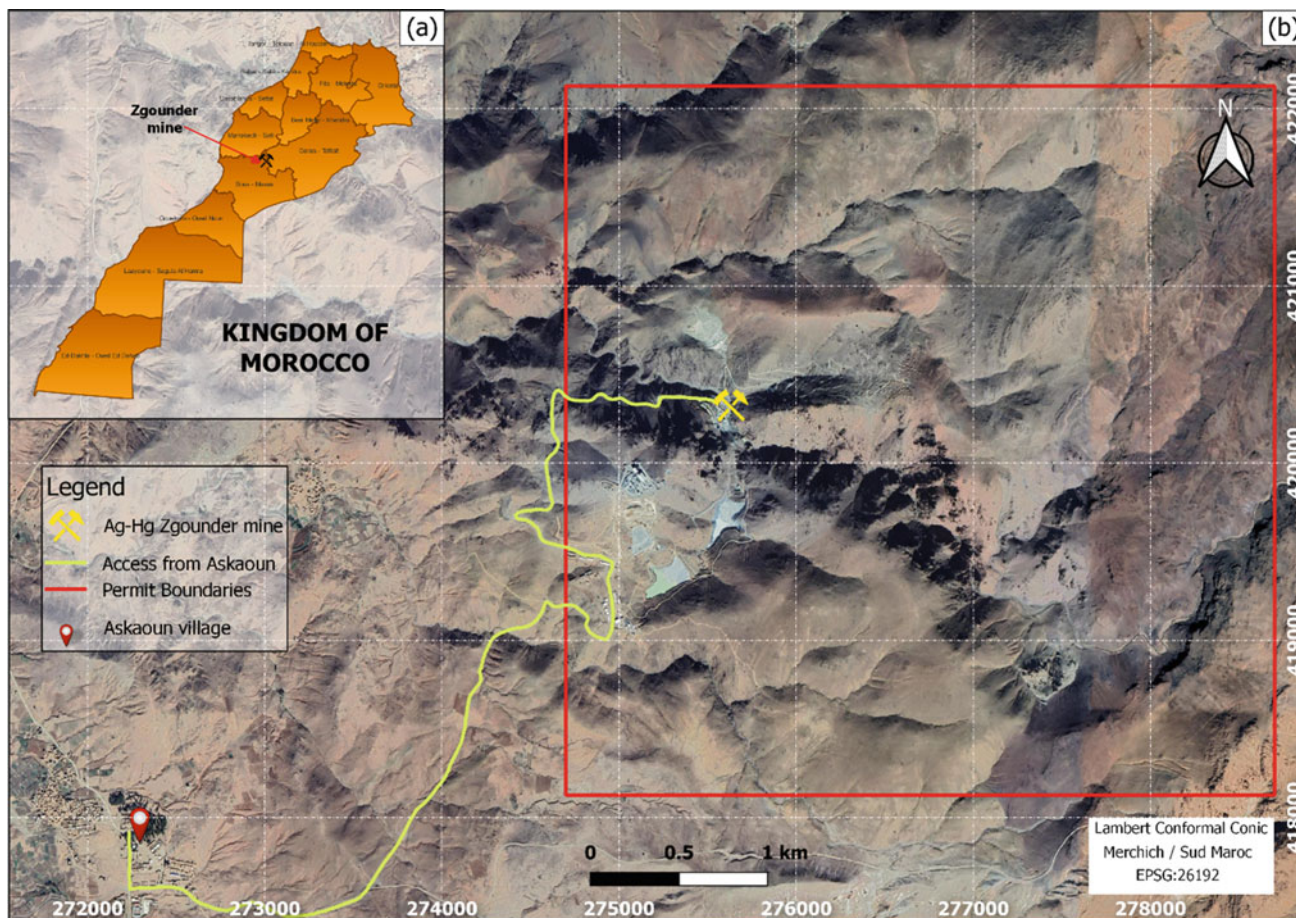


Fig. 1 Geographic presentation of the study area, illustrating: **a** administrative location of the Zgounder mine in the kingdom of Morocco; **b** access from Askaoun village to Zgounder mine site and permit boundaries

at ca. 580–540 Ma with the emplacement of late to post orogenic granites and coeval volcanic and volcanoclastic rocks (Tuduri et al., 2018 and references therein).

The present contribution focuses on the Ediacaran period which is exemplified by the occurrence of large felsic plutons and coeval pyroclastic units referred to as the Ouarzazate Supergroup (610–541 Ma). These rocks were studied by combining detailed field mapping, geochemistry (whole-rock major and trace elements including REEs) and Sm–Nd isotopic analyses. Therefore, we provide new insights on magmatic processes that prevailed during this time period and hence challenge the previously proposed geodynamic models.

2 Lithostratigraphy

The evolution of the Ouarzazate Supergroup in the OSS has been previously approached by several authors (Belkacim et al., 2017; Thomas et al., 2002, 2004; Toummite et al.,

2012). Previous studies on the geology of the region attributed the oldest sedimentary sequences along with intercalated volcanic rocks to the Saghro Group (620–610 Ma) that has been interpreted to be deposited during the uplift of the West African Craton (WAC). Following this event, the intrusive Tadmant Formation (rhyolite with some ignimbritic phases) represents the Bou-Salda Group according to Thomas et al., (2002) in the Zgounder mine region. Additionally, it reflects a different tectonic regime involving strike-slip pull-apart basins favoring the deposition of its 400–1000 m volcano-sedimentary successions. Yet, the local field relationships and cross-cutting information are not homogenous to both Tadmant Formation and its equivalent ‘Tamriwine Formation’ located further east of the Zgounder mine (Thomas et al., 2002). In addition, the attributed age for Bou-Salda Group has only been estimated by the dating of these two units. Lastly, The Ouarzazate Group successions are positioned to the west and defined by the multi-phase Askaoun granodiorite (Toummite et al., 2012). More scattered volcano-sedimentary units are found

to the east of the Zgounder mine and composed essentially of wide spread pyroclastic rocks (ignimbrite, lapilli tuff; Pelleter et al., 2016; Thomas et al., 2002). The whole complex is intruded by several dolerite and rhyolite dikes and covered locally by Neogene volcanic rocks of trachyte to trachy-andesite in composition.

3 Sampling and Analytical Methods

Twenty-seven samples were selected on the best-exposed outcrops as well as in various boreholes from Zgounder mine area; the goal is to ensure the freshness of the samples. Crushing and powdering of the rock samples designated for whole-rock and Sm–Nd isotopic analyses were performed at the facilities of the Zgounder Millennium Silver Mining Company (ZMSM). Analysis was carried out at the Activation Laboratories (ActLabs), Ancaster, Ontario, (Canada). Details on the procedure, precision and accuracy of ActLabs analysis are available at www.actlabs.com.

4 Results

4.1 Petrography

The studied volcanic rocks consist of basalt, andesite, dolerite and rhyolite, with some felsic pyroclastic terms (ignimbrite). Most mafic rocks are fine-grained and dark green to olive green in color. Felsic rocks are light pink to brownish. Under the microscope, mafic rocks contain fine-grained plagioclase and clinopyroxene phenocrysts dispersed in the groundmass. The texture is microlitic to microlitic-porphyrific for basalt and andesite. Dolerite shows intergranular texture. Rhyolite has a microcrystalline porphyritic texture, with phenocrysts of quartz and altered plagioclase and K-feldspars. Ignimbrite shows an eutaxitic texture with remarkable fiamme and dense welded volcanic glass, along with cryptocrystalline facies locally fluidal, mainly composed of quartz, opaque minerals, sericitized plagioclase and K-feldspars. The plutonic rocks consist of gabbro, granodiorite and granite. Gabbro is fine to medium-grained, with heavily altered pyroxenes and amphiboles. Granodiorite and granite show a homogenous coarse-grained texture. The loss on ignition (LOI) at 1100 °C is low for most samples (less than 3 wt%), except in some cases where it is higher than 3 wt% for basalt, gabbro and andesite. All rocks suffered a greenschist facies metamorphism with albite, chlorite, epidote, sericite, calcite, ilmenite and quartz as metamorphic phases.

4.2 Whole-Rock Geochemistry

Ediacaran magmatism of Zgounder mine (EMZM) consists of intrusive and extrusive rocks with compositions ranging from sub-alkaline basalt to rhyolite according to the Nb/Y–Zr/Ti diagram of Winchester and Floyd (1977; Fig. 2a). In the Harker diagrams, Al₂O₃, FeO, MgO, CaO and TiO₂ show a negative correlation with SiO₂, whereas major elements vs Zr show no significant correlations. Still, two groups could be recognized, the first one formed by mafic rocks and the second one formed by felsic-intermediate rocks. Discrimination based on the alkali-total iron-magnesium (AFM) diagram of Irvine and Baragar (1971) indicates that mafic rocks (SiO₂ < 52 wt%) plot within the tholeiitic area, while felsic-intermediate samples (SiO₂ > 61 wt%) plot in the calc-alkaline field. However, when using Zr/Y vs. Th/Yb diagram of Ross and Bédard (2009; Fig. 2b), the calc-alkaline affinity for the most felsic-intermediate rocks is clearly confirmed, except for one granite (Zg_115) and one rhyolite sample (Zg_106) that fell within the transitional field (Fig. 2b). On the other hand, mafic rocks display both a calc-alkaline signature for dolerite and transitional character for gabbro and one basalt sample (Fig. 2b). In the A/CNK–A/NK plot of Shand (1943; Fig. 2c); mafic and intermediate samples are metaluminous, while felsic samples display a peraluminous character.

Mafic and andesite samples show coherent chondrite-normalized rare earth element patterns (Boynton, 1984) with slight LREEs enrichments ((La/Yb)_N = 1.83–7.36), HREE depletions, and no negative Eu anomalies ($\delta\text{Eu} = 0.52\text{--}1.28$) (Fig. 2d). The primitive mantle-normalized trace element patterns (after Sun and McDonough 1989) exhibit a slight enrichment in large ion lithophile elements (LILE), depletions in high field strength elements (HFSE) and positive Pb anomalies. Nevertheless, felsic and granodiorite samples show slight LREE enrichment ((La/Yb)_N = 0.89–17.93) and strongly negative Eu anomalies ($\delta\text{Eu} = 0.04\text{--}0.61$). In the primitive mantle-normalized diagram, they are enriched in Nd, Sm, Pb and LILE (e.g., Rb, U, and Th) and depleted in Ba, Sr and HFSE (e.g., Nb and Ti).

4.3 Sm–Nd Isotopic Data

The $\epsilon\text{Nd}_{(570)}$ of mafic rocks range from – 0.4 to + 4.3 (– 0.4 for doleritic dyke, + 2.8 for basalt and + 4.3 for gabbro) and TDM model age range from 1197 to 1526 Ma. Felsic-intermediate rocks show $\epsilon\text{Nd}_{(570)}$ between – 0.9 to + 1.1 (– 0.1 and – 0.9 for rhyolite, 0 for granite and + 1.1 for granodiorite) and TDM model age between 1252 and 1483 Ma.

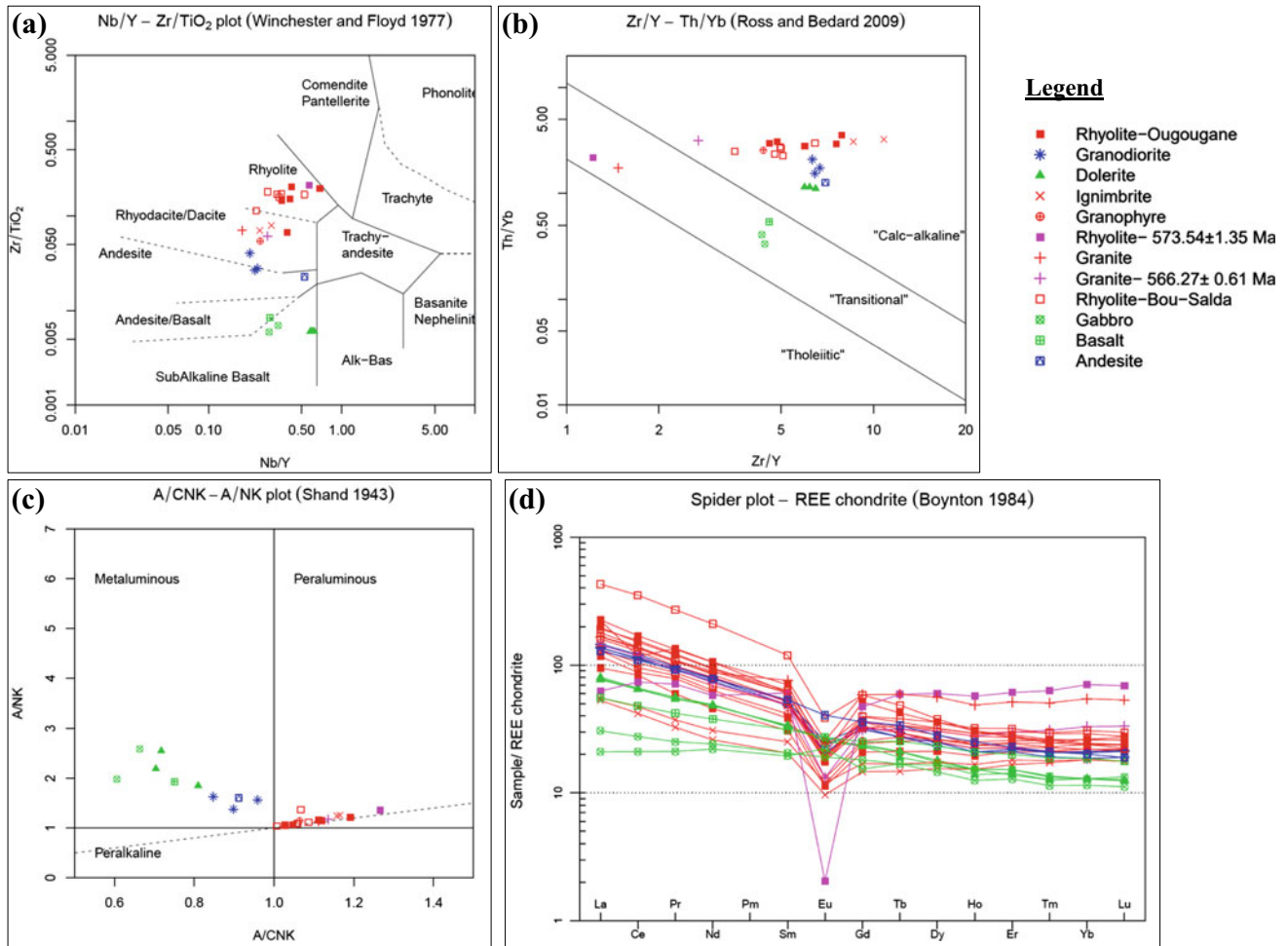


Fig. 2 Analyzed samples plotted in **a** (Nb/Y–Zr/Ti diagram of Winchester and Floyd (1977) for classification; **b** Zr/Y versus Th/Yb diagram of Ross and Bédard (2009); **c** A/CNK–A/NK plot of Shand

(1943) for the metaluminous and peraluminous character; **d** REE elements normalized to chondrite diagram (Boynton 1984)

In the Sirwa Massif, no Mesoproterozoic crust has been found (except few dikes in the western Anti-Atlas). Hence, this hybrid isotopic signature ($\epsilon\text{Nd}_{(570)} = -0.9$ to $+4.3$ and TDM model ages from 1197 to 1526 Ma) indicates mixing between a depleted source (probably depleted mantle) and an enriched source (probably a Paleoproterozoic crust).

5 Discussion

The studied rocks belong to the Ouarzazate Supergroup (610–541 Ma), representing evidence of syn-to-post-collisional magmatism recorded over the whole Anti-Atlas, with strong extensional tectonics and orogenic collapse at the end of the Pan-African orogeny (Gasquet et al., 2008; Thomas et al., 2004). Based on geochemical proxies (major and trace elements), the EMZM appear to comprise two magmatic associations: (1) mafic metaluminous rocks of within plate and calc-alkaline to transitional

affinity; and (2) felsic-intermediate rocks of peraluminous and High-K calc-alkaline affinity. The origin of these two distinct magmatic series could be derived either from fractional crystallization and contamination/assimilation of primary mafic lithologies to produce felsic-intermediate rocks, or from different magmatic sources. The lack of significant correlation between all rock types and the silica gap between mafic and felsic-intermediate rocks does not support co-genetic signature between the two groups. The origin of these groups could be explained by the source of the magma, where the magma in the first group (mafic rocks) is derived from the partial melting of high-K mafic rocks, and magma in the second group (intermediate and felsic rocks) could be generated by the melting of metasediments based on major elements concentration diagram of Laurent et al. (2014). Furthermore, the hybrid isotopic signature for both groups indicates a mixture between a depleted mantle source and an enriched Paleoproterozoic crust.

In light of these results, the EMZM may have been emplaced during a long-lived geotectonic process evolving from a transpressive to a transtensive regime, without significant crustal or lithospheric thickening (Belkacim et al., 2017; Ennih & Liégeois, 2008). Geochronological data support that the magmatic activity of the Ouarzazate Supergroup was emplaced via at least three pulses (flare-ups) (Belkacim et al., 2021; Tuduri et al., 2018). Such long-lived magmatic activity with the subsequent huge volume of mostly felsic magma is typical of a Silicic Large Igneous Province (SLIP) as defined by Ernst (2014). Within this framework, intense metallogenic activity occurred giving rise to numerous world-class precious and base metal porphyry-epithermal deposits, including the Ag–Hg Zgounder deposit.

6 Conclusions

The Ediacaran magmatism of Zgounder deposit has been studied using lithostratigraphic, petrographic, and geochemical approaches. The examined rocks range in composition from sub-alkaline basalt to rhyolite, through basaltic-andesite, andesite and dacite. The two recorded magmatic series were emplaced during multiple pulses, typical of a Silicic Large Igneous Province, in a syn-to-post-collisional stage of the Pan-African orogeny. The subsequent orogenic collapse being the precursor of an intense metallogenic activity recorded over the Anti-Atlas. Our isotopic data indicate the importance of mixing between mantle-derived magmas and Paleoproterozoic continental crust during magma genesis.

References

- Belkacim, S., Gasquet, D., Liégeois, J. P., Arai, S., Gahlan, H. A., Ahmed, H., Ishida, Y., Ikenne, M. (2017). The Ediacaran volcanic rocks and associated mafic dykes of the Ouarzazate Group (Anti-Atlas, Morocco): Clinopyroxene composition, whole-rock geochemistry and Sr–Nd isotopes constraints from the Ouzellarh–Siroua salient (Tifnoute valley). *Journal of African Earth Sciences*, 127, 113–135. (2017). <https://doi.org/10.1016/j.jafrearsci.2016.08.002>
- Belkacim, S., Perrot M., Davies, J., Ikenne, M., Liégeois, J. P. (2021). *The Ediacaran Ouarzazate Group, a metacratonic silicic large igneous province (SLIP): new U–Pb zircon ages from Ouzellarh–Siroua Salient (Tifnoute Valley)*. Geological Society of America Northeastern Section (NEGSA). Abstracts with Programs. Online meeting. March 14–15, 2021.
- Boynton, W. V. (1984). Cosmochemistry of the rare earth elements: meteorite studies. In *Developments in geochemistry, Elsevier*, 2, 63–114.
- Ennih, N., & Liégeois, J. P. (2008). The boundaries of the West African craton, with special reference to the basement of the Moroccan metacratonic Anti-Atlas belt. *Geological Society, London, Special Publications*, 297(1), 1–17. <https://doi.org/10.1144/SP297.1>
- Ernst, R. E. (2014). *Large igneous provinces*. Cambridge University Press.
- Gasquet, D., Ennih, N., Liégeois, J. P., Soulaïmani, A., & Michard, A. (2008). The Pan-African Belt. In A. Michard, O. Saddiqi, A. Chalouan, D. Frizon de Lamotte (Eds.), *Continental evolution: The geology of Morocco*. Lecturer Notes in Earth Science (Vol. 116, pp. 33–64).
- Irvine, T. N., & Baragar, W. R. A. (1971). A guide to the chemical classification of the common volcanic rocks. *Canadian journal of earth sciences*, 8(5), 523–548.
- Laurent, O., Martin, H., Moyaen J. F., Doucelance, R. (2014). The diversity and evolution of late-Archean granites: Evidence for the onset of a “modern-style” plate tectonics between 3.0 and 2.5 Ga. *Lithos*, 205, 208–235. <https://doi.org/10.1016/j.lithos.2014.05.011>
- Pelleter, E., Cheilletz, A., Gasquet, D., Mouttaqi, A., Annich, M., Camus, Q., & Ouchtouban, L. (2016). U/Pb ages of magmatism in the zgounder epithermal Ag–Hg deposit, Sirwa Window, Anti-Atlas, Morocco. In *Mineral deposits of North Africa*. (pp. 143–165). Springer. https://doi.org/10.1007/978-3-319-31733-5_5
- Ross, P. S., & Bédard, J. H. (2009). Magmatic affinity of modern and ancient subalkaline volcanic rocks determined from trace-element discriminant diagrams. *Canadian Journal of Earth Sciences*, 46 (11), 823–839.
- Shand, S. J. (1943). Eruptive rocks; their genesis, composition, classification, and their relation to ore-deposits with a chapter on meteorite. *New York: John Wiley & Sons*.
- Sun, S. S., & McDonough, W. F. (1989). Chemical and isotopic systematics of oceanic basalts: implications for mantle composition and processes. *Geological Society, London, Special Publications*, 42(1), 313–345.
- Thomas, R. J., Chevallier, L., Gresse, P., Harmer, R., Eglington, B., Armstrong, R., de Beer, C. H., Martini, J. E. J., De Kock, G. S., Macey, P. H., & Ingram, B. Precambrian evolution of the Sirwa Window, Anti-Atlas Orogen, Morocco. *Precambrian Research*, 118 (1–2), 1–57 (2002). [https://doi.org/10.1016/S0301-9268\(02\)00075-X](https://doi.org/10.1016/S0301-9268(02)00075-X)
- Thomas, R. J., Fekkak, A., Ennih, N., Errami, E., Loughlin, S. C., Gresse, P. G., Chevallier, L. P., & Liégeois, J. P. (2004). A new lithostratigraphic framework for the Anti-Atlas Orogen, Morocco. *Journal of African Earth Sciences*, 39(3–5), 217–226 (2004). <https://doi.org/10.1016/j.jafrearsci.2004.07.046>
- Toummite, A., Liégeois, J. P., Gasquet, D., Bruguier, O., Beraaouz, E. H., & Ikenne, M. (2012). Field, geochemistry and Sr–Nd isotopes of the Pan-African granitoids from the Tifnoute Valley (Sirwa, Anti-Atlas, Morocco): a post-collisional event in a metacratonic setting. *Mineralogy and Petrology*, 107(5), 739–763 (2012). <https://doi.org/10.1007/s00710-012-0245-3>
- Tuduri, J., Chauvet, A., Barbanson, L., Bourdier, J. L., Labriki, M., Ennaciri, A., Badra, L., Dubois, M., Ebbaciri-Leloix, C., & Maacha, L. (2018). The jbel saghro Au (–Ag, Cu) and Ag–Hg metallogenic province: product of a long-lived Ediacaran tectono-magmatic evolution in the Moroccan Anti-Atlas. *Minerals*, 8(12), 592 (2018). <https://doi.org/10.3390/min8120592>
- Winchester, J. A., & Floyd, P. A. (1977). Geochemical discrimination of different magma series and their differentiation products using immobile elements. *Chemical geology*, 20, 325–343.



Characterization and Valorization of Clay Deposits from the Region of Beni Mellal-Khenifra in the Ceramic Industry (Morocco)

Soukaina Bedda, Toufik Remmal, Fouad Amraoui, and Assia Laroussi

Abstract

The state of the clay reserves of the exploited or potentially exploitable sites is diagnosed, integrating the geological, physico-chemical and mechanical aspects in order to better valorize these resources. This study focused on 15 representative samples collected in different geological contexts. The particle size distribution, Atterberg limits, X-ray diffraction (XRD), X-ray fluorescence (XRF), total organic content and calcimetry were determined. The mechanical characteristics were revealed by studying the shrinkage after drying/firing process, loss on ignition (LOI), the bending test and water absorption capacity (WAC). The studied clays presented a silty to sandy-silty composition with a clay fraction not exceeding 12.5% and a plasticity index (PI) between 20 and 30%. The carbonate and organic matter contents are low ($\text{CaCO}_{3T} < 12.5\%$, $\text{OM} < 2.5\%$). The bulk mineralogy is dominated by quartz (5–36%), K-feldspar (3.3–19.7%) and goethite (8.8–25%). The clay mineral content is between 12 and 25.2%. It is dominated by illite (5–90%), kaolinite (0–70%) and chlorite (0–45%). Smectite, vermiculite and mixed-layer clays are rarely identified. The chemical composition is dominated by SiO_2 (44.9–62.2%) and Al_2O_3 (10.5–19.6%). Technological and mechanical tests show a high bending strength (BS) (5.01–13.02 N/mm²) which is positively correlated with the quartz content but inversely proportional to the calcium carbonate content. The LOI (8.69–29.78%) and the WAC (7.88–35.72%) are tolerable. The drying shrinkage (DS) (0.31–14.43%) and firing shrinkage (FS) (0.24–5.59%) coefficients are low. The suitability of clays from the Beni Mellal-Khenifra region to be used in ceramic manufacturing is constrained by pretreatments

(crushing, grinding, sieving) and formulation to balance the composition and/or the particle size curve or to correct the plasticity.

Keywords

Clay • Pottery • Beni Mellal-Khenifra • Characterization • Valorization

1 Introduction

Clay is a very abundant raw material, with a wide range of applications due to its physico-chemical and technological properties.

In the Beni Mellal-Khenifra region, the exploitation of clays in pottery is entirely artisanal, founded and managed by the artisans themselves who draw the raw material near their workshops. Economically, pottery plays an important role in employment as it is a significant source of financial gain for the local population. The recognition of the supply sites as well as the exploitation methods and treatment of clays come first from experience inherited from generation to generation. Nevertheless, the pottery sector is not well managed in terms of quantity and quality and is increasingly subject to many constraints related generally to the quality of the pottery produced as well as the problems of raw material supply. These two factors are major elements that can slow down productivity and cause a serious decline of activity in the region.

The purpose of this study is to make a diagnosis of the clay reserves' state in the Beni Mellal-Khenifra region, integrating the geological aspects of the exploited or potentially exploitable sites as well as the physico-chemical and technological aspects of clays, and also, to identify opportunities for valorization and optimization to ensure the quantitative and qualitative availability of these clays for the artisanal pottery sector.

S. Bedda (✉) · T. Remmal · F. Amraoui · A. Laroussi
Laboratory of Applied Geosciences to Development Engineering,
Faculty of Sciences Ain Chock, Hassan II University of
Casablanca, B.P 5366 Maarif, Casablanca, Morocco
e-mail: soukaina.bedda-etu@etu.univh2c.ma

Therefore, this study constitutes a scientific and technical contribution in the knowledge, the characterization and the enhancement of clay materials in the Beni Mellal-Khenifra region, which is an essential phase to control a sustainable supply for the potters in the area.

2 Materials and Methods

2.1 Materials

The studies had focused on 15 representative samples taken from six main sites exploited by the potters of the Beni Mellal-Khenifra region (see Fig. 1).

The targeted clay formations concern the recent alluvial terraces, the Cretaceous marls, the red formations underlining the Upper Triassic-Lias transition, the granitic arena of the Eopermian complex and the flysch of the Viséan basement.

2.2 Methods

The performed analyses for the 15 samples include physico-chemical, mineralogical and technological analyses.

The particle size distribution was carried out using sieving analysis according to the NF P 94-056 (1996) standard and laser diffraction analysis using a Horiba LA-920 laser analyzer. The Atterberg limits were determined according to the NF P 94-052-1 (1995) and NF P 94-051 (1993) standards. The organic matter content was determined according to XP P 94-047 (1998) standard. The content of CaCO_3 was determined according to the NF P 94-048 (1996) standard. The mineralogical analysis was performed by X-ray diffraction using a Bruker D8-Advance diffractometer. The chemical analysis was performed by X-ray fluorescence using a PANalytical Axios spectrometer.

For each clay sample, shrinkage, loss on ignition, capacity of water absorption and bending strength were determined on bricks made in the laboratory.

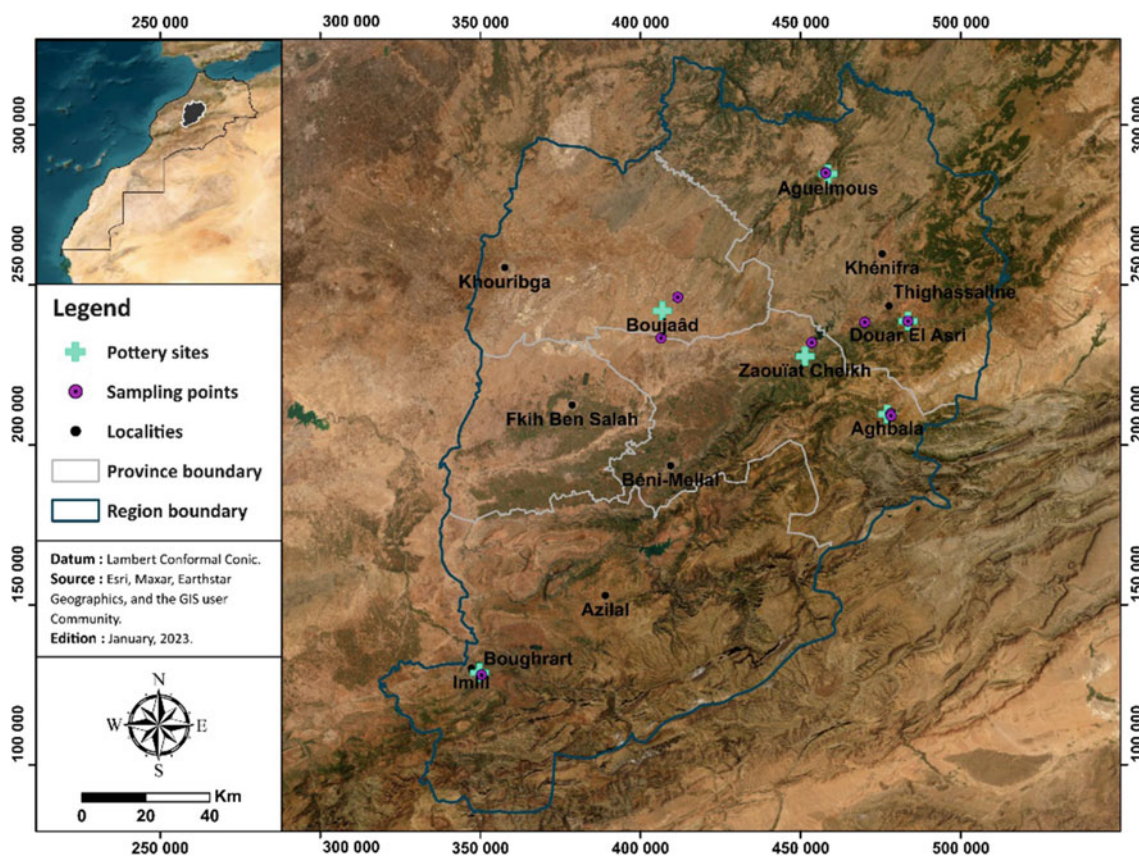


Fig. 1 Geographical context of the Beni Mellal-Khenifra region

3 Results

3.1 Characterization of the Raw Clay Samples

The particle size analysis shows a wide variation in grain size with a dominant silty fraction for most samples (see Fig. 2) (McManus, 1988). The Atterberg limits show that most of the studied samples have liquidity limit values above 35% and are then considered as moderately plastic materials according to Holtz and Kovacs (1981). The organic matter analysis shows that the studied samples have low organic

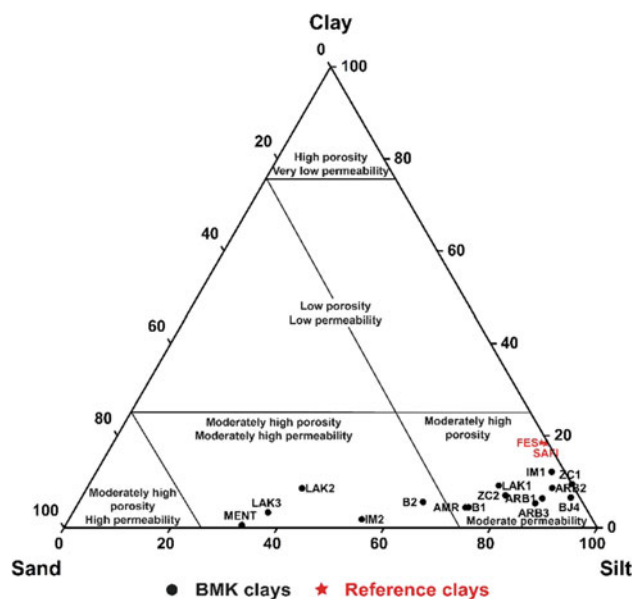


Fig. 2 Typology of raw clays and reference clays according to their grain size distribution

matter content. The calcimetric analysis shows that the studied samples present a large variation in CaCO₃ content.

The bulk mineralogy analysis revealed that samples consist mainly of quartz, feldspar, clay minerals and goethite (see Fig. 3), while the clay fraction analysis revealed that the samples consist mainly of illite, kaolinite and chlorite (see Fig. 3).

The chemical analysis revealed that the most abundant oxides in the studied samples are SiO₂ (44.9–62.2%) and Al₂O₃ (10.5–19.6%) (see Fig. 4).

3.2 Characterization of the Clay Bricks

Technological and mechanical tests show a high BS (5.01–13.02 N/mm²) which is positively correlated with the quartz content but inversely proportional to the calcium carbonate content. The LOI (8.69–29.78%) and the WAC (7.88–35.72%) are tolerable. The DS (0.31–14.43%) and FS (0.24–5.59%) coefficients are low (see Table 1).

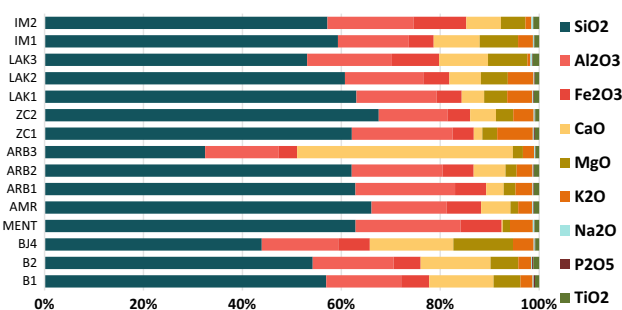


Fig. 4 Chemical composition of the studied samples

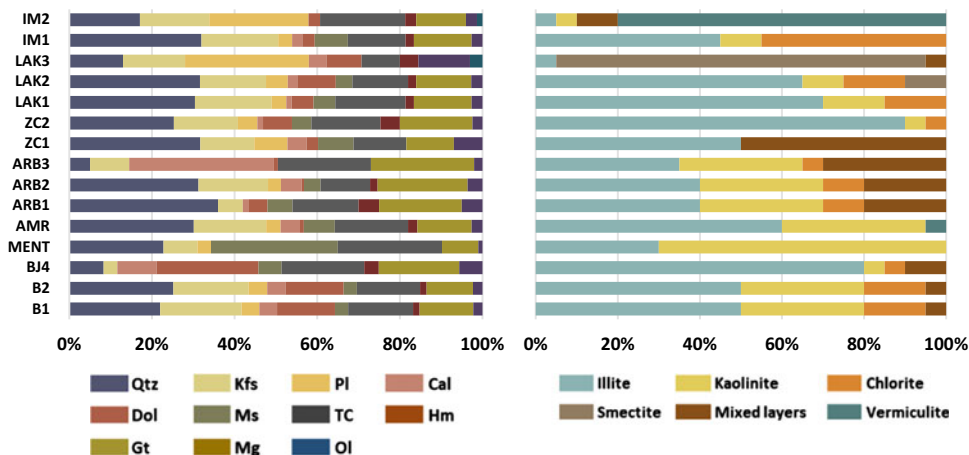


Fig. 3 Composition of the bulk mineral and the clay fraction of the studied samples. Qtz: Quartz, Cal: Calcite, Kfs: K-Feldspar, Dol: Dolomite, Pl: Plagioclase, Ms: Muscovite, TC: Total clay, Hem:

Hematite, Mag: Magnetite, Gt: Goethite, Ol: Olivine, Ill: Illite, Kln: Kaolinite, Chl: Chlorite, Sme: Smectite, ML: Mixed layers, Vrm: Vermiculite, Plg: Palygorskite

Table 1 Results of technological tests on the studied samples

	DS (%)	FS (%)	LOI (%)	WAC (%)	BS (N/mm ²)
B ₁	3.82	0.52	22.55	28.44	5.69
B ₂	5.21	0.26	18.81	21.25	6.24
BJ ₄	9.02	2.59	27.64	16.33	8.24
MENT	4.14	0.35	9.29	17.05	7.89
AMR	3.62	0.4	13.09	16.65	7.44
ARB ₁	6.57	0.39	10.73	12.13	11.33
ARB ₂	5.42	0.71	13.17	12.36	11.56
ARB ₃	5.30	0.67	29.78	35.72	5.01
ZC ₁	14.43	5.59	21.48	7.88	13.02
ZC ₂	0.31	0.85	9.0	17.27	6.77
LAK ₁	1.39	0.24	8.77	18.05	7.07
LAK ₂	4.09	0.30	10.93	16.53	8.54
LAK ₃	ND	ND	ND	ND	ND
IM ₁	1.87	0.35	8.69	18.61	7.32
IM ₂	5.98	1.16	14.03	13.39	11.98

DS drying shrinkage; FS firing shrinkage; LOI loss on ignition; WAC water absorption capacity; BS bending strength

4 Discussion

The suitability of clay materials for use in pottery is controlled and determined by their physical, chemical, mineralogical and technological properties (Daoudi et al., 2014; El Ouahabi et al., 2014; Nasri et al., 2019). The representation of the obtained results in multi-criteria diagrams can reveal relationship existing between the different characteristics of clays, hence the study of their potentiality for the exploitation in the pottery.

Overall, the raw clays used by potters are of acceptable quality, due to their grain distribution, mineralogical and chemical composition (Augustinik, 1956; Fiori et al., 1989; Strazzer et al., 1997; Winkler, 1954) and are suitable for making usual Moroccan pottery (tajines, majmars, kasaâs and jars).

5 Conclusions

The physico-chemical and technological characterization of the clays coming from the Beni Mellal-Khenifra region allowed to classify these studied materials in three categories according to their relevance to the use in pottery: six of them are not adapted to the manufacture of pottery products, five are acceptable but require modifications and four can be used alone, without modification. Therefore, in order to adapt

these materials to this application, it is advisable to proceed to some pretreatments (crushing, grinding and sieving) as well as to opt for mixtures with more appropriate formulations.

References

- Augustinik, A. J. (1957). W woprosu o metodikie issliedoeanija drierwiej keramiki. In A. J. Augustinik (Ed.), *Kratk. Soobszcz. IIMK, nr 64, 1956: [recenzja]/EF. Kwartalnik Historii Kultury Materialnej* (Vol. 5, No. 2).
- Daoudi, L., El Boudour El Idrissi, H., Saadi, L., Albizane, A., Bennazha, J., Waqif, M., El Ouahabi, M., & Fagel, N. (2014). Characteristics and ceramic properties of clayey materials from Ameziz region (Western High Atlas, Morocco). *Applied Clay Science, 102*, 139–147.
- El Ouahabi, M., Daoudi, L., De Vleeschouwer, F., Bindler, R., & Fagel, N. (2014). Potentiality of clay raw materials from northern Morocco in ceramic industry: Tetouan and Meknes areas. *Journal of Minerals and Materials Characterization and Engineering, 2*, 145–159.
- Fiori, C., Fabbri, B., Donati, G., & Venturi, I. (1989). Mineralogical composition of the clay bodies used in the Italian tile industry. *Applied Clay Science, 4*, 461–473.
- Holtz, R. D., & Kovacs, W. D. (1981). *An introduction to geotechnical engineering* (Vol. 747).
- McManus, J. (1988). Grain size distribution and interpretation. In M. E. Tucker (Ed.), *Techniques in sedimentology* (pp. 63–85). Blackwell Scientific Publications.
- Nasri, H., Azdimousa, A., El Hammouti, K., El Haddar, A., & El Ouahabi, M. (2019). Characterization of Neogene marls from the

- Kert Basin (northeast Morocco): Suitability for the ceramics industry. *Clay Minerals*, 54(4), 379–392.
- Strazzer, B., Dondi, M., & Marsigli, M. (1997). Composition and ceramic properties of tertiary-136 clays from southern Sardinia (Italy). *Applied Clay Science*, 12(3), 247–266.
- Winkler, V. H. (1954). Bedeutung der Korngrößenverteilung und des Mineralbestandes von Tonen für die Herstellung grobkeramischer Erzeugnisse. *Berichte der Deutschen Keramischen Gesellschaft*, 31 (10), 337–343.



3D Modeling and Resources Estimation of Coal Old Piles in Jerada Mine, Oriental Morocco

Ayoub El Aallaoui, Mustapha El Ghorfi, Abdellatif Elghali, Hamza Zine, Ayoub Bayoussef, Yassine Taha, Mostafa Benzaazoua, and Rachid Hakkou

Abstract

Besides being a cause of environmental problems, tailings and waste rock can also be potential sources of valuable minerals and metals. The Jerada mine (JM) in the eastern region of Morocco operated by Moroccan Coal Mines (MCD) for coal extraction is one of the many overburden mines in Morocco with large amounts of overburden since 2000 without rehabilitation plans. The main objective of this study is the coupling between 3D model as a tool to estimate the ore resources and evaluate the economic potential of coal mine waste rock (CMWR) piles and metallurgical study in the valorization of abandoned rejects. The study will initially focus on the 3D modeling of the CMWR piles and the estimation of their resources based on drill sampling to highlight the vast quantities of CMWR piles deposited on site. Physical–chemical characterization was performed using XRF, XRD, SEM, total C-S measurement and QEMSCAN. Eight CMWR piles (T01, T02, T03, T04, T05, T06, T07 and T08) were the target of our work to uncover the huge tonnages of coal stored in these stockpiles. The 3D model blocks show a total volume of 8.64 Mm³ of waste, which corresponds to 15.3 Mt on the piles. Chemical analyses have highlighted the presence of

significant concentrations of carbon, T08 with nearly 50% of the tonnage 7.36 Mt and a %C that is close to 8.5 wt%; T01 and T02 with 5.31 Mt and a %C of 12.75 wt% and T03, T04, T05, T06 and T07 regrouping 1.84 Mt. It should be noted that the %S in the T08 approaches 2 wt% with a high degree of oxidation, which may represent a source of acid mine drainage (AMD). The high carbon content and the large tonnages obtained indicate that the waste can be reused by re-exploitation or reused in other fields to limit and reduce its environmental impact.

Keywords

3D modeling • Mine waste • Jerada mine • Geochemistry • Coal mine waste rock

1 Introduction

Jerada coal is the only and oldest coal mine in Morocco and is considered as an anthracite-type deposit, located in the eastern region 60 km from Oujda and extended over 25 km from the east to the west with an extension of 4 km. Geologically, the Jerada basin is a part of the Paleozoic meseta massifs, characterized by the presence of early Syn-metamorphic folds on which rest in unconformity the Viseo-Namurien series. This Paleozoic massif is generally constituted by an alternation of volcano-sedimentary series dated from the inferior carboniferous surmounted by a Westphalian coal series (A, B and C). The whole basin is affected by folds with E-W direction, covered by the discordant Mesozoic series of the Atlasic highlands. The Westphalian C called the “productive coal” or “Jerada bed” (Essamoud, 2011; Owodenko, 1976) is marked by the deposition of 8 layers of coal (A, B, C, D, E, F and H), but only layers A, B, C and F are exploited. This productive coal has been subdivided by Owodenko (1976) into two main basins: a northern basin that contains only the layers A, B, C

A. E. Aallaoui (✉) · M. E. Ghorfi
Laboratory of Geo Resources, Geo Environment and Civil
Engineering, Faculty of Science and Technology Gueliz,
Cadi Ayyad University, Avenue A. Elkhatabi,
BP549, 40000 Marrakech, Morocco
e-mail: ayoub.elaallaoui@ced.uca.ma

M. E. Ghorfi · A. Elghali · H. Zine · Y. Taha · M. Benzaazoua ·
R. Hakkou
Geology and Sustainable Mining Institute (GSMI), Mohammad VI
Polytechnic University, Lot 660. Hay Moulay Rachid,
43150 Ben Guerir, Morocco

A. Bayoussef · R. Hakkou
Materials and Environmental Chemistry Laboratory (IMED-Lab),
Faculty of Science and Technology Gueliz, Cadi Ayyad
University, Avenue A. Elkhatabi, BP549 40000 Marrakech,
Morocco

and D of shallow depth, and a southern one where all layers are present and crossed by several faults and fractures. The three layers exploited in Jerada are dipping between 20° to over 45° , which shows the sinking of the east and therefore the probable existence of coal reserves that deserve further exploration. The Jerada basin shows a low volatile matter variability (3–7%) and a sulfur content that remains generally lower than 3% (Berkhli et al., 1999; Essamoud, 2011). Despite the low sulfur content of these wastes, the generation of acid mine drainage (AMD) represents one of the greatest environmental risks. The factor has prompted numerous studies and research to characterize the reuse of these mining wastes in other fields in order to reduce their environmental impact and possibly prevent the negative effects of AMD on nearby ecosystems (Amrani et al., 2020; Taha et al., 2016).

2 Materials and Methods

The abandoned mine of Jerada has generated throughout its working period, 8 CMWR piles T01, T02, T03, T04, T05, T06, T07 and T08, divided into old piles as the case of the huge CMWR pile T08 and new or young ones as the case of the other piles T01, T02 (Fig. 1). The modeling study will focus principally on the study of three piles among the eight, given the constraints of accessibility and sampling, that are successively T01, T02 and T08.

The drilling technique of bottom hole (FT) was used to collect the samples, which were then transported to the laboratory in plastic bags. To ensure representative samples, an adjustable channel sample divider was used to quarter each sample. The samples were then dried at 115°C for 12 h and pre-ground with a jaw crusher to achieve uniformity. Afterward, an oscillating disk mill was used to grind 50 mL of each sample to a final particle size of less than $200\ \mu\text{m}$. Physical–chemical characterization was performed using laser granulometry analyze. The Malvern Panalytical Epsilon 4 was used for X-ray fluorescence (XRF) analysis, and total S/C was measured with an induction furnace (ELTRA CS-2000) with a detection limit of 0.09%. Mineralogical identification and quantification were confirmed by X-ray diffraction (XRD) using an X'pert3 Powder Smart Lab diffractometer with $\text{Cu K}\alpha$ ($\lambda = 1.540593\ \text{\AA}$) irradiation. The data were collected from 20° to 70° in the 2θ range with a step size of $2^\circ/\text{min}$. An optical microscope (OM) under reflected light, specifically an Olympus BH2-UMA microscope combined with a Leica EC4 microscope camera, was used for petrographic analysis. Scanning electron microscopy (SEM) and quantitative scanning electron microscope (QEMSCAN) were used for a quantitative evaluation of the morphology and microstructural properties of the CMWR samples. The 3D topo-photogrammetric images were obtained using drone imagery and were then used to estimate the volumes of CMWR piles. Characterization data were imported into Datamine RM software to create accurate 3D block models.

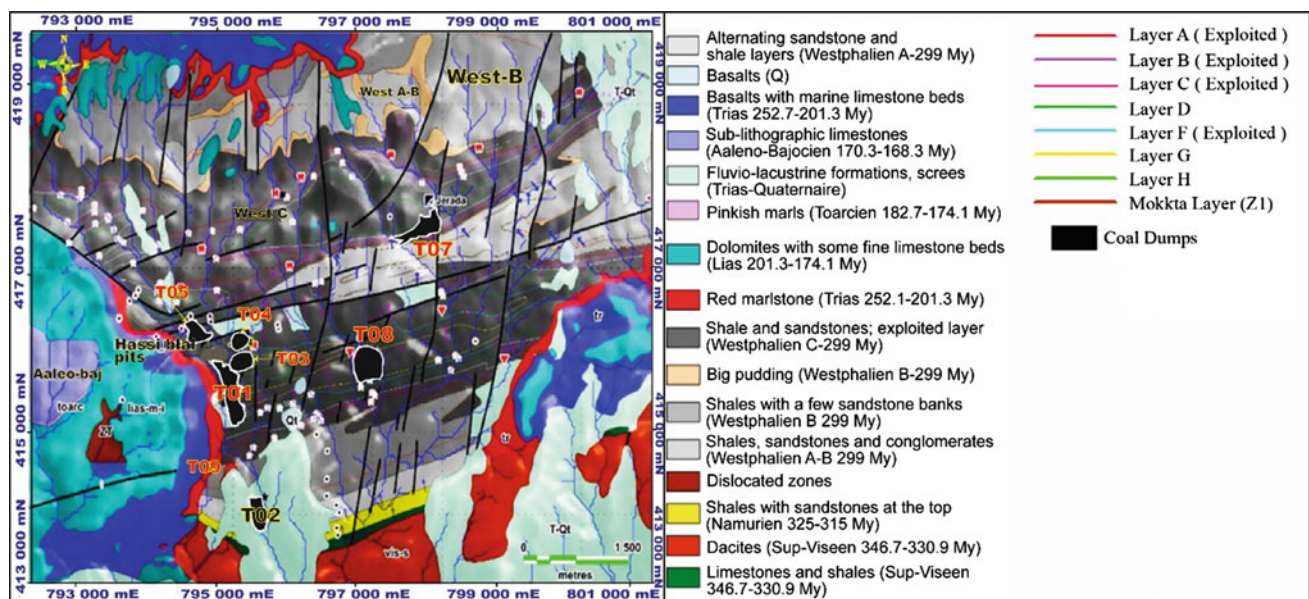


Fig. 1 Geological map of the study area (Jerada mine) showing the areal carbon distribution (T01, T02 and T08 piles)

3 Results

The results obtained via physical-chemical, mineralogical characterizations and 3D geo-metallurgical modeling considering the ability of valorization of JM CMWR piles are given here. This valorization is based on the two principal aspects.

3.1 Chemical Characterization

The chemical and mineralogical characterization aims to distinguish the existing mineralogical phases and to describe the textural relationship between them, as well as to estimate the carbon and sulfur content, elements that may influence the probability of generating acid mine drainage (Fig. 2).

3.2 3D Modeling and Reserve Estimation

The 3D topo-photogrammetric model blocks have made it possible to estimate the available resources and highlight the large tonnages stored in these CMWR piles using Datamine RM software. The density of 1.6 kg/m^3 was taken into account, resulting in a total tonnage of approximately 13.82 Mt. They established a chemical–mineralogical database that has been verified in 3D software, and the digital terrain model (DTM) and 3D digital model (3DM) were created by Datamine RM software to locate metal-rich areas, making it easier to target them for re-exploitation in the future. In our study, we considered the simple geometric

form of the dumps, semi-regular sampling grid and a moderate number of samples. We used the inverse distance weighting method (IDW) to interpolate the average chemical element content (C wt.%, S wt.%) of each block or sub-block within the mineralized solids from the available composites around the block. The presented block models were confirmed using research ellipsoids with different research radii (Fig. 3; Tables 1, 2 and 3).

4 Discussion

The results of the XRF have revealed the abundance of oxides represented generally by SiO_2 (45–57%), Al_2O_3 (16–23%), Fe_2O_3 (5–12%), MgO (0.8–1.5%) and CaO (0.4–2%), in lighting the presence of silico-alumina and iron oxides, confirmed by mineralogical examination by XRD. The other oxides such as TiO_2 and P_2O_5 are barely existent in our samples. SEM analysis was able to validate the presence of alumino-silicate gangue, pyrite, iron oxides and hydroxides and quartz, as well as to present the different forms in which anthracite exists and its relationship with the other phases. Pyrite is often oxidized with high Fe contents and without traces of sulfur. The 3D modeling highlights the overall volume on each CMWR pile, moreover, the state of the reality of the site on the tonnage of residual materials and on the grades of the piles, with a tonnage of 7.36 Mt only for T08, 8.37 (wt.%) of carbon for a density of 1.6 kg/m^3 . However, the piles T01 and T02 have recorded 2.76 Mt with an average of carbon 11.4 (wt.%) and 1.06 Mt with 14.15 (wt.%) as carbon average, respectively.

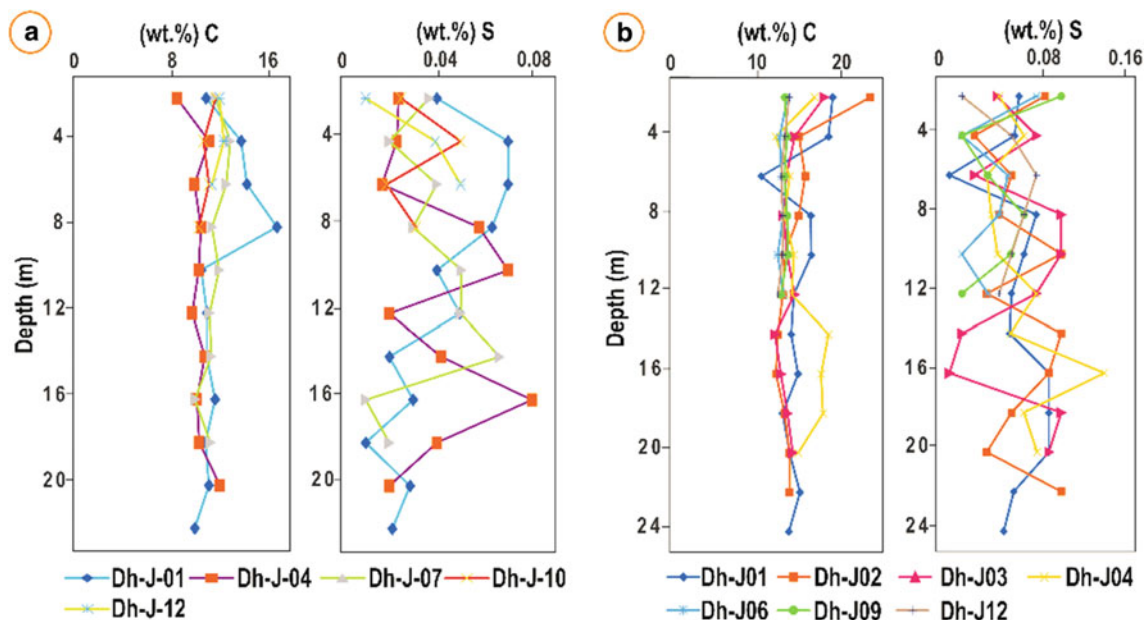


Fig. 2 Carbon and sulfur content distribution in the young piles T01 and T02

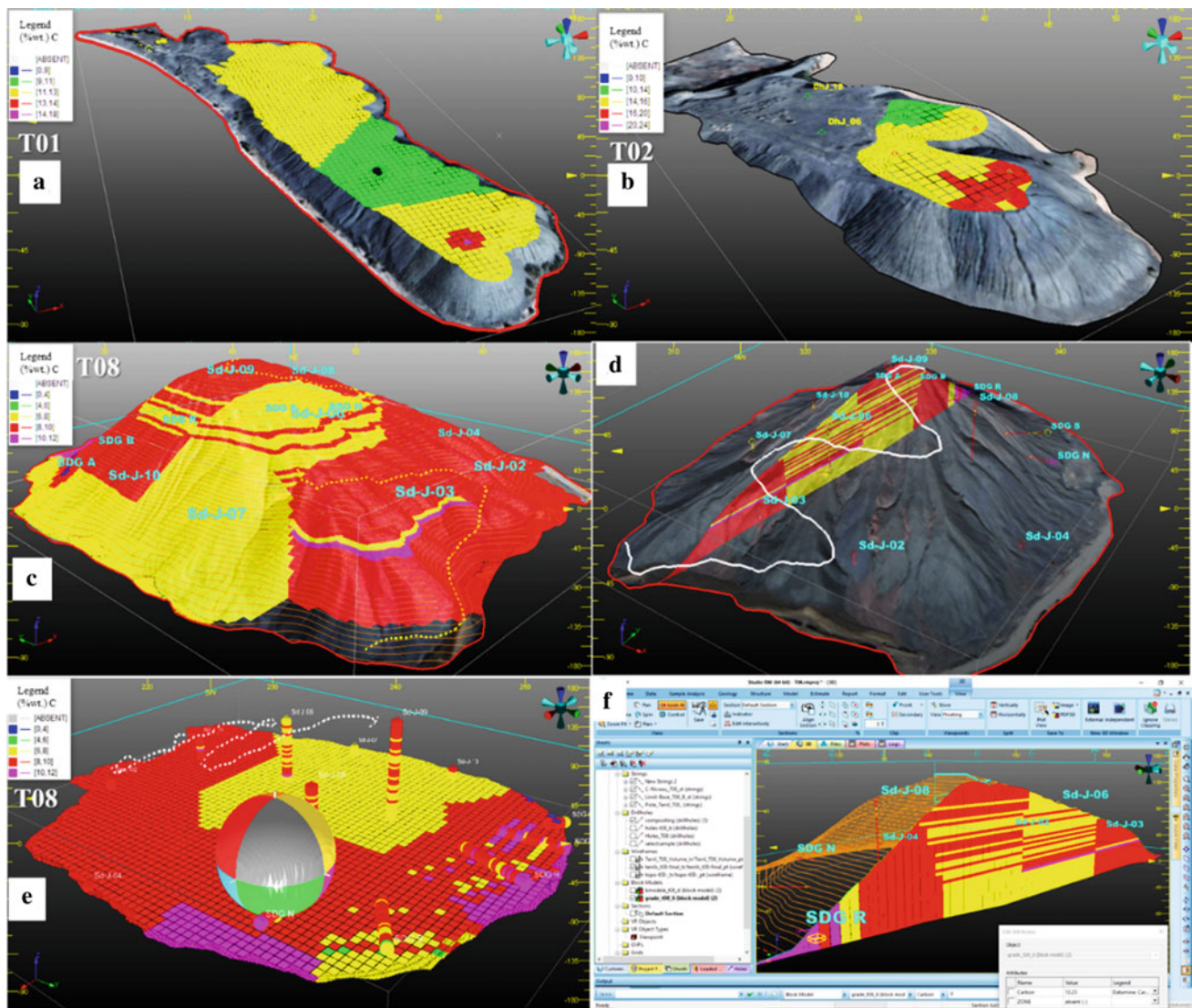


Fig. 3 a 3D model block of T01 showing the spatial distribution of the coal ore; **b** for T02 and **c** for T08; **d** model block T08 with research ellipsoid extended to the sphere in cross section and **e** in horizontal section; **f** model block in horizontal section, by clicking on each point of this block you get spatial information in 3D, and shows the presence of stratification of coal layers deposited in this CMWR piles

Table 1 Coal mineral resources for the T08 pile in Jerada

Category	BlockID	Density	Tons (t)	Volume (m ³)	C (wt%)	Verification
[ABSENT]	1.61	1.60	32,325	20,203	–	32,325
[0–4]	1.61	1.60	2455	1534	0.72	2455
[4–6]	1.61	1.60	2319	1449	5.68	2319
[6–8]	1.61	1.60	2,311,306	1,444,566	7.72	2,311,306
[8–10]	1.61	1.60	4,768,412	2,980,257	8.59	4,768,412
[10–12]	1.61	1.60	244,155	152,597	10.41	244,155
Total	–	1.60	7,360,971	4,600,607	8.37	7,360,971

The chemical analysis results support the tailings recovery scenario as they show a richness in carbon concentration in the new piles (T01, T02, T03, T04 and T05) with a carbon content that varies between 10 and 23 wt% in comparison

with the old Jerada pile (T08) that shows a variation of carbon contents between 5 to 11%wt. with almost no harmful elements (As, Cd...) and weak sulfur contents generally lower than 1% in the totality of the piles. But even if the sulfur

Table 2 Coal mineral resources for the T01 pile in Jerada

Category	BlockID	Density	Tons (t)	Volume (m ³)	C (wt%)	Verification
[ABSENT]	1.01	–	0	0	–	–
[0–9]	1.01	–	0	0	–	–
[9–11]	1.01	1.60	719,406	449,629	10.41	719,406
[11–13]	1.01	1.60	2,042,105	1,276,315	11.76	2,042,105
[13–14]	1.01	1.60	7578	4736	13.23	7578
[14–18]	1.01	1.60	614	384	14.25	614
Total	–	1.60	2,769,703	1,731,064	11.4	2,769,703

Table 3 Coal mineral resources for the T02 pile in Jerada

Category	BlockID	Density	Tons (t)	Volume (m ³)	C (wt%)	Verification
[ABSENT]	1.01	1.60	14	9	–	14
[0–10]	1.01	–	0	0	–	–
[10–14]	1.01	1.60	533,785	333,615	13.48	533,785
[14–16]	1.01	1.60	507,780	317,362	14.74	507,780
[16–20]	1.01	1.60	28,031	17,520	16.37	28 031
Total	–	1.60	1,069,610	668,506	14.15	1,069,610

Table 4 Summary of tonnages and volumes in the studied piles

Name	X	Y	Volume (RM) m ³	Tonnage (Tons)
T01	795,000	415,350	1,731,067	2,769,707
T02	795,370	413,940	668,505	1,069,609
T08	796,900	415,900	4,600,607	7,360,973
Total			7,000,179	11,200,289

content is low, this does not mean that these piles cannot generate acidic water during the oxidation process.

5 Conclusions

The characterization results present the tonnage giving a total volume of the eight CMWR piles examined of about 8.15 Mm³ and a tonnage of 13.04 Mt. From all the above, we conclude that the Jerada piles are characterized by the presence of carbon in relatively important proportions, reaching up to 20 wt.%. This carbon content can makes the case for using this waste in the production of civil engineering materials because of its ability to reduce the sintering temperature, as shown by previous research. It is also possible to valorize these proportions of carbon, which is of the type anthracite, the richest in carbon and recover energy. It should be noted that some CMWR piles are currently the subject of coal mining either by cooperatives or even worse, are being mined clandestinely (Table 4).

References

- Amrani, M., Taha, Y., El Haloui, Y., & Benzaazoua, M. (2020). *Sustainable reuse of coal mine waste : Experimental and economic assessments for embankments and pavement layer applications in Morocco*.
- Berkhli, M., Vachard, D., Tahiri, A., & Paicheler, J. (2000). Caractères sédimentologiques et structuraux des dépôts volcanoclastiques du Viséen supérieur – Serpoukhovien de la Meseta orientale marocaine (Vol. 22(1999), pp. 1–8).
- Essamoud, R. (2011). Le bassin houiller de Jerada (Chaîne des Horsts, Maroc oriental)/The Jerada Coal Basin (Horst Chain, Eastern Morocco).
- Owodenko, B. (1976). *Le bassin houiller de Jerada (Maroc oriental). Essai de synthèse et de paléogéographie* (p. 148). Notes Mém. Serv. Géol. Maroc, 207 bis.
- Taha, Y., Benzaazoua, M., Hakkou, R., & Mansori, M. (2016). Coal mine wastes recycling for coal recovery and eco-friendly bricks production. *Minerals Engineering* 1–16. <https://doi.org/10.1016/j.mineng.2016.09.001>



Investigation on the Flotation Recovery of Mixed Copper Ore Through an Integrated Mineralogical Approach

Rachid Faouzi, Khalid Naji, Intissar Benzakour, Hakim Faqir, Hind Tahari, Hassan Oumesaoud, and Moulay Abdelazize Aboulhassan

Abstract

The flotation behavior of mixed copper ore during selective copper flotation was investigated using a geometallurgical approach. To this end, samples were taken from a production block at the Ouansimi copper deposit and subjected to laboratory batch kinetics tests and quantitative mineral analyses. Using a range of ore samples from different location in the same deposit, the influence of mineralogy on flotation performance was studied. The automated quantitative mineralogy technique was utilized to characterize the samples, revealing that bornite, chalcopyrite, and chalcocite are the copper-bearing sulfide minerals, whereas malachite is the major copper-bearing carbonate mineral. In order to construct a robust model with the highest quality data (Q^2) and excellent goodness of fit (R^2), the deposit was divided into two homogeneous geometallurgical domains using a K-means clustering algorithm based on mineralogical and metallurgical information. Copper recovery of samples by geometallurgical domain was correlated to the feed mineralogy through statistical algorithms for principal component analysis (PCA) and partial least squares regression (PLS) regression to look for relationships between mineralogical features and flotation recovery. For the domain 1, a significant negative correlation was found between copper recovery and the middling and locked copper association (iron oxide with a trace of copper, copper associated with gangue like biotite, barite, kaolinite, chalcocite locked and delafossite). By contrast, in domain 2, a negative effect on copper recovery was

established due to the presence of iron oxide with a trace of copper and malachite and bornite.

Keywords

Mixed copper ore • Automated quantitative mineralogy • Geometallurgy • Flotation modeling • K-means clustering • Principal component analysis (PCA) • Partial least squares regression (PLS)

1 Introduction

The use of geometallurgical approaches can provide valuable solutions for maximizing the value of an ore body, reducing technical and operational risks, and creating a more resilient operation. By identifying key attributes that contribute to the overall value of a resource, geometallurgy enables the processing of variable ores into the flow sheet (Suazo et al., 2010; Whiteman et al., 2016), infrastructure design, and production and grade forecasts over the entire mine life. Understanding the geological and mineralogical drivers of metallurgical response can help prevent processing surprises and ensure a timely return on investment (Dominy et al., 2018b; Lishchuk et al., 2019). The application of mineralogical and statistical algorithms can be a powerful tool for developing a predictive geometallurgical program (Tungpalan et al., 2021). In this study, the process mineralogy and batch test flotation of the Ouansimi deposit ores were conducted to determine the significant impact of mineralogy on recovery and to establish a predictive geometallurgy model.

2 Materials and Methods

The geochemical analysis was carried out for flotation feeds and products. The major oxides were analyzed by X-ray fluorescence (XRF) on fused rock powders. Multielement

R. Faouzi (✉) · H. Oumesaoud · M. A. Aboulhassan
Laboratory of Mechanic Process Energy and Environment,
National School of Applied Sciences, Ibn Zohr University,
PO Box 1136/S Agadir, Morocco
e-mail: rachid.faouzi@edu.uiz.ac.ma

R. Faouzi · K. Naji · I. Benzakour · H. Faqir · H. Tahari
Reminex Research Centre, Site de Guemassa,
PO Box 469 Marrakech, Morocco

assay was realized using a combination of digestion methods with inductively coupled plasma optical emission spectroscopy (ICP-OES). An Agilent 511 ICP-OES analyzer was used for this purpose. Carbon and sulfur were measured by ELTRA CS-2000 analyzer and furnace. The assays were used for grade-recovery calculations.

Modal mineralogy, element department, liberation and associations were studied on polished thin sections from composite samples. Each composite was ground to a P80 of 120 μm . Graphite was used in the preparation of samples in order to disperse the particles, minimize settling, and segregation due to different mineral-specific gravities. Automated quantitative mineralogy (AQM) was utilized for the quantitative mineralogical analysis at the REMINEX research center (located in the industrial complex of Gue-massa, Morocco). The AQM method involves a Carl Zeiss Sigma VP automated mineralogy system which is coupled with Bruker detectors and is processed by ZEISS Mineralogic Mining software. The 16 samples were prepared as polished sections and the mineralogical data, including mineralogical mapping, distribution of target elements, and liberation, was obtained using Mineralogic software. The time required for the automated scanning was adjusted based on the number of grains, with a typical duration of 3 h per sample containing 3000 grains. The analysis was performed using BSE detectors, a tension of 20 kV, and a diaphragm aperture of 120 μm .

Using quantitative mineralogical data, chemistry analysis, and statistical tools (PCA and PLS), a model is developed that can be used to predict changes in mixed copper flotation performance based on in-deposit mineralogical variability. The work in this study follows five major steps. First, the geological and metallurgical background for the orientation study. Second, samples were collected from 16 different operational locations in the Ouansimi mine using underground panel samples as a linear sampling method (Dominy et al., 2018a). Third, inductively coupled plasma optical emission spectroscopy (ICP-OES) was used to accomplish the geochemical investigation on the composite samples. The automated quantitative mineralogy (AQM) was employed to produce the quantitative mineralogy data. Fourth, experimental testing with standard operating conditions was conducted to establish the flotation performance for each sample. Finally, the metallurgical data together with the mineralogical database are used to create predictive models of copper recovery in domain-based modeling. The PCA-PLS regression method was used as a tool in the process modeling.

2.1 Mineralogical Composition

The modal mineralogy of composite samples shows that the main gangue sulfide minerals present in all samples is pyrite, with a small amount of pyrrhotite. Considering the gangue has no sulfide, the dominant minerals are dolomite, quartz, and biotite. Barite content reaches up to 20 mass%, while muscovite and calcite present a maximum of 14 mass% and 11 mass%, respectively. All the other silicate and oxide minerals such as kaolinite, wollastonite, and iron oxide constitute less than 3 mass%. The identified copper-bearing minerals correspond to sulfides, represented by chalcocite, bornite, and chalcopyrite with a small amount of covellite; carbonate is defined by malachite; oxides are expressed by cuprite, delafossite, and iron oxide with a trace of copper. Native copper was detected in a limited number of samples. Twenty-one minerals were detected in total, of which those present in trace quantities, specifically silver, sphalerite, albite, goethite, rutile, chamosite, clinocllore, chrysocolla, and titanite, were grouped as “others.”

2.2 Kinetic Flotation Study

The kinetics results in Table 1 show a large variability in copper recovery ranging from 61 to 99%. The differences in recovery between samples are correlated to the depth of the sample and ore mineralogy. The experimental data of the flotation tests were fitted using the rectangular distribution model with the HSC chemistry model. The precision and the Root Mean Square Error of the fitting are respectively ($R^2 = 99.4\%$ and $\text{RMSE} = 1.34$). In the statistical analysis, the kinetic constants (K_{max}), maximum recovery (R_{max}) and recovery ($R_{\text{at } 9 \text{ min}}$), as well as the final grade (G), are used as dependent variables.

3 Mineralogical Prediction Results and Discussion

Based on all geometallurgical matrix data, K-means algorithms were used to establish a two-homogeneity domain with high extern variance of 83.48% and low intern variance of 16.52%. The first domain was formed by four samples (from C1 to C4), and the second domain was formed with 12 samples (from C5 to C16). PLS was used in conjunction with PCA to determine the most sensitive and critical response variables for production parameters of each domain. The recovery Cu predictive models' equations for each domain are:

Table 1 Kinetics flotation results

Sample	%R _{at 9 max}	%G	%R _{max}	K _{max}
C1	61.20	10.20	89.45	0.30
C2	85.60	7.64	87.16	2.59
C3	90.75	24.49	72.58	2.23
C4	76.59	7.65	76.87	2.92
C5	95.98	7.34	96.71	6.08
C6	83.96	6.57	97.07	3.97
C7	99.24	14.56	99.46	6.52
C8	98.21	7.09	98.14	7.23
C9	90.88	11.45	92.39	2.81
C10	98.63	23.04	99.48	4.05
C11	98.63	13.03	99.00	5.14
C12	98.22	8.55	98.34	6.96
C13	99.47	9.13	99.52	7.36
C14	99.17	8.14	100.00	3.68
C15	99.28	11.11	100.00	5.39
C16	99.02	19.05	100.00	1.96

Domain 1 ($Q^2 = 97.9\%$ and $R^2 = 95.06\%$, Fig. 1a):

$$\begin{aligned}
 R_{Cu} = & 84 + (2.77 * 10^{-4} * \text{Depth}) - (1.34 * 10^{-2} * \text{Fe_Ox_Cu}) \\
 & - (5.38 * 10^{-2} * \text{Dela}) - (1.97 * 10^{-2} * \text{Adr}) \\
 & - (5.09 * 10^{-2} * \text{Cct Locked}) - (3.44 * 10^{-3} * \text{DBi}) \\
 & - (6.92 * 10^{-2} * \text{DBar}) - (6.92 * 10^{-2} * \text{DKln}) \\
 & + (3.89 * 10^3 * \text{DNative_Cu})
 \end{aligned}$$

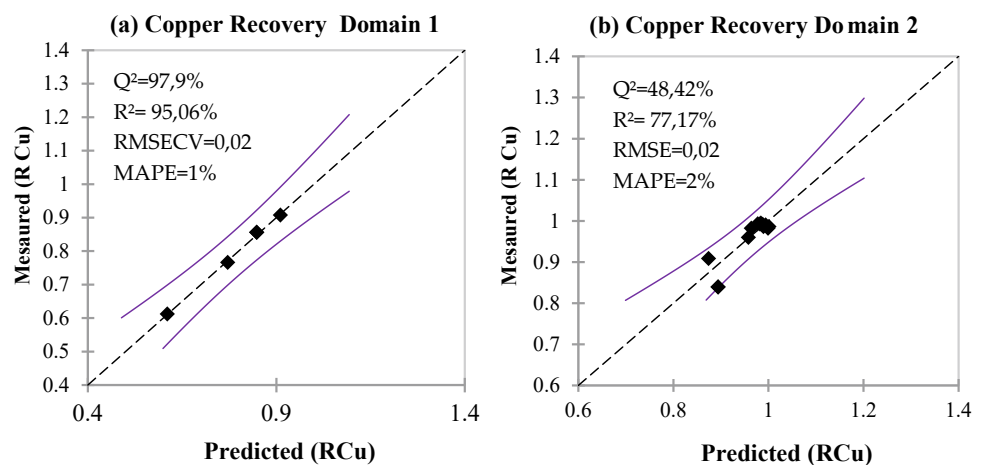
Domain 2 ($Q^2 = 48\%$ and $R^2 = 77\%$, Fig. 1b):

$$\begin{aligned}
 R_{Cu} = & 96 - (5.40 * 10^{-3} * \text{Fe_Ox_Cu}) - (9.57 * 10^{-3} * \text{Cal}) \\
 & - (5.37 * 10^{-3} * \text{DFe_Ox_Cu}) - (2.40 * 10^{-4} * \text{DBn}) \\
 & - (6.07 * 10^{-3} * \text{DMal})
 \end{aligned}$$

The domain 1 represents the near-surface zone with a maximum depth of 100 m. The samples are collected from

the oxidized level – 50 m and the transition level – 100 m. These zones are characterized by a high oxidation rate and the dominance of copper oxide and quartz as gangue. The copper recovery model shows that the more we go deeply, the more recovery is enhanced. On the other hand, the presence of native copper as well as iron oxide with a trace of copper, delafossite and copper associated with biotite, barite, kaolinite, and chalcocite locked negatively impacts the recovery of copper.

The domain 2 expresses the depth from – 365 to – 450 m, which is dominated by low-rate oxidation and the dominance of chalcopyrite with pyrite and dolomite as gangue. The copper recovery model reveals the negative effect of the minimum abundance of iron oxide with a trace of copper, malachite, and the bornite that may be depressed with pyrite.

Fig. 1 Predicted versus measured values for the copper recovery in each domain

4 Conclusions

The application of geometallurgical approaches, which incorporate mineralogy and statistical algorithms, can provide a powerful tool for developing predictive models for mixed copper ore flotation performance. The study conducted on the Ouansimi copper deposit showed that the mineralogical composition of the ore plays a significant role in flotation performance, and the use of quantitative mineralogy techniques can aid in determining the mineralogical drivers of metallurgical response. The results of the study indicate that chalcopyrite, chalcocite, malachite, and bornite are the main copper-bearing minerals hosted in a silico-carbonate gangue within the deposit. Additionally, using a K-means algorithm, the deposit can be divided into two geometallurgical domains, each with distinct mineralogical characteristics and metallurgical responses. Statistical methods such as PCA and PLS can be employed to identify the key mineralogical features that influence copper recovery and aid in developing predictive models for each domain. These models can be used to optimize flotation parameters and improve the recovery of copper from the deposit. In summary, the study underscores the importance of applying geometallurgical approaches in processing variable ores and designing a more resilient operation.

References

- Dominy, S. C., O'Connor, L., Glass, H. J., Purevgerel, S., & Xie, Y. (2018a). Towards representative metallurgical sampling and gold recovery testwork programmes. *Minerals*, 8(5). <https://doi.org/10.3390/min8050193>
- Dominy, S. C., O'Connor, L., Parbhakar-Fox, A., Glass, H. J., & Purevgerel, S. (2018b). Geometallurgy—A route to more resilient mine operations. *Minerals*, 8(12), 1–33. <https://doi.org/10.3390/min8120560>
- Lishchuk, V., Koch, P. H., Ghorbani, Y., & Butcher, A. R. (2020). Towards integrated geometallurgical approach: Critical review of current practices and future trends. *Minerals Engineering*, 145, 106072. <https://doi.org/10.1016/j.mineng.2019.106072>
- Suazo, C. J., Kracht, W., & Alruiz, O. M. (2010). Geometallurgical modelling of the Collahuasi flotation circuit. *Minerals Engineering*, 23(2), 137–142. <https://doi.org/10.1016/j.mineng.2009.11.005>
- Tungpalan, K., Wightman, E., Keeney, L., & Manlapig, E. (2021). A geometallurgical approach for predicting separation performance. *Minerals Engineering*, 171, 107065. <https://doi.org/10.1016/j.mineng.2021.107065>
- Whiteman, E., Lotter, N. O., & Amos, S. R. (2016). Process mineralogy as a predictive tool for flowsheet design to advance the Kamao project. *Minerals Engineering*, 96–97, 185–193. <https://doi.org/10.1016/j.mineng.2016.05.004>



Sensor-Based Sorting in Mining Industry: Selection of Appropriate Sensing Technologies for a Copper Deposit

Samira Es-sahly, Brahim Lakssir, Khalid Naji, Hakim Faqir, Jihad Zahir, Abdelaziz El Basbas, and Slimane Dadi

Abstract

Mining companies are increasingly turning to industry 4.0 to tackle economic challenges and to boost production efficiency. As one of the technological advances, sensor-based sorting systems (SBS) are increasingly used. It enables dry separation in early stage of raw material processing. The selection of appropriate sensing technologies is a vital aspect of implementing SBS systems, and there are not many research studies that treat the approach used to select the appropriate sensors; therefore, this paper demonstrates the selection of two combinations of sensors to pre-concentrate ore from a Moroccan copper deposit called Tizert. The approach used to select these combinations is based on analyzing the intersection between the detection principle of sensing technologies and preliminary geological and mineralogical characterization of the copper ore fragments. Results of this approach are two combinations of sensing techniques. The first is near-infrared spectroscopy combined with microwave treatment followed by infrared thermal imaging; this combination guarantees the detection of all copper-bearing minerals; the second combination is dual-energy X-ray transmission with X-ray fluorescence; it allows to detect valuable fragments and reduce surface-to-volume correlation errors as well as overcoming the resolution limitations of the XRT sensors. The

strategy followed gives as result two combinations of sensors that allow researchers to concentrate at first on potential technologies.

Keywords

Sensor-based sorting • Copper ore • Sensing technologies • Mineralogical characteristics

1 Introduction

SBS is a trendy technology in mining industry. It has beneficial influence on water and reagent consumption, transport costs, and environmental impact, and it allows decreasing the cut-off-grade for greenfield operation of low grade resources (Robben et al., 2020). While the current context of the copper industry is critical, according to the World Bank Group (2020), demand for copper is predicted to exceed 29 Mt by 2050; on the other hand, the average copper ore head grade decreases from 4% in 1900 to 0, 56% in 2018 (Schodde, 2019). Thus, SBS systems allow meeting rising demand, falling head grade, and fluctuating market prices. Different sensing technologies are used, depending on the nature of the mineralization, gangue, and casing. Consequently, this paper studies the choice of the appropriate sensing technologies to classify raw material.

2 Approach Used to Choose the Suitable Sensing Technologies

The strategy followed to select the appropriate detection technologies is divided to three stages. The first stage consists of a global study of the geological and mineralogical characteristics of the deposit and the selection of detection properties that allow valuable fragments to be separated from waste. The second stage is benchmarking of current

S. Es-sahly (✉) · A. El Basbas · S. Dadi
National School of Mines of Rabat, Rabat, Morocco
e-mail: sahlysamira@gmail.com

S. Es-sahly · B. Lakssir
Moroccan Foundation for Advanced Science, Innovation and Research, Rabat, Morocco

K. Naji · H. Faqir
MANAGEM Group, REMINEX SA, Casablanca, Morocco

J. Zahir
Faculty of Science and Technology, Cadi Ayyad University, Marrakech, Morocco

state of the art of sensing technologies, besides the associated detection criteria, and the last stage is finding the intersection between the classification and the detection criteria, in other words studying the amenability of the ore raw material to be sorted using the sensing technologies chosen.

2.1 Global Geological and Mineralogical Analysis

The mineralization studied in this paper originates from a sediment-hosted copper deposit located at the Anti-Atlas, Morocco. It contains various classes of Cu-bearing and gangue minerals distributed across different facies and has been subjected to a weathering process. Copper-bearing minerals are disseminated or in vein in the rock and are carried by dolomites, sandstones, siltstones, and conglomerates. The deposit is composed of a primary mineralization and a supergene mineralization resulting from weathering process (Poot et al., 2020). For further precision on the mineralogy, X-ray diffraction and mineral liberation analysis reports, elaborated in the research and development center REMINEX, have been investigated. As conclusion, copper is contained by carbonates (malachite), sulfides (Chalcocite, Bornite, Chalcopyrite), and oxides (Cuprite). Gangue minerals are distributed in silicates (Quartz), carbonates (dolomite), and oxides (hematite). Because of the diversity of copper-bearing minerals and gangue minerals, considering only one classification criteria is unfeasible; hence, an analysis of the behavior of Tizert ore in response to several technologies was conducted.

2.2 Sensing Technologies Currently in Use for Copper Ore Deposits

Based on previous test works and applications of SBS systems, copper ore deposits are amenable to be sorted by various technologies including X-ray fluorescence (XRF), Prompt Gamma Neutron Activation Analysis (PGNAA), infrared spectroscopy (NIR), hyperspectral imagery, microwave treatment and infrared thermal imaging (MW/IRT), and dual-energy X-rays transmission (DE-XRT) (Batchelor et al., 2016; Dalm et al., 2014; Lessard et al., 2015; Li et al., 2020). Each of these technologies allows classifying on the basis of a sorting criteria, respectively, surface elementary chemical composition, absorption and emission of prompt gamma rays, reflection/absorption of SWIR, VIS, and NIR radiations, thermal conductivity, X-rays attenuation coefficient or density contrast.

3 Tizert Ore Amenability to Sensor-Based Sorting Technologies

Geological and mineralogical characteristics combined with classification criteria on which copper-related technologies are based have allowed to select four sensing technologies, namely DE-XRT, XRF, MW/IR, and NIR spectroscopy; thereafter, the behavior of ore fragments is examined in relation to these technologies.

(a) DE-XRT-Based Sorting

DE-XRT sensors use as classification criterion the density contrast. Copper-bearing minerals in Tizert deposit have a higher density, ranging between 3.6 and 6.6, compared to gangue minerals, varying between 2.5 and 3.4. This disparity between densities combined with the capacity to quantify the bulk fragments characteristic, recognize it as a viable separation strategy. Despite its potential advantages, it has also limitations when applied to Tizert deposit. The first is the presence of oxides gangue minerals such as hematite that have high density ranging from 4.9 to 5.3 similar to Cu-bearing minerals and the second is mineral grain size; economic minerals are disseminated and can measure up to 50 μm , especially for dolomite and sandstone. As a result, high-performance sensors are required.

(b) XRF-Based Sorting

Tizert deposit heterogeneity requires a well-adapted method capable of detecting copper in all carried minerals, regardless of class (carbonates, sulfides, oxides), this need can be met by using the XRF technology, given its quantitative response to element concentrations and rapid measuring. Otherwise, the physical principle of XRF is based on the excitation of atoms on the ore particle surface; hence, the accuracy of sorting depends on the ability to correlate the particle bulk grade to sensor responses.

(c) MW/IRT-Based Sorting

MW/IRT is pre-selected for Tizert copper deposit based on the physical properties of minerals, mainly the dielectric properties. Sulfides Cu-bearing minerals heated rapidly when exposed to microwaves compared to the majority of gangue minerals (Quartz, dolomite) (Batchelor et al., 2016), as a result, rapid heated fragments may be considered as valuable fragments while low temperature fragments as waste. The challenges of applying this method to Tizert ore are the low heat rate of malachite and the high heat rate of hematite, they may provide deviation in the separation

process. Moreover, the ability of minerals to absorb microwave energy when arranged with other minerals in rocks is a difficulty. Consequently, it is more significant to understand the behavior the fragments instead of Cu-bearing and gangue minerals independently.

(c) NIR Spectroscopy-Based Sorting

NIR spectroscopy has been widely used for porphyry copper deposit (Dalm et al., 2014). Tizert deposit contains malachite, Cu-bearing mineral, characterized by an absorption feature in the SWIR range, in 2275 and 2360 nm (Iyakwari et al., 2013). As a result, this technique may be suitable to identify malachite-rich fragments, specifically dolomite copper rich fragments where the mineralization is disseminated. The other encouraging factor to use this method is the existence of supergene mineralization that may provide associations between alteration minerals, active in the NIR range (chlorite, muscovite) and copper-bearing minerals, featureless in the SWIR range (Dalm et al., 2014).

4 Results and Discussions

Using the proposed approach, four technologies were pre-selected, and the behavior of Tizert ore in response to them has been studied. It is found that, when used on the studied deposit, each method offers advantages and disadvantages (Table 1).

Consequently, combined two detection methods could be designed for an effectively sorting. The first suggestion is MW/IR and NIRS; this combination guarantees detection of sulfides, using MW/IR, and carbonates using NIR spectroscopy; the second suggestion is DE-XRT and XRF; it

provides quantification of copper surface content using X-ray fluorescence and separation based on volume characteristics using DE-XRT; this combination will allow reducing surface-to-volume correlation errors besides overcoming the resolution limitations of the XRT sensors.

5 Conclusions

Dry separation and pre-concentration are becoming increasingly prominent in the mining industry, and choosing the appropriate detection-discrimination technique is critical. This separation technique necessitates a profound understanding of the mineralogical characterizations of economic and gangue minerals using advanced tools as the mineral liberation analyzer. It is also recommended to take into consideration several criteria, such as detection accuracy and speed, operating cost, adaptability to the mining environment, and sample preparation to implement a sorting solution.

Acknowledgements This work was supported by the Ministry of Higher Education, Scientific Research and Innovation, the Digital Development Agency, the CNRST of Morocco, Managem Group, Reminex SA, MAScIR and National School of Mines of Rabat.

References

- Batchelor, A. R., Ferrari-John, R. S., Katrib, J., Udoudo, O., Jones, D. A., Dodds, C., & Kingman, S. W. (2016). Pilot scale microwave sorting of porphyry copper ores: Part 1—Laboratory investigations. *Minerals Engineering*, *10*, 1016.
- Dalm, M., Buxton, M. W. N., Ruitenbeek, F. J. A., & Voncken, J. (2014). Application of near-infrared spectroscopy to sensor based sorting of a porphyry copper ore. *Minerals Engineering*, *58*, 7–16.
- Iyakwari, S., Glassa, H. J., & Kowalczyk, P.B. (2013). Potential for near infrared sensor-based sorting of hydrothermally-formed minerals. *Journal of Near Infrared Spectroscopy*, *223*–229.
- Lessard, J., Sweetser, W., Bartram, K., Figueroa, J., & McHugh, L. (2015). Bridging the gap: Understanding the economic impact of ore sorting on a mineral processing circuit. *Minerals Engineering*, *0892*–6875.
- Li, G., Klein, B., Sun, C., & Kou, J. (2020). Applying receiver-operating-characteristic (ROC) to bulk ore sorting using XRF. *Minerals Engineering*, *146*, 106117.
- Poot, J., Verhaert, M., Dekoninck, A., Oummouch, A., El Basbas, A., Maacha, L., & Yans, J. (2020). Characterization of weathering processes of the giant copper deposit of Tizert (Igherm Inlier, Anti-Atlas, Morocco). *Minerals*.
- Robben, C., Condorib, P., Pintob, A., Machacab, R., & Takala, A. (2020). X-ray-transmission based ore sorting at the San Rafael tin mine. *Minerals Engineering*, *145*, 105870.
- Schodde, R. (2019). Role of technology and innovation for identifying and growing economic resources. In *AMIRA International's 12th Biennial Exploration Managers Conference*.

Table 1 Comparison of sensing technologies for Tizert copper deposit

Sensing technology	Advantages	Challenges
DE-XRT	Bulk measurements	Mineral grain size
XRF	Measure the copper concentration in the surface of the sample	Sample preparation Correlation between surface grade and bulk grade
MW/IR	Bulk measurement	Detection of malachite Elimination of hematite effect
NIRS	Fast and secure	Sample preparation, surface measurement, correlation between NIR spectra and copper grade



A Kinetic Test Method to Assess the Long-Term Acid Generation Behavior of Sludge/Slag and Mine Tailings of Mine a (Quebec, Canada)

Mohamed Jalal El Hamidi, Abdelkabir Maqsoud, and Tikou Belem

Abstract

The mine A tailings storage was used successively for the deposition of sulfide tailings, and the co-deposition of sludge and slag. With the objective to evaluate the hydrochemical behavior of these materials, humidity cell tests were used. These cell tests internationally operated to simulate sulfide mineral oxidation and acid generation at controlled laboratory conditions. It consists of weekly wetting and drying cycles using deionized water flush of the studied material. At the end of each cycle, water flush was analyzed for several geochemical parameters in order to compare their oxidation rates, generation of alkalinity, and metal leaching potential (As, Cu, Fe, Pb, and Zn). Four cell tests were performed for 16 cycles (105 days) on the mine tailing and the sludge/slag materials. Indeed, this study enhances our understanding of the reactivity of the sulfur generated by the mine tailing and the high concentrations of sludge/slag material in Cu. These materials generate contaminated water and are therefore likely to affect the quality of the surrounding environment.

Keywords

Sulfide tailings • Sludge and slag • Humidity cell tests • Geochemistry

1 Introduction

The mining industry produces a high quantity of tailings, which frequently contain a high amount of sulfide minerals. Some tailings when they are exposed to atmospheric conditions (occurrence of water and oxygen) can generate acidity allowing to increase metal dissolution. These materials generate contaminated water, well known as acid mine drainage (AMD) phenomenon (Kleinmann & Crerar, 1981). It has a severe effect on the ecosystem, affecting the water resources, agricultural lands, historical sites, and wild animals and is therefore likely to affect the quality of the surrounding environment.

Researchers have largely used static tests (such as acid–base accounting tests or ABA) to estimate the AMD risk since they are fast and low-priced (Villeneuve, 2004). The ABA tests, on the other hand, feature an uncertainty zone in which it is hard to say with certainty the long-term acidity production potential (Ferguson & Morin, 1991). Static tests can reveal that a sample is not acid generating, but it can still generate contaminated neutral drainage. Hence, kinetic tests are required when a particular tailing is in the uncertainty interval, or when a better understanding of the future geochemical behavior of tailings is required. Kinetic tests, indeed, can also provide additional information about mineral weathering, reaction kinetics, lag time, etc. Field-based pad tests, laboratory column tests, and humidity cell tests (HCT) are the most typical kinetic tests (Frostad & Klein, 2000; Lapakko, 2000; Lawrence, 1990; Price & Kwong, 1997; Sapsford et al., 2008). All of these kinetic tests are based on the alteration of materials under controlled conditions in order to assess their long-term evolution, which provides information on a material ability to produce acidity or release metalloids contaminants.

In this study, the acid-generating potential, as well as the potential of pollutants release, was determined using the acid–base accounting and HCT. The current research focuses on the humidity cell testing process.

M. J. El Hamidi (✉) · A. Maqsoud · T. Belem
Institut de recherche – mines et environnement (IRME), Université
du Québec en Abitibi-Témiscamingue (UQAT), Rouyn-Noranda,
Québec, Canada
e-mail: mohamedjalal.elhamidi@uqat.ca

2 Materials and Methods

The mine A tailings storage facility (TSF) (Quebec, Canada) was used successively for the deposition of sulfide tailings, and the co-deposition of sludge and slag. In the mine A site, two material samples (mine tailing and sludge/slag) were collected and delivered to the laboratory in plastic buckets, and they were dried in a 100 °C for 48 h. These materials were characterized and submitted to kinetic test. In the following section, one can find a description of these evaluation.

2.1 Mineralogical Characterization

For the mineralogical composition, the used materials were characterized using the X-ray diffraction. The instrument used in this characterization was a Bruker D8 Endeavor diffractometer equipped with Cu X-ray source. The TOPAS software (v 2.1) applying Rietveld refinement was used to quantify the abundance of all recognized mineral species, and the DiffracPlus EVA software (v.9.0 rel. 2003) was utilized to identify mineral species. The main results of these characterizations are presented in Table 1.

This table shows that the sludge and slag materials contain abundance minerals such as fayalite, magnetite/chromite, gypsum, and amorphous. While in the mine tailing, materials contain sulfide minerals such as chalcocite, and also it encloses quartz, albite, gypsum, and carbonates such as ankerite FeO₂, dolomite, and siderite.

2.2 Geochemical Characterization

For the kinetic tests, the HCT were used to evaluate the geochemistry of the mine A tailing storage and intentionally operated to accelerate sulfide mineral oxidation and acid generation. These tests were carried out in a Plexiglas chamber with air input and output. The cells were filled with 1 kg of material and set on a perforated plate covered with two geo-textile layers. The cells have an interior diameter of 20.3 cm and a height of 10.2 cm.

Four cells were used for the kinetic test, with the first and second cells containing mine tailing materials, the second and third cells containing sludge and slag materials. These replicate materials on Cell#1 (Cell#2) and Cell#3(Cell#4) are important because they can be used in order to prove the validity of the performed tests.

Throughout the test, steady dry and humid air fluxes (1–1.5 L/min) and a humidifier's water temperature (25–30 °C to provide 99 percent air moisture) were used. The HCT were operated with the dry air cycle lasting 3 days followed by the humid air cycle lasting 3 days ending with flushing of the studied material by 1L of demineralized water, and it was soaked for about 4 h.

The leachate out was collected in a flask after the week cycle, the volume was noted, and it was then filtered into a 1000 mL polyethylene container. The water collected at the end of each cycle was analyzed for several physical and chemical parameters (using ICP-AES and ICP-MS) in order to compare their oxidation rates, generation of alkalinity, and metal leaching potential (As, Cu, Fe, Pb, and Zn).

Table 1 Mineral abundances of the mine tailings and sludge/slag (weight %)

Materials	Mine tailings		Sludge and slag	
	Sample 1	Sample 2	Sample 3	Sample 4
Quartz	13.2	15	n.d	n.d
Albite	45.7	44.4	n.d	n.d
Gypsum	6.4	7.2	12.5	10.1
Chalcocite	2.8	0.9	n.d	n.d
Lepidolite 2M1	8.4	16.9	n.d	n.d
Muscovite 2M1	0.6	0.3	n.d	n.d
Clinochlor	0.6	3.0	n.d	n.d
Ankerite	7.7	8.7	n.d	n.d
Dolomite	8.3	10.9	n.d	n.d.-
Siderite	n.d	2.6	n.d	n.d
Fayalite	3.7	1.7	32.4	34.5
Staurolite	1.4	1.7	n.d	n.d
Arsenolite	1.1	1.7	n.d	n.d
Magnetite/chromite	n.d	n.d	23.9	26.9
Amorphous	n.d	n.d	31.2	28.5

n.d.: not detected

3 Results

Cell tests (from Cells#1 to 4) were performed for 16 cycles (105 days) on the material of the sludge/slag and mine tailings. Figure 1 displays the most significant results of the HCT. Results of the replicated materials on Cell#1/Cell#2 and Cell#3/Cell#4 are similar; they prove the validity of the performed tests. Over 105 tests, the pH of the cell leachates has remained relatively neutral. The sludge/slag shows generally lower pH values (6.2–7.0) than the mine tailing (7.0–8.3) during the 105 days. The electrical conductivity of the water flush from the mine tailing between 944 and 3750 $\mu\text{S}/\text{cm}$ is higher than the one from sludge/slag until the last leaching cycle. The sludge/slag generates higher Zn and Cu concentrations than mine tailing (Zn up to 0.13 mg/L for

Cells#1 and 2 (tailing) and up to 2.25 mg/L for Cells#3 and 4 (sludge/slug); Cu up to 0.03 mg/L for tailing and up to 4.34 mg/L for sludge/slug. According to the directive 019 requirements (Environnement Quebec, 2012), the concentration of Zn, after 42 days, becomes acceptable ($< 1 \text{ mg/L}$). Moreover, a significant difference between S (sulfur) values is noticed between the sludge/slug and mine tailing (12–1018 mg/L). The Fe concentrations from the sludge/slag and from the mine tailing are very close to or below the detection limit (0.007 mg/L) throughout the tests. Moreover, the alkalinity of the water flush from the mine tailing is higher than sludge/slag (214–13 mgCaO₃/L). However, this study enhances our understanding of the reactivity of the sulfur generated by the mine tailing and the high concentrations of sludge/slag material in Cu ($> 0.6 \text{ mg/L}$).

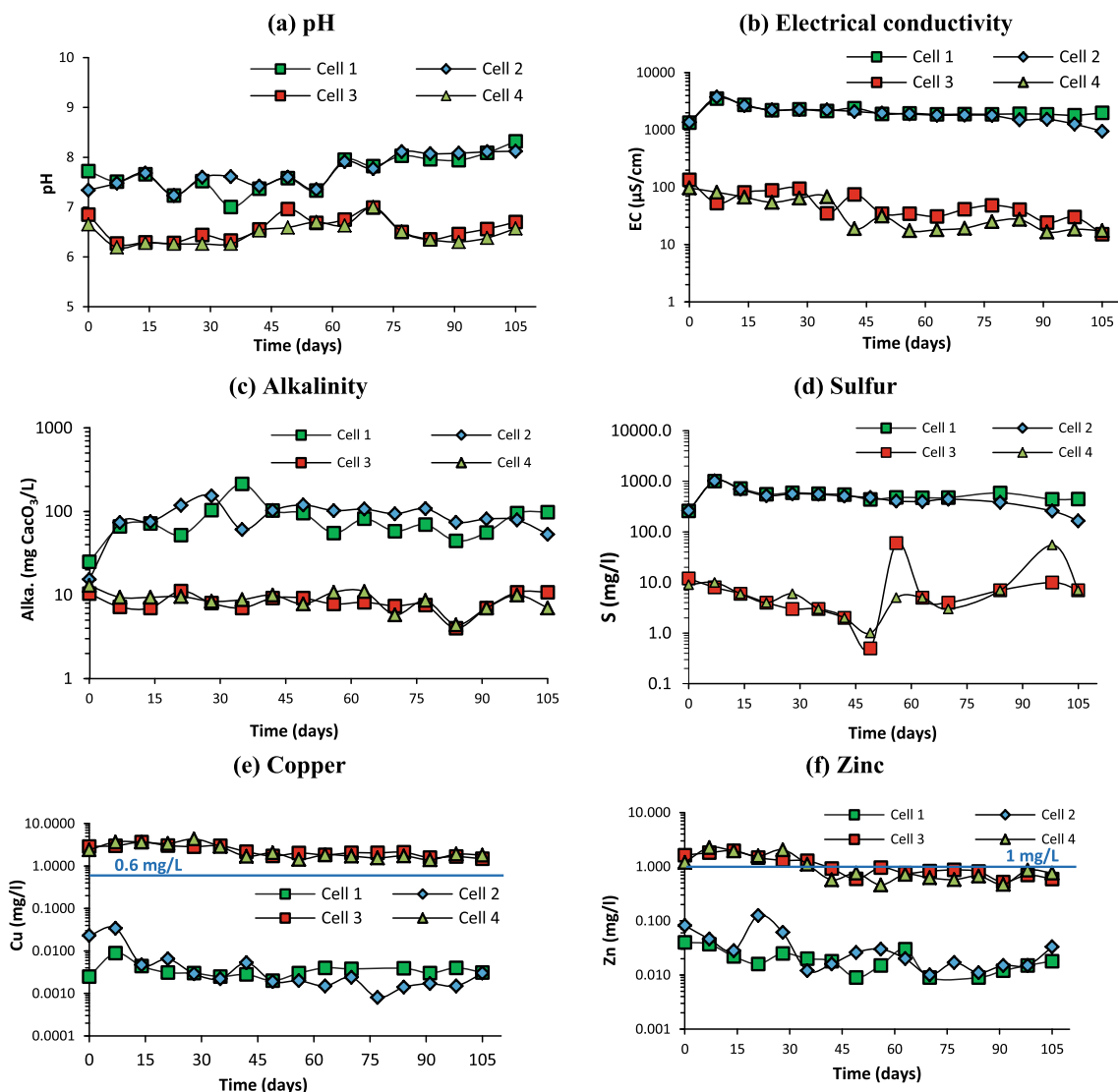


Fig. 1 Evolution of a pH, b electric conductivity, c alkalinity, d sulfur, e copper, and f zinc concentrations in HCT

4 Conclusions

Four humidity cells kinetic tests were performed on mine tailings and sludge and slag samples. The analysis conducted for this study has shown that the used materials have the capacity to produce and release pollutants S, Cu, and Zn into the solution. However, the concentration of Zn becomes acceptable after 42 days. In mine tailing samples, the high concentration in sulfur in the presence of oxygen and water may produce acidity. Acidity produced by the oxidation of sulfides is neutralized by the subsequent dissolution of neutralizing minerals leading to neutral mine drainage (NMD), and near-neutral pH conditions were maintained throughout the tailings site facility and the water flush of the mine tailing samples are more alkaline.

Moreover, the sludge/slag sample generates higher Cu concentrations. This copper must be treated and ensure that the effluents respect the directive 019 requirements. Furthermore, immediate action must be taken to reduce contaminated water in the mine site.

References

- Environnement Quebec. (2012). *Directive 019 sur l'industrie manière, Québec, Canada* (105p). Report available on https://www.environnement.gouv.qc.ca/milieu_ind/directive019/
- Ferguson, K. D., & Morin, K. A. (1991). The prediction of acid rock drainage—Lessons from the data base. In *Second International Conference on the Abatement of Acidic Drainage, Montréal, Canada* (Vol. 3, pp. 83–106).
- Frostad, S., & Klein, B. (2000). Lawrence RW: Evaluation of laboratory kinetic test methods for measuring rates of weathering. *Mine Water and the Environment*, 21, 183–192.
- Kleinmann, R. L. P., Crerar, D. A., Pacellil, R. R. (1981). Biogeochemistry of acid mine drainage and a method to control acid formation. *Mining Engineering*, 33(3), 300–304 (1981)
- Lapakko, K. A., & White III, W. W. (2000). Modification of the AstM5744—96 kinetic test. In *Proceedings of the International Conference on Acid rock Drainage* (pp. 631–639). SME.
- Lawrence, R. E. (1990). Laboratory procedures for the prediction of long-term Weathering characteristics of mining wastes. In *Proceedings of the symposium on Acid Mine Drainage; Annual Meeting Geological Association of Canada and Mineralogical Association, VCH, Canada*.
- Price, W. A., & Kwong, Y. T. J. (1997). Waste rock weathering, sampling and analysis: Observations from the British Columbia ministry of employment and investment database. In *Proceedings of the 4th International Conference on Acid Mine Drainage, Vancouver, BC* (pp. 31–45).
- Sapsford, D. J., Bowell, R. J., Dey, M., & Williams, K. P. (2008). Humidity cell tests for the prediction of acid rock drainage. *Minerals Engineering*, 22(1), 25–36.
- Villeneuve, M. (2004). *Évaluation du comportement géochimique à long terme de rejets miniers à faible potentiel de génération d'acide à l'aide d'essais cinétique* (Masters thesis, École Polytechnique de Montréal, Canada).

**Geodynamics, Tectonics, Structural Geology,
Petroleum Geology**



The First Geological Investigation of Mekong River Rapids, Loei Province: Implications for a New Geologic Map and Tectonics in the Thai-Laos Boundary

Vimoltip Singtuen and Prawit Bumroongroch

Abstract

The Mekong River Rapids outcrop in Loei Province appeared in the middle part of the Mekong River, a site of national geoheritage at the boundary between Thailand and Laos PDR. These rapids are not systematically classified on the geological map, and no studies have researched the rocks around the rapids in detail. This work aims to study petrography and the rocks' chemical composition to explain the origin and to specify the names by field observation, petrography, and geochemistry. According to petrographical analysis, the studied rocks are classified into four groups: (1) a microcrystalline volcanic rock (alkaline rhyolite and rhyolite), (2) a garnet-pyroxene skarn, (3) a biotite-hornblende monzogranite, and (4) a dolomitic limestone. Major elements classify the studied rocks as rhyolite and dacite, while trace elements group them into rhyodacite and andesite fields. Geochemical data indicate that volcanic rocks generated from calc-alkaline magma erupted at the volcanic arcs related to subduction activities. Therefore, this work can hypothesize the geological model as granitic rocks intruded into carbonate hosts and metamorphosed into the skarn zone due to contact metamorphism. Meanwhile, the chill margin of the granite pluton rapidly formed as fine-grained igneous rocks with a volcanic eruption, which appeared at the Mekong Rapids.

Keywords

Volcanic rocks • Volcanic arc • Rhyolite • Skarn • Calc-alkaline magma • Silicification

1 Introduction

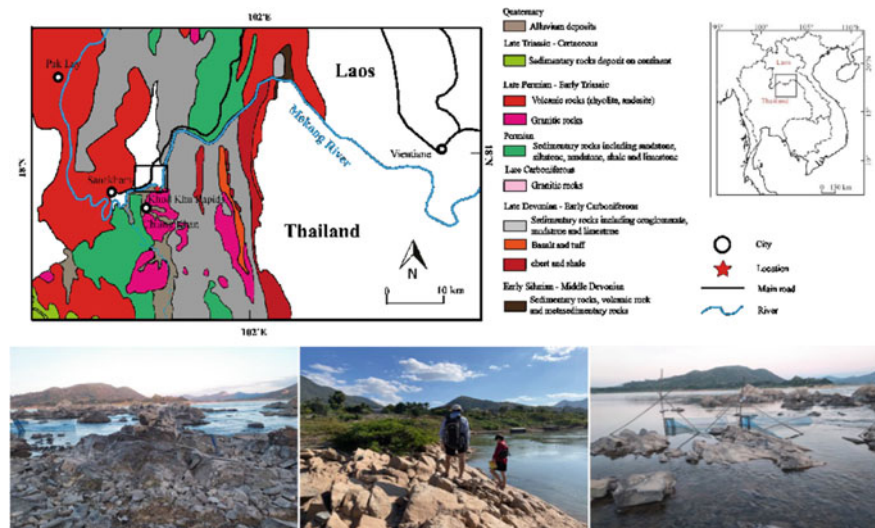
The Mekong Transboundary River Rapids in Chiang Khan District, Northern Loei Province, are one of the largest rapids in Thailand and bordered by Laos PDR. Thai geologists reported the river rapids as dioritic and granodioritic dikes that cross the Mekong River in the N-S direction and intrude into the sedimentary and tuffaceous rocks (DMR, 2012). The Chiang Khan area, Loei Province, is covered by Paleozoic sedimentary rocks, middle Carboniferous in the east that were metamorphosed into hornfels, quartzite, and marble by granodioritic intrusion, whereas in the west there are middle Permian rocks, consisted of sandstone, shale, and limestone. The found limestone has a layered and lens-like appearance and granite that intruded into the limestone during the upper Permian to lower Triassic related to the mineral deposits (Fe and Au) (Nakhonsri et al., 1987). Diorite (Fe-ore deposit) emplacement in Chiang Khan occurred, as it was indicated, in the middle Triassic (239 Ma) related to the volcanic arc activity during the initial stage of the Sibumasu and the Indochina collision in the early to the middle Triassic period (250–239 Ma) (Jiang et al., 2021; Nualkhao et al., 2018). Although many researchers have studied geology in Loei Province, the Mekong River Rapids are not systematically classified in the geological map. No research has been undertaken in detail (Fig. 1). Thus, this work aims to study petrography and geochemistry to give the names to the rocks and to explain their origin.

2 Materials and Methods

The primary method for this study is a field investigation at the Mekong River Rapids, Loei Province, between the borders of Thailand and Laos PDR (Fig. 1). Outcrops are present in the middle of the river with many joint directions. These rapids are covered by various rock types, felsic volcanic rocks associated with some plutonic and metamorphic

V. Singtuen (✉) · P. Bumroongroch
Department of Geotechnology, Faculty of Technology,
Khon Kaen University, 123 Moo 16 Mitparp Rd, Nai-Muang,
Muang Khon Kaen, Khon Kaen, 40002, Thailand
e-mail: vimoltipst@gmail.com

Fig. 1 Geologic map of northern Loei and Laos showing the major rock units (DGM, 1990; DMR, 2007) and outcrops in the Mekong River, Loei Province



rocks as well as dolomitic limestone. A petrographical examination was conducted on fifteen rocks at Khon Kaen University's Department of Geotechnology using ZEN core Imaging Software, connecting ZEISS imaging. For the geochemical study, seven samples with the least amount of alteration were selected for whole rock analysis. The major oxides were analyzed by the Axios model at SGS (Thailand) Co., Ltd. In addition, trace elements and REEs were analyzed using 5300DV ICP-OES and nexion300X ICP-MS at the SGS-CSTC Standards Technical Services Co., Ltd., China.

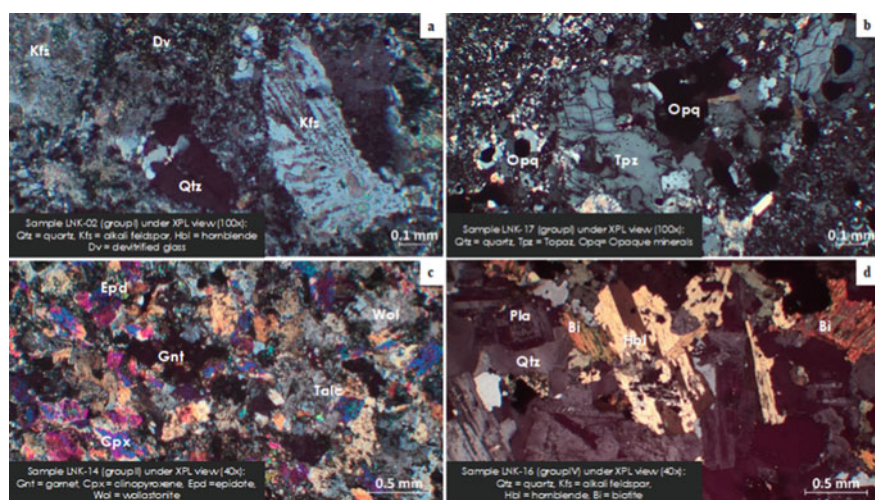
3 Results

3.1 Petrography

Petrography classified the rocks in Mekong River Rapids into four groups, microcrystalline volcanic rocks (alkaline

rhyolite and rhyolite), garnet-pyroxene skarn, dolomitic limestone, and biotite-hornblende monzogranite (Fig. 3). The alkali rhyolite and rhyolite present quartz and alkali feldspar microphenocrysts (porphyritic texture) with devitrified glass groundmass. This rock group has a low proportion of mafic minerals, but shows silica (silicification), topaz, and fine-white mica secondary replacement. Meanwhile, garnet-pyroxene skarn presents a granoblastic texture and consists mainly of garnet and pyroxene (prograde alteration), associated with wollastonite and talc (retrograde alteration). The biotite-hornblende monzogranite demonstrates a medium-grain of 32.78% quartz, 27.42% alkaline feldspar, and 39.80% plagioclase. In addition, mafic minerals are invariably biotite and hornblende (moderately altered to chlorite) that can classify them to I-type Granitoids. Meanwhile, dolomitic limestone is only one sedimentary rock unit, presenting an abundance of calcite and dolomite with small amounts of epidote and opaque minerals. The rocks have a crystalline texture and are classified as

Fig. 2 Photomicrograph (crossed nicols) of the studied rocks in Mekong River Rapids: **a** alkali rhyolite, **b** rhyolite, **c** garnet-pyroxene skarn, and **d** biotite-hornblende monzogranite



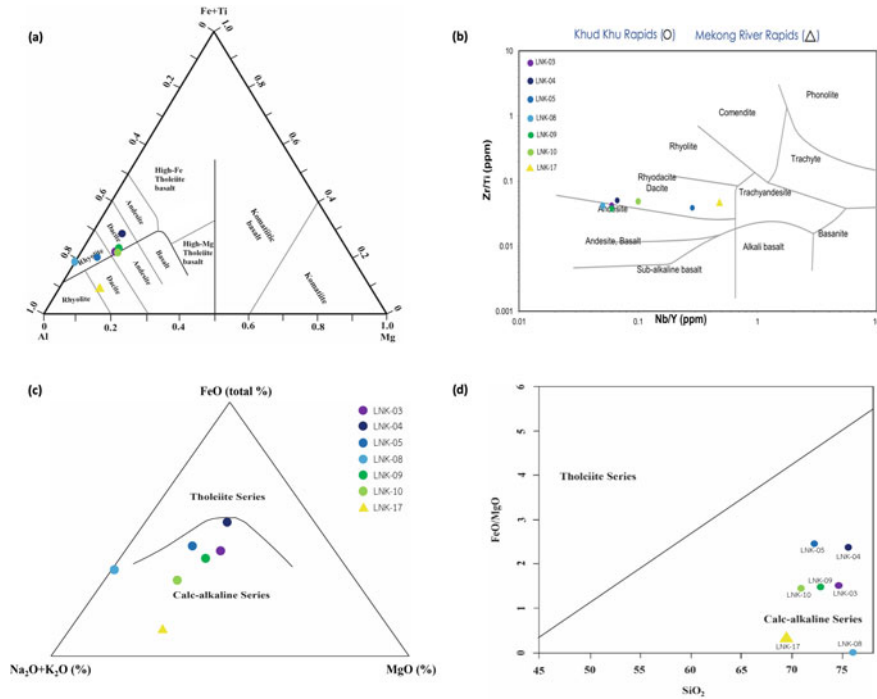


Fig. 3 Geochemical classification of the studied rocks in Mekong River Rapids: **a** ternary diagram of Fe + Ti–Al–Mg (Jensen, 1976), **b** diagram of Zr/Ti vs. Nb/Y (Winchester & Floyd, 1977), **c** diagram plots of FeO, Na₂O + K₂O and MgO (Irvine & Baragar, 1971), and **d** diagram plots of FeO/MgO against SiO₂ (Miyashiro, 1974)

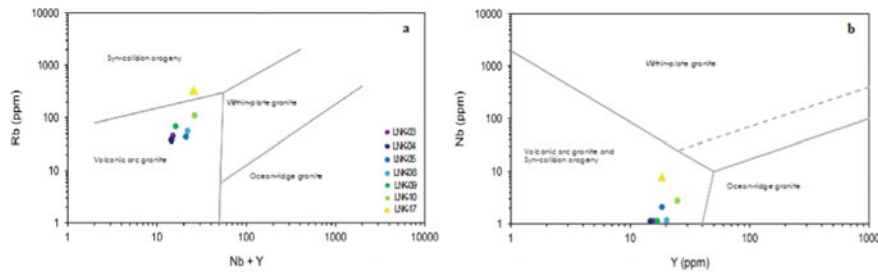


Fig. 4 Discrimination diagrams of the studied rocks in Mekong River Rapids: **a** Rb versus Nb + Y and **b** Nb versus Y (Pearce et al., 1984)

dolomitic limestone based on 54.32% CaO and 40.98% MgO from chemical analysis (by using Vanta handheld X-ray fluorescence) (Fig. 2).

3.2 Whole-Rock Geochemistry

Seven representative samples were analyzed to determine content of major oxides, trace elements, and rare earth elements (REEs). Major oxides (Fe + Ti–Al–Mg) suggest that the studied volcanic rocks are rhyolite and dacite (Fig. 3a), similar to the total alkaline versus SiO₂ classification diagram of Le Maitre et al. (Maitre et al., 1989), presenting 69.33–77.07% SiO₂, 2.24–6.38% total alkaline (Na₂O +

K₂O). Meanwhile, trace elements also identified them as andesite and rhyodacite (Fig. 3b). According to chemical data, these volcanic rocks were generated from calc-alkaline magma series (Fig. 3c-d) in volcanic arc tectonic setting related to the subduction zone (Fig. 4a, b).

4 Discussion

Based on geological data in the area comparable to the geomorphology of Thailand during the Permian to the early Triassic period, there was a massive intrusion and eruption of igneous rock in the Loei Fold Belt (Jiang et al., 2021; Nualkhao et al., 2018). This is evidenced by the emergence

of volcanic rocks such as andesite, dacite, and rhyolite, as well as intrusive igneous rocks such as monzogranites.

According to previous works and data from the present study, these volcanic and granitic rocks occurred due to the influence of the subduction of Paleotethys under the Indochina subcontinent during the formation process of the Indosinian Mountains (Jiang et al., 2021; Nualkhao et al., 2018), as mentioned above in the classification of the tectonic conditions of volcanic rocks that are plotted in the volcanic arc and collisional zone.

The sequence of rock formations in the area started from the precipitation of carbonate rocks (dolomite limestone), which is thought to have been formed during the Carboniferous to Permian period. After that, there was intrusion of igneous masses in the late Permian to the Early Triassic. As the mass of rocks pushed up, there was an eruption of magma along a large crack, causing volcanic eruption and lava flow. The composition of the lava ranges from rhyolite to andesite, which corresponds to a felsic to intermediate magma composition. The exposure of igneous rock masses to local carbonate rocks caused them to be metamorphosed, occurring ions exchange between igneous rock and carbonate rock leading to skarn zone formation. This skarn is considered as an endoskarn since is closer to the igneous body. This hypothesis can be proved by the mineral constituents that tend to occur in temperature ranges. The findings of this study will be used in a new geological map and also applied to a geological fieldwork course for university students, as well as promoted via a geotourism development.

5 Conclusions

The Mekong River Rapids in Loei Province are made up of multiphase of rocks, including volcanic, plutonic, metamorphic, and sedimentary rocks. Petrographic and geochemical data classified the studied rocks into four groups, consisting of an alkaline rhyolite-rhyolite, a garnet-pyroxene skarn, a biotite-hornblende monzogranite, and a dolomitic limestone. Petrography suggests that the volcanic rocks are highly altered and replaced by secondary minerals (silica-topaz) as silicification, presenting with microphe-notocrysts. The biotite and hornblende in monzogranite

suggest that they were generated from an igneous source (I-Type). In addition, skarns are rich in garnet and pyroxene, pointed out its classification as endoskarn, closing to the igneous body and metamorphosed from dolomitic limestone. Furthermore, geochemical data identified volcanic rocks as rhyolite and dacite (major oxides) and were also classified as rhyodacite and andesite by trace elements. These volcanic suites were generated from the calc-alkaline magma series in volcanic arcs related to the subduction zone.

References

- DGM. (1990). *Lao P.D.R. Geological and Mineral Occurrence Map 1: 1,000,000*. Department of Geology and Mines of Lao P.D.R., Vientiane.
- DMR. (2007). *Geologic map of Loei Province scale 1: 1,000,000*. Department of Mineral Resources of Thailand, Bangkok.
- DMR. (2012). *Geology of Loei Province and geological conservation sites*. Department of Mineral Resources of Thailand, Bangkok.
- Irvine, T. N., & Baragar, W. R. A. (1971). A guide to the chemical classification of the common volcanic rocks. *Canadian Journal of Earth Sciences*, 8(5), 523–548.
- Jensen, L. S. (1976). *A new cation plot for classifying subalkalic volcanic rocks* (Vol. 66). Ministry of Natural Resources, Ontario Geological Survey.
- Jiang, H., Li, W. Q., Zhao, K. D., Zhang, D., & Jiang, S. Y. (2021). Middle Triassic diorites from the Loei Fold Belt, NE Thailand: Petrogenesis and tectonic implications in the context of Paleotethyan subduction. *Lithos*, 382, 105955.
- Le Maitre, R. W., Bateman, P., Dudek, A., Keller, J., Lameyre, J., Le Bas, M. J., Sabine, P. A., Schmid, R., Sorensen, H., Streckeisen, A., Woolley, A. R., & Zanettin, B. (1989). *A Classification of igneous rocks and glossary of terms: Recommendations of the International Union of Geological Sciences Subcommittee on the Systematics of Igneous Rocks*. Blackwell Scientific.
- Nakhonsri, N., Chairangsi, Ch., & Masubchroen, S. (1987). *Geologic map of Chiang Khan District, Loei Province*. Department of Mineral Resources of Thailand, Bangkok.
- Nualkhao, P., Takahashi, R., Imai, A., & Charusiri, P. (2018). Petrochemistry of granitoids along the Loei Fold Belt, Northeastern Thailand. *Resource Geology*, 68, 395–424.
- Miyashiro, A. (1974). Volcanic rock series in island arcs and active continental margins. *American Journal of Science*, 274, 321–355.
- Pearce, J. A., Harris, N. B., & Tindle, A. G. (1984). Trace element discrimination diagrams for the tectonic interpretation of granitic rocks. *Journal of Petrology*, 25(4), 956–983.
- Winchester, J. A., & Floyd, P. A. (1977). Geochemical discrimination of different magma series and their differentiation products using immobile elements. *Chemical Geology*, 20, 325–343.



Multi-scale Analysis of the Mylonitized Giant Quartz Veins of the Cap de Creus and Canigó Massifs (Pyrenees)

Eloi González-Esvertit, Josep Maria Casas, Àngels Canals, Paul D. Bons, Claudia Prieto-Torrell, Gabriel Cofrade, and Enrique Gomez-Rivas

Abstract

Quartz veins with widths ranging from meters to hundreds of meters and lengths from tens of meters to kilometers, known as Giant Quartz Veins (GQVs), are ubiquitous in orogenic belts worldwide. These veins are very useful to gain understanding of fluid flow, quartz precipitation, and deformation mechanisms and also to unravel the geochemical history of their host rocks. The present work is dealing with multi-scale analysis (from orogen-to microscopic-scales) of the mylonitized GQVs encountered in the Cap de Creus and Canigó Massifs, Eastern Pyrenees, SW Europe. Despite being hosted in variable rocks and emplaced along different structures, the studied GQVs share various similar features: (1) the development of silicification halos, (2) evidence of different mechanisms of quartz growth through host rock replacement, host rock dissolution related to the opening of cm-wide vein networks, and aggregation of multiple crack-seal veins, and (3) a strong structural control on their emplacement. The GQVs postdate the development of regional cleavages but are affected by a mylonitic/phyllonitic foliation, showing evidence of deformation by dislocation creep and a wide range of microscopic shear sense indicators. The pre-existing structures along which

the Roses GQV was formed vary even within hundreds of meters, from a brittle thrust fault to a mylonitic band. In the Esquerdas de Rojà GQV, an incipient to well-developed low temperature mylonitic fabric is present along more than 15 km, and grain-size reduction is mainly achieved along cataclastic bands. These features can be representative of the more than 700 GQVs that have been mapped in the Pyrenees.

Keywords

Giant quartz vein • Mapping • Microstructures • Pyrenees

1 Introduction

Giant Quartz Veins (GQVs), up to hundreds of meters in width and kilometers in length, are often related to hydrothermal ore deposits and represent large-scale fingerprints of the structural and geochemical history of their host rocks (Sharp et al., 2005; Wagner et al., 2010). However, the tectonic and geochemical controls on their emplacement are not well understood yet. This work presents a multi-scale study of two sectors in the Pyrenees (SW Europe), where GQVs are ubiquitous and hosted by different rock types, aiming to gain insight into their structural evolution from the orogenic to the thin section scale.

2 Zooming in into the Canigó and Cap de Creus Veins

The Pyrenees (Fig. 1a) is an Alpine fold-and-thrust belt formed after the collision between the Iberian and the Eurasian plates (Muñoz, 1992). It exposes an exhumed late-Neoproterozoic to Carboniferous metasedimentary succession that records Sardinian, Variscan and Alpine deformation

E. González-Esvertit (✉) · À. Canals · C. Prieto-Torrell · G. Cofrade · E. Gomez-Rivas
Departament de Mineralogia, Petrologia i Geologia Aplicada, Facultat de Ciències de la Terra, Universitat de Barcelona, 08028 Barcelona, Spain
e-mail: e.gonzalez-esvertit@ub.edu

J. M. Casas
Departament de Dinàmica de la Terra i l'Oceà, Facultat de Ciències de la Terra, Universitat de Barcelona, 08028 Barcelona, Spain

P. D. Bons
Department of Geosciences, Tübingen University, 72076 Tübingen, Germany

P. D. Bons
China University of Geosciences, Beijing, China

events, Cadomian, Ordovician and Carboniferous igneous rocks, and was affected by a Variscan regional metamorphism (Casas et al., 2019). At least 741 GQVs, defined as those that can be mapped at 1:25,000 scale, are emplaced at different structural levels of the Pyrenees along different brittle and ductile structures (González-Esvertit et al., 2022).

The age of these structures is under discussion. Most of them have been attributed to the Variscan Orogeny (ca 330 to 290 Ma), but in the southern and northern slopes of the chain, some GQVs are hosted in sedimentary rocks of

Jurassic to Eocene age. In the Canigó Massif, the Esquerdes de Rojà GQVs (Figs. 1a, b and 2a) are hosted in the Canigó gneiss and the Costabona granite. At the outcrop scale, the structures along which these GQVs could have been emplaced are unclear, and vein quartz exhibits two main deformation structures: an E-W-oriented mylonitic foliation (Fig. 2b), which can be correlated with other mylonitic belts with same orientation across de Pyrenees, and a N-S fracture system. The development of silicification haloes around the GQVs (Figs. 1b and 2c) and the existence of

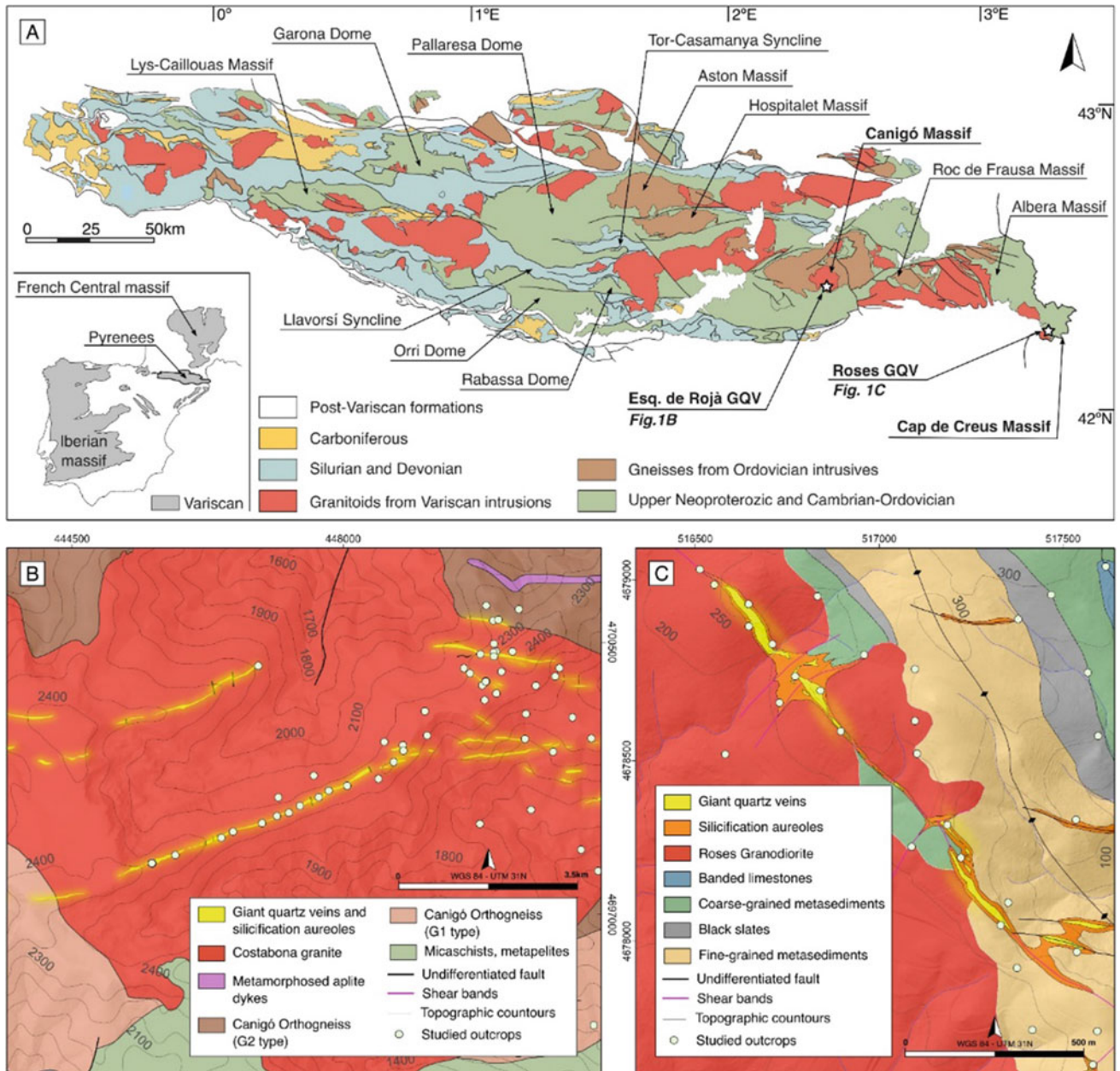


Fig. 1 Geological sketch map of the pre-Variscan basement rocks of the Pyrenees (a), and of the Esquerdes de Rojà (Canigó Massif) (b) and Roses (Cap de Creus Massif) (c) areas

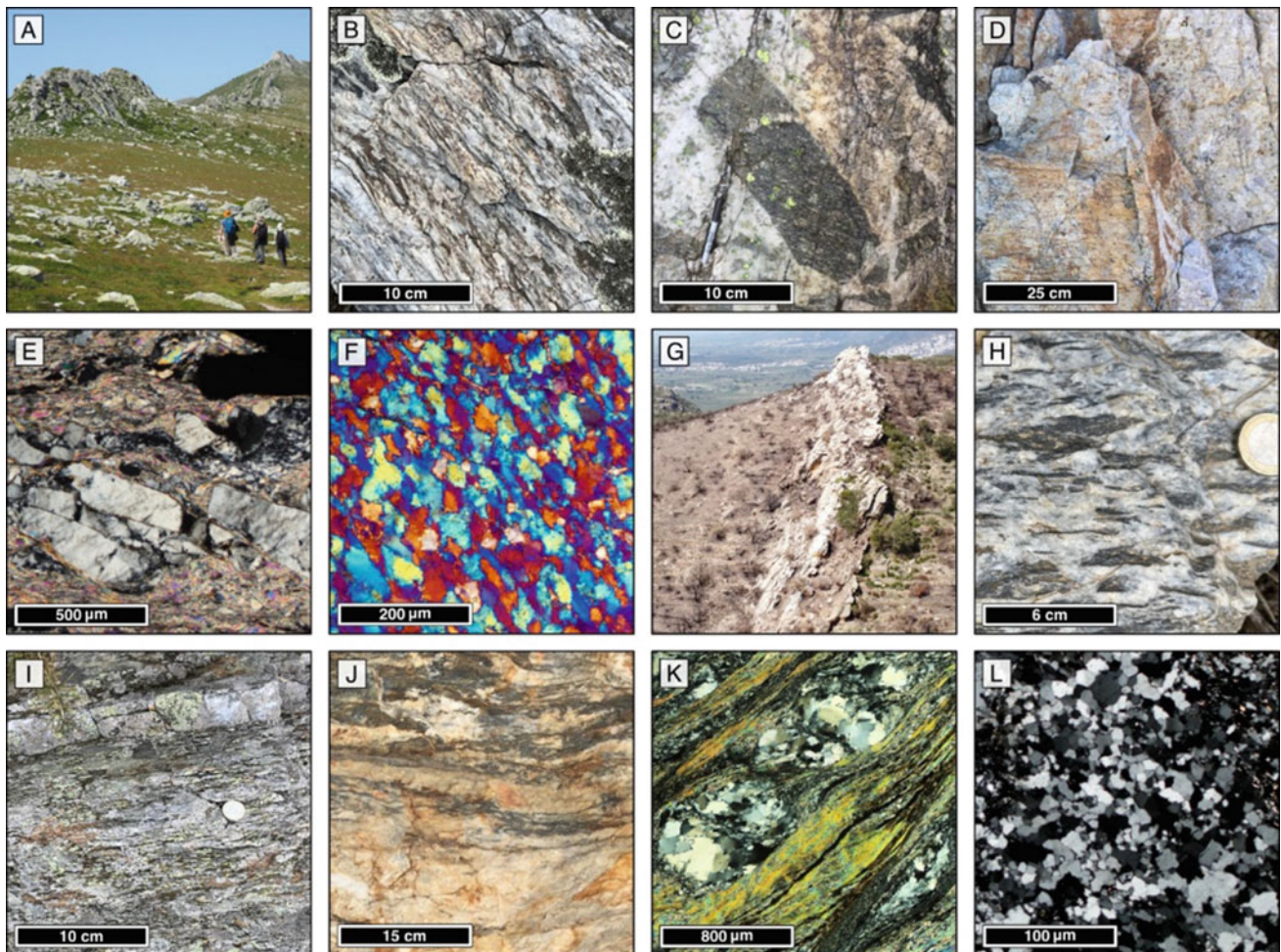


Fig. 2 Progressive zooming into the Esquerdes de Rojà (a–f) and Roses (g–l) Giant Quartz Veins. Microphotographs are in cross-polarized light (XPL) except for (f), which is in XPL plus retardation lambda plate. See text for detailed descriptions

metasomatically altered areas with biotite loss and feldspatization in the adjacent rocks (Fig. 2d) are also common features. At the thin section scale, microstructures mainly show crystal-plastic deformation and cataclastic grain-size reduction. A well exposed mylonitic fabric, with tectonically reworked quartz grains and fractured feldspar porphyroclasts, is the dominant microstructure in both the GQVs and their host rocks (Fig. 2e). This may indicate that deformation took place below 450 °C (initial temperature for k-feldspar recrystallization), although the existence of chemical potentials and diffusion processes could bias this interpretation. Quartz dynamic recrystallization is mainly achieved through bulging and dominantly sub-grain rotation (Fig. 2e, f). Tectonically reworked quartz often shows a weak crystallographic preferred orientation defining a continuous foliation that suggests, according to c-axis fabrics, a sinistral sense of shearing (Fig. 2f). This is also confirmed by other kinematic indicators, such lepidoblastic muscovite mica fish, fragmented porphyroclasts, and an S-C fabric

dominated by C' shear bands (Fig. 2e). Diffusion creep microstructures within the GQVs are represented by pressure solution between quartz grains, as well as by fractures defining cataclastic grain-size reduction bands.

In the Cap de Creus Massif (Figs. 1a, c and 2g), the Roses GQV is hosted in pre-Variscan fine- to coarse-grained low-grade metasedimentary and metavolcanic rocks, as well as by the 290–300 Ma-old Roses Granodiorite. Quartz bodies that crop out in the SE sector of this area are emplaced along a SE-NW-oriented thrust, while the NW segment of the Roses GQV follows the main trend of a sheared quartz-schist. At the outcrop scale, silicification of the host rocks, as in the Canigó Massif, is the most dominant feature (Figs. 1c and 2h). The Roses GQV is affected by a strong NW–SE-oriented and moderately-to-strongly SW-dipping mylonitic/phyllonitic foliation along which 1–5 cm-wide “late” quartz veins are common (Fig. 2i). Next to the GQV walls, evidence of different mechanisms of quartz growth through host rock replacement, host rock

pressure-dissolution related to the opening of cm-wide veins, and aggregation of unoriented “late” crack-seal veins are common features (Fig. 2j). At the thin section scale, host rocks juxtaposing the GQV show a strong anastomosing phyllonitic foliation, which bends around polycrystalline quartz porphyroclasts that show small new grains formed by bulging recrystallization along the contacts between relict grains (Fig. 2k). Quartz from the GQV shows a fine-grained mylonitic fabric defined by the orientation of Fe–Ti oxides and phyllosilicates, as well as by a weak elongation of some quartz grains. Sub-grain rotation is the dominant crystal-plastic deformation mechanism, although lobate boundaries, the absence of undulous extinction, and the occurrence of window and pining structures also suggest grain boundary migration. Occasional polygonal fabrics with triple junctions at 120° suggest the occurrence of static grain growth through grain boundary area reduction (Fig. 2l).

3 Concluding Remarks

Giant quartz veins can act either as conduits or barriers to heat and mass within the Earth’s crust, can also be associated with hydrothermal ore deposits, and hold information about the deformational and geochemical history of their host rocks. In the Eastern Pyrenees, the Canigó and Cap de Creus areas represent key locations for the understanding of the origin and significance of these structures. The studied veins share similar features such as silicification processes in the adjacent rocks, replacement textures within the main quartz

body, and brittle and ductile deformation microstructures. Further investigations on the deformation microstructures could help to understand the complete evolution of this veins and, therefore, to unravel their formation age and kinematics.

References

- Casas, J. M., Álvaro, J. J., Clausen, S., Padel, M., Puddu, C., Sanz-López, J., Sánchez-García, T., Navidad, M., Castiñeiras, P., Liesa, M. (2019). Palaeozoic basement of the pyrenees. In Quesada, C., Oliveira, J. T. (Eds.), *The geology of Iberia: A geodynamic approach* (pp. 229–259). Regional Geology Reviews; Springer International Publishing. ISBN 978-3-030-10518-1.
- González-Esvertit, E., Canals, A., Bons, P. D., Casas, J. M., & Gomez-Rivas, E. (2022). Compiling regional structures in geological databases: The giant quartz veins of the pyrenees as a case study. *Journal of Structural Geology*, 163, 104705. <https://doi.org/10.1016/j.jsg.2022.104705>
- Muñoz, J. A. (1992). Evolution of a continental collision belt: ECORS-pyrenees crustal balanced cross-section. In McClay, K. R. (Ed.), *Thrust tectonics* (pp. 235–246). Springer Netherlands. ISBN 978-0-412-43900-1.
- Sharp, Z. D., Masson, H., & Lucchini, R. (2005). Stable isotope geochemistry and formation mechanisms of quartz veins; extreme paleoaltitudes of the Central Alps in the Neogene. *American Journal of Science*, 305, 187–219. <https://doi.org/10.2475/ajs.305.3.187>
- Wagner, T., Boyce, A. J., & Erzinger, J. (2010). Fluid-rock interaction during formation of metamorphic quartz veins: A REE and stable isotope study from the Rhenish Massif, Germany. *American Journal of Science*, 310, 645–682. <https://doi.org/10.2475/07.2010.04>



Tracking the Southern Tethys Margin in NW Africa (Rif Belt, Morocco)

André Michard, Aboubaker Farah, Omar Saddiqi, Youssef Driouch, Abdeltif Lahfid, Ahmed Chalouan, Hervé Bertrand, Moulley Charaf Chabou, and Nasrddine Youbi

Abstract

Along NW Africa, scarce relics of the Alpine Tethys crust are associated with the Maghrebian Flyschs. In the Rif belt, a string of potential relics extends as tectonic slivers within the stacked external nappes from the Beni Malek serpentinite massif to the Bou Adel gabbro massif. These relics define the transported “Mesorif Suture Zone” (MSZ), whose interpretation is controversial. Here, we report on the large Bou Adel gabbro, based on detailed mapping and sampling. A thin, tectonic envelope of hydrothermally altered basalts followed upward by marbles and volcanoclastic carbonate meta-breccias is identified. The greenschist-facies metamorphism of the marbles is coeval with the imprint of a flat-lying foliation that affects both the clasts and matrix. Geochemical signature of the meta-basalts compare with that of the Central Atlantic Magmatic Province (CAMP) whereas the 190–196 Ma-old gabbro exhibits composition between E-MORB and OIB. Consistently, we hypothesize that the gabbro intruded a Late Triassic-Lower Liassic volcanic passive margin that evolved into a magma-poor transform

margin. During the Lower-Middle Jurassic rifting climax, normal faulting and metamorphism would have affected the gabbro envelope subsequently overlain by extensional rafts from the proximal margin. The Ocean-Continent Transition (OCT) domain (Beni Malek) would have developed later further north. Non-inverted analogs could be found in the Limpopo and Namibia margins.

Keywords

Rif • CAMP • Volcanic passive margin • Magma-poor transform margin • Gondwana rifting

A. Michard (✉)

Paris-Saclay University, Paris, France
e-mail: andremichard@orange.fr

A. Farah · O. Saddiqi

Hassan II University, Casablanca, Morocco

Y. Driouch

Sidi Mohammed Ben Abdallah University, Fes, Morocco

A. Lahfid

BRGM, Orléans, France

A. Chalouan

Mohamed V University, Rabat, Morocco

H. Bertrand

Ecole Normale Supérieure, Lyon, France

M. C. Chabou

Ferhat Abbas University, Setif, Algeria

N. Youbi

Cadi Ayyad University, Marrakech, Morocco

1 Introduction

The Bou Adel gabbro massif is the westernmost gabbro tectonic lenses that herald the transported Mesorif Suture Zone (MSZ), together with the Beni Malek serpentinite massif (Benzaggagh, 2014) (Fig. 1). The gabbroic lenses have been regarded either as derived from an Early-Mid Jurassic oceanic crust of the south-westernmost, Maghrebian Tethys (Michard et al., 2014, 2018) or from CAMP intrusions in the crust of the African continental margin (Gimeno-Vives et al., 2019).

The rocks that overlie the gabbro slivers and thus could represent the hosting rocks of the intrusion were not precisely described so far. Here, we document the nature and structure of this envelope based on detailed mapping and sampling of the well-exposed, western tip of the Bou Adel gabbro massif.

2 Settings, Materials and Methods

The studied rock units from the Senhadja Nappe (Fig. 1) include from bottom to top, (i) gabbro and associated plagiogranite pockets and veins (400 × 2500 m in horizontal



Fig. 1 **a** Structure of the Rif belt and magmatic occurrences of the MSZ (after 1, 3, 6, 7). BA: Bou Adel; BM: Beni Malek; DA: Douar Alami; DB: Dar bou Aza; DR: Douar Roukba; JM: Jorf el Melha; KG:

Kef-el-Ghar; LK: Laklaia; DR: Douar Roukba; TA: Taineste; TF: Trois-Fourches; TL: Taounat Lechkar; Z: Zitouna. **b** Schematic southward nappe stacking

size, > 150 m of thickness); (ii) a discontinuous envelope (< 40 m) involving meta-basalts/meta-volcanoclastic breccias and clastic marbles (Benzaggagh, 2014), and (iii) the massive to bedded, fossiliferous platform limestones classified as Lower Jurassic (~300 m; see references in Benzaggagh, 2014). The latter form the base of a Jurassic sequence that includes Middle and Upper Jurassic deposits further to the east (Benzaggagh, 2014; Gimeno-Vives et al., 2019; Gimeno-Vives et al., 2020).

Mapping at 1:7,000 of the Bou Adel outcrops was carried out on both sides of the Oued Azrou valley (Fig. 2). Structural analysis was implemented both in the field and thin section. Samples were collected for petrography, geochemistry and geothermometry (in progress). Mineralogical determination was performed by electronic microscopy (Christian Chopin courtesy, ENS Paris).

3 Results

The hydrothermally altered basaltic/volcanoclastic envelope (Benzaggagh, 2014) overlies the gabbro through a clear-cut shallow-dipping fault, which truncates the steeply dipping magmatic structures. Instead, the clastic marbles are stratigraphically linked to the basaltic envelope as they rework

clasts of the latter. Lastly, a metric fault gouge and carnegneule breccias with striated mirrors highlight the base of the Liassic limestones.

The clastic marbles and associated Fe-rich metapelites are affected by low-grade greenschist-facies metamorphism coeval with the imprint of a foliation, which nearly parallels the bedding and affects both the clasts and matrix. The mineral assemblage contains dolomite and talc in the carbonate matrix, and chlorite, albite, sphene, calcite, epidote and quartz in the volcanic clasts.

4 Discussion

Based on the results reported above, we assume that the greenschist-facies basalts and clastic marbles are relics of the former host rocks of the Bou Adel gabbro. The lack of any relic of continental crust rock does not support the setting proposed by Gimeno-Vives et al. (2019). Taking into account the CAMP affinities of the basaltic envelope (Haissen et al., 2021), we propose that the gabbro emplaced within a volcanic-sedimentary pile of Upper Triassic age located outward the North Africa margin, consistent with the occurrence of shallow-water limestone clasts in the clastic marbles (Fig. 3a). This portrays a volcanic passive margin

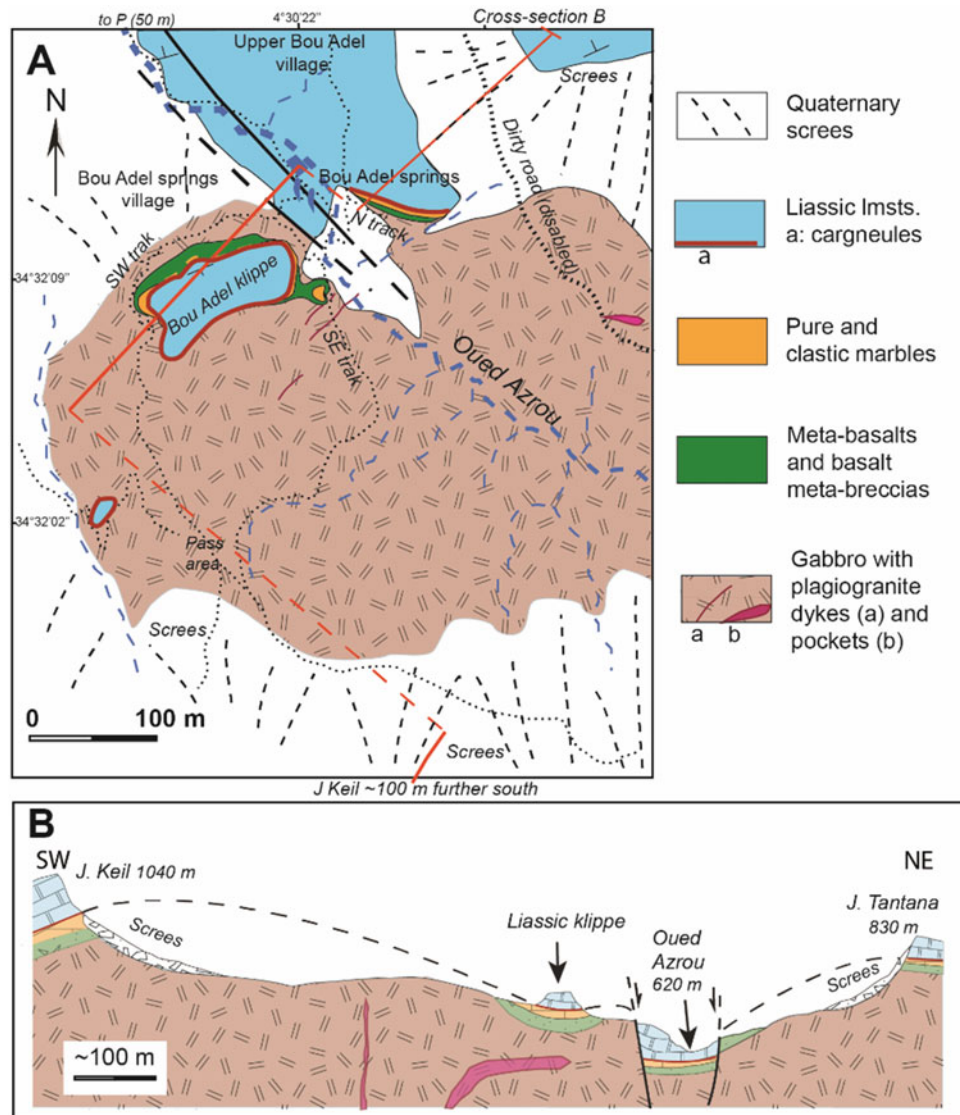


Fig. 2 **a** Detail map of the western tip of the Bou Adel gabbro lens showing the thin metamorphic envelope beneath the thick Liassic limestones of the Senhadja nappe. **b** Cross section of the Bou Adel gabbro western tip and overlying rock units

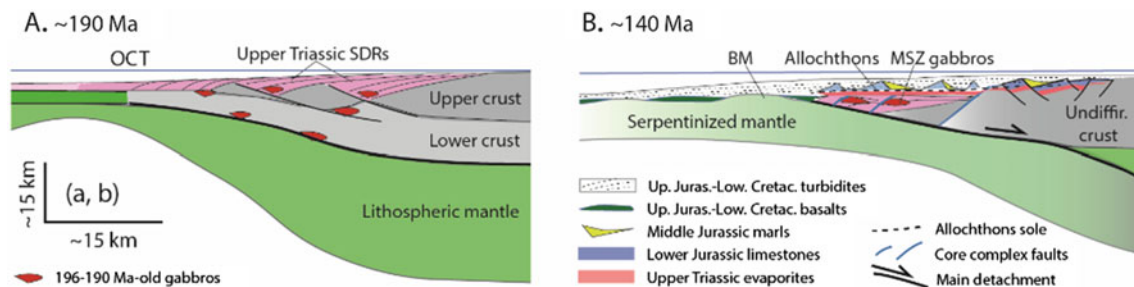


Fig. 3 New interpretation of the emplacement of the Bou Adel gabbro. **a** End of the VPM margin stage. **b** End of the magma-poor transform margin stage, after exhumation of the gabbro and sliding of the proximal Allochthons (Senhadja units)

(VPM) accumulation of Sea-Dipping Reflectors (SDRs) developed around 200–195 Ma. The SDRs could have been intruded by gabbro bodies as suggested by the 190–196 Ma U–Pb dates available for the Bou Adel gabbro (Gimeno-Vives et al., 2019; Michard et al., 2018). Then, the Bou Adel gabbro would have been exhumed in the footwall of a shallow-dipping normal fault zone, which could be now recognized beneath the basalts and marbles (Fig. 2).

Synkinematic, high-temperature, low-pressure (HT-LP) metamorphism of the host rocks of the gabbro and alteration of the gabbro itself would have developed during the rifting climax [175–170 Ma, (Gimeno-Vives et al., 2020)], with intense shear deformation along the marble ductile envelope of the gabbro body (Fig. 3b). The emplacement of the Liassic, shallow-water carbonate sequence of the Senhadja nappe and overlying Jurassic deposits above the metamorphic marble/basalt units requires a syn/post-metamorphic tectonic event, which was described as the oceanward sliding of extensional rafts from the proximal margin associated with salt tectonics (Gimeno-Vives et al., 2019; Michard et al., 2020). This would have occurred during the Late Jurassic–Early Cretaceous, i.e., at the time when the former VPM was converted into a magma-poor transform margin (MPTM) typical of the Alpine and Maghrebian Tethys. The latest pre-orogenic extensional events (160–140 Ma) allowed mantle exhumation in the OCT domain (Beni Malek massif) and E-MORB basalt flows in the distal Ketama Allochthon (Benzaggagh, 2014; Michard et al., 2018) and the proximal Mesorif-Internal Prerif zone (Benzaggagh, 2014). Tectonic sampling of slivers from the OCT and distal margin domains occurred during the onset of plate convergence (Eocene–Oligocene) and building of the Maghrebian tectonic prism up to the Neogene (Michard et al., 2018; Gimeno-Vives et al., 2020 and references therein).

5 Conclusion

Data gaps explain the recent controversy about the origin of the Bou Adel gabbro and eastern analogs (Gimeno-Vives et al., 2020; Michard et al., 2020). Re-examination of the Bou Adel case allows us to assume that the gabbro emplaced there in the SDRs of a VPM likely connected westward to the Central Atlantic, Early Jurassic margin. Then, this margin segment evolved toward the MPTM type during the

Middle-Late Jurassic/Early Cretaceous [cf. Namibia and Limpopo examples; (Roche et al., 2022; Geoffroy et al., 2022)], which caused firstly the gabbro exhumation, and secondly the sliding of sedimentary rafts from the proximal margin.

References

- Benzaggagh, M. (2014). Oceanic units in the core of the External Rif (Morocco): Intramargin hiatus or South-Tethyan remnants? *Journal of Geodynamics*, 77, 4–21.
- Gimeno-Vives, O., Mohn, G., Bosse, V., Haissen, F., Zaghoul, M. N., Atouabat, A., & Frizon de Lamotte, D. (2019). The Mesozoic margin of the Maghrebian Tethys in the Rif belt (Morocco): Evidence for polyphase rifting and related magmatic activity. *Tectonics*, 38, 2894–2918 (2019)
- Geoffroy, L., Chauvet, F., & Rigenbach, J.-C. (2022). Middle-lower continental crust exhumed at the distal edges of volcanic passive margins. *Communications Earth & Environment* <https://doi.org/10.1038/s43247-022-00420-x>
- Gimeno-Vives, O., Mohn, G., Bosse, V., Haissen, F., Zaghoul, M. N., Atouabat, A., & Frizon de Lamotte, D. (2020). Reply to comments by Michard et al. on “The Mesozoic Margin of the Maghrebian Tethys in the Rif Belt (Morocco): Evidence for polyphase rifting and related magmatic activity. *Tectonics*, 0–2. <https://doi.org/10.1029/2020tc006165>
- Haissen, F., Zaghoul M. N., Dilek, Y., Gimeno-Vives, O., Mohn, G., Cambeses A., Frizon de Lamotte, D., Bosse, V. (2021). Geochemistry and petrogenesis of Lower Jurassic mafic rock suites in the External Rif Belt, and chemical geodynamics of the Central Atlantic Magmatic Province (CAMP) in NW Morocco. *The Journal of Geology*, 129, <https://doi.org/10.1086/716499>
- Michard, A., Saddiqi, O., Chalouan, A., Chabou, M. C., Lach, P., Rossi, P., et al. (2020). Comment on «The Mesozoic margin of the Maghrebian Tethys in the Rif Belt (Morocco): Evidence for polyphase rifting and related magmatic activity” by Gimeno-Vives et al. *Tectonics*, 38. <https://doi.org/10.1029/2019TC006004>
- Michard, A., Mokhtari, A., Chalouan, A., Saddiqi, O., Rossi, P., & Rjimati, E. (2014). New ophiolite slivers in the External Rif Belt, and tentative restoration of a dual Tethyan suture in the Western Maghrebides. *Bulletin de la Société géologique de France*, 185, 313–328.
- Michard, A., Mokhtari, A., Lach, P., Rossi, P., Chalouan, A., Saddiqi, O., & Rjimati, E. C. (2018). Liassic age of an oceanic gabbro of the External Rif (Morocco): Implications for the Jurassic continent–ocean boundary of Northwest Africa. *Comptes Rendus Geoscience*, 350, 299–309.
- Roche, V., Leroy, S., Guillocheau, F., et al. (2021) The Limpopo magma-rich transform margin, South Mozambique. Implications for the Gondwana breakup. *Tectonics*, 40, e2021TC006914.



Les Avellanes Diapir, South-Central Pyrenees: Reconstructing the Kinematics of a Salt Diapir Inside a Fold-and-Thrust Belt: Preliminary Results

Gabriel Cofrade, Òscar Gratacós, Irene Cantarero, Oriol Ferrer, Pedro Ramirez-Perez, Eduard Roca, and Anna Travé

Abstract

In salt-detached fold-and-thrust belts, salt can be accumulated along the front where can extrude locally. The nature and timing of salt accumulations were studied at the South-Central Pyrenees, along *Les Avellanes* diapir surroundings. Field data collected is used for mapping and the construction of a cross section covering the outer part of the fold-and-thrust belt, restituted until the base of the Eocene. The primary welding of the synclines during the Eocene obstructed lateral flow which created an underground accumulation. The collapse of the crest atop facilitated the extrusion of the diapir.

Keywords

Salt tectonics • Tectonostratigraphy • Fold-and-thrust belt • Southern Pyrenees • Les Avellanes Diapir

1 Introduction, Geological Setting, and Objectives

In salt-detached fold-and-thrust belts, such as in the South-Central Pyrenees (Fig. 1a, b), salt is accumulated near the outer areas where can locally outcrop (Camara & Flinch,

2017). Those salt accumulations can either result from pre-orogenic structures, or from syn-tectonic migration due to sedimentary and tectonic loading. Thus, the nature, timing, and evolution of those external salt structures are generally, not well understood.

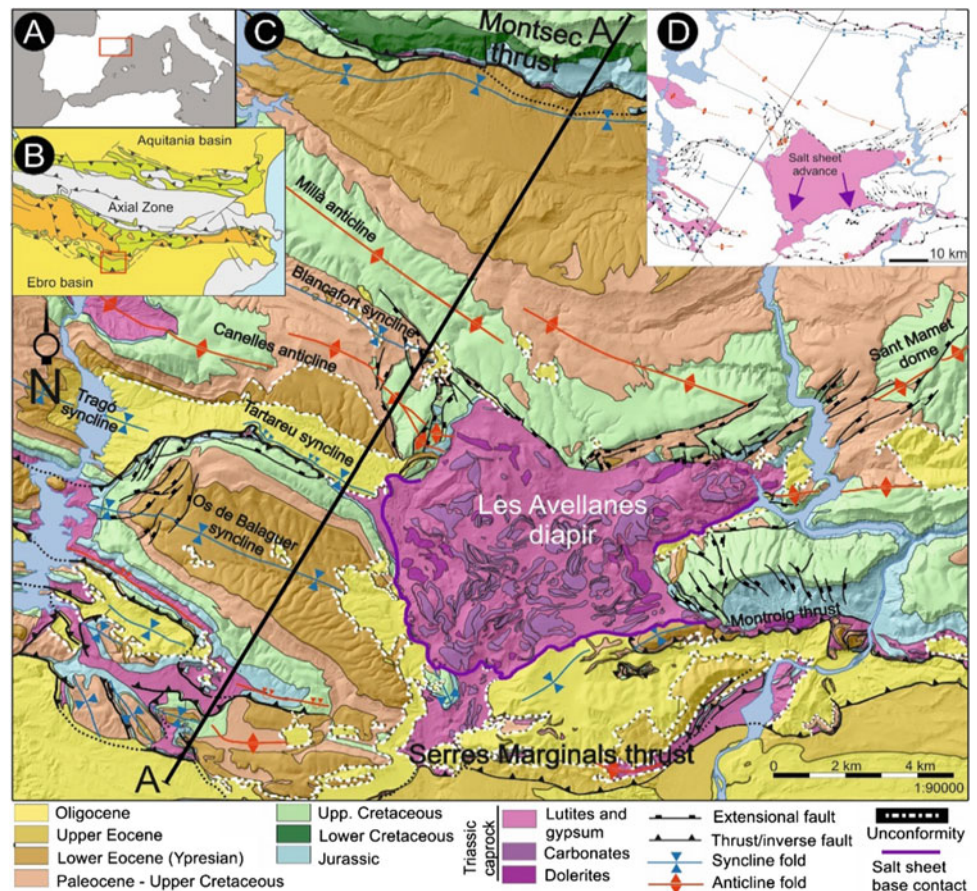
The Pyrenees is a collisional orogen formed by the subduction of the Iberian plate under the European plate during the Upper Cretaceous to Oligocene times. It is made by two opposite vergent fold-and-thrust belts and a hinterland core (Axial Zone). The orogenic building is mainly controlled by (1) the inversion of a late Jurassic-Lower Cretaceous hyperextended margin and (2) the uneven extension and thickness of both, the Triassic evaporites and the foreland evaporites (upp. Eocene–Oligocene in age) (Camara & Flinch, 2017; Muñoz et al., 2018). The South-Central fold-and-thrust belt is characterized by three thrust sheets branching southward in a piggy-back sequence detached on the Triassic salt: the Upper Cretaceous (Bóixols thrust sheet), the lower Eocene (Montsec thrust sheet), and the Oligocene (Serres Marginals (SM) thrust sheet), being this last one the outermost and the studied area of this work. The SM thrust sheet contains a detached sedimentary cover, thickening northward, deposited at the distal tip of the pre-orogenic basin (Muñoz et al., 2018). This sequence is formed of late Triassic-Jurassic carbonates, Upp. Cretaceous calcarenites, Paleocene detritics and carbonates, low. Eocene limestones, and med.-late Eocene–Oligocene conglomerates and evaporites. Along this thrust sheet there are several diapirs piercing this cover, and *Les Avellanes* diapir, is one of the most extensive among them. The large extension of the outcropping diapir body (Fig. 1) suggests first, the sub-surface salt accumulation in the studied area followed by the piercing of the diapir, being the mechanism and the timing of those processes the main aim of this work.

G. Cofrade (✉) · I. Cantarero · P. Ramirez-Perez · A. Travé
Departament de Mineralogia, Petrologia i Geologia Aplicada,
Facultat de Ciències de la Terra, Universitat de Barcelona (UB),
c/Martí i Franquès s/n, 08028 Barcelona, Spain
e-mail: gcofrade@ub.edu

Ò. Gratacós · O. Ferrer · E. Roca
Departament de Dinàmica de la Terra i de l'Oceà, Facultat de
Ciències de la Terra, Universitat de Barcelona (UB),
c/Martí i Franquès s/n, 08028 Barcelona, Spain

G. Cofrade · Ò. Gratacós · I. Cantarero · O. Ferrer ·
P. Ramirez-Perez · E. Roca · A. Travé
Institut de Recerca Geomodels, Universitat de Barcelona (UB),
c/ Martí i Franquès s/n, 08028 Barcelona, Spain

Fig. 1 a, b location and simplified map of the Pyrenees. c, d geological and structural map of the study area



2 Methods

Structural and sedimentological data was collected and georeferenced on-field. Geological maps were finally done integrating information already published in ICGC (<https://www.icgc.cat/en/Downloads>). Digital elevation models at 2×2 m resolution derived from LiDAR data [available at (<https://www.icgc.cat/en/Downloads>)] have been used as a base to extract new dip data (using GOCAD and in-house plugins), as well as, to construct the geological maps (Fig. 1). Using the geological maps and the structural data, a cross section has been constructed and restored in SW-NE direction. Cross section construction and restoration were done using MOVE software with flexural slip unfolding, and fault parallel flow algorithms without considering the compaction of sediments.

3 Structural and Tectonostratigraphic Observations

The outcropping salt body of *Les Avellanes* diapir is mainly represented by a caprock made of stacked, Triassic blocks, where halite is missing. The diapir body displays an irregular shape, whose boundaries are the combination of (1) the interconnection of the salt with the regional tectonic structures and (2) the outer boundary of a salt sheet sourced in the main structure which advanced southward during the early Oligocene (Cofrade et al., 2021) (Fig. 1c, d). The salt sheet obscures partially the real geometry of the diapir, although its surrounding area is well exposed.

The area is characterized by a set of WNW-ESE folds, showing gentle and broad synclines followed by tight, verticalized, anticlines. The thickness of the sedimentary units

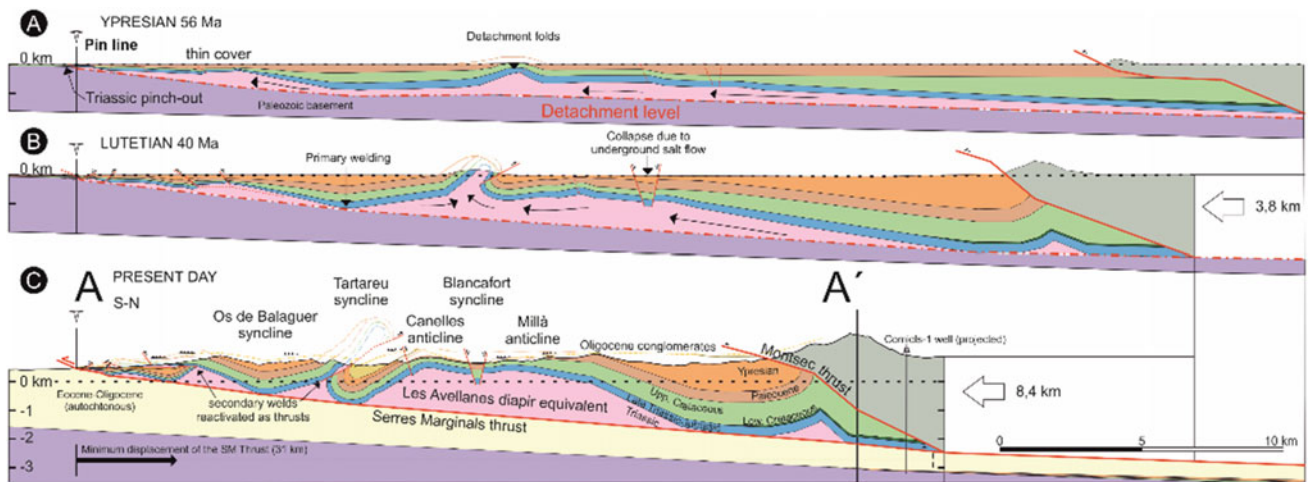


Fig. 2 Sequential restoration of the A-A' cross section (preliminar) from the present to the Ypresian. See trace and location in Fig. 1c

controls the syncline fold wavelength, becoming greater northward. At the core of the synclines, the Paleocene and the lower Eocene (Ypresian), present growth strata architectures adjacent to the verticalize anticline limbs and growth thicker toward the hinge of the synclines.

Superimposed on the folds, two orthogonal NW–SE and SW–NE sets of extensional faults are developed in the northern area (Fig. 1c, d). The resulting horst-and-graben array extends outward from the diapir and reaches the NE Sant Mamet dome (Fig. 1c). The north boundary of the diapir is mostly coincident with some of the fault escarpments (Fig. 1c, d). Postdating the extensional faults and onlapping the diapir at the north, there are Oligocene conglomerates.

4 Discussion

During the Paleocene (Fig. 2a), early Pyrenean shortening formed narrow and elongated detached folds mainly in an orthogonal-to-compression trending direction. In between, synclines show a wider geometry due to sedimentary loading, triggering underground salt flow. During the early Eocene (Ypresian times, Fig. 2b), as deformation progressed southward the Montsec thrust began to form. Shortening caused the evolution of the detached folds. Limbs rotated while the anticline crests were uplifted, exposing the salt at the surface by erosion. The synclines continued to sink accommodating sedimentation until some were welded at the bottom. The primary welding compartmentalized the salt which accumulated below the cover forming a bulge whose broad crest collapsed inward resulting in the formation of grabens parallel to the fold axis. The formation of those grabens during the late Eocene–Oligocene facilitated the piercing of the salt laterally eastwards of the cross section (Fig. 2c).

5 Conclusions

Accumulation of Triassic salt at the front of the South-Pyrenean fold-and-thrust belt was due to both, sedimentary and tectonic loading from, at least, Paleocene to early Oligocene times. Contraction formed salt pillows, evolving into detached folds. Synclines sunk as they captured sedimentation until their bottom welded, obstructing salt lateral flow. Then, salt accumulated under a bulge whose crest collapsed inwards creating grabens parallel to the fold axis which, laterally eastward, facilitated the piercing of *Les Avellanes* diapir.

Acknowledgements Work supported by Institut de Recerca Geomodels (project CGL2017- 85532-P (AEI/FEDER)), Grups Consolidats de Recerca “Geologia Sedimentària” (2017SGR-824) and “Geodinàmica i Anàlisi de Conques (2017SGR-596), DGICYT PID2021-122467NB-C22, PGC2018-093903-B-C22 (MCIU/FEDER, UE), SABREM PID2020-117598GB-I00 MCIN/AEI/<https://doi.org/10.13039/501100011033>, and the scholarship PREDOC-UB1 5660400. Petex and Emerson are also acknowledged for providing academic licenses for Move and Gocad, respectively.

References

- Camara, P., & Flinch, J. (2017). *The Southern Pyrenees: A salt-based fold and thrust belt* (pp. 395–415). Permo-Triassic Salt Provinces of Europe, North Africa and the Atlantic Margins.
- Cofrade et al. *Study of the Oligocene sediments in the SW boundary of Les Avellanes diapir (NE Spain)*, MedGU2021 conference proceedings (in progress).
- ICGC. Mapa geològic de Catalunya, 1:25.000, [Camarasa, Os de Balaguer, Ager, Figuerola]. 1:25.000 series Elevation dataset. Webpage: <https://www.icgc.cat/en/Downloads>
- Muñoz et al. (2018). The structure of the South-Central-Pyrenean fold and thrust belt as constrained by subsurface data. *Geologica Acta*, 16(4), 439–460.



Using Paleomagnetic and Field Data for the Paleogeometric Reconstruction of the Northern Border of the Central High Atlas

Bennacer Moussaid, Antonio Casas-Sainz, Juan José Villalaín, Hmidou El Ouardi, Belen Oliva, Sara Torres-López, Teresa Roman-Berdiel, Ruth Soto, Nawal Bouya, and Hassan El Makrini

Abstract

In this work, we present results of the application of paleomagnetism and the analysis of synsedimentary structures in order to clarify the age and origin of transversal anticlinal ridges in the northern border of the Central High Atlas (CHA). The results are interpreted in terms of paleogeometry of the main structures. The High Atlas fold-and-thrust belt is the result of intracontinental basin inversion during the Cenozoic convergence between the African and European plates. The studied ridges separate the three main synclines of the northern border of the CHA, namely Ait Attab, Ouaouizaght and Taguelft. Samples have been collected along the Tansrift ridge separating the Taguelft and Ouaouizaght synclines and to the west, Ouaouizaght syncline from the Ait Attab syncline. Paleomagnetic data reveal the presence of a magnetization component, stable in different lithologies in the ridges. This magnetization is carried by hematite, as evidenced by rock magnetism experiments on

representative samples and by the results of thermal demagnetization of the studied samples, showing a maximum unblocking temperature around 680 °C. The paleomagnetic stable component observed in different specimens shows a systematic normal polarity. This component corresponds to the generalized widespread remagnetization known in the CHA, dated at 100 Ma. Directional analysis shows that this remagnetization is syntectonic (inter-folding), indicating that the studied anticlinal ridges were partially uplifted before 100 Ma, predating basin inversion during the Cenozoic convergence. Synsedimentary structures studied at the borders of these three synclines prove synsedimentary uplifting. These results allow to consider these three synclines as confined mini-basins separated by diapiric ridges at least since Bathonian time.

Keywords

Paleomagnetism • Syntectonic remagnetization • Synsedimentary structures • Anticlinal ridges • Mini-basins • Central high atlas • Morocco

B. Moussaid (✉)

Bio-Geosciences and Materials Engineering Laboratory, Ecole Normale Supérieure, Hassan II University of Casablanca, 50069 Casablanca, Morocco
e-mail: bnmous@hotmail.fr

A. Casas-Sainz · B. Oliva · T. Roman-Berdiel
Geotransfer, Instituto de Investigación en Ciencias Ambientales (UCA), Universidad de Zaragoza, Zaragoza, Spain

J. J. Villalaín
Laboratorio de Paleomagnetismo, Departamento de Física, Universidad de Burgos, Burgos, Spain

H. E. Ouardi · N. Bouya · H. E. Makrini
Département de Géologie, Faculté Des Sciences de Meknès, Université Moulay Ismail, Meknes, Maroc

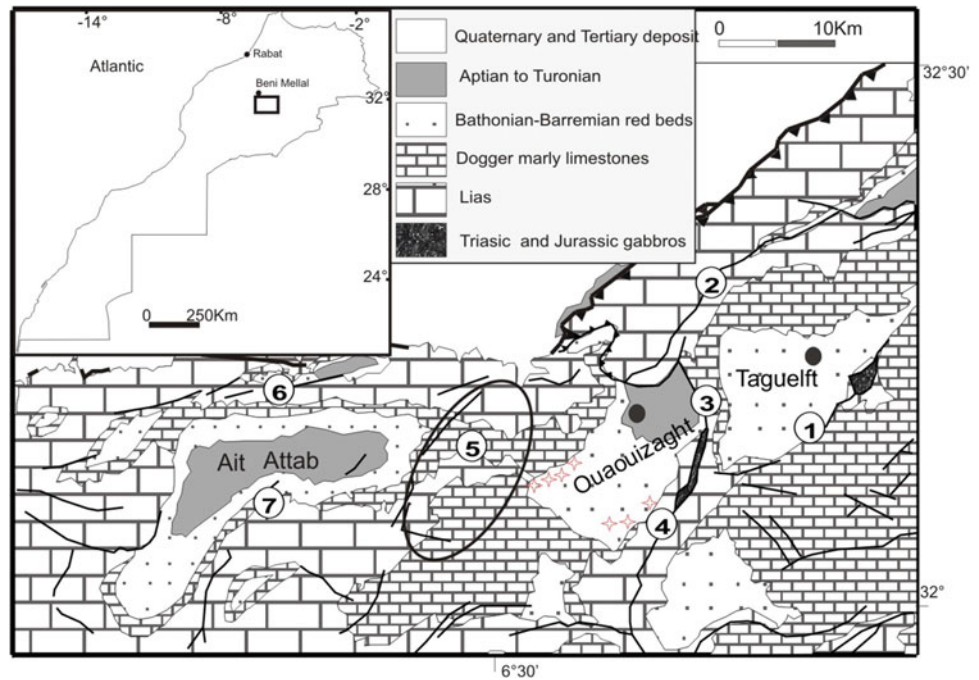
S. Torres-López
Departamento de Geología y Geoquímica, Universidad Autónoma de Madrid, Madrid, Spain

R. Soto
Instituto Geológico y Minero de España, Universidad de Zaragoza, Zaragoza, Spain

1 Introduction

In this work, we present the results of a paleomagnetic study in sedimentary rocks of the northern border of the Central High Atlas and their confrontation with field data in order to reconstruct the paleostructures inherited from the basinal stage. The northern boundary of the Central High Atlas is part of an intracontinental chain (Mattaouer et al., 1977; Michard, 1975), interpreted as a result of abortion of an intracontinental rift (Ibouh, 2004; Laville, 1985). Basin inversion took place during the Alpine Orogeny, Cenozoic to the present day for some authors (e.g. Frizon de Lamotte et al., 2000; Teixell et al., 2003; Arboleya et al., 2004) and for others (Ambroggi, 1963; Ibouh et al., 1994; Laville &

Fig. 1 Géological map of the studied area. (1, 2, 3, 4, 5, 7) ridges and mini-basins boundaries evidenced by paleomagnetism (Moussaid et al., 2015; Moussaid et al., in press, and this work for 4 and 5 ridges) and geological data and (6) mini-basin boundary evidenced by syndimentary structures. The empty stars indicate the locations of the sampling sites used in this work. Excerpt from geological map of Beni Mellal 1/100,000 (Monbaron, 1985)



Piqué, 1992; Souhel, 1996) it's began since Late Jurassic to Early Cretaceous times. The northern border of the Central High Atlas is characterized by synclines, mainly trending NE-SW, where Cretaceous units are well preserved. Our study is dealing with the Ait Attab, Ouaouizaght and Taguelft synclines. In the Ouaouizaght area, the main Cretaceous red bed sequence thins or disappears near the Jbel Abbadine anticline ridge. This progressive decrease in thickness and other indicators were interpreted as geological arguments of syndimentary uplift of anticline ridges during the sedimentation stage (Laville, 1985; Laville et Piqué, 1992, Ibouh, 2004; Michard et al., 2011). In this work, we use the remagnetization vectors of Cenomanian age obtained in Jurassic limestones and Lower Cretaceous red beds (Moussaid et al., 2015; Moussaid et al., in press) to reconstruct the paleogeometry of the studied area at the moment of the remagnetization event. The paleomagnetic results reveal a remagnetization carried especially by hematite in red beds. The use of these paleomagnetic data leads to evidence that at least the anticline ridges of the basin borders were partially folded and uplifted before the remagnetization stage, thus defining an Early Cretaceous age for the deformation of the present-day basin borders (Fig. 1).

2 Sampling and Methodology

In the three synclines of the northern boundary of the High Atlas, 87 paleomagnetic sites were taken in order to cover the whole accessible area and the stratigraphic series from the Bajocian to the Albo-Cenomanian. The collection of

samples in the field was performed using a portable electric drill machine powered by a gasoline generator or batteries in the case of sampling clays. An average of 10 samples was taken in red beds and marly limestones. Seven to eight specimens per site were subjected of thermal demagnetization. The measurement of NRM was done using a 2G755 cryogenic magnetometer and thermal demagnetization with a TD48-SC thermal demagnetizer. The low magnetic field susceptibility during demagnetization process was measured using a KLY4S (AGICO) Kappabridge after each demagnetization step, in order to supervise the mineralogical changes when heating. Several rock magnetism experiments as IRM acquisition, three orthogonal axes IRM thermal demagnetization were done following Lowrie method (Lowrie, 1990) on a Pulse Magnetizer and 2G755 Cryogenic Magnetometer. All measurements and analyses were performed in the Paleomagnetic laboratory of Burgos University, Spain.

3 Results

In this work, we will present only the result of seven sites from the Ouaouizaght syncline. All selected sites were collected in red bed. The studied samples reveal a simple behaviour, with Zijderveld diagrams showing a characteristic component with unblocking temperatures between 300 and 660 to 680 °C (Fig. 2a). The NRM intensities decrease strongly around 630 °C to 660 °C. A few specimens show another component with reverse polarities isolated above 640–680 °C.

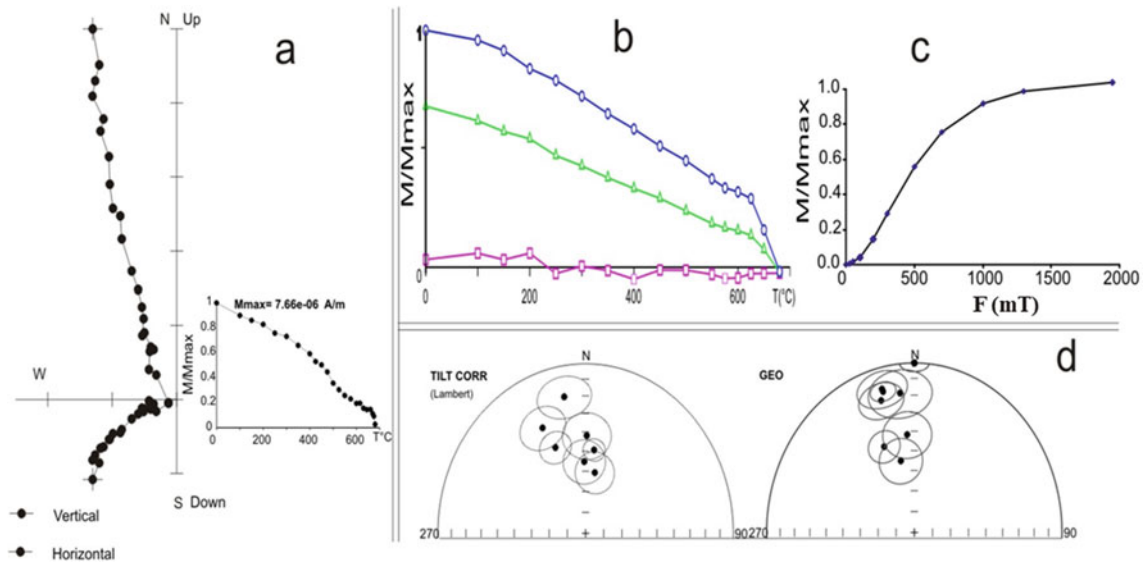


Fig. 2 **a** Representative Zijderveld diagram of thermal demagnetization and magnetization versus Temperature evolution. **b** Thermal demagnetization of IRM 3D. **c** IRM acquisition diagram. **d** Stereoplot of site-mean paleomagnetic direction before and after bedding correction

The results of magnetic mineralogy experiments reveal the dominance of high coercivity phases as carriers of remagnetization. Hematite is the dominant phase as evidenced by no saturation of IRM curves at 1 T and the sharp drop of the hard phase (2 T) in the 3D IRM demagnetization spectrum around 680 °C, which coincides with the Curie temperature of the hematite (Fig. 2b, c).

4 Discussion

The paleomagnetic directions of the characteristic component display normal polarities in all measured specimens. Since the analysed sequence covers magnetozones with normal and reverse polarities, this result indicates that the magnetization obtained from the Jurassic to Lower Cretaceous rocks of the Ouauizaght syncline is probably the main remagnetization found in other sectors of the High Atlas (Torres-López et al., 2014; Moussaid et al., 2015; Moussaid et al., in press) and dated in the Early Cenomanian, according to the Global Apparent Polar Wander Path (GAPWP, Torsvik et al., 2012). The mean paleomagnetic directions of sites are dispersed before and after bedding corrections (Fig. 2d).

Although further work is necessary to account for the details of syn-folding remagnetization in the lower studied sequence, from these results it can be stated that the Jurassic to infra-Aptian studied series record a portion of tilting before the age of remagnetization. The studied sites of these series were taken in the Ouauizaght basin boundaries formed by very narrow and tight anticlines. The Jurassic-Early Cretaceous uplift of these structures was encountered by geological evidence in the axial zone of the High Atlasic belt (e.g.

Laville et al., 2004). The paleomagnetic results found in this work confirm this assumption and imply the pre-Albian folding of series near the basin boundaries, what can explain the disappearance of Upper Jurassic series in the southern boundary of the Ouauizaght basin. The uplift of the anticline ridges was related to the diapiric activity of the Triassic series occurred since the Early Jurassic times (Saura et al., 2013), favoured by the gabbroic intrusions intruded in the ridge's cores (Schaer and Persoz, 1976; Laville, 1985) and the differential subsidence between different area of mini-basins. To the east, in the Taguelft syncline, paleomagnetic data reveal the pre-Albian tilting of the Jurassic series in the basin borders and in some localities in the whole area (Moussaid et al., in press). To the west, the remagnetization dated at 100 Ma in the Ait Attab syncline was considered in the almost sites as post-folding. However, in some sites collected near to the boundary faults (example of Ait Sri Fault, Moussaid et al., 2015), the results indicate that synsedimentary folds pre-date the remagnetization. Far from the core of the syncline, where remagnetization is pre-folding, field data show geological evidence of the diapiric activity and uplift of the margin of the Ait Attab syncline. According to this, we can consider the grouping of mean directions in the Ait Attab syncline as linked to the geological position, because almost all site were collected in the central area of the syncline, where tilting is mostly linked to Cenozoic inversion. To the east, the Tansrift ridge separating the Ouauizaght and Taguelft synclines reveals paleomagnetic and geological markers of uplift in pre-remagnetization times.

As a result of the observations stated above, the three synclines of the northern part of the Central High Atlas were bordered by synsedimentary diapiric / extensional ridges to

south and north. These structures were also separated by transverse N–S or NNE–SSW ridges. These ridges formed paleogeographic heights separating three confined areas at least since Bathonian times. The seven ridges and basin borders shown on the map (Fig. 1) pre-date the remagnetization. The neighbouring area shows important paleodips indicating pre-remagnetization tilting as evidenced by paleomagnetic studies (Moussaid et al., 2015 for ridge 7, Moussaid et al., in press for ridges 1, 3, 2; and this work for ridges 4, 5 and 6).

5 Conclusions

Paleomagnetic and field data in the Jurassic series of three synclines of the northern border of the Central High Atlas were used in order to reconstruct the paleogeometry of this area at the moment of remagnetization acquisition. Collected samples of red beds, at the borders of Taguelft and Ouauizaght synclines, show a stable component of high temperature, similar to the one obtained in the same lithologies in other sectors of the Central High Atlas. Remagnetization in red beds is carried by hematite and shows systematic normal polarities. This component is syn-folding and evidences an uplifting of basin borders before its acquisition (100 Ma). The others ridges (basin borders), not sampled, show synsedimentary evidences of this basinal uplifting of basin borders. Both, paleomagnetic data and synsedimentary structures, attest that the three studied synclines were separated by transverse synsedimentary ridges and to the south, from others depocentres, by NE–SW trending ridges. All in all, the northern border of the Central High Atlas, which displays features as a Jurassic continuous trough, was divided before 100 Ma, into three separated mini-basins bordered by ridges. The uplifting of ridges can be explained as related to diapiric activity and the differential subsidence under an extensional regime.

References

- Ambroggi, R. (1963). Etude géologique du versant méridional du Haut Atlas occidental et de la plaine du Souss. *Notes & Mém. Serv. Géol. Maroc*, 157, 322.
- Arboleya, M. L., Teixell, A., Charroud, M., & Julivert, M. (2004). A structural transect through the high and middle Atlas of Morocco. *Journal of African Earth Sciences*, 39, 319–327.
- Frizon de Lamotte, D., Saint Bézar, B., Bracène, R., & Mercier, E. (2000) The two main steps of the Atlas building and geodynamics of the western Mediterranean. *Tectonics*, 19, 740–761.
- Ibouh, H. (2004). *Du rift avorté au bassin sur décrochement, contrôles tectonique et sédimentaire pendant le Jurassique (Haut-Atlas central, Maroc)* (p. 224). Université Cadi Ayyad, Marrakech.
- Ibouh, H., Bouabdelli, M., & Zargouni, F. (1994). Indices de tectonique synsédimentaire dans les dépôts aaléno-bajocien de la région d 'Imilchil (Haut Atlas Central, Maroc). *Miscellanea Servo Geol. Naz. Roma*, 5, 305–310.
- Laville, E. (1985). Evolution sédimentaire, tectonique et magmatique du Bassin jurassique du Haut Atlas (Maroc): modèle en relais multiples de décrochements, Unpubl. Thesis Univ. Sci. Techn. Languedoc Montpellier (Vol. 166).
- Laville, E., & Piqué, A. (1992). Jurassic penetrative deformation and Cenozoic uplift in the Central High Atlas (Morocco): A tectonic model. Structural and orogenic inversions. *Geol. Rundsch.* 81, 157e170. <https://doi.org/10.1007/BF01764546>
- Laville, E., Piqué, A., Amrhar, M., & Charroud, M. (2004). A restatement of the Mesozoic atlasic rifting (Morocco). *Journal of African Earth Sciences*, 38, 145e153. <https://doi.org/10.1016/j.jafrearsci.2003.12.003>
- Lowrie, W. (1990). Identification of ferromagnetic minerals in a rock by coercivity and unblocking temperature properties. *Geophysical Research Letters*, 17, 159–162.
- Mattauer, M., Tapponier, P., & Proust, F. (1977). Sur les mécanismes de formation des chaînes intracontinentales. L'exemple des chaînes atlasiques du Maroc. *Bull. Soc. géol. Fr.*, 19(7), 521–526.
- Michard, A., Ibouh, H., & Charriere, A. (2011). Syncline-topped anticlinal ridges from the high Atlas: A Moroccan conundrum, and inspiring structures from the Syrian arc, Israel. *Terra Nov.*, 23, 314e323. <https://doi.org/10.1111/j.1365-3121.2011.01016.x>
- Monbaron, M. (1985). Carte géologique au 1/100 000 de Beni Mellal. Notes et Mém. Serv. Géol. Maroc, No. 341.
- Moussaid, B., Villalain, J. J., Casas-Sainz, A., El Ouardi, H., Oliva-Urcia, B., Soto, R., Roman-Berdiel, T., & Torres-López, S. (2015). Primary vs. secondary curved fold axes: Deciphering the origin of the Aït Attab syncline (Moroccan High Atlas) using paleomagnetic data. *Journal of Structural Geology*, 70, 65e77. <https://doi.org/10.1016/j.jsg.2014.11.004>
- Saura, E., Vergés, J., Martin-Martin, J. D., Messenger, G., Moragas, M., Razin, P., Grélaud, C., Joussiaume, R., Malaval, M., Homke, S., & Hunt, D. (2013). Syn- to post-rift diapirism and minibasins of the Central High Atlas (Morocco): The changing face of a mountain belt. *Journal of the Geological Society London*, 171, 97–105.
- Souhel, A. (1996). *Le Mésozoïque dans le Haut-Atlas de Beni-Mellal (Maroc): Stratigraphie, sédimentologie et évolution géodynamique*. Université Paul Sabatier, Toulouse.
- Teixell, A., Arboleya, M.-L., Charroud, M., & Julivert, M. (2003). Tectonic shortening and topography in the central High Atlas (Morocco). *Tectonics*, 22(5), 1051.
- Torres-López, S., Villalain, J. J., Casas, A. M., EL Ouardi, H., Moussaid, B., Ruiz-Martínez, V. C. (2014). Widespread Cretaceous secondary magnetization in the High Atlas (Morocco). A common origin for the Cretaceous remagnetizations in the western Tethys? *Journal of Geological Society London*, 171, 673e687. <https://doi.org/10.1144/jgs2013-107>
- Torsvik, T. H., Van der Voo, R., Preden, U., Mc Niocaill, C., Steinberger, B., Doubrovine, P. V., Van Hinsbergen, D., Domeier, M., Gaina, C., Tohver, E., Meert, J. G., McCausland, P. J. A., & Cocks, L. R. M. (2012). Phanerozoic polar wander, palaeogeography and dynamics. *Earth-Science Reviews*, 114, 325–368.



Evidence of Brittle Tectonic Continuity Between Precambrian Basement of Air and Its Sedimentary Cover (Northeast Niger)

Souley Baraou Idi, Abdoulwahid Sani, and Moussa Konaté

Abstract

Air Precambrian basement (NE Niger) is unconformably overlain by deposits of the Tim Mersoi basin at West and of the Tenere basin at Southeast. The present work addresses the structural relationship between the basement and the overlying sedimentary cover. A methodological approach combining geophysical data (magnetic and seismic) interpretation and fieldwork was implemented. The field observation carried out along the major unconformity between the Tim Mersoi basin and Air basement revealed a fault and fracture system mostly oriented N135° to N180° (NNW-SSE) affecting similarly the sandstone formations called “Agadez sandstones” and its underlying basement formations. Structural interpretation of magnetic and seismic maps highlighted two regional lineament systems: the NNW-SSE seismic lineament affecting both the Air basement and Tenere basin in the East (Termit basin) and the magnetic one corresponds to the regional N-S In-Azaoua-Arlit fault system prolonged in the Tim Mersoi basin in the west. Interpretation of seismic section across the petroleum system of Termit basin showed that the same NNW-SSE fault system revealed by the fieldwork and seismic map affects similarly the sedimentary cover and the underlying basement. The combined analysis of obtained data reveals a continuum of brittle tectonic between Air basement and Tim Mersoi basin in the west and Tenere basin in the east. In the Tim Mersoi basin, this brittle tectonic would control the setup of the uranium mineralization in Arlit region, and in Tenere basin it constitutes a NNW-SSE petroleum system of Termit basin. This regional brittle deformation, deriving

from the reactivation of sub-meridian Raghane shear zone (8° 30') which was considered as a late to post Pan-African tectonic lineament.

Keywords

Brittle tectonic • Air basement • Tim Mersoi Basin • Tenere basin • Northeastern Niger

1 Introduction

The study area corresponds to the southern part of Precambrian basement of Air and the overlying sedimentary cover, Tim Mersoi basin in West and Tenere basin in East (Fig. 1). The basement outcrops are represented by the metamorphic (schists gneiss) and magmatic (granites, basalts, gabbros) rocks. The sedimentary cover exhibits a succession from Devonian to Lower Cretaceous as revealed by the previous geological data (Clermonté et al., 1991). These lithounits are separated by a major unconformity and all affected by a brittle deformations in the shape of regional faults and or fractures (Fig. 1b). Previous structural data limited to aeromagnetic (PRDSM, 2005) and seismic (Wahab, 2017) cartography. They revealed regional lineaments cutting Precambrian basement as well as its sedimentary cover but not supported by field data. This study focuses on the structural relationship between the basement and the overlying sedimentary cover. A methodological approach integrating structural interpretation of magnetic and seismic data and field study was implemented.

2 Materials and Methods

To highlight the brittle tectonic continuity between the different lithounits, this study integrated (i) the interpretation of geophysical data derived from previous papers (PRDSM,

S. B. Idi (✉) · A. Sani

Faculty of Sciences and Technology, University of Agadez, Niger,
P.O. Box 199 Agadez, Niger
e-mail: univ.agadez@gmail.com

M. Konaté

Faculty of Sciences and Technology, Abdou Moumouni
University of Niamey, Niger, BP 13619, Niamey, Niger

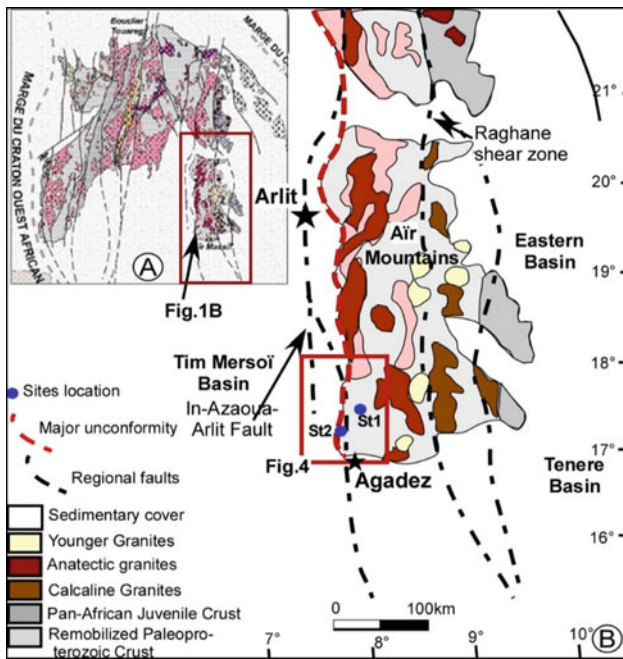


Fig. 1 Lineaments map from interpretation of aeromagnetic data showing the N-S fault systems of Air Precambrian basement (PRDSM, 2005)

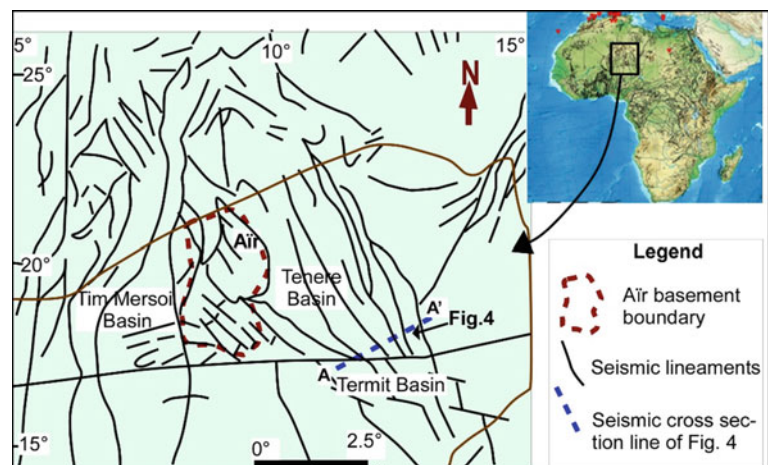
2005); (Wahab, 2017) and (ii) the original data of the present study derived from fieldwork. The interpretation of geophysical data consists of lineaments extraction from aeromagnetic and seismic maps. The field study involves in situ identification and structural measurement of fracture planes. The obtained data were processed by using the ArcGIS 10.1 and Drawing Software Canvas 11.

3 Results and Discussion

3.1 Interpretation of Magnetic Data

The interpretation of extracted lineaments from aeromagnetic map obtained by PRDSM (2005) highlighted two N-S

Fig. 2 Structural map from interpretation of seismic data (Wahab, 2017)



regional lineament systems: the In-Azaoua-Arlit fault system prolonged in the Tim Mersoï basin in West and Raghane fault system affecting similarly the Precambrian Air basement and Tenere basin in East (Fig. 1b). These two fault systems, described in Air Mountains and its sedimentary cover were the focus of three seismic events (4 July 1969, in 19 May 1967, and 18 January 2017, (Wahab, 2017; Baraou et al., 2022). According to geological data obtained in Hoggar (2017), these regional fault systems derive from the reactivation of three major sub-meridian shear zones in Hoggar: East Ouzzal shear zone, Tekouyat shear zone, and Raghane shear zone.

3.2 Interpretation of Seismic Data

Structural interpretation of seismic map (Wahab, 2017) highlighted two regional lineament systems: the NNW-SSE seismic lineament affecting both the Air basement and Tenere basin in East and N-S fault system prolonged in the Tim Mersoï basin in West (Fig. 2). The structural analysis of seismic section (Fig. 3) from the petroleum system of Tenere basin (Bang et al., 2015) showed that the same NNW-SSE fault system revealed by the fieldwork (Fig. 4) and seismic map (Fig. 2) affects similarly the sedimentary cover and the underlying basement. The combined analysis of obtained data reveals a continuum of brittle tectonic between Air basement and Tim Mersoï basin in West and Tenere basin in East. In the Tim Mersoï basin, this brittle tectonic would control the setup of the uranium mineralization in Arlit region (Wagani et al., 2019), and in Tenere basin it constitutes a NNW-SSE petroleum system of Termit basin (Bang et al., 2015).

3.3 Structural Analysis of Field Data

The field observation was carried out along the major unconformity between Air basement and overlying

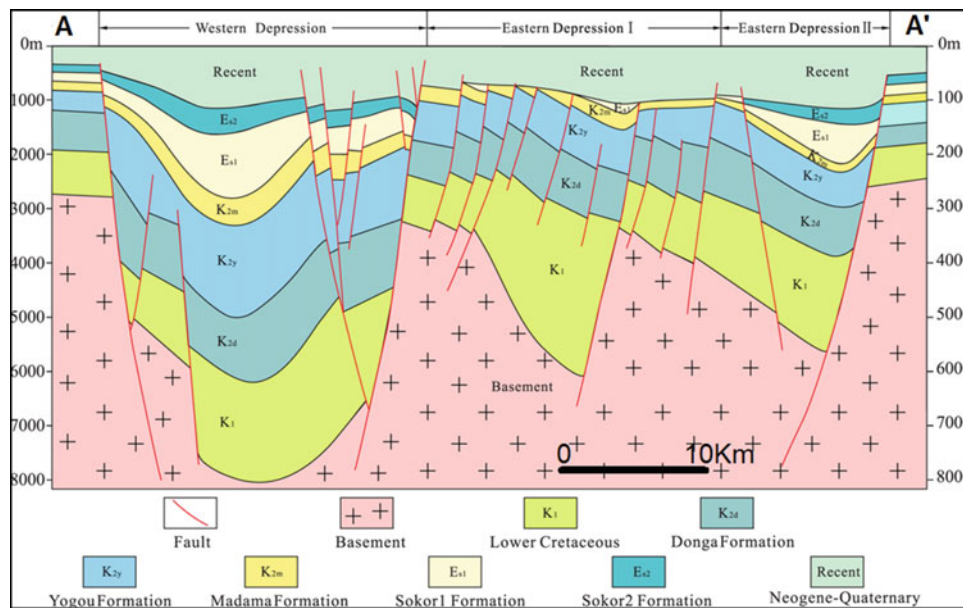


Fig. 3 Cross section of Tenere basin from interpretation of seismic data (Bang et al., 2015)

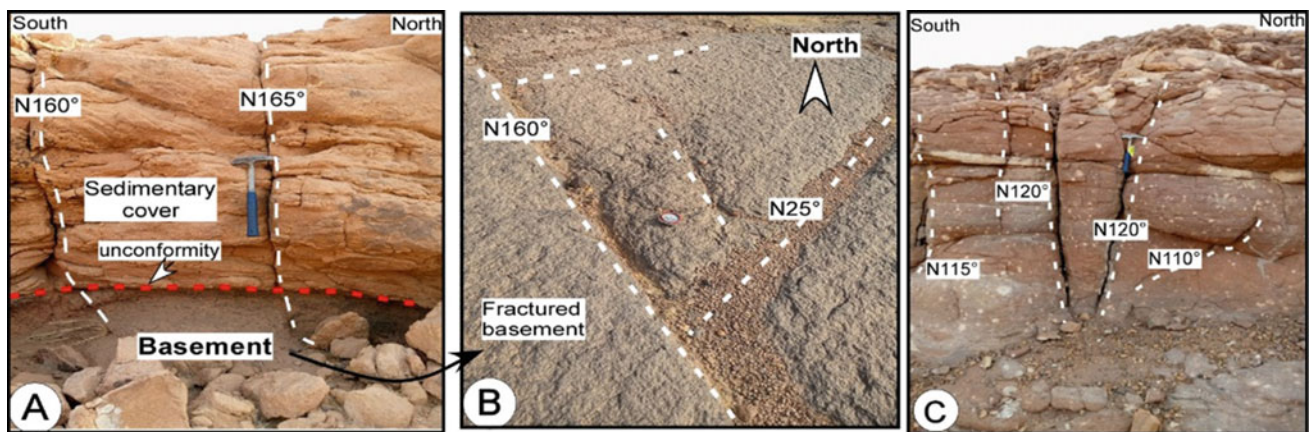


Fig. 4 In situ photographs from field study. **a** major unconformity between Air basement and overlying sedimentary cover and associated fractures, **b** fractured basement, **c** fractured sandstone

Table 1 Microtectonic data of fractures planes from site 1

Site (St1)	E 7.94894°		N 17.05633°		
Direction	Dip	Dip sector	Direction	Dip	Dip sector
N120°	85°	SW	N140°	85	SW
N150°	75	NE	N35°	90	V
N80°	90	V	N85°	90	V
N150°	90	V	N160°	90	V
N90°	80	S	N180°	70	E
N50°	70	SE	N40°	70	SE
N70°	90	V	N85°	90	V
N135°	80	SW	N100°	50	SSW

Note S: South, N: North, W: West, E: East, V: Vertical

Table 2 Microtectonic data from site 2

Site (St2)	E7.93205°		N17.03608°		
Direction	Dip	Dip sector	Direction	Dip	Dip sector
N25°	70	NWW	N 80°	80	SWW
N165°	85	NEE	N145°	70	SW
N160°	80	NEE	N140°	80	NE
N10°	90	V	N65°	75	SE
N140°	80	SE	N65°	90	V
N15°	60	NWW	N170°	90	V
N160°	90	V	N10°	90	V
N25°	90	V	N115°	90	V
N110°	45	SW	N30°	85	SEE

Note S: South, N: North, W: West, E: East, V: Vertical

sedimentary cover. In the investigated zone, the structures of brittle tectonic are represented by fractures. Figure 4 represents images from outcrops showing fractures system. The microtectonic data are presented in Tables 1 and 2. The structural analysis of obtained data showed a fracture system mostly oriented N165° to N110°, affecting both the sandstone formations called “Agadez sandstones” and its underlying basement formations (Fig. 4).

4 Conclusions

This study focused on structural relationship between Precambrian basement of Air and its sedimentary cover. The obtained results shown how seismic, aeromagnetic, and fieldwork contributed to provide the evidence of brittle tectonic continuity between Precambrian basement and its sedimentary cover. This study helps to better understand the geodynamic context leading to uranium deposits in Tim Mersoï basin and formation of petroleum system of Tenere basin.

References

- Aissa, D. E., & Christian, M. (2017). Controls on gold deposits in Hoggar, Tuareg Shield (Southern Algeria). *Journal of African Earth Sciences*, 127, 136–145.
- Bang, L., Guangya, Z., Fengjun, M., Jiguo, L., Dingsheng, C., & Mingsheng, L. (2015). The petroleum system of the Tenere Basin: Oil geochemistry from the SH-1 wildcat well in eastern Niger. *Petroleum Geoscience*. <https://doi.org/10.1144/petgeo2015-067>
- Baraou, I. S., Abdoulwahid, S., Abdoul, W. D. M., & Moussa, K. (2022). Geotechnical risk assessment and geological origin of building fracturation in Agadez city (North Niger). *Journal of Environmental & Earth Sciences*, 4(2) (2022). <https://doi.org/10.30564/jees.v4i2.4697>
- Clermonté, J., Moussa, Y., & Lang, J. (1991). Paleozoic and Mesozoic basin in a strike-slip zone: the Tim Mersoï in the Arlit Region, in the western l’Air. Meeting report of Sciences academy. *Paris*, 312, II. 1189–1195 (Origin language: French).
- PRDSM. (2005). *Geophysic interpretation map of Air Mountains* (p. 55). Ministry of Mines and Industrial development, Ministry of Mines and Industries, Niger (Origin language: French).
- Wagani, I., Maman, S. B., & Alhassane, I. (2019). Structural study of Akola uranium ore deposit and geotechnical risk related to the extracting method in the Cominak, Niger. *Rev. Ivoir. Sci. Technol.* 34, 230–246 (Origin language: French).
- Wahab, D. M. A. (2017). *Location map of seismic focus on the African continent*, OTICE Department, HANEA, Niger (Origin language: French).



Tectonics and Geodynamics of a Narrow Continental Rift: Barmer Basin, Rajasthan, India

Swagato Dasgupta, Soumyajit Mukherjee, and Rima Chatterjee

Abstract

The Barmer petroliferous basin in W Rajasthan (India) is ~ 50 km wide and ~ 200 km long trending NNW. The Barmer basin experienced a two-phase (NW–SE followed by NE–SW) extension during Early Cretaceous and Late Cretaceous–Paleocene times. It consists of fluvial to shallow marine sediments deposited between Jurassic to Miocene, with some distinct hiatus in between. Late Proterozoic Malani igneous suite/Malani rhyolite is the basement rock. The western margin rift shoulder consists of Malani basement isostatic flexural uplifts, while the eastern margin comprises thick sedimentary cover and is fault-bound. The objective is to understand the rift kinematics, structural inheritance and the type of deformation from field based studies. We carried out structural field studies along the rift margins that helped in deciphering the two-phase (NW–SE followed by NE–SW) extension through brittle shear tectonics. Cross-cutting relation among the NW and NE fault planes connotes the relative timing of the two extension phases. Other key observations from field studies are (1) presence of mega-scale transfer zones along the N margin of the basin, (2) NW trending rift faults inherited the pre-existing structures, (3) variation in strike and cross-cutting nature of fault planes in eastern and western rift margins. Paleostress analysis further interprets the stress regime and relative timing of the tectonic events. Thus, the analysis helps in deciphering the rift evolution and the type of extensions related to tectonic inheritance.

Keywords

Rift basin • Brittle shear • Tectonics • Structural inheritance • Paleostress

1 Introduction

The Barmer rift basin is a major hydrocarbon producing basin in Rajasthan, western India. Three sedimentary basins—Jaisalmer, Barmer and Bikaner-Nagaur—crop out in western Rajasthan (Biswas et al., 2022; Bladon et al., 2015; Dasgupta & Mukherjee, 2017), India. The former two basins consist of thick Mesozoic and Tertiary sediments. The Barmer failed narrow-rift basin is ~ 200 km long along the NNW and is ~ 50 km wide (Bladon et al., 2015; Dasgupta & Mukherjee, 2017). It is separated from the Jaisalmer basin at north by the NE trending Devikot-Fatehgarh structural high.

The entire area of western Rajasthan is covered by the Thar Desert with few outcrops. Google Earth Pro satellite images were used to identify the exposures in and around the Barmer basin (Dasgupta & Mukherjee, 2017, 2019). The field-based structural study was done along the Barmer rift margins (see Fig. 1, L1–L7) to understand: (1) fracture trends and type of movements, (2) the effect of structural inheritance and (3) relative timing of the rifting events from paleostress analyses.

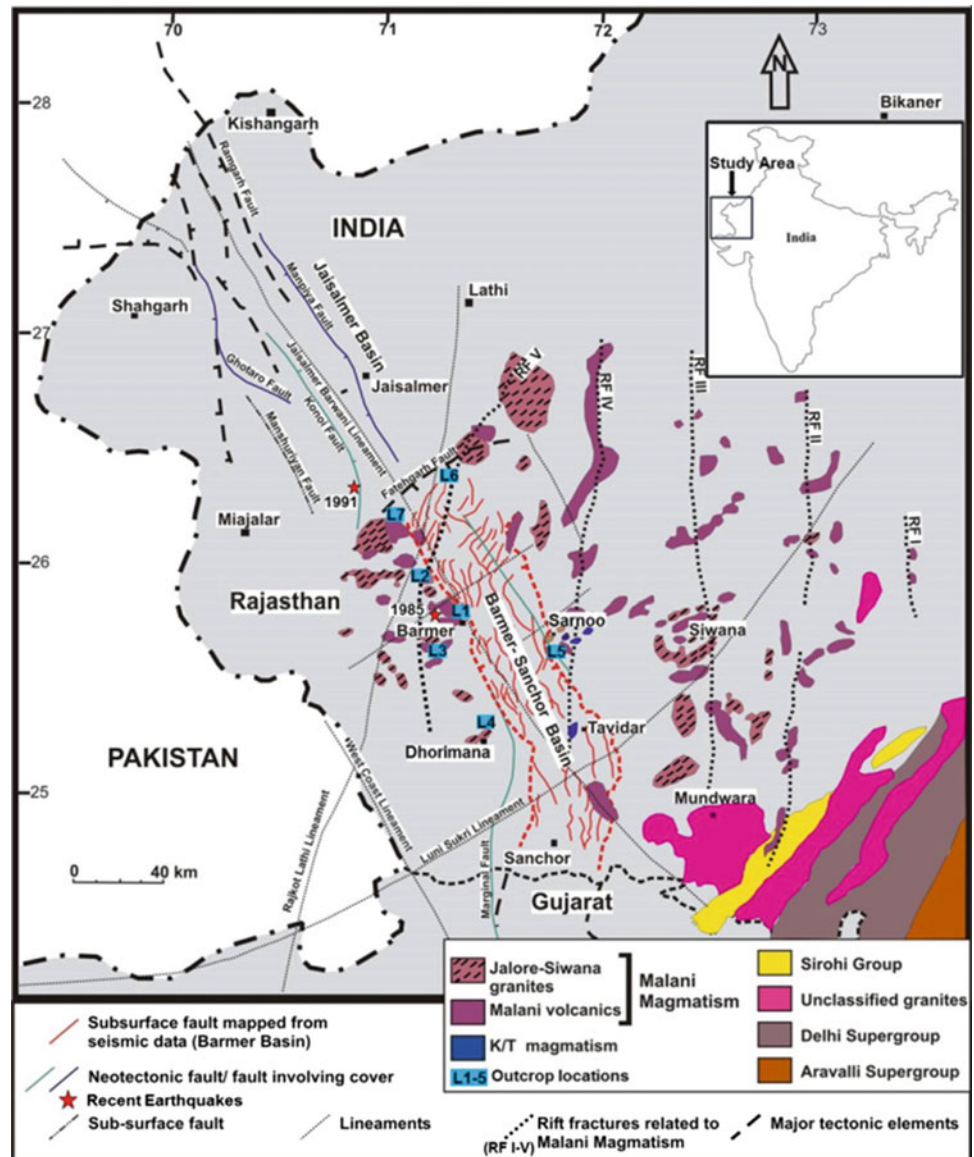
2 Tectonic and Geological Settings

The Barmer intracontinental rift basin developed over Late Proterozoic basement rock—Malani igneous suite/rhyolites (MIS) (Biswas et al., 2022; Dasgupta & Mukherjee, 2017). The basin experienced two distinct phases of extension, i.e. NW–SE followed by NE–SW (Bladon et al., 2015; Dasgupta & Mukherjee, 2017).

S. Dasgupta (✉) · R. Chatterjee
Department of Applied Geophysics, Indian Institute of Technology (ISM) Dhanbad, Jharkhand, 826004, India
e-mail: swagato.dasgupta38@gmail.com

S. Mukherjee
Department of Earth Sciences, Indian Institute of Technology Bombay, Powai, Mumbai, Maharashtra 400076, India

Fig. 1 Tectonic map of western Rajasthan showing Barmer basin with different fault trends and field outcrop locations (L1–L7)



The rift geometry is deciphered from the Bouguer gravity anomaly and seismic (2D and 3D) data-driven maps (Bladon et al., 2015; Dasgupta & Mukherjee, 2017). The basin deepens towards S and SE. The sedimentation in the Barmer rift was discontinuous resulting in distinct hiatuses during Mid-Late Jurassic to Early Cretaceous, in Late Cretaceous, and in Late Tertiary time (Dasgupta & Mukherjee, 2017). Sediments linked to a first phase of rifting of Aptian–Albian age are exposed near Sarnoo in eastern rift shoulder. The Paleocene-Eocene deposits, linked to a second phase of rifting, are the major hydrocarbon producing reservoirs of the basin (Bladon et al., 2015). Pre-cursor of Deccan volcanism is documented at places in the eastern margin (Dasgupta & Mukherjee, 2017). The MIS is exposed along the western basin margin in and around Barmer, towards south near Dhorimana.

3 Results and Deductions

Numerous ~ NW, ~ NNW, ~ NE and ~ E trending brittle shear faults were identified from the structural field work (L1–L7 locations). We further identified: (1) ~ NE trending mega-scale transfer zones along the Fatehgarh fault trend, N margin of the basin, (2) crosscutting fault planes—in E and W margins: NE faults cut by NW faults and NE faults cut the ~ E trending faults, (3) The pre-existing fractures of MIS and cross faults of first phase of rifting govern the second and main ~ NW trending rift faults.

Around 500 fault slip data were collected from outcrops [L1–L5]. T-Tecto studio X5 and Win-Tensor (v.5.9.2) software (Delvaux & Sperner, 2003; Žalohar & Vrabec, 2007) were used for paleostress analyses which resulted in

Table 1 Paleostress analyses results as obtained from fault slip data

Area	No	Sense of Slip	Dominant Rock Type	No. of Fault Slip data	σ_1 (trend/plunge, in °)	σ_2 (trend/plunge, in °)	σ_3 (trend/plunge, in °)	Stress Ratio (unitless)		Stress Regime (unitless)	SHMax (T-Tecto, in °)
								D	R'		
W Margin— Barner	1	Normal	MIS	12	105/24	291/66	22/0	0.7	1.27	S1—Pure Strike Slip	105
W Margin— Barner	2	Reverse	MIS	9	110/0	200/85	32/5	0.2	1.5	S1—Strike Slip to Transpressive	113
W Margin— Dhorimana	7	Normal	MIS	19	82/35	273/55	172/8	0.2	1.45	S1—Pure Strike Slip	68
W Margin— Dhorimana	8	Normal (Dyke Parallel)	MIS	22	75/1	264/89	162/0	1	1.5	S1—Strike Slip to Transpressive	87
E Margin— Samoo	13	Normal	Sandstone	7	283/55	65/29	163/15	1	0.85	S1—Extensive to Transpressive	80
E Margin— Samoo	14	Normal	Sandstone	6	96/17	303/71	180/11	0.5	1.7	S1—Pure Strike Slip	90
W Margin— Barner	3	Normal	MIS	8	353/84	229/3	138/4	0.5	0.5	S2—Pure Extensive	55
E Margin— Samoo	15	Normal	Sandstone	30	138/80	234/1	144/0	0.3	0.56	S2—Pure Extensive	63
E Margin— Samoo	16	Normal	Sandstone	22	160/61	255/2	346/29	0.2	0.62	S2—Pure Extensive	60
W Margin— Barner	4	Normal	MIS	6	27/28	210/62	113/3	0.5	1.34	S3—Pure Strike Slip	26
W Margin— Dhorimana	9	Normal	MIS	12	163/69	37/31	302/18	0.3	1.5	S3—Pure Strike Slip	15
E Margin— Samoo	17	Normal	Sandstone	12	60/46	168/16	271/39	0.7	0.86	S3—Extensive to Transpressive	0
E Margin— Samoo	18	Normal	Sandstone	7	239/70	9/13	102/13	0.5	0.63	S3—Extensive to Transpressive	15

(continued)

Table 1 (continued)

Area	No	Sense of Slip	Dominant Rock Type	No. of Fault Slip data	σ_1 (trend/plunge, in $^\circ$)	σ_2 (trend/plunge, in $^\circ$)	σ_3 (trend/plunge, in $^\circ$)	Stress Ratio (unitless)		SHMax (T-Tecto, in $^\circ$)
								D	R'	
W Margin—Barner	5	Normal	MIS	25	194/77	348/11	79/5	0.4	0.5	S4a—Pure Extensive 170
W Margin—Barner	6	Normal	MIS	10	132/44	277/40	24/20	0.4	0.82	S4a—Extensive to Transensive 113
W Margin—Dhorimana	10	Normal	MIS	10	117/40	347/37	230/31	0.4	0.85	S4a—Extensive to Transensive 136
E Margin—Samoo	19	Normal	Sandstone	26	32/61	136/8	230/27	0.2	0.66	S4a—Pure Extensive 160
E Margin—Samoo	20	Normal	Sandstone	14	267/77	153/5	62/12	0	0.64	S4a—Extensive 120
W Margin—Dhorimana	11	Normal	MIS	22	7/30	181/60	90/0	0.6	1.41	S4b—Pure Strike Slip 177
W Margin—Dhorimana	12	Reverse	MIS	7	303/11	193/60	39/27	0.4	2.11	S4b—Transpressive to Compressive 129
E Margin—Samoo	21	Normal	Sandstone	9	126/7	311/83	43/0	0.7	1.52	S4b—Strike Slip to Transensive 129
E Margin—Samoo	22	Reverse	Sandstone	6	172/0	262/39	99/49	0.1	2.3	S4b—Compressive to Transpressive 183

four stress regimes (S1–S4) based upon the stress ratio and maximum horizontal stress direction (SHMax). These stress regimes are as follows. S1—strike slip regime, initiation of oblique extension in Early Cretaceous (SHMax ~ E), S2—Extensional regime in Early Cretaceous resulting in the first phase of synrift deposition during Albian-Aptian (SHMax ~ NE), S3—strike slip to transtensive regime in Mid-Late Cretaceous (SHMax ~ N to NNE). S1–S3 are linked to Madagascar separation from West Indian plate. S4 stress regime is sub-divided into two parts, i.e. S4a—extensive to transtensive linked to 2nd and main rift phase of rifting (SHMax ~ SE), and S4b—strike slip transpressive to compressive regime likely linked to progressive phase of Barmer rifting in Early Tertiary (SHMax ~ SSE). Stress regime S4 is coeval with the Seychelles–India separation and northward drift of Indian plate (Dasgupta & Mukherjee, 2017) (Table 1).

4 Conclusion

We were able to establish the following: (1) relative timing of the faults from crosscutting nature identified in the field, (2) transfer zones in N margin identified from remote sensing and field observations, (3) four main paleostress regimes

obtained from the analyses, S1-S3 indicates stress rotation from ~ E to NNE during Cretaceous and (4) structural inheritance plays a key role in rift fault propagation.

References

- Biswas, M., Puniya, M.K., Gogoi, M.P., Dasgupta, S., Mukherjee, S., Kar, N. R. (2022). Morphotectonic analysis of petroliferous Barmer rift basin (Rajasthan, India). *Journal of Earth System Science*, 131, 1–31. <https://doi.org/10.1007/s12040-022-01871-8>
- Bladon, A. J., Clarke, S. M., & Burley, S. D. (2015). Complex rift geometries resulting from inheritance of pre-existing structures: Insights and regional implications from the Barmer Basin rift. *Journal of Structural Geology*, 71, 136–154.
- Dasgupta, S., & Mukherjee, S. (2017). Brittle shear tectonics in a narrow continental rift: Asymmetric non-volcanic Barmer basin (Rajasthan, India). *The Journal of Geology*, 125, 561–591.
- Dasgupta, S., Mukherjee, S. (2019). Remote sensing in lineament identification: Examples from Western India. In Andrea, B., & Åke, F. (Eds.), *Developments in structural geology and tectonics* (pp. 205–221). Elsevier. ISSN 2542-9000, ISBN 9780128140482.
- Delvaux, D., & Sperner, B. (2003). New aspects of tectonic stress inversion with reference to the TENSOR program. *Geological Society*, 212, 75–100.
- Žalohar, J., & Vrabec, M. (2007). Paleostress analysis of heterogeneous fault-slip data: The Gauss method. *Journal of Structural Geology*, 29, 1798–1810.



Successive Fracturing and Fluid Flow Events During Thrust Sheet Emplacement: The Montsec Thrust Sheet (Southern Pyrenees)

Daniel Muñoz-López, Wissam Aziz, David Cruset, Irene Cantarero, Vinyet Baqués, Ardiansyah Koeshidayatullah, and Anna Travé

Abstract

Field data together with petrographic and geochemical analyses ($\delta^{13}\text{C}$, $\delta^{18}\text{O}$) of vein cements and host rocks are used to reconstruct the fluid flow evolution in a well-exposed carbonate thrust zone, the Montsec thrust sheet, Southern Pyrenees. The Montsec thrust places Upper Cretaceous marine limestones over Paleocene non-marine carbonates and clays. Within this thrust zone, four fracture sets including bed-parallel and bed-perpendicular fractures (F1 and F2, respectively), bed-parallel slip surfaces (F3) and strike slip faults (F4) have been identified. These fractures have been filled with four generations of calcite cements (Cc1-Cc4). Consequently, stable isotope analyses applied to these cements indicate three different geochemical trends: (i) similar $\delta^{13}\text{C}$ values between all cements and their related host rocks (from 0 to + 2 ‰_{VDPDB}) that has been interpreted as buffering of the cement-forming fluids by the host carbonates; (ii) a progressive depletion in $\delta^{18}\text{O}$ values from Cc1 to Cc3 (from - 7 to - 12 ‰_{VDPDB}) that is either attributed to a change in the fluid origin, a dilution of the fluid composition and/or an increase in the fluid temperature and (iii) an enrichment in the $\delta^{18}\text{O}$ values from Cc3 to Cc4 (from - 12 to - 9 ‰_{VDPDB}), probably indicating the infiltration of a low-temperature, likely meteoric, fluid during thrust sheet exhumation and piggy-back transport of this thrust towards the south. The formation of

successive fracture/vein sets as well as the geochemical variation of the vein cements through time indicates changes in the fluid origin, pathways and the extent of fluid-rock interaction during the emplacement of the Montsec thrust. Therefore, this study highlights how the evolution of carbonate veins could inform the fluid flow events during the geodynamic evolution of fold-and-thrust belt systems.

Keywords

Fluid flow • Calcite veins • Geochemistry • Montsec thrust sheet • Southern Pyrenees

1 Introduction

Diagenetic products such as vein cements that develop during the evolution of a fault zone are important fingerprints of vein-forming fluids and can be used to unravel the timing, history and origin of fluids that migrate during deformation (Sun et al., 2022; Travé et al., 1997). Consequently, exhumed fault zones, and their related vein sets, represent important field analogues to examine the fluid flow and deformation relationships in the upper crust (Cruset et al., 2018; Roure et al., 2005). Understanding the interplay between fluid flow and deformation is key to constrain the controlling factors of fluid flow and fluid-rock interactions and to assess when fluid migration occurs and when fractures act as seals or pathways (Muñoz-López et al., 2020, 2022; Sun et al., 2021). This information has direct implications in economic-strategic fields mainly related to the exploration of alternative energy resources or the selection of potential storage sites (Ramirez-Perez et al., 2023). In this respect, using a combination of field data and petrographic-isotopic analyses of vein cements and host rocks, this study aims to reconstruct the fluid flow regimes during the evolution of the Montsec thrust sheet in the Southern Pyrenees.

W. Aziz · I. Cantarero · V. Baqués · A. Travé
Departament de Mineralogia, Petrologia i Geologia Aplicada,
Facultat de Ciències de La Terra, Universitat de Barcelona (UB),
c/Martí i Franquès s/n., 08028 Barcelona, Spain

D. Cruset
Group of Dynamics of the Lithosphere, Geosciences Barcelona
(GEO3BCN-CSIC), Lluís Solé I Sabaris s/n, 08028 Barcelona,
Spain

D. Muñoz-López (✉) · A. Koeshidayatullah
College of Petroleum Engineering and Geosciences, King Fahd
University of Petroleum and Minerals, Dhahran, Saudi Arabia
e-mail: j.munozlopez@kfupm.edu.sa

2 The Montsec Thrust Sheet: Fractures and Calcite Cements

The South Pyrenean fold-and-thrust belt comprises a piggy-back imbrication of south verging and East–West striking thrust sheets involving Mesozoic–Cenozoic cover rocks detached along Late Triassic evaporites (Choukroune, 1989; Roure et al., 1989). One of these major imbricated structures, the Montsec thrust sheet, was emplaced during the late Ypresian placing Upper Cretaceous marine limestones over Paleocene non-marine carbonates and clays (Vergés & Muñoz, 1990). Within this thrust zone, four fracture sets (F1 to F4) including bed-parallel and bed-perpendicular fractures (F1 and F2, respectively), bed-parallel slip surfaces (F3) and strike slip faults (F4) have been identified. Within these fracture sets, four different generations of calcite cements (Cc1–Cc4) were identified according to their petrographic and geochemical characteristics (Fig. 1). The stable isotope data of these cements reveal three different geochemical trends: (i) similar $\delta^{13}\text{C}$ values between all cements and their related host rocks (from 0 to +2 ‰_{VPDB}); (ii) a progressive depletion in $\delta^{18}\text{O}$ values from Cc1 to Cc3 (from –7 to –12 ‰_{VPDB}) and (iii) an enrichment in the $\delta^{18}\text{O}$ values from Cc3 to Cc4 (from –12 to –9 ‰_{VPDB}) (Fig. 1).

3 Discussion of Fluid Flow and Thrust Emplacement Relationships

The evolution of the fluid regimes in the Montsec thrust is revealed by the three geochemical trends of fracture-filling calcite cements. Accordingly, the similar $\delta^{13}\text{C}$ values between all cements and their related host rocks (Fig. 1) has

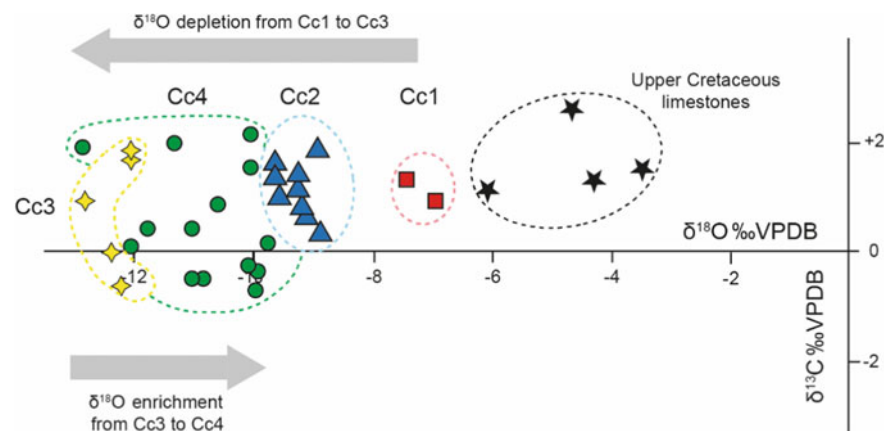
been interpreted as buffering of the cement-forming fluids by the host carbonates. Indeed, the progressive depletion in $\delta^{18}\text{O}$ values from Cc1 to Cc3 (from –7 to –12 ‰_{VPDB}) has been either attributed to a continuous change in the fluid origin, a dilution of the fluid composition and/or a progressive increase in the fluid temperature. Finally, the enrichment in the $\delta^{18}\text{O}$ values from Cc3 to Cc4 (from –12 to –9 ‰_{VPDB}) is interpreted to record the infiltration of a low-temperature, likely meteoric fluid during thrust sheet exhumation and piggy-back transport of this thrust towards the south during the emplacement of the Serres Marginals thrust imbrication.

In conclusion, we suggest that the formation of successive fracturing events and related calcite cementation phases indicate that fractures created new pathways for fluids but were rapidly occluded with calcite, indicating a transient permeability (Muñoz-López et al., 2020). Furthermore, the variation of the geochemistry of calcite cements in the Montsec thrust through time indicates changes in the fluid origin, pathways and the extent of fluid–rock interaction during the evolution of thrust sheet emplacement.

4 Conclusions

Four fracture-filling calcite cements were identified in the Montsec thrust. The geochemistry of these cements reveals (i) buffering of the vein-forming fluids by the host carbonates as suggested by their similar $\delta^{13}\text{C}$ values; (ii) a progressive change in the fluid origin, composition or temperature as revealed by their continuous depletion in $\delta^{18}\text{O}$ values from Cc1 to Cc3 and (iii) the infiltration of a later, likely meteoric, fluid during thrust sheet exhumation as indicated by enrichment in $\delta^{18}\text{O}$ values from Cc3 to Cc4.

Fig. 1 $\delta^{18}\text{O}$ versus $\delta^{13}\text{C}$ cross-plot of the calcite cements and carbonate host rocks studied in the Montsec thrust



Acknowledgements This is a contribution to the DGICYT Spanish Projects PID2021-122467NB-C22 and PGC2018-093903-B-C22 (MCIU/AEI/FEDER, UE) and the Grup Consolidat de Recerca “Geologia Sedimentària” (2021 SGR 00349).

References

- Choukroune, P. (1989). The Ecors Pyrenean deep seismic profile reflection data and the overall structure of an orogenic belt. *Tectonics*, 8, 23–39.
- Cruset, D., Cantarero, I., Vergés, J., John, C. M., Muñoz-López, D., & Travé, A. (2018). Changes in fluid regime in syn-orogenic sediments during the growth of the south Pyrenean fold and thrust belt. *Glob Planet Change*, 171, 207–224.
- Muñoz-López, D., Cruset, D., Cantarero, I., Benedicto, A., John, C. M., & Travé, A. (2020). Fluid dynamics in a thrust fault inferred from petrology and geochemistry of calcite veins: An example from the Southern Pyrenees. *Geofluids*, 2020, 1–25. <https://doi.org/10.1155/2020/8815729>
- Muñoz-López, D., Cruset, D., Vergés, J., Cantarero, I., Benedicto, A., Mangenot, X., Albert, R., Gerdes, A., Beranoaguirre, A., & Travé, A. (2022). Spatio-temporal variation of fluid flow behavior along a fold: The Bóixols-Sant Corneli anticline (Southern Pyrenees) from U-Pb dating and structural, petrographic and geochemical constraints. *Marine and Petroleum Geology*, 143, 105788. <https://doi.org/10.1016/j.marpetgeo.2022.105788>
- Ramirez-Perez, P., Cantarero, I., Cofrade, G., Muñoz-López, D., Cruset, D., Sizun, J.-P., & Travé, A. (2023). Petrological, petrophysical and petrothermal study of a folded sedimentary succession: The Oliana anticline (Southern Pyrenees), outcrop analogue of a geothermal reservoir. *Glob Planet Change*, 222, 104057. <https://doi.org/10.1016/j.gloplacha.2023.104057>
- Roure, F., Choukroune, P., Berastegui, X., Munoz, J. A., Villien, A., Matheron, P., Bareyt, M., Seguret, M., Camara, P., & Deramond, J. (1989). Ecors deep seismic data and balanced cross sections: Geometric constraints on the evolution of the Pyrenees. *Tectonics*, 8, 41–50. <https://doi.org/10.1029/TC008i001p00041>
- Roure, F., Swennen, R., Schneider, F., Faure, J. L., Ferket, H., Guilhaumou, N., Osadetz, K., Robion, P., & Vandeginste, V. (2005). Incidence and importance of tectonics and natural fluid migration on reservoir evolution in foreland fold-and-thrust belts. *Oil and Gas Science and Technology*, 60, 67–106.
- Sun, X., Gomez-Rivas, E., Alcalde, J., Martín-Martín, J. D., Ma, C., Muñoz-López, D., Cruset, D., Cantarero, I., Griera, A., & Travé, A. (2021). Fracture distribution in a folded fluvial succession: The Puig-reig anticline (south-eastern Pyrenees). *Marine and Petroleum Geology*, 132, 105169. <https://doi.org/10.1016/j.marpetgeo.2021.105169>
- Sun, X., Gomez-Rivas, E., Cruset, D., Alcalde, J., Muñoz-López, D., Cantarero, I., Martín-Martín, J. D., John, C. M., & Travé, A. (2022). Origin and distribution of calcite cements in a folded fluvial succession: The Puig-reig anticline (south-eastern Pyrenees). *Sedimentology*. <https://doi.org/10.1111/sed.12994>
- Travé, A., Labaume, P., Calvet, F., & Soler, A. (1997). Sediment dewatering and pore fluid migration along thrust faults in a foreland basin inferred from isotopic and elemental geochemical analyses (Eocene southern Pyrenees, Spain). *Tectonophysics*, 282, 375–398.
- Vergés, J., & Muñoz, J. A. (1990). Thrust sequences in the southern central Pyrenees. *Bulletin Societe Geologique De France*, 6, 265–271.



CTX Gale Crater Basemap

FatimaEzzahra Jadid and Hasnaa Chennaoui Aoudjehane

Abstract

Gale Crater is one of the best-known sites on the Martian surface. It is located at 5.3°S, 222.3°W (137.7°E), and is ~ 155 km in diameter. It has become a target of particular interest because of the large mound of stratified material that occupies the crater entrance (~5000 m). Gale Crater is the landing site of the Mars Science Laboratory (MSL) rover Curiosity, which landed on the Martian surface on August 5, 2012 (NASA JPL, 2017). This work aims to provide a basemap that will serve as a reference map on which we can overlay data from other layers such as mineralogy and visualize geographic and geomorphological information. We used calibrated radiometric data from the Mars Reconnaissance Orbiter (MRO) Context Camera (CTX) which is currently orbiting Mars and acquiring grey-scale images at a scale of 6 m/pixel over a 30-km-wide swath (Malin et al. in *Journal of Geophysical Research*: 112-E5, 2007), to generate a 6 m/pixel resolution mosaic of the entire crater, which will serve as the basemap for our studies of this site. The processing was done with ArcMap 10.6 and Qgis 3.28.0 software. The wide coverage and resolution of the CTX make it a good tool for geomorphological mapping of the surrounding units. The crater comprises sedimentary deposits, a bowl-shaped depression, and a central mountain (Blake et al. in *Science* 341-6153, 2013). The crater rim is quite degraded but still clearly identifiable, and the surrounding terrain has a bumpy, mantled appearance (Le Deit et al. in *Journal of Geophysical Research* 118-12, 2013), visible on the CTX mosaic. The generated basemap provides the geomorphic context for the various investigations we are conducting to study the Martian surface, in particular Gale Crater.

Keywords

Mars • Gale crater • CTX • Basemap • DTM • 3D

1 Introduction

Gale Crater is a prominent and extensively studied site on the Martian surface, situated at coordinates 5.3°S, 222.3°W (137.7°E) and spanning an estimated diameter of 155 km. The crater's distinguishing feature is a significant stratified mound located at the crater's entrance, which towers approximately 5000 m high. The MSL rover Curiosity was specifically tasked with exploring the Gale Crater and landed successfully on August 5, 2012, and has since carried out extensive scientific investigations of the site.

Gale Crater is located south of Elysium Planitia, northwest of Terra Cimmeria, and on the edge of Aeolis Mensae (Fig. 1).

2 Method and Materials

In this study, we used calibrated radiometric data from the CTX MRO to generate a 6 m/pixel resolution mosaic of the entire Gale Crater. This basemap was created from 15 CTX images and will serve as a critical tool for further studies at this site. To better understand the topography of the crater, we also generated a digital terrain model (DTM) that allows for 3D visualization of the crater, with a 3× exaggeration of the relief.

The individual images on which we based are listed in Table 1.

The CTX data that support the results of this study were obtained free of charge from the Planetary Data System

F. Jadid (✉) · H. C. Aoudjehane
Hassan II University of Casablanca, FSAC, Casablanca, Morocco
e-mail: fatimaezzahra.jadid-etu@etu.univh2c.ma

Fig. 1 Martian globe and location of Gale Crater

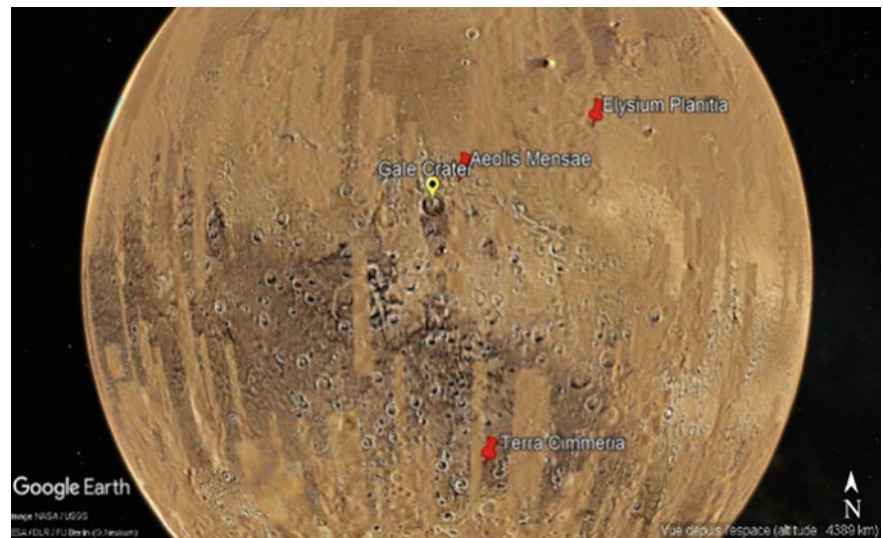


Table 1 List of CTX images

ID	CTX observation
1	P01_001356_1747_XN_05S221W
2	P01_001422_1747_XN_05S222W
3	P01_001488_1751_XI_04S222W
4	P01_001554_1745_XI_05S221W
5	P01_001620_1749_XI_05S222W
6	P02_001752_1753_XI_04S222W
7	P03_002253_1746_XN_05S221W
8	P04_002464_1746_XI_05S221W
9	P04_002530_1745_XI_05S223W
10	P04_002675_1746_XI_05S222W
11	P06_003453_1752_XI_04S222W
12	P13_005998_1746_XI_05S222W
13	P13_006143_1745_XN_05S223W
14	P14_006644_1747_XI_05S222W
15	P15_006855_1746_XN_05S222W
16	P16_007356_1749_XI_05S222W

(PDS) and are publicly available online at <https://pds.nasa.gov/index.shtml>. The mosaic was generated with ArcMap 10.6 software. The DTM and 3D view were produced using the latest version of Qgis software (3.28.0).

3 Results and Discussion

Our analysis of the data obtained from processing (Basemap, DTM, and 3D view) has revealed several significant features within Gale Crater, in agreement with previous studies

(Blake et al., 2013). The crater is composed of Layered deposits (Fig. 3b, c), a bowl-shaped depression, a delta located northwest of the crater (Fig. 3a) (Palucis et al., 2014), and a central mountain. The rim of the crater, with its multiple rings, while quite weathered, is still clearly identifiable, and the surrounding terrain has a bumpy, manicured appearance (Le Deit et al., 2013), as visible in the generated CTX mosaic (Fig. 2).

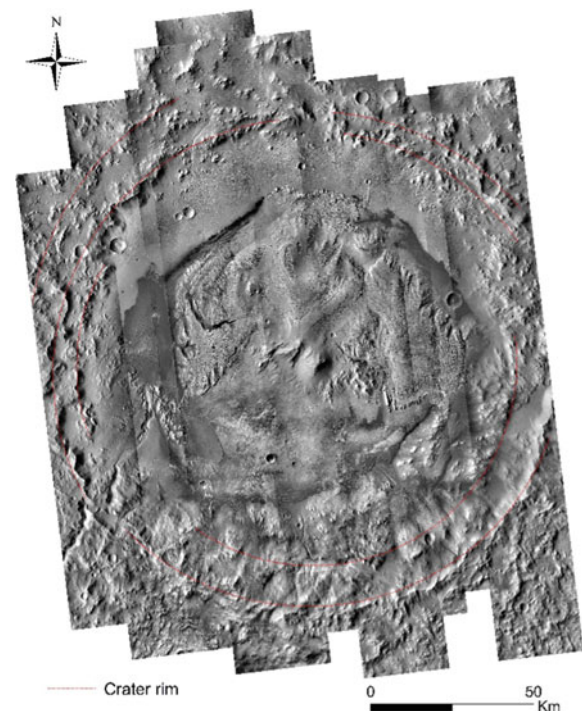
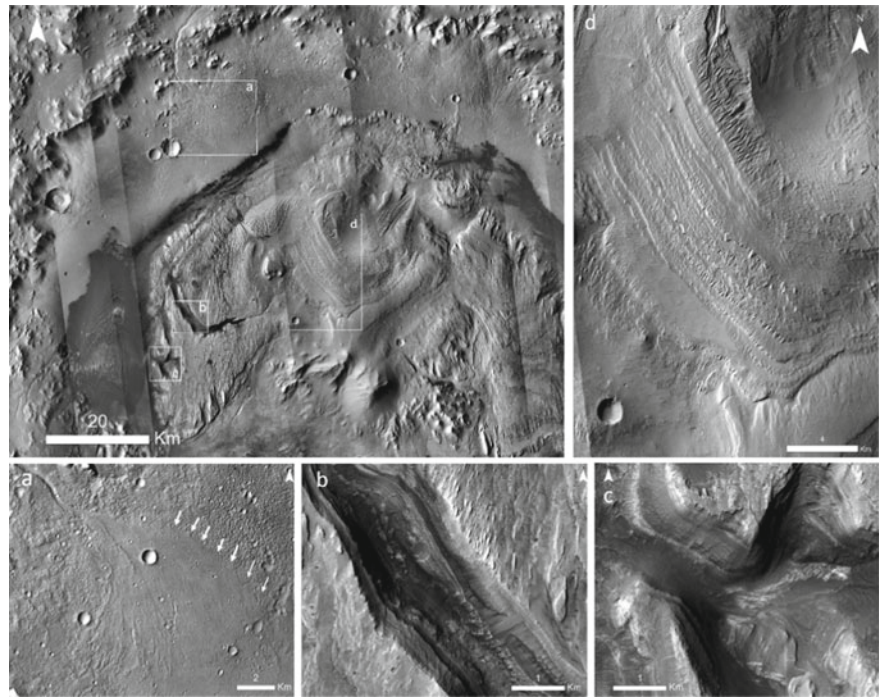


Fig. 2 Gale Crater basemap

Fig. 3 Northern region of Gale Crater **a** Delta fan (Peace Vallis) with distinct margins (e.g. white arrows), **b, c** layered deposits (Valleys) and **(d)** layered deposits (central mound of the crater)

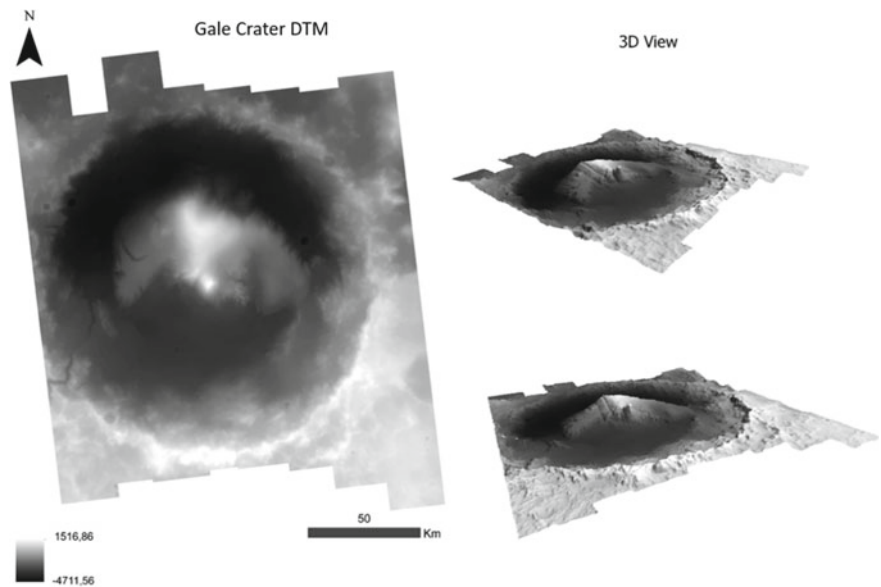


The high-resolution basemap and digital terrain model provide critical context for our ongoing investigations of the Martian surface, particularly within Gale Crater. By allowing us to visualize the topography and sedimentary deposits in 3D, we can better understand the formation processes that shaped the crater and surrounding landscape. Additionally, the broad coverage and high resolution of the CTX mosaic make it an ideal tool for geomorphic mapping of the surrounding units (Fig. 4).

4 Conclusions

In conclusion, our study of Gale Crater has provided critical information about the geomorphic architecture of the site and the potential for future studies of the geologic history and habitability of Mars. While previous studies have provided important information about the site, our use of updated, high-resolution orbital data has allowed us to

Fig. 4 Digital terrain model and perspective view of Gale Crater



generate a more detailed basemap and digital terrain model, enabling new analyses of the site.

We plan to continue our research on Gale Crater, focusing specifically on the mineralogy of the site and its geologic context. Using data from CRISM and other sources, we will explore the distribution and composition of minerals in the crater layers, with the ultimate goal of better understanding the ancient environmental conditions of Mars.

Our work on Gale Crater represents an important step in our understanding of the history of Mars and the possibility of past or present life on the planet. We believe that future research at this site will continue to provide critical information about the evolution of Mars and the potential for habitable environments beyond our own planet.

References

- Blake, D. F., Morris, R. V., Kocurek, G., Morrison, S. M., Downs, R. T., Bish, D., Ming, W., Edgett, K., Rubin, D., Goetz, W., Madsen, M. B., Sullivan, R., Gellert, R., Campbell, I., Treiman, A.H., McLennan, S. M., Yen, A. S., Grotzinger, J., Vaniman, D. T., Chipera, S. J., Achilles, Rampe, E. D., Sumner, D., Meslin, P.-Y., Maurice, S., Forni, O., Gasnault, O., Fisk, M., Schmidt, M. P., Mahaffy, P., Leshin, L. A., Glavin, D., Steele, A., Freissinet, C., Navarro-González, R., Yingst, R. A., Kah, L. C., Bridges, N., Lewis, K. W., Bristow, T. F., Farmer, J. D., Crisp, J. A., Stolper, E. M., Des Marais, D. J., Sarrazin, P. MSL Science Team. (2013). Curiosity at Gale Crater, Mars: Characterization and analysis of the rocknest sand shadow. In *Science* (pp. 341–6153).
- Le Deit, L., Hauber, E., Fueten, F., Pondrelli, M., Rossi, P. A., Jaumann, R. (2013). Sequence of infilling events in Gale Crater, Mars: Results from morphology, stratigraphy, and mineralogy, *Journal of Geophysical Research* 118(12).
- Malin, M. C., Bell, F. J., Cantor, B. A., Caplinger, M. A., Calvin, W. M., Clancy, T. R., Edgett, K. S., Lawrence, E., Haberle, R. M., James, P. B., Lee, S. W., Rvine, M. A., Thomas, P. C., Wolff, M. J. (2007). Context camera investigation on board the Mars reconnaissance orbiter. *Journal of Geophysical Research* 112-E5.
- NASA JPL. <https://www.jpl.nasa.gov/videos/a-guide-to-gale-crater>
- Palusic, M. C., Dietrich, W. E., Hayes, A. G., Williams, R. M. E., Gupta, S., Mangold, N., Newsom, H., Hardgove, C., Calef III, F., Sumner, D. Y. (2014). The origin and evolution of the Peace Vallis fan system that drains to the Curiosity landing area, Gale Crater, Mars. *Journal of Geophysical Research* 705–904.



On the Nature of Fossil Fuel

Andrey Shilovskiy

Abstract

The term fossil fuel refers to oil, gas, coal, and oil shale. Recently, more and more often, they consider hydrogen as a fossil. In southern Australia, they even began to issue licenses for the search and exploration of hydrogen accumulations. Currently, the main hypothesis of the origin of fossil fuels is the organic theory, which implies the origin of fossil hydrocarbon fuels as a product of catagenesis (late stage of diagenesis) of organic sediments. However, to date, a huge amount of accumulated evidence indicates the significant possibility inorganic origin of fossil fuels. On the one hand, a concept develop the idea based on the generation of hydrocarbons occurs in the deep layers of the Earth due to inorganic synthesis. On the other hand, more than 40 years ago, a discovery of previously unknown phenomenon of transformation of the organic matter of sedimentary rocks under the influence of tectonic and seismic processes of the earth's crust because of mechanochemical reactions arising under the action of variable mechanical stresses was experimentally established and registered. The theory of different cycles of the carbon cycle on Earth developed in the last two decades, in combination with the above, leads to the conclusion that the planet's hydrocarbon resources are renewable under certain conditions and allow us to consider hydrogen as a fossil fuel.

Keywords

Fossil fuel • Hydrogen • Organic theory • Degassing of the Earth • Renewable hydrocarbon resources

1 Introduction

The term fossil fuel today refers to oil, gas, coal, and oil shale. Recently, more and more often hydrogen acquires signs of a combustible mineral. The advantages of hydrogen are the most common element on the surface of the Earth and in outer space, the maximum heat of combustion of hydrogen, and the product of combustion in oxygen is water (which is also involved into the circulation of hydrogen energy). However, the high cost of hydrogen production by existing methods, from two to 10 \$/kg (from steam reforming of methane to electrolysis of water) (https://en.wikipedia.org/wiki/Hydrogen_economy), significantly limits the widespread use of hydrogen. A completely different situation develops if hydrogen is a mineral. In southern Australia, they even began to issue licenses for the search and exploration of hydrogen accumulations. The reason for this is clear: given the economic and environmental benefits of using hydrogen as an energy source, fossil hydrogen, if it is possible to develop a reliable technology for the search, exploration and development of hydrogen deposits, will be the cheapest compared to any other methods of obtaining it.

2 Settings or Methods or Materials and Methods or ... Etc.

Currently, the main hypothesis of the origin of fossil fuels is the organic theory, which implies the origin of fossil hydrocarbon fuels because of catagenesis (late stage of diagenesis) of organic sediments. The current practice of determining the resource potential of oil and gas fields postulates the invariability, at least on the scale of geological time, of the amount of hydrocarbons in deposits.

However, to date, a huge number of accumulated facts indicate a significant possibility of the inorganic origin of fossil fuels.

A. Shilovskiy (✉)
Oil and Gas Research Institute of Russian Academy of Science,
Moscow, Russia
e-mail: ashilovsky08@gmail.com

3 Data and Results

For almost 200 years, there have been two concepts of the origin of the hydrocarbon potential of the subsoil.

There is a mechanism of degassing of the Earth.

In 1982, the discovery of a mechanochemical mechanism for the generation of hydrocarbons in the depths was registered.

A biospheric concept of different cycles of the carbon cycle on Earth developed more than 20 years ago.

4 Discussion

On the one hand, there is a concept based on the idea that the generation of hydrocarbons occurs in the deep layers of the Earth due to inorganic synthesis. The resulting hydrocarbon fluid under high pressure enters the crystalline basement and sedimentary stratum through deep faults and in the presence of reservoirs forms hydrocarbon deposits. Within the framework of this concept, oil and gas potential is one of the manifestations of the natural degassing of the Earth.

On the other hand, more than 40 years ago, a discovery (Ryzhenko et al., 2015; <https://odysseus.prometeus.nsc.ru/patent/invent/d-326.ssi>) was registered. The essence of which was that a previously unknown phenomenon of transformation of any form of carbon (in the composition of dispersed organic matter of sedimentary rocks or carbon dioxide dissolved in formation waters) was experimentally established as a result of mechanochemical reactions arising under the action of variable mechanical stresses (tectonic and seismic processes of the earth crust). The scientific significance of the discovery lies in the fact that for the first time it was proved that the driving force behind the processes of transformation of fossil organic matter is not only the thermal component of the released energy of the Earth, but also the mechanical one. This made it possible to substantiate the position on the possibility of the formation of a wide range of hydrocarbons in natural conditions at low formation temperatures of less than 60–70 °C, in zones with increased tectonic-seismic activity. It is important to note that these processes demonstrate the generation of significant amounts of free hydrogen. A group of scientists from the School of Natural and Environmental Sciences at Newcastle University (UK) recently came to similar conclusions and independently discovered the phenomenon of the formation of hydrogen peroxide (H₂O₂), and therefore oxygen and hydrogen, because of the interaction of rocks with seeping through water cracks during the movement of tectonic faults (Stone et al., 2022).

In addition, the theory of different cycles of the carbon cycle on Earth, developed more than 20 years ago

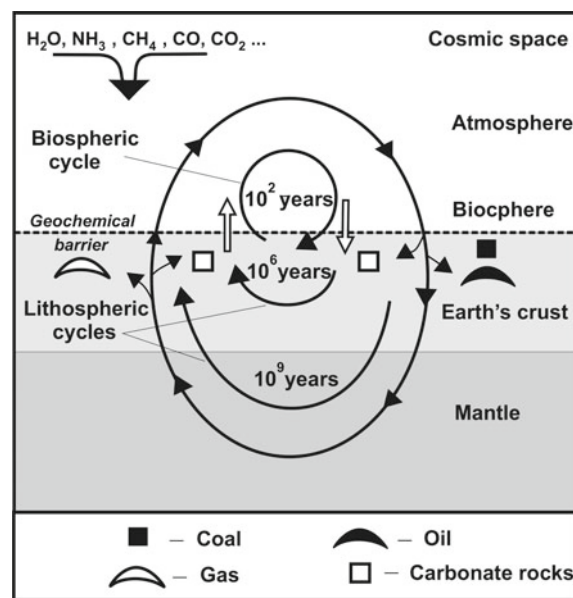


Fig. 1 Schematic layout of biosphere carbon geochemical cycle of the Earth (Zakirov et al., 2016)

(Stone et al., 2022), revealed the participation of the biospheric cycle of carbon cycle through the earth's surface in oil and gas formation, which had not previously been taken into account by either geologists or climatologists (Fig. 1). In the figure, this is the top loop. Based on the discoveries of Russian scientists, this concept generalized the organic (middle cycle in the figure) and mineral hypothesis of the origin of oil and gas (lower cycle in the figure), ensuring the balance of carbon and water cycles in the biosphere, taking into account the processes of oil and gas formation in the subsoil and modern human economic activity.

The biospheric concept theoretically explained the phenomenon of replenishment of oil and gas in exploited fields and established the characteristic time of this process at 30–40 years. Therefore, during the development of oil and gas fields, which takes several decades, the hydrocarbon potential of the deposits is in one way or another experiencing recovery. According to the conclusions of the biospheric concept, confirmed in practice, it is possible to implement a field operation regime in which the extraction of hydrocarbons from deposits corresponds to the level of their natural replenishment.

5 Conclusions

All of the above together allows us to conclude that under certain conditions the hydrocarbon resources of the planet are renewable. In addition, it allows us to consider hydrogen, which is a by-product in the process of renewal of

hydrocarbon resources, as a fossil fuel produced based on existing oil and gas technologies.

References

- Diploma №326, Application N OT-10572 dated April 21, 1982, A.A. Trofimuk, acad. Academy of Sciences of the USSR, N.V. Chersky, acad. USSR Academy of Sciences, V.P. Tsarev, Doctor of Geology and Mathematics and T.I. Soroko, Ph.D. The phenomenon of transformation of organic matter of sedimentary rocks under the action of tectonic and seismic processes of the earth's crust, priority, April 21, 1982. <https://odysseus.prometeus.nsc.ru/patent/invent/d-326.ssi>
- Hydrogen economy. From Wikipedia, the free encyclopedia. https://en.wikipedia.org/wiki/Hydrogen_economy
- Ryzhenko, B. N., Sidkina, E. S., & Cherkasova, E. V. (2015). Thermodynamic modeling of water-rock systems to evaluate their generative potential for hydrocarbons. *Geochemistry International*, 53, 825–837. <https://doi.org/10.1134/S0016702915090062>
- Stone, J., Edgar, J. O., Gould, J. A., et al. (2022). Tectonically-driven oxidant production in the hot biosphere. *Nature Communications*, 13, 4529. <https://doi.org/10.1038/s41467-022-32129-y>
- Zakirov, S., Barenbaum, A., Zakirov, E., et al. (2016). Revisiting the development of oil deposits with low permeability reservoirs. *Indian Journal of Science and Technology* 9, 2016/11/17. <https://doi.org/10.17485/ijst/2016/v9i42/104219>



Reservoir Characteristic of Sa'adi Formation, Southern Iraq

Mohanad Al-Jaberi and Adyan Ali Musban

Abstract

The Sa'adi Formation (Santonian-Campanian) is one of the important reservoirs hydrocarbon-bearing zones in the southern Iraq. According to the reservoir quality, the Sa'adi reservoir is considered a clean tight reservoir (moderate to low permeability less than 20 mD) in all study area. The Sa'adi Formation subdivided into two members; the upper member is chalky limestone rocks and the lower member is limestone, the lower member can be further divided clearly into three units (A, B, and C) according to wells logs. Petrophysical properties showed a relationship with facies distribution, the relationship between porosity and permeability in some study wells through Winland R35 method, four types of pore throat sizes have been identified (nanopores, micropores, mesopores, and macropores). Upper Sa'adi and lower Sa'adi Unit C have the low quality related to medium average values of porosity less than 12% and permeability less than 2mD while it's absence of oil saturation. The micropores and nanopores dominate of this flow and related to mud-supported microfacies of outer ramp and mid-ramp facies associations. While lower Sa'adi Unit A and B, mesopores and macropores marked with grain-support facies related to inner-ramp facies associations, which reflect to high porosity is 17% and medium permeability less than 20 mD with high oil saturation at (78–65%), it represents the best flow unit of Sa'adi Formation in West Qurna I and West Qurna II Oilfields.

Keywords

Sa'adi • Basrah • West Qurna • Facies • Iraq • Reservoir

1 Introduction

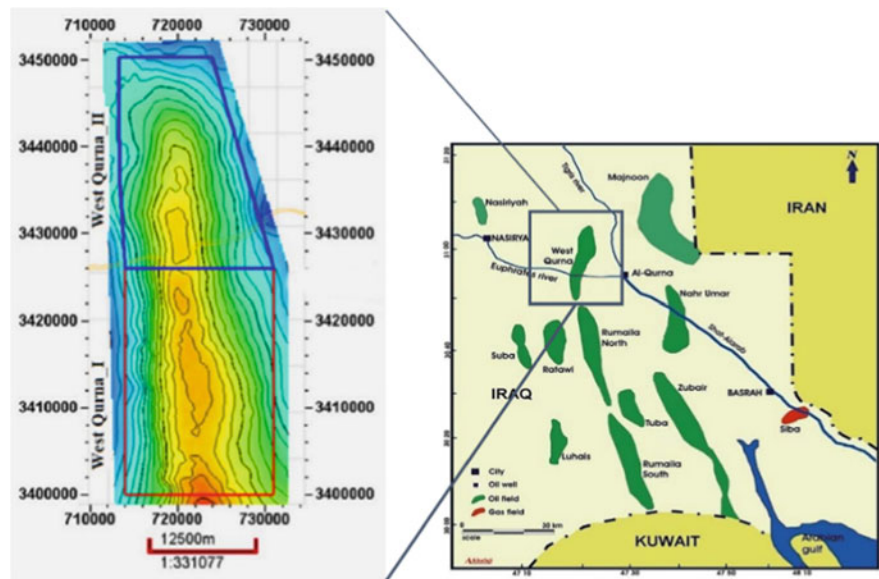
The West Qurna I (WQI) and West Qurna II (WQII) supergiant oilfields are one of the largest oil-producing fields. The oilfields are located in Mesopotamia hydrocarbon province north part of the Arabian plate, southern Iraq (Fouad, 2010). These structures are an extension of the unstable shelf of the Arabian plat (Jassim & Goff, 2006). Structurally, the fields represent the northern extensions of the northern Rumaila fold (Fig. 1). Within these oilfields, most of the oil production in the West Qurna I and II oilfield is from the middle Cretaceous of Mishrif reservoir and minor oil production from Late Cretaceous of Sa'adi reservoir in West Qurna I (Abdullah, 2021). The Sa'adi Formation is the highest, youngest, thickest, and most widespread formation compared to the megasequence AP9 (Khasib and Tanuma) in Iraq (Buday, 1980). The first description of the formation originates from Rabanit (1952). The upper boundary of the Sa'adi Formation is usually unconformable and overlain by Hartha Formation, and its lower contact is conformable and gradational only where it is in contacts with the Tanuma Formation. The Sa'adi Formation in the West Qurna oilfield can be subdivided into two members in the type locality includes, the upper member of the Sa'adi is chalky, and the thickness was about 100–110 m and the lower member of the Sa'adi limestone with marly limestone, while thickness was about 25–30 m (Al-Shawosh, 2002). The lower member can be further divided into three units (A, B, and C) according to wells logs and petrophysical properties. The main aims of this study are to identify reservoir quality based on petrophysical properties.

2 Materials and Methods

The preliminary information was collected from the final reports of the wells of the study area, as well as the wells containing the log data and core analysis required for the

M. Al-Jaberi (✉) · A. A. Musban
Geology Department, College of Science,
University of Basrah, Basrah, Iraq
e-mail: muhanad.abood@uobasrah.edu.iq

Fig. 1 Location map of study area (Abdullah, 2021)



study were identified. Seventy-Five Core samples were analyzed (porosity and permeability) for Sa’adi Formation distributed on ten wells represented by five well in the West Qurna I and five wells in West Qurna II, whether used plugs core samples or whole core section give a precise measurement of grain density and pores volume using gas (Helium) expansion method. Using the Winland (1976) method to determine the pore throat, this method allows predicting flow units’ distribution within Sa’adi Formation succession. GEOLOG8 software is used to analysis of wireline logging data to calculate petrophysics properties such as the water and oil saturation (Sw and So) by using Archie equations (Archie, 1942).

to determine Pore-Throat Radius (R35). The R35 of a given rock type effects reservoir performance by reflecting its diagenetic fabric and depositional (Hartmann & Coalson, 1990). As a result, using the Winland Eq. (1) to predict R35 from core data (Fig. 2) shows the distribution of R35 in wells West Qurna I and West Qurna II. The water and oil saturation (Sw and So) were calculated by Archie equation, and oil storage units have been identified, as shown in Fig. 2b.

$$\text{Log } R35 = 0.732 + 0.588 \log(\phi_e) - 0.864 \log(k), \quad (1)$$

where K = permeability, ϕ_e = effective porosity.

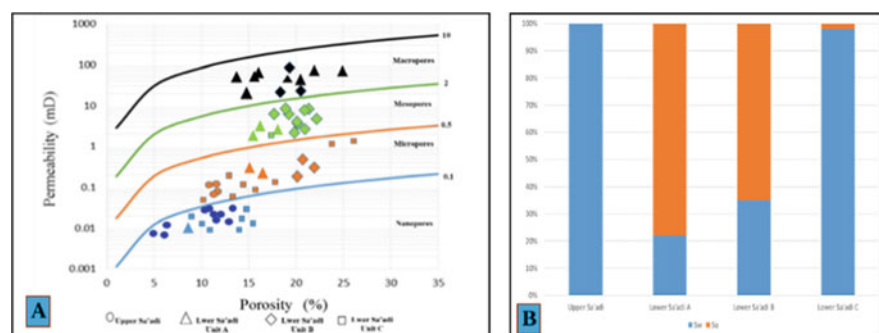
3 Results and Discussion

The relationship between porosity and permeability are the most important parameters used to evaluate of the reservoir quality. The available core porosity and permeability data for Sa’adi reservoir in West Qurna I and II oilfield was utilized

3.1 Upper Sa’adi and Lower Sa’adi (Unit C)

This flow unit is characterized by lowest average permeability, which reaches 1.6 mD. The average porosity is 12% reduce the reservoir quality of this unit, while its absence of oil saturation. The proportion of micropores in this flow unit and remarkably increased with the association of nanopores.

Fig. 2 a Pore throat radius for wells of West Qurna I and II Oilfields. b The percentage of water and oil saturation in the Sa’adi reservoir from 10 wells in West Qurna I and II Oilfields



Therefore, it is consisting only of outer ramp (deep marine and basinal facies in upper and mid-ramp facies in lower association characterized by mud-supported texture.

3.2 Lower Sa'adi (Unit a and Unit B)

In this unit, a clear increase in porosity is 17% and average permeability (20–15) mD with high oil saturation at (78–65%); it is considered of medium quality. Pore throat types are mainly mesopores and macropores. However, it represents the best flow unit of Sa'adi Formation in West Qurna I and West Qurna II Oilfields. Large pore sizes are existed in grain-supported microfacies related to inner-ramp (shoal and shallow open marine) facies association.

4 Conclusions

According to Winland R35 method, four types of pore throat sizes have been identified (nanopores, micropores, mesopores, and macropores). Based on pores radius and oil saturation, the reservoir quality increases lower Sa'adi and decreased in upper Sa'adi. The porosity–permeability limits and pore throat size (R35) controlled the flow unit characteristics in the Sa'adi Formation. Lower Sa'adi A and B represent the best flow unit due to high porosity and permeability values with high oil saturation, the dominance of mesopores and macropores. Lowest reservoir quality is observed in upper Sa'adi and lower Sa'adi C, the high porosity of this unit does not contribute in enhancing its reservoir properties because it is of micropore and nonpore types, where minimum permeability values are recorded

while its absence of oil saturation. Finally, the study concludes that the Sa'adi reservoir is considered a clean tight reservoir (moderate to low permeability less than 20 mD) and poor reservoir in all wells of West Qurna I and II Oilfields.

References

- Abdullah, R. A., & Al-Shahwan, M. (2021) Structural geometry analysis of Khasib formation in West Qurna I and II supergiant oilfields, Southern Iraq. *Iraqi Geological Journal*, 54–66.
- Al-Shawesh, M. A. (2016). Sequence stratigraphy of Late 'Turonian-Early Campanian Sa'adi, Tanuma and Khasib formation in West Qurna southern of Iraq, Unpublished M.Sc. Thesis, University of Basrah.
- Aqrabi, A. A. M., Goff, J. G., Horbury, A. D., & Sadooni, F. N. (2010). The petroleum geology of Iraq. Published by Scientific Press Ltd PO Box 21, Beaconsfield, Bucks HP9 1NS, UK (p. 424).
- Archie, G. E. (1942). The electrical resistivity log as an aid in determining some reservoir characteristics. *AIME*, 146, 54.
- Buday, T. (1980). The regional geology of Iraq. In Kassab, I. I., & Jassim, S. Z. (Eds.), *Stratigraphy and paleogeography* (p. 445). Dar Al-Kutub Publ. House, Mosul, Iraq.
- Fouad, S. F. A. (2010). Tectonic and structural evolution of the Mesopotamia foredeep, Iraq. *Iraqi Bulletin of Geology and Mining*, 6(2), 41–53.
- Hartmann, D. J., & Coalson, E. B. (1990). *Evaluation of the morrow sandstone in Sorrento field*. Cheyenne County, Colorado.
- Jassim, S. Z., & Goff, J. C. (2006). *Geology of Iraq*. DOLIN, distributed by Geological Society of London.
- Owen, R. M. S., & Nasir, S. N. (1958). The stratigraphy of the Kuwait-Basrah area. In Weeks, G. L. (Eds.), *Habitat of oil a symposium*. Amer. Assoc. Pet. Geol. Tulsa.
- Winland, H. D. (1976). *Evaluation of gas slippage and pore aperture size in carbonate and sandstone reservoirs: Amoco Production Company Report F76-G-5* (p. 25). Tulsa, Oklahoma.



Interpretation of Geophysical and Spectrometric Airborne Data of the Eastern Part of the Moroccan Central Massif

Nawal Bouya, Bennacer Moussaid, Ahmed Manar, and Hmidou El Ouardi

Abstract

This work aims to analyze and interpret a geophysical airborne dataset and to correlate them to field geological data in the order to study structures and subsurface bodies in the eastern part of the Paleozoic central massif of Morocco. This area is one of the most extended outcrops as inliers of Paleozoic basement affected by Variscan compressional events, covered by meso-cenozoic subtabular cover. Megastructures are organized as succession of anticlinoria and synclinoria with a NE-SW main trend. This area is characterized by important diversity of magmatic rocks and plutonic bodies and tectonic structures. Results of airborne data, aeromagnetic and spectrometric of Th element, show a very clear consistency of anomalies with superficial structures. They allow also to marking out and detailed mapping (i) ment granitic body and its surrounding metamorphic aureole rocks, (ii) basaltic flow of plio-quatarnary age, and (iii) the main Variscan strike-slip faults as well as NE-SW to ENE-WSW structures corresponding to the main trend of Variscan structures of this range and their probable alpine bending in the central area against the granitic body. Filters and analysis applied on magnetic data such as, reduction to pole, vertical derivative, Euler deconvolution and upward continuations processing PVH, allow to

enhancing anomalies and also to carrying out others deeper anomalies south-westward of Ment granitic bodies which can correspond to deeper plutonic bodies.

Keywords

Airborne magnetic data • Spectrometric • Mapping • Geological structures • Massif Central

1 Introduction

The central massif is one of the largest inliers of Meseta Variscan belt of Moroccan. Despite its great mining interest and geological diversity, this part of Variscan is not well reached by an accurate geological mapping coverage. However, the area is well studied by several geological works (Michard et al., 2008 and references there in). Currently, aeromagnetic and spectrometric data analyses are used worldwide for regional geological survey and metallogenic and mining research (Abderbi & Khattach, 2011; Bouya et al., 2013a, 2013b). Recently, aeromagnetic and gravity surveying data were widely used to spot and follow large structures or for punctual geological mapping and exploration of mining deposits (e.g., Bouya et al., 2013a, 2013b; Boutirame et al., 2019; Nait Bba et al., 2019). The present work aims to mapping a wide area of central massif using airborne geophysical data, especially aeromagnetic, which allow to establish a map of subsurface structures and to detect deep anomalies. The spectrometric method of Th element was also used in order to have more reliability and precision in subsurface map.

2 Geological Setting

The studied area, central massif, is located at the eastern part of the wide Variscan inlier «Central Meseta» of western Meseta. It is limited to the North by the Sehoul zone; to the

N. Bouya (✉) · H. El Ouardi
Département de Géologie, Faculty of Sciences, Moulay Ismail
University of Meknès, Meknes, Morocco
e-mail: bouyan288@gmail.com

H. El Ouardi
e-mail: h.elouardi@umi.ac.ma

B. Moussaid
«BGIM» Laboratory, Ecole Normale Supérieure, Hassan II
University, Casablanca, Morocco
e-mail: b.moussaid@enscasa.ma

A. Manar
Département de Géologie, Ministère de L'énergie Et Des Mines,
Rabat, Morocco
e-mail: a.manar@mem.gov.ma

West by the Western Meseta shear zone to the South by the atlasic belts (Atlas Paleozoic transform zone) and to the East by the tabular Middle Atlas and Saiss basin. The Central Massif, the Sidi Bettache Basin, the central and eastern parts of the Rehamna and Jebilet massifs, and most of the High Atlas Massif form the Central Meseta Block, where two subzones can be distinguished, separated by the Smaala-Oulmes fault zone the Western Central Meseta and the Eastern Central Meseta. This area was a thinned crustal domain during the Late Devonian Early Carboniferous as evidenced by the amount of mafic magmatism and turbiditic deposits. The Paleozoic series overlie the Neoproterozoic basement represented by rhyolitic and granitic outcrops as recently dated in the central area (Ouabid et al., 2017), Rabat-Tiflet fault (Tahiri et al., 2010) or previously highlighted in the literature, in the western part El Jadida (e.g., Gigout, 1951), and Rehamna (Corsini et al., 1988) areas. This belt is structured by the Variscan orogeny (e.g., Bouabdelli, 1994; Michard et al., 2008). These series began with, the Lower and Middle Cambrian strata (600 m) showing facies characterized by limestones and marbles covered by slates and greywacke. These formers show intercalation of tuffs and tholeiitic basaltic flows (Ouali et al., 2003). Cambrian strata are covered by thick series (3000 m) of quartzites (Cailleux, 1994). The Silurian is mainly represented by Graptolitic black shales. However, the Devonian is characterized by thick pelitic intervals with minor interbedded limestones and becomes dominated by sandstones and shales at the top of series. The carboniferous is mainly dominated by turbiditic series with intercalations of basaltic sill or flows. During the Westphalian, sedimentation becomes conglomeratic and still during the Permian time. The Mesetian belt was structured by the Variscan orogenic events, and surely its current structures record some Alpine deformations. The central Meseta is strongly shortened during the latest Variscan phases (Upper Carboniferous-Permian) with NW-verging NE-SW folds, duplexes and nappes. These folds are syn-foliation with a main foliation parallel to axial surface showing a N40°E main trend. Structures related to an early compressional phase (Tournaisian-Early Visean) are only exhibited in the most eastern part of the central Meseta (Nappe Zone, Azrou-Khénifra and Fourhal Basins) (Fig. 1).

3 Materials and Methods

The used data in this study are from airborne magnetic surveys acquired by the airborne magnetism campaign (African Geophysical Company, 1970), entrusted by the Ministry of Energy and Mines of Morocco. These surveys were recorded at a barometric flight altitude of 1000 m. The spacing between the flight lines is respectively 3 km and 5 km for aeromagnetic and radiometric data. After applying the

preliminary corrections of the measurements, the acquired data were analyzed and displayed in the maps of isovalues curves. Used data, in this work, were provided as maps of isovalues curves of the residual magnetic field at a scale of 1/100,000. Digital processing of the both magnetic and Th element maps of the study area by Oasis Montaj 7.0.1 software was performed in order to make other treatment leading to enhance and elaborate anomalies maps. Field data were also collected for verification of obtained anomalies and for interpretation and to add the undetectable small-scale structures, as the spaced-out flight lines don't allow it.

4 Results

4.1 Magnetic Anomalies Map (Fig. 2a)

After digitization of all intersections between flight lines and isovalues curves of the studied area, an interpolation of collected data was done following a regular grid with equal steps of 125 m. The first map obtained, by this process, images the residual magnetic field of the studied area. To make anomalies stackable to magnetic sources we performed a calculation of magnetic map reduced to the magnetic pole (RTMP or RMP) from the digital aeromagnetic information, which allows the compensation geomagnetic field influence. The map of the RMP shows the existence of zones with different magnetization intensities and by their geometric shapes (Fig. 2a). The main anomalies areas observed can be summarized as following: (i) areas with sub-circular shapes and showing high magnetic intensity. These anomalies cover the central part of studied and also, its southwestern and southeastern ends, (ii) linear shaped anomalies showing a main NE-SW trend, (iii) bent-shaped anomalies which correspond probably to the limit between two contrasted facies (the area located between the two dashed lines at the north of the anomaly 2 (Fig. 2a) (iv) a very low intensity anomaly in the northern end of the studied area, and (v) very high intensity anomaly extending along the Ifrane river with an ESE-WNW trend.

4.2 Radiometric Th Element Anomalies Map (Fig. 2b)

The airborne spectrometric data of Th element is an additional method for the aeromagnetic mapping thanks to its ability to give more precision regarding the subsurface information. The spectrometric map of studied area displays as well as anomalies with different intensities, shapes, and sizes: (i) sub-circular anomaly of very high intensity in the center of western part of the studied area (area 2 in Fig. 2b), (ii) aligned anomalies showing a NE-SW trend and

Fig. 1 Geological map of the Eastern part of Central massif of Morocco (1/100000) modified after (Fadli et al., 2007)

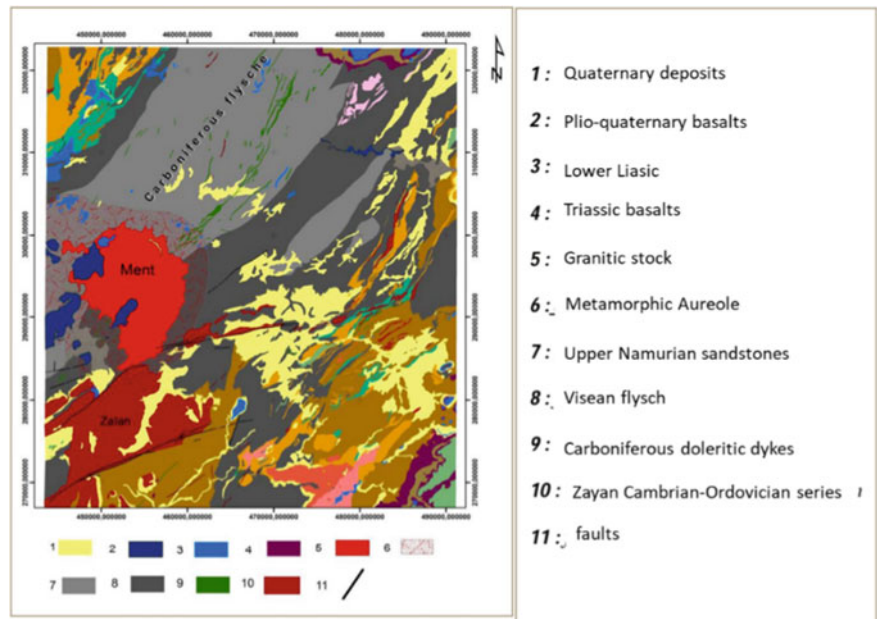
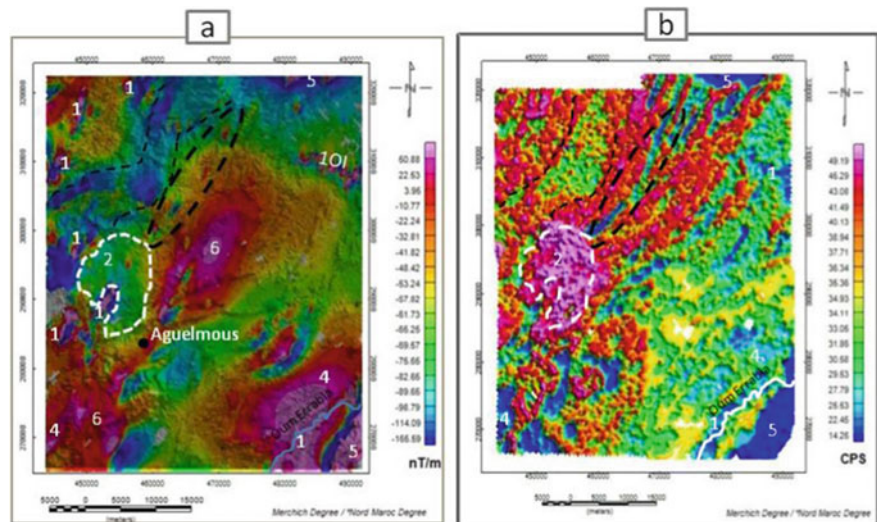


Fig. 2 a RMP map of magnetic anomalies superposed to the MNT of the studied area. b Airborne colored map of Th element of the eastern part of Moroccan central massif



superimposed to the high magnetic anomalies (6 in Fig. 2a), (iii) low concentration of Th element anomalies which coincide with very high magnetic intensity anomalies observed on the RMP map (10I, 1, 4 and 5 in Figs. 2a and b), and (iv) NE-SW linear anomalies at the north-eastern part of Ment Granitic body. These anomalies show a clear trend change near to the granitic stock, becoming ENE-WSW.

5 Discussion

The results obtained by treatment of magnetic and spectrometric data are interpreted using correlations between the both methods and those of field collected data and also compiled

information from previous works. The aeromagnetic and spectrometric anomalies maps display very well correspondence with the main geological structures of the studied area when these formers were superposed to the geological information. Magnetic and spectrometric anomalies show a NE-SW dominant trend, aligned with the direction of the main structures of the central massif. The sub-circular anomaly of very strong Th element concentration and low magnetic intensities is consistent with silica-rich body corresponding to the Ment granitic Stock (area 2, Fig. 2). However, the very low Th element anomaly which was recorded on the area showing higher magnetic intensity in the south-easternmost end of the maps correspond to the response of basaltic flow of Triassic time (area 5, Fig. 2). The same result was observed in

the Triassic basalts of the tabular middle atlasic eastern zone (area 5 in the northern end of the maps). Results show also a good consistency with quaternary basaltic flow (Oued Ifrane area), and others basalts, phonolites and tephrite in the whole eastern part of the studied area and along the Oum Errabiaa river (1 in Fig. 2). Following a north-east trend to Ment granitic body, the Th concentration displays a linear repartition corresponding to numerous fractures and faults which seem to control the distribution of Th element. The high Th concentration in these areas can be also linked to linear granitic bodies as attested by the presence of some granitic outcrops along the main Kilometric faults at the north of the Ment Granit. These anomalies show curved shapes near to the Ment granit, the bent linear structures can be the result of alpine deformation, subsequent to granitic body emplacement and attest a sinistral reactivation of Variscan structures during African and European plates convergence and their bending against the competent granitic stock. The low Th anomalies surrounded by the dashed elliptic marker in Fig. 2 correspond to carboniferous doleritic dykes and display high magnetic intensities. The anomalies 4 in Fig. 2 correspond to the outcrops of Cambrian-Ordovician volcano-sedimentary series showing high magnetic intensity and low Th element concentration. However, the aligned anomalies showing high magnetic intensities and alternation of high and low bands of Th element concentration, marked 6 in Fig. 2, coincide with quartzite series of the Ordovician and can be linked to the deeper influence of volcano-sedimentary or to magnetic mineral deposits along the major fault zone affecting this area in a NE-SW direction. This interpretation is more consistent with high Th element bands observed in part of the studied area.

6 Conclusions

This work represents the analysis of airborne magnetic and spectrometric data compared to field collected data. The enhancement techniques, namely reduction to pole, were used in identifying different magnetic anomalies and to well define structural trends representing the main structures linked to the Variscan orogeny which are observed to trend in NE-SW direction. Magnetic and Th maps display also wide anomaly areas corresponding to different magmatic bodies and others lithologies of the studied area. All in all, the present study reveals a good matching of the geological mapping, especially of kilometric scale structures and outcrops and the airborne magnetic and radiometric data.

References

- Abderbi, J., & Khattach, D. (2011). Apport des données aéromagnétiques et gravimétriques à l'étude de la structure géologique des Hauts Plateaux méridionaux (Maroc). *Journal of Hydrocarbons Mines and Environmental Research*, 2, 111–118.
- Bouabdelli, M. (1994). Tectonique de l'est du massif central (zone d'Azrou- Khénifra). *Bulletin of the Scientific Institute, Rabat*, 18, 145–168.
- Boutirame, I., Boukdir, A., Akhssas, A., & Manar, A. (2019). Geological structures mapping using aeromagnetic prospecting and remote sensing data in the karstic massif of Beni Mellal Atlas, Morocco. *Bulletin of the Mineral Research and Exploration*, 160 (160), 213–229.
- Bouya N., et al. (2013a). Aeromagnetic data used for mapping the Agourai plateau structures (Tabular Middle Atlas, Morocco). *Africa Geoscience Review*, 20.
- Bouya, N., et al. (2013b). *Geological interpretation of the aeromagnetic survey in the Agourai area (Central Morocco)*. Central European Geology.
- Cailleux, Y. (1994). Le Cambrien et l'Ordovicien du Maroc central septentrional. In A. El Hassani, A. Piqué, A. Tahiri (Eds.), *Le Massif central marocain et la Meseta orientale*, *Bulletin of the Scientific Institute, Rabat*, 18, 10–31.
- Corsini, M., Muller, J., Cornée, J. J., & Diot, M. (1988a). Découverte de la série basale du Cambrien et de son substratum dans les Rehamna centraux, haut-fond au Cambrien (Meseta marocaine). *Prémices de l'orogénèse hercynienne*. *C. R. Acad. Sci. Paris*, 306 (II), 63–68.
- Fadli D., Bouabdelli M., Cailleux Y., El Hassani A., El Wartiti M., Hoepffner C., Kharbouch F., Tahiri A., & Zahraoui M. (2007). Carte Géologique du massif hercynien central du Maroc (1/200.000).
- Gigout, M. (1951). Etudes géologiques sur la Meseta marocaine occidentale (arrière-pays de Casablanca, entre Mazagan et Safi). *Notes Et Mémoires Service Géologique Maroc*, 86, 507.
- Michard, A., Saddiqi, O., Chalouan, A., & De Lamotte, F. (2008). *Continental evolution: The geology of Morocco: Structure, stratigraphy, and tectonics of the Africa-Atlantic-Mediterranean triple junction* (pp. 65–121). Springer.
- Nait Bba, A., Boujamaoui, M., Amiri, A., Hejja, Y., Rezouki, I., Baïdder, L., Inoubli, M. H., Manar, A., & Jabour, H. (2019). Structural modeling of the hidden parts of a Paleozoic belt: Insights from gravity and aeromagnetic data (Tadla Basin and Phosphates Plateau, Morocco). *Journal of African Earth Sciences*, 151, 506–522.
- Ouabid, M., Garrido, C. J., Acosta-Vigil, A., Román-Alpiste, M. J., Dautria, J.-M., Marchesi, C., & Hidas, K. (2017). Neoproterozoic granitoids in the basement of the Moroccan Central Meseta: Correlation with the Anti-Atlas at the NW paleo-margin of Gondwana. *Precambrian Research*, 299, 34–57.
- Ouali, H., Briand, B., Bouchardon, J. L., & Capiez, P. (2003). Le volcanisme cambrien du Maroc central: implications géodynamiques. *C. R. Geoscience*, 335, 425–433.
- Tahiri, A., Montero, P., El Hadi, H., Martínez Poyatos, D., Azor, A., Bea, F., Simancas, J. F., & González Lodeiro, F. (2010). Geochronological data on the Rabat-Tiflet granitoids: Their bearing on the tectonics of the Moroccan Variscides. *Journal of African Earth Sciences*, 57, 1–13.



Hydrocarbon Generation Centers in the Meso-Cenozoic Complex of the Black Sea-Caspian Region

Rustam Mustaev, Vagif Kerimov, Elena Lavrenova, and Uliana Serikova

Abstract

As a result of the studies within the study area, four areas of stable subsidence (hollows) were identified for the entire period of formation of the plate cover: Karkinit-skaya, Indolo-Kubanskaya, East Kubanskaya, and Terek-Caspian. Each of the basins is characterized by a unique evolution, which manifests itself in differences in the tectonic regime and the rate of sedimentation. This determined the features of the geological structure of the basins, the sources of generation in them and the critical moment characterizing the process of generation–migration–accumulation of hydrocarbons in the system. In the centers of generation of hydrocarbons, the critical moment happened, when more than 50% of hydrocarbons emigrated from the source rock and accumulated in traps. As a rule, the springs are confined to the most submerged parts of the sedimentary basin, in which the deposits are in more severe thermobaric conditions. Based on the levels of modern maturity and transformation of OM of the identified and proposed oil and gas source rocks, as well as the obtained estimates of the specific densities of hydrocarbon emigration at 5 stratigraphic levels, independent generation centers were identified. The combination of steady subsidence of generation sources and uplift of adjacent areas of the Scythian Plate in the Neogene-Quaternary provided the conditions for long-range migration of hydrocarbons. This significantly expanded the area of probable accumulation and the area of the territory promising for the search for hydrocarbons.

Keywords

Sedimentary basin • Hydrocarbon system • Generation center • Plate cover • Tectonic regime • Sedimentation rate • Basin analysis • Source rocks • Black Sea-Caspian region

1 Introduction

The conducted studies have resulted in distinguishing the following four areas of persistent (basin) subsidence throughout the entire period of plate cover formation within the examined territory: the Karkinit, Indolo-Kuban, East Kuban, and Terek-Caspian Basins. Each basin has undergone its own unique evolution, manifested in the differences in tectonic regime and sedimentation rates. This determined specific aspects of the geologic framework of basins, kitchen areas within their limits and the critical moment that defines the process of hydrocarbon generation–migration–accumulation in the system (Kerimov et al., 2014, 2017).

2 Modeling Technique

Basin analysis and hydrocarbon system modeling were performed using Schlumberger's PetroMod software package and modeling technologies. The results produced by basin analysis determined the modeling strategy and the scope of tasks to be solved. These tasks involve identifying the main oil and gas kitchen areas, determining specific aspects of the evolution undergone by oil and gas source rocks and their realization of hydrocarbon-generating potential, establishing a relationship between actual oil and gas occurrence in the sedimentary cover and hydrocarbon kitchen areas, and identifying areas with the most probable hydrocarbon accumulation (Magoon & Dow, 1994). The analyzed indications of oil and gas occurrence suggest the

R. Mustaev · E. Lavrenova (✉) · U. Serikova
Sergo Ordzhonikidze Russian State University for Geological
Prospecting, 117997 Moscow, Russian Federation
e-mail: elena.lavrenova.70@inbox.ru

V. Kerimov
Oil and Gas Institute of Azerbaijan's National Academy
of Sciences, AZ1000 Baku, Azerbaijan

existence of several independent GAHS in each of the basins. Their specific aspects of evolution and interaction control the hydrocarbon potential of sedimentary basins and adjoining territories. Numerical basin modeling in the space–time domain was done with a view to achieving a deeper understanding of how this intricate interconnected system of hydrocarbon systems is functioning (Lapidus et al., 2018).

3 Results

According to the GAHS concept, **the critical moment** is the time that most precisely defines the process of hydrocarbon generation–migration–accumulation in a system, when more than 50% of hydrocarbons have expelled from an oil and gas source rock and accumulated in traps (Kerimov et al., 2016). The critical moment is surpassed in hydrocarbon kitchen areas—they are usually represented by oil and gas source rock intervals within the main zone of oil generation. The kitchens are usually confined to the most subsided parts of the sedimentary basin, where deposits are found under more severe P–T conditions. This determined the onset of hydrocarbon expulsion and migration from these areas into reservoir horizons.

In order to identify oil and gas kitchen areas and map their boundaries, we used maps showing specific density of hydrocarbon expulsion obtained via 3D modeling (Figs. 1 and 2).

For legend see Fig. 1b

As a result, oil and gas kitchens have been established at five stratigraphic levels in the Indolo-Kuban and Terek-Caspian Basins (Middle Jurassic, Cretaceous, Paleogene, Maikopian and Miocene), at four levels in the East Kuban

Basin (Middle Jurassic, Cretaceous, Paleogene, and Maikopian), and at three levels in the Karkinit Basin (Cretaceous, Paleogene, Maikopian) (Guliev et al., 2018).

Thus, the thermal maturity modeling of rocks in the sedimentary cover resulted in detecting differences in the studied basins with respect to the presence of hydrocarbon kitchen areas and their breakdown per stratigraphic levels.

4 Conclusions

The following independent kitchen areas have been identified at five stratigraphic levels based on the levels of present-day maturity and organic matter alteration in known and inferred oil and gas source rocks, as well as based on the obtained estimates of specific density of hydrocarbon expulsion: *Middle Jurassic* (Indolo-Kuban, East Kuban, Terek-Caspian), *Lower Cretaceous* (Karkinit, Indolo-Kuban, East Kuban, Terek-Caspian), *Eocene* (Karkinit, Indolo-Kuban, East Kuban, Terek-Caspian), *Maikopian* (Karkinit, Indolo-Kuban, East Kuban, Terek-Caspian), and *Miocene* (Indolo-Kuban, Terek-Caspian). Thus, the sedimentary basins under study differ, among other things, in the presence and distribution of hydrocarbon kitchen areas throughout the section.

Variations in basin subsidence rates at different stages of their evolution had a critical impact on the realization of hydrocarbon-generating potential by oil and gas source rocks. As a result, coeval oil and gas source rock intervals of the basins surpassed the critical moment at different points in time and by now have realized their hydrocarbon-generating potential to a varying degree.

The main prospective complex within the territory under study is made up of Cretaceous deposits. Their hydrocarbon

Fig. 1 Maps showing specific density of hydrocarbon expulsion from oil and gas source rock intervals in Middle Jurassic (a) and Lower Cretaceous and (b) deposits

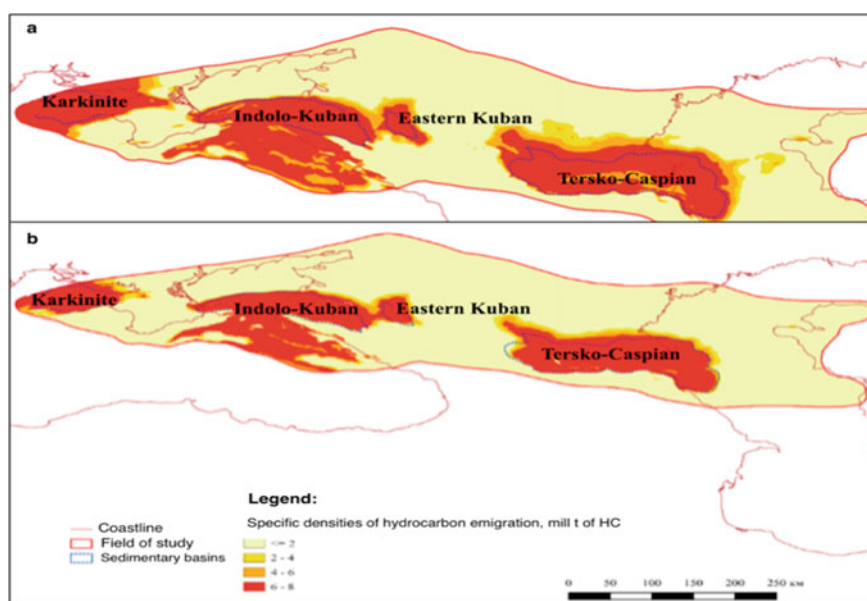
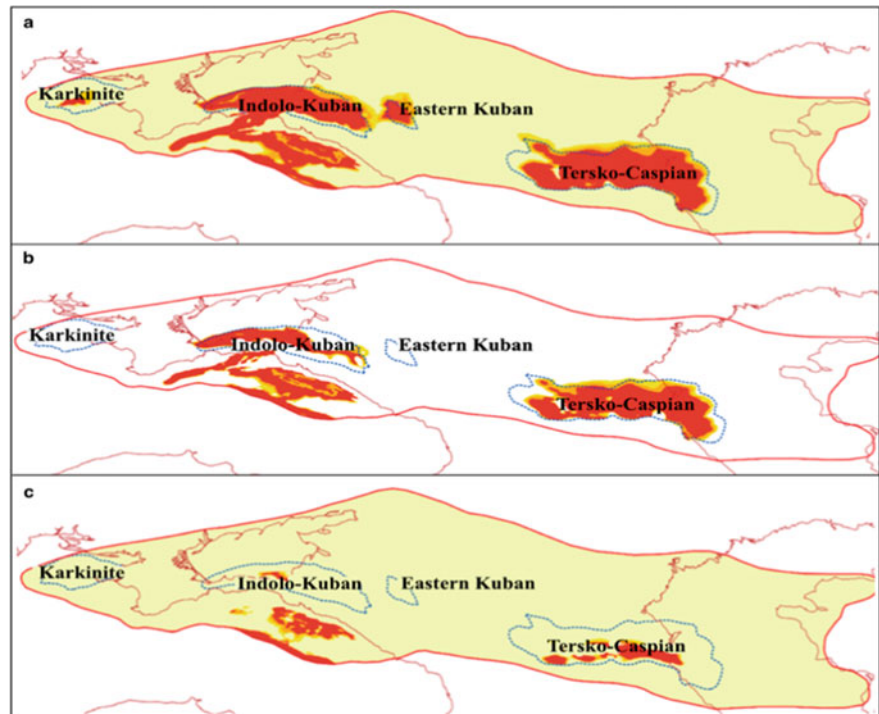


Fig. 2 Maps showing specific density of hydrocarbon expulsion from oil and gas source rock intervals in Eocene (a), Maikopian (b), and Miocene (c) deposits



saturation is provided both by their own oil and gas source rock interval and by flows from the deeper horizons in the sedimentary cover. The Paleogene complex ranks second in importance.

References

- Guliev, I. S., Mustaev, R. N., Kerimov, V. Y., & Yudin, M. N. (2018). Degassing of the Earth: Scale and implications. *Gornyi Zhurnal*, 11, 38–42.
- Kerimov, V. Y., Osipov, A. V., Mustaev, R. N., Monakova, A. S. (2014). Modeling of petroleum systems in regions with complex geological structure. In *16th Science and applied research conference on oil and gas geological exploration and development*, GEOMODEL 2014.
- Kerimov, V. Yu., Shilov, G. Ya., Mustaev, R. N., & Dmitrievsky, S. S. (2016). Thermobaric conditions of hydrocarbons accumulations formation in the shale low-permeability oil reservoirs of khadam suite of the Ciscaucasia. *Neftyanoe Khozyaystvo*, 2, 8–11.
- Kerimov, V. Y., Bondarev, A. V., & Mustaev, R. N. (2017). Estimation of geological risks in searching and exploration of hydrocarbon deposits. *Neftyanoe Khozyaystvo*, 8, 36–41.
- Lapidus, A. L., Kerimov, V. Y., Mustaev, R. N., Salikhova, I. M., & Zhagfarov, F. G. (2018). Natural Bitumens: Physicochemical properties and production technologies. *Solid Fuel Chemistry*, 52 (6), 344–355.
- Magoon, L. B., Dow, W. G. (1994). The petroleum system. In: L.B. Magoon, W.G. Dow (Eds.), *The petroleum system—From source to trap* (Vol. 60, pp. 3–24). AAPG Memoire.



Modeling Hydrocarbon Migration and Accumulation Processes in the Meso-Cenozoic Complex of the Black Sea-Caspian Region

Vagif Kerimov, Rustam Mustaev, Elena Lavrenova, and Pavel Romanov

Abstract

The article is devoted to the study of the processes of migration and accumulation of hydrocarbons in the Meso-Cenozoic complex of the Black Sea-Caspian region. The simulation results made it possible to study and model the processes of migration and accumulation of hydrocarbons in the hydrocarbon systems of the Meso-Cenozoic complex of the Black Sea-Caspian region. All modeled hydrocarbon systems are characterized by migration from the main reservoir, which lies directly above the modeled oil and gas source formations, to the overlying ones. This is due to the peculiarities of the formation of sedimentary formations under conditions of alternating regressions and transgressions. The factor stimulating migration is the active tectonic regime of the studied sedimentary basins. Based on the modeling results, the conclusion about the wide development of hydrocarbon filtration processes is consistent with the presence of multilayer deposits. It has been established that the areas of subsidence are characterized by extended catagenetic zoning, which is due to the high rates of sedimentation and subsidence and, accordingly, the large thickness of oil source deposits in the area of oil formation. As a result of the research, four areas of stable subsidence (hollows) were identified for the entire period of formation of the plate cover: Karkinitzskaya, Indolo-Kubanskaya, East Kubanskaya, and Terek-Caspian. All modeled generation-accumulation hydrocarbon systems are characterized by flows (to a greater or lesser extent) from the main reservoir, which lies directly above the modeled source reservoirs, to the overlying ones. A joint analysis of the actual oil and gas potential and

hydrocarbon accumulations predicted by the modeling results within the study area showed that the vast majority of discovered deposits and manifestations are genetically related to generation centers located within the identified sedimentary basins.

Keywords

Black Sea-Caspian region • Modeling • Migration • Accumulation • Oil and gas source strata • Deposit • Sediments • Organic matter

1 Introduction

The Black Sea-Caspian region is one of the oldest oil-producing regions. To date, 39 oil and gas fields have been discovered within the West Pre-Caucasian Petroleum Area (PA), including 17 gas fields, 21 gas condensate fields, and one oil field. A total of 32 oil and gas fields have been discovered within the East Kuban Petroleum Area, including 5 gas fields, 25 gas condensate/oil and gas condensate fields, and 2 oil fields. A total of 128 oil and gas fields have been discovered within the West Kuban Petroleum Area, including 90 oil fields and oil and gas fields, 23 gas fields, and 15 gas condensate fields. More than 200 oil and gas fields are found in the Terek-Caspian Petroleum Basin. The range of commercial oil and gas occurrence encompasses the entire complex of deposits overlapping the basement and spanning from the Triassic to Neogene (Kerimov et al., 2014, 2017a; Senin et al., 2020).

2 Research Technique

Hydrocarbon migration and accumulation processes in the Meso-Cenozoic complex of the Black Sea-Caspian region were modeled in the PetroMod software package. In order to characterize oil source rock intervals during modeling, we

V. Kerimov · R. Mustaev (✉) · E. Lavrenova · P. Romanov
Sergo Ordzhonikidze Russian State University for Geological
Prospecting, 117997 Moscow, Russian Federation
e-mail: mustaevrn@mgri.ru

V. Kerimov
Oil and Gas Institute of Azerbaijan's National Academy
of Sciences, AZ1000 Baku, Azerbaijan

used the following initial values of geochemical parameters: TOC—the percentage of organic carbon in sedimentary rocks; HI (hydrogen index)—the ratio between the amount of generated hydrocarbons (the S2 peak on a Rock–Eval

pyrolysis diagram) and the TOC; the type of organic matter, i.e., the type of kerogen, which is largely determined based on chemical and coal petrographic characteristics of kerogen (Lapidus et al., 2018).

Fig. 1 Models on the migration of hydrocarbons from Upper Jurassic (a) and Cretaceous (b) oil and gas source rock intervals (migration pathways of liquid and gaseous hydrocarbons are marked with respective green and red lines) (Kerimov et al., 2016, 2017b, 2018)

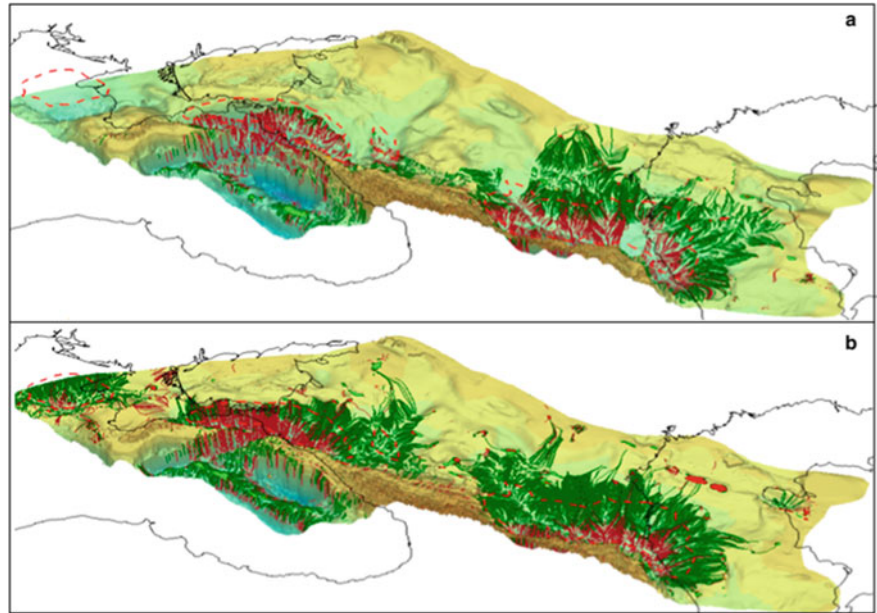
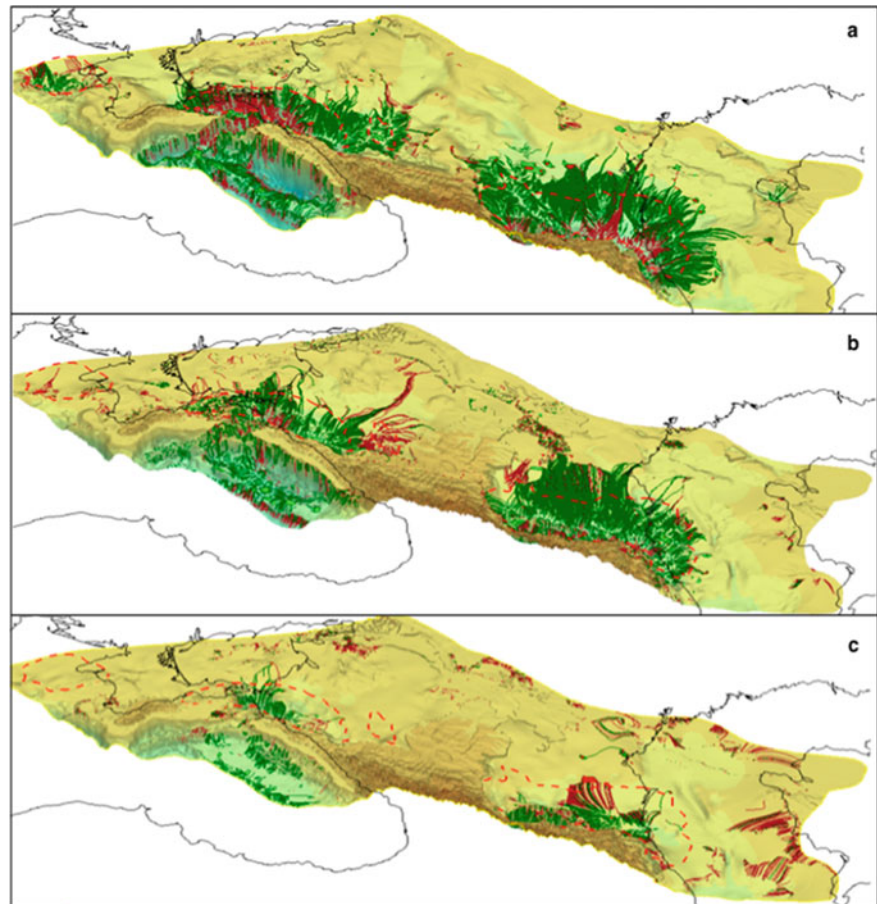


Fig. 2 Model on the migration of hydrocarbons from Eocene (a), Maikopian (b), and Miocene (c) oil and gas source rock intervals (migration pathways of liquid and gaseous hydrocarbons are marked with respective green and red lines) (Guliev et al., 2018; Kerimov et al., 2015; Rachinsky & Kerimov, 2015)



3 Results

The modeling results enabled us to examine and model the processes of hydrocarbon migration and accumulation in hydrocarbon systems in the Meso-Cenozoic complex of the Black Sea-Caspian region. The modeling results indicate (if we take persistent subsidence of the studied basins into account) that hydrocarbon migration proceeds toward their flanks. Hence, flank and near-flank zones represent areas where hydrocarbon accumulation is most probable (Figs. 1 and 2). The traps in the Central Stavropol system of uplifts are filled with hydrocarbons supplied from two sources. The East Kuban kitchen area supplies hydrocarbons from the west, while the Terek-Caspian kitchen area—from the east.

4 Conclusions

The modeling results have shown that the studied region comprises seven main sedimentary complexes (Upper Jurassic, Cretaceous, Paleocene-Eocene, Maikopian, Miocene, Pliocene, and Quaternary) separated by regional unconformity surfaces. The main prospective complex within the territory under study is made up of Cretaceous deposits. Their hydrocarbon saturation is provided both by their own oil and gas source rock interval and by flows from the deeper horizons in the sedimentary cover. The Paleogene complex ranks second in importance.

References

- Guliev, I. S., Mustaev, R. N., Kerimov, V. Y., Yudin, M. N. (2018) Degassing of the Earth: Scale and implications. *Gornyi Zhurnal*, 11, 38–42.
- Kerimov, V. Y., Osipov, A. V., Mustaev, R. N., Monakova, A. S. (2014). Modeling of petroleum systems in regions with complex geological structure. In *16th Science and applied research conference on oil and gas geological exploration and development*, GEOMODEL.
- Kerimov, V. Yu., Mustaev, R. N., Dmitrievsky, S. S., Yandarbiev, N. Sh., Kozlova, E. V. (2015). The shale hydrocarbons prospects in the low permeability khadam formation of the Pre-Caucasus. *Neftyanoe Khozyaystvo*, 10, 50–53.
- Kerimov, V. Yu., Shilov, G. Ya., Mustaev, R. N., Dmitrievsky, S. S. (2016). Thermobaric conditions of hydrocarbons accumulations formation in the shale low-permeability oil reservoirs of khadam suite of the Ciscaucasia. *Neftyanoe Khozyaystvo*, 2, 8–11.
- Kerimov, V. Yu., Lapidus, A. L., Yandarbiev, N. Sh., Movsumzade, E. M., Mustaev, R. N. (2017) Physicochemical properties of shale strata in the Maikop series of Ciscaucasia. *Solid Fuel Chemistry*, 51 (2), 122–130.
- Kerimov, V. Yu., Rachinsky, M. Z., Mustaev, R. N., Serikova, U. S. (2018). Geothermal conditions of hydrocarbon formation in the South Caspian basin. *Iranian Journal of Earth Sciences*, 10(1), 78–89.
- Kerimov, V. Y., Bondarev, A. V., & Mustaev, R. N. (2017a). Estimation of geological risks in searching and exploration of hydrocarbon deposits. *Neftyanoe Khozyaystvo*, 8, 36–41.
- Lapidus, A. L., Kerimov, V. Y., Mustaev, R. N., Salikhova, I. M., & Zhagfarov, F. G. (2018). Natural Bitumens: Physicochemical properties and production technologies. *Solid Fuel Chemistry*, 52 (6), 344–355.
- Rachinsky, M. Z., Kerimov, V. Yu. (2015). *Fluid dynamics of oil and gas reservoirs* (617 p). Wiley.
- Senin, B. V., Kerimov, V. Yu., Bogoyavlensky, V. I., Leonchik, M. I., & Mustaev, R. N. (2020). *Oil and gas bearing provinces of the seas of Russia and adjacent water areas* (340 p). Publishing House Nedra.



The Impact of Structural-Geodynamic Systems on the Formation and Distribution of Hydrocarbon Potential in the Black Sea-Caspian Region

Boris Senin, Rustam Mustaev, Vagif Kerimov, and Uliana Serikova

Abstract

The article presents the results of reconstruction and analysis of geodynamic conditions for the formation of the main structural elements in the Black Sea-Caspian region. The paper considers the basement and the sedimentary cover, united by the same type of reaction from an external or internal source of tectonic energy. The results of the research indicate that the predominantly offshore deep water Black Sea and South Caspian provinces are controlled by tectonic mega depressions that formed in the Alpine and recent epochs of tectogenesis. At the same time, both provinces include in their internal structure both elements that arose at different stages of Alpine and recent structure formation, as well as fragments of older plate and folded structures, reworked in these epochs and buried under Cenozoic or Cretaceous-Cenozoic deposits to varying degrees. The latter, in turn, partially or completely controls the position and configuration of the oil and gas regions within these provinces. We supplemented the data on the phase composition of hydrocarbon deposits with the results of the analysis of the location of deposits in relation to structural-geodynamic and basin systems of different ages. This allowed us to present a predictive scheme of zones of possible predominance of various types of fluids in the composition of potential accumulations and manifestations of hydrocarbons in the territories and offshore area of the region.

Keywords

Black Sea-Caspian region • Structural and geodynamic systems • Oil and gas provinces • Sedimentary basins • Phase composition • Hydrocarbon potential

1 Introduction

Hydrocarbon accumulations in the Black Sea-Caspian region (BCR) are found in four petroleum provinces. Of these, three provinces (the Black Sea Province, the Black Sea-North Caucasian-Mangyshlak Province and the South Caspian Province) lie nearly completely within the region, whereas the Caspian Province touches it with its southern part, while geographically belonging to the North Caspian shallow waters and the adjoining lowland territories of the Caspian Basin.

The Black Sea-Caspian region includes mature oil and gas producing areas, which are characterized by a fairly high degree of geological and geophysical exploration (including geological surveys, seismic, gravity and magnetic exploration, prospecting and exploration drilling and geochemical studies). At the same time, upon closer examination, it is obvious that most of the data (e.g., seismic surveys) obtained in the 70–90 s of the last century are characterized by low quality and resolution, which does not allow them to be used to solve geological problems at the modern technological level.

There are a large number of generalizing works, some of which are outdated and do not correspond to newly obtained data. Nevertheless, the existing scientific groundwork has formed a reliable basis for revising and rethinking retrospective and modern geological materials, updating geological models, integration and analysis from the standpoint of the concept of generation-accumulation hydrocarbon systems. This kind of comprehensive research has not been previously carried out, although the need for data systematization is long overdue.

B. Senin
Soyuzmorgeo OJSC, 353461 Gelendzhik, Russia

R. Mustaev · V. Kerimov (✉) · U. Serikova
Sergo Ordzhonikidze Russian State University for Geological
Prospecting, 117997 Moscow, Russian Federation
e-mail: vagif.kerimov@mail.ru

V. Kerimov
Oil and Gas Institute of Azerbaijan's National Academy
of Sciences, AZ1000 Baku, Azerbaijan

2 Research Technique

In the course of our studies, structural-geodynamic systems were examined by applying classical approaches to reconstructing depositional conditions (facies and thickness analysis, formational analysis of deposits and hiatuses and unconformities) using available archived and published data. The reconstruction of the evolution undergone by the sedimentary basins throughout the entire geologic history was based on structural-geodynamic paleoreconstructions and was conducted using the technologies of basin analysis and hydrocarbon system modeling in Schlumberger's PetroMod software package. The results from these studies were integrated into 3D models while taking geodynamics and geofluid dynamics into consideration. The modeling of generation-accumulation hydrocarbon systems (GAHS) is a modification of basin analysis based on the numerical modeling of geologic processes such as the deposition of sediments, their compaction, thermal regime, hydrocarbon generation, expulsion, migration and accumulation proceeding in sedimentary basins.

3 Results

The following work was completed as part of our studies into the conditions conducive to the formation of sedimentary basins in the BCR and regularities behind their distribution: we performed basin analysis, summarized the results from earlier studies, constructed lithologic-paleogeographic schematic maps, paleogeographic maps and maps showing the extent of sedimentary basins. Basin analysis involved generating depth structure maps and thickness maps based on the reviewed G&G data. These maps allowed us to trace a

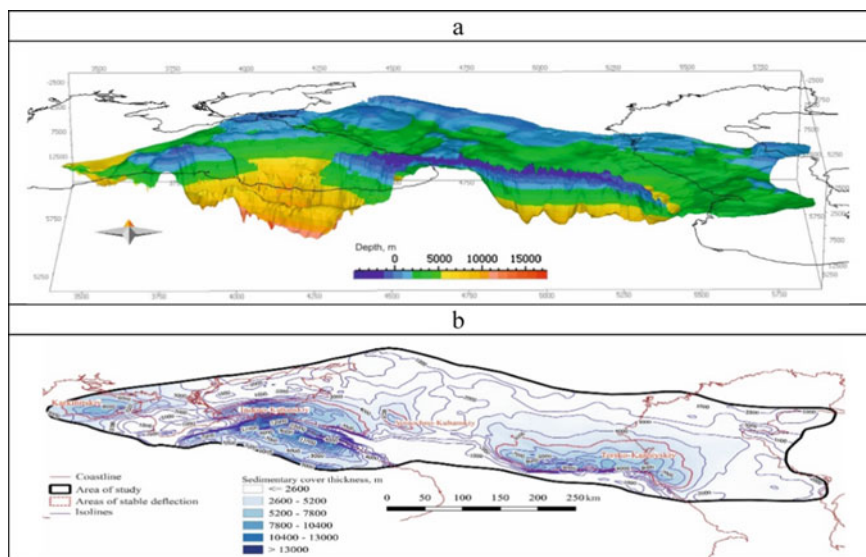
shift in the depocenters, identify particular aspects related to the formation of sedimentary basins, define their boundaries, and distinguish sizeable areas of persistent downwarping (Fig. 1).

The plate cover in the detailed analysis zone within the Scythian-Turan basin system as well as the necessary elements for the Mesozoic generation-accumulation systems began to take shape in the framework of Alpine structural-geodynamic systems. The maximum expression of sedimentary basins is attributed to the transgressive Cretaceous period, which saw the expansion of areas taken up by pre-existing basins and the appearance of new depocenters. The analysis of their areal extent in terms of structural-geodynamic systems shows that the depressions lay within different systems and in different tectonic settings. Notably, two groups of Cretaceous basins can be identified. The first one includes the Karkinit, Greater Caucasian, West Kuban, Central Caspian and Terek-Caspian basins, which are confined to the areas of general extension and subsidence in regions dominated by the continental or transitional Earth's crust, or areas with a reversive geodynamic regime dominated by extension and subsidence within the boundaries of cratons and mobile areas. The basins of this group are marked by relatively higher than average sedimentation rates and thicknesses exceeding 1500 m. Sediments attain their maximum thickness (up to 5000 m and more) in the Greater Caucasian and Karkinit Cretaceous depocenters.

By collating the distribution of hydrocarbon fields with areas taken up by heterochronous structural-geodynamic systems (Fig. 2), we can see differences in their component composition depending on which system they territorially belong to.

With respect to the Paleozoic structural-geodynamic system (see Fig. 2a) it should be primarily noted that it

Fig. 1 Model (a) and Scheme (b) of sedimentary basins —areas of stable subsidence of the Black Sea-Caspian region



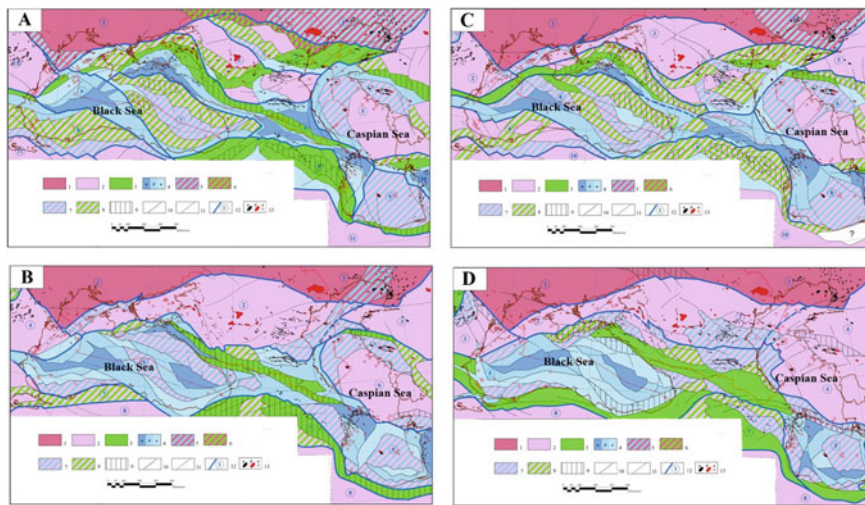
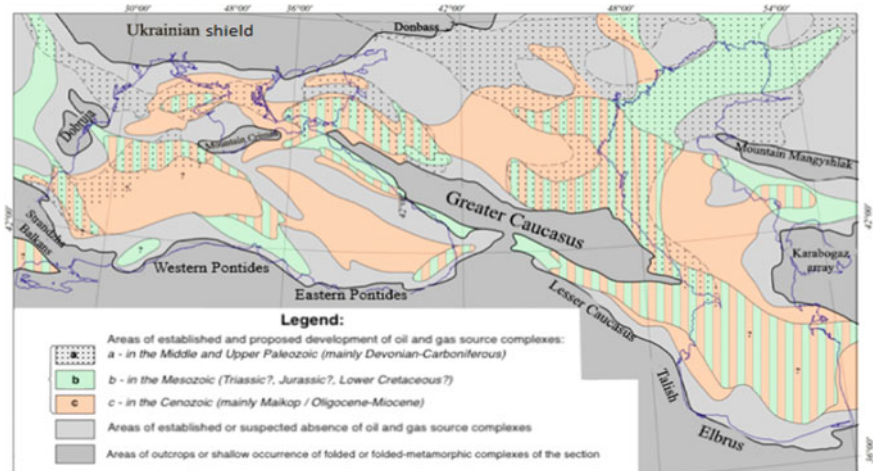


Fig. 2 Distribution of hydrocarbon fields/accumulations relative to heterochronous structural-geodynamic systems (Kerimov et al., 2014) Legend: **a** Late Paleozoic, **b** Mesozoic, **c** Alpine, **d** Recent. 1–3—Areas of overall compression, predominant uplift or relative stabilization in the setting of cratons, moving cratons, folded orogenic belts, systems: 1—Continental blocks/megablocks of cratons, 2—Same of mobile platforms 3—Folded orogenic belts, systems, 4—Areas of overall extension and subsidence in the regions dominated by continental or transitional crust: **a** Axial (rift-driven?) troughs with local areas of transitional or oceanic crust; **b** Intense crushing and subsidence of continental blocks; **c** Relative compression and subtle uplift in the belts and zones of overall extension; 5–8—Areas of alternate/pulsating (reversing) geodynamic regime: 5—Dominated by extension and subsidence settings within craton boundaries, 6—Dominated by compression and uplift within craton boundaries, 7—Dominated by

extension and subsidence in mobile areas, 8—Dominated by compression and uplift in mobile areas, 9—Localized folded orogenic and arched—block uplifts/assemblages, 10—Boundaries of structural-tectonic elements, 11—Rupture dislocations, major tectonic lineaments, 12—Structural-geodynamic systems and their indexes (1—Southern margin of the East European Craton, 2—Donetsk-Astrakhan/Buzachi-Embin, 3—North Scythian (Scythian), 4—Crimean-Caucasian, 5—West Turanian, 6—West Black Sea, 7—Eastern Black Sea, 8—Pontian-Transcaucasian, 9—South Caspian, 10—South Turkmenian/Kopet Dag, 11—Anatolian-Iranian, 12—Mizian), 13—Fields: **a** Oil fields, **b** Gas and gas condensate fields, **c** Areas that have not yielded positive results (see also Fig. 1). Other notations: Red dotted line—State borders of the Russian Federation and some internationally recognized delimitation lines of maritime boundaries

Fig. 3 Schematic map showing possible distribution of heterochronous oil source rock complexes in the Black Sea-Caspian region (Kerimov et al., 2016)



had formed much earlier than the overwhelming majority of the region’s fields, as has been shown above. Oil and gas source rock horizons which had been in basin structures during the period of its formation were substantially metamorphosed over vast swathes or destroyed by movements (Kerimov et al., 2017).

Still, several structural elements that formed during this epoch or earlier epochs of structure formation and that retained relative mobility during the latest periods, had a definite impact on the distribution of both single-component gas fields and multi-component fields located along linear structures that bound or cut them (see Fig. 2a).

Fields with a considerable or absolute prevalence of the gaseous component are concentrated in the northern and western parts of the region. During the Mesozoic and Cenozoic, (see Fig. 2b–d) they are largely marked by platform stabilization settings or an alternate regime dominated by compression and weak swell.

Results obtained by generalizing data on the oil and gas source rock properties of geologic section in the areas of the Black Sea-Caspian region and lithologic-paleogeographic reconstructions enabled us to model a generalized schematic map showing the possible distribution of heterochronous oil source rock complexes within the region's boundaries (Fig. 3).

4 Conclusions

The results of the research make it possible to present a generalized scheme of the prospects for the oil and gas potential of the region. It is based on the analysis of the location of deposits in relation to structural-geodynamic and basin systems of different ages, the assessment of the

resources of its territories and offshore areas (Guliev et al., 2018; Lapidus et al., 2018).

References

- Guliev, I. S., Mustaev, R. N., Kerimov, V. Y., Yudin, M. N. (2018). Degassing of the Earth: Scale and implications. *Gornyi Zhurnal*, 11, 38–42.
- Kerimov, V. Y., Osipov, A. V., Mustaev, R. N., Monakova, A. S. (2014). Modeling of petroleum systems in regions with complex geological structure. In: *16th Science and Applied Research Conference on Oil and Gas Geological Exploration and Development*, GEOMODEL 2014.
- Kerimov, V. Yu., Shilov, G. Ya., Mustaev, R. N., Dmitrievsky, S. S. (2016). Thermobaric conditions of hydrocarbons accumulations formation in the shale low-permeability oil reservoirs of khadum suite of the Ciscaucasia. *Neftyanoe Khozyaystvo*, 2, 8–11.
- Kerimov, V. Y., Bondarev, A. V., & Mustaev, R. N. (2017). Estimation of geological risks in searching and exploration of hydrocarbon deposits. *Neftyanoe Khozyaystvo*, 8, 36–41.
- Lapidus, A. L., Kerimov, V. Y., Mustaev, R. N., Salikhova, I. M., & Zhagfarov, F. G. (2018). Natural Bitumens: Physicochemical properties and production technologies. *Solid Fuel Chemistry*, 52 (6), 344–355.



Generation and Emigration of Hydrocarbons in the Meso-Cenozoic Complex of the Black Sea-Caspian Region

Vagif Kerimov, Rustam Mustaev, Elena Lavrenova, and Uliana Serikova

Abstract

As part of the assessment of the oil and gas content of the study area, numerical modeling of hydrocarbon generation and accumulation systems was performed, as a result of which hydrocarbon generation centers located within sedimentary basins were identified. Based on the levels of modern maturity and transformation of organic matter of established and proposed oil and gas source rocks, as well as the obtained estimates of the specific densities of hydrocarbon emigration at different stratigraphic levels, independent generation centers were identified: Middle Jurassic, Lower Cretaceous, Eocene, Maikop, and Miocene. Fluctuations in the sinking rate of basins at different stages of their development had a decisive influence on the realization of their generation potential by oil and gas source strata. As a result, the coeval oil and gas source strata of the basins at different times overcame the critical moment and by now have realized their potential to varying degrees. In basins with low subsidence rates, there is a delay in the emigration process in relation to generation, which is not typical for basins with high rates. The main promising complex within the study area is Cretaceous deposits, the hydrocarbon saturation of which is provided both by their own oil and gas source strata and by outcrops from deeper horizons of the sedimentary cover. The second most important is the Paleogene complex. Periodic tectonic activity within the study area, starting from the end of the Paleogene, created conditions for vertical hydrocarbon flows and the formation of multilayer deposits.

V. Kerimov · R. Mustaev (✉) · E. Lavrenova · U. Serikova
Sergo Ordzhonikidze Russian State University for Geological
Prospecting, 117997 Moscow, Russian Federation
e-mail: mustaevrn@mgri.ru

V. Kerimov
Oil and Gas Institute of Azerbaijan's National Academy
of Sciences, AZ1000 Baku, Azerbaijan

Keywords

Black Sea-Caspian region · Meso-Cenozoic complex ·
Catagenetic zoning · Modern maturity of deposits ·
Degree of transformation of organic matter ·
Generation · Emigration · Critical moment

1 Introduction

Patterns behind the distribution of hydrocarbon accumulations in the Meso-Cenozoic complex of the Black Sea-Caspian region are linked with the evolution of generation-accumulation systems found in the region's plate cover. The plate cover and the elements of the Mesozoic generation-accumulation systems began to take shape in the structure of Alpine structural-geodynamic systems. The most significant events that determined specific aspects of GAHS evolution are attributed to the recent time (Guliev et al., 2018).

2 Research Technique and Input Data for Modeling

Numerical basin modeling in the space-time domain was performed using Schlumberger's PetroMod software package and modeling technologies. It was aimed at achieving a more profound understanding of how the intricate interconnected system of hydrocarbon systems is functioning.

The numerical modeling of GAHS involved analyzing the impact of the tectonic evolution of sedimentary basins on the realization of hydrocarbon-generating potential and expulsion potential by oil and gas source rock intervals. As has been pointed out above, in order to do this, identical initial geochemical characteristics (TOC, hydrogen index, kinetic reaction) were assigned to the modeled oil and gas source rock intervals at each stratigraphic level. Hence,

differences in the realization of initial potential will be dictated solely by specific features of tectonic and thermal regimes of sedimentary basins hosting them (Kerimov et al., 2017).

3 Results

The results obtained by basin analysis determined the modeling strategy and the scope of tasks to be solved. These tasks involve identifying the main oil and gas kitchen areas, determining specific aspects of the evolution undergone by oil and gas source rocks and their realization of hydrocarbon-generating potential, establishing a relationship between actual oil and gas occurrence in the sedimentary cover and hydrocarbon kitchen areas, identifying areas with the most probable hydrocarbon accumulation and selecting new directions in prospecting.

The 3D modeling produced maps showing the present-day maturity of organic matter in modeled oil and gas source rock intervals (Figs. 1 and 2). The maturity of rocks is determined by the depth of their burial and rises with increasing age. By way of example, the highest values of calculated vitrinite reflectance were obtained for the Middle Jurassic oil and gas source rock interval. Within the identified basins (except the Karkinit Basin, where Middle Jurassic rocks are missing), organic matter maturity matches the level of predominant gas generation or is overheated (in the Indolo-Kuban depocenters and the southwestern part of the Terek-Caspian depocenter). Mature rocks extend also beyond the identified basins.

High present-day maturity is also typical of the Cretaceous oil and gas source rock interval. Its organic matter is overheated in the western part of the Indolo-Kuban Basin. In others, organic matter maturity varies from late oil generation to late gas generation.

Fig. 1 Maps showing present-day maturity: **a**—of Middle Jurassic deposits; **b**—of Lower Cretaceous deposits (Kerimov et al., 2014)

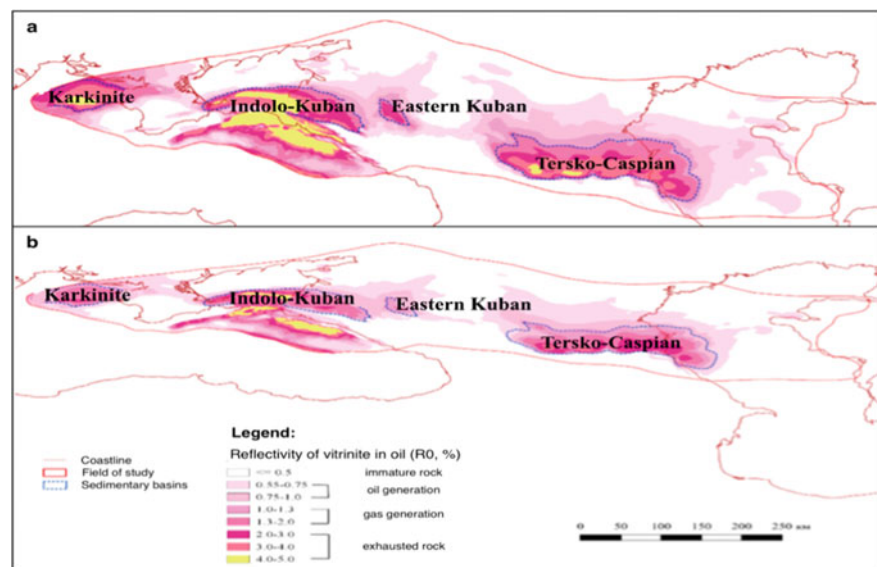
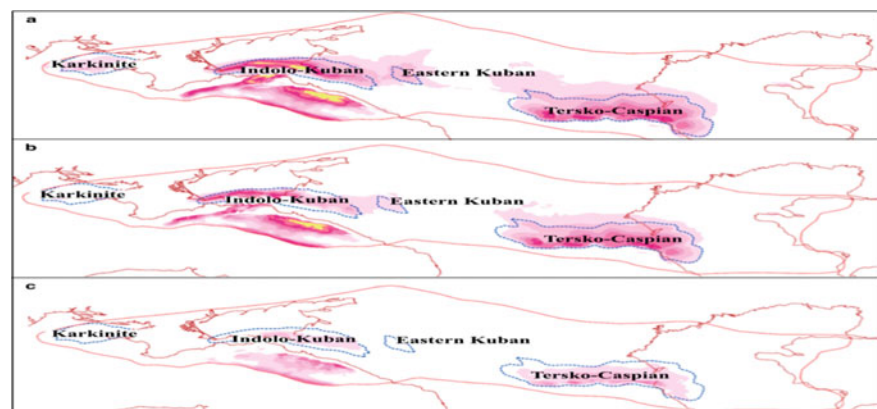


Fig. 2 Maps showing the present-day maturity of Eocene (a), Maikopian (b) deposits, and Miocene (c) deposits (Lapidus et al., 2018). For legend see Fig. 1b



In the Indolo-Kuban and Terek-Caspian Basins, the organic matter maturity in the Paleogene oil and gas source rock interval is almost on a par with that of the Cretaceous source rock interval. In the Karkinit and East Kuban depocenters, maturity is lower, i.e., on a par with the oil window.

In the Maikopian deposits, high levels of organic matter maturity persist in the Indolo-Kuban and Terek-Caspian Basins. In the East Kuban Basin, OM maturity does not exceed the level of early oil generation, while it is immature in the Karkinit Basin over much of the basin.

In the Miocene section, mature rocks are predicted solely in the Indolo-Kuban and Terek-Caspian Basins. Their maturity does not exceed the level of early oil generation.

The degree of catagenetic alteration reached by oil and gas source rock intervals found within it is the main characteristic of a hydrocarbon kitchen area. Together with the type of initial organic matter it determines the fluid content of generated fluids (Kerimov et al., 2016). The position of the main oil generation zone was determined using calculated vitrinite reflectance values.

The 3D modeling has resulted in producing maps of the calculated TR index representing the present-day alteration of organic matter (kerogen) in modeled oil and gas source rock intervals.

4 Conclusions

The following independent hydrocarbon kitchen areas have been distinguished at five stratigraphic levels based on the levels of present-day maturity and organic matter alteration

in known and inferred oil and gas source rocks as well as based on the obtained estimates of specific density of hydrocarbon expulsion: *Middle Jurassic* (Indolo-Kuban, East Kuban, Terek-Caspian), *Lower Cretaceous* (Karkinit, Indolo-Kuban, East Kuban, Terek-Caspian), *Eocene* (Karkinit, Indolo-Kuban, East Kuban, Terek-Caspian), *Maikopian* (Karkinit, Indolo-Kuban, East Kuban, Terek-Caspian), and *Miocene* (Indolo-Kuban, Terek-Caspian). Thus, the sedimentary basins under study differ, among other things, in the presence and distribution of hydrocarbon kitchen areas throughout the section.

References

- Guliev, I. S., Mustaev, R. N., Kerimov, V. Y., & Yudin, M. N. (2018). Degassing of the Earth: Scale and implications. *Gornyi Zhurnal*, 11, 38–42.
- Kerimov, V. Y., Osipov, A. V., Mustaev, R. N., & Monakova, A. S. (2014). Modeling of petroleum systems in regions with complex geological structure. In *16th science and applied research conference on oil and gas geological exploration and development*, GEOMODEL.
- Kerimov, V. Yu., Shilov, G. Ya., Mustaev, R. N., & Dmitrievsky, S. S. (2016). Thermobaric conditions of hydrocarbons accumulations formation in the shale low-permeability oil reservoirs of khadum suite of the Ciscaucasia. *Neftyanoe Khozyaystvo*, 2, 8–11.
- Kerimov, V. Y., Bondarev, A. V., & Mustaev, R. N. (2017). Estimation of geological risks in searching and exploration of hydrocarbon deposits. *Neftyanoe Khozyaystvo*, 8, 36–41.
- Lapidus, A. L., Kerimov, V. Y., Mustaev, R. N., Salikhova, I. M., & Zhagfarov, F. G. (2018). Natural Bitumens: Physicochemical properties and production technologies. *Solid Fuel Chemistry*, 52 (6), 344–355.

Geochemistry and Volcanology



Model Validation of Passive Gas Dispersion: Examples from La Solfatara (Campi Flegrei, Italy) and Caldeiras Da Ribeira Grande (São Miguel Island, Azores)

Silvia Massaro, Manuel Stocchi, Giancarlo Tamburello, Fabio Dioguardi, Antonio Costa, Laura Sandri, Jacopo Selva, Giovanni Macedonio, Arnau Folch, Fátima Viveiros, Giovanni Chiodini, Stefano Caliro, and César Andrade

Abstract

The emission of volcanic gases can occur during both eruptive and quiescent stages of volcanic activity, affecting air quality in the surrounding areas and threatening human health when the concentrations exceed species-specific thresholds. In this regard, quantitative studies of model validation are essential before applying a simulator for probabilistic volcanic hazard assessment. Here, we provide a model validation aimed at testing the accuracy in providing realistic values of CO₂ concentration at two active volcanic sites affected by persistent passive gas dispersion: La Solfatara (a maar crater within Campi Flegrei caldera, Italy) and Caldeiras da Ribeira Grande located in the north flank of Fogo volcano (São Miguel Island, Azores). We used published and original CO₂ flux data as input for numerical simulations run through VIGIL, an open-source workflow for parallel simulations and probabilistic output using two Eulerian models,

which account for the passive and gravity-driven gas transport, respectively. At Solfatara, we compared a 1-month-long simulation during June 2020 with CO₂ concentration acquired by the INGV measurement station at 4 m from the ground in a selected point close to Pisciarelli vent: Our results showed a good correlation between the daily simulated and observed averages of CO₂ concentrations. At Caldeiras da Ribeira Grande, we quantified the CO₂ concentration at 43 tracking points, each referring to a specific acquisition (in space and time) during 13 selected days in July 2021. The comparison between the 1-month-long simulation and the observed data provided acceptable accordance. In both cases, we noted that the daily averaged concentrations provided by the model do not exceed the gas hazardous threshold limits. However, for shorter timescales (hours), a higher data acquisition rate is needed for future investigation.

Keywords

CO₂ flux • Passive gas dispersion • Model validation

S. Massaro (✉) · F. Dioguardi
Dipartimento Di Scienze Della Terra E Geomambientali,
Università Degli Studi Di Bari, Via E. Orabona 4,
70125 Bari, Italy
e-mail: silvia.massaro@uniba.it

S. Massaro · M. Stocchi · G. Tamburello · A. Costa · L. Sandri ·
J. Selva · G. Chiodini
Istituto Nazionale Di Geofisica E Vulcanologia,
Sezione Di Bologna, Via D. Creti 12, 40128 Bologna, Italy

G. Macedonio · S. Caliro
Istituto Nazionale Di Geofisica E Vulcanologia, Via Diocleziano
328, 80124 Napoli, Osservatorio Vesuviano, Italy

A. Folch
Geosciencias Barcelona (GEO3BCN-CSIC),
Carrer de Lluís Solé I Sabarís, 08028 Barcelona, Spain

F. Viveiros · C. Andrade
Universidade Dos Açores, Rua da Mãe de Deus,
9501-801 Ponta Delgada, Portugal

C. Andrade
University of the Azores, Ponta Delgada, Portugal

1 Introduction

Active volcanoes emit gases continuously and may present a long-term hazard for the type and concentration levels of the volcanic species dispersed in the atmosphere (e.g., CO₂, H₂S, and SO₂). The threats for humans cover a wide spectrum of effects from respiratory irritation to death, for animals and environment in terms of crop failure and famine (e.g., Costa et al., 2005). In the last decades, density-driven and passive volcanic gas transport models have been largely employed in active volcanic areas for gas dispersal validations and for probabilistic volcanic hazard assessment applications (e.g., Massaro et al., 2021). In this work, we present a model validation at two sites, La Solfatara crater (Campi Flegrei, Italy) and Caldeiras da Ribeira Grande (São

Miguel Island, Azores), aimed to test whether the statistical properties of the natural variability displayed by the observed averages of CO₂ concentrations are satisfactorily reproduced by numerical simulations, confirming this procedure as key tool to produce unbiased hazard quantification in the future.

2 Methods

To carry on the model validation, we used VIGIL (v.1.2; (Dioguardi et al., 2022)), a probabilistic workflow which uses two Eulerian codes for passive and/or density-driven gas dispersion (DISGAS, v. 2.3; (Costa & Macedonio, 2016); TWODEE-2, v. 2.3; (Folch et al., 2009)) that are coupled with the mass-consistent Diagnostic Wind Model (DIAGNO; (Douglas et al., 1990)).

La Solfatara (Campi Flegrei; Fig. 1a) is characterized by a widespread soil release of CO₂ that is passively emitted by the most active fumarolic vents, located in the eastern slope and inside the crater. For this case study, we performed a 1-month-long simulation of dilute gas emission and dispersal using DISGAS. As weather data, we considered the daily local wind conditions acquired by the meteorological sensor placed on the INGV measurement station (Fig. 1a) at 4 m above the ground. The diffusive gas sources were simulated by discretizing in the emission area the total constant emission of ca. 6.7 kg s⁻¹ (Massaro et al., 2022), along with fumaroles at Pisciarelli (6.94 kg s⁻¹; Tamburello et al., 2019) and within the crater (ca. 3.22 kg s⁻¹; Massaro et al., 2022). The simulated and observed concentrations were compared at 4 m above the ground considering that the weather measurements are referred to that height.

At Caldeiras da Ribeira Grande, a survey was carried out on the north flank of the volcano to acquire soil CO₂ flux and concentration in the atmosphere (Fig. 2a). We simulated a continuous CO₂ dispersion, focusing the attention on 43 tracking points, each of them corresponding to a specific

acquisition of CO₂ concentration (in space and time) during 13 selected days in July 2021 (Fig. 2b). The corresponding observed data were obtained by calculating the mean and the variance of all the available concentration measurements performed 30 min before and after the tracking point acquisition and within a 20 m radius. The meteorological conditions were retrieved from the local weather station whose sensors are set about 1 m above the ground.

3 Results

At La Solfatara, the monthly average of the simulated CO₂ concentrations within the computational domain is shown in Fig. 1a, with values less than 5000 ppm (i.e., time weighted limit for human health, 8 h/day for 5 days a week). We compared the observed and simulated CO₂ concentrations, providing the daily, 12-h and 4-h averages along with the confidence interval at 90% represented by the black and red shaded bands, respectively (Fig. 1b). The Pearson's product-moment correlation was calculated with 3 time-averaging windows: at the significance level 0.05, only the daily-averaged time series show a significant correlation ($R: 0.49$; p -value: 0.0007), while shorter time intervals seem to be affected by poor weather and concentration acquisition frequency (2 h), which may strongly impact averages over few hours.

At Caldeiras da Ribeira Grande, we compared the observed and simulated data at 1.5 m from the ground for the 43 tracking points (Fig. 2b). We used the approach presented in Massaro et al. (2021) calculating the Empirical Cumulative Density Functions (ECDFs). In order to reproduce the observed concentrations, we scaled the fumarolic flux by different scaling factors. Preliminary results (Fig. 2c), based on the calculation of the Aida indexes and bias [e.g., (Poret et al., 2017)], indicate the best agreement between simulated and observed data scaled by a factor of 150; however, further investigations are still in progress.

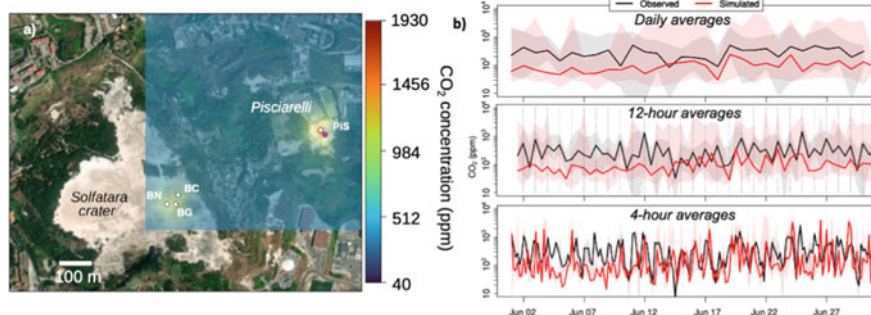


Fig. 1 a Map of La Solfatara crater (Campi Flegrei) showing the fumarolic sources and the measurement station; overlaid the map showing the simulated monthly average of CO₂ concentration;

b observed and simulated averages of CO₂ concentration (ppm) at 4 m from the ground for June 2020 performed with VIGIL

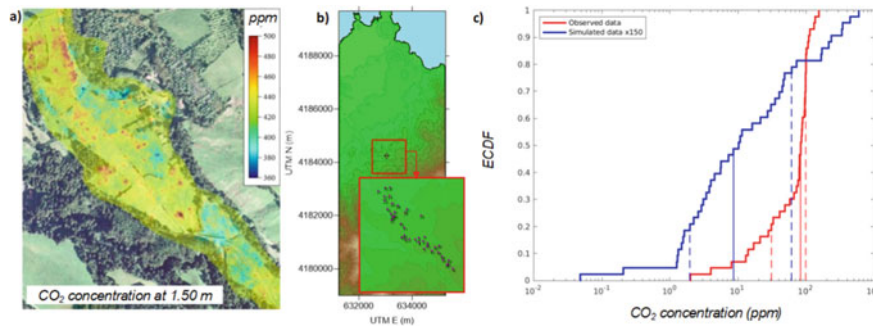


Fig. 2 a Map of the investigated area at Caldeiras da Ribeira Grande (Azores) showing the CO₂ concentration acquired in July/August 2021; b location of the 43 tracking points; c ECDFs showing the observed

data and simulated data obtained scaling the fumarolic flux by a factor of 150 (vertical lines are referred to 20th percentile (dotted) and 80th (solid))

4 Discussion and Conclusions

A model validation for testing the accuracy of DISGAS in providing realistic results was carried at two case studies. At La Solfatara, our results showed a good correlation between the daily simulated and observed averages of CO₂ concentrations at 4 m from the ground, in the selected point where concentration measurements were available. At Caldeiras da Ribeira Grande, the model validation is still in progress, but preliminary results indicate that a good accordance with observations can be found scaling the fumarolic flux by a factor of 150. It is worth noting that, for both case studies, we observed that the simulated monthly averaged concentration does not exceed the gas hazardous threshold limits for human health. However, new surveys will be planned to provide higher data acquisition rate needed for more accurate validations that represent a preliminary step to get probabilistic gas hazard assessments in active volcanic areas.

References

- Costa, A., Macedonio, G., & Chiodini, G. (2005). Numerical model of gas dispersion emitted from volcanic sources. *Annals of Geophysics*, 48, 4–5 (2016).
- Costa, A., & Macedonio, G. (2016). *DISGAS: A model for passive DISpersion of GAS*. Rapporti tecnici INGV. 332. Istituto Nazionale Di Geofisica e Vulcanologia, Italy.
- Dioguardi, F., Massaro, S., Costa, A., Chiodini, G., Folch, A., Macedonio, G., Sandri, L., Selva, J., & Tamburello, G. (2022). VIGIL: A python tool for automatized probabilistic Volcanic Gas dispersion modelling. *Annals of Geophysics*, 65(1), DM107.
- Douglas, S.G., Kessler, R.C., Carr, E.L. (1990). *User's guide for the urban airshed model* (Vol. 3). User's manual for the Diagnostic Wind Model (No. PB-91-131243/XAB). Systems Applications, Inc., San Rafael, CA (USA).
- Folch, A., Costa, A., & Hankin, R. K. S. (2009). TWODEE-2: A shallow layer model for dense gas dispersion on complex topography. *Computers & Geosciences*, 35, 667–674.
- Massaro, S., Dioguardi, F., Sandri, L., Tamburello, G., Selva, J., Moune, S., Jessop, D. E., Moretti, R., Komorowski, J.-C., & Costa, A. (2021). Testing gas dispersion modelling: A case study at La Soufrière volcano (Guadeloupe, Lesser Antilles). *Journal of Volcanology and Geothermal Research*, 417.
- Massaro, S., Stocchi, M., Tamburello, G., Costa, A., Sandri, L., Caliro, S., Chiodini, G., Selva, J., Dioguardi, F., & Folch, A. (2022). Validating gas dispersion modelling at La Solfatara Campi Flegrei, South Italy. *Nuovo Cimento Della Società Italiana Di Fisica C*, 45 (6), 186.
- Poret, M., Costa, A., Andronico, D., Scollo, S., Gouhier, M., & Cristaldi, A. (2017). Modeling eruption source parameters by integrating field, ground-based, and satellite-based measurements: The case of the 23 February 2013 Etna paroxysm. *Journal of Geophysical Research: Solid Earth*, 123, 5427–5450.
- Tamburello, G., Caliro, S., Chiodini, G., De Martino, P., Avino, R., Minopoli, C., Carandente, A., Rouwet, D., Aiuppa, A., Costa, A., Bitetto, M., Giudice, G., Francoforte, V., Ricci, T., Sciarra, A., Bagnato, E., & Capecchiacci, F. (2019). Escalating CO₂ degassing at the Pisciarelli fumarolic system, and implications for the ongoing Campi Flegrei unrest. *Journal of Volcanology and Geothermal Research*, 384, 151–157.



Vertical Geochemical Trends in the Juvenile Clasts from the 79 AD Plinian Fallout Deposits

Giulia Chiominto, Lorenzo Fedele, Claudio Scarpati, Annamaria Perrotta, and Ileana Santangelo

Abstract

The 79 AD Vesuvius eruption was characterized by two main phases: a sustained column Plinian phase, which deposited a thick white to grey pumice lapilli fallout deposit, followed by a column collapse phase, which emplaced several pyroclastic density current deposits. These latter are interstratified with five, minor, thin and lithic-rich fallout layers. The internal structure of the Plinian fallout deposit is weakly stratified, as observed at several studied locations from the Vesuvius slopes up to 20 km from the vent. Here we present chemical analyses for pumice lapilli samples collected at three type-locations representatives of the proximal, medial and distal facies of the deposits. The investigated samples display well-defined variations with respect to the stratigraphic height, both within the entire fallout sequence and within the individual layers recognized. The more evolved phonolitic white pumice clasts show a clear vertical gradient in all major and trace elements with, e.g. MgO, TiO₂ and Sr linearly increasing from 0.21 to 0.73 wt.%, 0.22 to 0.35 wt.% and 389 to 605 ppm, while Al₂O₃, Zr and Nb decrease from 21.8 to 20.6 wt.%, 350 to 312 ppm and 70 to 60 ppm, respectively. The tephriphonolitic grey pumice clasts have a less evolved composition (e.g. MgO 1.65–1.85 wt.%, TiO₂ 0.56–0.59 wt.%, Al₂O₃ 19.1–19.2 wt.%, Zr 270–297 ppm, Sr 845–915 ppm and Nb 49–50 ppm) and do not display appreciable vertical geochemical trends. These variations indicate a decrease in the degree of magma evolution as

eruption proceeded, likely related to the emptying of a stratified, compositionally zoned magma chamber, in line with previous literature. Interestingly, these vertical trends extend to the tephriphonolitic grey pumice clasts from the overlying post-Plinian lithic-rich fallout layers (e.g. MgO increasing from 1.93 to 3.03 wt.%, Nb decreasing from 51 to 45 ppm), analyzed here for the first time. This possibly supports the idea that also the lowermost portions of the magma chamber were compositionally stratified.

Keywords

Vesuvius • 79 AD • Plinian eruption • Fallout • Chemostratigraphy

1 Introduction

The petrochemical characterization of the juvenile components of the deposits of a volcanic eruption can provide useful insights both to the reconstruction of the pre- and syn-eruptive processes within magma reservoirs and feeding conduits, and to defining the factors involved and influencing the emplacement phase [e.g. (Fedele et al., 2016; Hildreth & Wilson, 2007; Williams et al., 2014)].

The 79 AD Vesuvius eruption consisted in a sustained column Plinian phase, producing a thick lapilli fallout deposit, more than 2 m thick, followed by a column collapse phase, which emplaced several pyroclastic density current deposits interstratified with minor lithic-rich fallout layers (Cioni et al., 1992, 1995, 1999). The deposits emplaced during the Plinian phase show a remarkable vertical chemical gradient in the juvenile component, from the lowermost white phonolitic to the topmost grey tephriphonolitic pumice clasts. In this paper, a chemostratigraphic characterization of selected type-sections for the 79 AD fallout deposits is reported.

G. Chiominto (✉) · L. Fedele · C. Scarpati · A. Perrotta · I. Santangelo
Dipartimento Di Scienze Della Terra, Dell'Ambiente E Delle Risorse (DiSTAR) – Università Degli Studi Di Napoli Federico II, Complesso Universitario Di Monte Sant'Angelo, Via Vicinale Cupa Cintia 21, 80126 Napoli, Italy
e-mail: giulia.chiominto@unina.it

2 Materials and Methods

The juvenile components of the 79 AD fallout deposits, belonging to both the Plinian and the post-Plinian eruptive phases, were sampled at various stratigraphic heights at three type-sections representative of proximal (Pompei), medial (Stabia) and distal exposures (Franche; Fig. 1). The 41 collected samples were processed and analyzed for petrochemical characterization at the DiSTAR laboratories (Naples). Samples were crushed, washed in deionized water, dried out and then pulverized in order to prepare pressed powder pellets, analyzed by XRF using a Panalytical Axios instrument. Uncertainties are within 1–2% and 5–10%, respectively, for major and trace elements. Weight loss on

ignition was determined gravimetrically after heating rock powders (pre-dried at ~ 150 °C overnight) at 950 °C for 3 h.

3 Results

The juvenile samples from the Plinian fallout deposits display a bimodal composition and a clear vertical geochemical gradient (Fig. 2). The compositional trends are evident not only within the entire sequence but also within the individual layers recognized, both in the medial and in the distal exposures. The lowermost, more evolved phonolitic white pumice clasts show a clear increase of MgO (0.21–0.73 wt.

Fig. 1 a DEM showing the location of the three stratigraphic sections where the juvenile clasts of the 79 AD fallout deposits were collected. Simplified composite stratigraphic sections of the studied outcrops are reported in b where the red dotted lines mark the distinction between the Plinian phase and the post-Plinian phase deposits

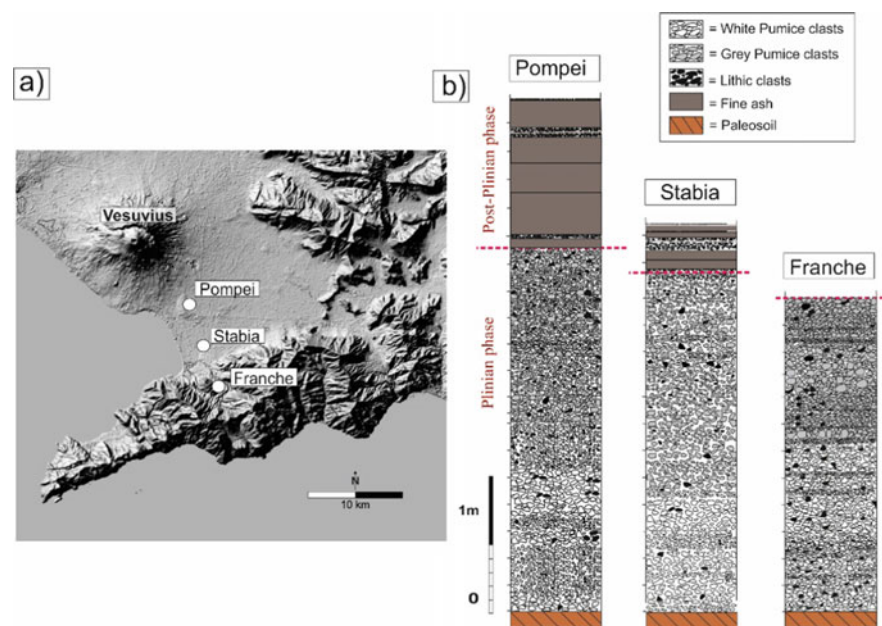
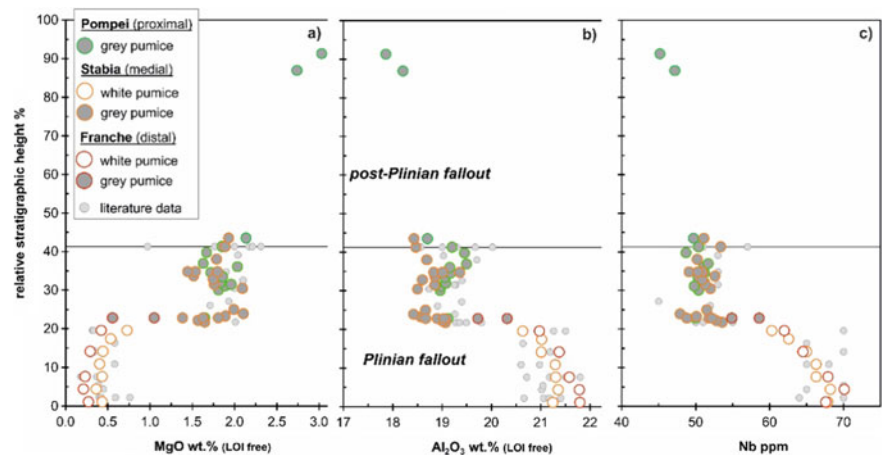


Fig. 2 Relative stratigraphic height versus a MgO, b Al_2O_3 and c Nb for the investigated juvenile samples from the 79 AD fallout deposits. Literature data from Cioni et al. (1992), Cioni et al. (1995), Barberi et al. (1981), Santacroce (1987), Civetta et al. (1991), Civetta and Santacroce (1992), Mues-Schumacher (1994)



%), TiO₂ (0.22–0.35 wt.%), Fe₂O₃tot (2.49–3.32 wt.%), Sr (389–605 ppm), Ba (185–611 ppm) and V (15–53 ppm) contents, together with a linear decline of Al₂O₃ (21.8–20.6 wt.%), Na₂O (6.65–5.40 wt.%), Rb (464–407 ppm), Zr (350–312 ppm) and Nb (70–60 ppm), with increasing stratigraphic height. The uppermost tephriphonolitic grey pumice clasts are less evolved in composition with, e.g. MgO 1.65–1.85 wt.%, TiO₂ 0.56–0.59 wt.%, Al₂O₃ 19.1–19.2 wt.%, Rb 366–378 ppm, Sr 845–915 ppm and Nb 49–50 ppm. No evident vertical geochemical trends can be recognized for these juvenile samples, except for few samples from the lowermost stratigraphic levels displaying a somewhat less evolved composition bridging the gap with the white pumice clasts.

The post-Plinian fallout deposits, recognized at proximal and medial exposures and sampled here for the first time, are characterized by tephriphonolitic grey pumice clasts with the least evolved compositions of the entire 79 AD sequence, and by a linear decrease of the degree of evolution with increasing stratigraphic height (e.g. MgO 1.93–3.03 wt.%, Zr 277–255 ppm and Nb 54–45 ppm; Fig. 2).

4 Discussion

The geochemical trends observed for the investigated 79 AD Plinian fallout deposits are consistent with the existence of a vertically stratified magma chamber, as already proposed in the literature [e.g. (Cioni et al., 1995; Mues-Schumacher, 1994; Santacroce, 1987)]. The first-erupted, topmost levels of this magma chamber represented by the white pumice clasts were also chemically stratified, as indicated by their evident vertical gradients, typically ascribed to fractional crystallization processes. No such evident trend is observed in the overlying grey pumice clasts, in line with models invoking complex mixing processes [mainly involving residual phonolitic and mafic magmas periodically refilling the 79 AD reservoir; (Cioni et al., 1995)]. The post-Plinian fallout deposits testify for a further compositionally distinct level of the magma chamber. The linear decrease in the degree of evolution recognized in these deposits extend the trend observed for the Plinian deposits to the topmost levels of the entire sequence, likely suggesting that the lowermost portions of the magma reservoir were compositionally stratified like the topmost ones.

5 Conclusions

The compositional spectra and the geochemical vertical gradients observed in juvenile clasts from the Plinian and post-Plinian fallout deposits of the 79 AD eruption provide some interesting clues to the modelling of the feeding reservoir. A remarkable compositional stratification is evident, though only the topmost and the lowermost levels display internal gradients likely ascribable to the major influence of fractional crystallization processes.

References

- Barberi, F., Bizouard, H., Clocchiatti, R., Metrich, N., Santacroce, R., & Sbrana, A. (1981). The Somma-Vesuvius magma chamber: A petrological and volcanological approach. *Bulletin of Volcanology*, 44, 295–315.
- Cioni, R., Civetta, L., Marianelli, P., Métrich, N., Santacroce, R., & Sbrana, A. (1995). Compositional layering and syn-eruptive mixing of a periodically refilled shallow magma chamber: The AD 79 plinian eruption of Vesuvius. *Journal of Petrology*, 36(3), 739–776.
- Cioni, R., Marianelli, P., & Sbrana, A. (1992). Dynamics of the AD 79 eruption: Stratigraphic, sedimentologic and geochemical data on the successions of the Somma-Vesuvius southern sector. *Acta Vulcanologica*, 2, 109–123.
- Cioni, R., Santacroce, R., & Sbrana, A. (1999). Pyroclastic deposits as a guide for reconstructing the multi-stage evolution of the Somma-Vesuvius Caldera. *Bulletin of Volcanology*, 61, 207–222.
- Civetta, L., Galati, R., & Santacroce, R. (1991). Magma mixing and convective compositional layering within the Vesuvius magma chamber. *Bulletin of Volcanology*, 53, 287–300.
- Civetta, L., & Santacroce, R. (1992). Steady state magma supply in the last 3400 years of Vesuvius activity. *Acta Vulcanologica*, 2, 147–159.
- Fedele, L., Scarpati, C., Sparice, D., Perrotta, A., & Laiena, F. (2016). A chemostratigraphic study of the Campanian Ignimbrite eruption (Campi Flegrei, Italy): Insights on magma chamber withdrawal and deposit accumulation as revealed by compositionally zoned stratigraphic and facies framework. *Journal of Volcanology and Geothermal Research*, 324, 105–117.
- Hildreth, W., & Wilson, C. J. N. (2007). Compositional zoning of the Bishop Tuff. *Journal of Petrology*, 48(5), 951–999.
- Mues-Schumacher, U. (1994). Chemical variations of the A.D. 79 pumice deposits of Vesuvius. *European Journal of Mineralogy*, 6, 387–395.
- Santacroce, R. (1987). Somma-Vesuvius. CNR Quaderni de La Ricerca Scientifica 114 (Vol. 8, 251 pp).
- Williams, R., Branney, M. J., & Barry, T. (2014). Temporal and spatial evolution of a waxing and waning catastrophic density current revealed by chemical mapping. *Geology*, 42(2), 107–110.



The Role of the White Pumice Clasts in the 79 AD Vesuvius Post-plinian PDC Deposits

Ileana Santangelo, Lorenzo Fedele, Claudio Scarpati, Annamaria Perrotta, and Giulia Chiominto

Abstract

Large explosive eruptions often generate compositionally zoned ignimbrites that provide evidence for the vertical stratification in the magma chamber and insights on magma withdrawal dynamics. In this regard, an excellent case is represented by the AD 79 eruption of Vesuvius, which consisted of two main phases. A first Plinian phase emplaced widespread fallout deposits and minor pyroclastic density currents (PDCs), characterized by a marked compositional variation from white phonolitic pumice clasts at the base, to grey tephriphonolitic pumice clasts at the top. This is commonly interpreted to reflect the emptying of a stratified magma chamber. A post-Plinian phase, emplacing mainly PDC deposits, followed, tapping the lowermost, tephriphonolitic “grey magma” still residing in the magma reservoir. Occasional occurrence of white juvenile clasts in the upper part of the sequence is also reported. We present here new geochemical data on the juvenile clasts from the 79 AD post-Plinian PDC deposits, collected at three type-locations representatives of the proximal and medial facies of the deposits in three different sectors around the volcano. Our dataset testifies the systematic coexistence of both grey and white pumice types at various stratigraphic levels. The grey pumice clasts depict quite regular vertical variations for both major and trace elements, with Fe_2O_3 tot and TiO_2 linearly increasing from 4.55 to 5.22 wt.% and from 0.51 to 0.65 wt.%, respectively, while Al_2O_3 and Zr regularly decrease from 19.2 to 16.9 wt.% and 294 to 255 ppm, respectively. The phonolitic white pumice clasts are much less common and do not display any regular vertical geochemical trend.

Two possible interpretations can be proposed for such coexistence: 1) batches of the phonolitic “white magma” had remained trapped in the magma chamber and were sporadically discharged during the eruption of the “grey magma”; 2) the white pumice clasts represent accidental cognate lithic clasts that were scraped off from the basal Plinian fallout deposits by the highly erosive post-Plinian PDCs.

Keywords

Vesuvius • 79 AD • Plinian eruption • PDC • Chemostratigraphy

1 Introduction

Defining the chemostratigraphy of the deposits from pyroclastic density currents (PDCs) by studying the compositional changes of the juvenile clasts, both in the vertical and horizontal directions, provides a significant aid in assessing what are the factors involved in that influence their emplacement (e.g. variability of the eruptive dynamics, topography and erosional processes (Branney & Kokelaar, 2002; Carrasco-Núñez & Branney, 2005; Fedele et al., 2016).

The 79 AD eruption of Vesuvius emplaced not only widespread fallout deposits during the initial Plinian phase, but also numerous post-Plinian PDC deposits (e.g. Cioni et al., 1992; Doronzo et al., 2022). The deposits of the first stage are characterized by a well-reported compositional variation from white phonolitic pumice clasts at the base, to grey tephriphonolitic pumice clasts at the top, whereas the second-stage deposits were fed only by tephriphonolitic grey magma batches. Occasional occurrence of white juvenile clasts in the upper part of the sequence is also reported (Cioni et al., 1992; Gurioli et al., 2002; Sbrana et al., 2020). Here we present a chemostratigraphic characterization of selected type-sections for the 79 AD post-Plinian PDC

I. Santangelo (✉) · L. Fedele · C. Scarpati · A. Perrotta · G. Chiominto
Dipartimento Di Scienze Della Terra, Dell’Ambiente E Delle Risorse (DiSTAR) – Università Degli Studi Di Napoli Federico II, Complesso Universitario Di Monte Sant’Angelo, Via Vicinale Cupa Cintia 21, 80126 Napoli, Italy
e-mail: ileana.santangelo@unina.it

deposits characterized by the presence of both types of pumice clasts at the same stratigraphic levels.

2 Materials and Methods

The juvenile components of the post-Plinian 79 AD PDC deposits were sampled at various stratigraphic levels at three sections in different sectors around the volcano, representative of proximal and medial exposures (Pollena, Pozzelle and Pompei; Fig. 1).

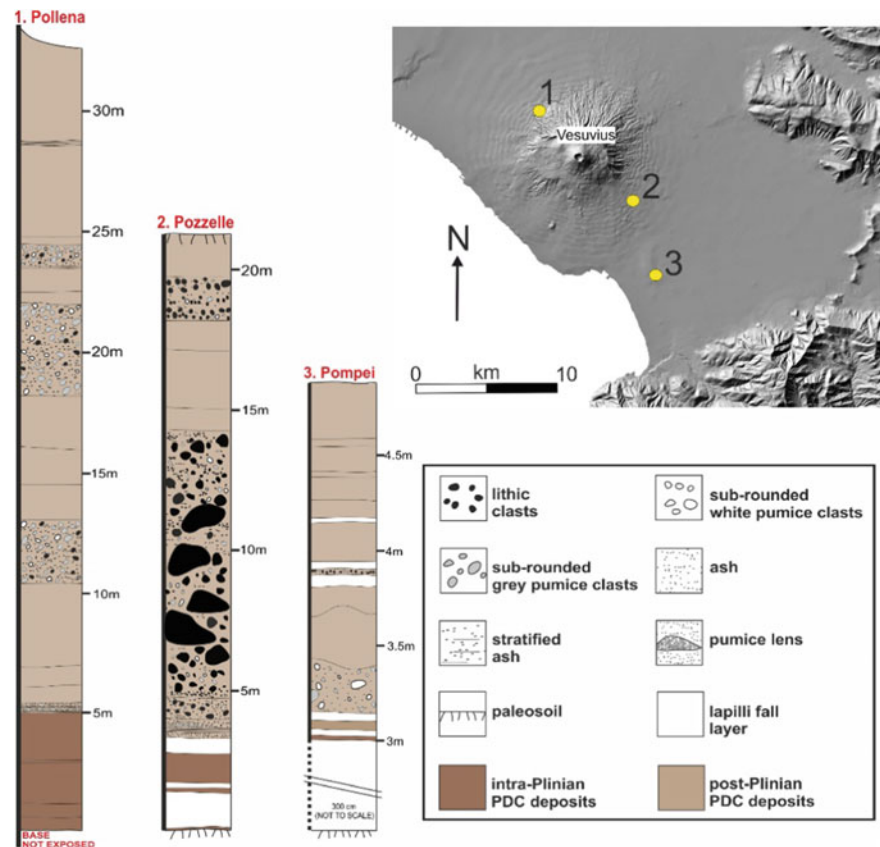
The collected 21 samples of white and grey pumice clasts were processed and analyzed for petrochemical characterization at the DiSTAR (University of Naples Federico II) laboratories. Samples were crushed, washed in deionized water, dried out and then pulverized in a low-blank agate mill in order to prepare pressed powder pellets, analyzed by XRF using a Panalytical Axios spectrometer. Uncertainties are within 1–2% and 5–10%, respectively, for major and trace elements. Weight loss on ignition (LOI) was determined gravimetrically after heating rock powders (pre-dried at ~ 150 °C overnight) at 950 °C for 3 h.

3 Results

A twofold behaviour can be observed in chemostratigraphic diagrams for the juvenile samples from the 79 AD post-Plinian PDC deposits (Fig. 2). The tephriphonolitic grey pumice clasts tend to show rather linear vertical trends, characterized by progressively less evolved compositions with increasing stratigraphic height. This is evident for each studied section and for the entire stratigraphic sequence, marked by an increase of TiO_2 0.51–0.65 wt.%, $\text{Fe}_2\text{O}_3\text{tot}$ (4.55–5.22 wt.%), Ba (1144–1321 ppm) and V (113–146 ppm), accompanied by decreasing Al_2O_3 (19.2–16.9 wt.%) and Zr (294–255 ppm).

As a whole, the grey pumice clast from the post-Plinian PDCs cover the spectrum defined by the grey pumice clasts of the Plinian fallout, extending to even less evolved compositions at the highest stratigraphic levels. On the other hand, the rarer phonolitic white pumice clasts show fluctuating composition, in line with those of the white pumice clasts from the Plinian fallout deposits but lacking any evident chemostratigraphic trend.

Fig. 1 Simplified stratigraphic columns for the three type-sections (locations indicated on the top of each column) where the juvenile clasts of the 79 AD post-plinian PDC deposits were collected. Different shades of brown are used to distinguish the intra-Plinian PDC deposits (dark) from the post-plinian PDC deposits (light)



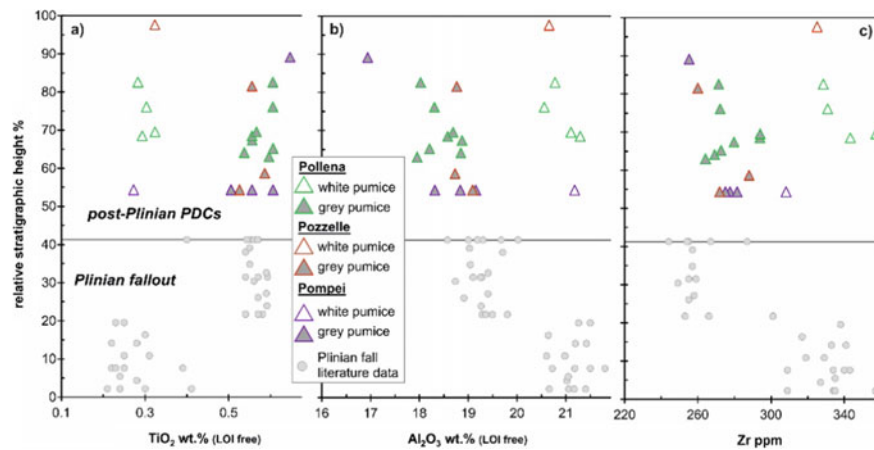


Fig. 2 Relative stratigraphic level % (referring to the entire 79 AD sequence) versus **a** TiO_2 , **b** Al_2O_3 and **c** Zr for the investigated juvenile samples from the 79 AD post-Plinian PDC deposits. Literature data for

the Plinian fallout from Cioni et al. (1992); Cioni et al., 1995; Barberi et al., 1981; Santacroce, 1987; Civetta et al., 1991; Civetta & Santacroce, 1992; Mues-Schumacher, 1994)

4 Discussion

The common coexistence of both pumice clast types in the post-Plinian PDC deposits, together with the recognition of some clear geochemical vertical profile in the grey pumice clasts only, defines a complex portrait for the overall chemostratigraphy of the 79 AD eruption deposits. This can have a notable impact on the models for the magma discharge during the eruption, as two different hypotheses can be proposed. A first scenario could involve the preservation of some batches of the phonolitic white magmas well after the eruption of the tephriphonolitic magmas of the Plinian fallout phase. Magmas from such batches would be occasionally tapped along with the more abundant grey magma throughout the last stages of the eruption. An alternative scenario would include erosion of the white pumice clasts from the basal Plinian fallout deposits by the following currents and then re-deposited and incorporated in the post-Plinian PDC deposits as accidental cognate lithic clasts. In such a framework, it is evident that part of the grey pumice clasts of the post-Plinian PDC deposits could have a similar origin.

5 Conclusions

The compositional spectra and the chemostratigraphic trends observed in the grey and white pumice clasts coexisting within the 79 AD post-Plinian PDC deposits provide some interesting insights not only for the reconstruction of the feeding reservoir and its emptying dynamics, but also for the processes related with the emplacement of the deposits. The rare white pumice clasts

could indeed testify for the limited persistence of some batches of evolved phonolitic magma or for the highly erosive action by the PDCs of the post-Plinian phase of the eruption.

References

- Branney, M. J., & Kokelaar, B. P. (2002). Pyroclastic density currents and the sedimentation of ignimbrites. *Geological Society of London Memoirs*, 27, 1–152.
- Carrasco-Núñez, G., & Branney, M. J. (2005). Progressive assembly of a massive layer of ignimbrite with a normal-to-reverse compositional zoning: The Zaragoza ignimbrite of central Mexico. *Bulletin of Volcanology*, 68, 3–20.
- Fedele, L., Scarpati, C., Sparice, D., Perrotta, A., & Laiena, F. (2016). A chemostratigraphic study of the Campanian Ignimbrite eruption (Campi Flegrei, Italy): Insights on magma chamber withdrawal and deposit accumulation as revealed by compositionally zoned stratigraphic and facies framework. *Journal of Volcanology and Geothermal Research*, 324, 105–117.
- Cioni, R., Marianelli, P., & Sbrana, A. (1992). Dynamics of the AD 79 eruption: Stratigraphic, sedimentologic and geochemical data on the successions of the Somma-Vesuvius southern sector. *Acta Vulcanologica*, 2, 109–123.
- Doranzo, D. M., Di Vito, M. A., Arienzo, I., Bini, M., Calusi, B., Cerminara, M., Corradini, S., de Vita, S., Giaccio, B., Gurioli, L., Mannella, G., Ricciardi, G. P., Rucco, I., Sparice, D., Todesco, M., Trasatti, E., & Zanchetta, G. (2022). The 79 CE eruption of Vesuvius: A lesson from the past and the need of a multidisciplinary approach for developments in volcanology. *Earth-Science Reviews*, 231, 104072.
- Gurioli, L., Cioni, R., Sbrana, A., & Zanella, E. (2002). Transport and deposition from pyroclastic flows over an inhabited area: The deposits of the AD 79 eruption of Vesuvius at Herculaneum. *Italy. Sedimentology*, 49, 929–953.
- Sbrana, A., Cioni, R., Marianelli, P., Sulpizio, R., Andronico, D., & Pasquini, G. (2020). Volcanic evolution of the Somma-Vesuvius complex (Italy). *Journal of Maps*, 16, 137–147.

- Cioni, R., Civetta, L., Marianelli, P., Métrich, N., Santacroce, R., & Sbrana, A. (1995). Compositional layering and syn-eruptive mixing of a periodically refilled shallow magma chamber: The AD 79 plinian eruption of Vesuvius. *Journal of Petrology*, *36*(3), 739–776.
- Barberi, F., Bizouard, H., Clocchiatti, R., Métrich, N., Santacroce, R., & Sbrana, A. (1981). The Somma-Vesuvius magma chamber: A petrological and volcanological approach. *Bulletin of Volcanology*, *44*, 295–315.
- Santacroce, R. (1987). Somma-Vesuvius. *CNR Quaderni de La Ricerca Scientifica* *114*, *8*, 251.
- Civetta, L., Galati, R., & Santacroce, R. (1991). Magma mixing and convective compositional layering within the vesuvius magma chamber. *Bulletin of Volcanology*, *53*, 287–300.
- Civetta, L., & Santacroce, R. (1992). Steady state magma supply in the last 3400 years of vesuvius activity. *Acta Vulcanologica*, *2*, 147–159.
- Mues-Schumacher, U. (1994). Chemical variations of the A.D. 79 pumice deposits of Vesuvius. *European Journal of Mineralogy*, *6*, 387–395.



Long-Term Probabilistic Volcanic Hazard Assessment for Tephra Fallout from Neapolitan Volcanoes on Southern Italy

Manuel Stocchi, Silvia Massaro, Beatriz Martínez Montesinos, Laura Sandri, Jacopo Selva, Antonio Costa, Roberto Sulpizio, Biagio Giaccio, Massimiliano Moscatelli, Edoardo Peronace, Marco Nocentini, Roberto Isaia, and Manuel Titos Luzòn

Abstract

Somma-Vesuvius, Campi Flegrei, and Ischia are three active volcanoes in the Neapolitan Area (Italy). In this work, we evaluated the combined tephra fallout hazard posed by the three volcanoes on a large-size (~ 600 km 700 km) and high-resolution (~ 3 km) domain. In order to explore the effect of the intrinsic variability in eruption and wind conditions on tephra hazard we used a probabilistic approach (probabilistic volcanic hazard assessment, PVHA). For Somma-Vesuvius and Campi Flegrei, we grouped the possible eruptive size classes into small-, medium- and large-scale eruptions, while for Ischia we considered only the large-scale scenario, as it is the only one that can affect the mainland. We created a synthetic dataset of ground loads by performing 1500 tephra

dispersion simulations for each eruption size class of each volcano (for a total of 10,500 simulations) using the numerical model Fall3D. For each simulation, we randomly sampled the eruptive parameters from suitable probability density functions and meteorological conditions from the ERA5 reanalysis dataset on the period 1990–2020. The hazard evaluation has been performed using a Bayesian Event Tree (BET) approach accounting for the results of the simulations, the variability in vent location and the mean annual rates of eruption for each volcano and eruption size class. In this way we obtained a set of hazard maps for Southern Italy showing the threshold tephra load that would be exceeded with selected mean annual rates within a 50-year exposure time. We found that greater tephra load thresholds are exceeded in the south–south-eastern regions.

M. Stocchi (✉) · S. Massaro · B. Martínez Montesinos · L. Sandri · J. Selva · A. Costa · R. Sulpizio
Istituto Nazionale Di Geofisica E Vulcanologia,
Sezione Di Bologna, Italy
e-mail: manuel.stocchi@ingv.it

Present Address:

S. Massaro · R. Sulpizio
Dipartimento Di Scienze Della Terra E Geoambientali,
Università Degli Studi Di Bari, Bari, Italy

R. Sulpizio · B. Giaccio · M. Moscatelli · E. Peronace · M. Nocentini
Istituto Di Geologia Ambientale E Geoingegneria,
Consiglio Nazionale Delle Ricerche, Roma, Italy

M. Nocentini
Dipartimento Servizio Geologico d'Italia, Istituto Superiore Per La Protezione E
La Ricerca Ambientale, Roma, Italy

R. Isaia
Istituto Nazionale Di Geofisica E Vulcanologia, Napoli,
Osservatorio Vesuviano, Italy

M. T. Luzòn
Signals Processing and Machine Learning,
University of Granada, Granada, Spain

J. Selva
University of Naples "Federico II", Naples, Italy

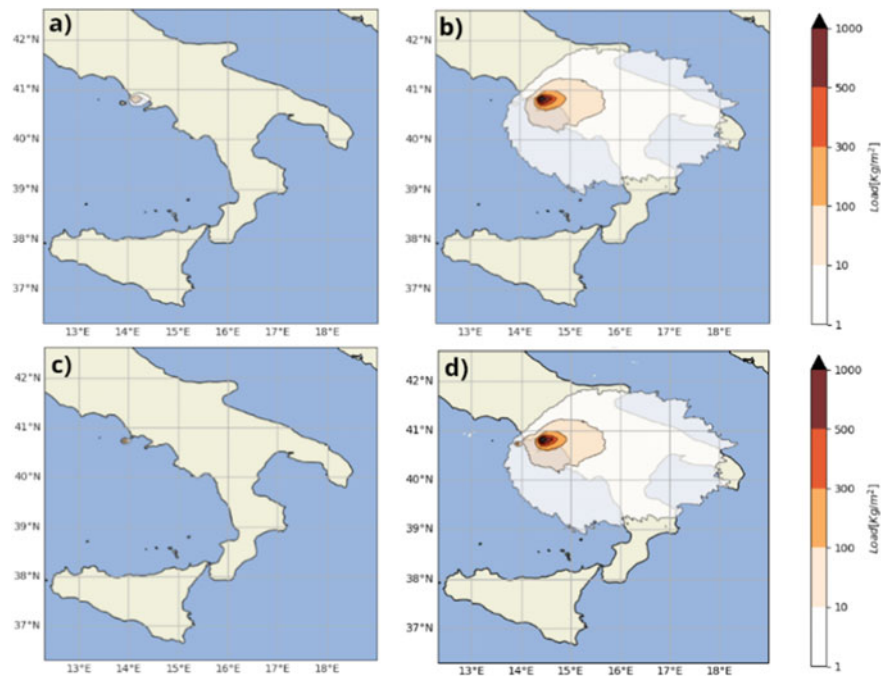
Keywords

PVHA · Tephra fallout · Neapolitan volcanoes · Bayesian event tree · Tephra dispersion simulation

1 Introduction

Within the area of Naples (Southern Italy), there are three active volcanoes, Somma-Vesuvius, Campi Flegrei and Ischia, which threaten an area where more than three millions of people live. The quantification of the hazard posed by tephra fallout is a crucial step in risk quantification and mitigation, as it is one of the most relevant hazard (*e.g.* (Newhall & Hobblit, 2002). As the physics involving tephra fallout is strongly influenced by highly variable eruptive parameters, as well as meteorological conditions, the Bayesian Event Tree approach (Martínez Montesinos et al., 2022; Marzocchi et al., 2010; Sandri et al., 2016) is often used to perform probabilistic volcanic hazard assessment (PVHA).

Fig. 1 Long-term maps reporting the absolute hazard intensity (tephra load, kg/m^2) that will be overcome with $\lambda = 0.02 \text{ yrs}^{-1}$. We show the maps relative to: **a** Somma-Vesuvius (aggregated eruption sizes: small, medium, large); **b** Campi Flegrei (aggregated eruption sizes: small, medium, large); **c** Ischia (large size class); **d** Long-term absolute hazard maps with the combined impact of the three volcanoes



We present a tephra fallout PVHA for the regions of Southern Italy by generalizing the workflow proposed by Martínez Montesinos et al., 2022 to take into account tephra fallout from Somma-Vesuvius, Campi Flegrei and Ischia and by using the mean annual eruption rates recently estimated by Selva et al., 2022.

2 Methodology

The hazard posed by ash fallout has been quantified through the mean annual frequency at which the tephra ground load overcomes a threshold Z in a location x within the computational domain given an exposure time window ΔT . The method is based on a Bayesian approach adapted from Sandri et al. (2016). For each of the three considered volcanoes, we identified a set of possible eruptive size classes σ_{ik} and a set of possible eruptive vent locations γ_{ij} . The mean annual frequency λ at which a selected threshold Z is overcome at location x due to an eruption of any of three volcanoes is calculated as

$$\lambda(Z, x) = \sum_{i,j,k} v_{ik} P(\gamma_{ij}|E_i) P(z > Z|E_i, \gamma_{ij}, \sigma_{ik}; x),$$

where $P(\gamma_{ij}|E_i)$ is the probability that, given an eruption of volcano E_i , the eruption will occur at vent γ_{ij} ; $P(z > Z|E_i, \gamma_{ij}, \sigma_{ik}; x)$ is the probability that tephra ground in x will overcome Z given an eruption of volcano E_i , size class σ_{ik} from vent γ_{ij} . For Somma-Vesuvius and Campi Flegrei,

we considered three eruption size classes: small (TEM 10^{10} – 10^{11} kg), medium (TEM 10^{11} – 10^{12} kg) and large (TEM 10^{12} – 10^{13} kg). For Ischia we considered only one eruption size class (Primerano et al., 2021). The variability in eruptive vent location has actually been considered only for Campi Flegrei by choosing a set of 40 possible vent locations spanning the caldera domain by approximately 12 km in longitude and 10 km in latitude. The term $P(z > Z|E_i, \gamma_{ij}, \sigma_{ik}; x)$ has been calculated performing numerical simulations with the model Fall3D (Folch et al., 2020) over a $0.03^\circ \times 0.03^\circ$ resolution domain from 36.31° to 42.61° in latitude and from 12.31° to 9.00° in longitude covering the target region of Southern Italy. We performed 1500 simulations per eruptive size for each volcano, with meteorological conditions obtained by sampling random days from 1990 to 2020 and downloading the relative meteorological data from the ECMWF ERA5 reanalysis database (ECMWF ERA5).

3 Results

The results of Eq. (1) over a set of ground load thresholds Z allow to obtain a hazard curve for every point x of the domain. These hazard curves can be cut at desired mean annual frequencies λ to obtain hazard maps showing the value of tephra ground load that will be overcome with the selected annual frequency. Figure 1 shows examples of hazard maps for Somma-Vesuvius (Fig. 1a), Campi Flegrei

(Fig. 1b) and Ischia (Fig. 1c) obtained by cutting the hazard curves at $2 \times 10^{-3} \text{ yrs}^{-1}$ (corresponding to an averaged return period of 500 years), while Fig. 1d shows the hazard map obtained by combining the contribution of the three volcanoes for $\Delta T = 50 \text{ yrs}$.

4 Discussions and Conclusions

Figure 1 shows the expected tephra loads with an average return time of 500 years. In proximal areas, where larger tephra loads are expected, the maximum values reach over 1000 kg/m^2 near Somma-Vesuvius. The distal areas like Apulia and Basilicata are expected to experience, with an average return period of 500 years, tephra loads in the order of 1 kg/m^2 that can be considered a critical value for ground traffic. The tephra load isolines extend in the South–South-East direction, in accordance with (Martínez Montesinos et al., 2022; Sandri et al., 2016).

By comparing Fig. 1a, b, and c, we see that Somma-Vesuvius gives the largest contribution to the total tephra load hazard with respect to Campi Flegrei and Ischia. This is likely due to its greater mean eruption rates (Selva et al., 2022), which are in general one order of magnitude greater than those of the other two volcanoes for similar eruption sizes.

References

- Newhall, C., & Hobblit, R. (2002). Constructing event trees for volcanic crises. *Bulletin of Volcanology*, 64(1), 3–20.
- Marzocchi, W., Sandri, L., & Selva, J. (2010). BET_EF: A probabilistic tool for long- and short-term eruption forecasting. *Bulletin of Volcanology*, 70(5), 623–632.
- Sandri, L., Costa, A., Selva, J., Tonini, R., Macedonio, G., Folch, A., & Sulpizio, R. (2016). Beyond eruptive scenarios: Assessing tephra fallout hazard from Neapolitan volcanoes. *Scientific Reports*, 6(1), 1–13.
- Martínez Montesinos, B., Titos Luzon, M., Sandri, L., Rudy, O., Cheptsov, A., Macedonio, G., Folch, A., Barsotti, S., Selva, J., Costa, A. (2022). On the feasibility and valuableness of High Performance Computing in probabilistic volcanic hazard assessment: an application to tephra hazard from Campi Flegrei. *Frontiers*, in review
- Selva, J., Sandri, L., Taroni, M., Sulpizio, R., Tierz, P., Costa, A. (2022). A simple two-state model interprets temporal modulations in eruptive activity and enhances multi-volcano hazard quantification. *Science Advances*, *Accepted*
- Primerano, P., Giordano, G., Costa, A., de Vita, S., & Di Vito, M. A. (2021). Reconstructing fallout features and dispersal of Cretaio Tephra (Ischia Island, Italy) through field data analysis and numerical modeling: Implications for hazard assessment. *Journal of Volcanology and Geothermal Research*, 415, 107248.
- Folch, A., Mingari, L., Gutierrez, N., Hanzich, M., Macedonio, G., & Costa, A. (2020). FALL3D-8.0: a computational model for atmospheric transport and deposition of particles, aerosols and radionuclides—Part 1: model physics and numerics. *Geoscientific Model Development*, 13(3), 1431–1458.
- ECMWF ERA5 database; <https://www.ecmwf.int/en/forecasts/datasets/reanalysis-datasets/era5>



Evidence for the Voluminous Silicic Volcanic Activity in the Permian–Triassic West Siberia

Anton Latyshev, Ivan Panchenko, Maria Smirnova, Petr Kulikov, Anastasia Tokmakova, and Yuliya Trushkova

Abstract

Permian–Triassic rifts of the West Siberian basin compose one of the largest continental rift systems in the world. They are nearly coeval to the Siberian Traps Large Igneous Province and mark the final stage of the amalgamation of the Northern Eurasia. Presence of acidic volcanic rocks along the mafic lavas is a specific feature of the West Siberian region. However, at this moment, felsic volcanics of this area are poorly studied. Here we present the first representative data on petrography, geochemistry, and U–Pb ages for silicic volcanic rocks from the drill cores of the deep boreholes in the Frolov-Krasnoleninsky region (the central part of the West Siberian basin). The largest rift structure of this area is Rogozhnikov-Nazym graben, composed of rhyolite-dacitic lavas. Lavas constitute the major part of the volcanic pile, while tuffs are subordinate (up to 15%). According to the seismic and well-logging data, the thickness of felsic volcanic rocks exceeds 0.7 km. Whole-rock chemistry of the silicic volcanic rocks of the Rogozhnikov-Nazym graben and other smaller rifts is very similar and corresponds to post-collisional extensional tectonic setting. Zircons from rhyolites and dacites yielded U–Pb (SHRIMP-II) ages ranging from 254 ± 2

to 248.2 ± 1.3 Ma (Late Permian–Early Triassic). Thus, volcanic activity in the Frolov-Krasnoleninsky region was nearly coeval to the main phase of the Siberian Traps emplacement in the Siberian platform.

Keywords

West Siberian basin • Continental rifts • Permian–Triassic boundary • Silicic volcanic activity

1 Introduction

Permian–Triassic volcanic rocks are widespread in the West Siberian basin and compose the upper structural floor of the Pre-Jurassic tectonic units. These volcanics are products of a widescale rifting stage, which is considered to be linked with the emplacement of Siberian Traps Large Igneous Province (LIP) (Reichow et al., 2009). The most prominent differences of the Permian–Triassic rocks of West Siberia from the Traps of the Siberian platform are: (1) their confinement mainly to multiple rift structures and (2) a significant part of silicic rocks which hardly occur within the Siberian platform. Permian–Triassic volcanic rocks are poorly accessible for the direct observation in the West Siberian basin, because the Pre-Jurassic basement is overlain by the thick sedimentary cover and is cut only with a limited number of deep boreholes. Therefore, volume and area of distribution of silicic volcanics, their relationships with basalts, and duration of magmatic activity are still poorly constrained.

Within this work, we studied volcanic rocks from the drill core of wells in the Frolov-Krasnoleninsky region (the central part of the West Siberia). In this area, silicic volcanics compose the large Rogozhnikov-Nazym graben, which is located at the junction of the Krasnoleninsky uplift and Frolov depression, and are widespread in many small rift-like structures (Fig. 1).

A. Latyshev (✉)

Faculty of Geology, Lomonosov Moscow State University,
1 Leninskie Gory, 119991 Moscow, Russia
e-mail: falseanton.latyshev@gmail.com

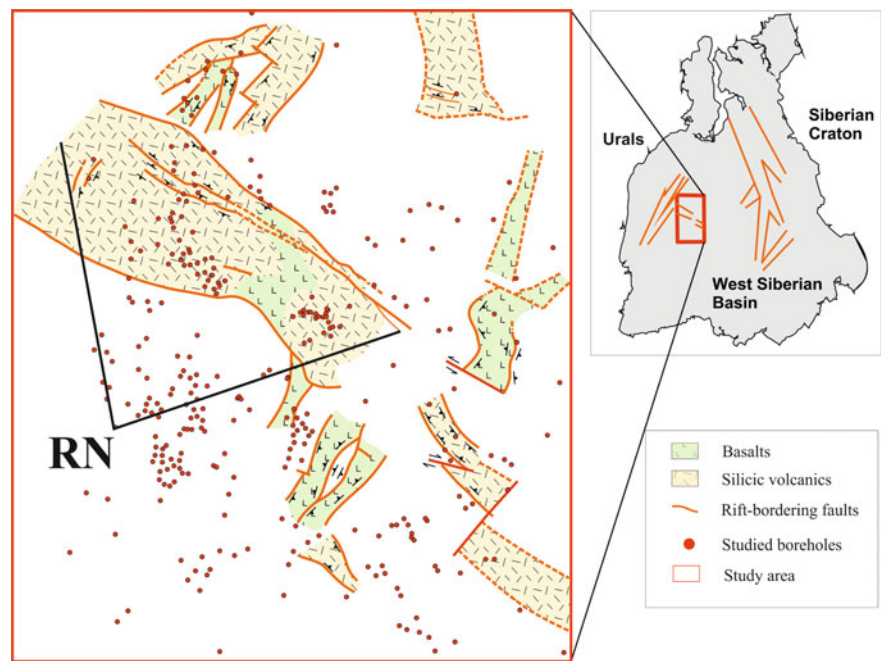
A. Latyshev

Schmidt Institute of the Physics of the Earth, Russian Academy
of Science, 10 Bolshaya Gruzinskaya St., 123242 Moscow, Russia

I. Panchenko · M. Smirnova · P. Kulikov · A. Tokmakova ·
Y. Trushkova

Closed Joint Stock Company “Modeling and Monitoring of
Geological Objects”, 21 B.1 Enthusiastov Highway, 111024
Moscow, Russia

Fig. 1 Sketch map of the rift structures in the Permian–Triassic complex of the Frolov-Krasnoleninsky region. RN—Rogozhnikov-Nazym graben



2 Materials and Methods

Here we present the first results of the comprehensive investigation of Permian–Triassic silicic volcanic rocks of the West Siberia. We performed the macroscopic analysis of drill cores from more than 30 boreholes and petrographic investigation of about 400 thin sections, as well as interpretation of well-logging, geochemical, and U–Pb data. To analyze the spatial distribution of volcanic rocks we used 2D and 3D seismic data. The main 3D volume is about 900 km² and 4.5 km in depth. 2D seismic surveys are about 2000 km in summary length. Major and trace element concentrations in rocks were analyzed using X-ray fluorescence (XRF) and inductively coupled plasma mass spectrometry (ICP-MS), respectively. Analyses were performed at the Institute of Microelectronics Technology and High Purity Materials of Russian Academy of Sciences (ICP-MS) and at the Institute of the Geology of Ore Deposits, Petrography, Mineralogy, and Geochemistry of Russian Academy of Sciences (XRF). U–Pb dating of zircons was performed on a sensitive high-resolution ion microprobe (SHRIMP-II) at the Center for Isotope Research (Karpinsky All-Russia Research Geological Institute, St. Petersburg). Zircon standard TEMORA [²⁰⁶Pb/²³⁸U = 0.0668 corresponding to 416.75 ± 0.24 Ma (Black et al., 2003)] was used to calibrate the U/Pb ratios, and zircon standard 91,500 (U = 81.2 ppm) was used for the calibration of U content.

3 Results

Acidic lavas and brecciated lavas (rhyolites, dacites, and rhyodacites) are predominant among the volcanic rocks of the Rogozhnikov-Nazym graben. Lavas usually have a porphyritic texture and contain phenocrysts of feldspars and occasionally quartz. Mafic phenocrysts are subordinate and represented by hornblende, rarely biotite or pyroxene. Lavas display massive, foliated, and perlitic structures. Felsic volcanoclastic rocks are rare and vary from ash tuffs to breccia with very diverse composition of clasts.

Other rift structures are composed of petrographically similar felsic volcanic rocks, mainly rhyolitic and dacitic lavas. In some boreholes we found porphyritic basalts and basaltic andesites, widespread in the Permian–Triassic rifts of West Siberian basin (Fig. 1). However, it should be noted that we did not find intercalated mafic and felsic volcanics in any studied borehole.

At seismic sections, Permian–Triassic volcanic rocks of the Rogozhnikov-Nazym graben correspond to gently dipping reflections, which form a series of calderas or a volcano-tectonic depression cut by steep faults. According to the seismic data, the total thickness of the volcanic pile exceeds 700 m. Felsic lavas form thick volcanic bodies, which can be traced at seismic profiles for 5–10 km. The thickness of individual bodies laterally varies from 70–80 to 10–20 m. We interpret these bodies as series of lava flows,

marking the local eruptive centers. Weathering crusts (10–25 m thick) are identified at the top of volcanic rocks and within thick lava piles. In some sections we found 3–5 weathering crusts within lava sequences. These levels may correspond to prolonged gaps between volcanic eruptions. Finally, volcanoclastic rocks form thin (5–25 m) horizons, traced across the entire studied area (> 10 km).

Geochemical peculiarities of volcanic rocks from the Rogozhnikov-Nazym graben and other studied areas of felsic volcanic activity are very uniform and close to each other. The most important features are: (1) predominance of acidic rocks (rhyolites, dacites, and trachydacites) mainly of high-potassium series (Fig. 2a); (2) negative anomaly in Ta-Nb, enrichment in Pb, possibly indicating the relics of supra-subduction tectonic setting (Fig. 2b); and (3) high enrichment in all incompatible elements. Based on these geochemical features, we suggest that this volcanic complex was emplaced in a post-collisional rifting geodynamic setting.

Nine zircon probes from rhyolites and dacites of the Rogozhnikov-Nazym graben and other structures yielded U–Pb ages ranging from 254 ± 2 to 248.2 ± 1.3 Ma, corresponding to the latest Permian–earliest Triassic (Fig. 3). The mean square weighted deviation varies from 0.045–0.13 to

3.2–5, and the probability of concordance is 0.025–0.83. Taking into account the error margins, we may assume that the total duration of felsic magmatic activity was not less than 2.5 M yr. However, it should be noted that the oldest and the youngest ages seem to be the least reliable due to the high MSWD and low probability of concordance.

4 Discussion

Analysis of facies and thicknesses of volcanic rocks reveals multiple local eruptive centers, which are marked by thick lava piles. The size of individual volcanic edifices is 1–5 km, typical for the modern felsic volcanic provinces. Volcanoclastic rocks constitute up to 15% of the volcanic province. Such a low proportion of products of explosive eruptions is uncommon for supra-subduction tectonic setting (Rittman, 1962) and favors an extensional post-collisional setting.

Layers of epiclastic volcanogenic sedimentary deposits among lavas and tuffs are rare and thin (< 1 m). This indicates the high intense volcanic activity and poorly dissected relief during eruptions, probably due to fast filling of local topographic depressions by lava and pyroclastic flows.

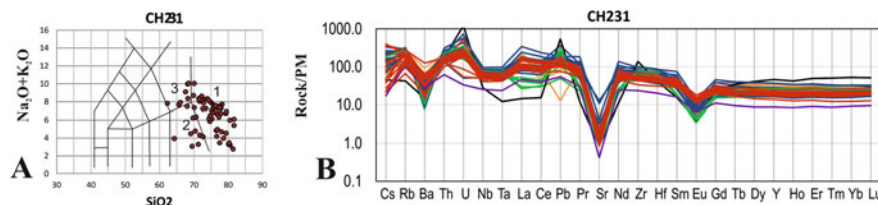
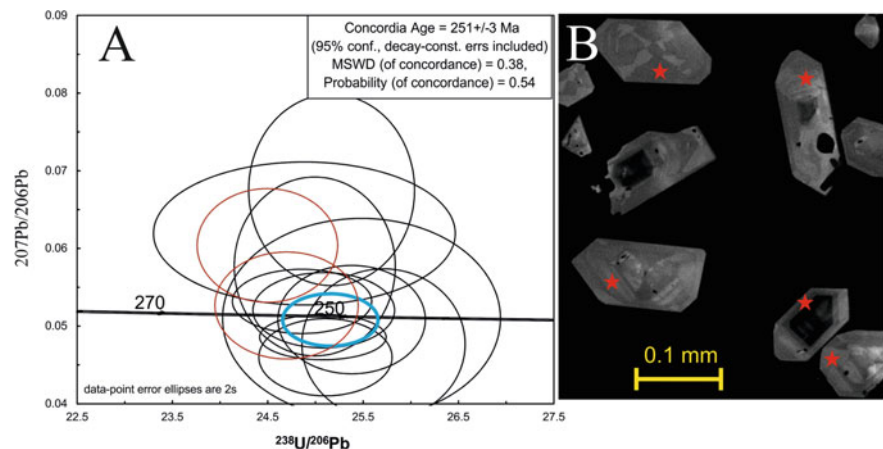


Fig. 2 Geochemical features of volcanic rocks. **a** TAS-diagram (Le Maitre, 2022) for volcanic rocks from one of the boreholes of the Rogozhnikov-Nazym graben; 1—Rhyolites, 2—Dacites, 3—Trachydacites. **b** PM-normalized [primitive mantle composition from Sun and

McDonough (1989)] spectra of incompatible elements for the same borehole (different colors correspond to different depths in the borehole without dividing by rock types)

Fig. 3 Results of U–Pb dating. **a** Concordia diagrams for one of the probes. **b** Cathodo luminescence images of zircons from the same probe. Points of analysis are shown as stars



Similar paleogeographic conditions were reported for felsic volcanic centers of the Okhotsk-Chukotka volcanic belt (Tikhomirov, 2021).

5 Conclusions

Eruptions of felsic volcanic rocks of the Rogozhnikov-Nazym graben and other smaller rifts took place near the Permian–Triassic boundary. Geochemical and paleogeographic features indicate a tectonic setting consistent with post-collisional rifting, probably marking the final stage of the amalgamation of Northern Eurasia. The exclusively acidic composition of volcanic rocks makes the Rogozhnikov-Nazym graben and related structures similar to Silicic Large Igneous Provinces (Bryan & Ernst, 2008). The new age constraints show that silicic rocks of the West Siberia are nearly coeval to the Siberian Traps LIP.

References

- Black, L. P., Kamo, S. L., Allen, C. M., Aleinikoff, J. N., Davis, D. W., Korsch, R. J., & Foudoulis, C. (2003). TEMORA 1: A new zircon standard for U-Pb geochronology. *Chemical Geology*, 200, 155–170.
- Bryan, S. E., & Ernst, R. E. (2008). Revised definition of Large Igneous Provinces (LIPs). *Earth-Science Reviews*, 86, 175–202.
- Le Maitre, R. W., Streckeisen, A., Zanettin, B., Le Bas M. J., Bonin, B., Bateman, P., Bellieni, G., Dudek, A., Efremova, S., Keller, J., Lameyre, J., Sabine, P. A., Schmid, R., Sorensen, H., & Wooley, A. R. (2002). *Igneous rocks. A classification and Glossary of Terms*. Cambridge University Press.
- Reichow, M. K., Pringle, M. S., Al’Mukhamedov, A. I., Allen, M. B., Andreichev, V. L., Buslov, M. M., Davies, C., Fedoseev, G. S., Fitton, J. G., Inger, S., Medvedev, A. Ya., Mitchell, C., Puchkov, V. N., Safonova, I. Yu., Scott, R. A., & Saunders, A. D. (2009). The timing and extent of the eruption of the Siberian Traps Large Igneous Province: Implications for the end-Permian environmental crisis. *Earth Planetary Sciences Letters*, 277, 9–20.
- Rittman, A. (1962). *Volcanoes and their activity*. Wiley.
- Sun, S. S., & McDonough, W. F. (1989). Chemical and isotopic systematics of oceanic basalts: Implications for mantle composition and processes. *Special Publication of the Geological Society of London*, 42, 313–345.
- Tikhomirov, P. L. (2021). *Cretaceous continental-margin magmatic activity of the northeastern Asia and problems of genesis of the largest Phanerozoic silicic igneous provinces*. GEOS.



Geochemical Perspective on the Diagenesis of the Buah Carbonates from the Jabal Al Akhdar, Oman Mountains

Arshad Ali, Mohamed El-Ghali, Iftikhar Abbasi, Leonardo Brandão Nogueira, and Mohamed Moustafa

Abstract

The Buah Formation has been recognized as an active exploration target due to the potential for exposed carbonate rocks, which can be used as a proxy for hidden subsurface reservoir rocks. Petrographical observations and geochemical investigations of carbonate rocks provide useful insight into the diagenetic alterations and their effects on reservoir quality. The distribution of carbonate sediments is controlled by a variety of environmental parameters, including temperature, substrate, salinity, and the presence of siliciclastic materials. Metastable minerals, such as aragonite and high-Mg calcite (HMC) tend to transition to low-Mg calcite (LMC) and dolomite. To study diagenetic alterations, geochemical data of carbonate rocks from outcrops of Wadi Bani Awf (WBA) and Wadi Bani Kharus (WBK) in Jabal Al Akhdar, Oman, have been obtained using the ICP-OES technique. The Mg/Ca and Sr/Ca ratios of studied samples are plotted to show the relationship between hypothetical carbonate endmembers and Buah carbonates along with literature data. The samples from WBA and WBK outcrops exhibit three distinct groups that are anticorrelated, i.e., a decrease in Sr/Ca with an increase in Mg/Ca. The trend is consistent with the fact that the rhombohedral calcite can accommodate smaller cations (e.g., ionic radius of $Mg^{2+} = 86$ pm), whereas orthorhombic aragonite prefers larger cations (e.g., ionic radius of $Sr^{2+} = 132$ pm). Furthermore, the data are compared with samples collected in the Gulf of

Mexico (e.g., 4193 and DIS2 from AC601 and GC53 sites, respectively). Some of the WBA samples match the data of sample 4193 precipitated from seepage of hydrocarbon-rich brine fluids with abundant micropores and shell material. While a few of the WBK samples have data that matches with micrite DIS2 sample precipitated from hydrocarbon-free brine fluids. The effect of diagenesis by incorporating Mg into the calcite mineral structure is represented by the third group, having samples from both WBA and WBK with the lowest Sr/Ca and highest Mg/Ca ratios. Our findings suggest that the anticorrelation of Mg/Ca and Sr/Ca ratios between three distinct groups of Buah carbonates may have been caused by varied diagenetic conditions ranging from micritization to mechanical and chemical compaction leading to dolomitization.

Keywords

Buah formation • Diagenesis • Calcite • Dolomite • Jabal Al Akhdar

1 Introduction

The Nafun Group (< 645–546 Ma; (Allen, 2007)) of the Huqf Supergroup in Oman is widely exposed in the Jabal Akhdar and to the south along the Huqf axis (Cozzi et al., 2004a, 2004b; Gorin et al., 1982), and contains the Hadash, Masirah Bay, Khufai, Shuram, and Buah formations (Yue & Vandeginste, 2020). The limestones and dolostones dominate the siliciclastic to carbonate sequences of the Shuram and Buah formations.

High strontium (Sr) contents are a result of the mineralogy, diagenesis, seawater Sr content, terrigenous clastic flux, and submarine hydrothermal flux of the Nafun Group carbonates (Yue & Vandeginste, 2020). Due to hydrothermal processes that occurred in parts of the Neoproterozoic period, seawater attained significant Sr flux, which was largely incorporated

A. Ali (✉) · M. El-Ghali
Earth Sciences Research Centre, Sultan Qaboos University,
Muscat, Oman
e-mail: arshadali@squ.edu.om

M. El-Ghali · I. Abbasi · M. Moustafa
Department of Earth Sciences, Sultan Qaboos University,
Muscat, Oman

L. B. Nogueira
Department of Geology, Federal University of Ouro Preto,
Ouro Preto, Brazil

into carbonate formations (Jacobsen & Kaufman, 1999). The Nafun Group offers an ideal place for study of the source of the carbon cycle, which could have had important implications for the evolution of life on Earth due to the existence of marked negative $\delta^{13}\text{C}$ excursions in carbonate-bearing sediments of the late Neoproterozoic period (Burns & Matter, 1993). The current study aims to evaluate the alkaline Earth elements such as calcium, magnesium, and strontium in carbonate rocks to understand the diagenetic processes.

2 Materials and Methods

Seventeen carbonate samples from the Buah formation (Jabal Al Akhdar) were collected from Wadi Bani Awf (WBA) and Wadi Bani Kharus (WBK) outcrops (Fig. 1). Major and trace elements were analyzed using inductively coupled plasma spectrometry at the Federal University of Ouro Preto, Brazil. Powdered samples were digested in HCl,

HF, and HNO_3 suprapur acids following the methods given in Nogueira et al. (2019).

3 Results

Data for alkaline Earth metals (e.g., Mg, Ca, and Sr) in Buah carbonates (Table 1) are plotted as Mg/Ca and Sr/Ca ratio (Fig. 1). These ratios are compared with those of the hypothetical carbonate endmembers (e.g., aragonite, detrital, biogenic calcite, high-Mg calcite, and low-Mg calcite (Bayon et al., 2007)).

4 Discussion

The Mg/Ca and Sr/Ca ratios indicate that the Buah carbonates are divided into three anticorrelated groups (i.e., G-1, G-2, and G-3) as shown in Fig. 2.

Fig. 1 a Location map of the central part of Jabal Akhdar, Oman, showing the Wadi Bani Awf and Wadi Bani Kharus. (taken from Al-Siyabi (2020)). b Sedimentology log of Wadi Bani Kharus. c Sedimentology log of Wadi Bani Awf. Note Sample locations are shown as red circles on (a) and (b)

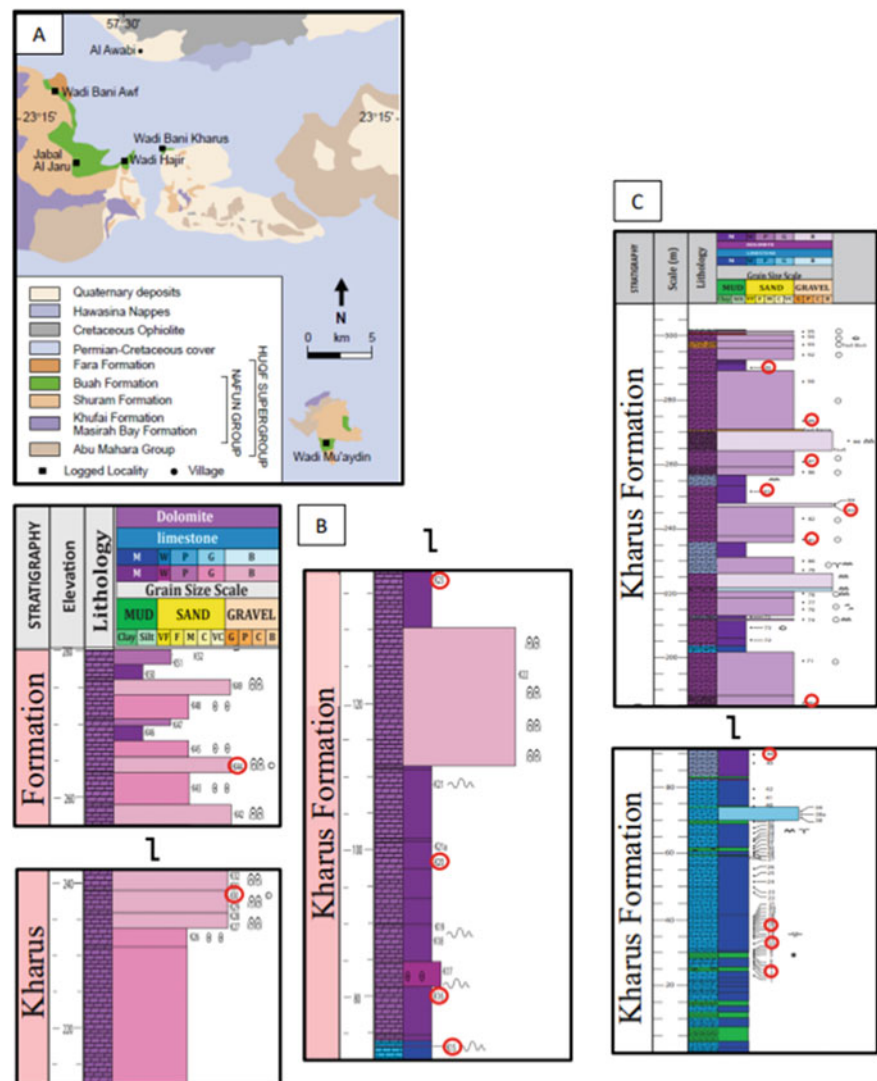


Table 1 Elemental compositions and their ratios for carbonates from Jabal Al Akhdar, Oman

Sample name	Depth (m)	Sr (ppm)	Mg (wt%)	Ca (wt%)	Mn (ppm)	Mg/Ca (mmol/mol)	Sr/Ca (mmol/mol)	Sr/Mn
<i>G-1</i>								
WA-K3	26	811	1.16	27.4	580	70.0	1.35	1.40
WA-K10	31	1325	1.49	28.8	1005	85.1	2.10	1.32
WA-K15	37	849	1.38	28.1	2712	80.9	1.38	0.31
<i>G-2</i>								
WK-K15	27	380	3.06	27.7	220	182.1	0.63	1.73
WK-K16	35	264	2.13	28.2	269	124.8	0.43	0.72
WK-K20	53	401	2.87	27.6	464	171.9	0.67	0.86
<i>G-3</i>								
WK-K23	70	69	11.5	21.1	108	897.7	0.15	0.64
WK-K30	87	92	11.7	20.3	103	946.8	0.21	0.90
WA-K44	89	52	11.6	20.4	149	938.6	0.12	0.35
WA-K70a	186	82	11.7	20.5	214	938.9	0.18	0.38
WK-K44	205	80	11.0	19.0	160	950.2	0.19	0.50
WA-K81	237	50	11.3	19.6	169	950.3	0.12	0.29
WA-K83	247	51	11.0	19.4	99	939.3	0.12	0.52
WA-K85	252	63	11.8	20.3	183	956.2	0.14	0.35
WA-K87	261	50	11.4	19.7	114	956.0	0.12	0.44
WA-K89	273	62	11.6	20.3	176	940.5	0.14	0.35
WA-K91	290	62	11.3	20.0	220	931.0	0.14	0.28

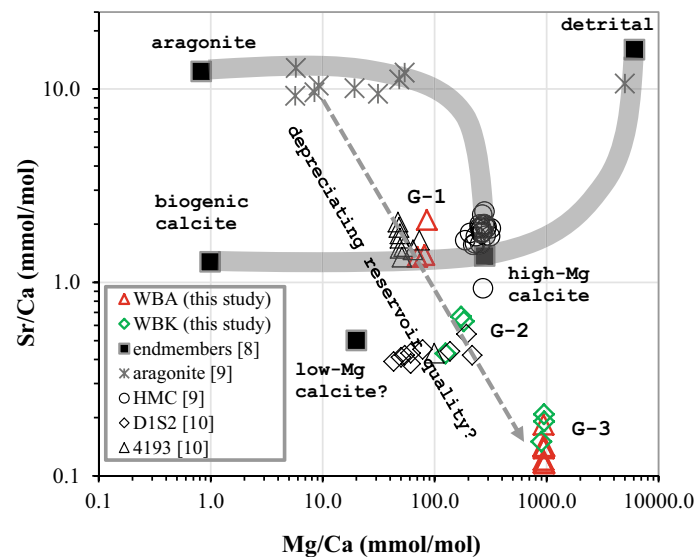


Fig. 2 Plot of Sr/Ca versus Mg/Ca of Buah carbonates. The filled squares represent endmembers (e.g., aragonite, detrital, biogenic calcite, high-Mg calcite, and low-Mg calcite) taken from Bayon et al. (2007). Data of aragonite (asterisks; Joseph et al., 2013) and high-Mg

calcite (circles; Joseph et al., 2013) are shown for reference. Data of samples from the Gulf of Mexico (e.g., D1S2 and 4193) are plotted for comparison (Huang et al., 2020). Abbreviations: WBA = Wadi Bani Awf, WBK = Wadi Bani Kharus, and HMC = high-Mg calcite

This trend is compatible with the fact that the rhombohedral calcite admits smaller Mg^{2+} cations (ionic radius = 86 pm) into the crystal structure than orthorhombic aragonite, which allows larger Sr^{2+} cations (ionic radius = 132

pm). It is observed that the data from samples precipitated from seepage of hydrocarbon-rich brine fluids with extensive micropores and shell material (i.e., 4193 from site AC601, Gulf of Mexico; Huang et al., 2020) matches G-1 samples.

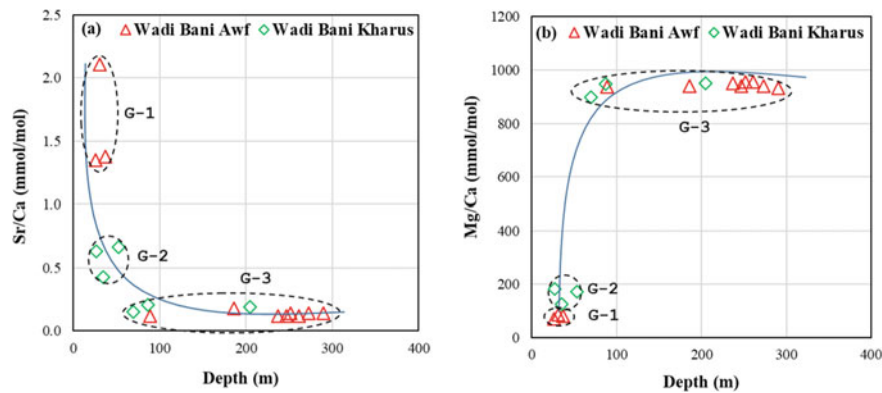


Fig. 3 Plot of Sr/Ca ratio (a) and Mg/Ca ratio (b) versus depth (m)

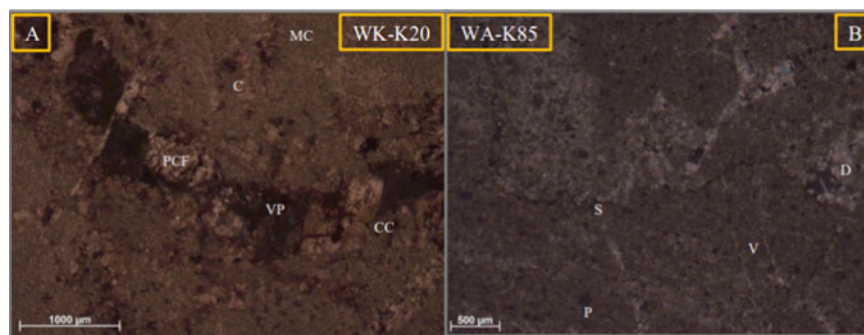


Fig. 4 (a) Photomicrograph of WK-K20 (G-2) showing micrite calcite (MC), calcite (C), calcite cement (CC), partial cemented fracture (PCF), and vuggy porosity (VP). (b) Photomicrograph of WA-K85 (G-3) showing stylolite (S), peloid (P), dolomite (D), and veins (V)

Furthermore, data from aphanite micrite samples precipitated from hydrocarbon-free brine fluids (i.e., D1S2 from site GC53, Gulf of Mexico; Huang et al., 2020) are comparable with the G-2 samples. The G-3 samples are characterized by the lowest Sr/Ca and the highest Mg/Ca values.

The main mineral percentages in G-1 (calcite = 74–91%; dolomite = 0–10%), G-2 (calcite = 30–55%; dolomite = 40–55%), and G-3 (calcite = 5–45%; dolomite = 38–82%) are also anticorrelated (Al-Siyabi, 2020). The Sr/Ca ratio decreases abruptly until a depth of 70–90 m for G-1 and G-2 samples and remains almost constant for the G-3 samples (Fig. 2). On the other hand, the Mg/Ca ratios of G-1 and G-2 are falling close to each other and below 200 mmol/mol, but there is a substantial difference between G-1, G-2 (Mg/Ca < 200 mmol/mol), and G-3 (Mg/Ca ~ 950 mmol/mol) (Fig. 3).

The anticorrelation between Sr/Ca and Mg/Ca ratios suggests that G-1 and G-2 samples precipitated at shallower depths and G-2 samples may have been affected by the first diagenetic phase (e.g., micritization) in the marine diagenetic environment. However, G-3 samples may have suffered from mechanical and chemical compaction, resulting in the destruction of the porosity due to dolomite cement (Al-Siyabi, 2020) as shown in Fig. 4. Taken together, it

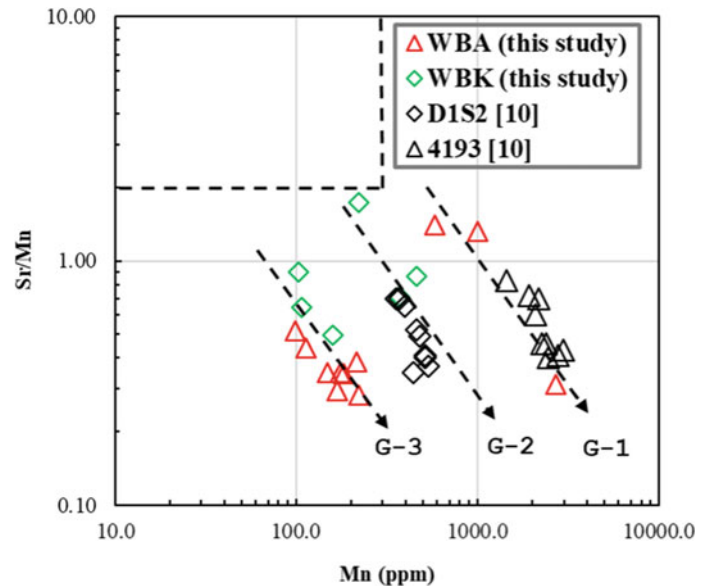
appears that the reservoir quality of Buah carbonates declined from G-1 to G-3 (Fig. 2).

Furthermore, the Mn contents in the studied samples range from 99 to 2712 ppm and decrease in the order of G-1 > G-2 > G-3. Sr and Mn (Sr/Mn vs. Mn) are often used to study the diagenetic alteration in marine carbonates (Brand & Veizer, 1980) because Mn is useful proxy for diagenetic alteration due to its mobility during burial, which can be used to track the progress of diagenesis (Fig. 4). The Sr/Mn ratio is also useful because it can help to differentiate between different diagenetic processes, such as recrystallization and cementation. All groups are found to be negatively correlated, and the G-1 and G-2 data agree with the 4193 and D1S2 data, respectively. Our results fall outside of the domain defined for carbonates retaining Sr isotopes of the original seawater (Denison et al., 1994) (Fig. 5).

5 Conclusions

The geochemical signatures of Buah carbonates suggest that the anticorrelation between Mg/Ca–Sr/Ca ratios and Sr/Mn ratio and Mn content may have been caused by variable diagenetic alterations, causing the samples to split into three

Fig. 5 Plot of Sr/Mn ratio versus Mn concentration of Buah carbonates (Jabal Al Akhdar) from WBA (red triangles) and WBK (green diamonds) outcrops along with D1S2 (open diamonds) and 4193 (open triangles) samples from the northern Gulf of Mexico. The dashed box represents the area where carbonates retain Sr isotopes of original seawater (Denison et al., 1994)



distinct groups. The alterations may have ranged from micritization to mechanical and chemical compaction, leading to dolomitization based on burial depth. The extent of reservoir quality reduction may have varied among the sample groups due to the water type from which they precipitated. We recommend the Sr isotope analysis of these samples to put better constraints on the reservoir quality evaluation.

References

- Al-Siyabi, S. M. S. (2020). *Depositional environment and diagenetic alteration of the pre-Cambrian Kharus Formation in the Jabal Al Akhdar, Northern Oman* (MS thesis, Department of Earth Sciences, College of Science, Sultan Qaboos University, Oman) (pp. 240).
- Allen, P. A. (2007) The Huqf supergroup of Oman: Basin development and context for Neoproterozoic glaciation. *Earth-Science Reviews*, 84, 139–185.
- Bayon, G., Pierre, C., Etoubleau, J., Voisset, M., Cauquil, E., Marsset, T., Sultan, N., Le Drezen, E., & Fouquet, Y. (2007). Sr/Ca and Mg/Ca ratios in Niger Delta sediments: Implications for authigenic carbonate genesis in cold seep environments. *Marine Geology*, 241, 93–109.
- Brand, U., & Veizer, J. (1980). Chemical diagenesis of a multicomponent carbonate system; 1, Trace elements. *Journal of Sedimentary Petrol.*, 50, 1219–1236.
- Burns, S. J., & Matter, A. (1993). Carbon isotopic record of the latest Proterozoic from Oman. *Eclogae Geologicae Helveticae*, 86, 595–607.
- Cozzi, A., Allen, P. A., & Grotzinger, J. P. (2004a). Understanding carbonate ramp dynamics using $\delta^{13}\text{C}$ profiles: Examples from the Neoproterozoic Buah Formation of Oman. *Terra Nova*, 16, 62–67.
- Cozzi, A., Grotzinger, J. P., & Allen, P. A. (2004b). Evolution of a Terminal Neoproterozoic carbonate ramp system (Buah Formation, Sultanate of Oman): Effects of basement paleotopography. *Geological Society of America Bulletin*, 116(11/12), 1367–1384.
- Denison, R. E., Koepnick, R. B., Fletcher, A., Howell, M. W., & Callaway, W. S. (1994). Criteria for the retention of original seawater $^{87}\text{Sr}/^{86}\text{Sr}$ in ancient shelf limestones. *Chemical Geology*, 112, 131–143.
- Gorin, G. E., Racz, L. G., & Walter, M. R. (1982). Late Precambrian-Cambrian sediments of Huqf Group, Sultanate of Oman. *American Association of Petroleum Geologists Bulletin*, 66, 2609–2627.
- Huang, H., Wang, X., Gong, S., Krake, N., Birgel, D., Peckmann, J., Chen, D., & Fend, D. (2020). Element patterns of primary low-magnesium calcite from the seafloor of the Gulf of Mexico. *Minerals*, 10, 299.
- Jacobsen, S. B., & Kaufman, A. J. (1999). The Sr, C and O isotopic evolution of Neoproterozoic seawater. *Chemical Geology*, 161, 37–57.
- Joseph, C., Campbell, K. A., Torres, M. E., Martin, R. A., Pohlman, J. W., Riedel, M., & Rose, K. (2013). Methane-derived authigenic carbonates from modern and paleoseeps on the Cascadia margin: Mechanisms of formation and diagenetic signals. *Palaeogeography, Palaeoclimatology, Palaeoecology*, 390, 52–67.
- Nogueira, L. B., Oliveira, V. Q., Araújo, L. P., Leão, L. P., Ali, A., Leite, M. G. P., Nalini, H. A., Jr., & Banerjee, N. R. (2019). Geochemistry and C and O isotope composition of carbonate rocks from Bemil and Lagoa Seca quarries, Gandarela Formation, Quedzilátero Ferrífero—Brazil. *Journal of South American Earth Sciences*, 92, 609–630.
- Yue, L., & Vandeginste, V. (2020). Neoproterozoic Nafun Group sediments from Oman affected by an active continental margin. *Minerals*, 10, 511.



Quantifying Gas Hazard with VIGIL (Automatized Probabilistic Volcanic Gas Dispersion Modelling)

Fabio Dioguardi, Silvia Massaro, Giovanni Chiodini, Antonio Costa,
Arnau Folch, Giovanni Macedonio, Laura Sandri, Jacopo Selva,
and Giancarlo Tamburello

Abstract

Volcanic gas emission represents a source of hazard to humans and the environment. They occur both during volcanic unrest, eruptions and in quiescent stages of the volcanic activity. Therefore, it is a widespread and frequent threat. Many gas species (e.g. CO₂, SO₂) can affect human health and even threaten life at concentrations and doses above species-specific thresholds. Depending on the relative buoyancy at the emission location, volcanic gas emissions can be generally classified as dilute passive degassing and dense gas flow. Numerical simulations of gas dispersion involve a workflow that can be complex and time-consuming, since it starts with the modelling of the wind field, proceeds with the gas dispersion simulation and ends with the postprocessing stage. This process should be repeated several times (hundreds to thousands) for probabilistic volcanic hazard applications, in which the uncertainty of the relevant input parameters (e.g. wind field, emission rates and source locations) is explored to obtain probabilistic outputs. Here we present VIGIL, a Python simulation tool that manages the gas dispersion simulation workflow and is interfaced with two dispersion

models: a dilute (DISGAS) and a dense gas (TWODEE-2) dispersion model. We show results from different applications showcasing the various capabilities of VIGIL.

Keywords

Atmospheric gas dispersion • Volcanic gases • Python workflow • Diagnostic wind model • Probabilistic volcanic hazard assessment

1 Introduction

In this work, we present VIGIL (automatized probabilistic Volcanic Gas Dispersion modelling) (Dioguardi et al., 2022), a Python tool designed to perform atmospheric gas dispersion modelling for both forecasting and probabilistic hazard assessment applications. Volcanic gas emissions occur in different geological contexts and therefore produce a wide range of potential impacts (Edmonds et al., 2018). For example, volcanic gases can be advected by winds (e.g., fumaroles, volcanic plumes) or accumulate and flow down valleys as a gravity flow, engulfing and asphyxiating people (Folch et al., 1986). In fact, volcanic gases are hazardous for human health and life above certain gas species-specific concentration levels and exposure times (IVHHN, 2015). In this conference paper we show an example of the application of the latest version of VIGIL, v1.3 (VIGILv1.3).

2 Materials and Methods

VIGIL is a collection of Python scripts that manage the entire workflow characterizing gas dispersion simulations, which consists of three stages: (1) meteorological data retrieval and processing; (2) gas dispersion simulations; (3) final postprocessing stage.

F. Dioguardi (✉) · S. Massaro
Dipartimento di Scienze Della Terra e Geoambientali,
Università Degli Studi di Bari “Aldo Moro”, Bari, Italy
e-mail: fabio.dioguardi@uniba.it

F. Dioguardi
British Geological Survey, The Lyell Centre, Edinburgh, UK

S. Massaro · G. Chiodini · A. Costa · L. Sandri · J. Selva ·
G. Tamburello
Istituto Nazionale di Geofisica e Vulcanologia,
Sezione di Bologna, Bologna, Italy

A. Folch
Geociencias Barcelona (GEO3BCN-CSIC), Barcelona, Spain

G. Macedonio
Istituto Nazionale di Geofisica e Vulcanologia,
Osservatorio Vesuviano, Naples, Italy

Meteorological data can be automatically retrieved from the NOAA-NCEP Global Forecast System (GFS) Numerical Weather Prediction (NWP) dataset (NOAA-NCEP Global Forecast System (GFS)) in forecast mode or the ECMWF ERA5 NWP dataset (Copernicus Climate Change Service (C3S) 2017) in reanalysis mode (e.g. for probabilistic hazard applications). User-provided data from local weather stations can also be used.

The meteorological data derived from the global models are then interpolated onto the location of interest. Subsequently, the wind field in the simulation domain is calculated from the meteorological data using the diagnostic wind model DIAGNO v1.1.6 (Douglas et al., 1990). The gas dispersion simulations are then performed using either DISGAS v.2.2.4 (Costa & Macedonio, 2016) or TWODEE-2 v.2.6 (Folch et al., 1986). The choice of the solver depends on the scenario: DISGAS for passive gas dispersion, TWODEE for cold dense gas flows. In the case of probabilistic applications, VIGIL allows to simultaneously perform N simulations by changing the meteorological conditions (e.g. sampling N different days with varying wind speed and direction) and the gas emission properties (gas flux, emission locations) in the simulations stage.

In the final postprocessing stage, the outputs of DISGAS or TWODEE are processed to produce graphical outputs. In the case of probabilistic hazard applications, the simulation outputs are combined to produce empirical cumulative density functions (ECDF) that can be then interrogated by the user to produce concentration maps at specified exceedance probabilities. Furthermore, VIGIL produces persistence maps, i.e. maps of the probability to overcome the concentration threshold for the exposure time or longer. Finally, hazard curves, i.e. plots of ECDF vs. concentration, can be created at selected locations.

3 Results

In this section, we show preliminary results of the probabilistic hazard application of VIGIL to the case of Mefite d'Ansanto.

Mefite d'Ansanto is the site of the largest natural emission of cold CO₂-rich gases from non-volcanic environment on Earth (Chiodini et al., 2010). Under low-wind conditions, the gas flows along W-E channel producing a persistent invisible gas river, which has already killed several people (Chiodini et al., 2010).

We consider CO₂ as the main tracer, and the outputs yield concentrations expressed as values in excess of background CO₂ levels in the air at heights selected by the user. One thousand four hours-long simulations were performed with TWODEE considering an emission of CO₂ from an area towards the east of the computational domain with an overall

flux of 23.18 kg s⁻¹ (Chiodini et al., 2010). The results were combined to obtain the ECDF of the CO₂ concentration and persistence maps at the last time step of the simulations at different heights above the ground. Figure 1 shows examples of probabilistic output for the test case, specifically a map of CO₂ concentration at 2 m above the ground at an exceedance probability of 1% (Fig. 1a) and a map of the probability of exceeding a CO₂ concentration of 100,000 for at least 1 h (Fig. 1b); the latter represents deadly conditions for human beings. It can be seen how, in the worst-case scenario (1% exceedance probability) very high concentration occurs in many areas of the domain and that deadly doses of CO₂ cannot be discarded in the source area and along the valley.

4 Discussion

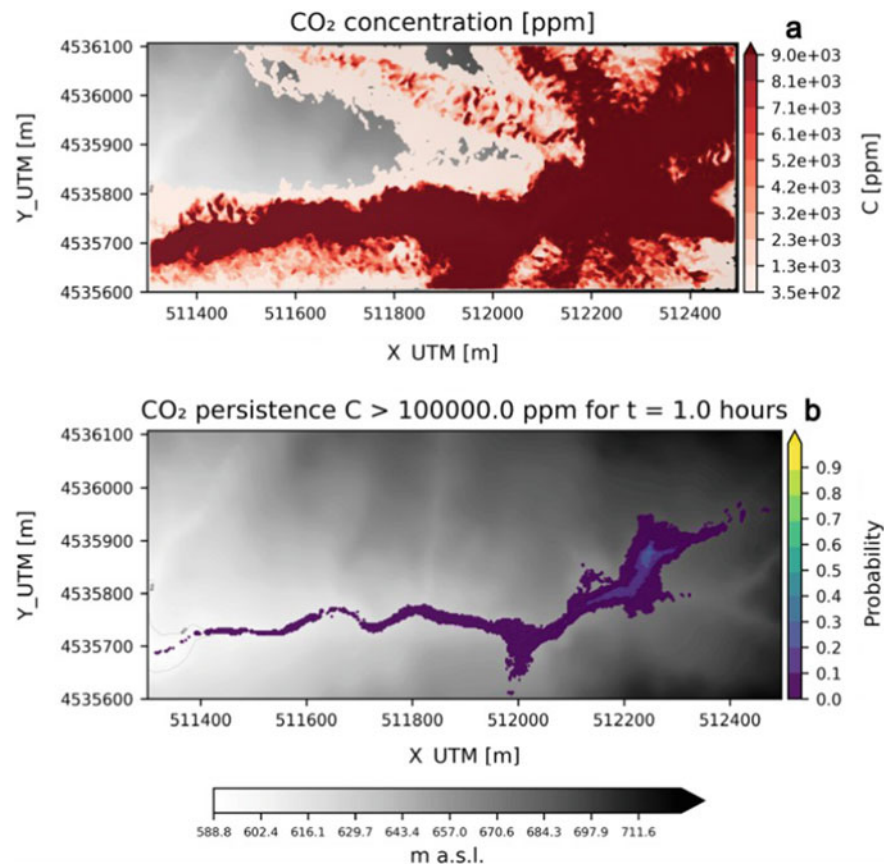
VIGIL is a workflow manager built for carrying out both forecast and reanalysis simulations of gas dispersal in the low troposphere close to the ground, both of volcanic and non-volcanic origin. In forecast mode it can be used by volcano observatories to carry out daily automatic forecasts of gas dispersal in areas of interest. On the other hand, in reanalysis mode it can be used for validation studies (e.g., replicate gas measurement campaigns with the dispersion models). But it is in the probabilistic hazard assessment application where the reanalysis mode of VIGIL demonstrates its importance and potential. In fact, it greatly simplifies the setting up, running and postprocessing of the large number of simulations that are normally required for these probabilistic applications.

The presented example shows how VIGIL can be used for probabilistic hazard assessment for gas emissions. The application to Mefite d'Ansanto showcased one of the possible applications of VIGIL and the importance of carrying out such studies. For example, Fig. 1a shows how the hazard posed by high concentrations of CO₂ cannot be neglected also outside the emission area and the W-E valley, which are the areas that are considered those at the highest level of danger. In fact, dangerously high concentrations of CO₂ can be seen towards the N, NE, E and SE of the emission area.

5 Conclusions

In this conference paper, we briefly introduced the latest version of VIGIL (VIGILv1) and preliminary results of one probabilistic application. Further test cases were originally presented in Dioguardi et al. (2022) and are fully described in the user manual of the latest version. All examples show the potential of VIGIL to be used for: (1) forecasting gas dispersion; (2) validating the gas dispersion models over long measurements campaigns and (3) carrying out

Fig. 1 Probabilistic outputs of the Mefite d'Ansanto test case. **a** CO₂ concentration at 2 m above the ground at an exceedance probability of 1%. **b** Probability of exceeding a concentration of 100,000 ppm for a duration of 1 h



probabilistic hazard assessments and producing meaningful outputs like concentration plots at user-specified exceedance probabilities, hazard curves and persistence maps.

VIGIL itself and the software linked with it are under constant maintenance and development. New capabilities already under implementation include the addition of new types of persistence maps, the improvement of the diagnostic wind model to be more flexible in terms of run duration and time step duration and numbers (currently restricted to 1 h and 24, respectively) and the implementation of maps in which buildings and infrastructures can be displayed.

References

- Chiodini, G., Granieri, D., Avino, R., Caliro, S., Costa, A., Minopoli, C., & Vilardo, G. (2010). Non-volcanic CO₂ Earth degassing: Case of Mefite d'Ansanto (Southern Apennines), Italy. *Geophysical Research Letters*, 37, 11.
- Copernicus Climate Change Service (C3S). (2017). ERA5: Fifth generation of ECMWF atmospheric reanalyses of the global climate. *Copernicus Climate Change Service Climate Data Store (CDS)*. <https://cds.climate.copernicus.eu/cdsapp#!/home>.
- Costa, A., & Macedonio, G. (2016). DISGAS: A model for passive DISpersion of GAS. *Rapporti tecnici INGV, Istituto Nazionale Di Geofisica e Vulcanologia, Italy*, 332, 2039e7941.
- Dioguardi, F., Massaro, S., Chiodini, G., Costa, A., Folch, A., Macedonio, G., Sandri, L., Selva, J., & Tamburello, G. (2022). VIGIL: A python tool for automatized probabilistic Volcanic Gas dispersion modelling. *Annals of Geophysics*, 65(1), DM107.
- Douglas, S. G., Kessler, R. C., & Carr, E. L. (1990). User's guide for the urban Airshed model. Volume 3. User's manual for the diagnostic wind model (No. PB-91-131243/XAB), systems applications. *Inc., San Rafael, CA (USA)*.
- Edmonds, M., Grattan, J., Michnowicz, S. (2018). Volcanic gas: Silent killers. In C. Fearnley, J. Bird, D.K. Haynes, W.J. McGuire, G. Jolly (Eds.), *Observing the volcano world: Volcano crisis communication*. Springer.
- Folch, A., Barcons, J., Kozono, T., Costa, A. (2017). High-resolution modelling of atmospheric dispersion of dense gas using TWODEE-2.1: Application to the 1986 Lake Nyos limnic eruption. *Natural Hazards and Earth System Sciences*, 17, 861–879.
- International Volcanic Health Hazard Network (IVHHN). (2015). *Volcanic gases and aerosols guidelines*. https://www.ivhnn.org/images/pdf/gas_guidelines.pdf.
- NOAA-NCEP Global Forecast System (GFS). <https://www.ncei.noaa.gov/products/weather-climate-models/global-forecast>.
- VIGIL v1.3. <https://github.com/BritishGeologicalSurvey/VIGIL/releases/tag/v1.3>.



Geochemical Characterization of Borehole Production Water in Southern Tunisia: Relationship with the Nature of the Reservoir and Environmental Quality of the Water Discharge

Amel Triki, Amina Mabrouk El Asmi, and Sonia Barbouchi

Abstract

Petroleum production is constantly coupled to the production of large quantities of water, called formation waters, which are originally associated to hydrocarbons from a given oil reservoir. In this work, we propose to chemically characterize and environmentally assess the waters produced from boreholes in the regions of Jeffara and the Ghadames basin in southern Tunisia. For that, water samples from the TAGI reservoir, Triassic in age, the Acacus reservoir, Upper Silurian in age, and the Bir Ben Tartar reservoir, Ordovician in age, which are major siliciclastic reservoirs producing oil in southern Tunisia, were the subject of a thorough sampling. A total of twenty-eight borehole water samples were collected from the wellheads (17 from the TAGI reservoir, 7 from the Acacus reservoir and 4 from Bir Ben Tartar reservoir) and two samples were recovered from the Waha treatment centre. All samples were analyzed in the Petroleum Research and Development Centre (CRDP) ETAP using the ICP-AES method. The geochemical results and the chemical facies evaluation show a tight similarity between all waters recovered from different reservoirs with a predominance of the chloride-sodium facies. This is despite that the three reservoirs are not connected. This resemblance is probably due to the common marine origin of these formation waters. Nevertheless, waters recovered from the Acacus reservoir are characterized by a strong

acidity and a very high salinity, which can reach 290 g/l. Produced waters are treated and discharged of traces of hydrocarbons (gas and liquid) and their solid loads in order to be reinjected into injection wells and the excess is injected into discharge wells. The quality of this water does not comply with the standards for discharge into the water environment. No produced water is currently discharged at the surface. Should the case arise in the future, the NT106.03 standards must be strictly obeyed. Potentially, excess production water from oil drilling can be recovered and adequately treated for use in agricultural irrigation networks.

Keywords

Production water • Bir Ben Tartar • Acacus • TAGI • Chemical facies • Sodium chloride • Marine origin • Standard NT106.03 • Ghadames basin

1 Introduction

Petroleum production is commonly accompanied by a substantial volume of formation water, which is generally conveyed through processing facilities and then reinjected for production or disposal purposes or discharged at the surface.

Accordingly, the need for the chemical characterization of such waters is of great environmental importance as it helps to verify its suitability for disposal into a given system.

In the present study, water samples were collected from three clastic reservoirs: the Triassic TAGI Fm, the Upper Silurian Acacus Fm and the Ordovician Bir Ben Tartar Fm, which are the major oil producing reservoirs in southern Tunisia. The study area covers the Jeffara and Ghadames areas.

All samples were analyzed in the Petroleum Research and Development Centre (CRDP) of ETAP (NOC Tunisia) using the ICP-AES method.

A. Triki (✉) · S. Barbouchi

Laboratory of Sedimentary Basins and Petroleum Geology (LR 18ES07), Geology Department, Faculty of Sciences of Tunis, University of Tunis El Manar, 2092 Tunis, Tunisia
e-mail: Amel.triki@etap.com.tn

S. Barbouchi

e-mail: Sonia.barbouchi@etap.com.tn

A. M. E. Asmi

Entreprise Tunisienne d'activités Pétrolières, Avenu Mohamed V, Tunis, Tunisia
e-mail: Amina.mabrouk@fst.utm.tn

The study area is located in Southern Tunisia and covers the Jeffara area to the northeast and the Ghadames basin to the southwest.

The structural setting is generally represented by a regional monoclinical trend dipping and deepening from Jeffara in the N–E to Ghadames in the S–W. Triassic sediments outcrop, northeast of the Jeffara are buried to approximately 3000 m to the southwest in the Ghadames basin (Fig. 1).

2 Materials and Methods

The samples were analyzed to determine the physical–chemical properties of the different formation waters and to verify reservoir connectivity between wells. The pH, electrical conductivity (EC) and TDS were measured in the field using HANNA apparatus.

The inductively coupled plasma atomic emission spectrometry (ICP-AES) was used for measuring the main

cations as well as heavy metal contents. Anions were determined by titration.

The software AqQA was used for the identification of water classes through Piper and Stiff diagrams. Sulin graph (Kurlov formula) was used to display the primary characterization of the water chemistry (Zaporozec, 1972).

3 Results

The hydro chemical facies as delineated from Piper and Sulin plots show that waters recovered from Ghadames basin are mainly of chloride calcium genetic water type, more saline sea water and submitting an old marine water origin, whereas in the Jeffara area water recovered from the TAGI area are of sulphate genetic water type, the salinity is less than the sea water suggesting an infiltrate meteoric water (Table 1; Fig. 2).

Fig. 1 Geological map of study area and samples locations

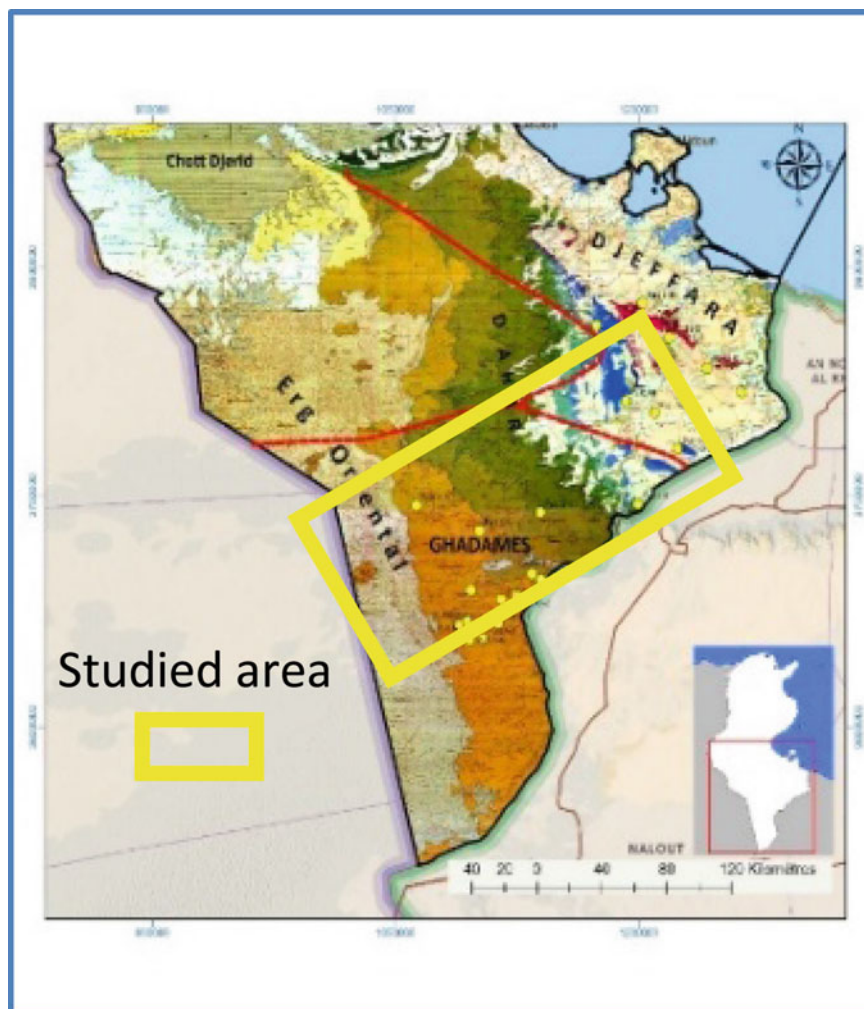
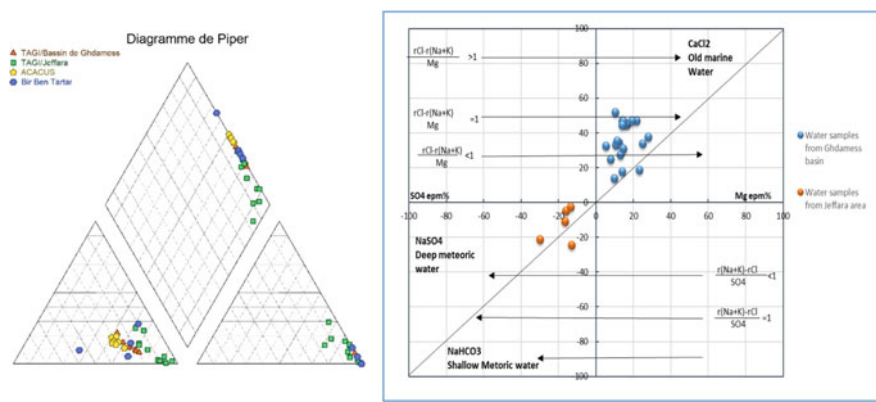


Table 1 Formation water analysis

Field	Unit	Ca ²⁺	Mg ²⁺	K ⁺	Na ⁺	SO ₄ ²⁻	Cl ⁻	HCO ₃ ⁻	TDS	pH
Av TAGI/Gah	epm	395.95	252.72	21.81	973.6	20.82	1645.6	3.1	94.32	7.8
	epm%	24.06	15.37	1.32	59.23	1.24	98.56	0.18		
Av TAGI/Jeff	epm	44.051	46.324	3.148	284.23	39.04	332	6.7	22.92	8
	epm%	11.66	12.26	0.83	75.24	10.3	87.9	1.78		
Av ACACUS	epm	1446.49	758.92	51.34	2541	0.15	4885	0	276.5	3.2
	epm%	30.14	15.81	1.07	52.96	0.003	99.2	0		
Av BBT	epm	372	319.62	8.19	1212.69	24.69	1939.75	1.74	114.05	7.7
	epm%	19.45	16.71	0.42	63.4	1.25	98.65	0.08		
SW	epm	2.07	9.83	0.975	46.23	5.4	54.55	0.23	35	8.8
	epm%	3.51	16.62	1.65	78.21	8.97	90.64	0.38		

Fig. 2 Formation waters types: piper and sulin plots

The mineral saturation indexes show that almost all the samples are carbonate oversaturated and sulphides under saturated (Fig. 3).

The TAGI formation salinity is extensively disseminated. It is rising from few grams per litre in shallow depth. The salinity increases with depth (Fig. 4).

4 CPF Processing Centre

Produced waters are treated and discharged of their solid loads in order to be reinjected into injection wells. The excess volumes are injected into disposal wells in the area (Table 2).

5 Discussion

The Na⁺, Ca²⁺ and Cl⁻ ions constitute more than 98% of the total TDS ranked as follows: Na⁺ > Ca²⁺ > Mg²⁺ > K⁺ and Cl⁻ > SO₄²⁻ > HCO₃⁻. Na⁺ and Cl⁻ are the predominant ions, with higher values recorded in wells of Ghadames basin area.

The formation waters recovered from the Acacus reservoir are characterized by an acidic pH (average 3.2), while those of the TAGI and Bir Ben Tartar reservoirs are basic.

Sulphates and bicarbonates exhibit a greater importance in samples of the Jeffara, while they are depleted in Ghadames basin.

6 Conclusions

Formation waters recovered from Ghadames basin are exclusively chloride-calcium type suggesting a marine water origin, whereas it is confirming a deep meteoric water in the Jeffara area. In Ghadames basin in general, the salinity increases with the depth with a special state of the Silurian ACACUS which shows the highest probably due to shale impact. TAGI reservoirs show remarkable decrease of the TDS from Ghadames to Jeffara, which can be related to the infiltration of the fresh rain waters into the TAGI reservoir exposed at the surface. Even the quality of the processed formation water is perfectly complying with the environmental discharge standards, no produced water is currently discharged at surface. Potentially, the excess production water can be recovered and adequately treated for use in agricultural irrigation networks.

Fig. 3 Mineral saturation index

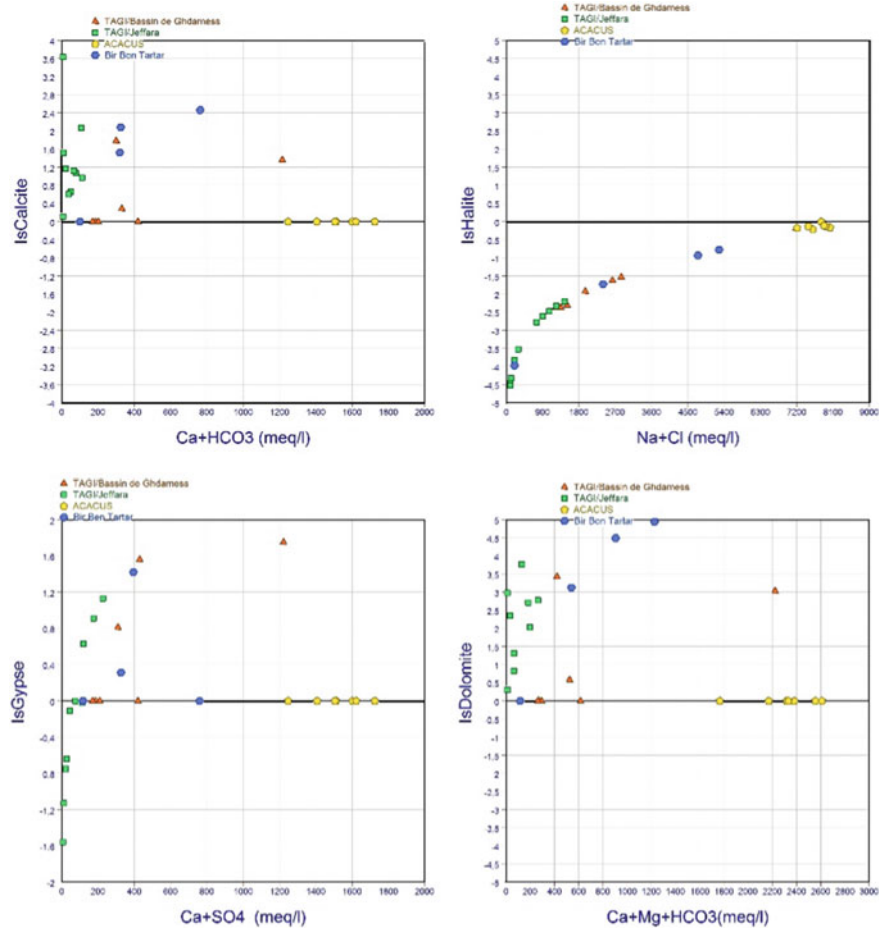


Fig. 4 Salinity distribution maps

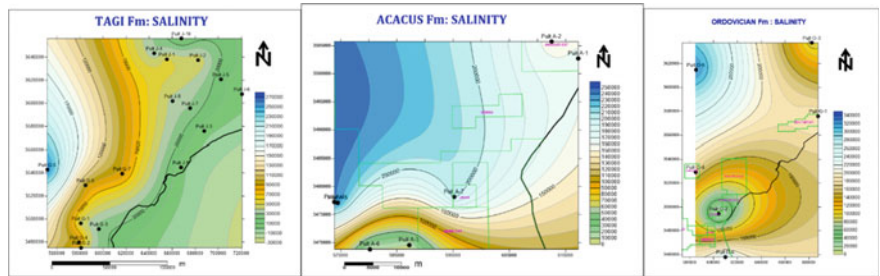


Table 2 Comparison of chemical analysis results before and after processing

	pH	Condu (S/cm)	DCO (mg/l)	DBO (mgO ₂ /L)	SS (mg/L)
Prod water (inlet separator)	4.5	231,000	227,00	130	437,00
Prod water (disposal well)	4	230,000	128,00	52	1910
DECREE 18/03/19 JORT	6.5 < pH < 8.5	5000	125	30	30

References

- Mackenzie, F. T., Byrne, R. H., Dubury, A. C. (2020) *Seawater*. Encycl. Br
- Piper, A. M. (1944). A graphic procedure in the geochemical interpretation of water analyses. *Transactions. American Geophysical Union*, 25, 914–923.
- Sullin, V. A. (1946). Waters of petroleum formations in the system of natural water.
- Zaporozec, A. (1972). Graphical interpretation of water quality data. *Ground Water*, 10(2), 32.



Peculiarities of the Vertical Profiles of CH₄ and CO₂ Concentrations in the Arctic Seas Sediments

Elena Tkachenko, Vyacheslav Sevastyanov, Veniamin Fedulov, Valery Fedulova, Olga Kuznetsova, Sergei Naimushin, Nikita Dushenko, Artem Krivenko, and Alyona Vinnikova-Malova

Abstract

The distribution of CH₄ and CO₂ concentrations along marine sediment vertical profiles (up to 4 m depth below the sea floor) from different sectors of the Kara, Laptev and East-Siberian Seas (Russian Arctic Seas) is presented. The symbiotic correlation between their concentrations was shown. The correlation coefficient (R) varied from 0.58 to 0.97 for the sediments of the Kara Sea and it did not depend on the CH₄ and CO₂ distribution along the vertical sediment profile. The concentrations of CH₄ and CO₂ synchronously increase with depth in the Kara Sea and the highest concentrations of CH₄ and CO₂ are observed at 170–190 cm. It has been shown that sulfate reduction process, acetogenesis, methanogenesis and methanogenesis involving dimethyl sulfide leads to CH₄ and CO₂ parallel formation. The $\delta^{13}\text{C}\text{-CO}_2$ value gradually decreases from -17 to -27‰ versus VPDB with the sediment depth. The evidence of CO₂ deep origin is the $\delta^{13}\text{C}$ high average value, varying from -18 to -10‰ .

Keywords

Marine sediments • Laptev sea • Kara sea • Methane • Seep fields • Carbon dioxide • Isotopic composition

1 Introduction

Formation processes of gases in marine sediments are still not clear, despite of the large number of investigations devoted to the organic matter (OM) and gases in Arctic Seas sediments (Coffin et al., 2013; Semenov et al., 2020). The main gaseous products of organic waste anaerobic decomposition are carbon dioxide, methane, dimethyl sulfide, lower alkanes and alkenes. Under anaerobic conditions, methane oxidation can occur by groups of methanotrophic archaea and sulfate-reducing bacteria (Boetius et al., 2000; Knittel & Boetius, 2009; Meister & Reyes, 2019). The purposes of this work were to study the vertical profiles and correlation of CH₄ and CO₂ concentrations in the sediments of the Kara, Laptev and East-Siberian Seas and understand the processes leading to the peculiarities in the gas distribution.

2 Methods and Materials

Marine sediment columns were sampled from Kara, Laptev and East-Siberian Seas using box corer (BC) and gravity corer (GC), during the Arctic voyages of the R/V Akademik Mstislav Keldysh (2017–2020 years). The lengths of BC columns are up to 50 cm and up to 500 cm for GC columns, respectively. Samples were sampled from 14 stations in the Kara Sea, 13 in the Laptev Sea (short columns), including seeps, and 6 stations in the East-Siberian Sea. Water depths ranged from 27 to 2987 m at these stations. The marine sediments were handle placed into the 0.5 L bottles with a saturated NaCl solution, then the bottles were placed in the ultrasonic bath and then into the oven. The gases were extracted into a He bubble (Sevastyanov et al., 2021). The CO₂ carbon isotopic composition isolated from sediments was measured by CF-IRMS method using an HP 6890 gas chromatograph and a Delta Plus mass spectrometer (Thermo Fisher Scientific, Bremen, Germany). The standard deviation was $< \pm 0.2 \text{‰}$.

E. Tkachenko (✉) · V. Sevastyanov · V. Fedulov · V. Fedulova · O. Kuznetsova · S. Naimushin · N. Dushenko · A. Krivenko · A. Vinnikova-Malova
Vernadsky Institute of Geochemistry and Analytical Chemistry of Russian Academy of Sciences, Kosygin st. 19, Moscow, Russia
e-mail: tkachenko@geokhi.ru

V. Sevastyanov
e-mail: vsev@geokhi.ru

3 Results

The correlation coefficients R between the concentrations of CH₄ and CO₂ gases were calculated for the sediment columns and are presented in Table 1. The concentrations of CO₂ changed from 188.4 up to 1389.9 µg/L and the concentrations of CH₄ changed from 0.548 up to 3.305 µg/L for Kara Sea sediments. Measured concentrations for Laptev Sea columns were shown in (Sevastyanov et al., 2021) and in references in (Sevastyanov et al., 2021) for East-Siberian Sea columns.

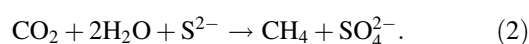
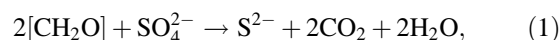
The gas formation processes in marine sediments associated with the OM transformation may have different nature. CH₄ and CO₂ gases concentrations distribution curves of sediment columns can significantly differ especially in the surface layer (0–15 cm). For example, in the columns 5960 and 5963, a positive correlation between CH₄ and CO₂ gases concentrations is observed in the shallower layers, while the correlation turns to be negative in the deeper layers (Table 1). Average gas concentrations in columns 6928 (CO₂ is 1389.9 µg/L and CH₄ is 2.798 µg/L) and 6245 (CO₂ is 517.6 µg/L and CH₄ is 1.896 µg/L) of sediments in the estuary of the Ob River exceed the gases concentrations in sediment columns at other columns (Sevastyanov et al., 2021): concentrations of CO₂ and CH₄ are 384.9 and 2.066 µg/L in column 6259, for example. In this case, the CO₂ average concentration exceeds the average CH₄ concentration by 100 times usually, and the average CH₄ concentration can exceed the average CH₃SCH₃ concentration by 2–10 times. Perhaps, CH₃SCH₃ (the concentrations were 0.364 and 9.347 µg/L in 6928 and 6245 columns,

respectively) is formed during the algae and the cyanobacteria decomposition (Zhuang et al., 2017). The CS₂ compound is oxidized to form COS in the sulfate reduction zone. The presence of high concentrations of sulfurous gases indicates to bacterial activity in marine sediments.

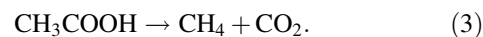
4 Discussion

The main reactions to form CH₄ and CO₂ due to sulfate reduction, acetogenic methanogenesis and methylotrophic methanogenesis with the participation of dimethyl sulfide can be presented as follows:

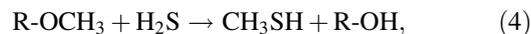
Sulfate reduction:



Acetogenic methanogenesis:



Methanogenesis involving dimethyl sulfide:



where R is H or an aromatic group.

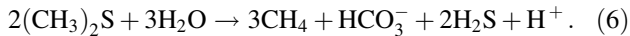
Then, due to the influence of bacterial enzymes, bicarbonate is fixed and methanethiol is methylated to form CH₃SCH₃:



Table 1 Correlation coefficients (R) between CH₄ and CO₂ concentrations in the sediment columns of Russian Arctic Seas

Seas	Columns	R	Seas	Columns	R
East-Siberian Sea	5602-2	0.45	Kara Sea	5966	0.40
Kara Sea	5636	0.97	Kara Sea	5967	0.57
Kara Sea	5644	0.44	Kara Sea	6239	0.13
Kara Sea	5943	0.67	Kara Sea	6245	0.95
Laptev Sea	5947	0.58	Kara Sea	6259	0.58
Laptev Sea	5949	0.05	Kara Sea	6261	0.80
Laptev Sea	5950	0.70	Kara Sea	6879	0.97
Laptev Sea	5953-1	0.01	Kara Sea	6883	0.93
Laptev Sea	5953-3	0.39	Kara Sea	6887	0.84
Laptev Sea	5954	0.59	Kara Sea	6907	0.97
Laptev Sea	5956-2	0.16	Kara Sea	6912	0.94
Laptev Sea	5958	0.58	Kara Sea	6916	0.81
Laptev Sea	5960	- 0.79	Kara Sea	6919	0.49
Laptev Sea	5962	0.68	Kara Sea	6928	0.93
Laptev Sea	5963	- 0.31			

Additionally, due to anaerobic conditions in the marine sediment, CH₃SCH₃ is converted to methane in a ratio of 1:1.5:



The studies carried out have shown that in Kara Sea sediments, in most cases, there are synchronous behaviors of the CH₄ and CO₂ concentrations. The correlation coefficient value R varies from 0.58 to 0.97 and does not depend on the nature of the gas concentration distribution in the marine sediments.

CH₃SCH₃ found in sediments let us to suggest that CH₄ and CO₂ are formed as a result of methylotrophic methanogenesis with the participation of CH₃SCH₃. Anyway, CO₂ and CH₄ can be originated by coupled processes of sulfate reduction and methanogenesis. These two processes are metabolically inextricably linked. According to thermodynamic calculations, sulfate-reducing bacteria suppress the rate of methanogenesis, thus CO₂ concentration in the sediment is significantly higher than CH₄ concentration. Most likely reactions (1) and (2), as well as hydrogenotrophic methanogenesis, run in parallel, and lead to methane concentration increase, in contrast to a high CO₂ concentration. Reactions (3) and (6) are less important, because they do not lead to a significant CO₂ concentration growth in the marine sediments.

For the 6239 and 6919 columns sediments no concentrations correlation were observed between CH₄ and CO₂ because of lithogenesis peculiarities (zones of vertical cracks in the fault structure) and deep thermogenic gas influx at the sampling sites. Column 6919 is located in the bay of the Novaya Zemlya archipelago, where a fault structure was recognized. A large accumulation of gases is located under column 6239. The average CH₄ concentration in column 6919 is 3.305 µg/L and it is higher than the average CH₄ concentrations in other columns of sediment from Kara and Laptev Seas.

Almost negligible concentration of CH₃SCH₃ indicates weak microbiological activity, whereas high concentration of CH₃SCH₃ suggests high microbial activity.

The high average value of the carbon isotope composition $\delta^{13}\text{C} = -10.46 \pm 0.89\text{‰}$ of CO₂ indicates to deep CO₂ source. The CO₂ carbon isotope composition for column 6907 is ^{12}C -enriched ($\delta^{13}\text{C} = -21.08 \pm 1.49\text{‰}$ versus VPDB), which indicates a biogenically originated CO₂ (Meister & Reyes, 2019).

CO₂-increased concentration in the sediments surface layers (0–15 cm) is observed, in comparison with the deeper horizons. This is associated with either aerobic methane oxidation by methanotrophs or anaerobic methane oxidation as a result of sulfate reduction. At the same time, the values of $\delta^{13}\text{C}$ -CO₂ are from -16 to -14 ‰ versus VPDB in the

surface layers of marine sediments. The $\delta^{13}\text{C}$ -CO₂ values increase in the near-surface sediment layers due to a CO₂ diffusion from the sediment into the aquatic environment.

5 Conclusions

The results of CH₄ and CO₂ concentrations distribution in the sediment columns from Kara Sea show a positive correlation between the two gases (R between 0.58 and 0.97) and it is not associated with nature of the CH₄ and CO₂ vertical distribution in the marine sediments.

Methanogenesis, coupled with sulfate reduction and hydrogenotrophic methanogenesis, leads to increasing of methane concentration at the background of high CO₂ concentration. Acetogenic methanogenesis and methylotrophic methanogenesis with the dimethyl sulfide participation are of lesser importance, because they do not lead to the formation of significant CO₂ amount. The evidence of the methylotrophic methanogenesis occurrence is the presence of CH₃SCH₃ in marine sediments.

A significant fold CO₂ concentration increase in the sediments surface layer (0–15 cm) was fixed in comparison with deeper horizons in some cases: in column 5963 the CO₂ concentrations are 1800 µg/L (10 cm depth bsf) and 800 µg/L (22 cm depth bsf) (Sevastyanov et al., 2021). This is due to CH₄ aerobic oxidation by methanotrophs or CH₄ anaerobic oxidation as a result of the sulfate reduction. Based on the features of CH₄ and CO₂ gases distribution abundances in the marine sediments and biogenic gas content, we can assume microbial processes are mainly responsible of the gases formation. The thermogenic gases (generating from thermocatalytic breakdown of complex organic molecules as they are cleaved and subsequently saturated to form the C1–C5 alkanes of natural gas) enter to the sediments from faults in sedimentary rocks and then mix with biogenic gases formed in the upper part of the sediments. Thus the gas formation processes in the upper layers of the sediments are proceeding differently in comparison with the processes in the deep layers, and all of this leads to lower correlation coefficients between the CH₄ and CO₂ concentrations.

References

- Boetius, A., Ravensschlag, K., Schubert, C. J., Rickert, D., Widdel, F., Gieseke, A., Amann, R., Jürgensen, B. B., Witte, U., & Pfannkuche, O. (2000). A marine microbial consortium apparently mediating anaerobic oxidation of methane. *Nature*, 407, 623–626.
- Coffin, R. B., Smith, J. P., Plummer, R. E., Yoza, B., Larsen, R. K., Millholland, L. C., & Montgomery, M. T. (2013). Spatial variation in shallow sediment methane sources and cycling on the Alaskan Beaufort Sea Shelf/Slope. *Marine and Petroleum Geology*, 45, 186–197.

- Knittel, K., & Boetius, A. (2009). Anaerobic oxidation of methane: Progress with an unknown process. *Annual Review of Microbiology*, 63, 311–334.
- Meister, P., & Reyes, C. (2019). The carbon-isotope record of the sub-seafloor biosphere. *Geosciences*, 9(12), 507, 1–25.
- Semenov, P., Portnov, A., Krylov, A., Egorov, A., & Vanshtain, B. (2020). Geochemical evidence for seabed fluid flow linked to the subsea permafrost outer border in the South Kara Sea. *Geochemistry*, 80(3), 125509.
- Sevastyanov, V. S., Fedulova, V. Y., Stennikov, A. V., Kuznetsova O. V., Naimushin S. G., Dushenko, N. V., Krivenko, A.P. (2021). Features of the distribution of gases in the upper layer of sediments in the system of the continental shelf of the Laptev Sea—The Arctic Ocean. *Oceanology*, 61(4), 472–487.
- Zhuang, G.-C., Lin, Y.-S., Bowles, M. W., Heuer, V. B., Lever, M. A., Elvert, M., Hinrichs, K.-U. (2017). Distribution and isotopic composition of trimethylamine, dimethylsulfide and dimethylsulfoniopropionate in marine sediments. *Marine Chemistry*, 196, 35–46.

Geoenergy Science and Engineering



A Novel Practical Method to Determine the Crude Oil Brine Rock System Wettability from Modified Amott Test

Abhijit Dandekar

Abstract

Wettability measurement of a crude oil–brine–rock (COBR) system is an integral part of the special core analysis (SCAL) since it influences the oil and water distribution and microscopic displacement of the former by the latter in a reservoir rock pore space. Wettability depends on several factors such as the type of rock, oil, and water properties, and the amount of time the pore space has been exposed to a given phase, i.e., oil, water, or both. Amott or its variant, the Amott-Harvey test, is perhaps the most time-honored and accepted method for wettability determination. Given the fundamental characteristics or definition of wettability, the Amott method is the most “logical” because wettability is determined based on the spontaneous and forced displacement of the oil by water and vice-versa. In a typical Amott test for a core sample, four different displacement cycles are required, which can be very time-consuming. We have recently designed a modified Amott method that is based only on the spontaneous displacement, which is carried out simultaneously on a pair of core samples originating from the same formation. Excellent, unambiguous wettability results have been obtained on the tested COBR system that proves the efficacy of our novel approach. Finally, the step-by-step methodology included in our paper demonstrates that it is not only practical and efficient, but also reliable, which can be easily implemented in the wettability determination of a given COBR system.

Keywords

Amott • COBR • SCAL • Oil-wet • Water wet • Microscopic displacement

1 Introduction

Fluid phases such as (gas), oil and water/brine are ubiquitously in contact with the reservoir rock pore spaces until they are brought to the surface as part of the recovery process. This ensemble is sometimes simply referred to as COBR system in which two sets of forces are active at the interface, for example, between the oil and water and oil/brine and the reservoir rock. It is the combination of all the active forces that determine the wettability of reservoir rocks, vis-à-vis the affinity for a given liquid phase such as oil, brine, or both. Although wettability as a numerical parameter does not enter in any reservoir engineering calculations, the knowledge of the COBR system wettability is critical because it influences fluid distribution in the pore space, petrophysical properties, and most importantly the displacement processes for hydrocarbon recovery. As a matter of fact, the fundamental definition of capillary pressure is in terms of the pressure difference between the non-wetting and wetting phases, respectively. On a broad scale, three different types of wettability states are recognized (Dandekar, 2013), namely (1) water wet (pore surfaces have preference for water); (2) oil-wet (opposite of water wet); and (3) intermediate or sometimes referred to as neutral wet (equal preference for both phases).

The wettability of a given COBR system can be determined either qualitatively or quantitatively. In qualitative methods, wettability is inferred or deduced from other measurements such as capillary pressure or relative permeability curves. Quantitative methods are direct measurements on representative rock and fluid samples from the formation. Typically, wettability is reported via a contact angle or a certain wettability index, signifying the degree of brine, oil, or intermediate wetness. Among the many different wettability measurement experimental techniques, the author believes that Amott (1951) or its variant, the Amott-Harvey (Cuiec, 1984) test, is perhaps the most time-honored and accepted method for wettability determination, given the

A. Dandekar (✉)
Department of Petroleum Engineering, University of Alaska
Fairbanks, Fairbanks, AK 99775, USA
e-mail: adandekar@alaska.edu

logic of spontaneous and forced displacement of the oil by water and vice-versa.

Notwithstanding the standard protocol and routine use of the Amott test, there are two main issues. One is the time requirement of repeating a displacement sequence on a given core sample and two there is always a question of the representativity of the core sample used as far as the true or in-situ wettability is concerned. Because the rock samples may have undergone irreversible (wettability) alterations and consequently the COBR system changed from the time the sample is collected from the formation and brought to the laboratory for measurements. This is the primary motivation for the novel method proposed in this work that attempts to eliminate the aforementioned drawbacks and determines relative wetting simultaneously because the measurement is not dependent on one, but a comparison of two companion samples of the same formation.

2 Methodology

A somewhat self-explanatory Fig. 1 outlines the workflow and the various laboratory tools and setups used in executing the methodology that leads to the wettability assessment. Briefly, the procedure is as follows. The twin clean dry core samples labeled as *A* and *B* were dimensioned using a Vernier caliper and fully saturated with (tap) water and flashed Umiat oil (Hanks, 2012), respectively, using vacuum, until the bubbling ceased. The densities of both water and oil were measured at the room temperature using the Anton Paar densitometer. After recording the wet weights of both

samples, they were placed in the Amott cells containing Umiat oil and water, respectively, and left for 7 days for ensuring completion of the spontaneous displacement. Note that ample time was allowed given the first trial of the modified Amott method, which certainly can be reduced significantly in future tests as we plan to refine and standardize our method. Finally, visual observations and the spontaneously displaced volumes (see results) were employed to determine the wettability of the tested COBR system(s). In the last step, both samples were subjected to Dean–Stark extraction.

Porosity calculation and mass balance equations for saturations are as follows, in which ϕ , WW , DW , BV , ρ_o , ρ_w , S_w , and S_o are porosity, wet weight, dry weight, bulk volume, oil density, water density, water saturation, and oil saturation, respectively.

$$\phi = \frac{(WW - DW)}{BV \times \rho_o \text{ or } \rho_w}, \text{ fraction} \quad (1)$$

$$S_w + S_o = 1 \quad (2)$$

$$S_w = \frac{WW - DW - \phi BV \rho_o}{\phi BV (\rho_w - \rho_o)}, \text{ fraction} \quad (3)$$

3 Results

The various measured and calculated values for the experiments are shown in Table 1.

The main spontaneous displacement is shown in Fig. 2, and the results are discussed in the next section.

Fig. 1 Workflow and laboratory tools used in the determination of COBR system wettability using the modified Amott method

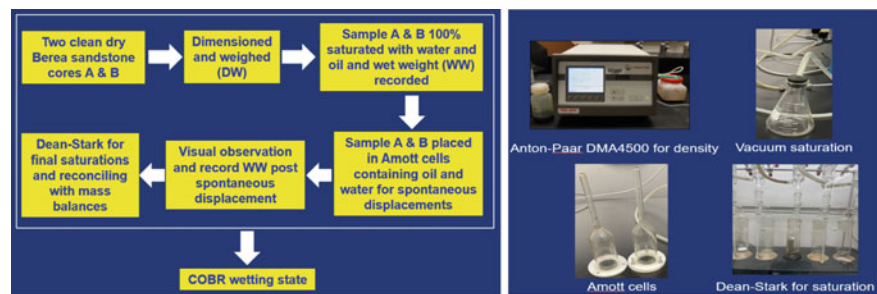


Table 1 Measured and calculated rock and fluid data for the COBR system. Note that ρ_o and ρ_w are 0.834 and 0.998 g/cm³

Variables	Sample A (water saturated)	Sample B (oil saturated)
L and D , cm; BV , cm ³	7.79 and 2.56; 40.22	7.79 and 2.57; 40.32
WW and DW , g	93.39 and 86.55	94.26 and 88.37
ϕ , fraction	0.17	0.17
Spont. Disp., cm ³	0 by oil	3.3 by water
WW after Amott, g	Not needed	94.89 g
V_w in sample (Eq. 3), cm ³	Same (100%)	3.87
V_w (Dean-Stark), cm ³	N/A	3.2

Note V_w denotes volume of water

Fig. 2 Amott cells containing 100% water- and oil-saturated samples *A* and *B* in oil and water, respectively, photographed after 7 days



(a) Sample A 100% saturated with water in Amott cell containing Umiat oil – no spontaneous displacement of water by oil



(b) Sample B 100% saturated with oil in Amott cell containing water – spontaneous displacement of oil by water clearly seen (a strongly water wet system)

4 Discussion

The bold italicized values shown in Table 1 basically represent the volume of water in sample *B* after the spontaneous displacement (of oil) by three different methods. The first one represents an equivalent of the oil volume displaced; the second one is based on the mass balance in Eq. 3 and the third actually measured using the Dean–Stark. Given the fact that all three are independent of each other, we took an average and calculated the % difference for each of them from the average, which ranged from 4.6 to 12.1%. We believe that this is a very reasonable and acceptable agreement as far as the reconciliation of the saturation data is concerned.

The logic behind the original Amott (1951) test, as stated by Amott is that these simple (spontaneous) displacement-type tests indicate in a reasonably direct manner the wettability of the porous rock surfaces. Accordingly, in the Amott test there are two spontaneous displacement steps that are carried out on a single or same sample twice, namely water by oil, followed by oil by water, at residual oil saturation and irreducible water saturation, respectively. In addition, companion forced displacements are also needed. The displaced volumes are used to calculate the oil and water wettability indices from which wettability is determined. A value approaching one for either oil or water is deemed as oil or water wet system, respectively, whereas a value of zero indicates neutral wetting system.

The uncertainty or potential non-representativity of in-situ wettability of a single core sample, four different displacement cycles, the redundant forced displacement, and

the need to calculate a wettability index are some of the drawbacks that we have addressed in our practical and modified Amott method. Although our proposed method requires two samples, only one spontaneous cycle each is necessary to unambiguously determine the wettability, because wetting tendencies should be readily obvious, merely on the basis of spontaneous displacements, as demonstrated in Fig. 2b, which is a strongly water wet system. Additionally, our proposed and proven method for the tested case eliminates the need for the forced displacement steps, and thus the calculation of any wettability indices. In our future work, we plan to test the modified Amott method on variety of COBR systems, including drill cuttings and geometrically uneven rock samples.

5 Conclusions

Our study offers the following main conclusions or takeaways:

- This work demonstrates the application of the modification of a well-established and logical experimental technique to determine the wettability of a COBR system.
- The proposed, proven approach has a universal appeal in that it can be easily and effectively applied to any COBR systems.
- Finally, the demonstrated technique is simple and practical and can be conducted in a basic rock and fluid properties laboratory, using the fundamental procedures outlined in this paper.

References

- Amott, E. (1951). Observations relating to the wettability of porous rocks. *AIME Transactions*, 192, 99.
- Cuiec, L. (1984). Rock/crude-oil interactions and wettability: An attempt to understand their relation. *Society of Petroleum Engineers SPE Paper Number, 13211*.
- Dandekar, A. Y. (2013). *Petroleum reservoir rock and fluid properties* (2nd ed.). CRC Press.
- Umiat oil (DOE report) Hanks, C. (2012). *Producing light oil from a frozen reservoir: Reservoir and fluid characterization of Umiat field, National Petroleum Reserve, Alaska*. United States, US DOE Final Report.



Kick Behavior Analysis and Modeling Methodologies

Fotios Zachopoulos and Nikolaos Kokkinos

Abstract

The current study reviews the techniques and methodologies used for analyzing and modeling a potentially disastrous event called a “kick.” Throughout the years, new and robust technologies have been developed to detect and mitigate such an event. Even so, there are still cases that the applied technologies fail and undetectable kick transform into catastrophic blowouts. This study aims to review the latest literature and provide a holistic approach to modeling and analyzing a kick, endeavoring to enhance the existing detection and mitigation techniques. PRISMA reporting system was employed to review the literature systematically. The review provided valuable information about the currently applied methodologies and the advances established throughout the years. Cubic equations of states and semi-empirical mathematical models were presented as the means to model the fluid flow and the thermodynamic state of the kick. Factors affecting the kick behavior, such as friction in annular space, fluid compressibility, heat transfer effects, the solubility of hydrocarbons, hydrogen sulfide, and carbon dioxide in drilling mud, changes in bottom hole pressure, and the gas bubble rise velocity, were also considered in the mathematical models. Afterward, the limitations of the reviewed models, such as the one-dimensional and single fluid flow patterns, the disregarded heat transfer effects, gas solubility, and temperature profiles, were investigated and discussed. Finally, considering the constraints and gaps in the literature review, the study recommends a

reliable and accurate methodology to analyze and model a hydrocarbon kick. The suggested method combines the existing equations of states and semi-empirical correlations with the power of computational fluid dynamics. Eventually, it aims to produce models based on three dimensions, accounting for transient conditions, dynamic flow regimes, and critical factors affecting the behavior of a kick.

Keywords

Oil and gas drilling • Kick • Drilling simulation • Computational fluid dynamics

1 Introduction

Early kick detection is of vital importance during drilling operations. Several technologies have been developed to detect and adequately mitigate unscheduled kicks (Carpenter, 2019; Tost, et al., 2020). The proper modeling and simulation of a kick could aid in improving or creating new technologies to reduce the occurrence of such events.

A holistic modeling approach should be able to account for all thermodynamic phenomena while accurately simulating the fluid’s transient multiphase flow. Specifically, the model must solve the pressure, temperature, velocity, phase fraction, and composition at any point in the wellbore. Mass, momentum, and energy balance equations simulate the fluid’s transient multiphase flow, including mass, and heat transfer effects. EOS and semi-empirical correlations can be utilized to calculate each phase’s thermodynamic conditions and composition. Such mathematical expressions must also account for the solubility of the kick fluid into the drilling mud and the effect of components such as H₂S and CO₂ in the fluid’s phase behavior. The most recently used approaches and mathematical models are systematically reviewed in the current study.

F. Zachopoulos · N. Kokkinos (✉)
Department of Chemistry, School of Science, International
Hellenic University, Ag. Loukas, 65404 Kavala, Greece
e-mail: nck@chem.ihu.gr

F. Zachopoulos · N. Kokkinos
Petroleum Institute, International Hellenic University, Ag. Loukas,
65404 Kavala, Greece

2 Methods

The Preferred Reporting Items for Systematic Reviews and Meta-Analyses (PRISMA) system was used in this work to review the literature systematically (Page et al., 2021). The research took place between June and August 2022 using Scopus and OnePetro databases. The search criteria included the query “gas AND kick AND (simulation OR model* OR analysis)” in the subject areas of engineering, mathematics, and energy. Searching in the title, abstract, and keywords of the articles, 870 results were obtained in total. After screening the results and removing all duplicates, 129 articles were considered for further investigation. Finally, 43 articles were excluded, due to not fulfilling the research purpose, leading to 86 articles finally used in this review paper.

3 Results and Discussion

In literature, several studies have been conducted to simulate a hydrocarbon kick. Both analytical and numerical solutions have been attempted, but in most cases, with various limitations. Mass and momentum conservation equations were used along with supplementary sub-models, such as the drift-flux model, to simulate the multiphase flow and to account for the non-uniform profiles of phase velocities (Gomes, et al., 2018; Nwaka et al., 2020; Patrício et al., 2019; Wei & Chen, 2021). Such models ignored the heat transfer between the wellbore fluids and surroundings and the temperature variations along the well. Fluid temperature and pressure are heavily affected by heat transfer and multiphase flow; consequently, parameters such as gas solubility and expansion are also influenced (Sleiti et al., 2020). However, most recent studies have widely incorporated the energy balance equation and various correlations into the models to account for such effects (Liao et al., 2022; Manikonda, et al., 2019; Zhang et al., 2022).

Most of the recent simulations were based on one-dimensional multiphase flow using variations of the drift-flux model for hydrodynamics. The friction factor along the wellbore was estimated using semi-empirical correlations such as Beggs–Brill and Perez-Tellez (Ambrus, et al., 2015; Jiang et al., 2019). The models also employed equations of states (EOS) and semi-empirical correlations to solve the fluid’s phase behavior, considering components such as CO₂ and H₂S. Ideal gas law, modified and original Peng–Robinson (PR) EOS, and van der Waals mixing rules were the most used among other EOS and correlations (Galdino et al., 2019; Manikonda, et al., 2019).

The drift-flux model (DFM) was commonly used in the literature to account for the non-uniform velocity profiles of

gas and liquid phases. DFM represents the multiphase flow as one single phase considering the drift velocity between the phases. Most studies assumed a homogeneous flow regime along the wellbore such as bubble, slug, churn, dispersed, or annular flow. The drift velocity (v_d) and the distribution parameter (C_o) were mathematically expressed based on the applied regime and the corresponding experimental studies (Sleiti et al., 2020).

Gas solubility is of vital importance while modeling a gas kick. An oil-based mud (OBM) can dissolve more gas than water-based mud leading to a slight increase in volume and consequently in pit gain (O’Byrne et al., 1988). O’Byrne and Bourgoyne (1990) found that the solubility increased as the pressure was increasing in an OBM. On the contrary, it decreased as the amount of drilling cuttings was increasing and the temperature was rising. Gas solubility can be modeled either by semi-empirical correlations or EOS. Manikonda et al. (2019), Petrosky and Farshad (1998), Standing (1947) developed correlations based on saturated and unsaturated conditions to account for gas solubility (R_s) and volume factor (B_o). A more objective approach can be achieved using EOS, where a wide range of pressures and temperatures can be covered. The Redlich–Kwong, Peng–Robinson, Soave–Redlich–Kwong, and van der Waals were the most used EOS for calculating gas solubility. Such models have recently developed but Omrani et al. (2019), Kim et al. (2015).

4 Conclusions and Recommendations

The systematic literature review resulted in several valuable models. Most of these models were limited to one-dimensional fluid flow, while most did not adequately account for heat transfer effects, gas solubility, and temperature profiles. Additionally, oversimplified models that assumed single flow patterns were usually used, leading to inaccurate simulations and predictions. Computational fluid dynamics (CFD) is recommended to develop three-dimensional multiphase flow systems by incorporating and numerically solving the Navier–Stokes equations. Existing EOS and semi-empirical correlations can be used to account for the heat transfer effects, the temperature profile along the wellbore and gas, H₂S and CO₂ solubility in the drilling mud. The CFD models should consider transient conditions and dynamic flow regimes to provide realistic results. Such a holistic model can, in turn, be used as input to drilling simulation systems to study the kick’s behavior and debug the models. Laboratory mockup test wells are also recommended to validate the results.

References

- Ambrus, A., et al. (2015). A simplified transient multi-phase model for automated well control applications. In *International petroleum technology conference*.
- Carpenter, C. (2019). Model simulates gas kicks in nonaqueous drilling fluids. *Journal of Petroleum Technology*, 71(01), 64–67.
- Galdino, J. F., et al. (2019). Gas kick detection and pressure transmission in thixotropic, compressible drilling fluids. *Journal of Petroleum Science and Engineering*, 180, 138–149.
- Gomes, D., et al. (2018). Transient modelling and sensitivity analysis of influxes in backpressure MPD systems. In *SPE Asia Pacific oil and gas conference and exhibition*.
- Jiang, H., et al. (2019). Numerical simulation of a new early gas kick detection method using UKF estimation and GLRT. *Journal of Petroleum Science and Engineering*, 173, 415–425.
- Kim, N. R., Ribeiro, P. R., & Pessôa-Filho, P. A. (2015). PVT behavior of methane and ester-based drilling emulsions. *Journal of Petroleum Science and Engineering*, 135, 360–366.
- Liao, Y., et al. (2022). Modeling of wellbore multiphase flow with free gas influx during horizontal drilling in marine hydrate reservoirs. *Journal of Natural Gas Science and Engineering*, 97, 104375.
- Manikonda, K., et al. (2019). Understanding gas kick behavior in water and oil-based drilling fluids. In *SPE Kuwait oil & gas show and conference*.
- Nwaka, N., et al. (2020). Hydrodynamic modeling of gas influx migration in slim hole annuli. *Experimental and Computational Multiphase Flow*, 2(3), 142–150.
- O'Bryan, P. L., et al. (1988). An experimental study of gas solubility in oil-based drilling fluids. *SPE Drilling Engineering*, 3(01), 33–42.
- O'Bryan, P. L., & Bourgoynne, A. T., Jr. (1990). Swelling of oil-based drilling fluids resulting from dissolved gas. *SPE Drilling Engineering*, 5(02), 149–155.
- Omrani, A. E., Franchek, M. A., & Tang, Y. (2019). BOP pressure and flowrate conditions during high pressure gas kick control. In *Offshore technology conference*.
- Page, M. J., et al. (2021). The PRISMA 2020 statement: An updated guideline for reporting systematic reviews. *BMJ*, 372, n71.
- Patrício, R. V., et al. (2019). Dynamic gas kick regulation through control reconfiguration under MPD scenario—Two-phase flow validation. *Journal of Petroleum Science and Engineering*, 172, 806–818.
- Petrosky, G. E., Jr., & Farshad, F. (1998). Pressure-volume-temperature correlations for Gulf of Mexico crude oils. *SPE Reservoir Evaluation & Engineering*, 1(05), 416–420.
- Sleiti, A. K., et al. (2020). Early gas kick detection in vertical wells via transient multiphase flow modelling: A review. *Journal of Natural Gas Science and Engineering*, 80, 103391.
- Standing, M. B. (1947). A pressure-volume-temperature correlation for mixtures of California oils and gases. In *Drilling and production practice*.
- Tost, B. C., et al. (2020). Early kick detection from downhole measurements: A novel method for reducing the frequency and magnitude of loss-of-well-control events. In: *Offshore technology conference*.
- Wei, C., & Chen, Y. (2021). On improving algorithm efficiency of gas-kick simulations toward automated influx management: a Robertson differential-algebraic-equation problem approach. *SPE Drilling & Completion*, 36(04), 943–966.
- Zhang, Z., et al. (2022). Intelligent well killing control method driven by coupling multiphase flow simulation and real-time data. *Journal of Petroleum Science and Engineering*, 213, 110337.



Insights on EU Strategy for Building Partnerships in Mediterranean Energy Policy to Meet Decarbonization Goals

Giacomo Di Foggia and Massimo Beccarello

Abstract

With the approval of the REPowerEU plan, the European Union intends to build partnerships to produce mutually beneficial gains by aiming to promote renewable energy and cooperate on green technologies and innovation. In addition to the increased supply of liquefied natural gas from the United States and Canada, it is necessary to intensify the southern gas transport corridor, formalize political agreements with gas suppliers such as Egypt and Israel to increase natural gas supplies, and boost the energy dialog with Algeria. Then, it is necessary to explore the export potential of sub-Saharan African countries. The shift to an economy less dependent on fossil energy offers significant opportunities beyond the issue of security and energy supply. Indeed, the new European decarbonization goals to rapidly advance the green transition pave the way for a new perspective in geostrategic cooperation in the Mediterranean. For the Mediterranean, geostrategic cooperation could combine economic development and renewable energy production. With this paper, we aim to estimate the energy potential of Mediterranean countries for renewable energy production to engage in more sustainable energy strategies, policies, and systems. We pay particular attention to infrastructural availability and plant capacity. We, therefore, intend to investigate possible synergies to combine energy and environmental policies in line with European climate policies.

Keywords

Energy policy • Renewables • Energy cooperation • Green deal

1 Introduction

Recently, European decarbonization goals have been significantly renewed, making a challenging climate change commitment that will lead the European continent to achieve climate neutrality goals by 2050, as stated in the 2050 strategy (Beccarello & Di Foggia, 2023). The transition to climate neutrality is an urgent challenge and an opportunity to build a more sustainable future. All parts of society and economic sectors will play a role in this challenge: we focus on the power sector and industry. The EU can lead the way by investing in prominent technological solutions aligning action in key areas, including industrial policy, while ensuring social fairness.

This engagement requires a significant cooperative effort within which different geopolitical areas must cooperate and gain mutual benefits. The worsening of the energy crisis following the pandemic period has highlighted the European difficulties in managing the transition path to decarbonization goals in terms of the security of the supply of natural gas, which is the energy source with the lowest environmental impact among fossil fuels and is needed to govern the transition process.

This new energy scenario, unanticipated when the decarbonization goals were launched with the “Fit for 55” package, has clarified that the energy transition path to 2030 cannot be achieved unless decarbonization goals are rethought with energy security goals. However, geopolitical tensions and growing global energy demand are causing a new concept of energy security to emerge (Lambert et al., 2022). This is a broader concept in which the supply of the least environmentally impactful fossil energy source, natural gas, must be integrated with a concept of security extended to the availability and control of the technology chains that will enable the replacement of fossil sources in energy production.

European decarbonization goals can be realized if Europe can promote this technological change while ensuring the

G. Di Foggia (✉) · M. Beccarello
Department of Business and Law, University of Milano - Bicocca,
Milan, Italy
e-mail: giacomo.difoggia@unimib.it

centrality of economic development and international cooperation goals.

The issue of industrial development in the area of new technologies for energy production is central both to the European continent and to accelerating the industrialization process of Mediterranean countries while avoiding risks of industrial relocation to other regions.

2 Background

The identification of a common development goal is crucial for geopolitical cooperation (Kraemer-Mbula et al., 2018). Through inclusive models of peer-to-peer industrial development cooperation, it will be possible to promote the progressive accession of neighboring areas by sharing and promoting synergies on the level of research and innovation within developing an integrated market area of green technologies.

The REPowerEU measure also identifies two main directions among the measures to escape the deepening gas crisis: a strategy to further increase renewable production targets and energy efficiency targets for consumption processes and a strategy of geopolitical diversification of natural gas supply routes (Osička et al., 2022).

These lines of intervention, to be effective, must not be reduced to the role of emergency and temporary responses but can and must represent the start of a process of inclusive cooperation among all countries that share the objectives of environmental sustainability and can mutually seize the opportunities for economic development arising from a policy for the energy transition. The Mediterranean area presents all the strategic elements to start a path of cooperation of the European continent with African and Middle Eastern countries that share the geopolitical perimeter.

Regarding natural gas availability, the Mediterranean area has a potential for natural gas availability that places the area eighth in deposits of proven natural gas reserves globally.

The Mediterranean area represents an even more important reservoir for the potential production of renewable sources and green hydrogen, a key energy vector for decarbonizing industrial processes, mainly green hydrogen. Natural gas and hydrogen represent the two basic energy factors for building an energy transition strategy (Mukelabai et al., 2022). In the short term, the availability of natural gas at competitive costs enables the resilience of industrial production in the countries that share the Mediterranean perimeter and could also ensure the affordability of one of the key factors for industrial reshoring of some energy-intensive production (gas and electricity). The analysis aims to assess the economic effects in terms of a development

driver of an integrated area that contains the potential to ensure security and affordability with respect to gas. Moreover, contextually, it intends to consider how, on the cooperative level, this competitive advantage can trigger a cooperative pathway in terms of industrial development of new green technologies—in other words, identifying how the development of cooperation dictated by an emergency contingency can be transformed into an opportunity for cooperation and development and leadership in the control of strategic supply chains for producing renewable energy, hydrogen, and energy conservation.

3 Expected Results

With this article, we aim to explore the factors that have led to the relocation of production of key green economy technologies to the Far East in recent years to understand what the strategies and benefits of relocation may be.

These factors include the high cost of the energy component in European production costs, labor costs, availability of raw materials, and strong economies of scale in technologically advanced production. By comparing the determinants of these factors within a new potential market constituted by the Mediterranean basin, we believe that it is also possible to look at the important investment program promoted by the European Commission from a different perspective.

In this regard, it is important to guarantee the healthy functioning of the market by promoting fair competition in energy and environmental industries (Di Foggia & Beccarello, 2021). The analysis aims to verify the potential of the Mediterranean perimeter both in terms of energy costs resulting from the shared exploitation of Mediterranean resources through an integrated optimization of resources. Of gas first of all but also of renewable energy production potential. Second, the analysis intends to verify whether the labor cost is still a hindering factor in initiating policies of reshoring the production of green technologies. From this perspective, integrated cooperation between the European and Mediterranean countries makes it possible to integrate a relevant and stable demand in relation to EU decarbonization goals, substantial funds for R&D, and competitive labor costs. These are all factors that could prove successful within an inclusive cooperation agreement based on the objectives of sustainability, energy security and affordability, and the development of production capacity with reference to strategic green economy supply chains.

According to the International Energy Agency, the hydrogen costs and supply from dedicated hybrid solar PV and onshore wind in Africa within 200 km of a serviceable

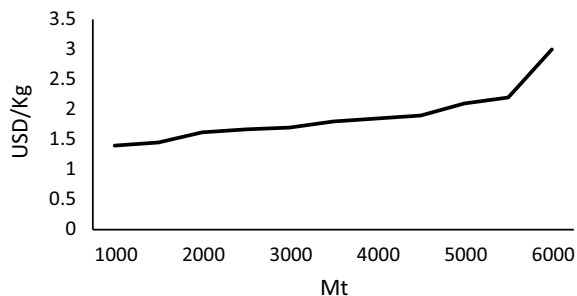


Fig. 1 Hydrogen production potential and cost. *Source* IEA (2022)

coast are expected to grow significantly, as reported in Fig. 1.

Building 1230 GW of new photovoltaic installations could achieve an annual solar hydrogen production of approximately fifty million tons by 2035. In detail, the main investment opportunities in the Mediterranean are in three countries: Mauritania, Morocco, and Egypt. In this regard, Fig. 2 provides insights into potential demand by sector.

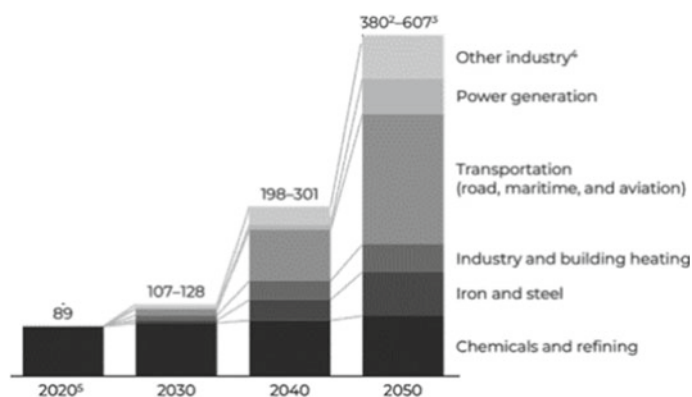
According to a recent report (EIB, 2022), there are three requirements to enable the production of 50 million tons of green hydrogen in Africa by 2035. First, there needs to be planning, efficient national incentives to mobilize private sector investment. Second, market-based partnerships are needed to enable the purchase and demand for green hydrogen on a national and international scale and increase cooperation to design, finance, build, and operate green

hydrogen production, storage, and distribution infrastructure. What mentioned above also seems plausible due to the number of projects currently in discussion or underway (Piebalgs, 2022). Clearly, for the benefits of such projects to happen, it is important to find the right enablers in terms of the ease of doing business and financial stability.

4 Conclusion

The European Union intends to build partnerships to produce energy that are mutually beneficial by aiming to promote renewable energy and cooperate on green technologies and innovation. We underline the fact that it is necessary to intensify the southern gas transport corridor and enhance political agreements among Mediterranean countries. The shift to an economy less dependent on fossil energy offers significant opportunities beyond the issue of security and energy supply. Indeed, the new European decarbonization goals to rapidly advance the green transition pave the way for a new perspective in geostrategic cooperation in the Mediterranean. For the Mediterranean, geostrategic cooperation could combine economic development and renewable energy production. We provide an early-stage appraisal of the energy potential of Mediterranean countries for renewable energy production to engage in more sustainable energy strategies, policies, and systems and possible synergies to combine energy and environmental policies.

Fig. 2 Global hydrogen demand forecasts by sector (Mt of hydrogen equivalent). *Fonte* AGHA (2022)



References

- AGHA. (2022). *Africa's green hydrogen potential*. Available at: https://climatechampions.unfccc.int/wp-content/uploads/2022/11/AGHA-Green-Hydrogen-Potential-v2_Final.pdf
- Beccarello, M., & Di Foggia, G. (2023). Review and perspectives of key decarbonization drivers to 2030. *Energies*, 16(3), 1345. <https://doi.org/10.3390/en16031345>
- Di Foggia, G., & Beccarello, M. (2021). Market structure of urban waste treatment and disposal: Empirical evidence from the Italian industry. *Sustainability*, 13(13), 7412. <https://doi.org/10.3390/su13137412>
- EIB. (2022). *Africa's extraordinary green hydrogen potential*. Available at: <https://www.eib.org/eib.org/attachments/press/africa-green-hydrogen-flyer.pdf>
- IEA. (2022). *Africa energy outlook 2022*. Available at: <https://www.iea.org/reports/africa-energy-outlook-2022>
- Kraemer-Mbula, E., Vaitas, C., & Essegbey, G. O. (2018). The dynamics of EU–Africa research and innovation cooperation programmes. *Africa-Europe Research and Innovation Cooperation: Global Challenges, Bi-regional Responses*, 39–63. https://doi.org/10.1007/978-3-319-69929-5_3
- Lambert, L. A., Tayah, J., Lee-Schmid, C., Abdalla, M., Abdallah, I., Ali, A. H., Esmail, S., & Ahmed, W. (2022). The EU's natural gas Cold War and diversification challenges. *Energy Strategy Reviews*, 43, 100934. <https://doi.org/10.1016/j.esr.2022.100934>
- Mukelabai, M. D., Wijayantha, U. K., & Blanchard, R. E. (2022). Renewable hydrogen economy outlook in Africa. *Renewable and Sustainable Energy Reviews*, 167, 112705. <https://doi.org/10.1016/j.rser.2022.112705>
- Osička, J., & Černoch, F. (2022). European energy politics after Ukraine: The road ahead. *Energy Research & Social Science*, 91, 102757. <https://doi.org/10.1016/j.erss.2022.102757>
- Piebalgs, A. (2022). *Has COP27 accelerated the development of Green Hydrogen in Africa?*



The Clustering of Source Rocks: A Spectral Approach

Vagia Ioanna Makri and Dimosthenis Pasadakis

Abstract

The identification of family affiliation of samples emerging from oils and source rocks is a topic of primary importance in the field of exploration geoscience. We demonstrate how spectral clustering can be applied in the context of chemometrics on a set of rock extracts from Western Greece, using quantitative information of normal alkane (nC15–nC35) concentrations. The developed method is based on the creation of a graph Laplacian matrix that represents the latent graphical structure of the samples, and the subsequent estimation of the underlying clusters based on the eigenvectors of this matrix. The number of clusters is determined by optimizing the modularity of the resulting graph, thus ensuring high intra-cluster and low inter-cluster similarity. Our results highlight that the proposed approach partitions the geological samples into groups with distinct concentration profiles of n-alkanes and attains higher modularity values than methods traditionally employed in hydrocarbon exploration. This empirical study showcases the reliability of spectral methods to support source rock classification and provides a way to facilitate geochemical interpretations.

Keywords

Source rock • Spectral clustering • Graph Laplacian • Geochemistry

V. I. Makri (✉)

Institute of GeoEnergy (FORTH/IG), Foundation for Research and Technology—Hellas, Chania, Greece
e-mail: vayanna@ipr.forth.gr

V. I. Makri

School of Mineral Resources Engineering, Technical University of Crete, Chania, Greece

D. Pasadakis

Institute of Computing, Università Della Svizzera Italiana, Lugano, Switzerland

1 Introduction

Oil-source correlation and source rock characterization are tasks of prime importance to the hydrocarbon exploration community. So far, methods such as k -means, principal component analysis (PCA), hierarchical clustering (HCA), and multidimensional scaling (MDS) have been extensively used in chemometrics for this kind of study (Peters et al., 2004; Wang et al., 2022). Contributing to this line of research, we present a direct multiway spectral clustering approach that allows the automatic selection of the optimal number of clusters. Spectral clustering (SC) is a long-established graph-based method that enjoys reasonable computation time, simplicity in its implementation, and overcomes the NP-hardness of other graph-theoretic algorithms (Bichot & Siarry, 2013). Nonlinear reformulations of the method have proven to lead to improved clustering assignments (Bühler & Hein, 2009; Pasadakis et al., 2022), and normalized variants have been shown to lead to the modularity maximization of the resulting clusters, allowing for the automatic detection of the optimal number of groups present in the graph (White & Smyth, 2005).

For this study, we consider a set of 83 rock extracts from Western Greece's potential source rocks. These samples are of multiple geological ages ranging from Triassic to Pliocene and are located in the so-called Ionian geotectonic zone of Greece. Using quantitative information of the normal alkanes and isoprenoids of the samples, we estimate their latent community structure. In the remaining text, we introduce the way our data were retrieved, and the algorithm used for their clustering in Sect. 2. In Sect. 3, we present our results and conclude this work in Sect. 4. The data and code used in this study are available online at <https://github.com/DmsPas/Spectral-clustering-of-source-rocks.git>. In what follows scalar quantities are denoted by lowercase, vectors by lowercase bold and matrices by uppercase bold characters. We denote the i th element of a vector \mathbf{v} by v_i , the (i, j) th entry of a matrix \mathbf{V} by v_{ij} , the

matrix identity by \mathbf{I} , and $\mathbf{A} \odot \mathbf{B}$ stands for the Hadamard product between matrices \mathbf{A} and \mathbf{B} .

2 Materials and Methods

In this section, we introduce the way our dataset was retrieved (Sect. 2.1) and outline the algorithm we used for the detection of communities (Sect. 2.2).

2.1 Dataset Retrieval

Solvent extraction of the samples was carried out in a Soxhlet apparatus with a DCM:MeOH 9:1 v/v mixture for sieved representative quantities of each sample for 24 h. The extracts were de-asphalted, generating maltene and asphaltene fractions. The former fraction was further separated into saturated, aromatic, and polar fractions using open-column $\text{SiO}_2\text{-Al}_2\text{O}_3$ chromatography, eluted with n-C5, toluene, and a mixture of Tol:MeOH (60:40 vol.), respectively. Gas chromatography-mass spectrometry (GC-MS) analysis was carried out for the saturated fractions, dissolved in n-C6, on an Agilent 7890A Gas Chromatograph coupled to an Agilent 5975E Mass Spectrometer. The GC was equipped with an electronic program controlled (EPC) split-splitless injector at 280 °C and an Agilent capillary column HP-5MS UI (60 m \times 250 μm \times 0.25 μm).

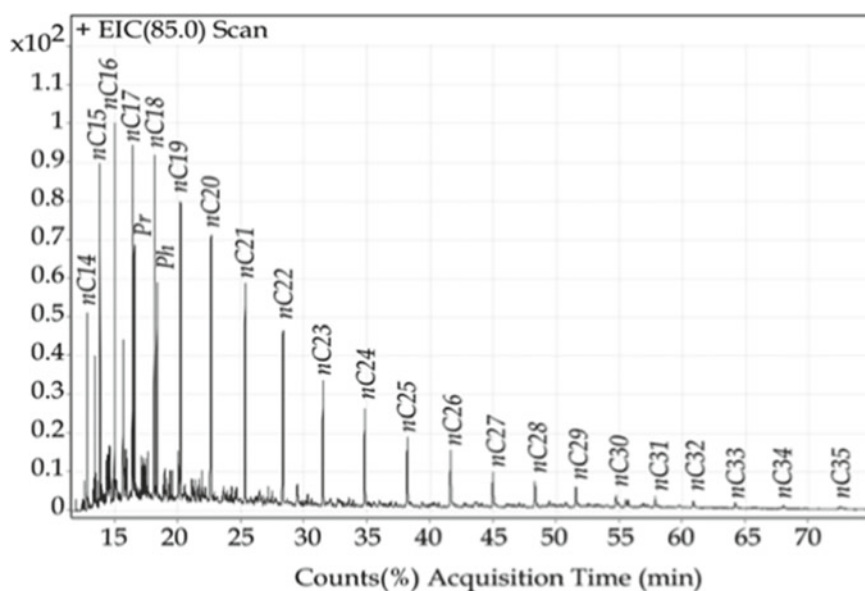
Using their relative retention times and spectrum patterns, n-alkanes (nC15-nC35) and isoprenoids (Pr, Ph) were identified using the ions m/z 57, 85 (Fig. 1). Their peak areas, representative of the relative quantity of each

compound, are used as input data for the SC algorithm introduced in the following subsection. This input has a dimension of $\mathbf{Y} \in \mathbb{R}^{n \times p}$, with $n = 83$ and $p = 34$ representing the samples and their data (coordinates, geological information, and peak areas), respectively.

2.2 A Spectral Approach for Source Rock Community Detection

Graph clustering aims to differentiate points in groups according to their similarities and can be considered a partitioning problem on an undirected weighted graph $\mathcal{G}(V, E, \mathbf{W})$. Its node set V represents the n data points, which are connected through the edges of the set E , and the similarity between the nodes is encoded in the elements $w_{ij} > 0$ of the adjacency matrix \mathbf{W} . The connectivity of \mathbf{W} is dictated by the matrix $\mathbf{G} \in \mathbb{R}^{n \times n}$, typically created from a k -nearest neighbors routine with the number of nearest neighbors (NN) set such that the resulting graph is connected. The weights of the edges are defined by the similarity matrix $\mathbf{S} \in \mathbb{R}^{n \times n}$ that captures the similarity between the data points as $s_{ij} = \max\{s_i(j), s_j(i)\}$ with $s_i(j) = \exp\left(-4 \frac{|y_i - y_j|^2}{\sigma_i^2}\right)$, with σ_i being the Euclidean distance between the i th data point and its k th nearest neighbor (Zelnik-Manor & Perona, 2005). The adjacency matrix is then created as $\mathbf{W} = \mathbf{G} \odot \mathbf{S}$. Normalized spectral methods are based on exploiting the information in the eigenvectors of the random walk Laplacian matrix \mathbf{L}_{rw} , which enables the partitioning of a graph into C_1, \dots, C_k clusters. The random walk \mathbf{L}_{rw} is a symmetric and positive semi-definite matrix

Fig. 1 GC-MS chromatogram of the ion m/z 85 of a sample used in this study



defined in terms of the adjacency \mathbf{W} and the diagonal degree matrix $\mathbf{D} \in \mathbb{R}^{n \times n}$, $\left(\mathbf{d}_i = \sum_{j=1}^n \mathbf{w}_{ij}\right)$, as $\mathbf{L}_{\text{rw}} = \mathbf{I} - \mathbf{D}^{-1}\mathbf{W}$. We estimate the mutually orthogonal eigenvectors $\mathbf{U} \in \mathbb{R}^{n \times k}$ associated with the smallest k eigenvalues of L_{rw} through the Rayleigh quotient minimization (Bhatia, 1997),

$$\begin{aligned} \text{minimize}_{\mathbf{U} \in \mathbb{R}^{n \times k}} & F_2(\mathbf{U}) = \text{Tr}(\mathbf{U}\mathbf{L}_{\text{rw}}\mathbf{U}) \\ \text{subject to} & \mathbf{U}^T\mathbf{D}\mathbf{U} = \mathbf{U}, \end{aligned} \quad (1)$$

with Tr denoting the trace of a matrix. The rows of \mathbf{U} are considered the spectral coordinates of the graph \mathcal{G} and are subsequently clustered with k-means into k groups (Shi & Malik, 2000). This is a relaxation approach corresponding to the maximization of the discrete graph cut metric modular-

ity, defined as $Q = \sum_l \left(\mathbf{d}_l - \left(\sum_m \mathbf{d}_m \right)^2 \right)$, with each element \mathbf{d}_m representing the degree of the edges that links nodes between clusters l and m , and d_l being the degree of the edges linking nodes within cluster l (White & Smyth, 2005). Modularity can be used as a metric to automatically select the optimal number of clusters k , and large values of Q have been shown to correlate with highly accurate graph clusterings (Newman, 2006; Newman & Girvan, 2004).

In the context of source rocks, high modularity values are expected to lead to the optimal number of clusters of the samples under consideration, displaying distinct geochemical characteristics. An outline of the algorithmic scheme that we employ for the normalized SC of source rock samples is offered in Algorithm 1.

Algorithm 1 SC of source rocks.

Input: Data $\mathbf{Y} \in \mathbb{R}^{n \times p}$	▷ Source rock data
Output: C_k	▷ Source rock clusters
1: Build adjacency matrix \mathbf{W}	▷ $\mathbf{W} = \mathbf{G} \odot \mathbf{S}$
2: Construct the graph Laplacian \mathbf{L}_{rw}	▷ $\mathbf{L}_{\text{rw}} = \mathbf{I} - \mathbf{D}^{-1}\mathbf{W}$
3: Rayleigh quotient min for the first $n/5$ eigenvectors \mathbf{U}	▷ Acc. Equation (1)
4: while $k \in [2, n/5]$ do	
5: Cluster \mathbf{U} in k groups ▷ Using k-means	
6: Compute the modularity Q_k of the k clusters	
7: end while	
8: Select the clusters C_k for which $Q = \max(Q_k)$	

3 Results

In this section, we present numerical experiments that demonstrate the efficacy of the normalized SC routine, summarized in Algorithm 1, in the identification of source rock groups with similar n-alkane concentration profiles. Our routine clusters the 83 potential source rocks in six distinct clusters, whose normalized concentration profiles are illustrated in Fig. 2. These profiles suggest the presence of clearly distinguishable families (groups) of source rocks across the study area, and thus their potentially genetic relationship.

Fig. 2 Normalized concentration profiles of the resulting clusters after applying Algorithm 1 on the source rock data

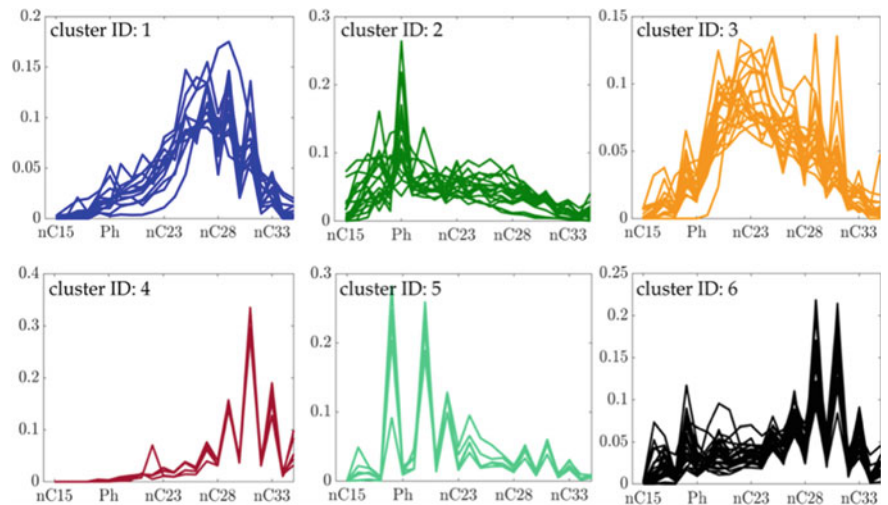
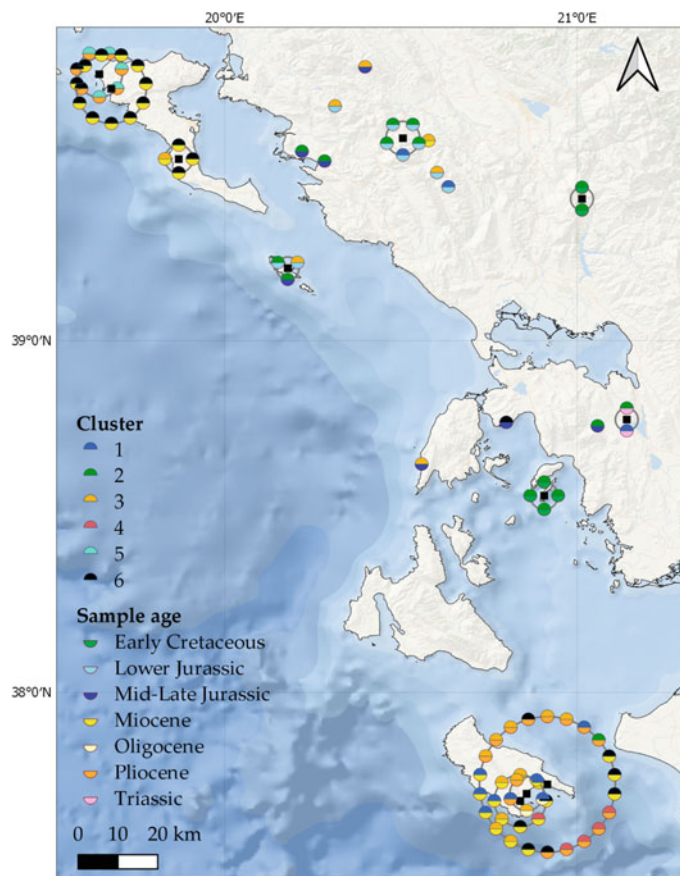


Fig. 3 Geographical distribution of the under-consideration samples. In areas with more than one sample, ring placement view was applied around a black square which represents the location point of the samples



In Fig. 3, we plot the clusters with respect to their geographical coordinates and their geological period and notice that the resulting groups do not solely contain source rocks of the same geological age. This could provide useful information regarding the source rock maturity and paleodepositional environment conditions (Diasty et al., 2020).

We additionally compare the value of modularity Q attained by our spectral approach on the constructed graph with 2 widely used clustering routines in the hydrocarbon exploration community. We consider (1) k -means initialized with multiple orthogonal and random initial guesses that generally lead to a stable result (Verma & Meila, 2005), and (2) a hierarchical agglomerative clustering method (HCA) (Yonggang & Wan, 2013). The modularity values for an increasing number of clusters k are presented in Fig. 4. Our approach (in blue) attains a maximum of $Q = 0.72$ for

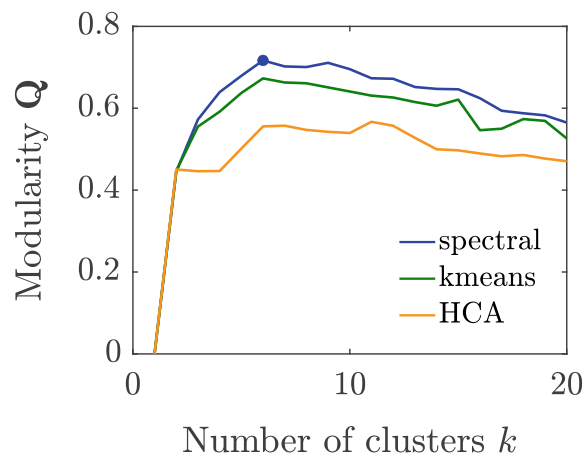


Fig. 4 Comparison of modularity values Q for an increasing number of clusters k

$k = 6$, while k -means (in green) reports a maximum of $Q = 0.67$ for $k = 6$ and HCA a maximum of $Q = 0.56$ for $k = 11$ clusters.

4 Discussion and Conclusions

Inspecting the chromatograms of each cluster in Fig. 2, we observe clear distinctions between the groups, originating from the relative concentrations of the n-alkanes and isoprenoids of each sample. Samples of the same cluster do not correspond solely neither to the same geographical areas nor to the same geological period, as illustrated in Fig. 3. The resulting groups are based on the similarity between n-alkane concentration profiles and thus may serve as the basis for further geochemical characterization and oil-source correlation studies.

Our empirical study has demonstrated the reliability of normalized SC to support the classification of source rocks. We considered input data of n-alkane and isoprenoids of samples obtained from Western Greece. Our approach provides higher modularity values compared to traditionally employed methods in geochemistry (like HCA and k -means), with these values corresponding to accurate sample groupings. Additionally, this method may be applied in studies involving chromatographic analytical data, such as oil fingerprinting and bioinformatics. In future work, we consider employing spectral methods in oil-source correlations and source rock geochemical characterization.

References

- Bhatia, R. (1997). *Matrix analysis*. (Vol. 169) Springer.
- Bichot, C., & Siarry, P. (2013). *Graph partitioning*. Wiley.
- Bühler, T., & Hein, M. (2009). Spectral clustering based on the graph p-Laplacian. In *Proceedings of the 26th annual international conference on machine learning* (pp. 81–88). Association for Computing Machinery.
- El Diasty, W. S., El Beialy, S. Y., Mostafa, A. R., Abo Ghonaim, A. A., & Peters, K. E. (2020). Chemometric differentiation of oil families and their potential source rocks in the gulf of Suez. *Natural Resources Research*, 29, 2063–2102.
- Lu, Y., & Yi, W. (2013). PHA: A fast potential-based hierarchical agglomerative clustering method. *Pattern Recognition*, 46(5), 1227–1239.
- Newman, M. (2006). Modularity and community structure in networks. *Proceedings of the National Academy of Sciences*, 103(23), 8577–8582.
- Newman, M., & Girvan, M. (2004). Finding and evaluating community structure in networks. *Physical Review E*, 69(2), 026113.
- Pasadakis, D., Alappat, C., Schenk, O., & Wellein, G. (2022). Multiway p-spectral graph cuts on Grassmann manifolds. *Machine Learning*, 111(2), 791–829.
- Peters, K., Walters, C., & Moldowan, J. (2004). Geochemical correlation and chemometrics. *The biomarker guide* (pp. 475–482). Cambridge University Press.
- Shi, J., & Malik, J. (2000). Normalized cuts and image segmentation. *IEEE Transactions on Pattern Analysis and Machine Intelligence*, 22(8), 888–905.
- D. Verma, & M. Meila (2005). *A comparison of spectral clustering algorithms* [White paper]. Department of CSE University of Washington Seattle, WA98195–2350.
- Wang, Y., Zhan, X., Zhou, X., Gao, Y., Wang, S., Xia, J., & Song, Z. (2022). The geochemical study of oil-oil and oil-source rock correlations in the Wushi Sag of the Beibu Gulf Basin, South China Sea. *Frontiers in Earth Science*, 10, 850922.
- White, S., & Smyth, P. (2005). A spectral clustering approach to finding communities in graphs. In *SIAM international conference on data mining*.
- Zelnik-Manor, L., & Perona, P. (2005). Self-tuning spectral clustering. In *Advances in neural information processing systems* (Vol. 17, pp. 1601–1608). MIT Press.



CNN-Transfer Learning-Based Prediction for Porosity and Absolute Permeability from Carbonate Rock Images

Ramanzani Kalule, Hamid Ait Abderrahmane, Waleed Alameri, and Mohamed Sassi

Abstract

This study is intended to compare the capabilities of three different deep learning-based convolutional neural network models in predicting reservoir rock porosity and absolute permeability from 2D carbonate rock images. We consider a comprehensive evaluation scenario to investigate the performance and training time involved in using the proposed models. These are studied and evaluated using 2D micro-CT images captured at various image resolutions from the four different core samples. The selected core samples demonstrate a wider range of absolute permeability and different levels of heterogeneity. We achieve model variability by adopting the transfer learning framework in two of the three designed models using pre-trained, VGG16, and MobileNetV2 models. Results obtained demonstrate that transfer learning improves model accuracy to predictions at the expense of computational time. With the influence of transfer learning, results show that the accuracy and computational time largely depend on the number of trained parameters being transferred. The proposed models can predict both the rock porosity and absolute permeability within a few seconds compared to numerical simulations and experiments which require larger amounts of time.

Keywords

Absolute permeability • Porosity • Carbonate rocks • Transfer learning • CNN

1 Introduction

Accurate and rapid prediction of reservoir rock properties is an essential step toward oil and gas resource exploration. Over the last few decades, several approaches for predicting reservoir rock properties have been proposed in the literature. These approaches mainly include numerical simulations, empirical correlations, mathematical modeling, field measurements, and experimental studies. However, most of these approaches are prohibitive due to the complex nature of the physics involved and the large computational requirement (Hong & Liu, 2020).

Deep learning (DL), a subset of machine learning (ML), is viewed as a viable alternative for predicting reservoir properties. This is due to the fact that DL can predict rock properties of various rock types in a matter of seconds with limited computational resources (Downton & Russell, 2020). Several studies utilizing DL to predict porosity and absolute permeability from rock images are available in the scientific literature. Alqahtani et al. (2018) used a convolutional neural network (CNN) to estimate porosity from 2D slice gray images of Berea sandstone with or without segmentation. Their findings correlated well with ground truth labels. In addition, CNNs were applied to 2D grayscale micro-CT images of rocks. In comparison with experimental measurements, they predicted porosity with a lower average error. Wu et al. (2018) proposed that with a physics-informed convolutional neural network (PIML-CNN) algorithm one can achieve better accuracy for the predictions of absolute permeability than the conventional CNN algorithm. They showed that DL can efficiently estimate absolute permeability compared to flow dynamics simulations and the Kozeny–Carman equation.

In this work, we analyze the capability of different CNN models in predicting porosity and absolute permeability from 2D images. We explore the influence of transfer learning, a technique that involves the transfer of pre-trained weights or parameters, to improve the performance and

R. Kalule (✉) · H. A. Abderrahmane · W. Alameri · M. Sassi
Khalifa University, Abu Dhabi, UAE
e-mail: 100053289@ku.ac.ae

computational time of the proposed CNN model. The proposed models are trained and tested on 2D micro-CT images from carbonate real rock samples of varying heterogeneity levels, a wide range of absolute permeability values, and scanned at various resolutions.

2 Methodology

2.1 Laboratory Measurements

The rock porosity was determined using a helium porosimeter, while the absolute permeability was estimated using Darcy's law based on water injection. Table 1 summarizes the experimental values of the four rock samples as well as the different image resolutions (Fig. 1). A dataset of 6500 images of size 224×244 was acquired. Then, this dataset was split with the ratio of 8:1:1 for the training set, validation set, and test dataset, respectively.

2.2 Image Processing

In image processing, segmentation techniques can be broadly categorized as manual or automatic segmentation. Manual segmentation algorithms are subjective in nature, relying on the expertise and experience of the operator (Arganda-Carreras et al., 2017; Kalule et al., 2023), hence limiting generalizability to all samples. On the other hand, automatic segmentation algorithms offer a less subjective approach and are more readily generalizable (Zhang et al., 2021). In this study, we employed the Otsu algorithm (Otsu, 1979), a well-established and efficient automatic segmentation algorithm.

2.3 Model Configuration and Evaluation

The CNN network consists of a series of convolutional kernels (C) (1C [32], 2C [64], 2C [128], 2C [256]), pooling layers (2, 2), fully connected perceptrons (Dense [1024, 512, 2]), activation functions (ReLU, sigmoid), and other relevant layers (such as the batch normalization layer: b_norm) all organized to obtain an intended target. To achieve model variability, we adopt transfer learning, by replacing all the convolutional layers in the architecture of the model with pre-trained layers. We adopt two pre-trained models, namely VGG16 (Simonyan & Zisserman, 2015) and a low latency model with a low number of pre-trained parameters MobileNetV2 (Sandler et al., 2018), proposed in the literature. We evaluate the models based on the loss functions, the mean squared error (MSE), and the mean absolute error (MAE) function, and we use the coefficient of determination to determine how well model predictions match actual values (R^2).

3 Results

Table 2 presents the overall performance results obtained in training and testing the four different networks after 200 epochs of training and testing. The best performance with the highest prediction capability is obtained with the CNN-MobileNetV2. A comparison between the three different CNN networks demonstrates the ability of transfer learning to improve prediction accuracy.

Figure 2 demonstrates the model training trends of the four proposed networks after 200 epochs of training. Results show that transfer learning weights can improve the model's prediction capabilities with the CNN-MobileNetV2 network

Table 1 Experimental values for the selected samples

Sample	Resolutions (μm)	Porosity (%)	Permeability (mD)
BB	14.01, 3.92	25.7	11.30
SD	13.24, 5.32	15.8	278.85
ALB	13.44, 4.24, 0.81	20.8	10.23
TC	3.93, 0.94	25.6	336.94

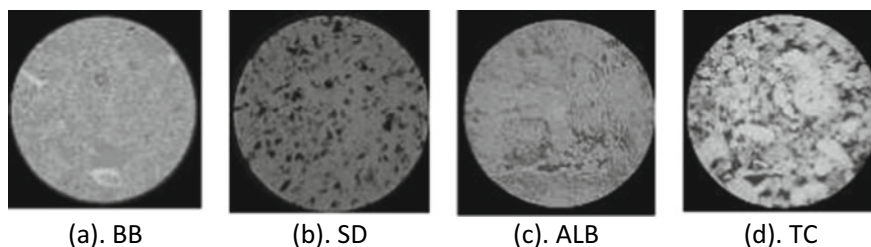


Fig. 1 2D micro-CT image slices of the selected carbonate rock samples. **a** BB: 14.01 μm , **b** SD: 5.32 μm , **c** ALB: 0.81 μm , **d** TC: 3.93 μm

Table 2 Model training and testing performance metrics

Model	MSE	MAE	Training (R^2)	Testing (R^2)	Training time (h)
CNN	0.083	0.149	0.796	0.771	1.47
CNN-VGG16	0.077	0.201	0.841	0.834	4.01
CNN-MobileNetV2	0.027	0.089	0.945	0.927	2.25

Fig. 2 Proposed models' 200-epoch training and validation loss

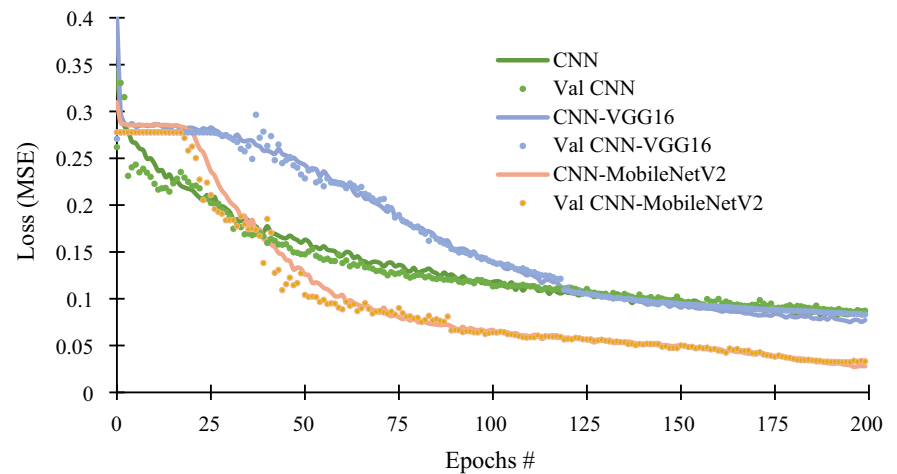


Table 3 Prediction of porosity and permeability from unseen data (CNN-MobileNetV2)

Sample	Ground truth		Prediction		Av. % error
	Porosity (%)	Permeability (mD)	Porosity (%)	Permeability (mD)	
BB	25.7	11.30	23.7	11.016	1.32
SD	15.8	278.85	15.5	284.848	1.08
ALB	20.8	10.23	19.7	10.126	0.55
TC	25.6	336.94	27.3	330.634	0.93

showing capabilities of improving the predictions even after 200 epochs. Table 3 presents the best model predictions against true values and the average percentage error corresponding to a specific rock sample in the proposed image dataset.

involved. However, the training process of all networks for the selected dataset takes only minutes while testing predictions are estimated within a few seconds. This is advantageous in comparison with the computational time required for numerical simulations and the time spent on laboratory experiments.

4 Discussion

In various studies, the MobileNetV2 network has been reported to be faster and more accurate than other pre-trained models due to its depth-wise separable convolutions, which reduce the number of parameters. It is also reported to be more prone to adversarial attacks (Muncsan & Kiss, 2021). These depth-wise separable convolutions cannot be directly supported by GPUs, therefore making the network training slower and running on CPUs. For this reason, the computational time is likely to increase during the training of the CNN-MobileNetV2. The CNN-VGG16 presents the highest computational time because of the large depth of the networks and the high number of pre-trained parameters

5 Conclusions

Our study highlights that methods based on deep learning are effective for predicting porosity and permeability from 2D micro-CT images. Unlike training models from scratch, transfer learning significantly improves prediction accuracy, model robustness, and dataset generalizability during training. CNN-MobileNetV2 was the most efficient model in terms of producing accurate predictions within seconds. Overall, our results indicate that the application of deep learning and transfer learning techniques can significantly improve the predictive accuracy and efficiency of micro-CT image-based petrophysical property predictions.

References

- Alqahtani, N., Armstrong, R. T., & Mostaghimi, P. (2018). Deep learning convolutional neural networks to predict porous media properties. In *Society of petroleum engineers—SPE Asia Pacific oil and gas conference and exhibition 2018, APOGCE 2018*. <https://doi.org/10.2118/191906-ms>
- Arganda-Carreras, I., Kaynig, V., Rueden, C., Eliceiri, K. W., Schindelin, J., Cardona, A., & Seung, H. S. (2017). Trainable Weka Segmentation: A machine learning tool for microscopy pixel classification. *Bioinformatics*, 33(15). <https://doi.org/10.1093/bioinformatics/btx180>
- Downton, J., & Russell, B. (2020). The hunt to use physics and machine learning to predict reservoir properties. In *CSEG-Symposium*, pp 1–6.
- Hong, J., & Liu, J. (2020). Rapid estimation of permeability from digital rock using 3D convolutional neural network. *Computational Geosciences, M*. <https://doi.org/10.1007/s10596-020-09941-w>
- Kalule, R., Abderrahmane, H. A., Alameri, W., & Sassi, M. (2023). Stacked ensemble machine learning for porosity and absolute permeability prediction of carbonate rock plugs. *Scientific Reports*, 13(0123456789), 1–17. <https://doi.org/10.1038/s41598-023-36096-2>
- Muncsan, T., & Kiss, A. (2021). Transferability of fast gradient sign method. *Advances in Intelligent Systems and Computing*, 1251(AISC(August)), 23–34. https://doi.org/10.1007/978-3-030-55187-2_3
- Otsu, N. (1979). A threshold selection method from gray-level histograms. *IEEE Transactions on Systems, Man and Cybernetics, SMC-9*(1), 62–66.
- Sandler, M., Howard, A., Zhu, M., Zhmoginov, A., & Chen, L. C. (2018). MobileNetV2: Inverted residuals and linear bottlenecks. In *Proceedings of the IEEE computer society conference on computer vision and pattern recognition* (pp. 4510–4520). <https://doi.org/10.1109/CVPR.2018.00474>
- Simonyan, K., & Zisserman, A. (2015). Very deep convolutional networks for large-scale image recognition. In *3rd international conference on learning representations, ICLR 2015—Conference track proceedings* (pp. 1–14).
- Wu, J., Yin, X., & Xiao, H. (2018). Seeing permeability from images: Fast prediction with convolutional neural networks. *Science Bulletin*, 63(18), 1215–1222. <https://doi.org/10.1016/j.scib.2018.08.006>
- Zhang, H., Abderrahmane, H., & Kobaisi, M. Al. (2021). Pore-scale characterization and PNM simulations of multiphase flow in carbonate rocks. *Energies*, 14(6897), 1–20. <https://doi.org/10.3390/en14216897>



Petrophysical Properties of the Late Carboniferous and Early Permian Glaciogenic Reservoirs: An Example from Al Khlata Formation, Block 56, Eastern Flank of South Oman Salt Basin

Elham K. S. Al-Nadabi, Mohamed A. K. El-Ghali, and Alex Ilic

Abstract

The Late Carboniferous and Early Permian Al Khlata Formation represent the lower unit of the Haushi Group, related to the third glacial event in the Arabian Plate. Al Khlata Formation, which is deposited in proglacial fluvial and deltaic systems, is an important hydrocarbon target in Oman. The accurate estimation of the amount of hydrocarbon that can be produced from Al Khlata reservoirs is very challenging because the rock properties between wells in the Block 56 vary significantly, and the distribution of the petrophysical properties is poorly understood. This study aims to construct a petrophysical model and predict the vertical and lateral distribution of the petrophysical properties of the Al Khlata sandstones in Block 56 within depositional facies and sequence stratigraphy. This study is based petrophysical analysis using wireline logs and drilling cuttings. However, the study revealed that the Al Khlata Formation consists of two sandstone bodies: sand 2 and sand 1, (from oldest to youngest), characterized by significant heterogeneity in lithology and petrophysical properties. The thickness of the correlatable sandstone bodies within the Al Khlata Formation varies from one well to another because their deposition was highly controlled by the salt movement during the Late Devonian to the Late Carboniferous hiatus. Moreover, this study has revealed that the correlation between wells allowed the prediction of the

influence of the glacial environments on the petrophysical properties of sandstone bodies. There is no consistent trend for the lateral and vertical distribution of porosity and permeability of the lacustrine and deltaic proglacial sandstone bodies, due to the complexity of the glacial environment. The degree of comparison between the two oil-bearing sandstones in terms of petrophysical properties is obvious. For example, sand 2 has good to excellent reservoir quality because of low average shale volume, and good average porosity. Sand 1 is a tight reservoir because it is enriched with shale, has poor porosity, and is very hard to drill because of diamictite. Subsequently, all of that has a significant impact on the hydrocarbon potentiality of each sand. Such modeling will help in drawing more efficient drilling, production, and recovery strategies.

Keywords

Al Khlata Formation • Petrophysical properties • Sandstone • Reservoir • Correlation • Log data • Porosity • Hydrocarbon

1 Introduction

The Late Carboniferous and Early Permian, glaciogenic Al Khlata Formation is well exposed in a series of Haushi-Huqf outcrops in the Huqf high (Fig. 1) (Heward & Penney, 2014) and in north Oman (El-Ghali et al., 2019). The formation outcrop formations can be easily recognized into two main areas in the Huqf region: Wadi Al Khlata and Wadi Shab Nakhad (Martin et al., 2012). Also, the Late Carboniferous and Early Permian, glaciogenic Al Khlata Formation is widely preserved in the subsurface of south and southcentral Oman (Osterloff et al., 2004).

Based on the palynological dating, the subsurface Al Khlata Formation (abbreviated as AK) is divided into three

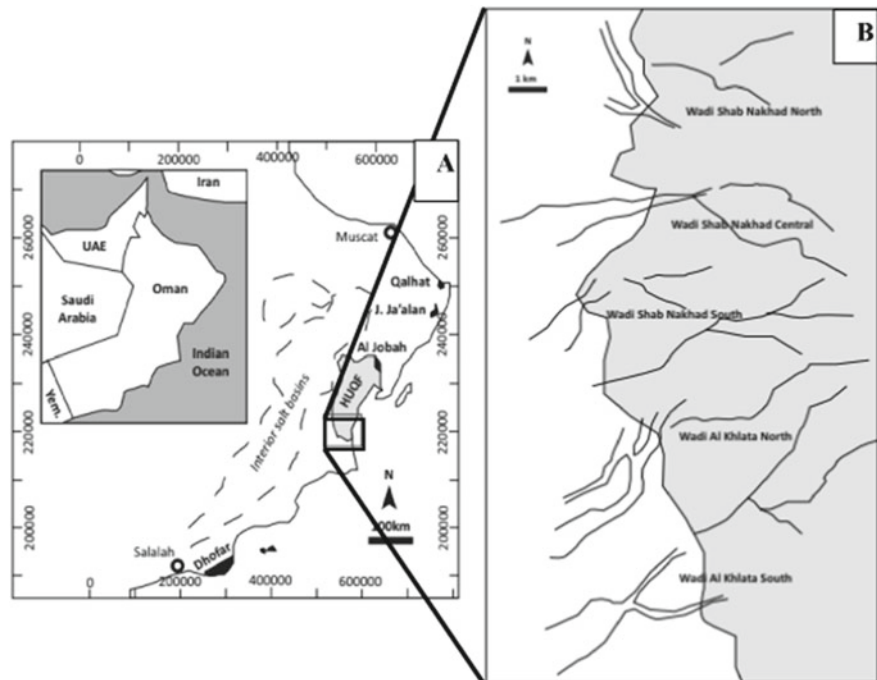
E. K. S. Al-Nadabi (✉) · M. A. K. El-Ghali
ROGII Company, Muscat, Oman
e-mail: S112430@squ.edu.om; s112430@student.squ.edu.om;
elham.alnadabi@rogii.com

M. A. K. El-Ghali
e-mail: melghali@squ.edu.om

M. A. K. El-Ghali
Earth Sciences Research Center, Sultan Qaboos University,
Muscat, Oman

A. Ilic
Tethys Oil Company, Muscat, Oman

Fig. 1 **a** Location map of Huqf area (light grey), the Latest Proterozoic salt basins of interior Oman (dashed outline) and exposed igneous basement (black). **b** Location map illustrates the western south margin of Huqf area and the major drainage systems of wadis Al Khlata and Shab Nakhad (Martin et al., 2012)



main successions (i.e., production units), which are AK P9, AK P5, and AK P1 respectively from oldest to the youngest (Osterloff et al., 2004). According to the Arabian Plate Sequence Stratigraphic framework, the subsurface of the Al Khlata Formation is divided into four depositional sequences, which are Carboniferous 30, Carboniferous-Permian, Permian 6 and Permian 8, each of the sequences presents only a time fraction of the deposition of a single or set of glaciation periods (Penney & Osterloff, 2002). The Late Carboniferous and Early Permian Al Khlata Formation comprise four major facies, which indicates different lithological units: diamictite facies, conglomerates facies, sandstone facies, and fine siltstone and mudstone facies (Levell et al., 1988). There is a complexity in estimating the recoverable reserves of the glaciogenic Al Khlata oil-bearing sandstones in Block 56. This is not only because of the limited occurrence of the Al Khlata reservoirs but several other causes that make the prediction of the amount of oil in place intricate such as diagenesis and lithological heterogeneity. The ultimate aim of this study is to predict the petrophysical properties of Al Khlata sandstones in Block 56 with the help of depositional and stratigraphic frameworks.

2 Materials and Methods

To achieve the main objectives of this study, a subsurface data set of nine drilled wells located in Block 56, southeast Oman targeting the Al Khlata Formation has been used. The

used well data includes wireline logs and drilling cuttings of two wells. Several qualitative and quantitative well-logging analyses were used to carry out a complete petrophysical analysis. Qualitative analyses were done by generating several cross-plots using Techlog Software including neutron/density plots for lithology identification, porosity/lithology cross-plots, and fluid saturation (Pickett plot). A quantitative approach was done for estimating the physical properties of the rocks using wireline logs.

3 Results

Herein, we report the preliminary results of an in-progress study to decipher the petrophysical properties of the Al Khlata Formation. Conventional gamma rays and spectral gamma rays aren't the only ones which that give good correlation results of Al Khlata Formation, but also resistivity logs give a perfect correlation for Al Khlata Formation. The distribution of the data points in the generated cross-plots such as litho-density and neutron-density cross-plots support the heterogeneity of Al Khlata and the abundance of shale lines within Al Khlata sand units. However, there is no typical trend of enhancing or destroying the petrophysical properties through the given wells recognized, and each well has its unique petrophysical properties. Reservoir properties of sand 2 (i.e., porosity, permeability, and net to gross) are generally better than reservoir properties in sand 1.

4 Discussion

Al Khlata Formation characteristics make gamma ray and resistivity logs very solid in correlating the sand units. To illustrate more, the diversity of Al Khlata lithology and mineralogy resulted in a distinctive gamma-ray log response, which makes the correlation of Al Khlata sand units much easier. In addition, the variation in the fluids of Al Khlata sand units makes it easy to correlate with the resistivity log where hydrocarbon zones have a distinct higher resistivity value compared with water zones. Due to the limited distance between the given wells, there was no specific trend recognized in destroying or enhancing the petrophysical properties, especially along the correlation profile. However, sand 2 in all wells has better reservoir quality properties compared with the reservoir quality properties of sand 1 in all wells. Herein, the depositional environment of each sand unit plays an essential role in the quality of sand reservoirs.

5 Conclusion

The overall objective of this study is to predict the petrophysical properties of the Late Carboniferous and Early Permian Al Khlata Formation in Block 56 with the help of depositional environment and stratigraphic framework.

The macroscale heterogeneity in Al Khlata sandstone units in Block 56 is characterized by depositional environments ranging from proglacial fluvial, deltaic, and lacustrine subenvironments. The lithology and mineral compositions, thicknesses, grain sizes, textural, sorting, and roundness of sandstone bodies tend to vary laterally and vertically. This suggests consistently a significant lateral and vertical heterogeneity in Al Khlata sandstone units. Therefore, it is obvious that the local depositional environments of Al

Khata Formation have stronger influence in the controlling the petrophysical properties of Al Khlata sandstone reservoirs. It is obvious that the local depositional environments of Al Khlata Formation have stronger influence in the controlling the petrophysical properties of Al Khlata sandstone reservoirs. Sand 2 is better in terms of petrophysical properties and therefore has better reservoir quality.

Acknowledgements This study is supported by Sultan Qaboos University and Tethys Oil Company in Oman.

References

- El-Ghali, M. A., Al-Hinai, N., Mandhari, K., & Khan, J. (2019). Diagenesis and reservoir quality of glacio-lacustrine sandstones: An example from the upper carboniferous-lower Permian Al Khlata Formation in Wadi Daiqa, Northern Oman. In *Conference of the Arabian Journal of Geosciences* (pp. 151–153). Springer.
- Heward, A. P., & Penney, R. A. (2014). Al Khlata glacial deposits in the Oman Mountains and their implications. *Geological Society, London, Special Publications*, 392(1), 279–301.
- Levell, B. K., Braakman, J. H., & Rutten, K. W. (1988). Oil-bearing sediments of Gondwana glaciation in Oman. *American Association of Petroleum Geologists Bulletin*, 72, 775–796.
- Martin, J. R., Redfern, J., & Williams, B. P. (2012). Evidence for multiple ice centres during the late Palaeozoic ice age in Oman: outcrop sedimentology and provenance of the Late Carboniferous-Early Permian Al Khlata Formation. *Geological Society, London, Special Publications*, 368(1), 229–256.
- Osterloff, P., Penney, R., Aitken, J., Clark, N., & Al-Husseini, M. (2004). Depositional sequences of the Al Khlata Formation, subsurface interior Oman. *Carboniferous, Permian and Early Triassic Arabian Stratigraphy. GeoArabia Special Publication, Gulf PetroLink, Bahrain*, 3, 61–81.
- Penney, R. A., & Osterloff, P. L. (2002). An improved palynostratigraphic zonation for the glaciogenic Al-Khlata Formation: Refinements and applications. In *5th Middle East Geosciences Conference, GEO 2002. GeoArabia, Abstract* (Vol. 7, no. 2, pp. 285–286).



Microfacies and Depositional Analysis of Mauddud Formation in Selected Wells at Three Oilfields—Southern Iraq

Zainab Abdul-Wahhab and Mohanad Al-Jaberi

Abstract

Mauddud Formation (Late Albian–Early Cenomanian) is one of Iraq’s most important carbonate hydrocarbon reservoirs. Fifty-four core samples and one hundred fifty thin sections were made from several wells of Mauddud Formation in Ratawi, south Rumaila, and west Qurna oilfields, southern Iraq. The mineralogy of this formation is limestone and dolomite. The microfacies analysis results in five main microfacies associated with Mauddud Formation, including mudstone, wackestone, packstone, grainstone, and dolostone. In addition to ten submicrofacies including planktonic mudstone, benthic wackestone, bioclastic wackestone, algal wackestone, peloidal wackestone, bioclastic packstone, benthic packstone, benthic grainstone, bioclastic grainstone, and peloidal grainstone. These facies are indicated to be shallow restricted, lagoon, shoal, open marine, and mid-ramp environments. It was deposited on a shallow carbonate platform with a ramp setting. Several diagenetic processes are affected in this formation: micritization, neomorphism, dissolution, cementation, dolomitization, and compaction are the main diagenetic processes. Dolomitization and dissolution processes improved the porosity and permeability with higher reservoir quality while cementation reduced the reservoir quality.

Keywords

Mauddud • Ratawi • Rumaila • West Qurna • Iraq

1 Introduction

Mauddud Formation (Late Albian–Early Cenomanian) is one of the essential formations deposited during the lower Cretaceous. It became important due to its petrophysical properties, which made it an oil reservoir in central and southern Iraq. The Mauddud Formation was initially described by Henson of the Qatar Petroleum Company’s subsurface section. The study area is located within the stable shelf in the Mesopotamian zone within the Zubair subzone (Buday, 1980). The average thickness of the formation in southern Iraq ranges between 110 and 148 m, while in northern Iraq, the thickness is up to 250 m (Jassim & Goff, 2006). The upper Qam-chuqa Formation is equivalent to the Mauddud Formation in Iraq (Aqrawi et al., 2010). Several authors, such as (Sadooni & Alsharhan, 2003) and (Manhi & Alsultani, 2021), have written a lot about the petrophysical properties and lithology of the Mauddud Formation in the three oil fields. The aim of this study is to recognize and define the paleoenvironment and lithological facies of Mauddud Formation, southern Iraq.

2 Methods

Fifty-four core samples were taken from 15 wells separated over three oilfields, as well as more than 150 thin sections were done for this study of the Mauddud Formation in Ratawi, West Qurna 1, and South Rumaila oilfields. These samples are divided into five wells for each oilfield represented by (RT-5, RT-7, RT17, RT14, and RT-23), (WQ-364, WQ-371, WQ-373, WQ-384, WQ-386), and (RU-1, RU-365, RU-383, RU-408, RU-410) (Fig. 1). The petrography of these wells was analyzed using a thin section, which was studied using a binocular microscope in the Department of Geology’s laboratory in the University of Basrah. The microfacies, diagenesis, and sedimentary environments were studied and interpreted using the

Z. Abdul-Wahhab · M. Al-Jaberi (✉)
University of Basrah, Basra, Iraq
e-mail: muhanad.abood@uobasrah.edu.iq

classification of Dunham. Wilson and Flugel were used to identify the depositional environment. Also, an XRD test was used to identify the mineralogy of sample content.

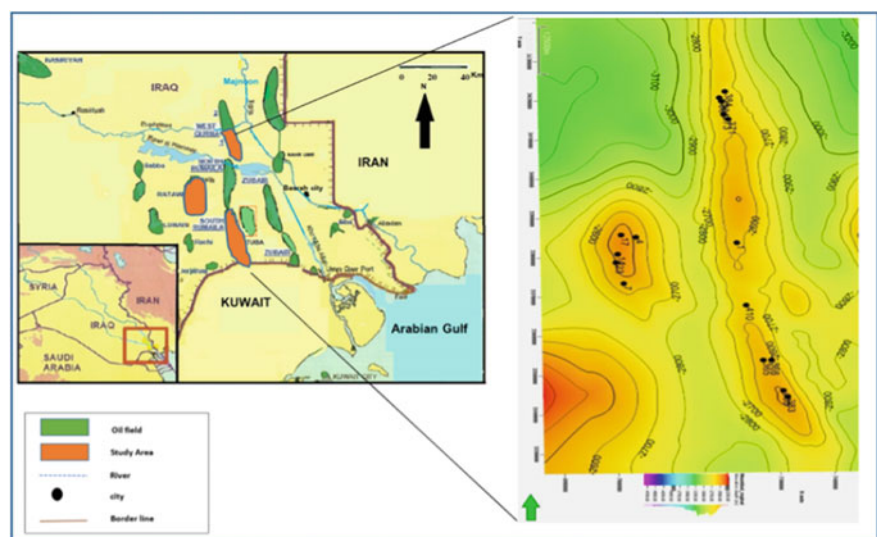
3 Results

3.1 Facies Analysis and Depositional Environments:

A modified version of Dunham's (1962) classification of carbonate rocks is used by Embry and Klaven to describe the facies (1971). The typical facies in the Mauddud formation are as follows:

- A. **Lime Mudstone Microfacies:** Carbonate grains make up less than 10% of mudstone microfacies, and it is equivalent to the (RMF5) (Flugel, 2010), which belongs to the mid-ramp and is further separated into planktonic submicrofacies (Plate 1a)
 - B. **Wackestone Microfacies:** These facies are common in Mauddud Formation. These microfacies are described as a skeletal and non-skeletal micrite matrix. These microfacies are further subdivided into four subfacies.
 1. Benthic wackestone submicrofacies: It is secondary facies, which characterized by the predominance of skeletal granules and represented by the benthic foraminifera such as *miliolid* asp., *orbitolina*, *nezazzata* submerged in a microscopic. It can be noted in (WQ-373 at depth 2636.6 and RT-17 at depth 2527.6) (Plate 2a).
 2. Bioclastic wackestone submicrofacies: These facies may be found as typical facies in the Mauddud Formation (Plate 1b) at the borehole WQ-373 at depth of 2651.6 m. These particular microfacies indicated the presence of a shallow lagoon with circulation (Flugel, 2010).
 3. Algal wackestone submicrofacies: The green dasy-cladales algae were a significant rock-forming fossil in the Mauddud Formation and red algae debris. It is an example of the RMF20 found in the FZ7 band (Hassan et al., 2022) (Plate 1c).
 4. Peloidal wackestone submicrofacies: These submicrofacies correlated with RMF8 and are located in zone FZ-7; the open marine environments microfacies present at depth of 2495.8 m in RT-17 (Plate 1e).
- C. **Packstone Microfacies:** These microfacies characterized grain support microfacies with the little spray matrix (Myzban et al., 2022).. These microfacies are common microfacies in the wells study area as second microfacies. It is can be divided into:
1. Bioclast Packstone submicrofacies: It is similar to (RMF-7) facies within the (FZ-6) range, as it is deposited in the environment of coral reefs and in front of reefs or shallow sea barriers (Plate 1h).
 2. Benthonic packstone submicrofacies: These facies are characterized by their high skeletal granular content represented by the benthic foraminifera (Plate 1f).
- D. **Grainstone Microfacies:** These facies can be considered within the shoal environment and medium to high energy environment; it is including the following:
1. Bioclast grainstone submicrofacies: these facies were found in reef and fore reef facies of FZ 6,7 (Flugel, 2010). (Plate 1g).
 2. Benthonic grainstone submicrofacies: The presence of numerous benthic foraminifera, particularly those belonging to the *orbitolinid* and *miliolids* subfamilies, is one of the requirements for this submicrofacies (Flugel, 2010). These submicrofacies

Fig. 1 Location map of the study area in southern Iraq



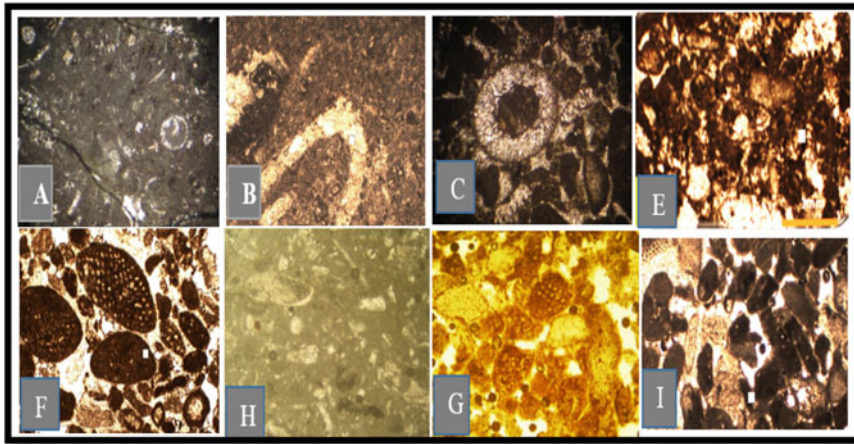


Plate 1 a Planktonic lime mudstone (mid-ramp). b Bioclastic wackestone (shallow open marine). c Algal Wackestone (lagoon). e Peloidal Wackestone (mid-ramp) f Benthic packstone (restricted). h Bioclastic packstone (restricted). g Bioclastic grainstone (shoal) i Peloidal grainstone (shoal)

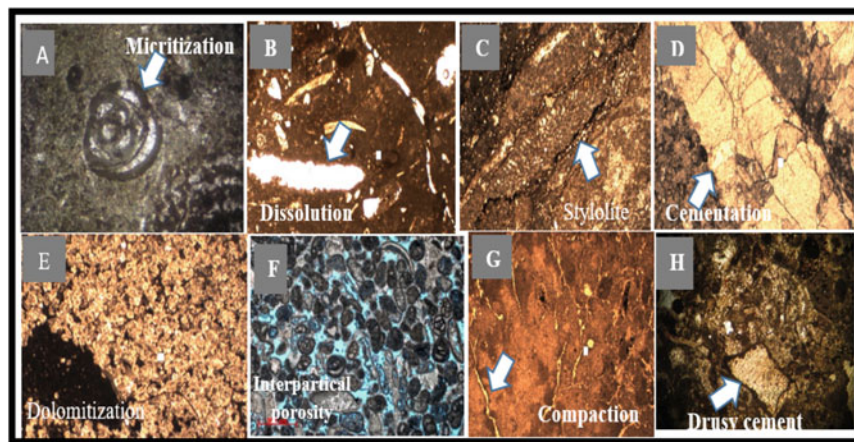


Plate 3 a Wackestone effected by micritization in RT-17; b dissolution in packstone c packstone effected by chemical compaction; d blocky cement in RT-17 at depth 2536.9 m; e Dolostone in RT-17 at depth 2558 m; f Grainstone with interparticulate porosity in WQ-373 in depth 2685 m; g v Lime mudstone microfacies with physical compaction in Rt-23, 2624.90 m; h drusy cement in Ru-1 at depth 2752.8 m

associated with RMF26 and the environment were classified as FZ8 (Plate 2f).

3. Peloidal grainstone submicrofacies: the peloidal resulting from the diagenesis process to which skeletal granules, nuts of biocrumbs, *echinoderms*, and *Echinacea*.

Comparative studies were conducted using RMF16, a model of the shoal and open sea found in FZ6. These facies were found in WQ-373 and RT-17.

E. **Dolostone Microfacies:** These facies contain very-fine faceless rhombic crystals representing the early dolomite stage. In other parts, we notice the dolomite rhombus grow larger to become large and full-faceted (Mahdi et al., 2022), representing the late dolomite stage. These microfacies are represented in wells

throughout the RT-17 at depth of 2543.50–2558 m and at depth of 2565.80 m (Plate 2e).

4 Discussion

Five facies associations were distinguished in the Mauddud Formation. Each represents a distinct depositional environment, including:

Facies association 1: Restricted environment: *miliolids* wackestone and mudstone to wackestone make up most of this relationship. *miliolids*, *textularia*, *nazzazata* (Plate 2a), identical to (RMF 13).

Facies association 2: Lagoon environment skeletal peloids and wackestone characterize this environment, and packstone fabric characterizes this environment's successions. Low fauna assemblages contained benthic foraminifera, including *miliolids*, thin shell bivalves, and rare abundance fragments of rudist and green algae (Schlager, 2005), corresponding to (RMF 17) (Plate 1c).

Facies association 3: Shallow open marine: It is the most common facies association in the Mauddud Formation. Four major microfacies characterize the shallow open marine conditions. They include benthonic foraminiferal bioclastic wackestone to packstone and echinoderm bioclastic wackestone to packstone (Plate 1b). The main diagenetic processes affecting these microfacies are compaction, cementation, and dolomitization (Plate 2g, h). This corresponds to RMF 13, 16, 17, and 18.

Facies association 4: Shoal Environment: The shoal environment is represented by peloidal bioclastic grainstone and fossiliferous peloidal packstone to grainstone (Manhi & Alsultan, 2021). (Plate 1g, i). The main diagenetic changes affecting these associations are dissolution, neomorphism, and cementation (Plate 2d). These associations may reflect sea word skeletal shoals of the mid-ramp. They correspond to RMF 26 and 27.

Facies association 5: Mid-ramp Environment: The bioclastic wackestone and packstone comprise most of the mid-ramp facies association. Rudist packstone and orbitolina wackestone are two other significant microfacies; the primary diagenetic processes in this facies relationship are dolomitization and dissolution, corresponding to (RMF 5) (Plates 1a and 2e).

5 Conclusions

The Mauddud Formation in southern Iraq was deposited in several shallow carbonate platform subenvironments. It was designed using the homoclinal ramp setting. A gradational

carbonate succession is relatively thick within the inner ramp, and lateral facies shifts from supratidal to restricted marine occur gradually to the shoal, shallow open marine to the mid-ramp. Diagenesis' influence on porosity has substantially altered formation and reservoir quality.

References

- Aqrabi, A. A. M., Goff, J. G., Horbury, A. D., & Sadooni, F. N. (2010). *The petroleum geology of Iraq* (p. 424). Scientific Press Ltd.
- Buday, T. (1980). In I. I. Kassab & S. Z. Jassim (Eds.), *The regional geology of Iraq: Stratigraphy and paleogeography* (p. 445). Dar Al-Kutub Publishing House.
- Dunham, R. J. (1962). Classification of carbonate rocks according to depositional texture. *American Association of Petroleum Geologists Memoir, 1*, 108–121.
- Flügel, E. (2010). *Microfacies of carbonate rocks* (p. 984). Springer.
- Jassim, S. Z., & Goff, J. C. (Eds.). (2006). *Geology of Iraq* (p. 341). Dolin, Prague and Moravian Museum, Berno.
- Hassan, K. A., Al-Jaberi, M. H., & Salim, L. N. (2022). Depositional properties of the Middle Miocene Fatha (Lower Fars) Formation. *K-Oilfield Southern Iraq, 55*(2B), 139–152.
- Mahdi, M. M., Ismail M. J., & Mahammad, O. A. M. (2022). The integration of wireline logs and sedimentological data to predict sequence stratigraphic framework in carbonate rocks: An example from Rumaila Formation (Cenomanian), West Qurna Oil Field, Southern Iraq. *Stratigraphy and Geological Correlation, 360–377*.
- Manhi, M. R., & Alsultan, H. A. A. (2021). Stratigraphy and depositional environment of Mauddud Formation in Ratawi Oil well of Southern Iraq. *IOP Conference Series: Earth and Environmental Science, 877*.
- Myzban, A. A., Al-Jaberi, M. H., & Al-Jafar, M. K. (2022). Microfacies analysis and depositional environment of lower Sa'adi formation, Southern Iraq. *Iraqi Geological Journal, 55*(2C), 93–105.
- Sadooni, F., & Alsharhan, A. (2003). *Stratigraphy, microfacies, and petroleum potential of the Mauddud Formation (Albian–Cenomanian) in the Arabian Gulf Basin*.
- Schlager, W. (2005). Carbonate sedimentology and sequence stratigraphy. In *SEPM concepts in sedimentology and paleontology series* (Vol. 8, p. 200). SEPM.



Setting Up an Infinite Slope Stability Analysis on a High-Resolution DEM ($0.21 \times 0.21 \text{ m}^2$) of a Mechanically Terraced Slope in Cyprus

Corrado Camera, Mattia Gentile, Hakan Djuma, Christos Zoumides, Christos Keleshis, Andreani Papageorgiou, Christos Constantinides, Andreas Leonidou, Marina Faka, and Adriana Bruggeman

Abstract

For centuries, the landscape of Mediterranean mountains has been shaped by the construction of terraces often supported by dry-stone walls, to allow farming activities. Nowadays, traditional dry-stone wall terraces are often replaced or combined with mechanically constructed terraces. Compared to dry-stone terraces, these behave differently regarding water retention, soil erosion and slope stability. The aims of this study are (i) to characterize a mechanically terraced slope (0.1 km^2) partially protected by dry-stone walls and (ii) to set up a high-resolution stability analysis to verify its capabilities in predicting instabilities. The study site is located in the Troodos Mountains (Cyprus). Field observations were made between October 2021 and April 2022. Measurements of depth, hydraulic conductivity and bulk density, as well as the collection of samples for texture analyses, were performed for the physical characterization of soils. The study site was visited after several storms to map areas affected by instabilities. Rainfall was measured by a local meteorological station. A photogrammetric survey was made with a GoPro9 camera mounted on an unmanned aerial vehicle developed by the Unmanned System Research Laboratory of The Cyprus Institute both in firmware and software. The collected data were used as input into FSLAM, an open-source model that couples a

simplified hydrologic model with an infinite slope stability analysis. The soil was a loamy sand, with a depth ranging between 0.30 and 0.80 m, an average bulk density of 1.70 g/cm^3 and a hydraulic conductivity of $2.05 \times 10^{-3} \text{ m/s}$. From the UAV flights, a DEM with a horizontal resolution of 0.035 m was produced. However, for modelling purposes the DEM was resampled at 0.21 m, to reduce calculation times and avoid high depth-to-length ratios at the single cell (infinite slope assumption). Preliminary results from multiple runs showed that the model responds reasonably well to flow accumulation and variations in soil depth. The model predicts higher instabilities for wetter deep soils. However, at this resolution it was not able to identify specific locations of failure. To improve the model output, FSLAM could be integrated with a routine able to process variable soil depths (now constant within soil units) and to route surface runoff.

Keywords

Mountain terraces • Shallow landslides • Soil loss • FSLAM • UAV • Eastern Mediterranean

C. Camera (✉) · M. Gentile
Dipartimento di Scienze Della terra “A. Desio”, Università Degli Studi di Milano, 20133 Milano, Italy
e-mail: corrado.camera@unimi.it

H. Djuma · C. Zoumides · A. Bruggeman
Energy, Environment and Water Research Center, The Cyprus Institute, 2121 Aglantzia, Cyprus

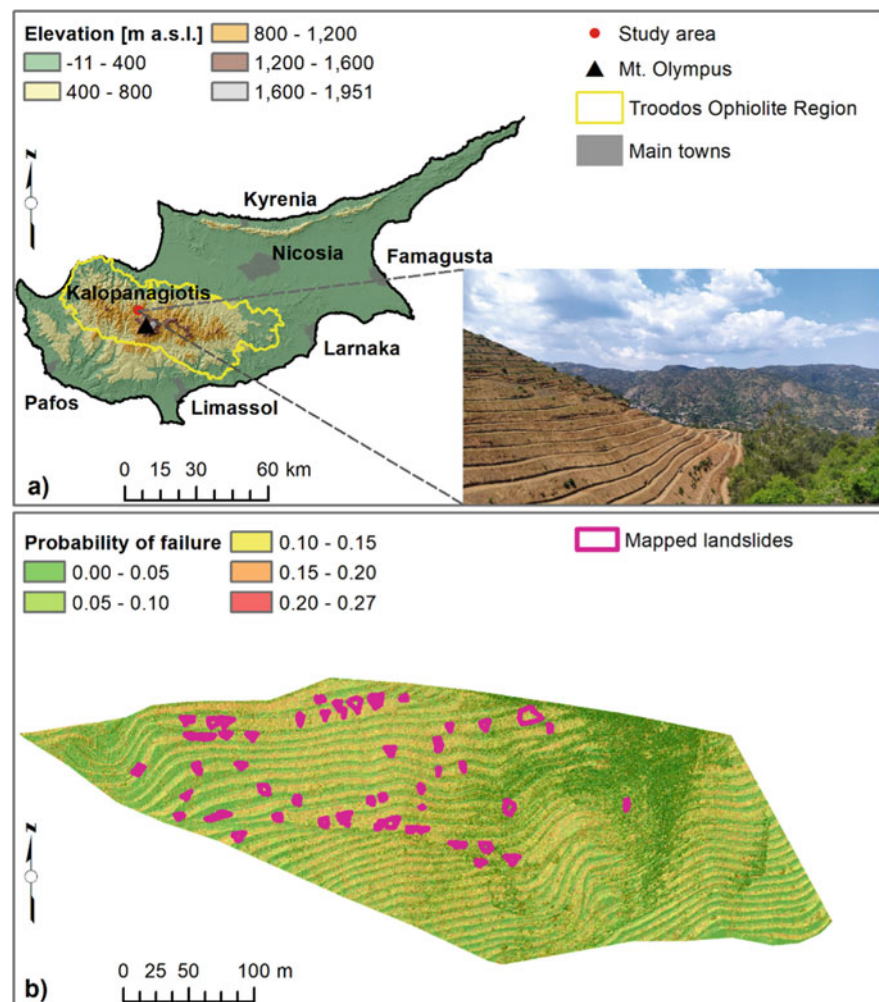
C. Keleshis · A. Papageorgiou · C. Constantinides · A. Leonidou
Climate and Atmosphere Research Center, The Cyprus Institute, 2121 Aglantzia, Cyprus

M. Faka
Science and Technology in Archaeology and Culture Research Center, The Cyprus Institute, 2121 Aglantzia, Cyprus

1 Introduction

In Cyprus, the number of small, family-based wineries has grown in the last 30 years, causing a positive impact on rural development in the mountain areas (Zoumides et al., 2022). Given the steep slopes, for an effective vine growth most wineries rely on terraces, which are either existing or renovated dry-stone terraces or sometimes built anew. For this last option, terraces are usually mechanically constructed. Compared to traditional dry-stone terraces these new structures behave differently regarding water retention, soil erosion and slope stability. While traditional dry-stone terraces have been widely studied for stability (Camera et al., 2015; Preti et al.,

Fig. 1 **a** Location of the study area with an image taken in May 2022 (Photo by C. Camera); **b** probability of failure for a simulation with soil depth equal to 0.8 m and wall height equal to 0.4 m, forced with precipitation inputs as occurred at the end of December 2021, compared with failures mapped on the field in January 2022



2018a), erosion processes (Camera et al., 2018; Nunes et al., 2018) and water circulation (Nunes et al., 2018; Preti et al., 2018b), few studies are available on mechanized terraced. Mechanization is increasing the management challenge for soil conservation and sustainable terrace management (Pijl et al., 2019). The aims of this study were (i) to characterize a mechanically terraced slope (0.1 km^2) partially protected by dry-stone walls located in the Troodos Mountains of Cyprus and (ii) to set up a high-resolution stability analysis to verify its capabilities in predicting instabilities.

2 Study Area

The central part of the Mediterranean island of Cyprus (9251 km^2) is characterized by the Troodos Mountains, an ophiolitic complex that extends for 2332 km^2 , with a mean slope gradient of 31% and elevations up to 1952 m a.s.l. (Mount Olympus, Fig. 1a). The region experiences a semi-arid climate with dry summers and wet winters and a mean annual precipitation that varies with elevation from around

600 mm to around 1000 mm (Camera et al., 2014b). Also, the Troodos region is Cyprus primary production area of permanent crops such as vineyards, other deciduous fruit and nut trees, which are typically cultivated on terraces. Specifically, this study focused on a mechanically terraced slope (0.1 km^2 , mean altitude 1005 m a.s.l., mean gradient 43°), partially protected by dry-stone walls and cultivated with vineyards, located near the village of Kalopanayiotis, in the north-western ranges of the Troodos Mountains (Fig. 1a).

3 Methods

To evaluate the stability of the study area, the open-source “Fast Shallow Landslide Assessment Model” (FSLAM) was selected (Medina et al., 2021). FSLAM consists of a simplified hydrologic model coupled with a routine to calculate the probability of failure of an area through the infinite slope approach. As input the model requires soil properties (cohesion, friction angle, bulk density, depth), vegetation-related data (root cohesion reinforcement), information on

Table 1 Ranges of shear strength and other model parameter values are assigned to the different materials characterizing the study area; c is cohesion; φ is friction angle; γ_d is the dry bulk density; n is porosity; H is soil depth

Soil unit	c (kPa)	φ (deg)	γ_d (g/cm ³)	n (-)	H (m)
Loamy sand	0–15	24–36	1.7	0.36	0.2–0.8
Dry-stone wall	15–50	45–55	2.0–2.4	0.25	0.2–0.4

the combination of soil and land cover (curve number, CN), a digital elevation model (DEM), and antecedent and event rainfall data. The hydrologic routine transforms the input rainfall in a water table height (and thereby, soil saturation degree, based on known soil depth). Following, the probability of failure is stochastically calculated from ranges of shear strength parameters (cohesion and friction angle).

To develop a high-resolution DEM that includes dry-stone walls, a photogrammetric survey was performed with a GoPro9 camera mounted on an unmanned aerial vehicle (UAV). Both the firmware and software to operate the UAV were developed by the Unmanned System Research Laboratory of The Cyprus Institute. The acquired images were georeferenced based on target points, the location of which was derived through differential GPS.

To parametrize the model, field observations and measurements were made between October 2021 and April 2022. Soil depth was measured by driving a steel rod into the ground. Hydraulic conductivity was measured through Mini-Disk Infiltrometer tests. Bulk density was estimated through the excavation method (Grossman & Reinsch, 2002). Samples for texture analyses were collected, and shear strength parameters were estimated from literature based on the resulting granulometric curves (e.g. Carter & Bentley, 2016). The granulometric curve was derived based on sieving and sedimentation analyses conducted according to ASTM standards (ASTM, 2017; ASTM D1140-00, 2017) and classified following the FAO guidelines (Jahn et al., 2006). Dry-stone walls mechanical properties were taken and slightly revised from Camera et al., (2014a). As rainfall input, several combinations of antecedent rainfall (10-day average intensity [mm/day]) and event rainfall (event total [mm]) were extracted from the time series of a local meteorological station. Vegetation-related parameters were assigned according to vegetation variations observed in the field and from orthophotos. For model output verification, the study site was visited after several storms to map areas affected by instabilities.

4 Results

From the field and laboratory characterization, the soil was classified as a loamy sand, with a depth ranging between 0.20 and 0.80 m, an average bulk density of 1.70 g/cm³ and

a hydraulic conductivity of 2.05×10^{-3} m/s. The derived shear strength parameters, assigned to the model, are reported in Table 1. The UAV and GPS campaign took one day. From the UAV flights, a DEM with a horizontal resolution of 0.035 m was produced. However, for modelling purposes the DEM was resampled at 0.21 m to reduce calculation times and avoid high depth-to-length ratios at the single cell (infinite slope assumption). Two sub-areas were recognized in terms of vegetation, a drier one characterized by vineyards in the higher part of the slope (CN = 77) and a wetter one characterized by natural vegetation in the lower part of the slope (CN = 66). For both sub-areas, root cohesion was not parametrized and set to zero.

The model predicts higher instabilities for wetter deep soils. Antecedent rainfall appeared to have a great weight on determining instabilities, playing a crucial role in bringing soil close to saturation. For example, for the event shown in Fig. 1b, the average probability of failure over the study area is 6.7%, 7.0% and 7.6% for dry, post-antecedent-rainfall and post-event-rainfall conditions, respectively. In dry conditions, reducing soil depth from 0.8 to 0.4 m decreased the average probability of failure over the study area to 3.4%. In general, the model recognized portions of the slope most prone to failure (high slope, high flow accumulation area mainly located in the lower part of the study area); however, at this resolution, it was not able to identify specific locations of failure (Fig. 1b).

5 Discussion

For setting up a stability analysis on terraced slopes targeting the space–time prediction of failures, the implemented model has several limitations that need to be addressed. First, the infinite slope approach does not allow to evaluate the stabilizing effect of dry-stone walls on the upslope cells. To account for this effect, an approach based on the global limit equilibrium would be more appropriate (Camera et al., 2015). Regarding water, the hydrologic routine of FSLAM considers lateral flow for the water infiltrated as antecedent rainfall but only vertical flow for the water infiltrated as event rainfall. Also, it does not consider surface runoff and the possibility for water to re-infiltrate in lower portions of the terraced slope. These processes should be investigated as well for precise failure prediction assessments. Therefore,

the modelling performed with FSLAM can serve as a useful preliminary attempt to investigate stability issues on a mechanically terraced slope with dry-stone walls, returning an output that can be intended as a susceptibility map.

6 Conclusions

Combining literature data and field measurements to parametrize the FSLAM model, it was possible to generally identify areas that are most susceptible to instabilities on a mechanically established terraced slope that is partially protected by dry-stone walls. Future work will focus on developing and applying coupled hydrologic-stability models, explicitly considering surface runoff, re-infiltration and lateral flow processes, with a stability analysis based on the global limit equilibrium, to predict the space–time occurrence of failures in these complex environments.

Acknowledgements We would like to thank Mr. Viktor Finopoulos, Oenologist at Lampadistis Winery, for sharing knowledge and information.

References

- ASTM D1140-00. (2017). *Standard test methods for amount of material in soils finer than the No. 200 (75-um) Sieve*.
- ASTM D422-63. (2017). *Standard test method for particle-size analysis of soils*.
- Camera, C., Apuani, T., & Masetti, M. (2014a). Mechanisms of failure on terraced slopes: The Valtellina case (northern Italy). *Landslides*, *11*, 43–54.
- Camera, C., Apuani, T., & Masetti, M. (2015). Modeling the stability of terraced slopes: An approach from Valtellina (Northern Italy). *Environment and Earth Science*, *74*, 855–868.
- Camera, C., Bruggeman, A., Hadjinicolaou, P., Pashiardis, P., & Lange, M. A. (2014b). Evaluation of interpolation techniques for the creation of gridded daily precipitation ($1 \times 1 \text{ km}^2$); Cyprus, 1980–2010. *Journal of Geophysical Research: Atmospheres*, *119*, 693–712.
- Camera, C., Djuma, H., Bruggeman, A., Zoumides, C., Eliades, M., Charalambous, K., Abate, D., & Faka, M. (2018). Quantifying the effectiveness of mountain terraces on soil erosion protection with sediment traps and dry-stone wall laser scans. *CATENA*, *171*, 251–264.
- Carter, M., & Bentley, S. P. (2016). *Soils properties and their correlation* (2nd ed.). Wiley.
- Grossman, R. B., & Reinsch, T. G. (2002). Bulk density and linear extensibility. In J. H. Dane & G. C. Topp (Eds.), *Methods of soil analysis, part 4: Physical methods*. Soil Science Society of America Journal Book Series (Vol. 5, pp. 201–228). ASA and SSSA.
- Jahn, R., Blume, H. P., Asio, V. B., Spaargaren, O., & Schad, P. (2006). *Guidelines for soil description* (4th ed.). Land and Water Development Division.
- Medina, V., Hürlimann, M., Guo, Z., Lloret, A., & Vaunat, J. (2021). Fast physically-based model for rainfall-induced landslide susceptibility assessment at regional scale. *CATENA*, *201*, 105213.
- Nunes, J. P., Bernard-Jannin, L., Rodríguez Blanco, M. L., Santos, J. M., Coelho, C. O. A., & Keizer, J. J. (2018). Hydrological and erosion processes in terraced fields: Observations from a humid Mediterranean region in northern Portugal. *Land Degradation & Development*, *29*, 596–606.
- Pijl, A., Barneveld, P., Mauri, L., Borsato, E., Grigolato, S., & Tarolli, P. (2019). Impact of mechanization on soil loss in terraced vineyard landscapes. *Cuadernos De Investigación Geográfica*, *45*, 287–308.
- Preti, F., Errico, A., Caruso, M., Dani, A., & Guastini, E. (2018a). Dry-stone wall terrace monitoring and modelling. *Land Degradation and Development*, *29*, 1806–1818.
- Preti, F., Guastini, E., Penna, D., Dani, A., Cassiani, G., Boaga, J., Deiana, R., Romano, N., Nasta, P., Palladino, M., Errico, A., Giambastiani, Y., Trucchi, P., & Tarolli, P. (2018b). Conceptualization of water flow pathways in agricultural terraced landscapes. *Land Degradation and Development*, *29*, 651–662.
- Zoumides, C., Bruggeman, A., Giannakis, E., & Kyriakou, N. (2022). A future for mountain terraces: Experiences from mediterranean wineries. *Mountain Research and Development*, *42*, R35–R49.